

JAERI-Review

94-009



REACTOR ENGINEERING DEPARTMENT  
ANNUAL REPORT

[April 1, 1993 – March 31, 1994]

November 1994

Department of Reactor Engineering

日本原子力研究所  
Japan Atomic Energy Research Institute

本レポートは、日本原子力研究所が不定期に公開している研究報告書です。

入手の問合わせは、日本原子力研究所技術情報部情報資料課（〒319-11 茨城県那珂郡東海村）あて、お申し込みください。なお、このほかに財団法人原子力弘済会資料センター（〒319-11 茨城県那珂郡東海村日本原子力研究所内）で複写による実費領布をおこなっております。

This reports are issued irregularly.

Inquiries about availability of the reports should be addressed to Information Division Department of Technical Information, Japan Atomic Energy Research Institute, Tokaimura, Naka gun, Ibaraki-ken 319-11, Japan.

© Japan Atomic Energy Research Institute, 1994

編集兼発行 日本原子力研究所  
印刷 ニッセイエプロ株式会社

## **Reactor Engineering Department Annual Report**

(April 1, 1993 - March 31, 1994)

Department of Reactor Engineering

Tokai Research Establishment  
Japan Atomic Energy Research Institute  
Tokai-mura, Naka-gun, Ibaraki-ken

(Received October 21, 1994)

This report summarizes the research and development activities in the Department of Reactor Engineering during the fiscal year of 1993 (April 1, 1993 - March 31, 1994).

The major Department's programs promoted in the year are the design activities of advanced reactor system and development of a high energy proton linear accelerator for the engineering applications including TRU incineration.

Other major tasks of the Department are various basic researches on the nuclear data and group constants, the developments of theoretical methods and codes, the reactor physics experiments and their analyses, fusion neutronics, radiation shielding, reactor instrumentation, reactor control/diagnosis, thermohydraulics and technology developments related to the reactor engineering facilities, the accelerator facilities and the thermal-hydraulic facilities.

The cooperative works to JAERI's major projects such as the high temperature gas cooled reactor or the fusion reactor and to PNC's fast reactor project were also progressed.

The activities of the research committees organized by the Department are also summarized in this report.

**Keywords:** Reactor Engineering Department Annual Report, Advanced Reactor System, Nuclear Data and Atomic & Molecular Data, Reactor Physics, Thermohydraulics, Fusion Neutronics, Radiation Shielding, Reactor Instrumentation, Reactor Control/Diagnosis, Passive Safety Reactor, Transmutation System, Accelerator Engineering, Free Electron Laser

---

Board of Editors for Annual Report: Murao Y.(Chief Editor), Iijima S.(Associated Chief Editor), Kutsukake C., Shibata K., Fujimura T., Yamane T., Yagi H., Suzudo T., Sakamoto Y., Ohnuki A., Oyama Y., Araya F., Nishida T., Kusano J. and Ohkubo M.

Editorial Assistant : Koyanagi D.

平成5年度原子炉工学部年報

日本原子力研究所東海研究所  
原子炉工学部

(1994年10月21日受理)

本報告は、平成5年度における原子炉工学部の研究活動状況を取りまとめたものである。

当該年度に原子炉工学部において推進された主要な研究活動は、新型炉の概念設計、及び TRU 消滅処理等への工学的応用を図るための大強度陽子線形加速器の開発である。

原子炉工学部では、基礎基盤研究として、核データと群定数、炉理論並びにコード開発、炉物理実験並びに解析、核融合中性子工学、放射線遮蔽、原子炉計測・計装、原子炉制御・診断、伝熱流動、及び炉工学施設・加速器施設並びに伝熱流動実験施設等の技術開発を行っている。

また、高温ガス炉及び核融合等の原研全体の研究活動や、動燃事業団との高速炉の共同研究も推進している。

本報告では、原子炉工学部が組織する各種研究委員会の活動報告もとりまとめられている。

---

東海研究所：〒319-11 茨城県那珂郡東海村白方字白根2-4

原子炉工学部年報編集委員会：

村尾良夫（委員長）、飯島 進（副委員長）、沓掛忠三、柴田恵一、藤村統一郎、山根 剛、八木秀之、  
鈴木知明、坂本幸夫、大貫 晃、大山幸夫、新谷文将、西田雄彦、草野譲一、大久保牧夫、  
小柳大作（事務局）



## Contents

Preface .....	1
1. Nuclear Data, and Atomic and Molecular Data .....	7
1.1 Second Revision of JENDL-3 (JENDL-3.2) .....	8
1.2 Evaluation of Neutron Nuclear Data of $^{237}\text{U}$ , $^{236}\text{Np}$ and $^{238}\text{Np}$ .....	11
1.3 Evaluation of Neutron Nuclear Data of $^{244}\text{Pu}$ and $^{237}\text{Pu}$ .....	13
1.4 Evaluation of Covariance Matrices for Several Nuclear Data .....	16
1.5 Update of Gamma-ray Production Data for JENDL-3.2 .....	18
1.6 Evaluation of Neutron Cross Sections of $^1\text{H}$ and $^{12}\text{C}$ in the Intermediate-energy Region .....	20
1.7 Applicability of the Quantum Molecular Dynamics to Nucleon-nucleus Collisions .....	23
1.8 Evaluation of Nuclear Data for Neutron- and Proton-induced Reactions on $^{27}\text{Al}$ ..	25
1.9 Fermi-gas Model Parametrization of Nuclear Level Density .....	28
1.10 Evaluation and Compilation of Nuclear Structure and Decay Data for $A=123$ , $125$ and $126$ .....	31
1.11 Measurements of Activation Cross Sections at 18-30 MeV by Using the $^7\text{Li}(p,n)$ Quasi-monoenergetic Neutron Source at JAERI-TANDEM .....	34
1.12 New Measurements of Activation Cross Section for the $^{63}\text{Cu}(n,2n)^{62}\text{Cu}$ and $^{65}\text{Cu}(n,2n)^{64}\text{Cu}$ Reactions at Energy Range of 13.3 ~ 14.9 MeV .....	37
1.13 Measurements of Activation Cross Sections for the $^{187}\text{Re}(n,2n)^{186\text{m}}\text{Re}$ and $^{193}\text{Ir}(n,2n)^{192\text{m2}}\text{Ir}$ Reactions at 14 MeV Energy Region .....	40
1.14 Activation Cross Section Measurement of Reactions Producing Short-lived Nuclei at Neutron Energy between 13.4 MeV and 14.9 MeV .....	43
1.15 Benchmark Tests of JENDL-3.2 for Thermal and Fast Reactors .....	46
1.16 Mean-field for the Vibron Model: Dipole Moment Function of Diatomic Molecules .....	49
1.17 Spectral Data and Grottrian Diagrams for Highly Ionized Manganese, Mn VII - Mn XXV .....	51
1.18 Analytic Cross Sections for Collisions of $\text{H}$ , $\text{H}_2$ , $\text{He}$ and $\text{Li}$ Atoms and Ions with Atoms and Molecules. II .....	53
1.19 Radiative Electron Capture in Relativistic Atomic Collisions .....	55
2. Theoretical Method and Code Development .....	58
2.1 Bremsstrahlung Photon Emission Model in the MVP Vectorized Continuous Energy Monte Carlo Code .....	59
2.2 Parallel Computation by Monte Carlo Codes GMVP and MVP .....	61
2.3 Improvement of SRAC Code .....	64

2.4	Effect of (n,2n) Cross Section on Minor Actinide Production in the SRAC System .....	67
2.5	Development of Intelligent Reactor Design System IRDS (5) .....	70
2.6	Development of Nuclear Design Code System for Advanced Reactors .....	73
2.7	Development of New Analytical Nodal Method for Multi-group Neutron Diffusion Equation .....	76
3.	Reactor Physics Experiment and Analysis .....	79
3.1	Mockup Experiments of MOX-fueled LMFBR in FCA Assembly X VII-1 .....	80
3.2	Doppler Effect Experiment in MOX-LMFBR Mockup Core FCA Assembly X VII-1 .....	83
3.3	Analysis of High Temperature Doppler Effect Measured at FCA(Evaluation of Flux Perturbation Effect Caused by Structural Material in Experimental Device)...	86
3.4	Measurement and Analysis of $B_4C$ and Pu Sample Worth Distribution in FCA Assembly X VII-1 .....	89
3.5	Benchmark Experiment of Metallic-fueled LMFBR at FCA -Reaction Rate Ratio .....	92
3.6	Evaluation of Calculation Accuracy for Sodium Void Worth Based on FCA Measurement .....	94
3.7	Measurement of Control Rod Reactivity Worth in Axially Heterogeneous Fuel Core by PNS Method .....	97
3.8	Analysis of U-235 fueled Lead Cooled Fast Reactor Critical Experiments .....	100
4.	Advanced Reactor System Design Studies .....	103
4.1	Concept of JAERI Passive Safety Reactor JPSR .....	104
4.2	Nuclear Design Study for JPSR .....	107
4.3	Transient Thermal-hydraulic Analyses for Design of JPSR .....	110
4.4	Preliminary Design of Passive Residual Heat Removal and Containment Cooling System for JPSR .....	113
4.5	Outline of Emergency Coolant Injection Systems and Preliminary Test for Core Makeup Tank for JPSR .....	116
4.6	Analysis for Making Distributions of Temperature and Velocity in Downcomer Uniform for JPSR Design .....	119
4.7	Concept of Passive Safe Reactor SPWR .....	122
4.8	Seismicity and Economy for Inherent Safety Lead-cooled Fast Reactor .....	125
4.9	Burnup and Reactivity Coefficient Calculation of PWR Core Loaded with Weapons Pu Once-through Burning Fuel of $PuO_2-ZrO_2(Y,Gd)-Al_2O_3$ Type .....	128
4.10	An HTGR-MHD Combination for High Efficiency Power Generation .....	131
4.11	A Liquid Metal Cooled Pebble-bed Reactor for a Moon Base .....	134
5.	Fusion Neutronics .....	137
5.1	Completion of the JAERI/USDOE Collaborative Program on Fusion Blanket Neutronics	
	— Blanket Integral Experiment — .....	138

8.2	Modeling of Nonlinear Power Oscillation in NSRR .....	207
8.3	Real-time Nuclear Power Plant Monitoring with Neural Network .....	210
8.4	Noise Analysis for Plant Dynamics Identification of Nuclear Ship Mutsu ( II ) ...	212
8.5	Data Synthesis for 1993 Benchmark Test on Detection of Sodium/Water Reaction .....	215
8.6	Compensation of Ultrasonic Signal Distortion with Various Deconvolution Methods .....	217
8.7	One Consideration for a Class of Redundant Manipulator .....	220
9.	Heat Transfer and Fluid Flow .....	221
9.1	Large Scale Reflood Test Program .....	222
9.2	Development of REFLA/TRAC Code for Accident Analyses of Light Water Reactor — Assessment of Predictive Capability for Large Break LOCA of PWR — .....	225
9.3	Development of REFLA/TRAC Code for Accident Analyses of Light Water Reactor — Analysis of Large Break LOCA in a 4-loop PWR — .....	228
9.4	Assessment of Models in COBRA-TF Code for Turbulent Mixing in Single-phase Flow .....	231
9.5	Analysis of Density Wave Instability in a Boiling Flow Using a Characteristic Method .....	234
9.6	Analysis of Cooling Limit of Rotating Target for DT Neutron Source at FNS .....	237
9.7	Evaluation of Falling Water Mass Flux under Countercurrent Flow Limitation in Vertical Circular Tubes .....	240
9.8	Analytical Study on Critical Heat Flux under Countercurrent Flow Limitation in Vertical Channels .....	243
10.	Transmutation System and Partitioning-transmutation Fuel Cycle .....	246
10.1	Conceptual Design Study on Minor Actinide Molten Salt Transmutation System Driven by an Accelerator .....	247
10.2	Conceptual Design of Accelerator-based Liquid TRU-alloy Target and Molten-salt Blanket Transmutation System .....	250
10.3	Minor Actinide Burner Reactor and Influence of Transmutation on Fuel Cycle Facilities .....	253
10.4	Overall Assessment of Partitioning Process ( I ): Status of Partitioning Technology .....	256
10.5	Benchmark Calculations for the Cascade Codes NMTC/JAERI and NUCLEUS .....	259
10.6	Investigation of Nuclide Production Cross Sections for the Analysis of Integral Spallation Experiment .....	262
10.7	Measurements of Neutron-production Double-differential Cross Sections for Incident Protons of 0.8, 1.5 and 3.0 GeV .....	265
10.8	Measurements of the Absolute Detection Efficiency of NE-213 Scintillator for 20-100 MeV Neutrons .....	268

5.2	Completion of JAERI/USDOE Collaborative Program on Fusion Neutronics — Induced Radioactivity and Nuclear Heating Experiments —	141
5.3	Measurement of Low Energy Neutron Spectrum in Iron Assembly for Verification of Evaluated Nuclear Data	144
5.4	Verification of Secondary Gamma-ray Data in JENDL-3 through Analysis of Benchmark Experiments at FNS and OKTAVIAN	147
5.5	Integral Test of Kerma Data for SS304 Stainless Steel in the D-T Fusion Neutron Environment	150
5.6	Experiment and Analysis of Induced Radioactivity Characteristics in a Large SS-316 Stainless Steel Shielding Materials Bombarded with 14 MeV Neutrons	153
5.7	Performance Test of Fiber Scintillation Detectors for Fusion Application	156
6.	Radiation Shielding	159
6.1	Measurement and Analyses on Neutron Transmitted through Iron and Concrete Shields in Intermediate Energy Region	160
6.2	Attenuation Data of Point Isotropic Neutron Sources up to 400 MeV in Water, Ordinary Concrete and Iron	163
6.3	Stopping Power of Charged Particles from 10 eV/amu to 10 GeV/amu	166
6.4	Evaluation of Fluence to Dose Equivalent Conversion Factors for High Energy Radiations ( II )	169
6.5	Survey Calculation for Bulk Shielding Experiments (2) — Mock-up Experiment —	172
6.6	Bulk Shielding Experiments on a Large SS316 Assembly with Voids	175
7.	Reactor and Nuclear Instrumentation	178
7.1	Analysis of Background Count Rates in a Neutron Detection System	179
7.2	Simultaneous Estimation of Spontaneous Fission Rate and ( $\alpha$ , n ) Neutron Emission Rate	182
7.3	A New Method of Nondestructive Measurement for Assessment of Material Degradation of Aged Reactor Pressure Vessels	184
7.4	High Temperature Tests of Nicrosil-nisil Thermocouples	187
7.5	Measurement of Scintillation Emission Spectra	190
7.6	Absorption Characteristics of an Activated Charcoal Filter for Noble-gas FPs Having Short Half-life	193
7.7	A Selective Detection Method of Magnetic-flux Sources Using a System of Superconductors, Ferromagnetic Substance and a Magnetic Sensor	196
7.8	Inverse Estimation of Current Distribution from Magnetic Field Using a Combination Method of Neural-network and Genetic Algorithm	199
7.9	Study of Position Sensitive Fission Counter with Transmission Delay Line Structure	201
8.	Reactor Control, Diagnosis and Robotics	203
8.1	Filtering of Net Reactivity Based on $H_{\infty}$ Estimation Theory	204

11. Development of Proton Linear Accelerator, FEL and Superconducting Booster .....	271
11.1 A Progress in the High Intensity Proton Linear Accelerator Development .....	272
11.2 First Beam Test of the JAERI Radio Frequency Quadrupole (RFQ) .....	275
11.3 Development of a Drift Tube Linac for the Basic Technology Accelerator — Fabrication and RF Characteristics — .....	278
11.4 Performance of a High Brightness Hydrogen Ion Source for the BTA .....	281
11.5 Design of 100kW Proton Beam Stopper for BTA at JAERI .....	284
11.6 Status of the JAERI Free Electron Laser Facility .....	287
11.7 Status of Superconducting Booster .....	290
12. Facility Operation and Technique Development .....	293
12.1 Operation Report of FCA .....	294
12.2 Operation Report of VHTRC .....	295
12.3 Operation Report of FNS .....	296
12.4 Operation Report of Heat Transfer and Fluid Flow Test Facilities .....	297
12.5 Operation Report of Tandem Accelerator and Electron Linac .....	298
13. Activities of Research Committees .....	300
13.1 Activity of Japanese Nuclear Data Committee .....	301
13.2 Activities of the Research Committee on Reactor Physics .....	304
13.3 Activity of Atomic and Molecular Data Committee .....	307
13.4 Activities of the Research Committee on Advanced Reactors .....	308
13.5 Activities of the Research Committee on Partitioning and Transmutation .....	311
Publication List .....	312
Appendix I Department of Reactor Engineering Organization Chart .....	327
Appendix II Abbreviations .....	329

## Preface

The annual research activities of the Department of Reactor Engineering, Japan Atomic Energy Research Institute, during the fiscal year 1993 (April 1993 – March 1994) are presented in this report. The research activities of the Department had covered the broad area including fission reactor physics, fusion reactor neutronics, shielding, reactor instrumentation and control, thermohydraulics, nuclear energy systems analysis and intense accelerator technology.

The total number of people working in the department during the year had been 177. The Department was funded from JAERI expenditures amounted to about 2305 million yen for the fiscal year 1993, excluding nuclear fuel costs and personnel expenses. About 738 million yen had been also provided by research contracts with external organizations; Science and Technology Agency (STA) for non-destructive measurement technology of transuranic elements (TRU) and for large scale reflood test program and thermal hydraulic demonstration test for HCLWR, Power Reactor and Nuclear Fuel Development Corporation (PNC) for fast reactor physics and Mitsubishi Atomic Power Industries, Inc. (MAPI) for development of PWR reactor noise diagnostic system.

The research activities were conducted in the following laboratories and supporting divisions:

### Nuclear Data Center

This center has two research themes; nuclear data and atomic & molecular data. As to nuclear data, the research activities consist of nuclear data evaluation, high energy nuclear data and nuclear data measurements. As to atomic & molecular data, main efforts are devoted to compilation and evaluation of atomic and molecular collision data and of atomic spectrum data.

This center has a function of the National Center which disseminates the nuclear and atomic & molecular data to Japanese users, contacts the foreign and international centers and coordinates the international collaboration. This center also serves as a secretariat of Japanese Nuclear Data Committee and of Atomic and Molecular Data Committee.

### Reactor System Laboratory

This laboratory has two major research themes. One is feasibility study and preconceptional design of new type reactors. Effort is concentrated in design study of innovative FBRs of safety and economic features. Recently once-through type plutonium burner LWRs became one of the subjects. Another item is development and modifications of software (data/code) in reactor physics to serve for reactor design and analysis. It aims at high accuracy as achieved by Monte Carlo method and high speed as done by nodal method. Effort is now concentrated to develop comprehensive code system such as reactor core design including thermal hydraulics, core management and time depending problems.

### Fast Reactor Physics Laboratory

This laboratory has three research themes; study on reactor physics of advanced fuel fast reactors, study on reactivity characteristics of fast reactors, high temperature Doppler effect and sodium void effect and study on fast reactor for transmutation of minor actinides. In the first theme, data and method were evaluated for design of advanced fast reactors with metallic and nitride fuels using the mock-up experiments at the Fast Critical Facility (FCA). In the second theme, participation was made in the  $\beta_{\text{eff}}$  measurements at MASURCA of France under the framework of OECD/NEA. In the third theme, the nuclear data base was prepared for an actinide burner reactor under the collaborative effort with ORNL as a part of OMEGA program.

### Thermal Reactor Physics Laboratory

This laboratory has three research themes; experimental research of HTGR neutronics, study of compact reactors and experimental research of actinide transmutation using accelerator. In the first theme, works have been mainly conducted on reactor physics experiments at a critical assembly (Very High Temperature Reactor Critical Assembly: VHTRC) for the verification of the neutronics design of the High Temperature Engineering Test Reactor (HTTR). The second theme includes conceptual designs of space reactors and HTGR-MHD combination plants. In the third theme, spallation experiments have been conducted on a lead assembly bombarded by 500 MeV protons. A high energy particle transport code NMTC/JAERI is being verified and modified using the experimental data.

### Sensing Technology Laboratory

This laboratory carries out R&D works in the field of instrumentation and

measurement under two research themes. One covers general subjects of the nuclear and reactor instrumentation widely, where being performed are R&D of a new type of neutron detectors, nondestructive measuring technologies to assess the material degradation of reactor components, a beam current profile monitor, a fuel failure detection system for HTGRs, etc. The other is specified to the nondestructive measurement of TRU waste drums, where both the active and passive neutron assays are applied.

#### Control and AI Laboratory

This laboratory considers the contribution to safe operation of the nuclear power plants. For this purpose, the laboratory pays attention especially to the improvement of the reactor stability and early fault diagnosis based on reactor noise. The other concern is robotics for the hazardous environment; it involves, for example, manipulator technologies with redundant degrees of freedom and advanced sensing by ultrasonic sensor.

#### Shielding Laboratory

This laboratory has mainly focused their activity on high energy neutron and photon shielding for accelerators. As for experimental works, benchmark experiments have been done using quasi-monoenergetic neutrons in the AVF cyclotron facility TIARA, and energy responses of neutron detectors have been measured for neutrons above 20 MeV. While, a comprehensive data set of neutron attenuation up to 400 MeV was prepared with an intermediate energy group constant HILO86R for water, concrete and iron, and a point kernel integration code PKN-H was developed as a conventional shielding design method with the data set.

Besides, a couple of peripheral works around the accelerator shielding have been made concerning fluence to dose conversion factors of neutrons and photons up to 10 GeV and stopping power data for charged particles.

#### Heat Transfer and Fluid Flow Laboratory

This laboratory has three major research themes for upgrading of thermal hydraulic analyses of light water reactors. One is the development and verification of the best-estimate thermal hydraulic analysis codes for light water reactors. Another is the fundamental studies such as those for improving the mechanistic models of critical heat flux in the sub channels of fuel assembly and two-phase flow structure in the horizontal or vertical flow channels. The neutron radiography in the JRR-3M has been utilized for this purpose. The other is the



transient thermal hydraulic test program aiming at the verification of the core integrity during the design basis events of LWRs.

#### Fusion Neutronics Laboratory

Since the JAERI/USDOE Collaborative Program was being terminated in Oct. 1993, a big effort paid to summarize the achievements for ten years and to prepare joint reports and papers. At the same time, two workshops were held in both Japan and US in order to introduce the results to the fusion neutronics community world-widely. Under the ITER/EDA R&D program, a series of bulk shield experiments has been started based on the '93 & '94 Tasks along with benchmark experiments on functional materials have also been started or planned under the ITER program. Data tests of JENDL-3.2 for fusion neutronics application have been started. For this purpose, two cross section libraries, JSSTDDL-J3.2 and FSXLIB-J3.2 were prepared based on JENDL-3.2.

#### Passive Safety Reactor Systems Laboratory

This laboratory developed new concept of JAERI passive safety reactor (JPSR) for a next generation light water reactor. In order to develop and evaluate the concept, analytical studies such as nuclear calculations, safety analyses and probabilistic safety assessment (PSA) have been performed. Experimental studies are under way to investigate the important thermal-hydraulic phenomena including natural circulation, steady-state and transient DNB, gravity driven coolant injection, steam condensation and multi-dimensional flow in pressure vessel. A conceptual design of integral-type passive safety test reactor is in progress. A feasibility of active storage PWR which uses MOX fuel was confirmed and demonstration tests will be performed using a large scale hydraulic mock-up test facility.

#### Transmutation System Laboratory

This laboratory has two main research themes; the transmutation system using a reactor and the accelerator-based transmutation system. The first is the design study on the burner reactor and the fuel cycle facility taking into account the partitioning and transmutation cycle as described in the paragraphs 10.3 and 10.4. The international and internal collaboration work based on the OMEGA plan is also included here. The second consists of the conceptual design studies on three types of the accelerator-based transmutation system and the development of codes used for the design studies, including the cascade codes, as described in the paragraphs 10.1, 10.2 and 10.5.

### Accelerator Engineering Laboratory

This laboratory has been engaged in the R&D work for the design and construction of a high intensity proton accelerator. The Engineering Test Accelerator (ETA) with an energy of 1.5 GeV and average current of 10 mA has been proposed for accelerator-based nuclear waste transmutation and various basic researches with secondary beams of neutron, muon and pion. In the course of the development, the Basic Technology Accelerator (BTA, 10 MeV and 10 mA) are being studied because the maximum current and beam quality are mainly determined by the low energy portion. Major accelerator components such as ion source, radio frequency quadrupole (RFQ), drift tube linac (DTL) and RF source have been developed as a first step R&D work.

### Free Electron Laser Laboratory

This laboratory has undertaken a developmental program of the JAERI Free Electron Laser (FEL) system for a far-infrared region from the wavelength of 20  $\mu\text{m}$  to 80  $\mu\text{m}$ . The purpose of the present JAERI FEL program lies in constructing a very long pulse or quasi-continuous wave(cw) superconducting radio frequency (rf) linac electron accelerator and demonstrating a high-average power FEL in the far-infrared wavelength region.

### Reactor Engineering Facility Operation Division

This division operated four large-scale experiment facilities in accordance with each experiment program and mended carefully in the monthly or the annual inspection. Consequently safety operations of these facilities were achieved and contributed sufficiently to the execution of each experimental study.

### Accelerator Operation Division

This division operates a 20 MV tandem accelerator since 1982, which designed for ions with masses from 1 to 240 amu. The accelerator is used for a wide range of basic research in JAERI and outside users. As a special feature, the division has developed a superconducting tandem booster to increase the energy of the heavy ions from the tandem accelerator by approximately four times.

The Department has managed the Japanese Nuclear Data Committee, the Research Committee on Reactor Physics, the Atomic and Molecular Data Committee, the Research Committee on Advanced Reactors and the Research Committee on Partitioning and

transmutation.

The project-related research program by the Department has been:

- (1) Design study of advanced reactors,
- (2) Development of technology for partitioning and transmutation of nuclear wastes including R&D of the high intensity proton linear accelerator,
- (3) Development of Very High Temperature Gas-cooled Reactors (VHTR),
- (4) Engineering research for fusion reactors.

Activities by the Development in fiscal year 1993 have contributed to the essential progress in the field of reactor engineering.



Hiroyuki Yoshida, Director

Department of Reactor Engineering

September 1, 1994

## 1. Nuclear Data, and Atomic and Molecular Data

In nuclear data evaluation, much efforts have been devoted to providing JENDL-3 Revision 2 (JENDL-3.2) for which the data of 160 nuclides in JENDL-3.1 were revised and the data of 16 nuclides were newly added. The preliminary benchmark tests of JENDL-3.2 showed more satisfactory results than JENDL-3.1. The evaluation of JENDL Special Purpose Files has been continued for Actinoid Files and Covariance Files. Theoretical model was developed on the level density parameters.

The theoretical work and evaluation have been made for high energy data. The Quantum Molecular Dynamics (QMD) was applied to nucleon induced reactions. The evaluated data of H,  $^{12}\text{C}$  and  $^{27}\text{Al}$  in the high energy range were adopted in JENDL High Energy File.

Mass chain evaluation has been continued within international framework for ENSDF. The evaluations of mass chains of 123, 125 and 126 were completed and published in Nuclear Data Sheets.

As to the experimental activities of nuclear data, the activation cross sections of  $^{63}\text{Cu}(n,2n)$ ,  $^{65}\text{Cu}(n,2n)$ ,  $^{187}\text{Re}(n,2n)$  and  $^{193}\text{Ir}(n,2n)$  reactions and many reactions producing short-lived nuclei were measured near 14 MeV at JAERI/FNS. Activation cross sections were also measured at 18 - 30 MeV by using the  $^7\text{Li}(p,n)$  quasi-monoenergetic neutron source at JAERI-TANDEM.

With respect to atomic and molecular data, data evaluation has been continued for JEAMDL-4. The cross sections were evaluated for excitation and for spectral line emission in collisions of H,  $\text{H}_2$ , He and Li atoms and ions with atoms and molecules. The spectral data for highly ionized Mn ions were also evaluated. Calculations based on new theoretical approaches were made for dipole moment function of diatomic molecules and cross sections for radiative electron capture in relativistic atomic collisions.

In this chapter, the research activities, 1.1-1.10 and 1.16-1.19, were conducted at the Nuclear Data Center, and the benchmark test, 1.15, was done at the Reactor System Laboratory. The measurements, 1.11-1.14, were carried out at the Fusion Neutronics Laboratory.

## 1.1 Second Revision of JENDL-3 (JENDL-3.2)

### Nuclear Data Center and Japanese Nuclear Data Committee

The third version of Japanese Evaluated Nuclear Data Library (JENDL-3)<sup>1,2)</sup> has been updated to JENDL-3.2. This revision work started in 1992 to improve drawbacks of JENDL-3.1 which was released in 1990, and was done by the Nuclear Data Center and working groups of Japanese Nuclear Data Committee (JNDC). JENDL-3.2 provides the neutron induced reaction data for 340 nuclei in the energy range from  $10^{-5}$  eV to 20 MeV. Among those nuclides, the data of 16 nuclei are newly added to JENDL-3, and those of more than 180 nuclei were revised from previous evaluation. Main aspects of the present revision are summarized below:

#### Resonance Parameters of Important Actinides

The resolved resonance parameters of  $^{233}\text{U}$ ,  $^{235}\text{U}$ ,  $^{238}\text{U}$ ,  $^{239}\text{Pu}$  and  $^{241}\text{Pu}$  were updated with new evaluation based on the Reich-Moore formula. The energy range of the resolved resonance region was expanded to higher energies than JENDL-3.1. For example, the parameters of  $^{239}\text{Pu}$  were evaluated by Derrien<sup>3)</sup> by means of SAMMY code<sup>4)</sup> and recent measurements of fission and total cross sections. Its resonance region was extended from 1 keV of JENDL-3.1 to 2.5 keV. The unresolved resonance parameters were modified for  $^{235}\text{U}$  and  $^{238}\text{U}$ . The fission and capture cross sections of  $^{235}\text{U}$  were re-evaluated in the unresolved resonance region and the unresolved resonance parameters were determined to reproduce the new cross-section data. For  $^{238}\text{U}$ , the upper boundary of the unresolved resonance region was changed from 50 keV of JENDL-3.1 to 150 keV.

#### Inelastic Scattering Cross Sections of $^{233}\text{U}$ and $^{238}\text{U}$

After careful recalculation with sophisticated theoretical calculation method, these cross sections were slightly modified from JENDL-3.1.

#### Fission spectra of $^{233}\text{U}$ , $^{235}\text{U}$ , $^{238}\text{U}$ and $^{239}\text{Pu}$

These data were newly calculated with non-equitemperature Madland-Nix model proposed by Ohsawa<sup>5)</sup>, which takes account of different temperatures for two fission fragments and multi-chance fission process. Their spectra became softer than those in JENDL-3.1.

### Total Cross Sections of Structural Material

The total cross sections of  $^{14}\text{N}$ ,  $^{23}\text{Na}$  and Fe were reevaluated. Their drawbacks were revealed by benchmark calculation<sup>6)</sup> to Broomstick experiments. In the case of natural Fe, JENDL-3.1 was evaluated from fine resolution experimental data. However, the experimental data are broadened with a finite experimental resolution even in the very fine resolution experiments. The total cross section of Fe given in JENDL-3.1 was unfolded by considering the experimental resolution. Those of Cr and Ni were also modified with the same method. The total cross sections of  $^{14}\text{N}$  and  $^{23}\text{Na}$  were reevaluated by taking more reasonable data. Revised data are in very good agreement with the benchmark experiments.

### Double Differential Cross Sections

The double differential cross sections (DDX) are important for fusion neutronics. To improve the DDX, JENDL Fusion File<sup>7)</sup> is being provided, in which the DDX data are represented in MF6 of ENDF-6 format. The modified data for JENDL Fusion File were adopted in JENDL-3.2 by approximately transforming the MF6 representation to the conventional MF4-MF5 format. By the adoption of JENDL Fusion File, the data of the inelastic scattering, (n,2n), and other neutron emission cross sections and the angular and energy distributions of secondary neutrons were remarkably improved. Even in the conventional representation, JENDL-3.2 reproduces quit well the experimental DDX data measured at Osaka and Tohoku universities for many nuclides.

### Fission Product Nuclei

The resonance parameters and capture cross sections of many nuclei in the fission product region (from As to Tb) were modified. New experimental data reported after the previous evaluation were taken into consideration. The inelastic scattering cross sections of even mass isotopes of Sm were updated by adding the contributions from the direct process. The data of As, Zr, Mo and Sb were taken from JENDL Fusion File.

### Gamma-ray Production Data

New evaluation was made for seven nuclei. JENDL-3.2 contains, therefore, the  $\gamma$ -ray production data for 66 nuclei. The  $\gamma$ -ray spectra in the low energy region were calculated with CASTHY<sup>8)</sup>, and energy balance was carefully checked. The discrete  $\gamma$ -rays from the inelastic scattering of natural elements were separated from continuum spectra.

Preliminary benchmark calculations for JENDL-3.2 were made by working groups of JNDC for LWR, FBR and shielding of JNDC. It has been confirmed that JENDL-3.2 improves the drawbacks found in JENDL-3.1, and JENDL-3.2 provides the reliable neutron nuclear data for wide region of applications.

#### References

- 1) Shibata K., et al.: "Japanese Evaluated Nuclear Data Library, Version 3, - JENDL-3 -", JAERI 1319 (1990).
- 2) Kawai M., et al.: J. Nucl. Sci. Technol., 29, 195 (1992).
- 3) Derrien H.: J. Nucl. Sci. Technol., 30, 845 (1993).
- 4) Larson N.M.: "Updated Users' Guide for SAMMY: Multilevel R-Matrix Fits to Neutron Data Using Bayes' Equations", ORNL/TM-9179/R1 (1985).
- 5) Ohsawa T. and Shibata T.: "Analysis of Fission Neutron Spectra by Non-Equitemperature Madland-Nix Model", Proc. of Int. Conf. on Nuclear Data for Science and Technology, Juelich, 13-17 May, 1991, p.965 (1992).
- 6) Kawai M., et al.: "Shielding Benchmark Tests of JENDL-3", JAERI 1330 (1994).
- 7) Chiba S., Yu B. and Fukahori T.: "Evaluation of JENDL Fusion File", JAERI-M 92-027, p. 35 (1992).
- 8) Igarasi S. and Fukahori T.: "Program CASTHY - Statistical Model Calculation for Neutron Cross Sections and Gamma Ray Spectrum -", JAERI 1321 (1991).

## 1.2 Evaluation of Neutron Nuclear Data of $^{237}\text{U}$ , $^{236}\text{Np}$ and $^{238}\text{Np}$

T. Nakagawa and Y. Kikuchi

The evaluation of neutron nuclear data of  $^{237}\text{U}$ ,  $^{236}\text{Np}$  and  $^{238}\text{Np}$  was made in the neutron energy range from  $10^{-5}$  eV to 20 MeV. Quantities evaluated are the total, elastic and inelastic scattering, capture, fission, (n,2n) and (n,3n) reaction cross sections, the angular and energy distributions of secondary neutrons, and number of neutrons emitted per fission. For  $^{237}\text{U}$ , the cross sections in the energy range below 200 eV were represented with the resolved resonance parameters. Results were compiled in the ENDF format and adopted in JENDL-3.2. Figures 1.2.1 to 1.2.3 show the evaluated cross section data. In the case of  $^{237}\text{U}$ , the cross sections in the resolved resonance region are averaged in the suitable energy intervals. A report on this subject was published as JAERI-M 94-009 (1994). This work was performed under the contracts between the Power Reactor and Nuclear Fuel Development Corporation and Japan Atomic Energy Research Institute.

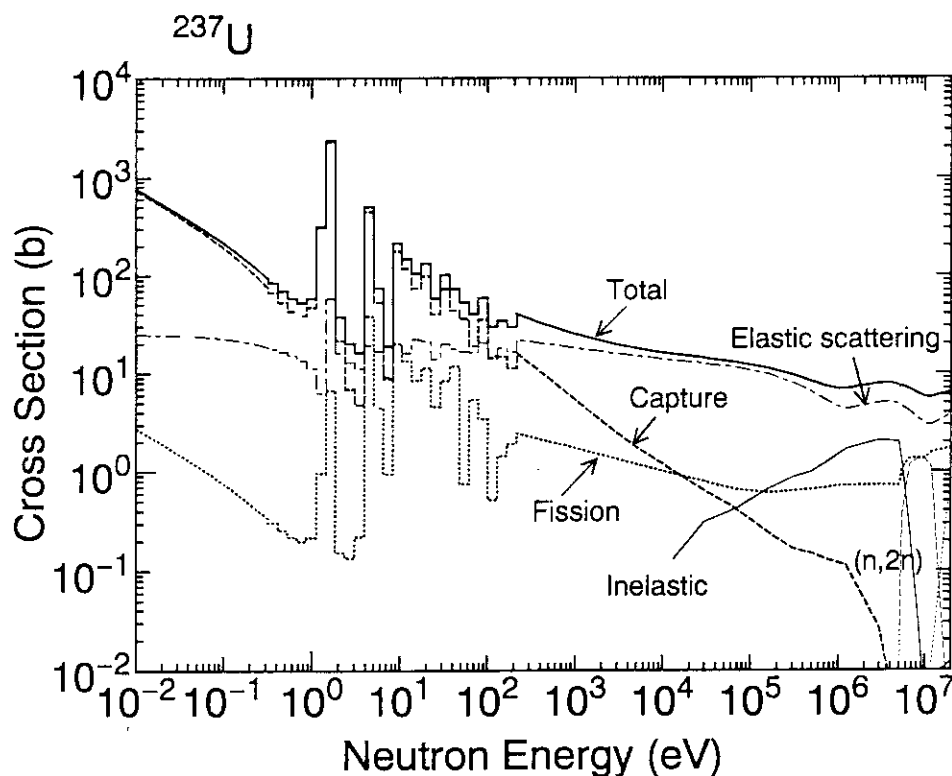
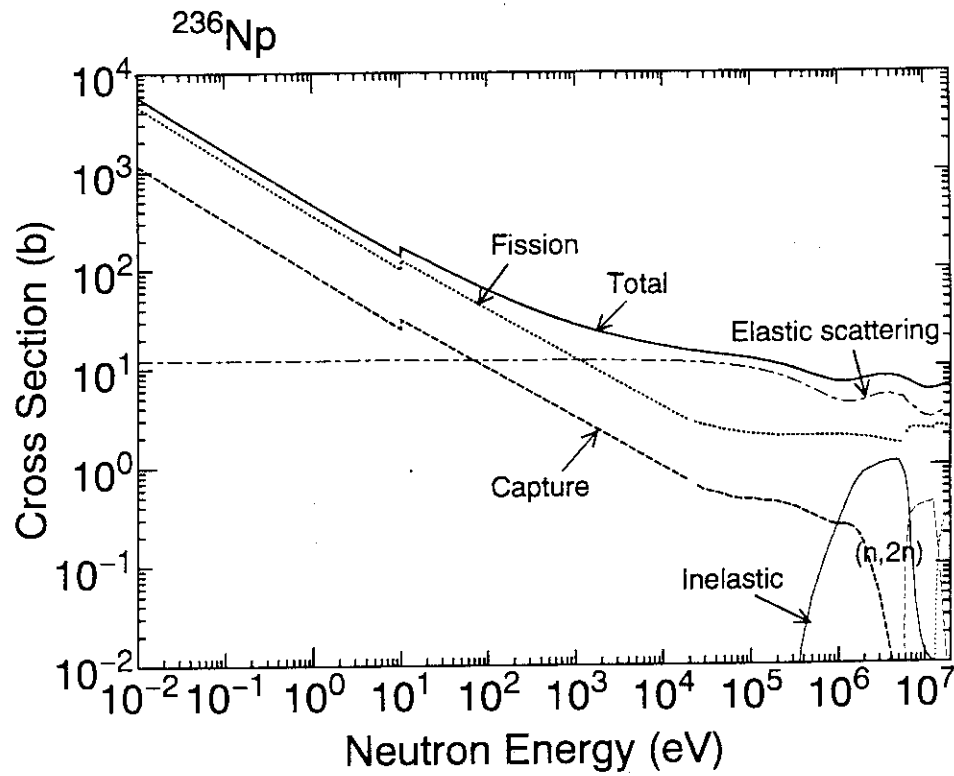
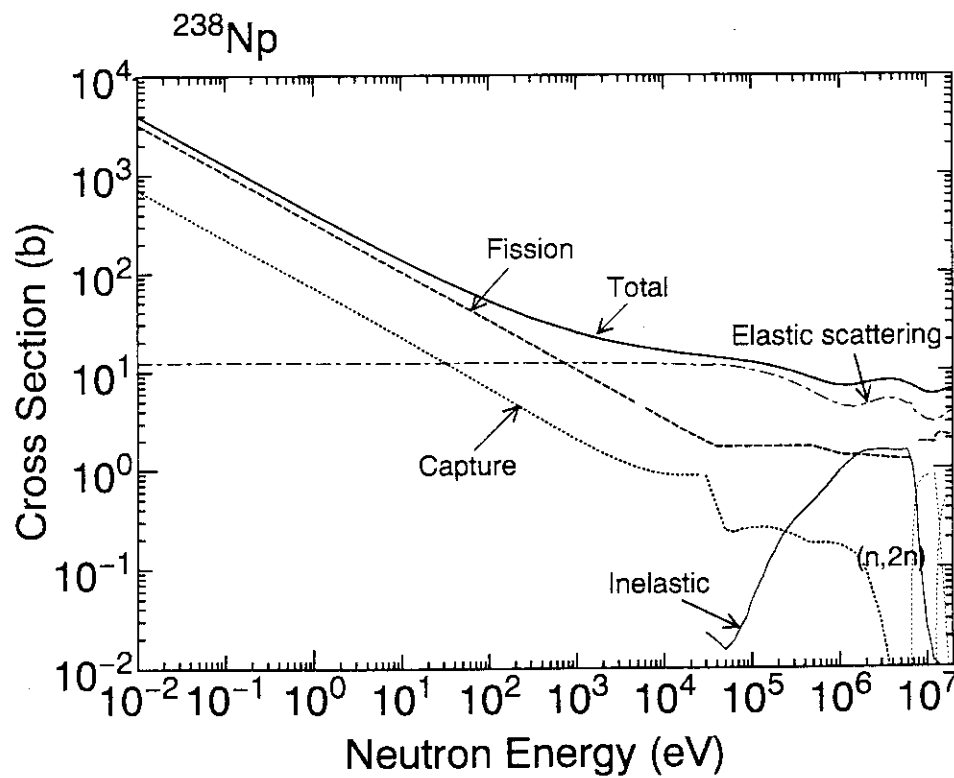


Fig. 1.2.1 Evaluated cross sections of  $^{237}\text{U}$



Fig. 1.2.2 Evaluated cross sections of  $^{236}\text{Np}$ Fig. 1.2.3 Evaluated cross sections of  $^{238}\text{Np}$

### 1.3 Evaluation of Neutron Nuclear Data of $^{244}\text{Pu}$ and $^{237}\text{Pu}$

T. Nakagawa and V. Konshin<sup>1</sup>

The evaluation of neutron nuclear data of  $^{244}\text{Pu}$  and  $^{237}\text{Pu}$  was made in the neutron energy range from  $10^{-5}$  eV to 20 MeV. Quantities evaluated are the total, elastic and inelastic scattering, capture, fission, (n,2n) and (n,3n) reaction cross sections, the angular and energy distributions of secondary neutrons, and number of neutrons emitted per fission.

#### $^{244}\text{Pu}$

The resolved resonance parameters were given in the energy range up to 290 eV on the basis of experimental data by Auchampaugh et al.<sup>1)</sup> The thermal fission and capture cross sections are 0.0017 b and 1.68 barns. Their resonance integrals are 5.07 barns and 50 barns, respectively. Above the resonance region, theoretical calculation was made with ECIS<sup>2)</sup>, STAPRE<sup>3)</sup> and CASTHY<sup>4)</sup>. The ECIS calculation was adopted for the total, shape elastic and direct inelastic scattering cross sections, and their angular distributions. The (n,2n), (n,3n) and fission cross sections, and energy distributions of neutrons due to the continuum inelastic scattering, (n,2n) and (n,3n) reactions were calculated with STAPRE. The fission cross sections below 8 MeV were determined from existing experimental data<sup>1),5)</sup> which are in agreement with the STAPRE calculation. The CASTHY was used to calculate the capture and compound scattering cross sections to discrete levels. The continuum inelastic scattering cross section was determined by subtracting a sum of the other partial cross sections from the total cross section. The number of prompt neutrons per fission ( $\nu_p$ ) was estimated as:

$$\nu_p = 2.79 + 0.163 \times E(\text{MeV}).$$

The number of delayed neutrons is 0.03 in the thermal energy region and 0.019 in the MeV region.

#### $^{237}\text{Pu}$

No resonance parameters were given. The thermal fission cross section was taken from

---

<sup>1</sup> Research fellow

Mughabghab's recommendation<sup>6)</sup> ( $2455 \pm 295$  barns). The capture cross section was assumed to be 500 b at 0.0253 eV, which is about 1/5 of the fission cross section. The ratio was obtained in the keV region. The resonance integral is 816 barns for the fission and 142 barns for the capture.

No experimental data are available for the cross sections of  $^{237}\text{Pu}$ . The fission cross section was assumed to be  $\sigma_R \times 0.85$  where  $\sigma_R$  is the total reaction cross section calculated with CASTHY and the factor of 0.85 was estimated at 100 keV by assuming the cross section is almost the same as  $^{239}\text{Pu}$ . Other quantities were evaluated with ECIS, STAPRE and CASTHY in the same manner as  $^{244}\text{Pu}$ . The number of prompt neutrons per fission was estimated as:

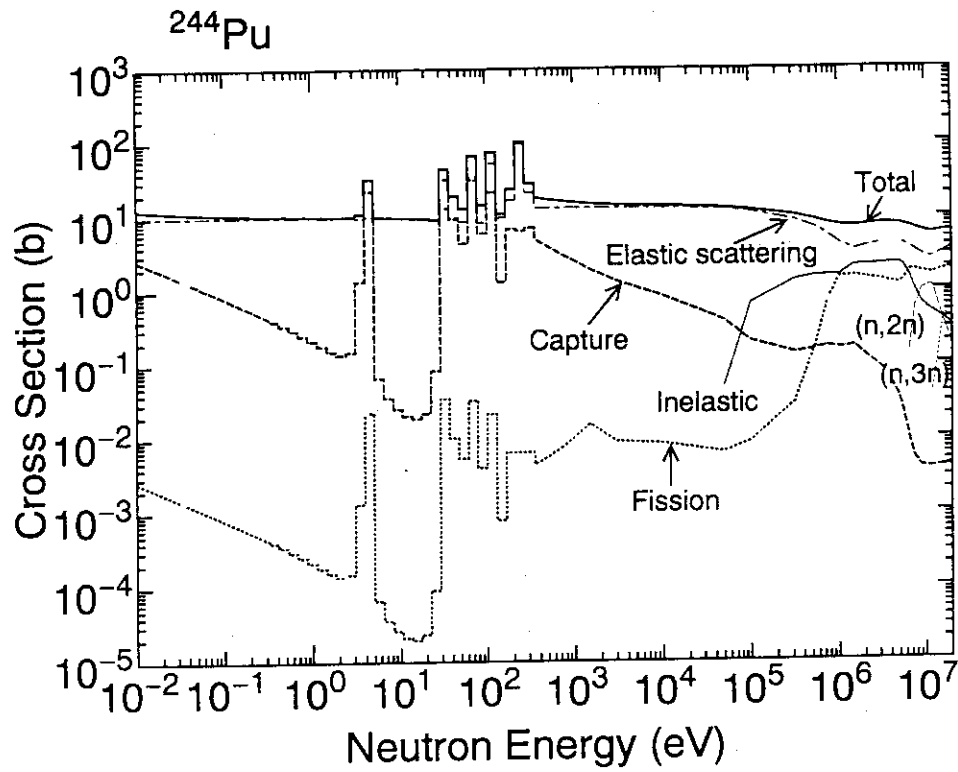
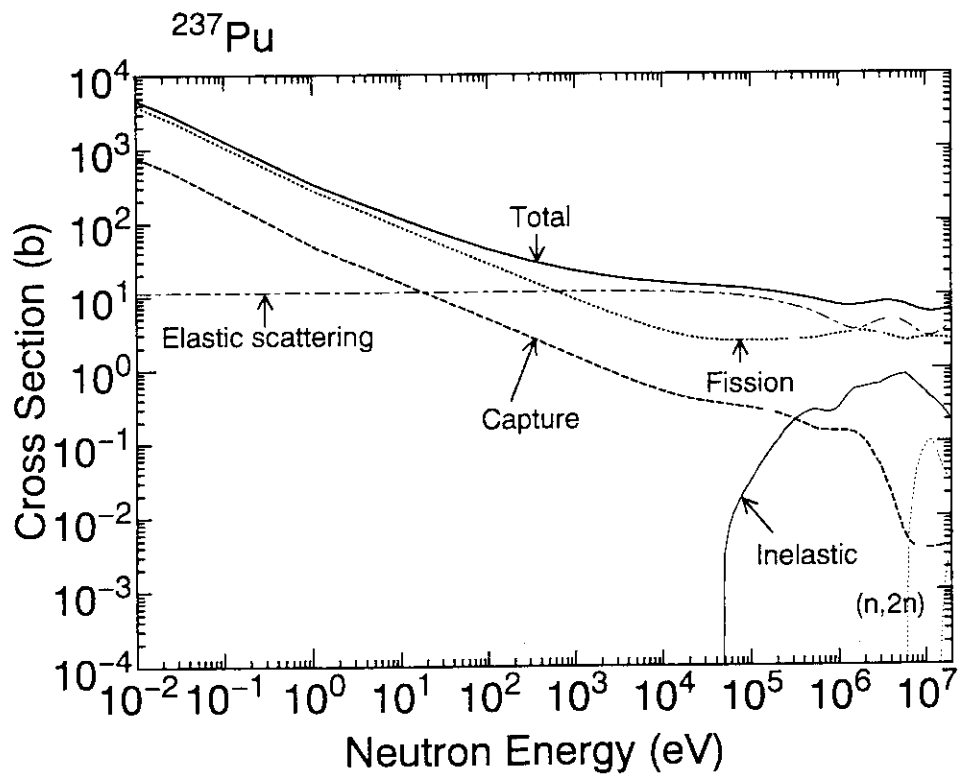
$$\nu_p = 2.863 + 0.123 \times E(\text{MeV}).$$

The number of delayed neutrons is 0.002 in the thermal energy region and 0.0014 in the MeV region.

The present results will be adopted in JENDL Actinoid File. Figures 1.3.1 and 1.3.2 show the evaluated cross section data. This work was performed under the contracts between the Power Reactor and Nuclear Fuel Development Corporation and Japan Atomic Energy Research Institute.

#### References

- 1) Auchampaugh G.F., Farrell J.A. and Bergen D.W.: Nucl. Phys., A171, 31(1971).
- 2) Raynal J.: unpublished.
- 3) Uhl M. and Stromaier B.: Report IRK-76/10 (1976).
- 4) Igarasi S. and Fukahori T.: "Program CASTHY - Statistical Model Calculation for Neutron Cross Sections and Gamma Ray Spectrum -", JAERI 1321 (1991).
- 5) Moore M.S., et al.: Proc. Int. Conf. on Nuclear Data for Science and Technol., Antwerp, 6-10 Sep. 1982, p.74 (1983).
- 6) Mughabghab S.F.: "Neutron Cross Sections, Vol. 1, Part B", Academic Press Inc. (1984).

Fig. 1.3.1 Evaluated cross sections of  $^{244}\text{Pu}$ Fig. 1.3.2 Evaluated cross sections of  $^{237}\text{Pu}$

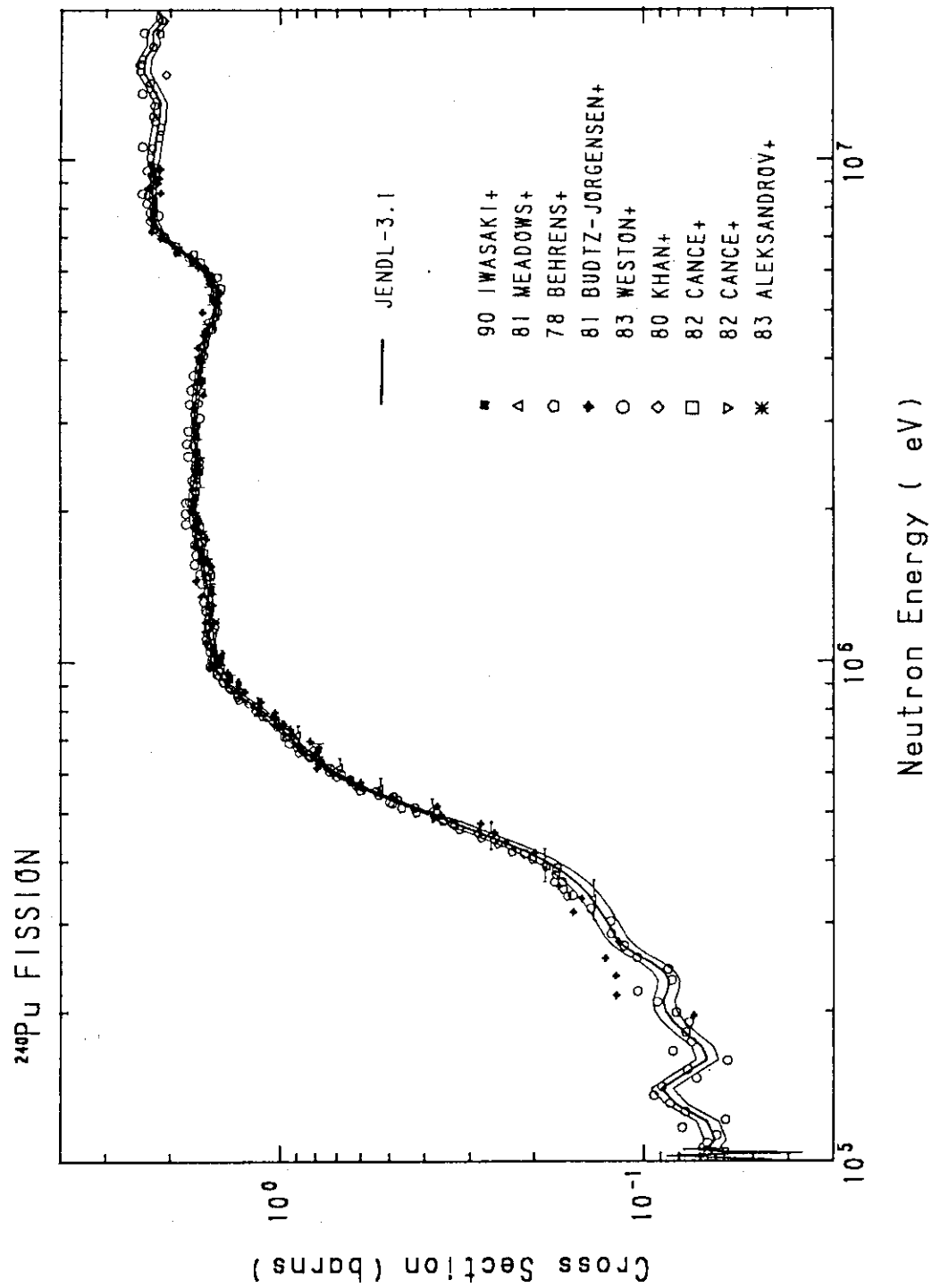
## 1.4 Evaluation of Covariance Matrices for Several Nuclear Data

T. Nakagawa, K. Shibata, S. Chiba and Y. Nakajima

Covariance matrices of evaluated nuclear data are important to estimate uncertainties of reactor performance parameters calculated from the evaluated data. Since the Japanese nuclear data library, JENDL-3, has no such information, Japanese Nuclear Data Committee has organized a working group to investigate evaluation method of the covariance matrices. On the other hand, the Power Reactor and Nuclear Fuel Development Corporation required us to estimate roughly the covariance matrices for several cross section data in JENDL-3. This work was made to meet the urgent requirement.

In the present work, the covariance matrices were given to the  $^{14}\text{N}$  elastic scattering cross section,  $^{14}\text{N}(\text{n,p})$  reaction cross section,  $^{15}\text{N}$  elastic scattering cross section,  $^{23}\text{Na}$  inelastic scattering cross section, Fe inelastic scattering cross section and  $^{240}\text{Pu}$  fission cross section. Their covariance matrices were determined by comparing JENDL-3 data with experimental data, and by taking into consideration of their evaluation method. The covariance matrices were given in the 18 energy group structure up to 20 MeV. In Fig. 1.4.1, the standard deviation given to the  $^{240}\text{Pu}$  fission cross section is compared with experimental data, which was determined by calculating deviations of experimental data from JENDL-3.

This work was performed under the contracts between the Power Reactor and Nuclear Fuel Development Corporation and Japan Atomic Energy Research Institute.

Fig. 1.4.1 The fission cross section of  $^{240}\text{Pu}$  and its standard deviation

## 1.5 Update of Gamma-ray Production Data for JENDL-3.2

S. Igarasi<sup>\*1</sup>, T. Asami<sup>\*2</sup>, K. Shibata, M. Mizumoto, K. Hida<sup>\*3</sup>, M. Igashira<sup>\*4</sup> and H. Kitazawa<sup>\*4</sup>

The third version of Japanese Evaluated Nuclear Data Library (JENDL-3)<sup>1)</sup> contained gamma-ray production data for 59 nuclides. It was the first experience for the members of Japanese Nuclear Data Committee (JNDC) to evaluate gamma-ray emission data although they had enough expertise regarding neutron emission data. Since the release of JENDL-3 in 1989, the gamma-ray production data have been compared with integral and differential measurements and some problems were found in the evaluated data. We were therefore requested to solve the problems and polish the gamma-ray production data for the second revision of JENDL-3 (JENDL-3.2).

Energy balance was the biggest problem of capture gamma-ray spectra at thermal energy. In the original JENDL-3 (JENDL-3.1), thermal spectra were evaluated on the basis of experimental data, but energy conservation was not fulfilled for many nuclides. We employed statistical-model calculations in order to solve this problem. In the calculation, branching ratios for primary transitions were taken into account and the energy was automatically conserved. Moreover, the Q-values of capture reactions on natural elements were recalculated by considering the isotopic abundance and cross section of each isotope. Figure 1.5.1 shows gamma-ray spectra from <sup>nat</sup>Ni at thermal energy.

As for natural elements composed of more than two isotopes in JENDL-3.1, line spectra originating from the inelastic scattering to discrete levels had been put into continuum spectra with a bin width of 500 keV. This treatment however caused a serious problem in the analysis<sup>2)</sup> of the gamma-ray spectra from an iron sphere measured at KFK. In JENDL-3.2, the line spectra were explicitly provided up to several MeV for natural elements. The revised data were found<sup>3)</sup> to reproduce the KFK experiments very well.

As a result, we revised gamma-ray production data of 49 nuclides. These data were used<sup>4)</sup> to analyze the integral experiments at FNS and OKTAVIAN, and it should be noted that the agreement between the measurements and calculations is quite good.

---

\*1 Nuclear Energy Data Center  
\*3 Toshiba

\*2 Data Engineering  
\*4 Tokyo Institute of Technology

## References

- 1) Shibata K., et al.: "Japanese Evaluated Nuclear Data Library Version-3 JENDL-3", JAERI 1319 (1990).
- 2) Yamano N.: Private communication (1993).
- 3) Ueki K., Ohashi A. and Yamano N.: "Integral Test of Secondary Gamma-ray Production Cross Sections of Iron in JENDL-3 with Continuous Energy Monte Carlo Analysis", JAERI-M 94-019, p. 362 (1994).
- 4) Maekawa F.: Private communication (1994).

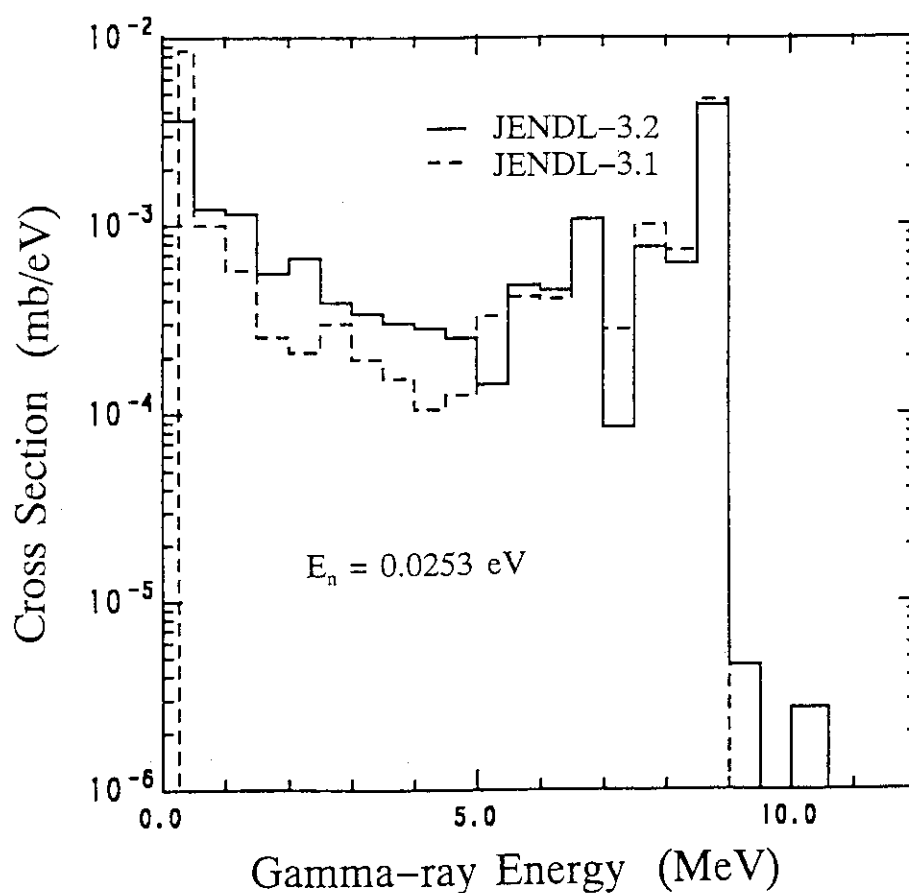


Fig. 1.5.1 Capture gamma-ray spectra from  $^{nat}\text{Ni}$



## 1.6 Evaluation of Neutron Cross Sections of $^1\text{H}$ and $^{12}\text{C}$ in the Intermediate-Energy Region

S. Chiba, T. Fukahori, S. Morioka<sup>1</sup>, Y. Watanabe<sup>2</sup>, Y. Koyama<sup>2</sup> and M. Harada<sup>2</sup>

Neutron cross sections of  $^1\text{H}$  and  $^{12}\text{C}$  have been evaluated in the energy region from 20 MeV to 1 GeV for  $^1\text{H}$  and 20 MeV to 50 MeV for  $^{12}\text{C}$  as a part of JENDL High-Energy Data File project<sup>1)</sup>.

Evaluation of the  $^1\text{H}$  data were performed mostly based on available experimental data. The total, elastic scattering, inelastic scattering (pion production) and radiative capture cross sections were evaluated. The total cross section was obtained by combining a result of the generalized least-squares analysis (GMA)<sup>2)</sup> and the prediction given from the phase-shift data of Arndt et al.<sup>3,4)</sup>. The result is shown in Fig. 1.6.1. Fig. 1.6.2 shows the error-correlation matrix, obtained from the GMA analysis, of the presently evaluated total cross section of  $^1\text{H}$ . The inelastic scattering ( $\text{np} \rightarrow \text{d}\pi^0$ ,  $\text{np}\pi^0$ ,  $\text{nn}\pi^+$ ,  $\text{pp}\pi^-$ ) cross section was obtained entirely from the phase-shift data. The capture cross section, on the other hand, was calculated from the  $\text{D}(\gamma, \text{n})\text{p}$  cross section with the aid of the principle of detailed balance. Below 140 MeV, the deuteron photo-disintegration cross section was taken from the work of Murata<sup>5)</sup>. Above this energy, the theoretical value of Feshbach and Schwinger<sup>6)</sup> was adopted.

The following quantities have been evaluated for  $^{12}\text{C}$ : the total, elastic scattering, inelastic scattering to the first  $2^+$  state, reaction cross section, radiative capture cross section and double-differential particle production cross sections. The experimental information was taken into consideration as much as possible. The total cross section, for example, was obtained by the GMA analysis. The angular distribution of elastically and inelastically ( $2^+$ ) scattered neutrons above 26 MeV were calculated by using a microscopic optical model potential, where the nucleon density distribution was obtained from the Skyrme-Hartree-Fock calculation<sup>7)</sup> and the density-dependent effective interaction was taken from the G-matrix calculation of Jeukenne, Lejeune and Mahaux<sup>8)</sup>. The presently evaluated elastic angular distribution is compared with experimental data in Fig. 1.6.3. The double-differential cross section was calculated by the SCINFUL/DDX program<sup>9,10)</sup>.

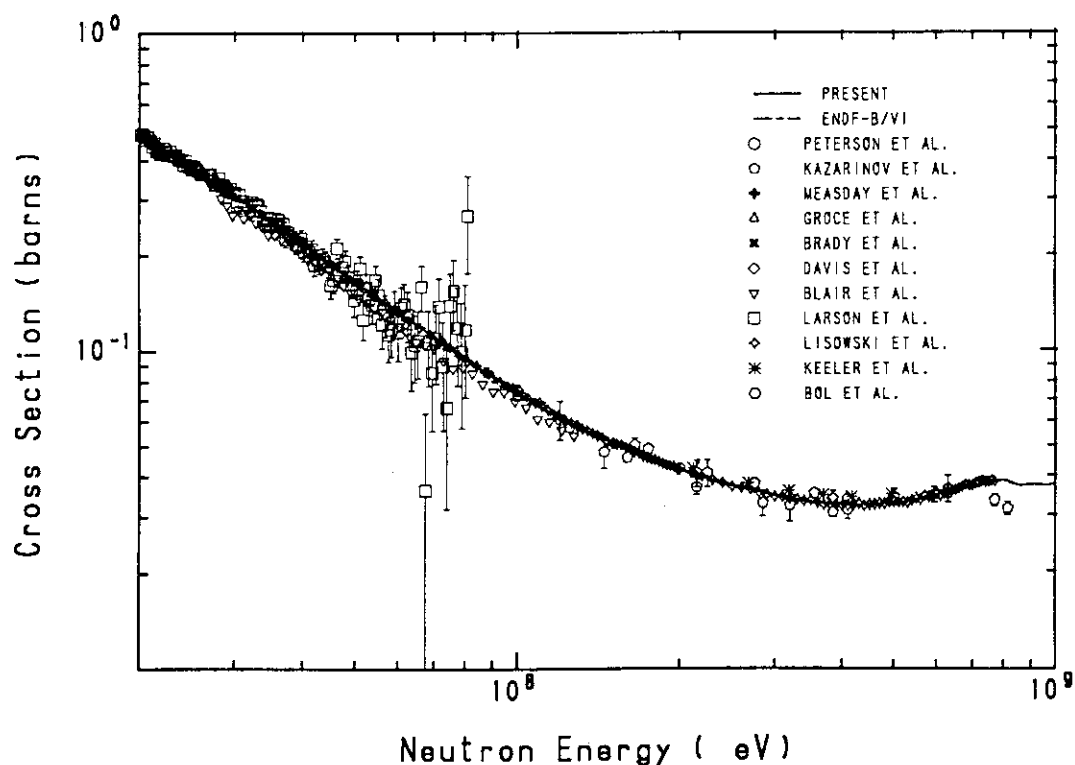
---

<sup>1</sup>CRC Research Institute, Chiba

<sup>2</sup> Kyushu University, Fukuoka

## References

- 1) Fukahori T., et al.: "STATUS OF NUCLEAR DATA EVALUATION FOR JENDL HIGH ENERGY FILE", Proc. of Int. Conf. on Nuclear Data for Science and Technology, May 9-13, 1994, Gatlinburg, Tennessee U.S.A.
- 2) Poenitz W.P.: "A Least-Squares Program for Nuclear Data Evaluation", BNL-NCS-51363, p.249 (1981).
- 3) Arndt R.A., et al.: Phys. Rev. D35, 128(1987).
- 4) Arndt R.A., et al.: Phys. Rev. D28, 97(1983).
- 5) Murata T.: JAERI-M 94-019, P.330 (1994).
- 6) Feshbach H. and Schwinger J.: Phys. Rev. 84, 194(1951).
- 7) Reihnard P.G.: Computational Nuclear Physics 1, p.28 (1991), Springer-Verlag.
- 8) Jeukenne J.P., Lejeune A. and Mahaux C.: Phys. Rev. 16, 80(1977).
- 9) Kashimoto H., et al.: JAERI-M 93-046, p.287(1993).
- 10) Dickens J.K.: ORNL-6462(1988), ORNL-6463(1988).

Fig. 1.6.1 The total cross section of  $^1\text{H}$

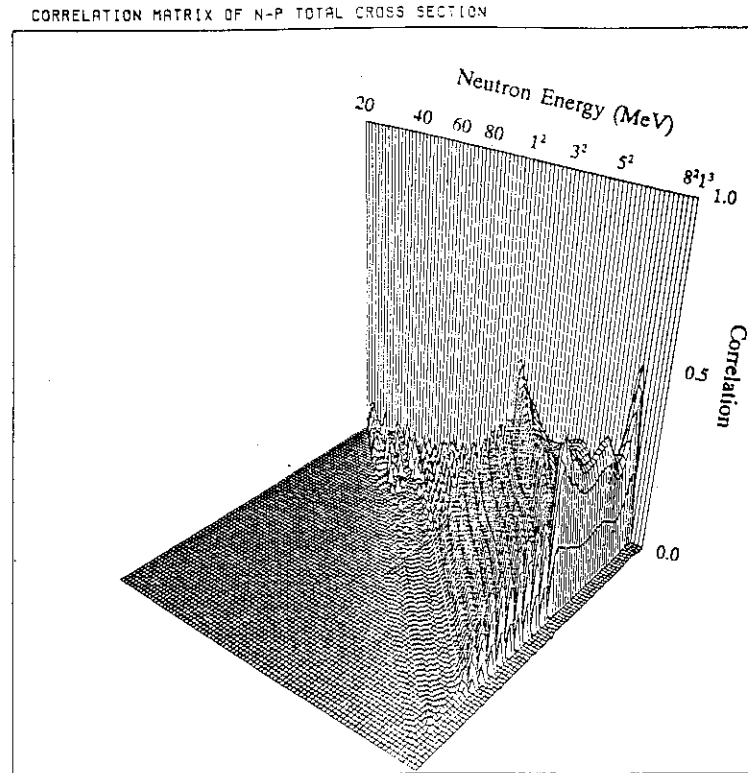


Fig. 1.6.2 The error-correlation matrix of the evaluated total cross section of hydrogen

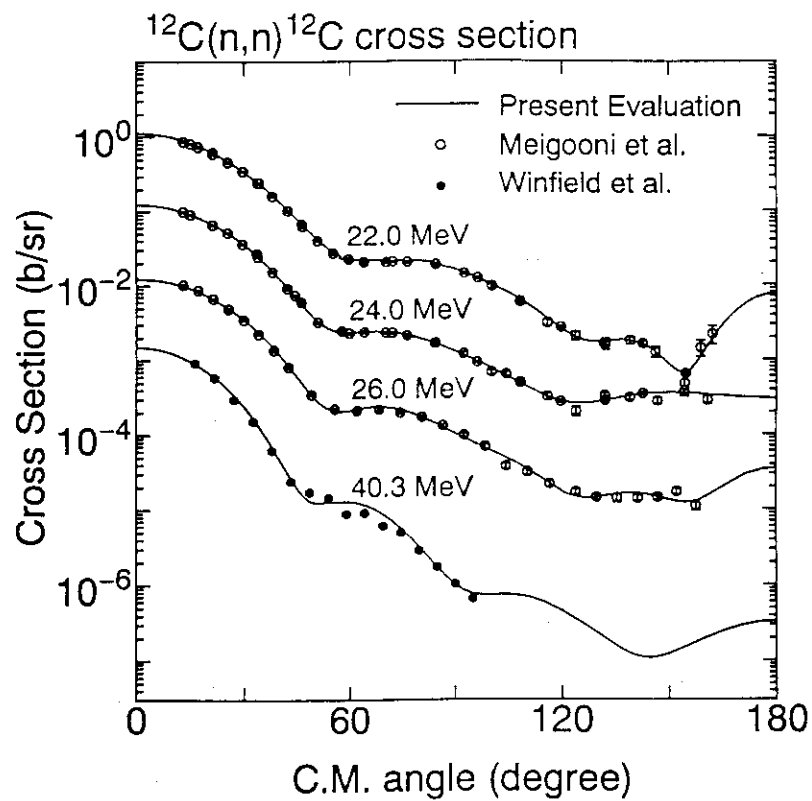


Fig. 1.6.3 The angular distribution of elastically scattered neutrons from  $^{12}\text{C}$

## 1.7 Applicability of the Quantum Molecular Dynamics to Nucleon-Nucleus Collisions

S. Chiba, H. Takada, T. Fukahori, T. Maruyama, K. Niita<sup>1</sup> and A. Iwamoto

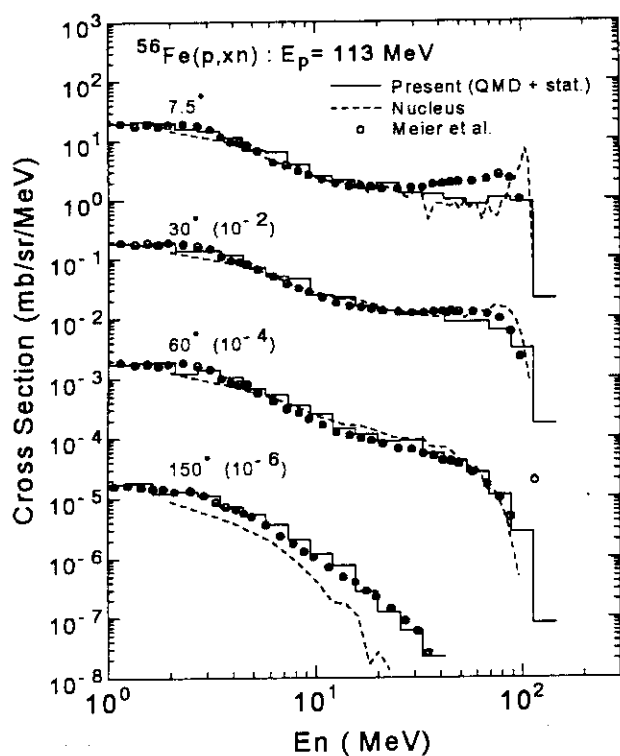
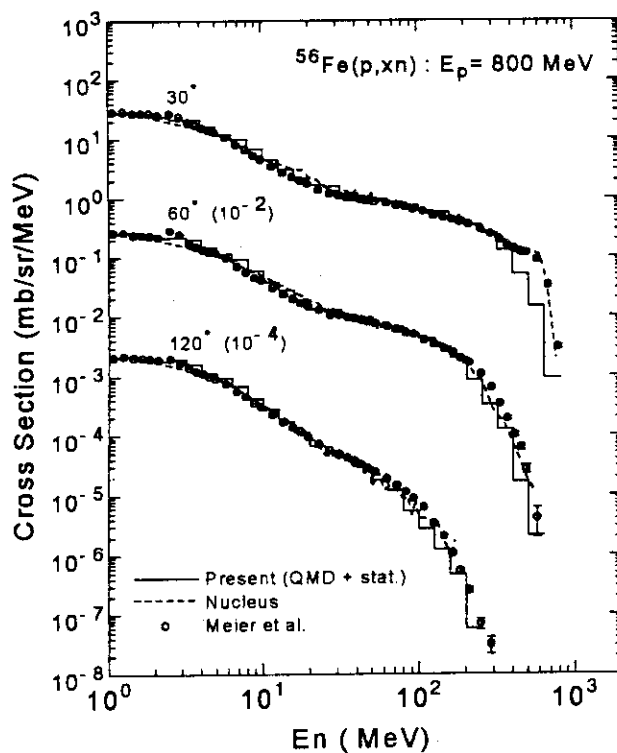
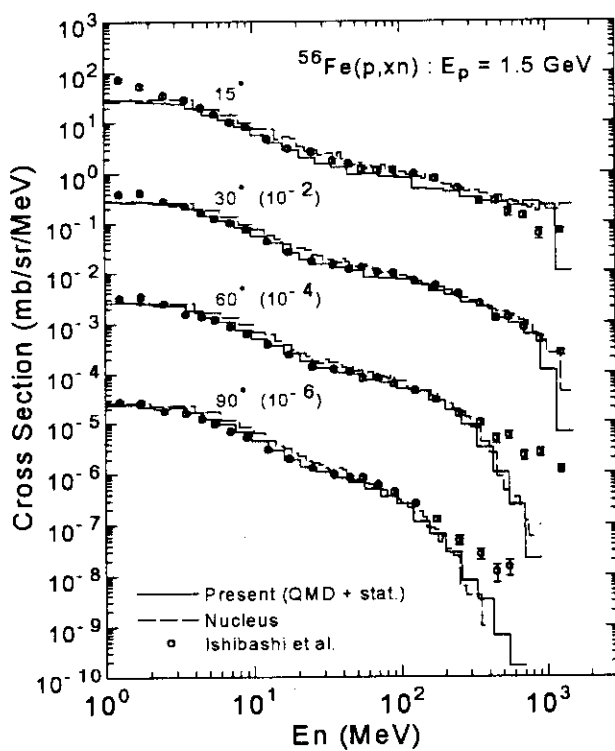
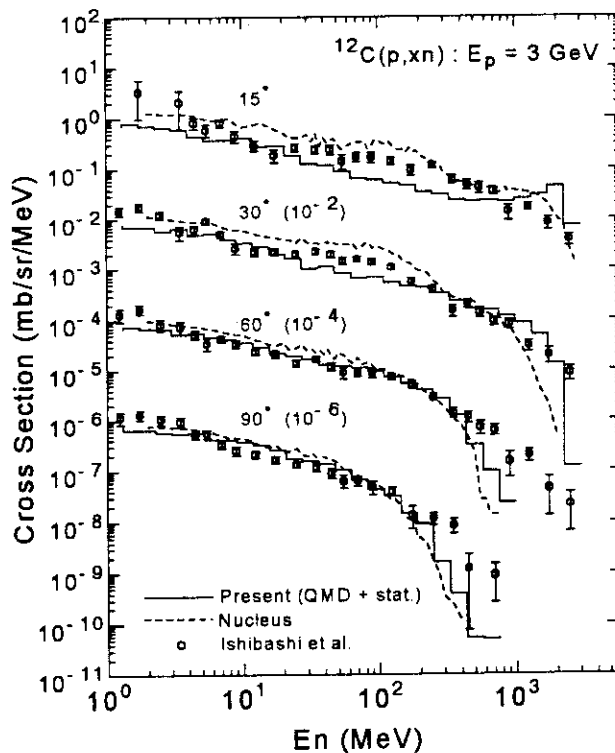
The Quantum Molecular Dynamics (QMD) theory has been developed in the heavy-ion physics and was proved to be quite successful in predicting various phenomena occurring in the reactions between heavy-ions<sup>1)</sup>. The applicability of QMD to nucleon-induced reactions, however, is still uncertain. In this work, the "QMD + statistical decay model<sup>2)</sup>" calculations have been carried out for (N,xN') reactions on C, Al and Fe in the energy region of 25 MeV to 3 GeV. In Figs 1.7.1 to 1.7.4 shown are the typical results of (p,xn) reactions for Fe and C with experimental data<sup>3,4)</sup> and predictions of cascade+evaporation code (Nucleus<sup>5)</sup>). At 113 MeV, the cascade model gives lower values compared with the experimental data at the most backward angle. The present results, on the contrary, reproduce the measured data satisfactorily over the whole angular region. Moreover, the agreement of the present calculation with the low energy neutron data confirms that the QMD gives a proper excitation spectra of residues from which the statistical neutron emission takes place. Therefore, it is clear that the present calculation based on QMD + statistical decay includes the following reaction mechanisms, i.e., the cascade (spallation), pre-equilibrium processes and formation of compound nucleus, in a unified framework. At 800 MeV to 3 GeV, the agreement of the present calculation with the measured data is also remarkable. This work was carried out in cooperation with the Research Group for Hadron Transport, Advanced Science Research Center, JAERI.

### References

- 1) Aichelin J., et al.: Phys. Rev. **C37**, 2451(1988).
- 2) Maruyama T., et al.: Prog. Theor. Phys. **98**, 1367(1992).
- 3) Meier M.M., et al.: LA-11518-MS, LANL(1989); M. Meier, private communication.
- 4) Ishibashi K., et al., "Measurements of Neutron-Production Double-Differential Cross Sections for Incident Protons of 0.8, 1.5 and 3 GeV", Int. Conf. on Nuclear Data for Science and Technology, Gatlinburg, Tennessee, U.S.A., May 9-13, 1994.
- 5) Nishida T., et al.: JAERI-M 86-116 (1986).

---

<sup>1</sup> Nuclear Energy Data Center, Tokai, Naka, Ibaraki, Japan

Fig. 1.7.1  $^{56}\text{Fe}(p,xn)$  cross section at 113 MeVFig. 1.7.2  $^{56}\text{Fe}(p,xn)$  cross section at 800 MeVFig. 1.7.3  $^{56}\text{Fe}(p,xn)$  cross section at 1.5 GeVFig. 1.7.4  $^{12}\text{C}(p,xn)$  cross section at 3 GeV

## 1.8 Evaluation of Nuclear Data for Neutron- and Proton-Induced Reactions on $^{27}\text{Al}$

T. Fukahori

Nuclear data in the intermediate energy range up to several GeV are necessary to many applications, such as accelerator-driven radioactive waste transmutation systems which need the neutron- and proton-induced reaction data as fundamental data for the calculation of shielding designs, spallation target characteristics, a transmutation rate, etc. However, evaluations in the intermediate energy region were reported only for  $^{56}\text{Fe}$ <sup>1)</sup> and for  $^{208}\text{Pb}$  and  $^{209}\text{Bi}$ <sup>2)</sup>, while neutron nuclear data below 20 MeV are well established for wide range of nuclei as the evaluated nuclear data libraries. On the other hand, the nucleus  $^{27}\text{Al}$  is one of the important nuclides as a candidate material for accelerator tubes and many equipments.

The present evaluation has been performed mainly by using the code system including the ALICE-F code. The code ALICE<sup>3,4)</sup> was produced by Blann using statistical model with Weisskopf-Ewing evaporation model<sup>5)</sup> and the preequilibrium process correction of the hybrid and geometry dependent hybrid model<sup>6)</sup>. The ALICE-F code is one of the improved version of ALICE. The improved points were the change of optical model parameters, the use of systematics<sup>2,7-9)</sup> of total, elastic scattering, total reaction and high-energy fission cross sections and double differential particle emission cross sections, the calculation of inverse cross sections, the inclusion of cluster particle emission in the preequilibrium process based on the Iwamoto-Harada model<sup>10,11)</sup>, the replace of mass table of the Wapstra's in 1988<sup>12)</sup>, and the addition of mass formula given by Tachibana et al.<sup>13)</sup>

The total (only for neutron), elastic and total reaction cross sections were calculated with Pearlstein's systematics. The elastic scattering angular distributions were based on a diffraction model<sup>14)</sup> amended for relativistic effects and empirical fits to high energy data.

The particle and isotope production cross sections were mainly obtained by the ALICE-F code. A few of the calculated results were normalized to reproduce the experimental data. The  $^{24}\text{Na}$  production cross section of proton-induced reaction on  $^{27}\text{Al}$  is shown in **Fig.1.8.1**. The experimental data above 50 MeV are separated into two groups, and the evaluated result agrees with the lower group, which includes more data.

The calculations of double differential cross sections (DDXs) were performed by the

semi-empirical formula of Kalbach for neutron and charged particles. **Figures 1.8.2** shows the neutron DDXs calculated at 100 MeV. The experimental data were measured by Kalend et al.<sup>15)</sup> at the proton energy of 90 MeV and by Meier et al.<sup>16)</sup> at 113 MeV. The evaluated results are in good agreement with the experimental data.

The nuclear data for  $^{27}\text{Al}$  for proton- and neutron-incident reactions at the energy region 20 MeV to 1 GeV were evaluated by using the ALICE-F code and systematics. The evaluated results were compiled in the ENDF-6 format, and will be stored in the JENDL High Energy File after a careful evaluation review.

#### References

- 1) Pearlstein S.: J. Astrophys., **346**, 1049 (1989).
- 2) Fukahori T. and Pearlstein S.: Proc. IAEA Advisory Group Meeting on Intermediate Energy Region Nuclear Data for Applications, **INDC(NDS)-245**, p.93 (1990).
- 3) Blann M.: CODE ALICE/85/300, UCID 20169, (1985).
- 4) Blann M.: CODE ALICE/89, private communication (1989).
- 5) Weisskopf V.F. and Ewing D.H.: Phys. Rev., **57**, 472 (1940).
- 6) Blann M. and Vonach H.K.: Phys. Rev., **C28**, 1475 (1983).
- 7) Pearlstein S.: Nucl. Sci. Eng., **95**, 116 (1987).
- 8) Kalbach C.: Phys. Rev., **C37**, 2350 (1988).
- 9) Kalbach C. and Mann F.M.: Phys. Rev., **C23**, 112 (1981).
- 10) Iwamoto A. and Harada K.: Phys. Rev., **C26**, 1821 (1982).
- 11) Sato K., Iwamoto A. and Harada K.: Phys. Rev., **C28**, 1527 (1983).
- 12) Wapstra A.H., Audi G. and Hoekstra R.: Atomic Data and Nuclear Data Tables, **39**, 281 (1988).
- 13) Tachibana T., et al.: Atomic Data and Nuclear Data Tables, **39**, 251 (1988).
- 14) Pearlstein S.: Nucl. Sci. Eng., **49**, 162 (1972).
- 15) Kalend A.M., et al.: Phys. Rev., **C28**, 105 (1983).
- 16) Meier M.M., et al.: "Differential Neutron Production Cross Sections and Neutron Yields from Stopping-Length Targets for 113-MeV Protons", **LA-11518-MS** (1989).

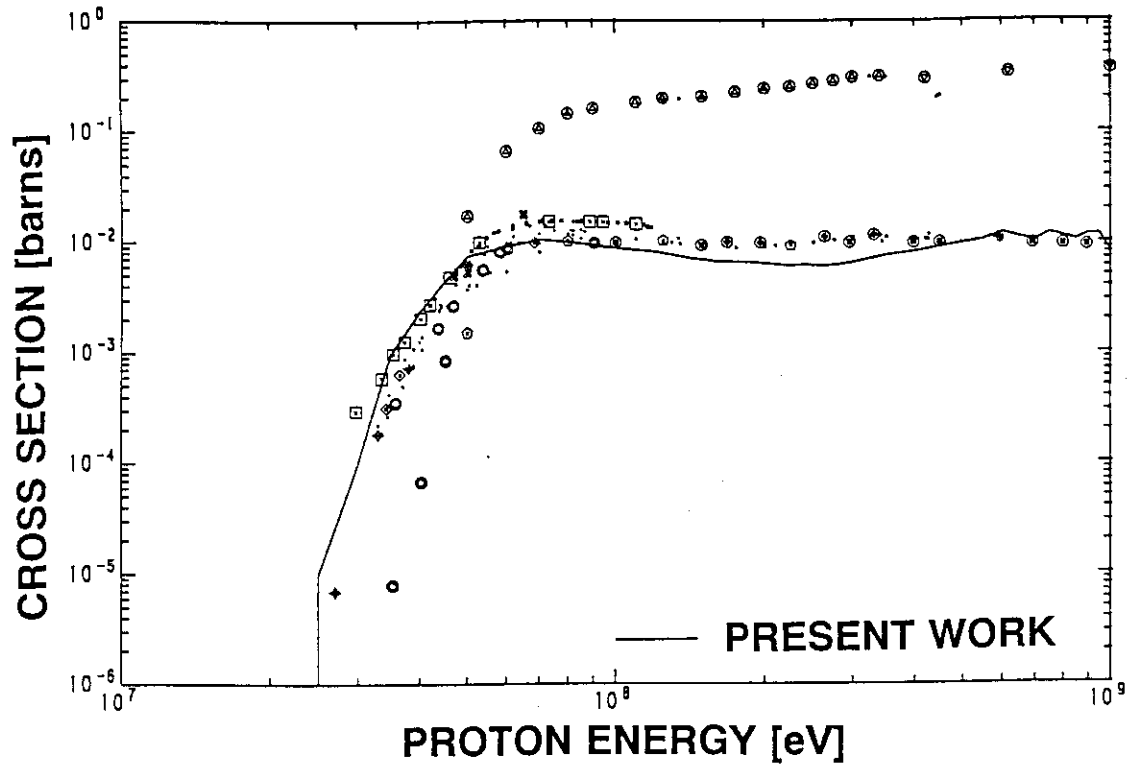


Fig.1.8.1 The  $^{24}\text{Na}$  production cross section of proton induced reaction of  $^{27}\text{Al}$ .

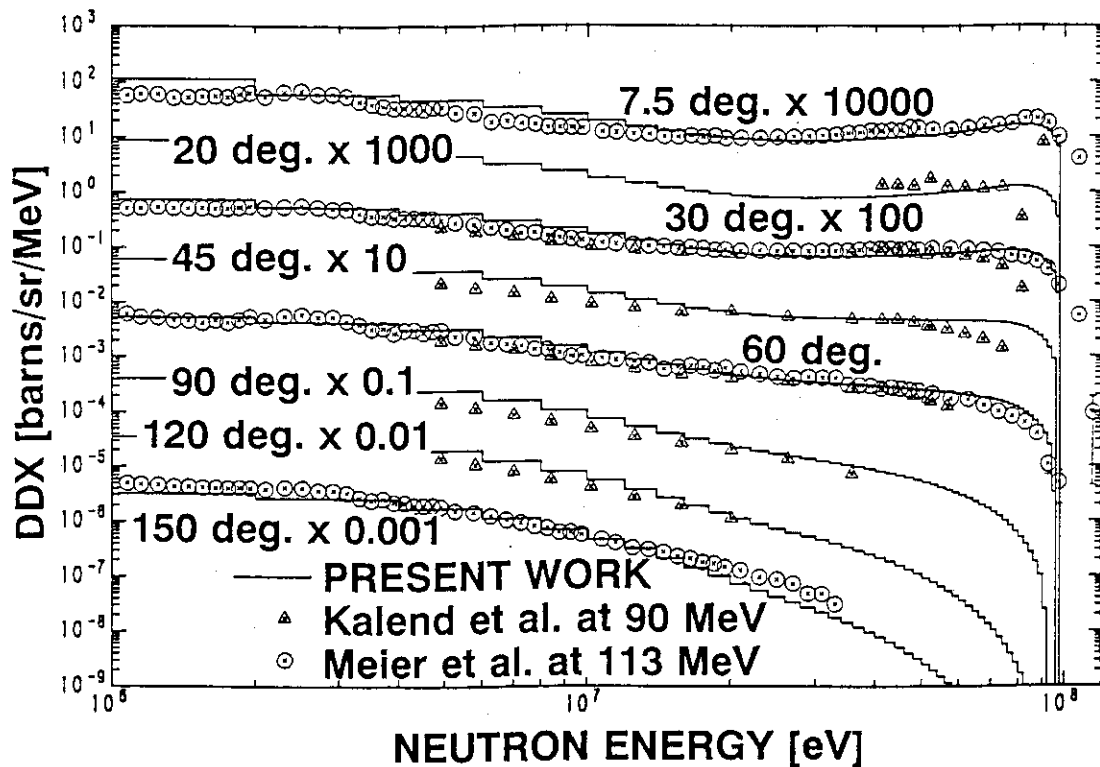


Fig.1.8.2 The double differential neutron emission cross section of  $^{27}\text{Al}$  at the proton energy of 100 MeV calculated from the evaluated result.



## 1.9 Fermi-Gas Model Parametrization of Nuclear Level Density

A. Mengoni<sup>1</sup> and Y. Nakajima

Reliable calculation of nuclear cross sections for basic and applied purposes, for instance in nuclear technology development and astrophysical applications to stellar nucleosynthesis, requires an accurate description of level densities for a broad range of excitation energies and a large number of nuclei.

We furnished a new parametrization of the Fermi-Gas model description of nuclear level densities at excitation energies corresponding to the neutron binding energy.<sup>1)</sup> The model adopted is the standard Fermi-Gas model, which is one of the simplest independent particle models and describes the level density of a set of non-interacting nucleons arranged on a single particle spectrum with equal spacing. In the Fermi-gas model the density of nuclear levels with total angular momentum  $J$  and parity  $\Pi$  is expressed by the following formula<sup>2)</sup>:

$$\rho_{Z,N}(U, J, \Pi) = \frac{\sqrt{\pi}}{12 a^{1/4} U^{5/4}} e^{2\sqrt{aU}} \frac{1}{2 \sigma^2 \sqrt{2 \pi \sigma^2}} e^{-\frac{J(J+1)}{2 \sigma^2}} \frac{1}{2},$$

where  $U$  is the excitation energy,  $\sigma$  the spin cutoff parameter and  $a$  the level density parameter. The level density parameters  $a$  of the model were deduced from reliable s-wave level spacings obtained from neutron resonance spectroscopy. The level density parameters  $a$  thus deduced fluctuate drastically as shown in Fig. 1.9.1. Pairing and shell corrections were applied to the level density parameters to smooth out the nuclear structure effects. The procedure for the evaluation of the corrected level density parameters  $a(*)$  has been applied to a data-base<sup>3)</sup> of 217 nuclei covering a mass range  $41 \leq A \leq 253$  and the results are shown in Fig. 1.9.2. The systematic behavior of the level density parameters  $a(*)$  is more moderate than  $a$ . The systematics of the  $a(*)$  parameter shown in Fig. 1.9.2 can be well described by a smooth function of the mass number  $A$

$$a(*) = \alpha A(1 - \beta A^{-\frac{1}{3}}),$$

---

<sup>1</sup>ENEA, v.le G. B. Ercolani, 8 I-40138 Bologna, Italy

where the two parameters  $\alpha$  and  $\beta$  can be determined from the least-squares fit to the  $a(^*)$  values. From the values plotted in Fig. 1.9.2 we have obtained

$$\alpha = 0.058 \text{ MeV}^{-1} \quad \text{and} \quad \beta = -5.91$$

with root mean square deviation,  $rms = 0.938 \text{ MeV}^{-1}$ . The function allows for a derivation of the level density parameters for nuclei where experimental information is not available.

We also developed a computer program, HERMES, that could provide the quantities usually needed in nuclear level density calculations, level density parameters and the global level density systematics.<sup>4)</sup> HERMES can be obtained upon request to the authors. It contains the program and all the databases necessary to the calculations.

By using the derived systematics we investigated the nuclear properties at the excitation of the neutron binding energy.<sup>5)</sup> The systematics of the level density parameters shows the deformation effects of the nuclei as in the same way as the residual energy in nuclear ground states.

## References

- 1) Mengoni A. and Nakajima Y.: J. Nucl. Sci. Technol., **31**, 151(1994).
- 2) Engelbrecht C.A. and Engelbrecht J.R.: Ann. Phys., **207**, 1(1991).
- 3) Mughabghab S.F., Divadeenam M. and Holden N.E.: "Neutron Cross Sections", Volume 1, Part A, Academic, New York, (1981); Mughabghab S.F.:ibid., Part B, Academic, New York, (1984).
- 4) Mengoni A. and Nakajima Y.: "HERMES: A Personal-Computer Program for Calculation of the Fermi-Gas Model Parameters of Nuclear Level Density", JAERI-M 93-177(1993).
- 5) Mengoni A. and Nakajima Y.: "Nuclear Level Density Parameter Systematics Revisited: Nuclear Deformation Effects", JAERI-M 94-019, P. 337(1994).

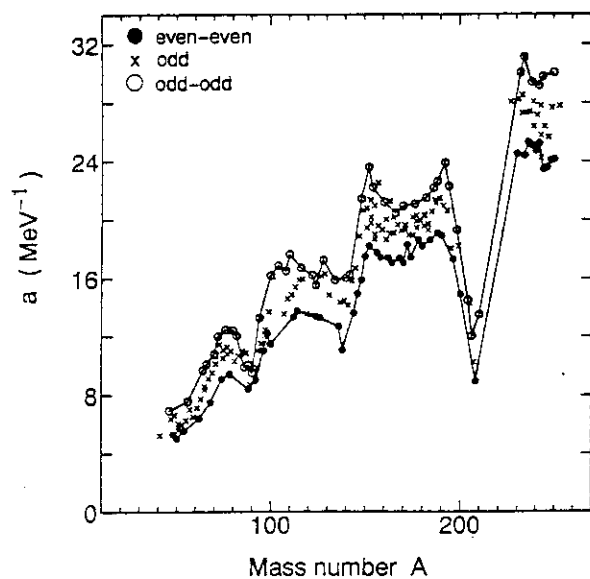


Fig. 1.9.1 Level density parameter

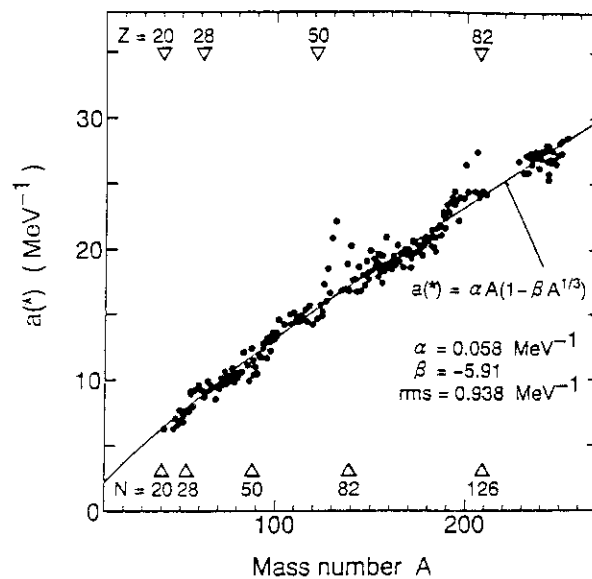


Fig. 1.9.2 Corrected level density parameters and their systematics

## 1.10 Evaluation and Compilation of Nuclear Structure and Decay Data for A=123, 125 and 126

J. Katakura, M. Oshima, K. Kitao\*, H. Iimura, S. Ohya\*\*, T. Tamura\*\*\* and K. Miyano\*\*

The international nuclear structure and decay data network aims at a complete and continuous nuclear structure data evaluation of all mass chains. As the new measurements of nuclear structure and decay data is accumulated continuously, the data are intended to be re-evaluated every 5 to 6 years. The newest evaluated data comprising the currently recommended "best values" of all nuclear structure and decay data are compiled as a data file of Evaluated Nuclear Structure Data File (ENSDF) and published in the Nuclear Data Sheets. The ENSDF file and its bibliographic file Nuclear Structure References (NSR) are the internationally recognized data base for nuclear level schemes, half-lives, decay gamma ray spectra, and so on, of all the known nuclear isotopes.

As a member of the network, Japanese group, whose data evaluation center is Nuclear Data Center, Japan Atomic Energy Research Institute, has responsibility for evaluating 12 mass chains with A=118-129. In the year of 1993, the evaluations of A=123, 125 and 126 mass chains were published in Nuclear Data Sheets.

### A=123<sup>1)</sup>

All data available before January 1, 1993, have been considered for inclusion in this evaluation. The data included in the evaluation are tabulated below.

Nuclide	Data Type	Nuclide	Data Type
<sup>123</sup> Ag	Adopted Levels	<sup>123</sup> Sn	<sup>122</sup> Sn(n,γ)
<sup>123</sup> Cd	Adopted Levels, Gammas		<sup>122</sup> Sn(d,p)
	<sup>123</sup> Ag β <sup>-</sup> Decay		<sup>122</sup> Sn(d,pγ)
<sup>123</sup> In	Adopted Levels, Gammas		<sup>122</sup> Sn(α, <sup>3</sup> He)
	<sup>123</sup> Cd β <sup>-</sup> Decay (2.10 s)		<sup>124</sup> Sn(p,d)
	<sup>123</sup> Cd β <sup>-</sup> Decay (1.82 s)		<sup>124</sup> Sn(p,d) IAR
	<sup>124</sup> Sn(d, <sup>3</sup> He)		<sup>124</sup> Sn(d,t)
	<sup>124</sup> Sn(t,α)		<sup>124</sup> Sn( <sup>80</sup> Se, <sup>80</sup> Se nγ)
<sup>123</sup> Sn	Adopted Levels, Gammas	<sup>123</sup> Sb	Adopted Levels, Gammas
	<sup>123</sup> In β <sup>-</sup> Decay (5.98 s)		<sup>123</sup> Sn β <sup>-</sup> Decay (129.2 d)
	<sup>123</sup> In β <sup>-</sup> Decay (47.8 s)		<sup>123</sup> Sn β <sup>-</sup> Decay (40.06 min)

\* Data Engineering Inc.

\*\* Niigata University

\*\*\* Institute of Radiation Measurements

Nuclide	Data Type	Nuclide	Data Type
$^{123}\text{Sb}$	$^{123}\text{Te}$ $\epsilon$ Decay	$^{123}\text{Te}$	$^{124}\text{Te}(\beta^+\text{He},\alpha)$
	$^{120}\text{Sn}(\alpha,p)$		$^{125}\text{Te}(p,t)$
	$^{122}\text{Sn}(\text{pol } p,p)$ IAR	$^{123}\text{I}$	Adopted Levels, Gammas
	$^{122}\text{Sn}(\beta^+\text{He},d)$		$^{123}\text{Xe}$ $\epsilon$ Decay
	$^{122}\text{Sn}(\beta^+\text{Li},\alpha 2n\gamma)$		$^{121}\text{Sb}(\alpha,2n\gamma), ^{120}\text{Sn}(\beta^+\text{Li},3n\gamma)$
	$^{123}\text{Sb}(\gamma,\gamma')$		$^{122}\text{Te}(p,p')$ IAR
	$^{123}\text{Sb}(n,n'\gamma)$		$^{122}\text{Te}(\beta^+\text{He},d)$
	$^{123}\text{Sb}(d,d')$	$^{123}\text{Xe}$	Adopted Levels, Gammas
	Coulomb Excitation		$^{123}\text{Cs}$ $\epsilon$ Decay
	$^{124}\text{Te}(t,a)$		$\text{Te}(\beta^+\text{He},xn\gamma), ^{110}\text{Cd}(\beta^+\text{O},3n\gamma)$
$^{123}\text{Te}$	Adopted Levels, Gammas	$^{123}\text{Cs}$	Adopted Levels, Gammas
	$^{123}\text{Te}$ IT Decay		$^{123}\text{Cs}$ IT Decay
	$^{123}\text{I}$ $\epsilon$ Decay		$^{123}\text{Ba}$ $\epsilon$ Decay
	$^{122}\text{Te}(n,\gamma)$ E=th		(HI,xn $\gamma$ )
	$^{122}\text{Te}(d,p)$	$^{123}\text{Ba}$	Adopted Levels, Gammas
	$^{123}\text{Sb}(p,n\gamma)$		$^{123}\text{La}$ $\epsilon$ Decay
	Coulomb Excitation		(HI,xn $\gamma$ )
	$^{124}\text{Sn}(\beta^+\text{He},4n\gamma), ^{123}\text{Sb}(d,2n\gamma)$	$^{123}\text{La}$	Adopted Levels, Gammas
	$^{124}\text{Te}(p,d)$		(HI,xn $\gamma$ )
	$^{124}\text{Te}(d,t)$	$^{123}\text{Ce}$	Adopted Levels

$A=125^{2)}$

All data available before March 31, 1992, have been considered for inclusion in this evaluation. The data included in the evaluation are tabulated below.

Nuclide	Data Type	Nuclide	Data Type
$^{125}\text{Cd}$	Adopted Levels, Gammas	$^{125}\text{Te}$	Adopted Levels, Gammas
$^{125}\text{In}$	Adopted Levels, Gammas		Coulomb Excitation
	$^{125}\text{Cd}$ $\beta^-$ Decay (0.65 s)		$^{124}\text{Sn}(\alpha,3n\gamma)$
	$^{125}\text{Cd}$ $\beta^-$ Decay (0.57 s)		$^{124}\text{Te}(d,p)$
$^{125}\text{Sn}$	Adopted Levels, Gammas		$^{124}\text{Te}(t,d)$
	$^{124}\text{Sn}(\alpha, \beta^+\text{He})$		$^{125}\text{I}$ $\epsilon$ Decay
	$^{124}\text{Sn}(d,p)$		$^{125}\text{Sb}$ $\beta^-$ Decay
	$^{124}\text{Sn}(d,p\gamma)$		$^{125}\text{Te}$ IT Decay
	$^{124}\text{Sn}(n,\gamma)$		$^{125}\text{Te}(d,d')$
	$^{125}\text{In}$ $\beta^-$ Decay (12.2 s)		$^{126}\text{Te}(d,t)$
	$^{125}\text{In}$ $\beta^-$ Decay (2.36 s)		$^{126}\text{Te}(\beta^+\text{He},\alpha)$
$^{125}\text{Sb}$	Adopted Levels, Gammas	$^{125}\text{I}$	Adopted Levels, Gammas
	$^{124}\text{Sn}(\text{pol } p,p)$ IAR		(HI,xn $\gamma$ )
	$^{124}\text{Sn}(\beta^+\text{He},d)$		$^{124}\text{Te}(\alpha,t)$
	$^{125}\text{Sn}$ $\beta^-$ Decay (9.52 min)		$^{124}\text{Te}(p,p),(p,p')$ IAR
	$^{125}\text{Sn}$ $\beta^-$ Decay (9.64 d)		$^{124}\text{Te}(\beta^+\text{He},d)$
	$^{126}\text{Te}(d,\beta^+\text{He})$		$^{125}\text{Xe}$ $\epsilon$ Decay
	$^{126}\text{Te}(t,\alpha)$	$^{125}\text{Xe}$	Adopted Levels, Gammas

Nuclide	Data Type	Nuclide	Data Type
$^{125}\text{Xe}$	(HI,xn $\gamma$ )	$^{125}\text{Ba}$	(HI,xn $\gamma$ )
	$^{125}\text{Cs}$ $\beta^+$ Decay		$^{125}\text{La}$ $\beta^+$ Decay
	$^{125}\text{Xe}$ IT Decay	$^{125}\text{La}$	Adopted Levels, Gammas
$^{125}\text{Cs}$	Adopted Levels, Gammas		$^{112}\text{Sn}(^{16}\text{O},2n\gamma)$
	(HI,xn $\gamma$ )		$^{125}\text{Ce}$ $\beta^+$ Decay
	$^{125}\text{Ba}$ $\beta^+$ Decay (3.5 min)	$^{125}\text{Ce}$	Adopted Levels
$^{125}\text{Ba}$	Adopted Levels, Gammas		

**A=126<sup>3)</sup>**

All data available before March 31, 1992, have been considered for inclusion in this evaluation. This evaluation, however, does not include the data which has not changed from the previous evaluation performed in 1982. The data included in the evaluation are tabulated below.

Nuclide	Data Type	Nuclide	Data Type
$^{126}\text{Cd}$	Adopted Levels	$^{126}\text{Xe}$	$^{126}\text{I}$ $\beta^-$ Decay
$^{126}\text{In}$	Adopted Levels, Gammas		$^{126}\text{Cs}$ $\beta^+$ Decay
	$^{125}\text{Cd}$ $\beta^-$ Decay		$^{116}\text{Cd}(^{13}\text{C},3n\gamma)$
$^{126}\text{Sn}$	Adopted Levels, Gammas		$^{123}\text{Te}(\alpha,n\gamma)$
	$^{126}\text{In}$ $\beta^-$ Decay (1.64 s)		$^{126}\text{Te}(^3\text{He},3n\gamma), ^{126}\text{Te}(\alpha,4n\gamma)$
	$^{126}\text{In}$ $\beta^-$ Decay (1.60 s)		$^{127}\text{I}(p,2n\gamma)$
	$^{124}\text{Sn}(t,p)$	$^{126}\text{Cs}$	Adopted Levels, Gammas
	$^{124}\text{Sn}(^{14}\text{C}, ^{12}\text{C})$	$^{126}\text{Ba}$	Adopted Levels, Gammas
$^{126}\text{Sb}$	Adopted Levels, Gammas		$^{126}\text{La}$ $\beta^+$ Decay
$^{126}\text{Te}$	Adopted Levels, Gammas		(HI,xn $\gamma$ )
	$^{126}\text{Sb}$ $\beta^-$ Decay (12.46 d)	$^{126}\text{La}$	Adopted Levels, Gammas
	$^{126}\text{Te}(n,n'\gamma)$		$^{126}\text{Ce}$ $\epsilon$ Decay
	Coulomb Excitation		(HI,xn $\gamma$ )
$^{126}\text{I}$	Adopted Levels, Gammas	$^{126}\text{Ce}$	Adopted Levels, Gammas
	$^{126}\text{Te}(p,n\gamma)$		$^{126}\text{Pr}$ $\beta^+$ Decay
	$^{127}\text{Te}(\gamma,n)$		$^{92}\text{Mo}(^{40}\text{Ca},2p\alpha\gamma)$
	$^{127}\text{I}(n,2n\gamma)$	$^{126}\text{Pr}$	Adopted Levels
$^{126}\text{Xe}$	Adopted Levels, Gammas		

**References**

- 1) Ohya S. and Tamura T.: Nucl. Data Sheets 70, 531 (1993)
- 2) Katakura J., Oshima M., Kitao K. and Iimura H.: Nucl. Data Sheets 70, 217 (1993)
- 3) Miyano K.: Nucl. Data Sheets 69, 429 (1993)

### 1.11 Measurements of Activation Cross Sections at 18-30 MeV by Using the ${}^7\text{Li}(p,n)$ Quasi-monoenergetic Neutron Source at JAERI-TANDEM

Y. Uno, S. Meigo, S. Chiba, T. Fukahori, Y. Kasugai\* and Y. Ikeda

The demands for neutron cross section data above 20 MeV have been increased recently. The experiment of neutron activation cross section measurement by using the  ${}^7\text{Li}(p,n)$  quasi-monoenergetic neutron source with 18-30 MeV has been started at the TANDEM accelerator facility of JAERI.

Protons of 20 and 25 MeV were injected into a thin  ${}^7\text{Li}$  target of 1.4-1.8 mm in thickness cooled by water. The cooling water layer was separated by a 0.1-mm-thick aluminum plate and the protons passing through the  ${}^7\text{Li}$  target are fully stopped in this water layer. The neutron energy spectrum in the forward direction was measured by a TOF method by using an NE213 liquid scintillation detector. The measured neutron energy spectra are shown in Figs. 1.11.1 and 1.11.2. A quasi-monoenergetic peak produced by the  ${}^7\text{Li}(p,n)$  reaction to the ground state and the first excited (0.429 MeV) state of  ${}^7\text{Be}$  was observed. There was a low energy neutron tail corresponding to the breakup of higher excitation states of  ${}^7\text{Be}$ , and to the interaction of protons with the cooling water and the structural materials of the target. The absolute flux of peak neutrons was measured by the proton recoil counter telescope detector. The characteristics of the p-Li neutron source are summarized in the Table 1.11.1. The angular distributions of the peak neutron yield were also measured via the NE213 detector.

The samples of Co, Nb, Cu, Y, Tm, Ti, Ni, Fe, Zr, W, Au and Al were irradiated at the distance of 10 cm from the Li target in the forward direction. After irradiation, gamma-rays of each samples were measured by the HP-Ge detectors and the reaction rates were derived from the measured induced activities. The obtained reaction rates include the contribution from the low energy neutrons. Therefore, the correction for this low energy neutrons is necessary, and the cross section values for the effective peak energy,  $\sigma$ , is calculated as follows:

$$\sigma = R \cdot \frac{\int_{E_{\min}}^{E_{\max}} \sigma_0(E) \cdot \phi(E) dE}{\int_{E_{th}}^{E_{\max}} \sigma_0(E) \cdot \phi(E) dE} \cdot \frac{1}{\phi_{peak}}, \quad (1.11.1)$$

---

\*Department of engineering, Nagoya University.

where  $R$  is the reaction rate,  $\sigma_0(E)$  the cross section taken from a literature,  $\phi(E)$  the measured neutron spectra,  $E_{max}$  and  $E_{min}$  the highest and the lowest energy of the peak neutrons respectively,  $E_{th}$  the threshold energy of the reaction, and  $\phi_{peak}$  the absolute yield of peak neutrons. The measured cross sections of  $^{197}\text{Au}(n,2n)^{196}\text{Au}$  and  $^{27}\text{Al}(n,\alpha)^{24}\text{Na}$  reactions are shown in Figs. 1.11.3 and 1.11.4. The cross section data evaluated by M. Wagner et al.<sup>1)</sup> were used as  $\sigma_0(E)$  in the eq. (1.11.1). The present results showed good agreements with the evaluated data.

#### Reference

- 1) Wagner M., et al. : PHYSICS DATA No. 13-5 (1990)

Table 1.11.1 The characteristics of the p-Li neutron source

Proton energy [MeV]	Thickness of Li [mm]	Mean energy of peak neutrons [MeV]	Peak neutron yield [#/Sr/ $\mu\text{C}$ ]
20	1.8	17.6	$6.05 \times 10^8$
25	1.45	22.7	$9.49 \times 10^8$

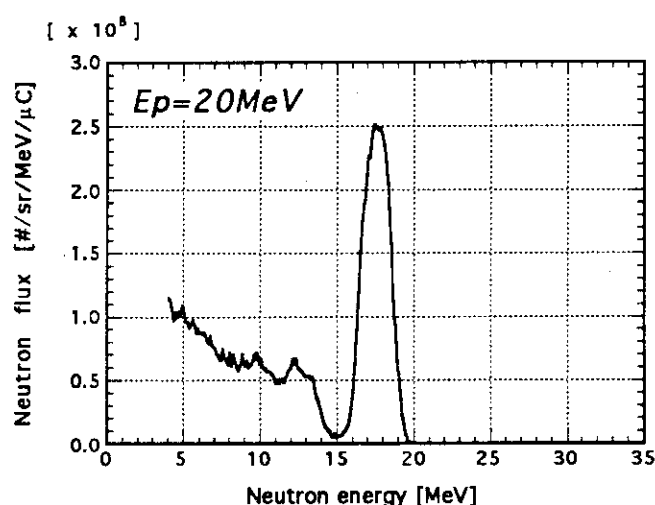


Fig. 1.11.2 Neutron spectrum by 20 MeV protons



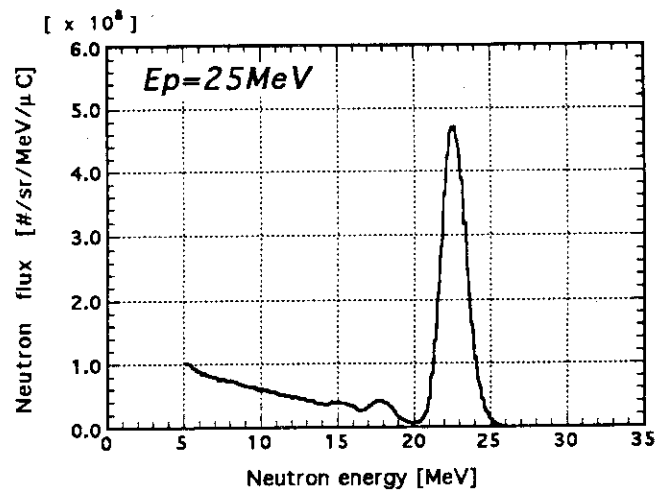
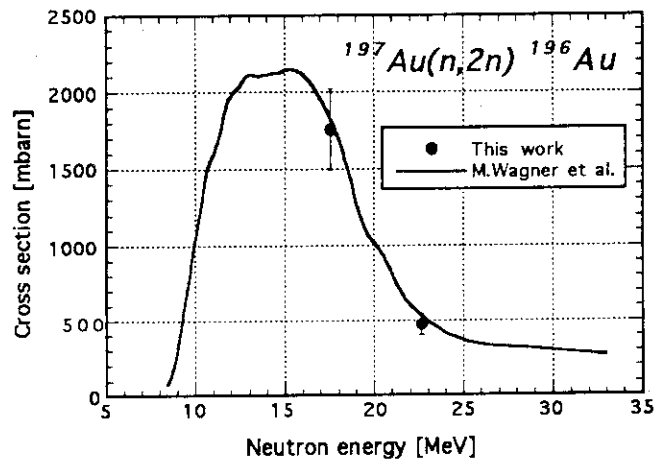
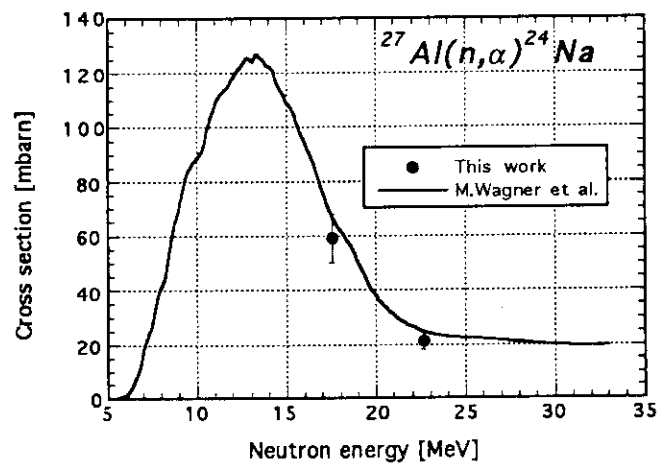


Fig. 1.11.2 Neutron spectrum by 25 MeV protons

Fig. 1.11.3 Cross section of  $^{197}\text{Au}(n,2n)^{196}\text{Au}$ Fig. 1.11.4 Cross section of  $^{27}\text{Al}(n,\alpha)^{24}\text{Na}$

## 1.12 New Measurements of Activation Cross Section for the $^{63}\text{Cu}(n,2n)^{62}\text{Cu}$ and $^{65}\text{Cu}(n,2n)^{64}\text{Cu}$ Reactions at Energy Range of 13.3~14.9 MeV

Y. Ikeda, D.L. Smith\*, Y. Uno, Y. Kasugai\*\*, C. Konno and H. Maekawa

Cross sections for  $^{63}\text{Cu}(n,2n)^{62}\text{Cu}$  and  $^{65}\text{Cu}(n,2n)^{64}\text{Cu}$  reactions have been extensively evaluated based on a large body of available experimental data, and used in many dosimetry applications. In particular, the  $^{63}\text{Cu}(n,2n)^{62}\text{Cu}$  reaction is employed not only in an ordinary foil activation study, but also, as a major detector, in the triton burn-up measurements in D-D plasma diagnostics in fusion devices, e.g., JT-60, TFTR and JET, utilizing its short-lived nature of activity and a high activity yield<sup>1)</sup>. A lot of mutually consistent experimental data for the  $^{65}\text{Cu}(n,2n)^{64}\text{Cu}$  reaction cross section enabled evaluations appreciably accurate. However, we found that the number of experimental data for the  $^{63}\text{Cu}(n,2n)^{62}\text{Cu}$  reaction are not sufficient, exhibiting largely scattered nature in comparison with data for the  $^{65}\text{Cu}(n,2n)^{64}\text{Cu}$  reaction.

In several preliminary experiments on this particular reaction cross sections under the program<sup>2,3)</sup> at the fusion neutronics source FNS, always we obtained appreciably lower value than those evaluations. The present measurement was conducted to provide new experimental data for these cross sections at energy range of 13.3 ~ 14.9 MeV and to investigate the possible source of discrepancies in the previous data for the  $^{63}\text{Cu}(n,2n)^{62}\text{Cu}$  reaction cross section.

The D-T neutrons were generated by bombarding a T target with a  $d^+$  beam of 2 mA and 350 keV at FNS. Two irradiation methods were applied for the short-lived  $^{62}\text{Cu}$  measurements. In the first scheme, natural copper samples of 10 mm in dia. and 0.2 mm thick were deployed at 100 mm from the D-T neutron source at angles of  $0^\circ$  to  $165^\circ$  to the incident  $d^+$  beam. Immediately after 3 min. irradiation, annihilation  $\gamma$ -rays from the Cu sample encapsuled in a 0.8 mm thick lead capsule were counted by a Ge detector. The irradiation was separated into four, and, in each, two samples at different angels were measured successeively. Each sample was measured at least three times at different cooling times in order to reduce the contribution annihilation  $\gamma$ -rays from  $^{64}\text{Cu}$  deacy and to subtract natural background component. Thus, the cross section for the  $^{65}\text{Cu}(n,2n)^{64}\text{Cu}$  was simultaneously obtained. The second scheme employed a pneumatic sample transfer sysetm in order to minimize a counting loss due to the decay of  $^{62}\text{Cu}$ . The ends of the eight tubes were fixed around the D-T source ranging from  $0^\circ$  to  $165^\circ$ . Irradiation and cooling time were 1 min., and 2 to 3 min., respectively. The irradiated Cu samples were exncapsuled with 0.8 mm-thick lead. The counting procedure was the same as in

---

\* Engineering Physics Division, Argonne National Laboratory

\*\* Faculty of Engineering, Nagoya University

the first scheme. In both schemes, for  $^{62}\text{Cu}$  decay, the lead capsule served to stop all energetic  $\beta^+$  ( $Q_{\beta^+} = 3.9 \text{ MeV}$ ) rays in a restricted region to avoid annihilation events far from the sample location. In this sample configuration, self-absorption of  $\gamma$ -ray plays major correction to derive the reaction rate. The component of annihilation  $\gamma$ -rays due to the decay of  $^{64}\text{Cu}$  as well as natural background contribution were subtracted using the decay curves of annihilation  $\gamma$ -rays measured. The neutron flux at the sample was monitored with the Al foils using  $^{27}\text{Al}(n,p)^{27}\text{Mg}$  reactions whose cross section values were calibrated by the  $^{93}\text{Nb}(n,2n)^{92\text{m}}\text{Nb}$  reaction cross section of  $459 \pm 15 \text{ mb}^4$ ). In **Table 1.12.1**, the decay data used in this work are presented.

**Figure 1.12.1** gives the presently measured data along with data in IRDF-90 and the JENDL Dosimetry File. The presently measured data for the  $^{63}\text{Cu}(n,2n)^{62}\text{Cu}$  reaction showed systematically lower than values in the comprehensive evaluations. From experimental consideration, we found that detector efficiency for annihilation  $\gamma$ -rays associated with a high energetic  $\beta^+$  emission tends to be higher than that of ideal point source, resulting in giving systematically larger cross sections. In conclusion, we recommended to re-evaluate this particular cross section for  $^{63}\text{Cu}(n,2n)^{62}\text{Cu}$  reaction. Apparently, the measured data show lower value in the energy range from 14 to 15 MeV. The value exhibits the lower limit in the expanded region encompassed by the previously reported experimental data. From the present extensive investigation for the source of uncertainty, we concluded that the data could not be larger than the present measured value. The measured cross sections for the  $^{65}\text{Cu}(n,2n)^{64}\text{Cu}$  reaction were in good agreement within experimental errors with the data previously measured at FNS<sup>2)</sup> as well as other data in the literature. The comparison of the present data with data in IRDF-90 and the JENDL Dosimetry File is given in **Fig. 1.12.2**. This demonstrated that the experimental procedure was consisted with the previous work, and it assured the validity of the data for the  $^{63}\text{Cu}(n,2n)^{62}\text{Cu}$  reaction, because there should be less uncertainty in the  $\gamma$ -ray self-absorption treatment for the lead capsule.

## References

- 1) Hoek M., Nishitani T., Ikeda Y. and Morioka A. : "Initial Results from Neutron Yield Measurements by Activation Technique at JT-60U," JAERI-M 94-002 (1994).
- 2) Ikeda Y., et al. : "Activation Cross Section Measurements for Fusion Reactor Structural Materials at Neutron Energy from 13.3 to 15.0 MeV Using FNS Facility," JAERI-1312 (1988).
- 3) Konno C., et al. : "Activation Cross Section Measurements at Neutron Energy from 13.3 to 14.9 MeV Using FNS Facility," JAERI-1329 (1993).
- 4) Ikeda Y., et al. : J. Nucl. Sci. & Technol., 30 [9] (1993) 26.
- 5) Browne E. and Firestone R. B. (Shirley V. S., Editor) : "Table of Radioactive

Isotopes" A Wiley-Interscience Publication, John Wiley & Sons (1986).

Table 1.12.1 Decay data used in the present experiment

Item	Reaction	
	$^{63}\text{Cu}(n,2n)^{62}\text{Cu}$	$^{65}\text{Cu}(n,2n)^{64}\text{Cu}$
Half-life	9.74 m	12.7 h
$\gamma$ -ray energy (keV)	511.	511.
$\gamma$ -branching	1.948	0.358
Abundance	0.691	0.309
Atomic mass	63.546	"
$Q_{\beta}$ -value (MeV)	3.949	1.675

Data were taken from Ref-5)

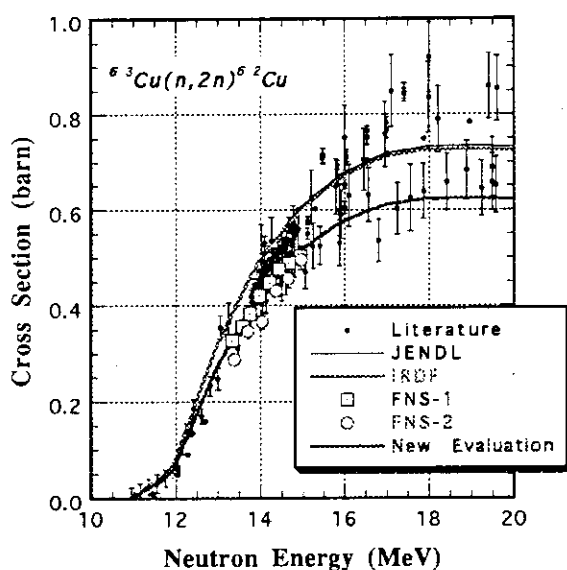


Fig. 1.12.1 Comparison of cross sections for the  $^{63}\text{Cu}(n,2n)^{62}\text{Cu}$  reaction.

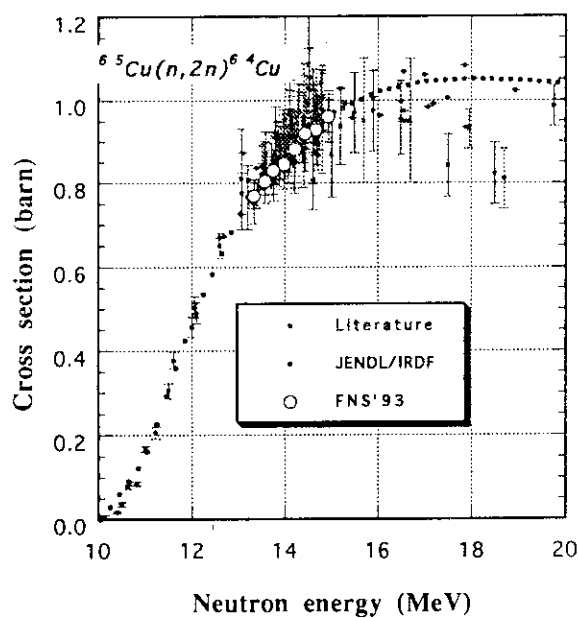


Fig. 1.12.2 Comparison of cross sections for the  $^{65}\text{Cu}(n,2n)^{64}\text{Cu}$  reaction

### 1.13 Measurements of Activation Cross Sections for the $^{187}\text{Re}(n,2n)^{186\text{m}}\text{Re}$ and $^{193}\text{Ir}(n,2n)^{192\text{m}2}\text{Ir}$ Reactions at 14 MeV Energy Region

Y. Ikeda, Y. Kasugai\*, Y. Uno, C. Konno and H. Maekawa

Long-lived radionuclides production by D-T neutrons is the most concern for the radioactive waste consideration of fusion reactors. Not only the major structural materials, but minor or rare impurity level elements create serious problems due to those long-lived characteristics. Thus all possible reaction channels have to be investigated. In order to meet the strong request from fusion reactor development, IAEA-CRP on "Cross Sections for the Generation of Long-Lived Radionuclides of Importance in Fusion Reactor Technology" has been conducted and the significant improvement in data accuracy has been achieved.<sup>1)</sup> There are, however, still lack of substantial data in some reactions, for which it is difficult to be measured due to inherent reasons of low activation yields, low emission probability, and low neutron source strength.

As a framework of the program for activation cross section measurements around 14 MeV at FNS<sup>2,3)</sup>, activation cross sections for the reactions of  $^{187}\text{Re}(n,2n)^{186\text{m}}\text{Re}$  [ $T_{1/2}=2.0 \times 10^5$  y] and  $^{193}\text{Ir}(n,2n)^{192\text{m}2}\text{Ir}$  [ $T_{1/2}=241$  y] at 14.9 MeV were measured. The measurements provided the experimental data to meet the initial purpose of the fusion reactor requirement.

As reported previously in the IAEA-CRP meeting<sup>1)</sup>, these cross sections are of significant difficult to be measured due to inherent low decay rates of low energy  $\gamma$ -rays, and due to existence of large interference activities. As regard to the importance of data for the fusion applications, efforts have been placed on reduction of the background to emerge weak  $\gamma$ -ray lines by using a Compton suppression  $\gamma$ -ray spectrometer.

The samples of Re with natural abundance and  $^{193}\text{Ir}$  with 98 % enrichment were irradiated with 14 MeV neutrons at FNS facility for 32 h and 40 h, respectively. The samples were placed at 2 cm distance from the D-T neutron source in the direction of incident  $d^+$  beam of FNS. The D-T neutron fluxes at these samples were derived from the activation rate of the monitor reaction,  $^{93}\text{Nb}(n,2n)^{92\text{m}}\text{Nb}$ .

The Compton suppression spectrometer consisting of two NaI(Tl) suppressers of 27.6 mm in dia. x 13.8 mm in thickness and a Ge detector. This detector configuration enabled significant reduction of background in the low energy region of interest. The system arrangement is shown in Fig. 1.13.1. The ordinary first-slow coincidence technique was adopted. The effective suppression ratio in the Compton scattering component was around 6. It was found that for the  $\gamma$ -ray sources with higher energy, the suppression ratio increased very

---

\* School of Nuclear Engineering, Faculty of Engineering, Nagoya University,

much. This was due to the detector arrangement with suppresser covering backward of the main Ge detector. As an example, a  $\gamma$ -ray spectrum for the activated Re sample is shown in Fig. 1.13.2. There was, as a result, remarkable suppression of background for the low energy region. Since each radioactivity of interest emits low energetic single  $\gamma$ -rays, there was no need to correct the summing counting loss. However, the detector efficiency calibration was essential. For this purpose, several radioactivities,  $^{47}\text{Sc}$ ,  $^{57}\text{Co}$  and  $^{99}\text{Mo}$ , which emit low energy  $\gamma$ -rays associating with no cascade  $\gamma$ -rays, were prepared by irradiating samples of Ti, Co, Mo. By using these  $\gamma$ -ray sources, the detector efficiency in the  $\gamma$ -ray energy range of 120 ~ 160 keV was determined. After 3.7 year and 1.5 year cooling times for Re and Ir samples, respectively, activities were measured with the Compton suppression spectrometer. The cross sections were derived by using the measured decay  $\gamma$ -ray counts, neutron flux and the other necessary correction factors. In Table 1.13.1, all data needed for the cross section reduction are listed with corresponding errors.

The cross section for  $^{187}\text{Re}(n,2n)^{186\text{m}}\text{Re}$  reaction at 14.9 MeV was obtained for the first time by the direct measurement in this work. The measured cross section of  $445 \pm 156$  mb were compared with a recent calculation by Yamamuro<sup>5)</sup> with SINCROS-II as well as the IRK evaluation<sup>1)</sup>. The measured cross section value was agreed with the calculation and the evaluation within rather large experimental error. As a whole, there was no serious inconsistency among the data. Still more accurate experimental data are strongly requested to give better evaluation.

The half-live of 241 y seems not so long to be measured. However, the spin state of the second isomeric state of  $^{192}\text{Ir}$  is hindering the deexcitement with isomeric transition, resulting in very low  $\gamma$ -ray emission probability. Only one experimental data was reported from China, IAE<sup>1)</sup> for this reaction. Surprisingly, the presently measured data of  $147 \pm 52$  mb was in good agreement with the data of IAE. Although experimental error was reduced significantly by the present experiment, still more accurate data are needed.

## References

- 1) Pashchenko A. B., Ed. :Proceedings of the Second Meeting of a Coordinated Research Program, Del Mar, California, U. S. A., April 29-30, 1993, INDC(NDS)-288, November 1993.
- 2) Ikeda Y., et al. : "Activation Cross Section Measurements for Fusion Reactor Structural Materials at Neutron Energy from 13.3 to 15.0 MeV Using FNS Facility," JAERI-1312 (1988).
- 3) Konno C., et al. : "Activation Cross Section Measurements at Neutron Energy from 13.3 to 14.9 MeV Using FNS Facility," JAERI-1329 (1993).

- 4) Browne E. and Firestone R. B. (Shirley V. S., Editor) : "Table of Radioactive Isotopes" A Wiley-Interscience Publication, John Wiley & Sons (1986).
- 5) Yamamuro N. : "Activation Cross Section Calculations on the Production of Long-Lived Radionuclides," to be published

Table 1.13.1 Sample irradiation, measurement conditions and decay properties

Items	Reactions	
	$^{187}\text{Re}(n,2n)^{186\text{m}}\text{Re}$	$^{193}\text{Ir}(n,2n)^{192\text{m}2}\text{Ir}$
Decay constant (/s)	1.0990e-13	9.1201e-11
Decay Mode	IT + $\beta^-$	IT (100 %)
Sample weight (g)	0.54287	0.09806*
Abundance	0.6293	0.9870*
Neutron flux	2.87e+9 (3.5%)	9.81e+9 (3.5 $\pm$ %)
Irradiation time (s)	2.8446e+5	2.853e+5
Cooling time (s)	1.29429e+8	5.3379e+7
Collection time (s)	4.16524e+5	4.9528e+5
g-ray energy (keV)	137.16	155.16
Detector efficiency	0.211 $\pm$ 0.010	0.188 $\pm$ 0.009
g-ray branching	0.100 ( $\pm$ 1.0 %)	0.00097 ( $\pm$ 4.0%)
counts	382. $\pm$ 130	1020. $\pm$ 352
Atomic mass	186.207	192.9629*

\* Enriched  $^{193}\text{Ir}$  isotope was used.  
Decay data were taken from Ref. 4)

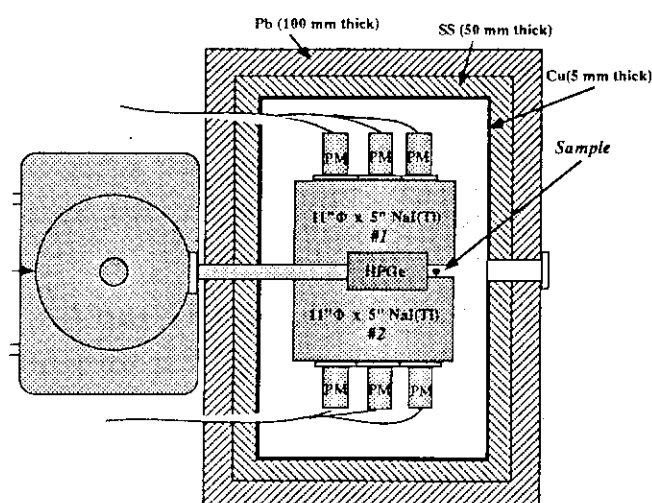
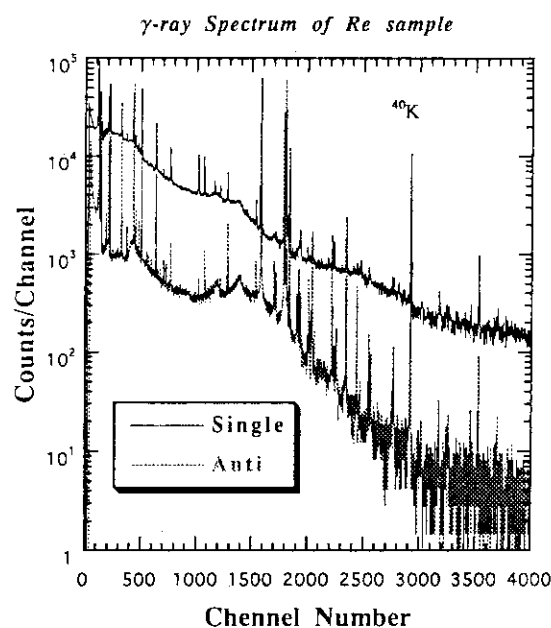


Fig. 1.13.1 Compton suppression spectrometer

Fig. 1.13.2 Measured  $\gamma$ -ray spectrum of the Re sample

### 1.14 Activation Cross Section Measurement of Reactions Producing Short-lived Nuclei at Neutron Energy between 13.4 MeV and 14.9 MeV

Y. Kasugai\*, Y. Ikeda, Y. Uno, H. Yamamoto\*, K. Kawade\* and H. Maekawa

Although many data of activation cross section around 14 MeV neutrons for various isotopes have been reported, there are still a lot of reactions whose cross sections have not been measured yet nor in a reasonable accuracy. In particular, the cross section data for the reactions producing short-lived nuclei are insufficient.

To meet the data needs from fusion application, the cross sections for twelve reactions producing the nuclei with half-lives between 18 s and 29 min. were measured in the energy range between 13.4 to 14.9 MeV by means of the activation method. The reactions investigated are listed in **Table 1.14.1** along with associated decay data and reaction Q-values. The neutrons were generated via the  $T(d,n)^4\text{He}$  reaction by bombarding a T target with  $d^+$  beam of 2 mA and 350 keV by using FNS. Eight pneumatic tubes were used to transport the samples. Separated isotopic samples were irradiated at angles of  $0^\circ$ ,  $45^\circ$ ,  $70^\circ$ ,  $95^\circ$ ,  $120^\circ$ , and  $155^\circ$  in order to cover the neutron energies ranging from 14.9 MeV to 13.4 MeV. The distance between the neutron source and the irradiation positions are 10 cm. The neutron flux at irradiation positions were around  $2 \times 10^8$  n/cm<sup>2</sup>/s. The effective energy of incident neutrons at each irradiation position was determined by the Nb/Zr method. The  $\gamma$ -rays emitted from the irradiated samples were measured with high-pure germanium detectors.

All cross section values were obtained relative to the cross section of the  $^{27}\text{Al}(n,p)^{27}\text{Mg}$  reaction which was determined by referring to the cross section of the  $^{27}\text{Al}(n,\alpha)^{24}\text{Na}$  reaction. Numerical data of the cross sections obtained are given in **Table 1.14.2**. The cross sections of  $^{57}\text{Fe}(n,p)^{57}\text{Mn}$  and  $^{96}\text{Zr}(n,np)^{95}\text{Y}$  reactions are shown in **Figs 1.14.1 and 1.14.2** along with the available experimental data and the evaluated library data. The cross sections of  $^{96}\text{Zr}(n,np)^{95}\text{Y}$ ,  $^{120}\text{Sn}(n,np)^{119\text{m}}\text{In}$  and  $^{180}\text{Hf}(n,p)^{180}\text{Lu}$  reactions were measured for the first time in the present study. For the other reactions, all previous data were obtained at only one energy point except for the reaction of  $^{68}\text{Zn}(n,p)^{68\text{m}}\text{Cu}$  reaction. The present data cover the wider energy range in comparison with the others. Some of the previous experimental and evaluated data are largely discrepant with the presently measured data as shown in **Figs. 1.14.1 and 1.14.2**.

In order to assure the data reliability of the particular (n,p) reaction cross sections with weak data base, the values were compared with the estimations from the empirical formula

---

\* School of Nuclear Engineering, Faculty of Engineering, Nagoya University,



which was derived based on the comprehensive experimental data taken at the FNS and OKTAVIAN facilities<sup>1-5</sup>). The formula is given by,

$$\sigma_{(n,p)}(mb) = \sigma_0 \exp\left(-32 \frac{N-Z+1}{A}\right), \quad (1.14.1)$$

$$\log \sigma_0 = 1.53 + 1.16 \log A - 0.124(\log A)^2,$$

where N, Z and A are the neutron, proton and mass numbers of target nuclei, respectively. The ratios between measured values and estimations are plotted in Fig. 1.14.2. The estimated values agree within  $\pm 30\%$  with the presently measured cross sections. This agreement demonstrates the validity of the present measurement as well as the feasibility of the formula proposed.

#### References

- 1) Kawade K., et al. : "Measurement of Formation Cross Sections of Short-lived Nuclei by 14 MeV Neutrons - Mg, Si, Cl, Cr, Zn, Ga, Y, In -", JAERI-M 90-171(1990).
- 2) Kawade K., et al. : "Measurement of Formation Cross Sections of Short-lived Nuclei by 14 MeV Neutrons - F, Mg, Si, Ti, Cr, Ni, Ga, Rb, Sr, Ag -", JAERI-M 92-020 (1992).
- 3) Kasugai Y., et al. : "Measurement of Formation Cross Sections of Short-lived Nuclei by 14 MeV Neutrons - Ru, Cd, Sn-", JAERI-M 93-124 (1993).
- 4) Ikeda Y., et al. : JAERI 1312 (1987).
- 5) Konno C., et al. : JAERI 1329 (1993).

Table 1.14.1 Reactions and associated decay data

Reaction	T <sub>1/2</sub>	E <sub>γ</sub>	I <sub>γ</sub>	Q(MeV)
<sup>46</sup> Ti(n, p) <sup>46m</sup> Sc	18.70(5) s	142.5	62.0(32)	-1.73
<sup>46</sup> Ti(n, np) <sup>46m</sup> Sc	18.70(5) s	142.5	62.0(32)	-10.60
<sup>57</sup> Fe(n, p) <sup>57</sup> Mn	1.45(3) m	122.1	10.8(9)	-1.91
<sup>68</sup> Zn(n, p) <sup>68m</sup> Cu	3.75(5) m	525.7	75.(15)	-4.39
<sup>74</sup> Ge(n, p) <sup>74m+g</sup> Ga	8.1(1) m	595.9	91.88(14)	-4.58
<sup>76</sup> Ge(n, p) <sup>76</sup> Ga	32.6(6) s	562.9	66.(3)	-5.99
(n, 2n) <sup>75m</sup> Ge	47.7(7) s	139.5	38.8(12)	-9.56
<sup>93</sup> Nb(n, nα) <sup>89m</sup> Y	16.06(4) s	909.2	99.14(<10)	-2.81
<sup>96</sup> Zr(n, np) <sup>95</sup> Y	10.3(2) m	954.1	19.0(21)	-11.52
<sup>100</sup> Ru(n, p) <sup>100</sup> Tc	15.8(1) s	539.5	7.0(7)	-2.42
<sup>120</sup> Sn(n, np) <sup>119g</sup> In	2.4(1) m	763.1	99.08(15)	-10.66
<sup>180</sup> Hf(n, p) <sup>180</sup> Lu	5.7(1) m	408.0	50.0(20)	-2.32

Table 1.14.2 Measured cross sections (mb)

Reactions	Neutron Energy (MeV)					
	14.95	14.66	14.36	14.03	13.70	13.38
$^{46}\text{Ti}(n, p)^{46\text{m}}\text{Sc}$	51(3)	51(3)	51(3)	54(4)	58(4)	59(4)
$^{47}\text{Ti}(n, n'p)^{46\text{m}}\text{Sc}$	10.6(9)	7.6(7)	5.0(6)	2.8(6)	1.8(4)	6.9(3)
$^{57}\text{Fe}(n, p)^{57}\text{Mn}$	53(4)	55(4)	59(4)	59(4)	60(4)	63(7)
$^{68}\text{Zn}(n, p)^{68\text{m}}\text{Cu}$	5.5(13)	----	4.0(12)	----	3.0(8)	4.9(6)
$^{74}\text{Ge}(n, p)^{74\text{m}}\text{Ga}$	12.1(6)	11.8(6)	12.1(6)	10.7(5)	9.1(5)	----
$^{76}\text{Ge}(n, p)^{76}\text{Ga}$	5.4(8)	3.7(6)	----	2.5(6)	2.1(7)	1.7(5)
$^{76}\text{Ge}(n, 2n)^{75\text{m}}\text{Ge}$	958(47)	914(45)	832(41)	794(39)	797(39)	----
$^{93}\text{Nb}(n, n'\alpha)^{89\text{m}}\text{Y}$	2.4(5)	2.1(4)	1.4(3)	1.2(3)	0.8(3)	0.9(3)
$^{96}\text{Zr}(n, n'p)^{95}\text{Y}$	0.52(21)	----	----	----	----	----
$^{100}\text{Ru}(n, p)^{100}\text{Tc}$	35(8)	33(8)	26(7)	18(6)	22(8)	----
$^{120}\text{Sn}(n, n'p)^{119\text{g}}\text{In}$	0.121(19)	----	----	----	----	----
$^{180}\text{Hf}(n, p)^{180}\text{Lu}$	3.2(6)	2.5(5)	2.1(4)	2.0(4)	1.4(3)	0.9(2)

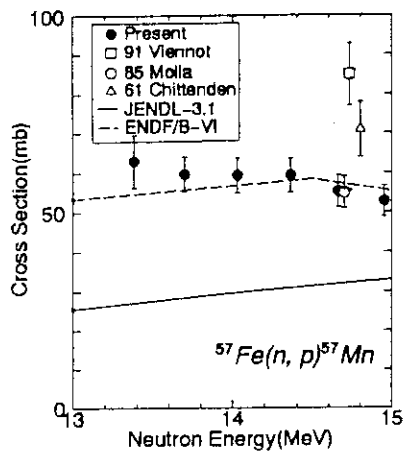
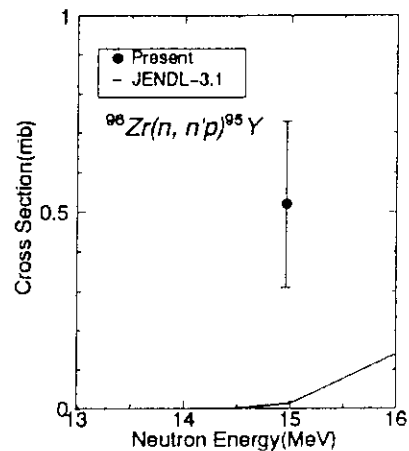
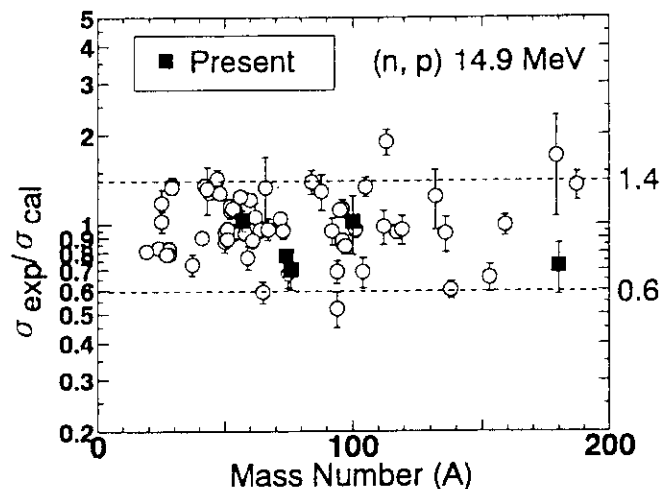
Fig.1.14.1 Cross sections of  $^{57}\text{Fe}(n, p)^{57}\text{Mn}$ Fig.1.14.2 Cross sections of  $^{96}\text{Zr}(n, np)^{95}\text{Y}$ 

Fig. 1.14.2 The ratios of the experimental to calculated cross sections.

## 1.15 Benchmark Tests of JENDL-3.2 for Thermal and Fast Reactors

H. Takano, H. Akie, T. Mori and K. Kaneko\*

JENDL-3.1<sup>1)</sup> was revised on the basis of much feedback information by various benchmark tests<sup>2)</sup>, and the benchmark calculations for the revised version JENDL-3.2<sup>3)</sup> have been performed<sup>4)</sup>.

### Thermal Reactor Benchmark

As thermal critical experiments selected were the uranium fuel cores TRX<sup>5)</sup> and TCA-UO<sub>2</sub><sup>6)</sup> with water moderated lattice of slightly enriched uranium metal and oxide rods, respectively, as plutonium fuel cores TCA-MOX with 3.0 wt% Pu rods. The benchmark calculations were performed with the continuous energy Monte Carlo code MVP and the integral transport code SRAC. Figure 1.15.1 shows the  $k_{\text{eff}}$  values and lattice parameters calculated for the TRX-2 core. The  $k_{\text{eff}}$  value of JENDL-3.2 is increased by 0.5 % compared with that of JENDL-3.1, because the capture resonance integral of <sup>235</sup>U is decreased in JENDL-3.2. The lattice parameters of  $\rho$ -28,  $\delta$ -25 and  $\delta$ -28 are better predicted with JENDL-3.2. The  $k_{\text{eff}}$  values calculated for the TCA with UO<sub>2</sub> rods were slightly overestimated. The  $k_{\text{eff}}$  values of the TCA cores with MOX rods are shown in Fig.1.15.2, and JENDL-3.2 predicts very well the experimental results.

### Fast Reactor Benchmark

Fast reactor benchmark cores consist of various critical assemblies such as the MONJU mock-up core FCA-VI-2, the large LMFBR mock-up core ZPPR-9, the FCA-IX cores with a wide variety of neutron spectrum shapes and very small cores of GODIVA, JEZEBEL and FLATTOP with very hard spectra. The  $k_{\text{eff}}$  values calculated for ZPPR-9 and FCA-VI-2 are 0.9967 and 0.9992, respectively. The results for small cores were as follows: The calculated  $k_{\text{eff}}$  values are slightly underestimated for Pu fueled cores. They are in good agreement with the experiments for <sup>235</sup>U fueled cores and overestimated for <sup>233</sup>U fueled cores. As shown in Fig.1.15.3, the  $k_{\text{eff}}$  values for FCA-IX assemblies which consist of <sup>235</sup>U fueled cores with intermediate spectrum moderated by graphite are improved with JENDL-3.2. Figure 1.15.4 shows the C/E values of sodium void reactivities

---

\*The Japan Research Institute, Ltd., Tokyo

with the increase of voided regions, and they are satisfactory for both of JENDL-3.1 and 3.2. The C/E values of control rod worth were well predicted. As for the C/E values of  $^{239}\text{Pu}$  fission rate radial distribution, and JENDL-3.2 overestimates slightly the experiments in the outer core region.

## References

- 1) Shibata K., et al.: "Japanese Evaluated Nuclear Data Library Version-3, JENDL-3," JAERI 1319 (1990).
- 2) Takano H., et al.: " Benchmark Tests of JENDL-3 for Thermal and Fast Reactors," Proc. Inter. Conf. Physics of Reactors, Marseille, April, Vol.3, PI-21 (1990).
- 3) Kikuchi Y.: "JENDL-3 Revision 2 (JENDL-3.2)," Inter. Conf. on Nuclear Data for Science and Technology, May 9-13, 1994, Gatlinburg.
- 4) Takano H., et al.: "Benchmark Tests of JENDL-3.2 for Thermal and Fast Reactors," *ibid*, (1994).
- 5) " Benchmark Specification," ENDF-202, BNL-10302 (1972).
- 6) Turuta H., et al.: " Critical Sizes of Light-Water Moderated  $\text{UO}_2$  and  $\text{PuO}_2\text{-UO}_2$  Lattices," JAERI 1254 (1978).

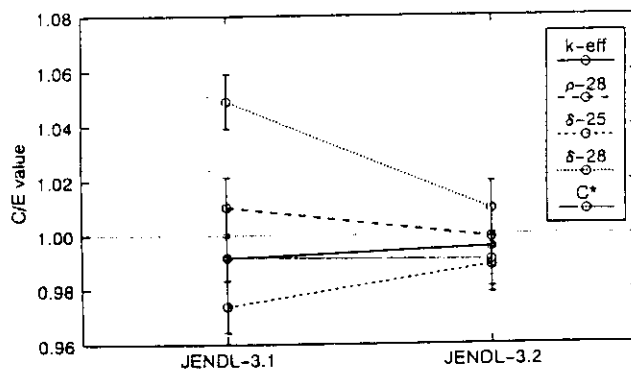


Fig.1.15.1 The C/E values of  $k_{\text{eff}}$  and lattice parameters

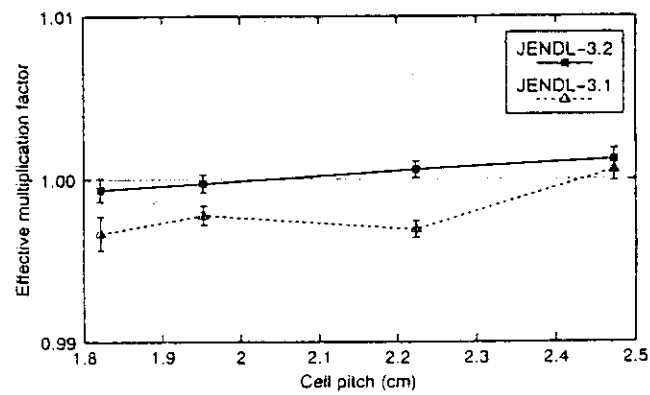
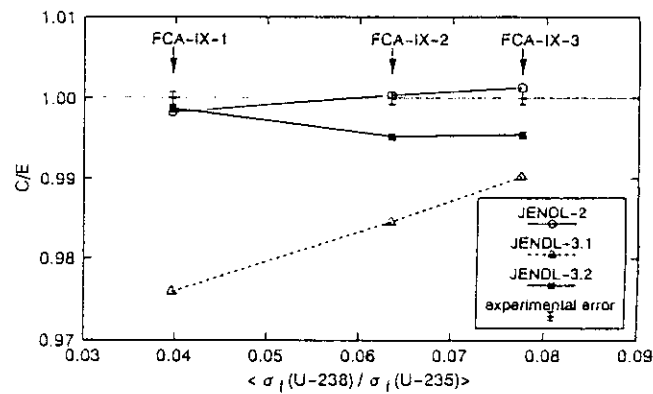
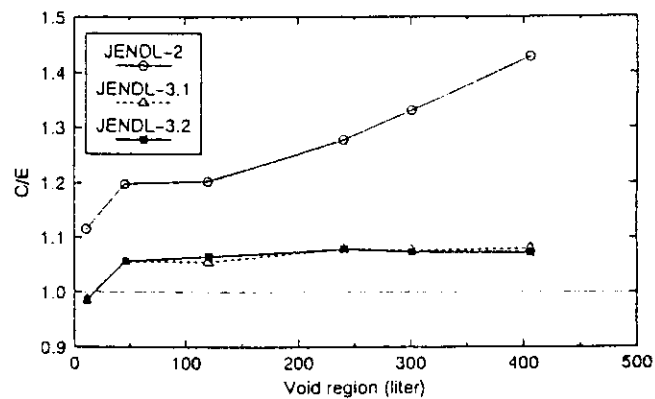
Fig.1.15.2 The  $k_{eff}$  values calculated for TCA-MOX coresFig.1.15.3 The C/E values of  $k_{eff}$  in FCA-IX-1,2 and 3

Fig.1.15.4 The C/E values of Na-void reactivity in ZPPR-9

## 1.16 Mean-field for the Vibron Model: Dipole Moment Function of Diatomic Molecules

A. Mengoni and T. Shirai

Recently, a model based on the Lie algebras has received considerable attention. The model, called the Vibron Model (VM), has been originally proposed for the treatment of rotational and vibrational degrees of freedom of diatomic molecules.<sup>1,2)</sup> As has been the case for an analogous model developed for the treatment of collective excitation of nuclei, the Interacting Boson Model,<sup>3)</sup> the mean-field approximation (MFA) has been applied to the VM in order to give a geometrical picture of an otherwise completely abstract approach.

In this work we have shown the relations necessary to go from the VM Hamiltonian to the potential energy surface as well as from the VM dipole operator to the dipole moment function of single molecular bonds (diatomic molecules). For the dipole moment function, the comparison is made with the up-to-date dipole moment function derived from a combination of *ab initio* and empirical models.

The result of this calculation is shown in Fig. 1.16.1. In this case a comparison is shown with the dipole moment function  $\mu(r)$  of the HF molecule,<sup>4)</sup> where  $r$  is the internuclear distance. The data are a combination of experimentally derived quantities (full dots in the figure) and extrapolations based on Padé approximants (crosses). We can see that the maximum of the dipole moment function coincides approximately with the experimentally derived value. At very large internuclear distances, however, the two models give a noticeable discrepancy. This is due to the fact that the calculations based on phenomenological models, including those shown in Fig. 1.16.1, assume a  $1/r^4$  dependence of  $\mu(r)$  at large  $r$ . The operator introduced here, instead, gives a dipole moment function proportional to  $\sqrt{\exp(-ar)}$  for large  $r$  with a positive constant  $a$ . Even though not immediately apparent, we can expect that an algebraic operator which gives the same large  $r$  behavior can be derived.

The accuracy of the present MFA calculation is comparable with that in an earlier work based on Padé approximants.<sup>5)</sup> To improve the agreement with the data of Ref. 4, additional terms in the dipole operator can be added.

Our analysis of the VM mean-field approximation showed that the relation derived here allows for a link between the real parameter  $\rho$  defining the VM boson condensate and the geometrical variable  $r$ . As far as the dipole moment function is concerned, even though the results of the mean-field approximation can be improved by adding more terms in the dipole operator, we can conclude that the VM dipole moment operator has the proper physical contents and that the general trend of the calculations is reliable.

In the simplest case analyzed here, namely that of a diatomic molecule, the only geometrical variable which has a physical contents is the internuclear distance  $r$ . It is, however, possible to extend the method to the interpretation of the multiple geometrical variables appearing in the description of polyatomic molecules.

#### References

- 1) Iachello F.: Chem. Phys. Lett. **78**, 581 (1981).
- 2) Iachello F. and Levine R. D.: J. Chem. Phys. **77**, 3046 (1982).
- 3) Iachello F. and Arima A.: "The Interacting Boson Model," Cambridge University Press, Cambridge, England, 1987.
- 4) Zemke W. T., et al.: J. Chem. Phys. **95**, 7846 (1991).
- 5) Ogilvie J. F., Rodwell W. R. and Tipping R. H.: J. Chem. Phys. **73**, 5221 (1980).

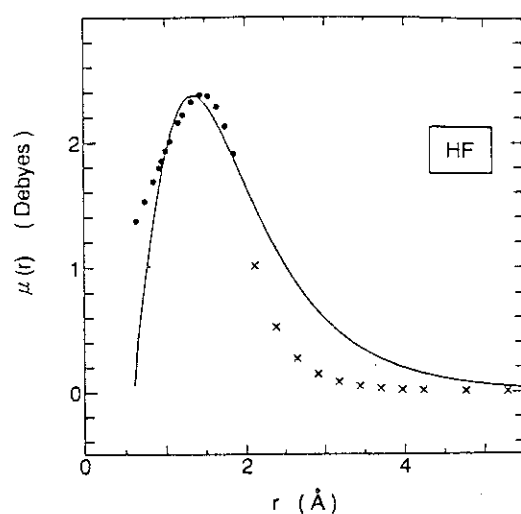


Fig. 1.16.1. Dipole moment functions of HF. The full dots are values derived from the experimental infrared transition matrix elements and the crosses are extrapolation values obtained using the Padé approximants.<sup>4)</sup> Solid line: this work.

### 1.17 Spectral Data and Grottrian Diagrams for Highly Ionized Manganese, Mn VII - Mn XXV

T. Shirai, T. Nakagaki, K. Okazaki\*, J. Sugar\*\* and W. L. Wiese\*\*

We have undertaken publication of a series of compilations of spectra of highly ionized atoms of particular interest to the fusion energy community. These selected elements occur as impurities in wall materials of fusion machines or are specifically injected into the hot plasmas for diagnostics. Much work on these spectra has appeared in recent years. We have critically compiled these data into single monographs for each element, including wavelengths, classifications, intensities, oscillator strengths, radiative transition probabilities, Grottrian diagrams, and a short review of the literature for each ion. Monographs<sup>1-8)</sup> are already published for Ti, V, Cr, Fe, Co, Ni, Cu and Mo. The present compilation contains data for Mn VII to Mn XXV.

All relevant papers on wavelengths and energy levels published through December 1992 were collected and surveyed, and the best measurements, in our judgement, were included in the tables. We consulted the following comprehensive compilations: for wavelengths, the tables by Kelly<sup>9)</sup>, for forbidden lines arising within ground configurations of the type  $ns^2np^k$  ( $n=2$  and  $3$ ,  $k=1$  to  $5$ ), the paper by Kaufman and Sugar<sup>10)</sup> and a review article by Fawcett.<sup>11)</sup>

Sugar and Corliss<sup>12)</sup> have published a comprehensive critical compilation of energy levels for the iron-group elements K to Ni in all stages of ionization. Their values are adopted for this compilation, except where superseded by more recent data. For the He- and H-sequences, only theoretical results are given since they are considered to be more accurate than the experimental values.

For atomic transition probabilities, calculations based on various multi-configurational approximations, including relativistic multi-configuration Dirac-Fock calculations, have been carried out for allowed and forbidden transitions. Brief reviews of such theoretical data are given in the critical data compilation of allowed and

---

\* Institute of Physical and Chemical Research, Wako

\*\* National Institute of Standards and Technology, Gaithersburg



forbidden lines by Martin et al.,<sup>13)</sup> from which the oscillator strength ( $f$ ) and transition probability ( $A$ ) data are taken.

In cases where no experimental wavelength data are available but for which  $f$ -values exist, the quoted wavelengths are calculated from the known energy levels using the Ritz combination principle. The wavelengths are then used to calculate  $A$ -values from the  $f$ -values.

We tabulate  $A$ -values and  $gf$ -values in order to provide a measure of the strengths of the lines. When these data are not available, we list the rough line intensity estimates provided in the literature.

## References

- 1) Mori K., et al.: Atom. Data and Nucl. Data Tables **34**, 79 (1986).
- 2) Shirai T., et al.: J. Phys. Chem. Ref. Data **21**, 273 (1992).
- 3) Shirai T., et al.: J. Phys. Chem. Ref. Data **22**, 1279 (1993).
- 4) Shirai T., et al.: J. Phys. Chem. Ref. Data **19**, 127 (1990).
- 5) Shirai T., et al.: J. Phys. Chem. Ref. Data **21**, 23 (1992).
- 6) Shirai T., et al.: Atom. Data and Nucl. Data Tables **37**, 235 (1987).
- 7) Shirai T., et al.: J. Phys. Chem. Ref. Data **20**, 1 (1991).
- 8) Shirai T., et al.: J. Phys. Chem. Ref. Data **16**, 327 (1987).
- 9) Kelly R.L.: J. Phys. Chem. Ref. Data **16**, Suppl. 1 (1987).
- 10) Kaufman V. and Sugar J.: J. Phys. Chem. Ref. Data **15**, 321 (1986).
- 11) Fawcett B.C.: J. Opt. Soc. Am. B **1**, 195 (1984).
- 12) Sugar J. and Corliss C.: J. Phys. Chem. Ref. Data **14**, Suppl. 2 (1985).
- 13) Martin G.A., Fuhr J.R. and Wiese W.L.: J. Phys. Chem. Ref. Data **17**, Suppl. 3 (1988).

## 1.18 Analytic Cross Sections for Collisions of H, H<sub>2</sub>, He and Li Atoms and Ions with Atoms and Molecules. II

R. Ito\*, T. Tabata\*, T. Shirai and R.A. Phaneuf\*\*

For diagnostics and modeling of plasmas in thermonuclear-fusion research, data on cross sections for inelastic collisions between atoms, molecules and ions, especially of the lightest elements, are important. Barnett<sup>1)</sup> published recommended data on such cross sections for the elements of hydrogen, helium and lithium. To facilitate interpolation, Barnett gave also least-squares Chebyshev polynomial fits to the recommended cross sections as a function of projectile energy. The polynomial fits, however, cannot be used for extrapolation, because they often show physically unreasonable behavior just outside the energy range of the data used. This inconvenience can be removed by using analytic expressions that approximate low-energy and high-energy asymptotic trends.

Green and McNeal<sup>2)</sup> proposed semiempirical expressions for inelastic collision cross sections of hydrogen atoms and ions with gaseous atoms and molecules. By using the same functional forms as the Green-McNeal expressions and some modified forms, Nakai *et al.*<sup>3)</sup> published a number of analytic cross sections for charge transfer of hydrogen atoms ions colliding with gaseous atoms and molecules. Analytic cross sections are also available for the following reactions: charge transfer of hydrogen atoms and ions colliding with metal vapors,<sup>4)</sup> single-electron capture of hydrogen ions leading to specified excited states of hydrogen,<sup>5)</sup> charge transfer of helium atoms and ions colliding with gaseous atoms and molecules,<sup>6)</sup> single-electron capture by multiply-charged ions colliding with H, H<sub>2</sub>, and He,<sup>7)</sup> and ionization of H, H<sub>2</sub>, and He by multiply-charged ions.<sup>8)</sup>

Presently a project of formulating analytic expressions fitted to Barnett's recommended data is in progress. In a previous report,<sup>9)</sup> analytic expressions for the cross sections of the following reactions were given:

- (1) electron capture by H, H<sup>+</sup>, H<sub>2</sub><sup>+</sup>, He<sup>+</sup>, and He<sup>2+</sup> colliding with atoms, molecules, and ions (H, He, Li; H<sub>2</sub>; H<sup>-</sup>, He<sup>+</sup>).

---

\* University of Osaka Prefecture

\*\* Oak Ridge National Laboratory

- (2) electron capture into excited states by  $H^+$ ,  $He^+$ , and  $He^{2+}$ , colliding with atoms and molecules (H, He, Li;  $H_2$ ).

The present report is a sequel to the previous report, and treats the cross sections of excitation and spectral line emission by H,  $H^+$ ,  $He^+$ ,  $He^+$ , and  $He^{2+}$  colliding with atoms and molecules (H, He, Li;  $H_2$ ). The possible error of analytic expressions when they are used for the extrapolation of the recommended data was discussed in the previous report.

## References

- 1) Barnett C.F., "Atomic Data for Fusion Volume 1: Collisions of H,  $H_2$ , He and Li Atoms and Ions with and Molecules," ed. Hunter H.T., et al., Oak Ridge Natl. Lab. Rep ORNL-6086/V1(1990).
- 2) Green A.E.S. and McNeal R.J.: J. Geophys. Res. **76**, 133 (1971).
- 3) Nakai Y., et al.: At. Data & Nucl. Data Tables **37**, 69 (1987).
- 4) Tabata T., et al.: Nucl. Instrum. & Methods **B31**, 375 (1988).
- 5) Tabata T., et al.: "Partial Cross-Sections for Single-Electron Capture of Hydrogen Ions Colliding with Gaseous Atoms and Molecules," Osaka Prefect. Radiat Res. Inst. Tech. Rep. **11** (1990).
- 6) Tabata T., et al.: "Cross Sections for Charge Transfer of Helium Atoms and Ions Colliding with Gaseous Atoms and Molecules," Radiat. Center Osaka Prefect. Tech. Rep. **7** (1987).
- 7) Nakai Y., et al.: Phys. Scr. **T28**, 77 (1989).
- 8) Tabata T., et al.: At. Plasma-Mater. Interact. Data for Fusion **2**, 91 (1992).
- 9) R. Ito, et al.: "Analytic Cross Sections for Collisions of H,  $H_2$ , He and Li Atoms and Ions Colliding with Atoms and Molecules. I," Jpn. Atm. Energ. Res. Inst. Rep. JAERI-M 93-117 (1993).

## 1.19 Radiative Electron Capture In Relativistic Atomic Collisions

A. Ichihara, T. Shirai and J. Eichler\*

Radiative electron capture (REC) is one of the basic processes occurring in relativistic atomic collisions. Differential cross sections for REC from light target atoms to fully stripped heavy ions have been calculated in the impulse approximation. Charge and energy dependence of the cross sections for radiative recombination (RR) with capture into the projectile K shell and the L subshells are presented in order to provide an estimate for the total REC cross sections.

The REC cross sections are estimated as follows: A loosely bound target electron may be regarded as approximately free in a high energy collision. In this limit, REC is identical with RR in which an electron initially moving with the momentum  $-\mathbf{p}_0$  in the projectile frame is captured into a bound state with the simultaneous emission of a photon. The RR is the inverse of the photoelectric effect and can be calculated by detailed balancing. The effect of electron in the target just gives rise to a momentum spread around  $-\mathbf{p}_0$  which is usually taken into account by the Compton profile.

A computer code has been developed to calculate the differential cross sections for the photoelectric effect and for the radiative recombination using exact Coulomb wave functions for the bound and continuum projectile states. The differential REC cross section is obtained by taking an average of the RR cross sections over the Hartree-Fock momentum distributions of electrons in their initial target states.

Figure 1.19.1 shows the angle-differential cross section for K-shell REC in 197 MeV/u  $\text{Xe}^{54+} + \text{Be}$  collision in comparison with the experimental results by Anholt *et al.*<sup>1)</sup> The values of calculated cross section are reduced by a factor of 0.8 for normalization at  $90^\circ$ . This excess of about 20% of the theoretical results over the experimental data is less than the systematic deviation in a recent observation by Stöhlker *et al.*<sup>2)</sup> Aside from the overall normalization, the experimental angular dependence is well reproduced in our calculation.

Figure 1.19.2 gives the K-REC differential cross section for 295 MeV/u  $\text{U}^{92+} + \text{N}$  collision. The contributions from spin-flip and non-spin-flip transitions are indicated

---

\* Hahn-Meitner-Institut Berlin, Germany

separately. In the nonrelativistic theory, the photon emission at forward and backward directions with respect to the electron momentum is forbidden, and the photon angular distribution shows a simple  $\sin^2\theta$  dependence. The present calculation shows pronounced deviations from the  $\sin^2\theta$  dependence owing to the relativistic spin-flip transition.

From the present study we have found that the laboratory angular distribution of K-REC cross section for medium  $Z$ -projectiles like  $\text{Xe}^{54+}$  has the simple  $\sin^2\theta$  dependence with respect to the beam axis as described in the nonrelativistic theory, while that for high- $Z$  projectiles deviates markedly from  $\sin^2\theta$  at forward angles. The importance of the spin-flip transitions, which can not be described nonrelativistically, is also demonstrated.

#### References

- 1) Anholt R., et al.: Phys. Rev. Lett., **53**, 234 (1984).
- 2) Stöhlker Th., et al.: Z. Phys. D, **23**, 121 (1992).

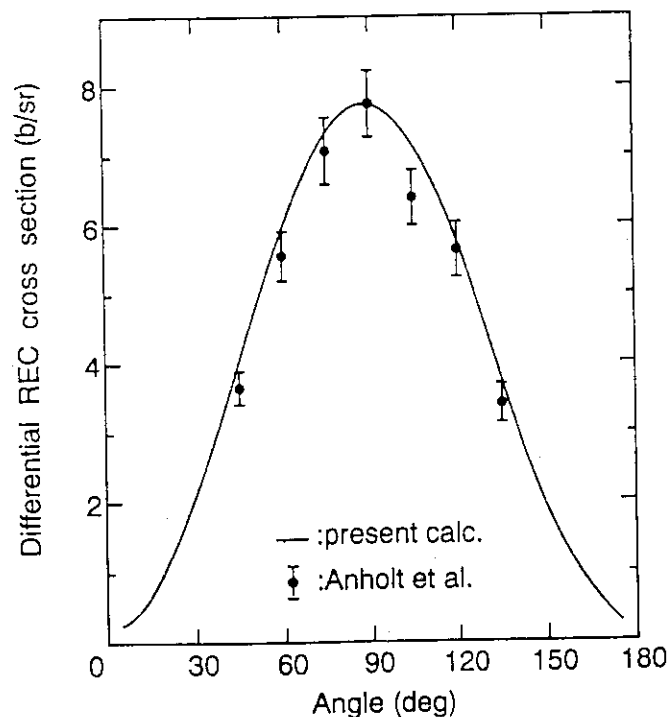


Fig.1.19.1 Differential K-REC cross section for 197 MeV/u  $\text{Xe}^{54+}$  on Be as a function of the laboratory angle. Measured values are from ref.1. Calculated cross section is multiplied with a normalization factor of 0.8.

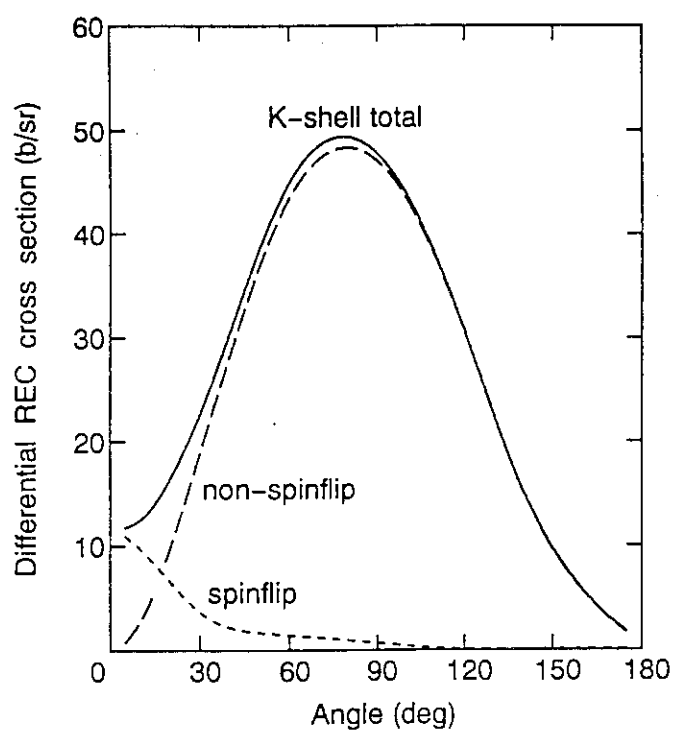


Fig.1.19.2 Differential K-REC cross section for 295 MeV/u  $U^{92+}$  on N as a function of the laboratory angle.

## 2. Theoretical Method and Code Development

Development of vectorized Monte Carlo codes: GMVP working with group cross sections, and MVP working with continuous energy ones has been continued. Effort was concentrated to develop a new module to generate bremsstrahlung photons so that accuracy of a photon reaction model was increased in MVP. A photon transport problem in an iron cylinder was solved. The performance was satisfactory.

For speedup of the above two codes, three types of parallelism were investigated. They are vector parallel by MONTE 4, massive parallel by AP1000, and workstation cluster linked through a network. The speedup efficiency by parallelism is high as far as the number of neutrons per batch per processor is enough large.

The latest version of SRAC: the JAERI thermal reactor standard neutronics design code system was fully released. It included source programs and several versions of cross section libraries. Major modifications done since the publication of the version 1986 are (1) permission of arbitrary temperature of composite materials, (2) several functions in cell burnup, (3) a new geometry for a hexagonal assembly in the CPM package.

A study was performed on the effect of  $(n,2n)$  reaction of minor actinide production above the upper energy limit 10 MeV of the SRAC. Reference calculations by MVP showed the reaction was underestimated by 10 - 15 % under the current group structure.

Successive effort has been devoted to develop the Intelligent Reactor Design System (IRDS). To extend the reactor type studied, several thermal hydraulics modules were newly installed. The window search function became available for neutronics parameters as well as for thermal hydraulics ones. A flow of design process of a lead-cooled fast breeder reactor was demonstrated on a SUN workstation.

A new burnup design code system has been developed. In this frame, a three dimensional (X-Y-Z) nodal diffusion module was developed based on a fourth-order polynomial nodal expansion method with a quadratic transverse leakage approximation. The performance examined in an IAEA benchmark problem was satisfactory. Another module was developed to feed cross section corresponding to arbitrary values of parameters. It will be used in core burnup and 3D kinetics codes. Another effort has been devoted to a nodal diffusion method based on an analytical expression.

The activities described in this chapter are contributed by Reactor System Laboratory.

## 2.1 Bremsstrahlung Photon Emission Model in the MVP Vectorized Continuous Energy Monte Carlo Code

T. Mori, M. Nakagawa and K. Kosako\*

Development of a vectorized continuous energy Monte Carlo code MVP<sup>1)</sup> has been continued. This code achieved a higher computation speed by a factor of 10–20 for coupled neutron–photon transport problems compared with conventional scalar codes.<sup>2)</sup> In the present work, a new module to generate bremsstrahlung photons, which are created by recoil electrons from incoherent Compton scattering, photo–electrons and so on, has been developed to increase accuracy of a photon reaction model in the MVP code.

The bremsstrahlung photon emission model of MVP consists of the following two steps: (1) generation of electrons/positrons by photon interactions with materials, and (2) bremsstrahlung photon emission by each electron or positron. At the first step, each photon creates one of an electron–positron pair, a Compton recoil electron and a photo–electron sometimes together with an auger electron. The generated electron and positron have the same weight as that of a parent photon and are emitted with an energy and a flight direction probabilistically selected on the basis of the physics model used in the ITS code<sup>3)</sup>. At the second step, the MVP code produces bremsstrahlung photons by applying the thick target approximation used in ITS<sup>3)</sup> to each electron or positron. The child photons are emitted with the same weight and flight direction with a parent electron (or positron). The number of emitted photons is determined by using bremsstrahlung cross sections.

Computation tasks for these two steps to generate bremsstrahlung photons have been fully vectorized and implemented as child–tasks which are started by the main task of collision analysis of photons. For the first task of electron/positron emission, the MVP code makes four temporary substacks for photons creating: (1) an electron–positron pair, (2) a Compton recoil electron, (3) a photo–electron and (4) an auger electron. Photons in each substack are independently processed to generate electrons or positrons. On the other hand, the generation of bremsstrahlung photons is simultaneously carried out for all electrons and

---

\*NEDAC, Nuclear Energy Data Center



positrons created by the first task.

To evaluate performance of the present module, we solved a photon transport problem in an iron cylinder of 20 cm radius and 20 cm thickness into which 8.25 MeV mono-directional photons enter. The result and the performance of MVP are compared with those of MCNP 4<sup>4)</sup> in Table 2.1.1. The computation speed of the MVP code strongly depends on the batch size which corresponds to the number of particles simultaneously tracked and proportional to the vector length of operations. With the batch size of 20,000, the computation speed of the MVP code is higher by a factor of about 36 compared with the MCNP 4 code.

#### References

- 1) Mori T., Nakagawa M. and Sasaki M.: J. Nucl. Sci. Technol. 29, 325 (1992).
- 2) Mori T., Nakagawa M. and Sasaki M.: JAERI-M 93-181, p.24, (1993).
- 3) Halpleib J.A., et al.: SAND 84-0573 ( or CCC-467) (1984).
- 4) "RSIC Computer Code Selection, MCNP 4," CCC-200A/B (1991).

Table 2.1.1 Comparison of performance between MVP and MCNP

	MVP		MCNP
	Batch size	2,000 20,000	---
Generated bremsstrahlung photons/source-photon		3.7	3.6
CPU time /total generated photon <sup>1)</sup> (μs)		16.5 8.27	296.
Ratio of computation speed		17.9 35.8	1.0

- 1) Generated photons = Source photons + Bremsstrahlung photons +  
Fluorescence photons + Annihilation photons

## 2.2 Parallel Computation by Monte Carlo Codes GMVP and MVP

M. Nakagawa, T. Mori, M. Sasaki\* and K. Suzuki\*\*

In order to speedup computations of neutron and photon transport, we have developed two codes, GMVP<sup>1)</sup> and MVP<sup>2)</sup> based on the multigroup and continuous energy models, respectively. They realized the speedup by a factor of about 15 compared with the conventional Monte Carlo codes. As another method for speedup, the parallel computation has high possibility as well known. We have investigated three types of parallelism by modifying them and evaluated their performance. Those are vector parallel, massive scalar parallel and workstation cluster linked on a network. Since both codes are programmed on the basis of the event based algorithm, it is rather simple to convert the programs for parallel machines.

### Parallel Computers Used

Vector parallel: MONTE4 at JAERI ( equivalent to NEC SX3 ) was used. This has 4 parallel vector processors and a shared core memory. Some additional pipelines are installed in MONTE4 but not used at the present work. OS is UNIX.

Massive parallel: The AP1000 parallel computer developed by Fujitsu was used. This consists of 1 ~ 512 RISC processors which are connected by a torus type network. Each processor has 16MB distributed memories.

Workstation cluster: Several workstations ( HP9000/720, HP9000/732, DECAXP3000 ) connected to Ethernet were used. The PVM software package was installed for parallel computations.

### Performance Evaluation

The performance of MVP on MONTE4 is shown in Table 2.2.1 for eigenvalue problems. The problem 1 is a whole core calculation of a PWR<sup>3)</sup> and 2 is a fast reactor fuel subassembly

---

\* The Japan Research Institute, Ltd, Tokyo

\*\* Fujitsu Ltd., Chiba

calculation. The speedup by FACOM VP2600 is achieved by vectorization and that on MONTE4 is through vectorization and parallelism and so the products of two factors give a total speedup factor for MONTE4. Since VP2600 has 4 pipeline sets, the vectorization efficiency is high. The speedup efficiency by parallel computation of MONTE4 is about 90%. The total speedup of MONTE4 is larger for the problem 1 and comparable for the problem 2 compared with VP2600. In the case of a fixed source problem, the speedup factor depends strongly on a problem type. Selection of a batch size is an important parameter because the vectorization efficiency is proportional to it but the parallel efficiency is not necessarily proportional due to the present algorithm, especially for a problem with a large number of zones.

Parallel efficiency of GMVP by AP1000 is shown in Fig.2.2.1 where an eigenvalue problem is solved. The total number of neutrons is 520 000 and a batch size is 16 000 which is equally divided to each processor and so the number of neutrons per batch per processor decreases with increase of the number of processors. If the number of particles decreases per batch, the fraction of overhead time increases and it reduces the efficiency as observed in the figure. If the total number of neutrons increases by 10 times, the parallel efficiency becomes about 100% which is an ideal value. A similar trend was observed for the MVP calculations for a fast reactor subassembly problem.

Parallel computations were performed using three workstations described above. A job (fast reactor subassembly calculation) is divided into 4 tasks and two tasks were carried out by HP9000/732 because its computation speed is highest among them. PVM is flexible in dividing tasks to parallel virtual machines. The estimated speedup factor of HP9000/720 is about a factor of four, so it is almost an ideal value. From this result, we can say that workstation cluster shows high performance when the number of machines is several. However, some traffic problems may happen on a network when the number of machines increase. The present investigation shows that both parallel versions of GMVP and MVP have high parallel efficiency about 70 ~ 100%. Further speedup could be expected by changing algorithm of a learning process on neighboring zones at the initial particle tracking.

## References

- 1) Nakagawa M., Mori T. and Sasaki M.: Nucl. Sci. Eng., 107, 58(1991)

2) Mori T., Nakagawa M. and Sasaki M.: J. Nucl. Sci. Technol., 29, 325(1992)

Table 2.2.1 Speedup of MVP by vector parallel computations on MONTE4

	cpu/ $10^4$ particles		Speedup by vector		Parallel	Total <sup>c)</sup>
	VP2600	MONTE4	VP2600	MONTE4	MONTE4	MONTE4
Prob.1 <sup>a)</sup>	7.36	5.7	12	5.0	3.6	18.2
Prob.2 <sup>b)</sup>	18.8	21.	18	4.9	3.8	18.7

<sup>a</sup> whole core calculation of a PWR (56 000 fuel pins)

<sup>b</sup> fast reactor fuel subassembly calculation (91 fuel pins)

<sup>c</sup> speedup factor by vector parallel computations using 4 cpus

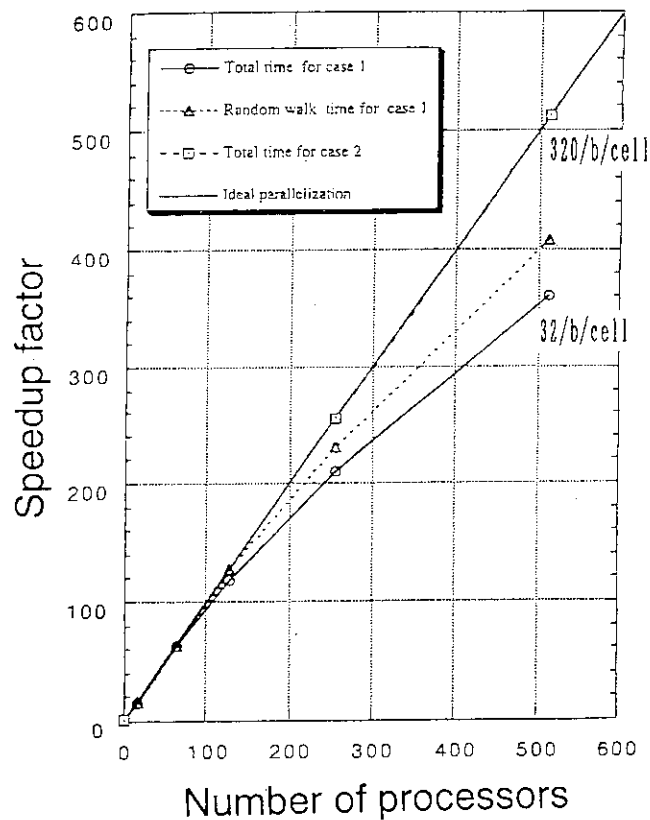


Fig.2.2.1 Speedup of GMVP by massive parallel computations on AP1000

## 2.3 Improvement of SRAC Code

– A Version to Allow Arbitrary Temperature Treatment and Release of the Latest Version SRAC93 –

T. Kugo, K. Tsuchihashi, H. Akie, H. Takano and K. Kaneko\*

A new version of the SRAC code has been developed to allow arbitrary temperature of composite materials for thermal scattering matrices and resonance absorption. Formerly calculations for thermal scattering were restricted to use any of the tabulated temperatures. Now the information of material specifications described in the section II.8 of the SRAC manual<sup>1)</sup> is used to specify the temperature. Interpolation is done by using the Lagrangian three point interpolation formula<sup>2)</sup>,

$$\begin{aligned}\sigma(T) = & (T - T_2)(T - T_3) \sigma(T_1) / (T_1 - T_2)(T_1 - T_3) \\ & + (T - T_1)(T - T_3) \sigma(T_2) / (T_2 - T_1)(T_2 - T_3) \\ & + (T - T_1)(T - T_2) \sigma(T_3) / (T_3 - T_1)(T_3 - T_2),\end{aligned}$$

where

$T$  : the specified temperature ,

$T_2$  : the nearest temperature to  $T$  in the tabulated temperatures ,

$T_1, T_3$  : the neighbouring temperatures of  $T_2$  among the tabulated temperatures .

Formation of resonance cross section of the specified temperature is executed. The algorithm to prepare cross sections for hyper-fine energy structure in resonance energy range is changed in the PEACO routine. The hyper-fine group cross sections of the fixed temperature of 300K are stored on MCROSS file. Doppler broadened cross sections are calculated on the specified temperature by using the SIGMA1 routine<sup>3)</sup> called from the PEACO routine and written on scratch UMCROS (user's MCROSS) file. This modification has reduced a large amount of data storage for the libraries and permitted the storage of various nuclides of minor actinides (MAs) and fission products (FPs) into the libraries. Consequently the accuracy has been improved in the burnup calculation where MAs and FPs are significant to burnup characteristics such as high conversion light water reactors.

---

\*The Japan Research Institute, Limited, Tokyo

In addition to this modification, a number of additions and modifications have been made and consequently we released the latest version SRAC93. Major points of the modifications are as follows:

(1) Several new functions related to cell burnup are installed.

- A kind of sensitivity calculation along a series of cell burnup calculations is available without repeating the input by burnup step. It is achieved by a combination of the modified input data of the standard case and the fixed nuclide densities obtained at each burnup step of the standard case.
- Additional edit such as changes of metallic weight by heavy nuclide and instantaneous conversion ratio is prepared.
- Burnup under fixed flux level.
- Inclusion of trans-plutonium isotopes in several new burnup chains.

(2) Dancoff correction factor by Tone's method<sup>4)</sup> is available. This method is expected to be effective for plate type fuel cell such as FCA, KUCA and so on, where a resonant nuclide exists in several composite materials with different number densities. However, it is not effective for normal pin type fuel cell.

(3) A new geometry of a hexagonal assembly is added to the collision probability package. The geometry is divided by triangular mesh and trapezoidal mesh near the outer boundary. Pin rods can be positioned at any grid point of triangular mesh. Size and composition of every pin do not have to be identical. This geometry can be used for assemblies of the hexagonal shape and of triangular pin rod arrangement such as those of HCLWR, LMFBR and pin-in-block type HTGR.

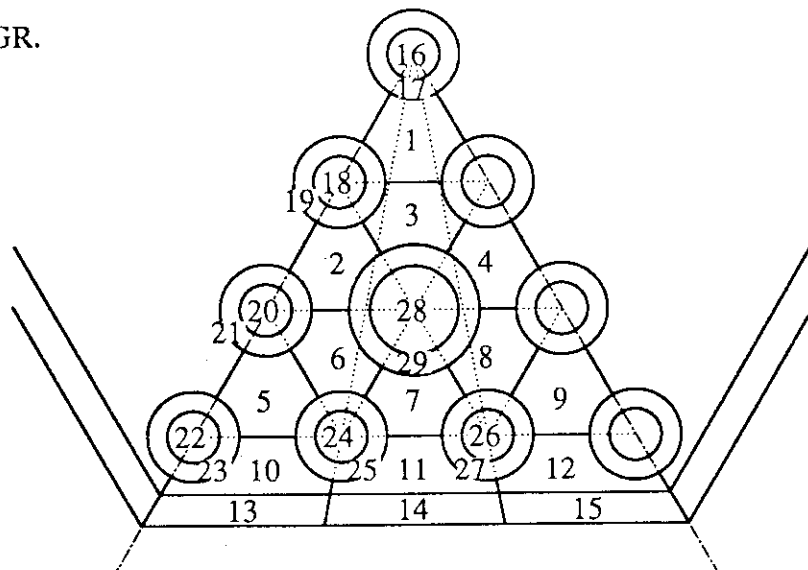


Fig.2.3.1 Hexagonal assembly with triangular pin rod arrangement

- (4) One point reactor calculation after an eigenvalue cell calculation is available.
- (5) Specification of neutron spectrum used for average of fission spectrum in a mixture is available. Formerly it was done using the asymptotic spectrum.
- (6) Use of large scale core memory for temporary storage of data was intended to reduce the I/O of the member repeatedly used from/into the Partitioned Data Set (PDS) files.
- (7) An engineering workstation (EWS) version SRAC-EWS has been developed. A main effort for SRAC-EWS has been paid for a PDS file management so as to reduce elapsed time by I/O from/into disk device. Use of a direct access file organization for PDS files required intolerable elapsed I/O time. Then, we have applied a sequential access file organization for the PDS file in addition to a large scale core memory for a temporary storage of data. In the sequential file organization, we use a tree structure of directories which was permitted by the UNIX OS, and can manage the data storage like PO file as follows:

[FACOM MSP-OS]		[EWS UNIX-OS]	
<u>File</u>	<u>Member</u>	<u>Directory</u>	<u>File</u>
		PDSFNAME / CNTL	
PDSFNAME.DATA (MEMBER01)		⇒ PDSFNAME / MEMBER01	
PDSFNAME.DATA (MEMBER02)		PDSFNAME / MEMBER02	
PDSFNAME.DATA (MEMBER03)		PDSFNAME / MEMBER03 .	

The application of the sequential file organization reduced the I/O time by a factor of five in comparison with the direct access file organization. The routines for the PDS file management were described in the Fortran language, and therefore, the compatibility was increased by this change.

## References

- 1) Tsuchihashi K., et. al.: "Revised SRAC Code Syetem", JAERI 1302 (1986).
- 2) Scarborough J. B.,: "Numerical Mathematical Analysis", The Johns Hopkins Press, Baltimore (1962).
- 3) Cullen D.E.,: "Program SIGMA1:Doppler-Broardened Evaluated Cross Sections in the Evaluated Nuclear Data File/Version B(ENDF/B) Format", UCRL-50400, Vol.17, Part B, Rev. 2 (1979).
- 4) Tone T.,: "A Numerical Study of Heterogeneity Effects in Fast Reactor Critical Assemblies", J. Nucl. Sci. Technol., 12(8), 467 (1975).

## 2.4 Effect of (n,2n) Cross Section on Minor Actinide Production in the SRAC System

H. Akie and H. Takano

For the estimation of minor actinides (MAs) production and transmutation characteristics in a new type reactor, whose neutron spectrum is unknown, it is necessary to use a spectrum calculation code such as the SRAC system. In the SRAC system, however, all the reactions are calculated with the upper energy limit of 10MeV, while a part of (n,2n) reaction is included in the energy region above 10MeV. It means that the SRAC system underestimates the (n,2n) reactions and the production rate of MAs such as Np-237, which is mainly produced through the (n,2n) reaction of U-238. For this reason, it was studied that the effect of the (n,2n) reactions above 10MeV on the production rate of MAs.

Unit pin cell calculations were carried out for the cell model of MOX fueled PWR and also of UO<sub>2</sub> fueled conventional PWR. The cell model of MOX fueled PWR is that of NEANSC benchmark calculation for plutonium recycling<sup>1)</sup> with "dirty" Pu composition. The conventional PWR data used are the results of isotope composition analysis of the spent fuels of the plants Genkai-1 and Mihama-3<sup>2)</sup>. The cell calculations were first carried out by using the continuous energy Monte Carlo code MVP with the upper energy limit of 20MeV. Two kinds of (n,2n) cross sections of the upper energy limit of 10 and 20MeV were evaluated from the result. Cell burnup calculations were next executed by SRAC with and without considering the contribution from the energy range between 10 and 20MeV.

Table 2.4.1 shows the (n,2n) cross sections of U-238 evaluated for the "dirty Pu" cell by using the JENDL-3.1 nuclear data library. In this table, the (n,2n) cross sections at 50GWd/t was calculated with the simulated fuel composition of 32 isotopes, which are included in the MVP cross section library. In the high temperature calculations, the MVP library of 900K are available only for U-235 and U-238. From this table, it is observed that about 15% of the U-238 (n,2n) reaction takes place in the energy range from 10 to 20MeV in this cell. The percentage does not depend on either the fuel burnup rate or temperature.

Taking into account the effect of (n,2n) reaction above 10MeV by multiplying the (n,2n) cross section by the factor evaluated above, a cell burnup calculation was performed by using SRAC. The result was compared with the original SRAC result of 10MeV upper energy limit. The Np-237 number densities of the two cases are compared in Fig. 2.4.1. There



can be seen about 9% difference in the density of Np-237 at 50GWd/t. In the same manner as the "dirty Pu" cell, cell calculations were made for the conventional PWR cell. The effect on the (n,2n) cross sections of both U-238 and Pu-239 was examined and it is about 12%. The calculation/experiment (C/E) ratios of Np-237 and Pu-238 amounts in the PWR cell are shown in Fig.2.4.2 and 2.4.3. The difference is about 2~3% of Np-237 amount between the two cases of (n,2n) cross sections with energy limits of 10 and 20MeV. There is also the effect on the amount of Pu-238 by about 2~5%. As a result, when the (n,2n) cross section is considered up to 20MeV, it improves the calculation accuracy of Np-237 and Pu-238 amount. From these results, it can be concluded for the accurate estimation of MA production that the SRAC system is necessary to calculate the (n,2n) reactions with the upper energy limit of higher than 10MeV.

#### References

- 1) Vergnes J., Wiese H.W. and Schlosser G. : "Benchmark Specification for Plutonium Recycling in PWRs", NSC/DOC(93)19, OECD Nuclear Energy Agency, Nuclear Science Committee (1993).
- 2) Naito Y., Kurosawa M. and Kaneko T. : "Databook of the Isotopic Composition of Spent Fuel in Light Water Reactors", JAERI-M 93-061, Japan Atomic Energy Research Institute, pp.162-170 (1993)(in Japanese).

Table 2.4.1 U-238 (n,2n) cross sections in the "dirty Pu" cell of NEANSC benchmark

Fuel Temp.	Code	Energy Range	$\sigma(n,2n)(\times 10^{-3}\text{barn})$	
			0GWd/t	50GWd/t <sup>1)</sup>
300K	MVP	$\leq 20\text{MeV}$	$5.89 \pm 2.4\%$	$5.85 \pm 2.5\%$
		$\leq 10\text{MeV}$	$5.02 \pm 2.5\%$ (0.852) <sup>3)</sup>	$4.98 \pm 2.4\%$ (0.851)
	SRAC	$\leq 10\text{MeV}$	4.75	4.76
900K <sup>2)</sup>	MVP	$\leq 20\text{MeV}$	$5.71 \pm 2.5\%$	$5.62 \pm 2.1\%$
		$\leq 10\text{MeV}$	$4.87 \pm 2.6\%$ (0.853)	$4.75 \pm 2.2\%$ (0.845)
	SRAC	$\leq 10\text{MeV}$	4.80	4.80

1) : Simulated fuel composition with 32 isotopes was used.

2) : Data of 900K are available only for U-235 and U-238 in MVP library.

3) : In parentheses is shown the ratio of the cases  $\leq 10\text{MeV} / \leq 20\text{MeV}$ .

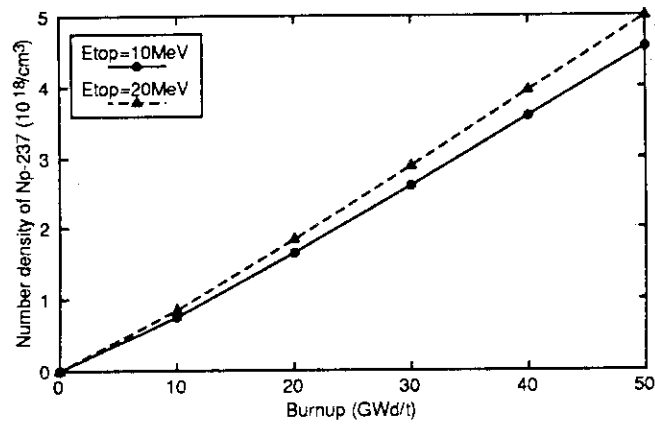


Fig. 2.4.1 Number density of Np-237 in "dirty Pu" cell of NEANS benchmark

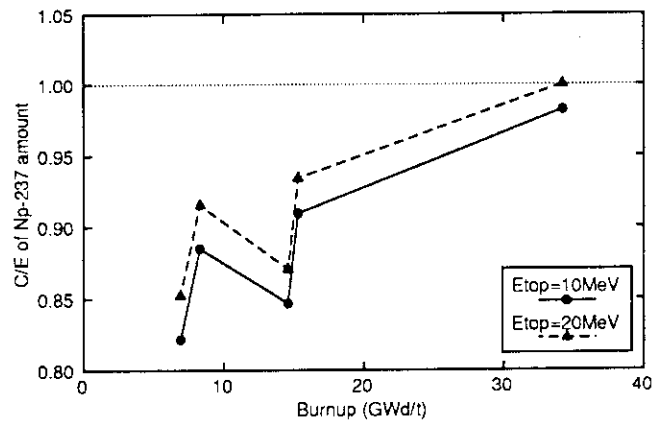


Fig. 2.4.2 Calculation/experiment ratio of Np-237 amount produced in PWR fuel

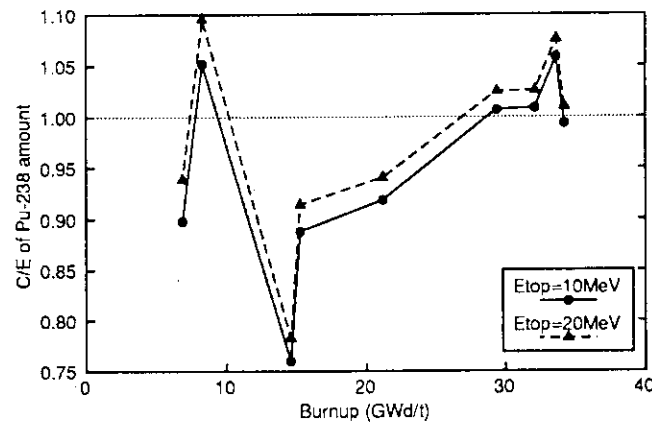


Fig. 2.4.3 Calculation/experiment ratio of Pu-238 amount produced in PWR fuel

## 2.5 Development of Intelligent Reactor Design System IRDS (5)

### - A Demonstration of a Prototype IRDS -

T. Kugo, K. Tsuchihashi, M. Nakagawa and T. Mori

We have developed a prototype of Intelligent Reactor Design System (IRDS)<sup>1)</sup> to support reactor core design in the fields of neutronics and thermal hydraulics. A main purpose of the system is to search a feasible region of design parameters and to decide an optimal set of them according to design criteria and goals. To achieve this purpose, functions of parametric survey calculation and design window search have been installed together with automatic generation of input data. The design process in the system is shown in Fig. 2.5.1. The design steps shown in this figure proceed interactively according to window menus. The system has been constructed on a SUN Workstation using the Open Windows system based on X-Windows adopted as a standard platform for UNIX system.

To cover overall reactor core analysis for various types of reactors, we added the following analysis modules into the system in FY 1993,

- COOLOD-N : A thermal hydraulic analysis for research reactor core with plate type fuel assemblies,
- CITATION : A recovery of core burnup analysis function included in CITATION,
- COBRA/HCLWR : Sub-channel analysis for LWR.

We extended frame structures of data base of reactor configuration to include thermal hydraulic information. Automatic input generation and output visualization become available for the above analysis modules.

We have developed a procedure to search a design window in two dimensional space with use of AI technique<sup>2)</sup>. This procedure is easy to extend to various technological fields because of its feature, that is, its easiness of addition of design parameters and design criteria in itself. We have applied this procedure to neutronics design. Design windows can be obtained from either viewpoint of neutronics or thermal hydraulics design. For the neutronics design, selected design parameters are pin diameter, pin pitch and fuel enrichment. As design criteria, we considered (i) the initial excess reactivity or discharged fuel burnup, (ii) coolant void reactivity and (iii) conversion or breeding ratio. They are specified by user's requests.

We applied the prototype system to fuel pin design of a lead cooled fast reactor. We

intended to find an optimal parameter set of pin diameter and pin pitch to realize high linear heat rate and low fuel enrichment as goals. In this problem, we considered the following conditions as thermal hydraulic design criteria; maximum cladding temperature  $< 720\text{ }^{\circ}\text{C}$  and pressure drop in a core  $< 2\text{ kg/cm}^2$ , in addition to the other typical design criteria. As for neutronics; the conditions considered were initial excess reactivity  $> 0.0$ , coolant void worth  $< 0.0$  and breeding ratio  $> 1.0$ . We obtained several design windows for pin diameter and pin pitch by changing linear heat rate and fuel enrichment. Figures 2.5.2 (a) and (b) are the windows to realize the lowest fuel enrichment and the highest linear heat rate, respectively. The intersection of the two windows is a feasible region from the viewpoint of both of neutronics and thermal hydraulics design as shown in Fig. 2.5.2 (c). Thus, a reactor designer could easily find and refine the feasible region of design parameters with the present system. The goals were linear heat rate =  $40\text{ kW/m}$  and Pu enrichment =  $11\text{ wt}\%$ .

#### References

- 1) Kugo T., et al.: M&C+SNA'93, Vol.2, p.199–209 (1993).
- 2) Nakagawa M., et al.: "Design Window Search Based on AI Technique", J. Nucl. Sci. Technol., 29, 1116 (1992).

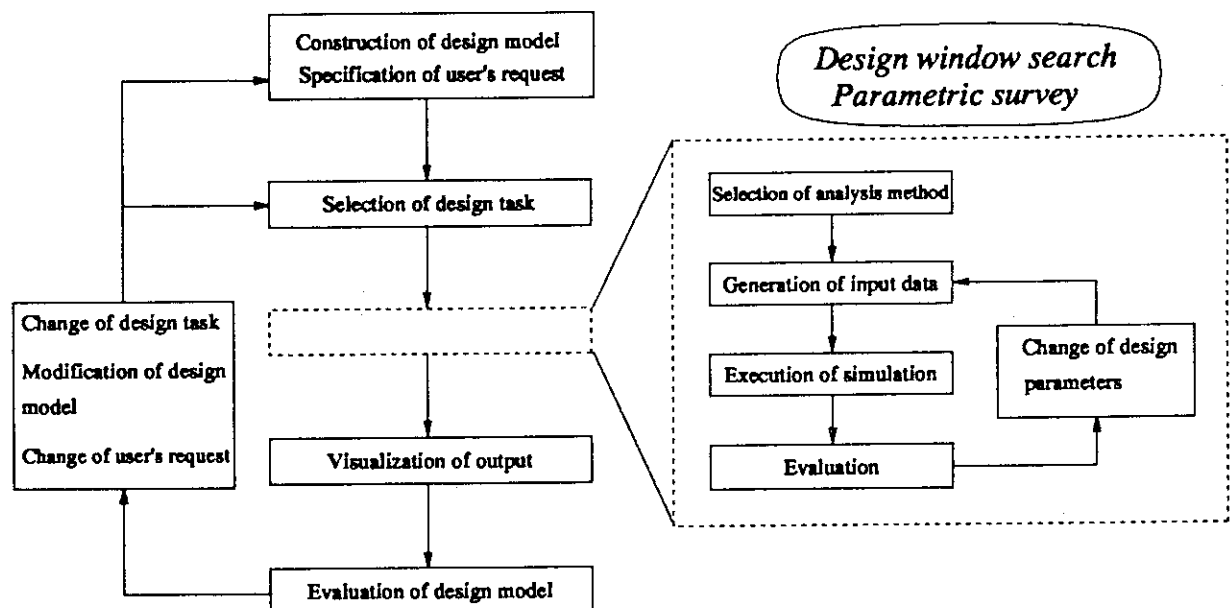
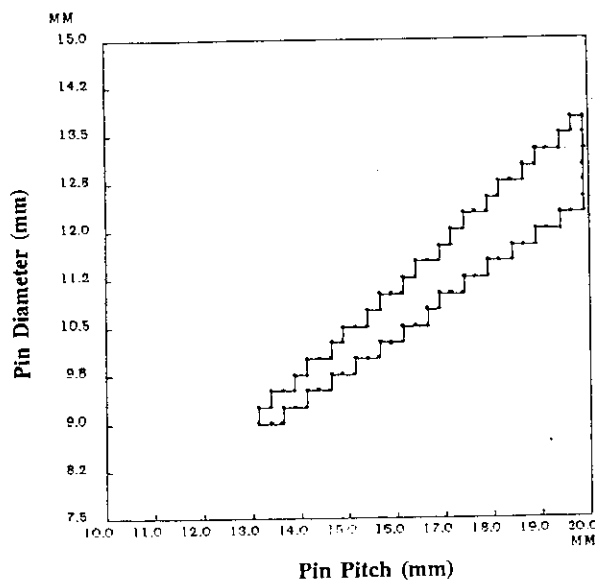
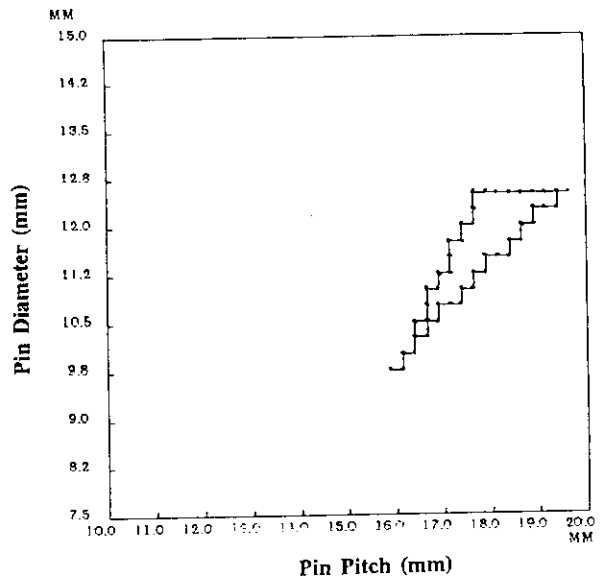


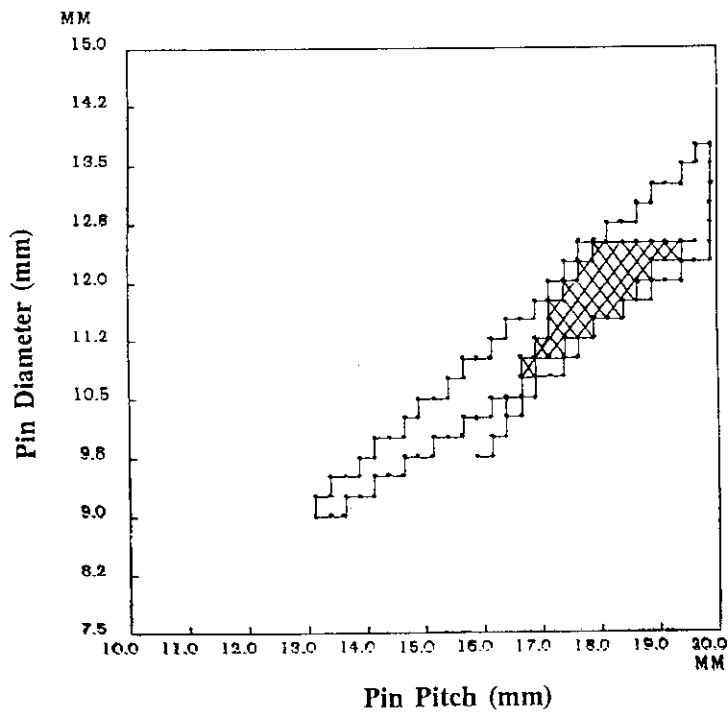
Fig. 2.5.1 Design process in prototype system of IRDS



(a) Neutronics



(b) Thermal hydraulics



(c) Intersection of (a) and (b)

Fig. 2.5.2 Design windows for pin diameter and pin pitch obtained by the present system

## 2.6 Development of Nuclear Design Code System for Advanced Reactors

K. Okumura

In research institutes or universities, the burnup management system well-coordinated for a restricted reactor is not necessary but the system applicable to unusual and various types of reactors is required. In order to reply to this requirement, a nuclear design code system for various types of advanced reactors is under development. The system consists of common frames to control overall calculational procedures, and several modules to solve neutronics equations or thermohydraulics equations. The modules are exchangeable depending on reactor types. It is favorable that several frames like a burnup management code or a space dependent kinetics code use common modules and common data files.

### Nodal Diffusion Calculation Module for Vector Processor

As a first work, a three-dimensional (X-Y-Z) nodal diffusion module was developed. It is based on a fourth-order polynomial nodal expansion method (NEM) with a quadratic transverse leakage approximation<sup>1)</sup>. The spatial coupling between the nodes is expressed by partial currents. The odd-even current sweep suitable for vector processors is adopted. In addition, the nodes adjacent to the boundaries are treated apart from other nodes, because many exceptional treatments for the nodes adjacent to the boundaries disturb efficient vector calculations.

In this module, various boundary conditions are available. They are extrapolated, reflective, periodic and rotational ones. One or two-dimensional calculations are available with the reflective boundary condition. Furthermore, internal blackness is also available. The internal blackness is treated as a usual material for fast groups but treated as an extrapolated boundary for some of thermal groups. The extrapolated constants of the blackness can be variable by blackness type and by group. This option is necessary especially for the research reactor which uses a lump of strong neutron absorber as a control rod. Other main features are an option to use discontinuity factor<sup>2)</sup>, finite difference calculational mode, and option to calculate kinetics parameters.

The performance of this module was examined in the well-known IAEA three-dimensional benchmark problem<sup>3)</sup>. Two cases of calculation were done; the case with 20cm of nodal width ( $\Delta=20\text{cm}$ ) and the case of  $\Delta=10\text{cm}$  in every direction. Fig.2.6.1 shows the results on  $k_{\text{eff}}$  and axially averaged sub-assembly power. They are compared with a reference solution<sup>3)</sup> ( $\Delta=0.0\text{cm}$ ), which is obtained by extrapolating the results of finite difference solutions with several mesh-widths by VENTURE code. Both of the present results show very good agreement with the reference solution. The accuracy of the results corresponds to

the solution of finite difference method with the mesh-width of 1cm. The computational times (CPU) are 2sec ( $\Delta=20\text{cm}$ ) and 13sec ( $\Delta=10\text{cm}$ ) with FACOM VP-2600 machine. Vectorization ratio is more than 99%, and speedup factor of 17~40 is achieved by the vectorization.

#### Feedback XS Preparing Module

In order to apply this system to various types of reactors, the module to produce macroscopic cross sections (XSs) must be general for the reactor types. By extending the XS feedback model of BWR, a general XS preparing module was developed. In this module, XSs are expressed as a function of 10 parameters as shown in the following equation.

$$\Sigma = \Sigma(F, R, E, \bar{U}, U, f_d, T_m, T_f, C_B, N_{Xe}) ,$$

- F : fuel type
- R : control rod type
- E : burnup degree
- $\bar{\rho}$  : relative historical coolant density (any coolant is acceptable)
- $\rho$  : relative instantaneous coolant density
- $f_d$  : control rod fraction
- $T_m$  : average coolant temperature
- $T_f$  : average fuel temperature
- $C_B$  : concentration of poison in coolant (any poison is acceptable)
- $N_{Xe}$  : number density of Xe-135

The XSs are produced by the combination of a table interpolation scheme and a polynomial fitting scheme with the XS-tables obtained by other sub-assembly burnup codes. The accuracy of the produced XSs depends on the table-length and the order of polynomial expression employed. They are optional depending on reactor types.

In this module, any system of units for the input parameters is acceptable. It is internally converted consistently with an external file. Therefore, this module can be easily connected to other neutronics or thermohydraulics modules. With the space dependent parameters obtained by neutronics and thermohydraulic modules, this module prepares space dependent XSs for any kind of reactors.

#### References

- 1) Finnemann F., Bennewitz F. and Wagner M.R. : "Interface Current Techniques for Multi-Dimensional Reactor Calculations", Atomkernenergie, **30**, pp123-128 (1977)
- 2) Smith K.S. : "Assembly Homogenization Techniques for Light Water Reactor Analysis", Progress in Nuclear Energy, **17**, No.3 pp303-pp335 (1986)
- 3) Argonne Code Center : "Bechmark Problem Book", ANL-7416, Supplement 2 (1977)

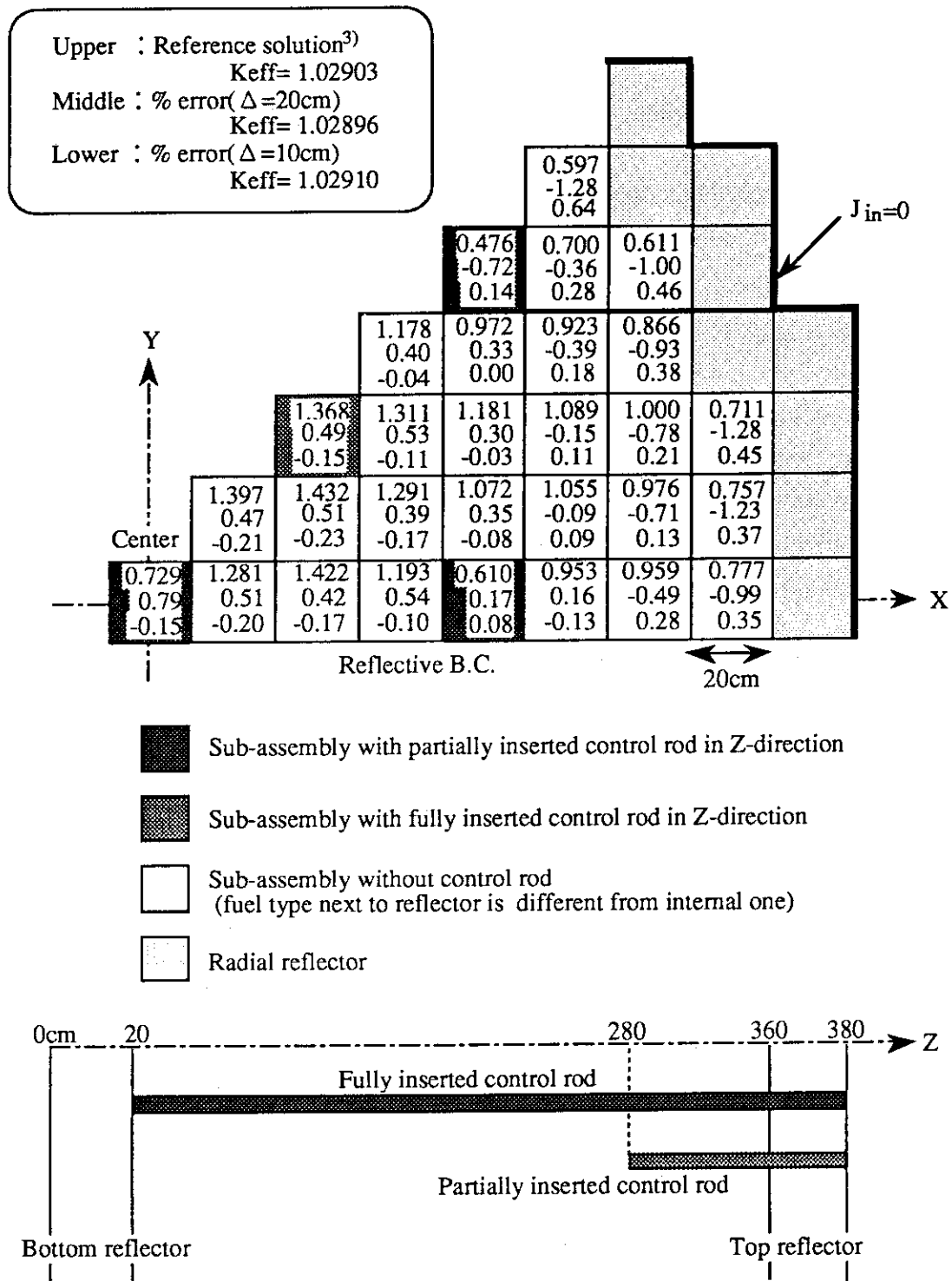


Fig.2.6.1 Nodal diffusion calculation results for IAEA 3D benchmark problem



## 2.7 Development of New Analytical Nodal Method for Multi-Group Neutron Diffusion Equation

Y. Asahi and T. Fujimura

Usually, the multi-dimensional, multi-group neutron diffusion equation is solved iteratively. In the so-called "inner iterations" in these iterative methods, we numerically solve for each group

$$D \nabla^2 \phi - \sigma \phi = -s, \quad (1)$$

where  $D$ ,  $\sigma$  and  $s$  are the diffusion constant, the macroscopic removal cross section and the neutron source, respectively.  $D$  and  $\sigma$  are assumed constant within a node. In the following, we consider a rectangular node ( $2a \times 2b \times 2c$ ) in the Cartesian coordinate system.

In an analytical nodal method, it is required to give an analytical expression for the solution to Eq. (1). In our present method, it will be given such that

$$\phi = \begin{pmatrix} \cosh(\alpha x) \\ \sinh(\alpha x) \end{pmatrix} \times \begin{pmatrix} \cosh(\beta y) \\ \sinh(\beta y) \end{pmatrix} \times \begin{pmatrix} \cosh(\gamma z) \\ \sinh(\gamma z) \end{pmatrix} + H(x, y, z) \quad (2)$$

where

$$\alpha^2 + \beta^2 + \gamma^2 = \frac{\sigma}{D}, \quad (3)$$

and

$$H(x, y, z) = \int_{-a}^a d\xi \int_{-b}^b d\eta \int_{-c}^c d\zeta G(x, y, z; \xi, \eta, \zeta) s(\xi, \eta, \zeta). \quad (4)$$

In Eqs. (2) and (3), among  $\alpha$ ,  $\beta$  and  $\gamma$ , at most, two of them can be purely imaginary, while, in Eq. (4),  $G$  is the Green's function associated with Eq. (1), which is normalized such that

$$\int_{-a}^a d\xi \int_{-b}^b d\eta \int_{-c}^c d\zeta G(x, y, z; \xi, \eta, \zeta) = \frac{1}{\sigma}. \quad (5)$$

First of all, we define the node-averaged flux  $\bar{\phi}$  such that

$$\bar{\phi} = \frac{1}{8} abc \int_{-a}^a dx \int_{-b}^b dy \int_{-c}^c dz \phi(x, y, z). \quad (6)$$

For the time being, we restrict ourselves to the x-direction. We define the x-averaged flux

$\varphi_x(x)$  such that

$$\varphi_x(x) = \frac{1}{4bc} \int_{-b}^b dy \int_{-c}^c dz \varphi(x, y, z) . \quad (7)$$

Let the surface-evaluated ( or interfacial ) quantities for flux  $\varphi$  and current  $J$  be defined such that

$$\varphi_{x\pm} = \varphi_x(\pm a) \quad (8)$$

and

$$J_{x\pm} = -D \left( \frac{d\varphi}{dx} \right)_{x=\pm a} . \quad (9)$$

Similarly, for  $H(x, y, z)$ , we define its surface-evaluated and node-averaged quantities. After algebraic manipulations, we obtain the following relationships among these quantities such that

$$\varphi_{x+} = \bar{\varphi} - \frac{p^x(J_{x+} + J_{x-})}{2} - \frac{q^x(J_{x+} - J_{x-})}{2} + \theta^x \quad (10)$$

and

$$\varphi_{x-} = \bar{\varphi} - \frac{p^x(J_{x+} + J_{x-})}{2} - \frac{q^x(J_{x+} - J_{x-})}{2} + \tau^x , \quad (11)$$

where

$$q^x = \frac{1}{D\alpha} \left( \frac{1}{\tanh(\alpha a)} - \frac{1}{\alpha a} \right) , \quad (12)$$

$$p^x = \frac{\tanh(\alpha a)}{D\alpha} , \quad (13)$$

$$\tau^x = H_{x-} - \bar{H} + \frac{D}{2} (p^x - q^x) \left( \frac{dH_x}{dx} \right)_+ + \frac{D}{2} (p^x + q^x) \left( \frac{dH_x}{dx} \right)_- \quad (14)$$

and

$$\theta^x = H_{x+} - \bar{H} - \frac{D}{2} (p^x + q^x) \left( \frac{dH_x}{dx} \right)_+ - \frac{D}{2} (p^x - q^x) \left( \frac{dH_x}{dx} \right)_- . \quad (15)$$

Node-averaged flux  $\bar{\varphi}$  defined by Eq. (6) is related to  $H$  and  $J$  such that

$$\begin{aligned} \bar{\varphi} &= \bar{H} + \frac{1}{2a\alpha^2} \left[ \left( \frac{dH_x}{dx} \right)_- - \left( \frac{dH_x}{dx} \right)_+ \right] - \frac{1}{2a\alpha^2 D} (J_{x+} - J_{x-}) \\ &= \bar{H} + \frac{1}{2b\beta^2} \left[ \left( \frac{dH_y}{dy} \right)_- - \left( \frac{dH_y}{dy} \right)_+ \right] - \frac{1}{2b\beta^2 D} (J_{y+} - J_{y-}) \\ &= \bar{H} + \frac{1}{2c\gamma^2} \left[ \left( \frac{dH_z}{dz} \right)_- - \left( \frac{dH_z}{dz} \right)_+ \right] - \frac{1}{2c\gamma^2 D} (J_{z+} - J_{z-}) . \end{aligned} \quad (16)$$

Suppose that neutron source  $s$  is constant within the node. Then, both  $\theta^x$  and  $\tau^x$  as well as the second term of RHS's of Eq. (16) vanish, since, with the help of Eq. (5), Eq. (4) yields

$$H(x, y, z) = \frac{s}{\sigma} \quad (a \text{ constant}) . \quad (17)$$

If we substitute Eqs. (10) and (11) into the continuity condition for  $\varphi$  at each node interface

$$(\varphi_{x+})_{\text{from-node}} = (\varphi_{x-})_{\text{to-node}} , \quad (18)$$

we obtain the tri-diagonal system of equations for interface neutron currents  $J_{xz}$ , which can be solved by means of the well known Thomas method. It should be noted that the preceding discussion for the  $x$ -direction is also applied to the  $y$ - and  $z$ -direction. Before entering the inner iteration, neutron source  $s$  will be calculated by using neutron flux given by Eq. (2).

The present analytical nodal method is characterized by the fact that the analytical expression for the solution to Eq. (1), namely, Eq. (2) is exact. In 1993, development of a computer code based on the formulation stated above was started.

## Reference

- 1) Kirk B. L., et al.: "An Iterative Algorithm for Solving the Multi-dimensional Neutron Diffusion Nodal Method Equations on Parallel Computers", Nucl. Sci. Eng., 11, 57 (1992).

### 3. Reactor Physics Experiment and Analysis

The MOX fueled LMFBR mock-up experiments were conducted on the assembly FCA XVII-1 at the Fast Critical Facility (FCA). The measurements and analysis were performed on the following items;

- Doppler effect measurements of  $^{238}\text{U}$  up to  $800^\circ\text{C}$ : the measurements were performed using metal, oxide and oxide with BeO admixture samples. The calculation of the ultra-fine group collision probability code "PEACO-X" agrees quite well with the experiments expect for the samples with BeO admixture.
- Doppler effect measurements up to  $1500^\circ\text{C}$ : the Doppler sample is contained in the tungsten capsule. To evaluate the flux perturbation due to tungsten, the Doppler effect was measured using two kinds of samples, one with thick tungsten capsule and the other with thin stainless steel capsule. It was concluded that the flux perturbation is well treated by the PEACO-X calculation of the effective cross sections of capsules.
- Measurements of the reaction rate ratio of  $^{238}\text{U}$  capture to  $^{239}\text{Pu}$ : measurements were carried out in this assembly and the metallic-fuel LMFBR mock-up assemblies. The collision probability calculation using JFS-3-J2 group constants agrees with the experiments within 1% for both MOX and metallic fuel cores.
- Analysis of the sodium void effects: measurements were performed in this assembly and in the metallic fuel mock-up assemblies. The analysis were carried out using JENDL-2 and JENDL-3.1 data library. The non-leakage term of the sodium void effect was well predicted by JENDL-3.1 calculation except for that of  $^{235}\text{U}$  core. The leakage term of the sodium void effect was well calculated when the detailed cell heterogeneity is taken into account.
- $\text{B}_4\text{C}$  and Pu sample worth distribution were measured in this assembly. For the analysis, the collision probability method and 70 group cross section set JFS-3-J3 were used for the cell calculation and the diffusion calculation was performed to obtain forward and adjoint fluxes. The calculated worth distributions agree well with the experimental ones.

As a part of the examination of the neutronics calculation code for the design of HTTR(High Temperature Test Reactor under construction), the reactivity worth of an HTTR mock-up control rod was measured by the pulsed neutron method in VHTRC-4 core. The experimental control rod worth was obtained by the Sjöstrand method and Kosály-Fisher method. Calculation was carried out using two methods, namely, 2-D Sn cell calculation/ 3-D diffusion core calculation and Monte Carlo method. The calculations agrees with the experiments within 10%.

The analysis of Russian critical experiments on  $^{235}\text{U}$  fueled Lead cooled Fast Reactor was carried out. The analysis was performed for the experiments in the assemblies of ROMB CA-1 to 6. In the analysis, the continuous energy Monte Carlo code MVP and JENDL-3.1 nuclear data library were used. The calculated results were compared with those of ENDF/B-IV, -V and JENDL-3.2 calculations.

### 3.1 Mockup Experiments of MOX-fueled LMFBR in FCA Assembly XVII-1

S. Iijima, H. Oigawa, T. Sakurai and A. Ohno

A critical experiment on oxide-fueled liquid metal fast breeder reactors was performed using the fast critical assembly (FCA) facility following to the experiments of metallic-fueled LMFBRs<sup>1), 2), 3)</sup>. Core physics parameters differ between an oxide-fueled core and a metallic-fueled core, particularly in spectrum-sensitive parameters such as Doppler reactivity and sodium void worth and in composition-dependent parameters such as breeding ratio. The purpose of the experiment was to examine the reliability of the current data and method by comparing the accuracy of physics parameter predictions in the oxide-fueled and the metallic-fueled mockup core.

FCA assembly XVII-1 was built as the reference core of oxide-fueled LMFBRs. The following physics properties were measured in assembly XVII-1;

- 1) sodium void, Doppler reactivity and  $B_4C$  control rod worths
- 2) axial fuel expansion reactivity worth
- 3) small sample worths for fuel and structure materials
- 4) reaction rate distributions and reaction rate ratios.

Assembly XVII-1 (shown in Fig.3.1.1 in horizontal cross-section, and in Fig.3.1.2 in r-z model) is a zone-type partial mockup core and has a cylindrical test region (~ 69 cm in diameter and ~ 152 cm high) in the inner part of the assembly. The test region is surrounded radially by the driver region, which serves to maintain criticality, and further enveloped by the radial blanket. The T2 drawers, which consists of the core cells and the axial blanket cells, are loaded in the test region. The plate arrangement of the drawer is shown in Fig.3.1.3. Plutonium enrichment of the core cell is 11wt%. The fissile material density of the driver region is about twice that of the test region.

The physics parameters are analyzed using the cross-section library JENDL-2<sup>4)</sup> and JAERI's standard calculation system for fast reactor neutronics<sup>5)</sup>. The JFS-3-J2 group constant set<sup>6)</sup> with a 70 energy group structure (0.25 lethergy width) is generated from JENDL-2. Infinite-medium cell calculations are made by using the JFS-3-J2 set. These basically involve two steps; resonance shielding for heavy isotopes by the "table lookup" method and calculation of the flux fine structure by the collision probability method. Cell averaged group constants are prepared by flux-volume weighting to preserve the reaction rates of the heterogeneous cell. Anisotropic diffusion coefficients are also prepared by Benoist's formula.<sup>7)</sup> The core calculation was made using the diffusion theory in r-z geometry and 70 energy groups. The reactivity worths such as sodium void and Doppler reactivity were calculated by perturbation method based on diffusion theory. The cell-averaged group

constants and the neutron flux from the core calculation were used. The reaction rates were also calculated by using the same group constants and the neutron flux. Another core calculation was made to analyze the criticality by using the diffusion theory in x-y-z geometry and 25 energy groups. Data used in the calculation were collapsed to 25 energy groups by the region-averaged spectra in the r-z calculation.

Assembly XVII-1 had features that facilitated comparison between oxide and metal cores. The results of assembly XVII-1 were compared to those of the prior metallic-fueled cores. The experiments and their analyses will be published in JAERI-M report.

## References

- 1) Iijima S., et al.: " Benchmark Physics Experiment of Metallic-Fueled LMFBR at FCA", Proc. of ANS Topical Meeting on Advances in Reactor Physics, 2-92. March 8-11, 1992, Charleston, S.C. (1992).
- 2) Iijima S., et al.: " Benchmark Physics Experiment of Metallic-Fueled LMFBR at FCA. - Core Design of FCA Assembly XVI-1 and Criticality -. JAERI-M 92-196 (1992).
- 3) Iijima S., et al.: " Benchmark Physics Experiment of Metallic-Fueled LMFBR at FCA. - Experiments of FCA Assembly XVI-1 and Their Analyses -. JAERI-M 93-186 (1993).
- 4) Nakagawa T.: " Summary of JENDL-2 general purpose file", JAERI-M 84-103 (1984).
- 5) Nakagawa M.: Calculation code system for fast reactor neutronics JAERI-M 83-066 (1983).
- 6) Takano H., et al.: "Production and benchmark tests of fast reactor group constants set JFS-3-J2", JAERI-M 82-135 (1982).
- 7) Benoist P.: "Streaming effects and collision probabilities on lattices", Nucl. Sci. Eng. 34(1968)285.

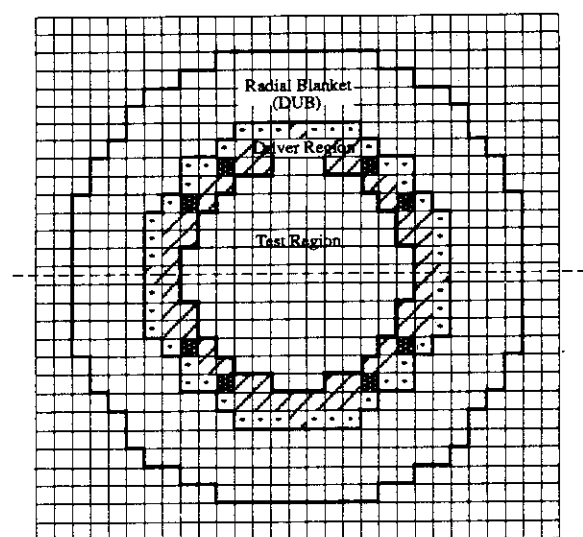


Fig. 3.1.1 Cross Sectional View of FCA Assembly XVII-1

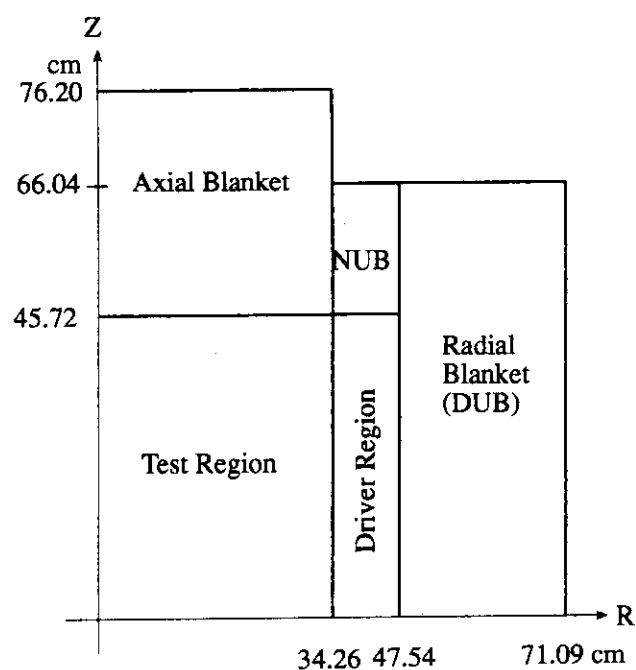


Fig. 3.1.2 RZ Model of FCA Assembly XVII-1

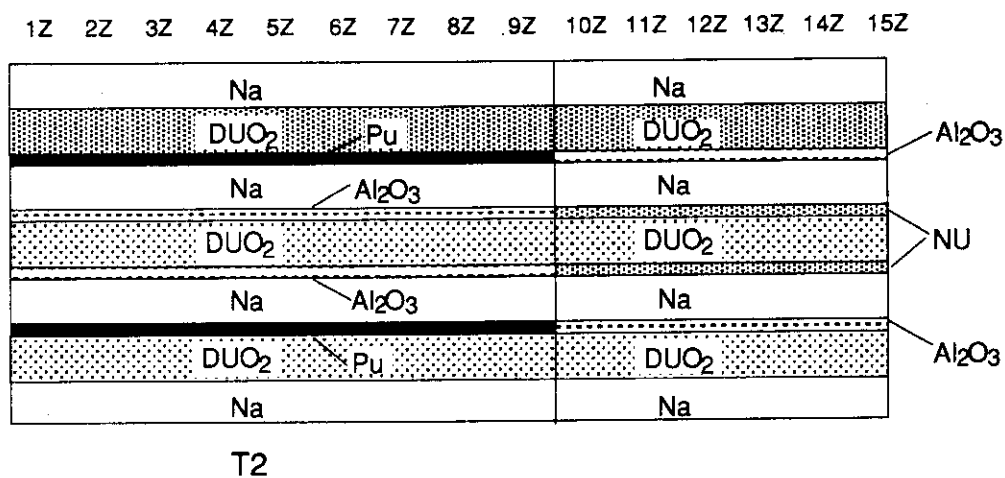


Fig. 3.1.3 Drawer Loading Pattern used in FCA Assembly XVII-1

### 3.2 Doppler Effect Experiment in MOX-LMFBR Mockup Core FCA Assembly XVII-1

M. Andoh, S. Okajima, H. Oigawa and T. Mukaiyama

In the analysis of Doppler effect experiment, an ultra-fine group collision probability code PEACO-X<sup>1)</sup> was developed to consider the resonance interaction effect between the Doppler sample and the adjacent core. We carried out Doppler effect experiments for six Doppler samples of different compositions. The accuracy of effective cross sections calculated by PEACO-X was evaluated using measured data.

Doppler effect of  $^{238}\text{U}$  was measured in temperature range up to 800 °C at FCA assembly XVII-1<sup>2)</sup> which is a mockup core of MOX-LMFBR. Doppler effect is obtained as a reactivity difference between the reactivity when a heated sample is placed at the core center and that of an unheated sample at the core center. Table 3.2.1 shows the size and weight of each sample used in the experiment and the experimental results at 800 °C.

In the analysis, Doppler reactivity worths were calculated by the first order perturbation theory using JENDL-3.1 library<sup>3)</sup>. Two calculation codes were used to obtain  $\delta\sigma$  of the Doppler samples (i.e., the effective cross section change caused by the temperature change of the sample). One is a conventional cell code, SLAROM<sup>4)</sup>, which calculates effective cross sections with a 70 group structure using shielding factor tables, and the other is PEACO-X. The real and adjoint fluxes with a 70 group structure were obtained from the two-dimensional diffusion calculation for the R-Z model using CITATION<sup>5)</sup>.

For the  $\text{UO}_2(2.5\text{cm}^3)$  sample, PEACO-X and SLAROM calculations are compared in Fig. 3.2.1 for  $\delta\sigma$  in  $^{238}\text{U}$  capture cross section and energy breakdown of Doppler reactivity worth at 800°C. As shown in the figure, considering the resonance interaction effect,  $\delta\sigma$  obtained from PEACO-X is larger than that from SLAROM above 300eV, which enlarges the Doppler reactivity worth by PEACO-X. A comparison between the calculated and measured Doppler reactivity worths at 800 °C is also shown in Table 3.2.1. By comparing the C/E values between SLAROM and PEACO-X calculations, it can be concluded that the PEACO-X calculations for all samples are better than the SLAROM calculations. For U(metal) and  $\text{UO}_2$  samples, PEACO-X calculations agree with experimental results quite well and there is no large discrepancy among these C/E values by PEACO-X. These results show that the  $\delta\sigma$  is improved by PEACO-X and that composition dependency of C/E values disappears for these samples.

For  $\text{UO}_2+\text{BeO}(1:1)$  and  $\text{UO}_2+\text{BeO}(1:5)$  samples, the PEACO-X calculation, however, underestimates the experimental values considerably. We assume that diffusion theory is not appropriate to calculate neutron flux distribution in the region which contains large amount of scattering materials such as BeO. Therefore a transport code TWOTRAN<sup>6)</sup> was used to



calculate real and adjoint fluxes for two samples which contains BeO. A comparison of C/E values between CITATION and TWOTRAN calculations is shown in Table 3.2.2. From the table, the C/E values of the  $\text{UO}_2+\text{BeO}(1:1)$  sample and of the  $\text{UO}_2+\text{BeO}(1:5)$  sample are improved about 8% and 18%, respectively. As for the  $\text{UO}_2+\text{BeO}(1:5)$  sample, the TWOTRAN calculation still underestimates the experimental value by more than 10%. Further investigation about TWOTRAN calculation (e.g., mesh points,  $S_N$  order) is under way.

## References

- 1) Okajima S., et al. : "Measurement of Doppler Effect up to 2000 °C at FCA (3) -Development of a Cell Code, PEACO-X, with Ultra-fine Group Structure-", JAERI-M 92-185, (in Japanese), (1992).
- 2) Iijima S., et al. : "Mock-up Experiments of MOX-fueled LMFBR in FCA assembly XVII-1", Section 3.1 in this report.
- 3) Shibata K., et al. : "Japan Evaluated Nuclear Data Library, Version-3 -JENDL-3-", JAERI 1319, (1990).
- 4) Nakagawa M. and Tsuchihashi K. : "SLAROM: A Code for Cell Homogenization Calculation of Fast Reactor", JAERI 1294, (1984).
- 5) Fowler T. B., et al. : "Nuclear Reactor Core Analysis Code; CITATION", ORNL-TM-2496, (1969).
- 6) Lathlop K. D. and Brinkly F. W. : "Theory and Use of the General Geometry TWOTRAN Program", LA-4432, (1970).

Table 3.2.1 Comparison between the calculated and measured Doppler reactivity worths at 800 °C for each sample

Sample composition*	Diameter*** (cm)	Mass of $^{238}\text{U}$ (g)	Expt. ( $10^{-6} \Delta k/k$ )	C/E value	
				SLAROM	PEACO-X
U(metal)	2.5	1337	$-16.78 \pm 1.4\%$	0.908	0.946
U(metal)	2.0	863	$-10.97 \pm 2.3\%$	0.909	0.953
$\text{UO}_2$	2.5	601	$-8.29 \pm 2.2\%$	0.884	0.952
$\text{UO}_2$	2.0	374	$-5.26 \pm 4.0\%$	0.875	0.952
$\text{UO}_2+\text{BeO}(1:1)^{**}$	2.5	292	$-4.89 \pm 3.5\%$	0.796	0.880
$\text{UO}_2+\text{BeO}(1:5)$	2.5	97	$-1.95 \pm 9.2\%$	0.623	0.733

\* : Uranium of all samples is natural Uranium.

\*\* : Values in parentheses are the volume ratio of  $\text{UO}_2$  to BeO.

\*\*\* : Length of all samples is 15 cm.

Table 3.2.2 Comparison of C/E values between CITATION and TWOTRAN calculations combined with PEACO-X\*

Sample	C/E value	
	CITATION	TWOTRAN
UO <sub>2</sub> +BeO(1:1)	0.880	0.938
UO <sub>2</sub> +BeO(1:5)	0.733	0.871

\* : It means that PEACO-X is used for the  $\delta\sigma$  calculation.

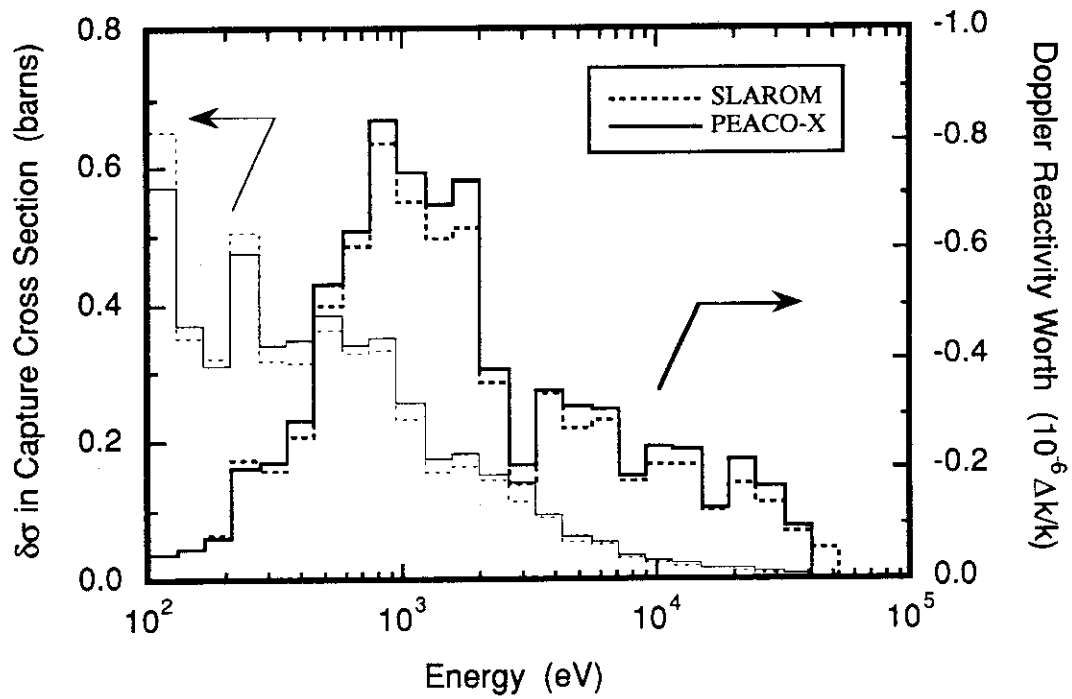


Fig. 3.2.1 Comparison of  $\delta\sigma$  in  $^{238}\text{U}$  capture cross section and energy breakdown of Doppler reactivity worths for UO<sub>2</sub>(2.5cm<sup>3</sup>) at 800 °C between SLAROM and PEACO-X calculations

### 3.3 Analysis of High Temperature Doppler Effect Measured at FCA (Evaluation of Flux Perturbation Effect Caused by Structural Material in Experimental Device)

S. Okajima, H. Oigawa, M. Andoh, T. Mukaiyama and K. Fushiki<sup>1</sup>

The high temperature Doppler effect measurements for  $^{238}\text{U}$  have been carried out using new experimental devices at FCA<sup>1), 2)</sup>. In the analysis of Doppler reactivity worth for temperature change up to 1500°C, the calculation still underestimated the experimental values about 10% after considering the following effects: the resonance interaction effects between the hot sample and the adjacent cold core<sup>3)</sup>, and the resonance overlapping effect between the sample and the structural material in the experimental devices. The discrepancy between the calculation and the experiment may be caused by the poor calculation of real and adjoint fluxes near the sample. In this area fluxes are perturbed considerably by the experimental device made of tungsten and stainless steel. In order to evaluate this flux perturbation effect, the Doppler reactivity worth was measured for the Doppler sample enclosed in a thick tungsten capsule (DUO2-20W). The measured data was compared with that for the Doppler sample enclosed in a thin stainless steel capsule (NUO2-20). The analyses were made for these measurements using the collision probability code with an ultra-fine group structure, PEACO-X<sup>4)</sup>.

Table 3.3.1 shows the composition of both Doppler samples. The measurement was carried out at the core center of FCA assembly XVII-1 which is a mockup core for the prototype MOX-fueled fast reactor<sup>5)</sup>. The experimental results are also shown in the table. The Doppler reactivity worth per unit mass of  $^{238}\text{U}$  for the DUO2-20W sample is smaller than that for the NUO2-20 sample since the tungsten capsule causes stronger flux depression.

The Doppler reactivity worth was calculated by the first order perturbation theory. The unperturbed real and adjoint fluxes with a 70-group structure were obtained from two-dimensional diffusion calculation for the R-Z geometry. This geometry contains the Doppler sample and the homogenized experimental device region. The conventional cell code, SLAROM<sup>6)</sup>, was used to calculate the effective cross sections of core and blanket regions. The PEACO-X code was used to calculate the effective cross section of the Doppler sample. The effective cross sections of the homogenized experimental device,  $\Sigma_{\text{eff}}^{\text{expt}}$ , were calculated using both cell codes and were compared. In this analysis, the JENDL-3.1 data<sup>7)</sup> was used.

The  $\Sigma_{\text{eff}}^{\text{expt}}$  are compared in Fig. 3.3.1 between SLAROM and PEACO-X calculations. The PEACO-X gives smaller value than the SLAROM below 10 keV since the PEACO-X

---

<sup>1</sup> Summer student from Nagoya university

calculation considers the self-shielding effect for the structural material of the experimental device. The C/E value for DUO2-20(W) increased by about 20%, as shown in Table 3.3.1. This effect for NUO2-20, however, was quite small because tungsten was not used. There is no large discrepancy between C/E values for both Doppler samples when the  $\Sigma_{\text{eff}}^{\text{expt}}$  of PEACO-X calculation was used in the flux calculation.

The flux perturbation effect was considered in analyzing the high temperature Doppler effect experiment. The C/E values are shown in Table 3.3.2 together with the previous calculations. The calculated Doppler reactivity worths increase by 8 % from the previous calculations. The discrepancy between the calculation and the experiment using the new experimental device is quite similar to earlier experiences below 800°C<sup>3)</sup> when the flux perturbation effect is taken into account.

#### References

- 1) Okajima S., Oigawa H., Mukaiyama T., et al. : Trans. Am. Nucl. Soc., 66, 523 (1992).
- 2) Okajima S., Oigawa H., Andoh M. and Mukaiyama T. : "Doppler Effect Measurement up to 2000 °C at FCA", Proc. Int. Conf. on Nuclear Data for Science and Technology, (Gatlinburg, USA) (1994).
- 3) Okajima S., Oigawa H. and Mukaiyama T. : J. Nucl. Sci. and Technol., 31, (1994) (to be published).
- 4) Okajima, S., Oigawa, H. and Mukaiyama, T. : "Measurement of Doppler Effect up to 2000 °C at FCA (3) -Development of a Cell Code, PEACO-X, with Ultra-fine Group Structure-", JAERI-M 92-185, (in Japanese), (1992).
- 5) Iijima S., et al. : "Mock-up Experiment in Mox-fueled LMFBR in FCA Assembly XVII-1", Section 3.1 in this report.
- 6) Nakagawa M. and Tsuchihashi, K. : "SLAROM: A code for cell Homogenization Calculation of Fast Reactor", JAERI 1294, (1984).
- 7) Shibata, K., et al. : "Japan Evaluated Nuclear Data Library, Version -3 -JENDL-3-", JAERI 1319, (1990).

Table 3.3.1 Compositions of Doppler sample and experimental results in a mockup core on MOX-fueled prototype fast reactor

Doppler sample	DUO2-20(W)*	NUO2-20
Dimension (dia.x length) (mm)	19.8x150	20.0x150
Total U (g)	389.2	376.7
Atom density ( $10^{22}$ #/cm <sup>3</sup> )		
<u>Doppler Sample</u>		
<sup>235</sup> U	0.006	0.014
<sup>238</sup> U	2.126	2.008
Oxygen	4.264	4.045
<u>Homo. expt. device</u>		
Chromium	0.519	0.493
Iron	1.888	1.794
Nickel	0.350	0.420
Tungsten	6.470	-
Experiment ( $\times 10^{-8} \Delta k/k$ /g of <sup>238</sup> U)	-1.28 $\pm$ 0.06	-1.41 $\pm$ 0.06
20°C - 800°C		
Calc./Expt.		
SLAROM	0.808	0.952
PEACO-X	0.970	0.953

\* This sample is prepared for evaluation of flux perturbation effect on Doppler reactivity worth. The sample is covered by tungsten metal of 3mm thickness. The outer diameter is 26.1 mm.

Table 3.3.2 C/E values for high temperature Doppler reactivity worths measured at a mockup core on MOX-fueled prototype fast reactor

Temperature change	C/E	
	Previous calc.	Present calc.*
20°C - 800°C	0.866	0.934
20°C - 1100°C	0.863	0.931
20°C - 1500°C	0.893	0.965

\* The flux perturbation effect is taken into account.

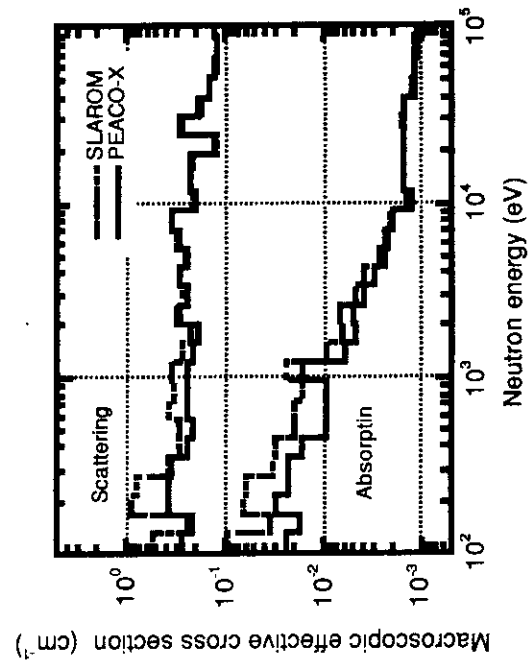


Fig. 3.3.1 Comparison of macroscopic effective cross section of the homogenized experimental device for DUO2-20W between SLAROM and PEACO-X

### 3.4 Measurement and Analysis of $B_4C$ and Pu Sample Worth Distribution in FCA Assembly XVII-1

Y. Nagaya, A. Ohno and T. Osugi

In order to investigate the spatial dependence of  $B_4C$  and Pu samples on the reactivity worth, the experiment was carried out in FCA Assembly XVII-1<sup>1)</sup> which was a typical MOX-fueled core. In this experiment central  $DUO_2$  plates in the central drawer of the fixed core were replaced with Al plates. Each Al plate was substituted for the sample of  $B_4C$  or Pu in turn. The sample worth was estimated from the reactivity difference between with the sample and without the sample.

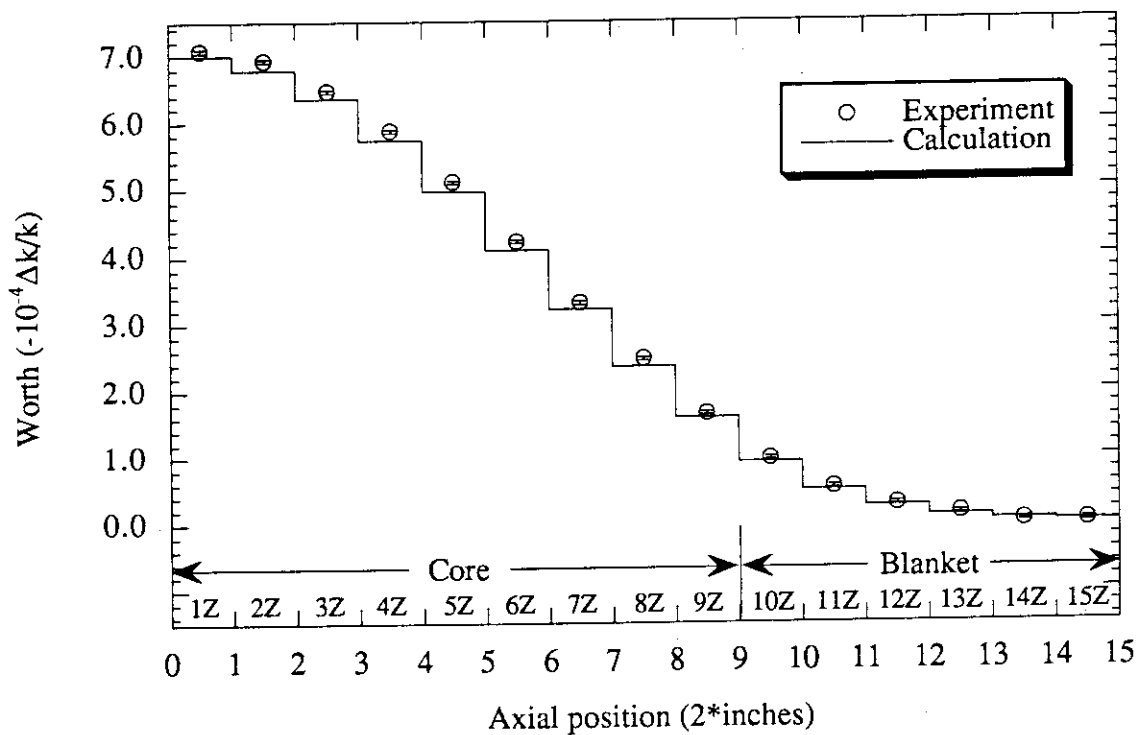
The analysis was also carried out using several models for calculation. Use was made of the collision probability code SLAROM<sup>2)</sup> with the 70 group cross section set JFS3-J3<sup>3)</sup> based on the evaluated data library JENDL-3.1<sup>4)</sup> to perform the cell calculation. Forward and adjoint fluxes were calculated by using the diffusion calculation code CITATION-FBR<sup>5)</sup> with the cross section data obtained by the cell calculation. The sample worth was then calculated by using the perturbation code CIPER<sup>6)</sup> based on the diffusion theory.

Figure 3.4.1 shows the comparison of  $B_4C$  sample worth between the experiment and the calculation. The calculated values in this figure were evaluated on the basis of the exact perturbation theory and taking mesh effect into consideration. The calculated values are in fairly good agreement with the experimental ones. Figure 3.4.2 shows the comparison of Pu sample worth between the experiment and the calculation. Pu sample worth was calculated in the same model as  $B_4C$  sample worth. Mesh effect was found to be negligibly small for Pu sample worth. Most of the calculated values are in fairly good agreement with the experimental ones. However, there is a large discrepancy between the calculated value and the experimental one at 1Z. The calculated values at 6Z, 8Z, 11Z and 15Z underestimate the experimental ones. The discrepancy at 1Z may be caused by the existence of stainless steel between the movable core and the fixed one.

Good results were obtained in the case of  $B_4C$ . However, further investigation is necessary to improve the results for Pu worth.

## References

- 1) Iijima S., et al. : This annual report, 3.1
- 2) Nakagawa M. and Tsuchihashi K. : "SLAROM: A Code for Cell Homogenization Calculation of Fast Reactor", JAERI 1294, (1984)
- 3) Takano H. : Private communication, (1994)
- 4) Shibata K., et al. : "Japanese Evaluated Nuclear Data Library, Version-3", JAERI 1319, (1990)
- 5) Iijima S., et al. : to be published
- 6) Nakagawa M. and Tokuno Y. : "CIPER: A Two- and Three- Dimensional perturbation code based on diffusion theory", JAERI-M 6722, (1976)

Fig. 3.4.1  $B_4C$  sample worth in FCA XVII-1 core

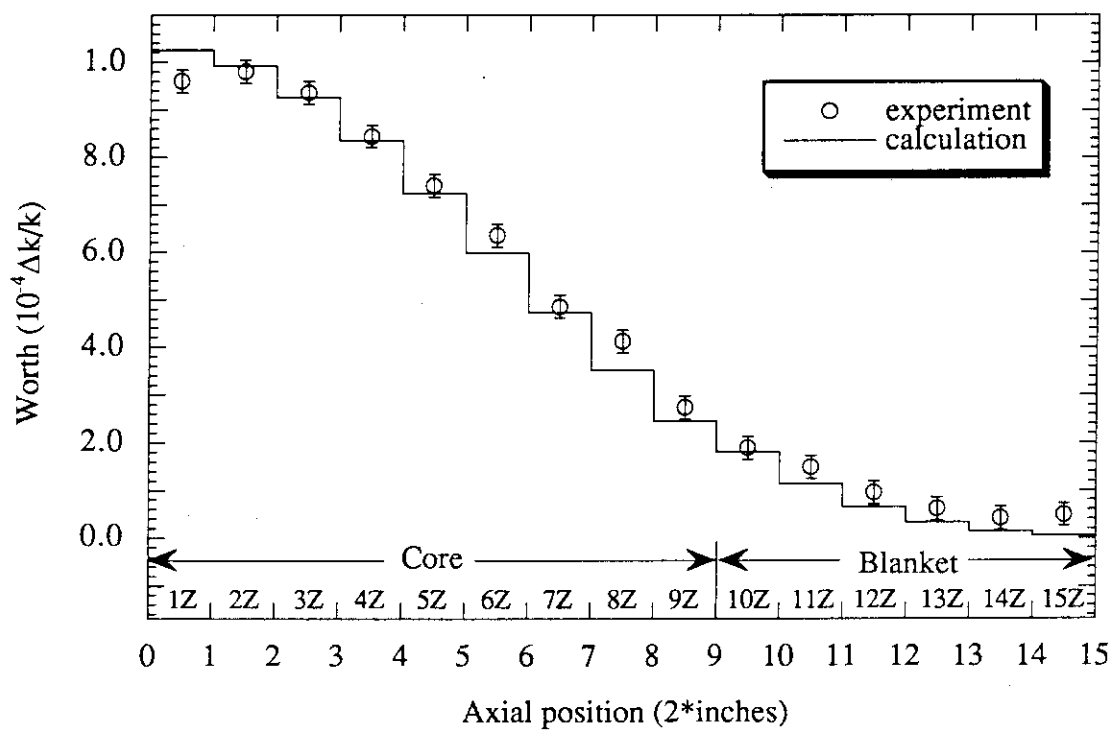


Fig. 3.4.2 Pu sample worth in FCA XVII-1 core



### 3.5 Benchmark Experiment of Metallic-fueled LMFBR at FCA - Reaction Rate Ratio

T. Sakurai, T. Nemoto and S. Iijima

Measurements of  $^{238}\text{U}$  capture to  $^{239}\text{Pu}$  fission rate ratio (C8/F9), which is important as an index of a breeding ratio, were made in metallic-fueled LMFBR mock-up cores (FCA assemblies XVI-1<sup>1)</sup> and XVI-2<sup>2)</sup>). The purpose of the present measurements was to evaluate the reliability of calculation for breeding behavior of a metallic-fueled LMFBR which has a harder neutron spectrum than a Mox-fueled one as shown in Fig.1. The measurement was made also in a Mox-fueled LMFBR mock-up core (FCA assembly XVII-1<sup>3)</sup>).

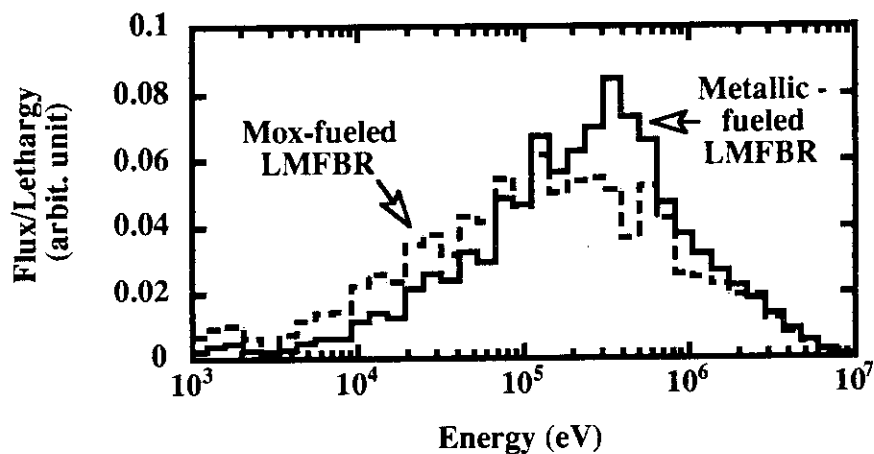


Fig.1 Comparison of calculated neutron spectra between metallic-fueled and Mox-fueled mock-up cores

Cell averaged values of the reaction rate ratios were measured by a foil activation technique<sup>1)</sup> at the core center where a spectrum of metallic-fueled core is well established. A comparison of the measured results of C8/F9 between the cores is shown in Fig.2. More than 20% smaller values of C8/F9 were observed in the metallic-fueled cores than in the Mox-fueled one. These large reductions are caused by a harder neutron spectrum of the metallic-fueled core than that of the Mox-fueled one.

Analyses of the reaction rates were made by using JFS-3-J2 group constants set<sup>4)</sup>. Effective cross sections were calculated by a collision probability method with SLAROM code<sup>5)</sup> in one dimensional infinite slab geometry. Neutron flux was calculated by 70-group anisotropic diffusion theory. Calculation to experiment ratios (C/E) of the C8/F9 are summarized in Fig.3. The calculated value agrees well with the experimental one within 1%

in all of the present mock-up cores where the value of C8/F9 varies considerably.

It was concluded that the accuracy of the calculation based on JFS-3-J2 group constants set on the central C8/F9 in the metallic-fueled core is the same as that in the Mox-fueled one.

#### References

- 1) Iijima S., et al.; JAERI-M 92-196 (1992) (in Japanese).
- 2) Iijima S., et al.; JAERI-M 93-181,37 (1993).
- 3) Iijima S., et al.; in this report.
- 4) Takano H., et al.; JAERI-M 82-135 (1982) (in Japanese).
- 5) Nakagawa M., et al.; JAERI 1294 (1984).

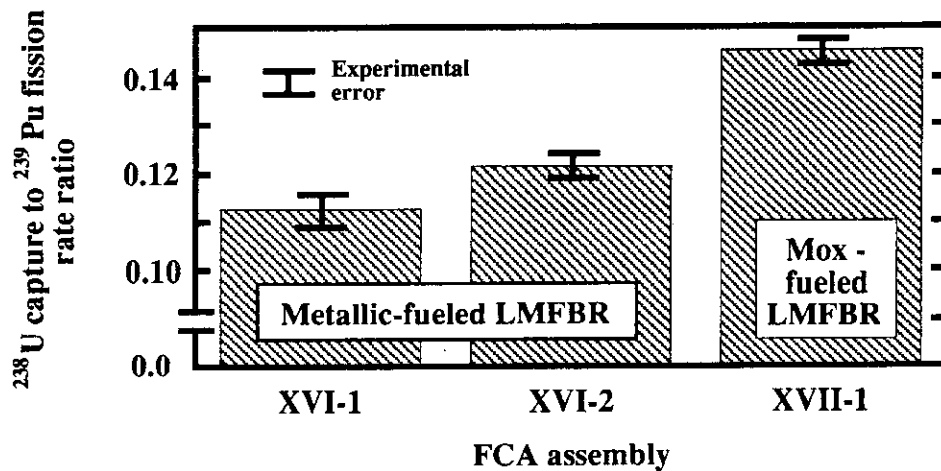


Fig.2 Comparison of measured  $^{238}\text{U}$  capture to  $^{239}\text{Pu}$  fission rate ratios

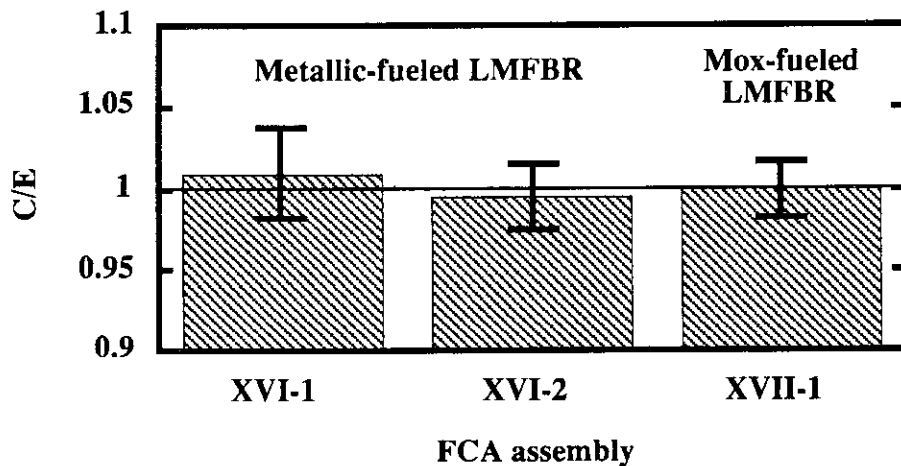


Fig.3 Comparison of C/Es of  $^{238}\text{U}$  capture to  $^{239}\text{Pu}$  fission rate ratio

### 3.6 Evaluation of Calculation Accuracy for Sodium Void Worth Based on FCA Measurement

H. Oigawa, S. Iijima and M. Andoh

Sodium void worth is one of the most important parameters that affect the safety of fast reactors. The accurate calculation is, however, very difficult since it consists of two contrary terms, namely, the positive non-leakage term and the negative leakage term. In this study, calculation accuracy of these two terms is separately evaluated using the measurements at FCA.

#### Experiment

Measured data at assemblies XVI-1, XVI-2 and XVII-1 were used for the evaluation. The former two assemblies are mock-up cores of metallic fueled fast reactors and the last one is that of MOX fueled fast reactor. Enriched uranium and plutonium were used as the fuel in XVI-1, while only plutonium was used in XVI-2 and XVII-1. These composition differences result in the differences of neutron spectra and adjoint neutron spectra, which largely affect the non-leakage term. Hence, the wide range of the calculation accuracy of the sodium void worth can be obtained based upon the measurements at these assemblies.

The axial distribution and the void volume dependence were measured. In these measurements, the sodium void was simulated in the central nine ( $3 \times 3$ ) drawers in the fixed half of the tube matrix of FCA by replacing sodium containing cans by void cans. For the axial distribution measurement, the area of the voided region was 17 cm x 17 cm, and the depth of it was 5 cm which corresponds to the cell size. For the volume dependence measurement, the area of the voided region was same as above, but the depth of it was varied from 10 cm to 46 cm, which correspond to the volume change from 2.8  $\ell$  to 12.5  $\ell$ .

The reactivity worth was obtained from the difference of excess reactivities caused by the replacement of the plates.

#### Calculation

Two sets of 70-group effective cross sections based on JENDL-2 and JENDL-3.1 were prepared using cell calculation code, SLAROM. The core calculation was performed by Benoist's anisotropic diffusion theory with rz-mode. The reactivity worth was then calculated by the first order perturbation theory for the axial distribution measurement and by the exact perturbation theory for the volume dependence measurement. The transport correction was applied to both calculations.

In the preparation of the anisotropic diffusion coefficients, detailed heterogeneity of sodium containing cans and void cans was considered to calculate the neutron streaming effect properly.

## Results

The ratios of the calculated sodium void worth to the measured one (C/E values) at the core center are shown in Table 3.6.1. Since the leakage term at the core center is negligible, C/E values in this table directly indicate the calculation accuracy of the non-leakage term. The calculation by JENDL-2 generally overestimates the measured sodium void worth by 10 to 20 %, while that by JENDL-3.1 agrees well with the measurements except for that at XVI-1 which contains U-235 in the inner core.

Energy breakdowns of the worths are also shown in Table 3.6.1. The smaller worth by JENDL-3.1 is mostly resulted by the smaller component in the energy range from 19 to 640 keV. In JENDL-3.1, the neutron capture cross section of U-238 is 10 % smaller than that in JENDL-2 around 100 keV. This change makes the adjoint neutron spectrum flat, and as a result, it reduces the positive reactivity worth caused by the neutron spectrum hardening.

To examine the calculation accuracy of the leakage term, the measured and the calculated axial distributions of sodium void worth are compared in Fig.3.6.1. In this figure, the non-leakage term of the calculation is multiplied by the inverse of the C/E values in Table 3.6.1, which are not affected by the leakage term, so as to exclude the error of the non-leakage term. Since the difference of the leakage term between JENDL-2 and JENDL-3.1 is small, the results calculated only by JENDL-3.1 are shown in the figure. The calculation agrees very well with the measurements even at the core edge where the magnitude of the leakage term is significant. If the detailed heterogeneity of the plates is not considered in the cell calculation, the absolute value of the leakage term generally decreases by 5 ~ 10 % because of the underestimation of the neutron streaming effect.

The results of the void volume dependence are shown in Table 3.6.2 for assembly XVII-1. Good C/E values after the correction of the non-leakage term suggest that the most part of the discrepancy between the measurement and the calculation comes from the non-leakage term and that the calculation accuracy of both terms are independent of the void volume.

The results of the accuracy evaluation are summarized as follows;

- 1) As to the non-leakage term, the calculation error by JENDL-3.1 is within 5 % for both metallic fueled fast reactors and MOX fueled ones, when their fuel does not contain U-235.
- 2) As to the leakage term, both JENDL-2 and JENDL-3.1 give fairly accurate values, when the detailed cell heterogeneity is taken into account.
- 3) These conclusions are independent of the void volume within the range of the present measurement.

Table 3.6.1 C/E values of sodium void worth at core center

Assembly	Fuel type (Fissile)	Data file	C/E	Energy breakdown ( $10^{-4}\Delta k/k$ )			
				Total	$\sim 19\text{keV}$	$19\sim 640\text{keV}$	$640\text{keV} \sim$
XVI-1	Metal (Pu+EU)	JENDL-2	1.22 (2.8%) <sup>(a)</sup>	0.93	-0.10	0.45	0.58
		JENDL-3.1	1.11	0.85	-0.10	0.37	0.58
XVI-2	Metal (Pu)	JENDL-2	1.08 (2.5%)	1.08	-0.08	0.76	0.40
		JENDL-3.1	0.96	0.96	-0.09	0.67	0.38
XVII-1	MOX (Pu)	JENDL-2	1.15 (4.5%)	0.62	-0.14	0.46	0.30
		JENDL-3.1	0.95	0.51	-0.15	0.37	0.29

(a) Experimental error

Table 3.6.2 Sodium void worth for large region (XVII-1)

Void volume ( $\ell$ )	Experiment ( $10^{-4}\Delta k/k$ )	Component <sup>(a)</sup> ( $10^{-4}\Delta k/k$ )		C/E		C/E after correction <sup>(b)</sup>	
		Non-leakage	Leakage	JENDL-2	JENDL-3.1	JENDL-2	JENDL-3.1
2.8	$1.01 \pm 0.02$	1.02	-0.04	1.20	0.98	1.01	1.02
8.4	$1.88 \pm 0.02$	2.62	-0.84	1.24	0.95	0.99	1.00
12.5	$0.97 \pm 0.02$	3.24	-2.36	1.61	0.90	1.01	1.04

(a) Calculated by JENDL-3.1

(b) Non-leakage term is divided by the C/E values in Table 3.6.1.

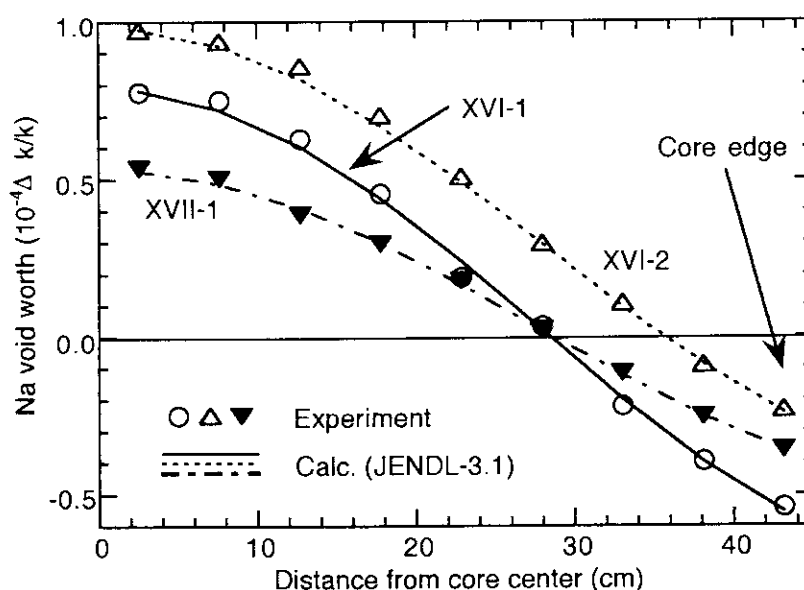


Fig.3.6.1 Comparison between calculated and measured axial distribution of sodium void worth  
(Non-leakage term is corrected by the C/E values in Table 3.6.1)

### 3.7 Measurement of Control Rod Reactivity Worth in Axially Heterogeneous Fuel Core by PNS Method

F. Akino, M. Takeuchi and T. Ono

In the design of the HTTR, the control rod worth and the reactor shutdown margin must be determined accurately. To examine the accuracy of neutronics calculation code, we measured the reactivity worth of an HTTR mockup control rod in the VHTRC-4 core by the pulsed neutron source (PNS) method.

The VHTRC-4 core is loaded with 2, 4 and 6wt% enriched fuel in an axially zoning pattern. This core reaches a critical point by 284 fuel rods. The HTTR mockup control rod consists of a stack of neutron absorbing pellets (outer diameter : 89.6mm, inner diameter : 60.0mm, height : 25.2mm, boron content : 38.3wt%, stack length : 1150mm) inserted into a stainless steel tube.

In the PNS experiments, the core loaded with 276 fuel rods was used and four  $\text{BF}_3$  counters were installed in the core. The PNS target was located near the center of back surface of the fixed half assembly. The fuel rod loading pattern and arrangements of the  $\text{BF}_3$  counters and the PNS target are shown in Fig.3.7.1. The subcritical reactivity of the core without the HTTR mockup control rod was 0.43\$ which was determined from the fuel rod worth measured in a critical core. The HTTR mockup control rod was inserted in a hole of the central column indicated in Fig.3.7.1. The  $\text{BF}_3$  counters were placed at 48 points in 12 fuel blocks. To get the most probable measured value, the experimental data were analyzed by two method, i. e., 1) integral version, 2) revised King-Simmons methods. The raw data were analyzed by the Sjöstrand method using the ALPHA-D code<sup>1)</sup>. Area ratios of the prompt to delayed modes by the Sjöstrand method were obtained at the 48 measuring points. The area ratios, i. e., the reactivity values are shown in Fig.3.7.2. The minimum and the maximum values were 13.5\$ and 52.3\$, respectively. Analyzing these results by the integral version of Kosály and Fisher's method<sup>2)</sup>, we obtained the reactivity worth of the HTTR mockup control rod as  $20.7 \pm 0.3\$$  ( $\overline{\rho}_{\text{st}}$ ). The reactivity worth ( $\rho_{\text{RKS}}$ ) obtained by the revised King-Simmon's pulsed neutron method<sup>3)</sup> is listed in the Table 3.7.1.

Calculations were carried out of the HTTR mockup control rod worth using the two methods, i. e., 1) two dimensional Sn method cell calculation/three dimensional diffusion core calculation, 2) Monte Carlo methods. Two calculational methods were adopted for comparison between homogeneous one region group constants model and heterogeneous two region group constants model for taking account of precise geometry of central block with the HTTR mockup control rod in the core calculation. The cell calculation was carried out by the SRAC code<sup>4)</sup> with ENDF/B-IV nuclear data library. The double heterogeneities of fuel rods

in a graphite block and coated particles in a fuel compact was taken into account in the calculation of group constants of fuel block. The group constants of central block with the HTTR mockup control rod were prepared by the Sn method using the TWOTRAN code (X-Y geometry,  $S_4$  approximation). Thermal neutrons in the energy range from 0.0eV to 1.125eV were divided into 39 groups and fast neutrons in the energy range from 1.125eV to 10MeV were divided into 22 groups. Using the neutron spectra obtained by the cell calculation, the cross sections of 61 groups were condensed into 24 groups for the core calculation. The group constants for reflector were condensed by means of asymptotic spectrum. The calculation of reactivity worth was carried out using these group constants by three dimensional diffusion approximation in the core calculation. For the Monte Carlo method, the group constants of fuel rod were calculated by pin rod cell model in the cell calculation and the group constants of central block with the HTTR mockup control rod were prepared by the collision probability method. The GMVP code<sup>9)</sup> was adopted for the Monte Carlo calculation to take account of the precise geometry of central block with the HTTR mockup control rod. The calculated values are shown in Table 3.7.1. The calculations by both methods predicted the experimental results with 10% accuracy.

#### References

- 1) Kaneko Y., et al. : Nucl. Sci. Eng., 50, 173 (1973)
- 2) Kosály G. and Fischer A. : J. Nucl. Energy, 26, 17 (1971)
- 3) Akino F., et al. : J. Nucl. Sci. Tech., 17, 593 (1980)
- 4) Tsuchihashi K., et al. : "Revised SRAC Code System", JAERI 1302 (1987)
- 5) Nakagawa M., et al. : Nucl. Sci. Eng., 107, 58 (1991)

Table 3.7.1 Measured and calculated values of HTTR mockup control rod worth in the VHTRC-4 core

Measured value(\$)		Calculated value(\$)	
$\rho_{SI}$	$\rho_{RKS}$	Sn/Diffusion	Monte Carlo
$20.7 \pm 0.3$	$19.4 \pm 0.3$	18.60	$19.0 \pm 0.3$

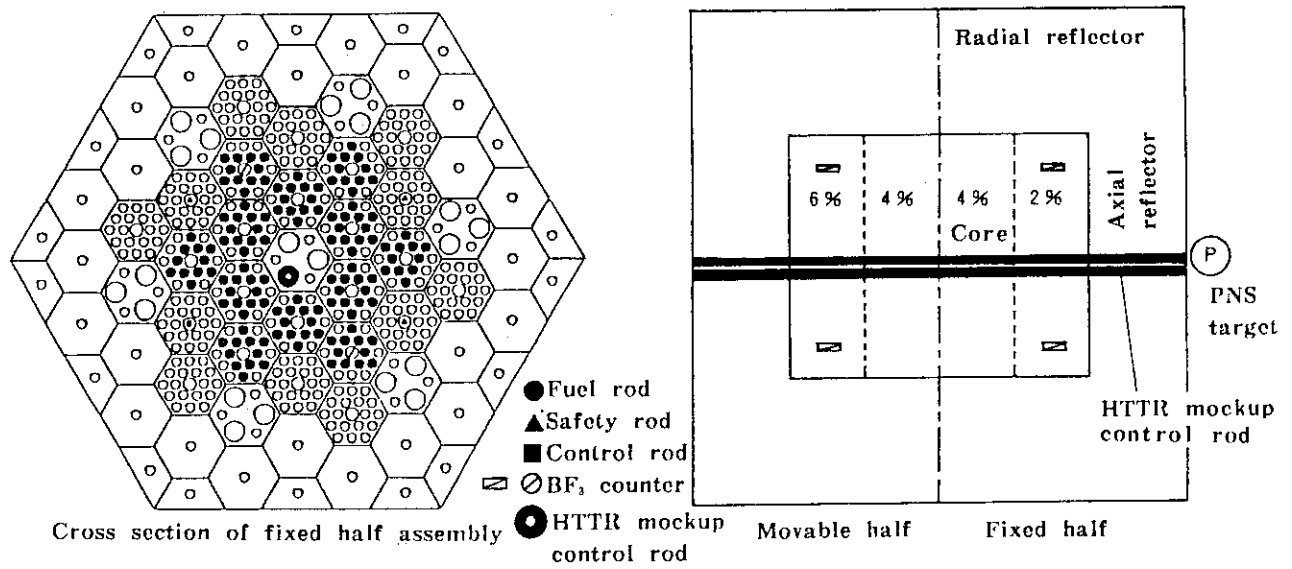


Fig. 3.7.1 Fuel rod loading pattern and arrangements of PNS target and BF<sub>3</sub> counters in the VHTRC-4 core.

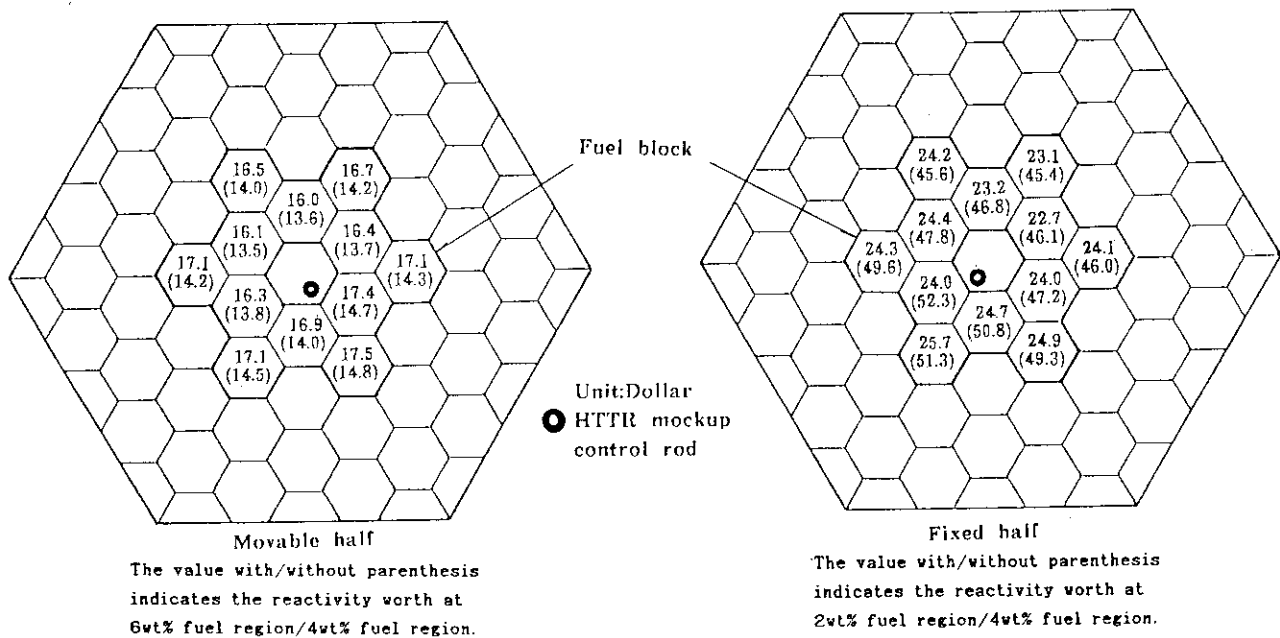


Fig. 3.7.2 Spatial dependence of reactivity worth by Sjöstrand method.



### 3.8 Analysis of U-235 fueled Lead Cooled Fast Reactor Critical Experiments

H. Akie, H. Takano and K. Kaneko\*

On developing lead cooled fast reactors, some critical experiments have been performed in Russia to validate the reactor physical data and methods used for the design calculations. These critical experiments have been also analysed in JAERI<sup>1)</sup>, and the results for the Pu fueled assembly BFS-61 were already reported last year in this annual report<sup>2)</sup>. Here, the results of the analysis of assemblies ROMB CA-1~6 are shown. These assemblies are the U-235 fueled cores of R-Z geometry surrounded by lead reflector, except that CA-1 has not reflector.

Analysis of these assemblies was carried out by using the continuous energy Monte Carlo code MVP. The evaluated nuclear data library JENDL-3.1 was mainly used, and intercomparison was also made between the results obtained with the different evaluated nuclear data libraries such as ENDF/B-IV, ENDF/B-V, and the latest evaluated data JENDL-3.2. From the results, the reliability of the nuclear data was also studied.

The multiplication factors calculated with MVP for the assemblies are summarized in Table 3.8.1. It is noticeable, first of all, that the results obtained by using the lead cross sections in JENDL-3.2 and ENDF/B-IV are overestimated about 0.5~3%. Figure 3.8.1 shows the elastic scattering cross section data of lead from ENDF/B-IV, JENDL-3.1 and JENDL-3.2. The large discrepancies are found in the 100keV energy range. The large elastic cross section leads to the small neutron leakage from the core, and causes the large multiplication factor.

Table 3.8.1 Effective multiplication factors of ROMB assemblies calculated by MVP code

	JENDL-3.1	J3.1+J3.2(Pb)	J3.1+B4(Pb)	J3.1+J3.2(U5)	J3.1+B5(U5)
CA-1	1.0013±0.05%	-	-	1.0008±0.07%	0.9957±0.08%
CA-2	1.0030±0.08%	1.0064±0.07%	1.0101±0.08%	1.0010±0.08%	0.9939±0.09%
CA-3	1.0015±0.09%	1.0049±0.05%	1.0112±0.09%	1.0000±0.08%	0.9961±0.10%
CA-4	1.0061±0.08%	1.0175±0.08%	1.0275±0.09%	1.0034±0.05%	0.9981±0.09%
CA-5	1.0061±0.08%	1.0214±0.09%	1.0333±0.10%	1.0047±0.10%	0.9950±0.10%
CA-6	1.0056±0.09%	1.0203±0.10%	1.0306±0.08%	1.0021±0.09%	0.9967±0.09%

J3.1 : JENDL-3.1, J3.2 : JENDL-3.2, B4 : ENDF/B-IV, B5 : ENDF/B-V and U5 : U-235

\* The Japan Research Institute, Ltd., Tokyo

In Table 3.8.1, it is also seen that the results calculated with the JENDL-3.1 data overestimate the multiplication factors by 0.1~0.6%. The overestimation can be related to the cross section of U-235, because CA-1 is almost completely composed of uranium. In the table, the

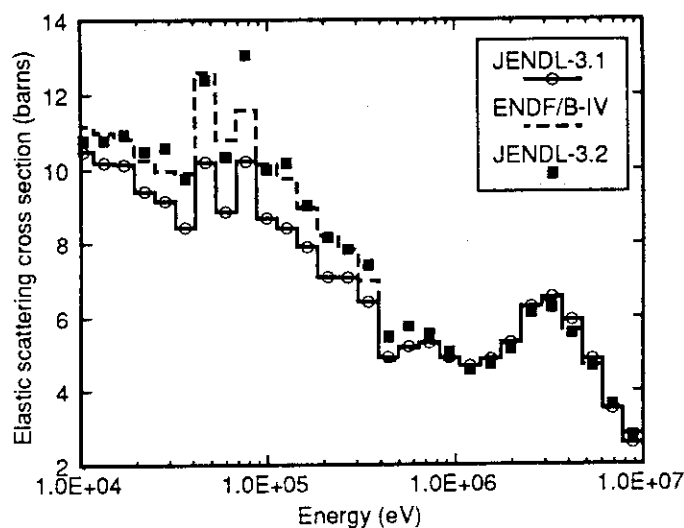


Fig. 3.8.1 Elastic scattering cross sections of Pb natural

U-235 data of ENDF/B-V underestimate slightly the multiplication factors and in better agreement with the experiment. The new data, JENDL-3.2, improves the overestimation of JENDL-3.1.

The one group effective cross sections of U-235 in the ROMB CA-1 assembly are compared in Table 3.8.2, to consider the differences between evaluated data files. It can be seen that the difference in fission cross section is small between JENDL-3.1 and JENDL-3.2, while the production cross sections ( $\nu\sigma_f$ ) differ each other. This indicates the discrepancies in  $\nu$  values. Both the fission and production cross sections of ENDF/B-V data are smaller than the JENDL-3.1 data. The  $\nu$  values evaluated as the ratio of  $\nu\sigma_f/\sigma_f$ , from the results of MVP calculation, are compared in Fig. 3.8.2. By comparing the JENDL-3.1 and -3.2 data, the discrepancies are found in the energy ranges  $E > 1\text{MeV}$  and  $E = 200\sim 300\text{keV}$ . In the MeV energy region,  $\nu$  value in JENDL-3.1 is larger than that in JENDL-3.2. The energy dependent structure of  $\nu$  observed between 200 and 300keV in JENDL-3.1 data disappeared in JENDL-3.2 data. For these reasons, the overestimated multiplication factors obtained by JENDL-3.1 data for U fueled cores are improved in the calculations with JENDL-3.2 data.

## References

- 1) Akie H., et al. : "Analysis of Critical Experiment BFS-61 by Using the Continuous Energy Monte Carlo Code MVP and the JENDL-3.1 Nuclear Data", Proc. Int. Topical Mtg. on Advanced Reactors Safety (ARS'94), April 1994, Pittsburgh, U.S.A., pp.544-548

(1994).

- 2) Akie H., Takano H. and Kaneko K. : "Benchmark Calculation of the Lead Cooled Fast Reactor Critical Assembly BFS-61", Reactor Engineering Department Annual Report, JAERI-M 93-181, Japan Atomic Energy Research Institute, pp.64-66 (1993).

Table 3.8.2 One group effective cross sections of U-235 in ROMB CA-1 (barns)

	$\nu\sigma_f$	$\sigma_f$	$\sigma_c$
JENDL-3.1	3.2802 (0.014%)	1.2555 (0.012%)	0.1393 (0.11%)
JENDL-3.2	3.2722 (0.017%)	1.2550 (0.014%)	0.1395 (0.10%)
ENDF/B-V	3.2624 (0.013%)	1.2516 (0.011%)	0.1311 (0.10%)

The values in parentheses show the errors., .

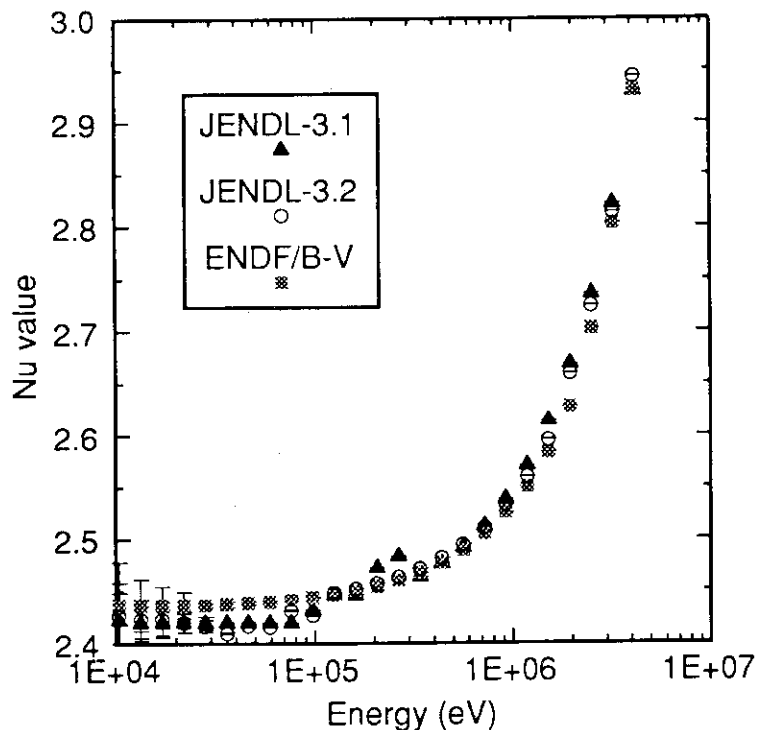


Fig. 3.8.2  $\nu$  values of U-235 evaluated from MVP calculation for CA-1

## 4 Advanced Reactor System Design Studies

Innovative concepts of advanced reactor systems have been developed to meet various needs for nuclear energy in next century.

A new concept of loop-type JAERI Passive Safety Reactor (JPSR) is being developed to reduce the manpower in operation and maintenance and influence of human error on reactor safety. The JPSR has the following features: an inherent matching nature of core heat generation and heat removal, in-vessel control rod drive mechanism units, low power density core, once-through steam generators, elimination of chemical shim, a large volume pressurizer, passive residual heat removal systems, passive engineered safety systems and elimination of emergency diesel generator. In order to develop and improve the reactor design, analytical and experimental studies have been performed.

The system-integrated pressurized water reactor (SPWR) is being continuously designed since 1986. The major features of SPWR are; an integral reactor in which all primary coolant system components are located in a reactor vessel, a passive shutdown system using poison tanks filled with high concentration borated water, passive emergency feed water system and heat removal system, and a water-filled containment vessel.

A feasibility study of lead-cooled fast reactor (LCFR) with nitride fuel assemblies has been performed from the view point of seismicity and plant cost. The results indicated that the reactor structure has the integrity against 2G seismic acceleration condition and the total cost can be reduced more 10 % than that of Na-cooled plant.

A concept of PWR with once-through weapons plutonium burning fuels were studied. In order to estimate the discharge burnup and plutonium transmutation characteristics, core burnup and reactivity coefficients calculations were performed.

A combination of pebble-bed type high temperature gas cooled reactor (HTGR) and magneto-hydrodynamic (MHD) generator has been proposed for high efficiency (57.3 %) electric power generation.

A conceptual studies of lithium cooled pebble bed reactor with a potassium Rankine cycle turbine generator has been performed for use in a moon base. The design efforts were made to increase safety during a launch phase and minimize the specific mass.

In this chapter, followings are in charge of sections in parenthesis: passive safety reactor systems laboratory (4.1 through 4.6), special researcher Dr. Sako (4.7), reactor system laboratory (4.8 and 4.9), and thermal reactor physics laboratory (4.10 and 4.11).

## 4.1 Concept of JAERI Passive Safety Reactor JPSR

Y. Murao, F. Araya, T. Iwamura and K. Okumura

The conceptual design of JAERI Passive Safety Reactor (JPSR) and flow diagram of primary system with passive safety system are shown in Figs.4.1.1 and 4.1.2, respectively. Major parameters of JPSR are listed in Table 4.1.1. The features of JPSR are describe. More detailed information on the JPSR design is explained in reference 1).

In the design of the inherent matching of core heat generation and heat removal in the nuclear steam supply system (NSSS), large reactivity coefficient on moderator density and small negative reactivity coefficient on fuel temperature (Doppler effect) and small dependency of steam temperature on heat removal rate were found to be essential for a closed primary coolant system from a pre-analysis<sup>1)</sup>. And the elimination of chemical shim is also found to be essential to increase reactivity coefficient on moderator density. In order to eliminate chemical shim in-vessel control rod drive mechanisms (CRDMs) which are being developed for a concept of a new marine reactor being designed at JAERI<sup>2)</sup> are adopted. The reasons are that the elimination of chemical shim requires increase of control rod drive mechanism units to compensate decrease in reactivity due to burnup of nuclear fuel and reactivity margin in cold state in the coolant. For reducing Doppler effect low power density core is adopted. And for obtaining independence of steam temperature on heat removal rate once-through type steam generators (SGs) are adopted. The low power density core is also effective to reduce thermal load on the fuel in emergency.

The chemical and volume control system (CVCS) can be dramatically simplified by adopting a large pressurizer, since volume control system of the primary coolant in operation and boron concentration control system are unnecessary and only chemical control system operated under high pressure condition is necessary. And by adoption of non-seal pumps as the primary coolant circulation pump, seal-water supply system is unnecessary. The charging and letdown systems are used for adjusting water level and system pressure in the pressurizer before nuclear heating in startup period and the charging system is also used for enough small leak events. Additionally actuation of pressure relief valves and even the pressure regulation in emergency are unnecessary. Thus the CVCS can be simplified and primary coolant is isolated in the containment. The control system in the NSSS can also be simple.

The passive residual heat removal and containment cooling system which does not require any auxiliary systems or components of the safety class are adopted in the JPSR. And a result, emergency diesel generators and active components such as valves and pumps can be eliminated. Two units of residual heat exchanger are installed outside the pressure vessel and each unit has a natural circulation loop connected to a gravity coolant injection pool cooled by

air cooler units outside the containment. The core residual heat is removed by the residual heat exchangers through single-phase natural circulation lines under high or low pressure and then transferred to the gravity coolant injection pool by single-phase or two-phase natural circulation under containment pressure. The pool is cooled by natural circulation of water under atmospheric pressure and the heat is transferred to the air coolers as final heat sink. Details of these systems are presented in section 4.4.

The passive engineering safety system consists of core makeup tanks (2 units), accumulators (2 units) and gravity coolant injection systems (2 units). The high pressure core makeup tanks with a pressure equalizing line are actuated by actively-operated valves and by passively-operated valves. When the system pressure decreases to a certain level, the accumulators are actuated by opening check valves and water is provided by nitrogen gas pressure. A large volume of gravity coolant injection pool is placed outside of the inner containment in the containment. This pool is used for reservoir for back-up water injection. Details of these systems is presented in Section 4.5.

#### References

- 1) Murao Y., Araya F. and Iwamura T.: presented at ARS'94, Pittsburgh, April 17-21, (1994).
- 2) Ishizaka Y., et al.: Proceedings of ANP'92, Vol.I, P4.6, Tokyo, Oct. 25-29, (1992).

Table 4.1.1 Major parameters for JPSR design

Reactor type	Two-loop PWR
SG type	OTSG
Control rod drive mechanism (CRDM)	In-vessel CRDM
Primary coolant pump	Canned-motor pump
Thermal reactor power	1853 MWt
Operating pressure	15.6 MPa
Total primary coolant flow rate	$32 \times 10^6$ kg/h
Core inlet temperature	558 K
Core outlet temperature	598 K
Pressure loss through the core	0.157 MPa
Primary coolant volume	319 m <sup>3</sup>
Pressurizer volume (total/steam region)	48 / 30 m <sup>3</sup>
Average linear heat generation rate	13.2 kW/m
Number of fuel bundle	145
Number of fuel rod per bundle	264
Outer diameter of fuel rod	9.5 mm
Thickness of cladding	0.57 mm
Fuel rod arrangement	Square lattice of 17x17
Active fuel length	3.66 m
Axial peaking factor (BOEC)	1.2393
Radial peaking factor (BOEC)	1.6159
Coolant density reactivity coefficient (BOEC)	$57.96$ \$/g/cm <sup>3</sup>
Coolant temperature reactivity coefficient (BOEC)	$-2.44 \times 10^{-4}$ \$/K
Doppler reactivity coefficient (BOEC)	$-4.02 \times 10^{-3}$ \$/K
Scram reactivity (BOEC)	-42.18 \$

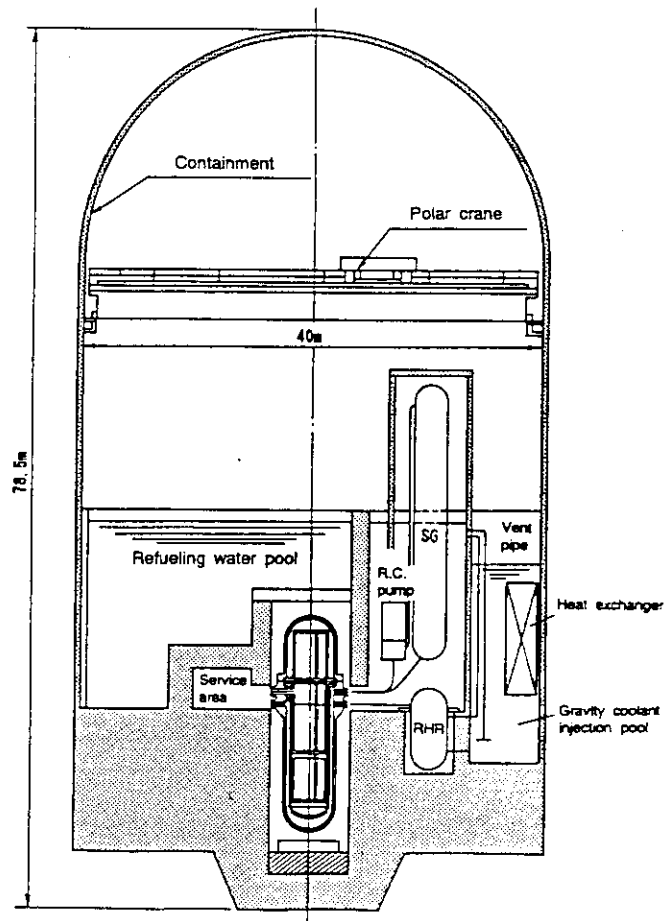


Fig. 4.1.1 Conceptual design of JP SR

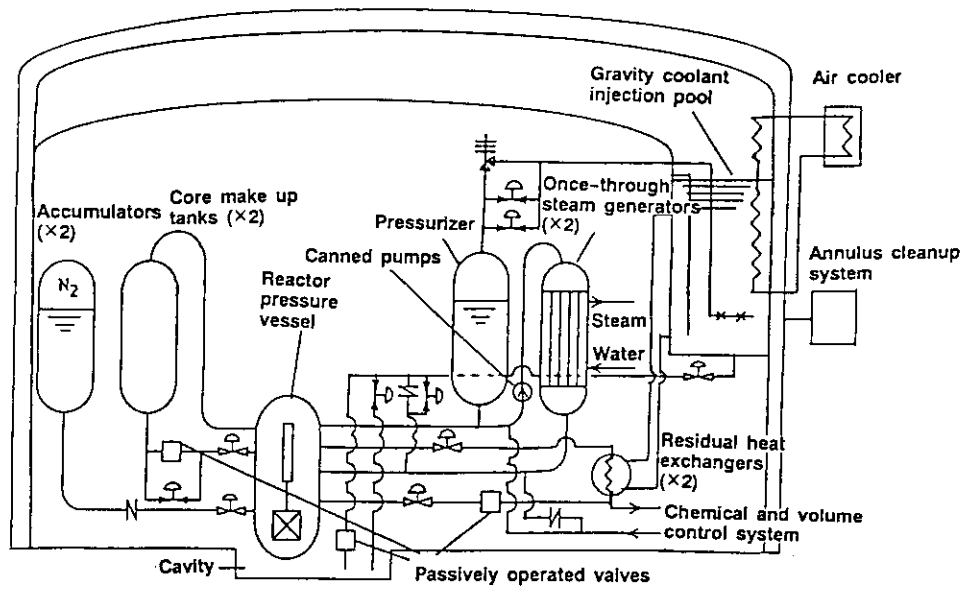


Fig. 4.1.2 Conceptual flow diagram of primary system with passive safety system

## 4.2 Nuclear Design Study for JPSR

K. Okumura and Y. Murao

Table 4.2.1 shows the main parameters of the JPSR core. The nuclear characteristics in this Table were evaluated by a three-dimensional core burn-up analysis with the SRAC code system<sup>1)</sup>. The gross electric and thermal outputs are fixed 660MWe and 1941MWt, respectively. The configuration of a fuel assembly is identical to that of a 17x17-type fuel assembly of typical PWRs. The core size is the same as the Takahama-3 PWR with three cooling loops. Thus the average power density is about 75% in comparison with current PWRs. As shown in Fig.4.2.1, four-batches refueling strategy is adopted to obtain high burn-up more than 45GWd/t without increase of excess reactivity. The disadvantage of shortening a cycle length is mitigated by the low power density.

From the preliminary transient analysis, it was found that relatively large reactivity coefficient on moderator density would be necessary to realize inherent load following capability.<sup>2)</sup> In current PWRs, the upper concentration of soluble boron in hot full power condition is limited so as to maintain negative feedback by moderator density decrease. In other words, the reactivity coefficient on moderator density is too small to realize the expecting inherent load following capability, especially at the beginning of a cycle.

In JPSR, all excess reactivities are compensated with control rod movements. The reactivity coefficients of JPSR in Table 4.2.1 were evaluated in the critical condition with control rods instead of the soluble boron. The suitable reactivity characteristics expected from the transient analysis was obtained through burn-up periods.

Table 4.2.2 shows the preliminary results on excess reactivity and control rod worth in cold condition at the beginning of cycle. Here, several types of cluster control rods are considered and they are assumed to be inserted in all fuel assemblies in the core with the in-vessel control rod drive mechanisms. From this Table, the conventional Ag-In-Cd control rods do not have enough worth to hold the sufficient subcriticality ( $\sim 5\% \Delta k/k$ ) in fuel exchanges. The  $B_4C$  control rod seems to be feasible, but such the strong neutron absorber has disadvantage to distort the power distribution in operating condition. Consequently, the use of two different types of control rods is preferable. They are a gray rod aiming to control burn-up excess reactivity and power distribution, and a strong absorber rod for emergency shutdown and for holding subcriticality. The detail of the control rods design is under optimizing.



## References

- 1) Tsuchihashi K., et al. : Revised SRAC Code System, JAERI-1302 (1983)
- 2) Araya F. and Murao Y. : A Study on Possibility of a Reactor with Highly-load Following Capability, JAERI-M 93-181, pp80-82 (1993)

Table 4.2.1 Major parameters for JPSR concept

Parameters	Value
Thermal output (MWt)	1853
Number of loops	2
Primary system pressure (Mpa)	15.73
Core inlet coolant temperature (K)	558
Core exit coolant temperature (K)	598
Core average coolant temperature (K)	578
Fuel assembly type	17×17 type
Number of fuel assemblies	145
Number of fuel rods per assembly	264
Fuel assembly pitch (mm)	215
Fuel rod pitch (mm)	12.6
Cladding outer diameter (mm)	9.5
Pellet outer diameter (mm)	8.19
U-235 enrichment (w/o)	[4.0] ~ 5.0
Effective core height (mm)	3660
Equivalent core diameter (mm)	2920
Average liner heat rate (KW/m)	13.2
Number of refueling batch	4
Discharge burn-up (GWd/t)	[47] ~ 58
Fuel cycle length (EFPM)	[14] ~ 18
Moderator density reactivity coefficient	
BOC / EOC (% $\Delta k/k/g/cm^3$ )	36 / 34 (35.2)
Doppler reactivity coefficient	
BOC / EOC (% $\Delta k/k/^\circ C$ )	$-2.5 \times 10^3 / -2.7 \times 10^3$ ( $-3.4 \times 10^3$ )

[ ] : case of 4.0w/o U-235

( ) : reference value expected from transient analysis<sup>2)</sup>

Table 4.2.2 Preliminary results on excess reactivity and control rod worth in cold condition at the beginning of cycle

Excess reactivity ( $\% \Delta k/k$ )	
Burnup	10.9
Xe effect	1.85
Power defect (HFP->CZP)	7.07
Total	19.82
Control rod worth ( $\% \Delta k/k$ )	
Ag-In-Cd	-23.58
B <sub>4</sub> C powder (natural B)	-30.99
B <sub>4</sub> C pellet (60% enriched B-10)	-42.07

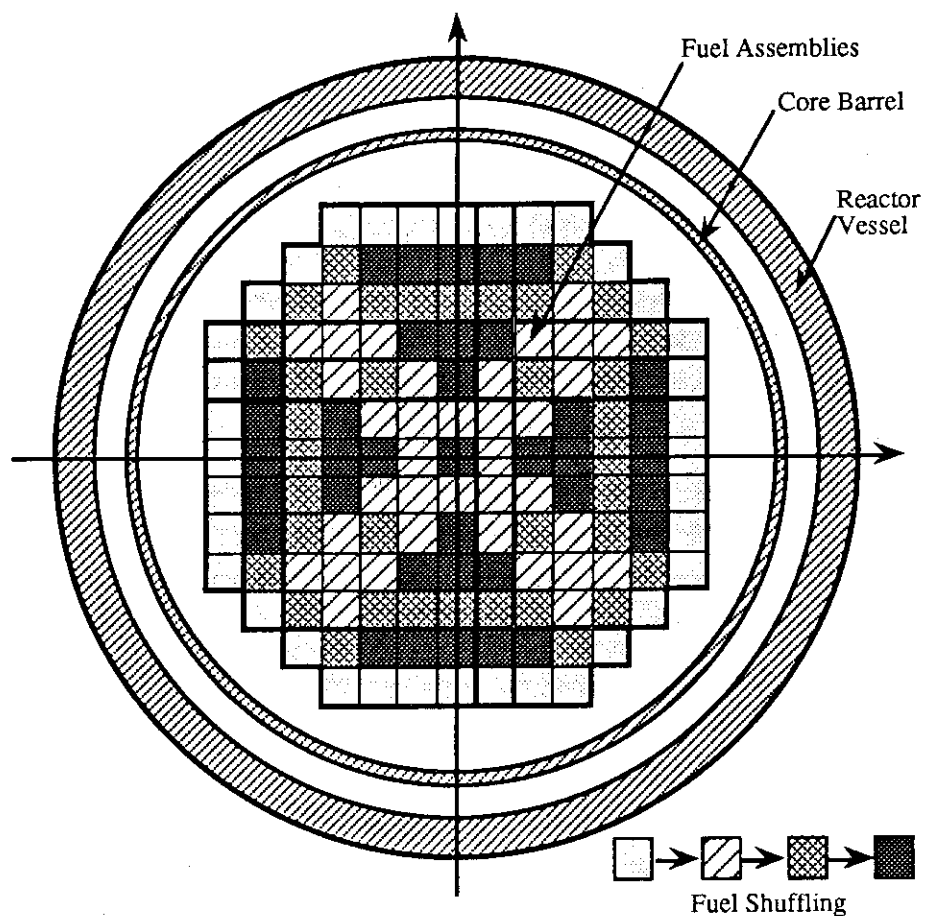


Fig.4.2.1 Horizontal cross section of JPSR core

### 4.3 Transient Thermal-Hydraulic Analyses for Design of JPSR

F. Araya, Y. Murao and T. Iwamura

A concept of JAERI Passive safety reactor (JPSR) has been studied confirming its safety by performing transient thermal-hydraulic analyses. The possibility of a pressurized water reactor concept with highly inherent matching nature of the core power to the heat removal rate has been confirmed<sup>1)</sup>. After the study, two transient analyses of the complete loss of flow accident and the loss of coolant accident were performed to determine the moment of inertia of canned-motor pumps as the main coolant pumps and to confirm effects of the core makeup tank on core cooling which were designed to be adopted in JPSR. The calculated results are presented in the following.

#### Complete loss of primary coolant flow accident

JPSR is designed to adopt canned-motor pumps as the main coolant pumps due to its high reliability<sup>2)</sup> and contribution to simplification of the chemical and volume control system (CVCS). Since the pump has low moment of inertia, flow coastdown transients following trip of primary coolant pumps becomes severe in view of occurrence of the departure from nucleate boiling (DNB). Therefore the rotor of the pump should be designed to have high inertia so as to inhibit the DNB occurrence. Since the complete loss of primary coolant flow accident following trip of all pumps is severest as described in the reference 2), the transient calculations have been performed to determine the inertia.

RETRAN-02/MOD3 code was used for the analysis. Since the interesting time period is short, the secondary system was neglected in the nodding model and the heat removal rate from the primary coolant loop was set to be constant during the calculation. The pump behavior was modeled with the built-in pump model by assuming loss of electric power supply. The rated head was determined so as to supply the pressure loss of the primary coolant loop at the rated condition. Other characteristic parameters were determined so as to satisfy the homologous law. The core power was calculated by the point reactor kinetics model. The reactor scram was assumed to be actuated by the trip signal on the low coolant flow of 80 %. The sensitivity calculations were carried out on the moment of inertia and the density reactivity coefficient which had effect on reduction of the core power during the transient.

The calculated results are shown in Fig 4.3.1. This figure shows that, for higher inertia than 8% of the ordinary PWR's,  $3110\text{kg}\cdot\text{m}^2$ , the occurrence of DNB can be inhibited in the present design of JPSR with regardless of the actuation of the reactor scram. This is because the core power is reduced by the effect of the density reactivity coefficient.

### Loss of coolant accident

In order to confirm the effect of the core makeup tank (CMT) on the core cooling, a large break loss-of-coolant accident (LBLOCA) was calculated. Two CMTs are designed to be adopted in JPSR as a passive coolant injection system under LOCAs and to make the reactor core subcritical by injecting borated water into the reactor core.

The nodding model used in the calculation includes the primary coolant system and the secondary side of the steam generators (SGs). The double ended break of a cold leg and 200% break area were assumed. The volume of CMT was determined so that a subcritical condition in the reactor core could be achieved by mixing the primary coolant and the borated water contained in a CMT with an assumption of 21000 ppm concentration of Boron in CMT. The reactor scram, the reactor coolant pump trip and the isolation of the SG secondary side were assumed.

The calculated results are shown in Fig. 4.3.2. As shown here, the pressure decrease is slow because JPSR has a large pressure vessel and two cold legs per one primary coolant loop. The actuation of the accumulator is about 53 seconds. The reverse flow is calculated in the core in most of the calculated time period. Since CMTs are designed to supply coolant into the upper plenum, the supplied coolant from CMTs flow down in the core region and contribute to cool the core. The maximum cladding temperature is calculated to be 823 K and to be low enough than the safety limit of peak cladding temperature. This is resulted from the CMT effect and the design feature that the linear heat generation rate is lower than that of the ordinary PWRs.

### References

- 1) Araya F. and Murao Y.: JAERI-M 93-181 ( 1993).
- 2) Tower S.N., et al.: Nuclear Engineering and Design, Vol. 109, pp147-154 (1988).

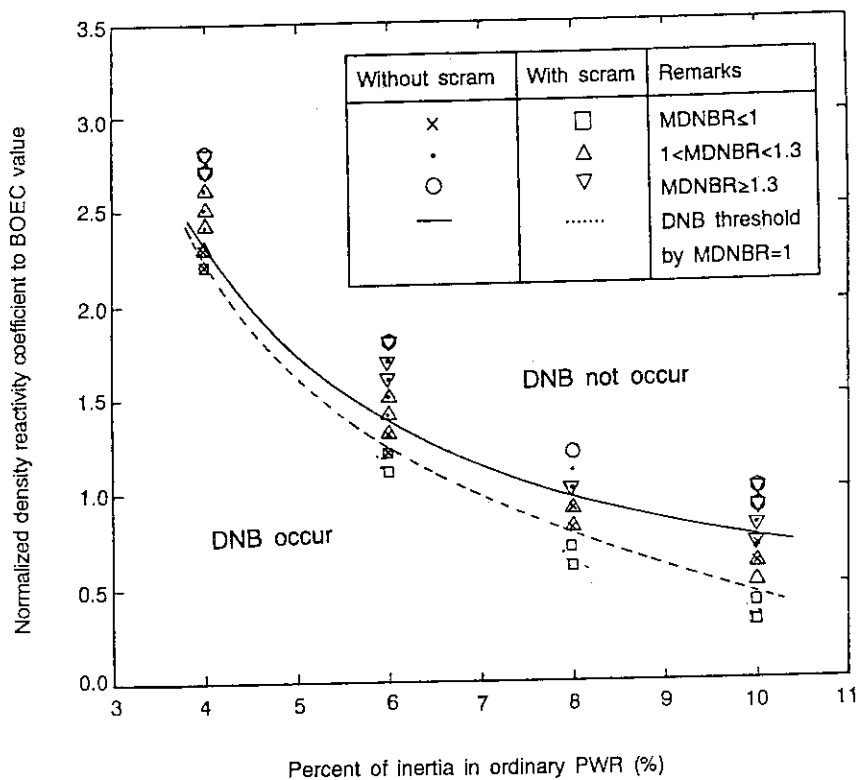


Fig. 4.3.1 DNB threshold related to pump inertia and density reactivity coefficient

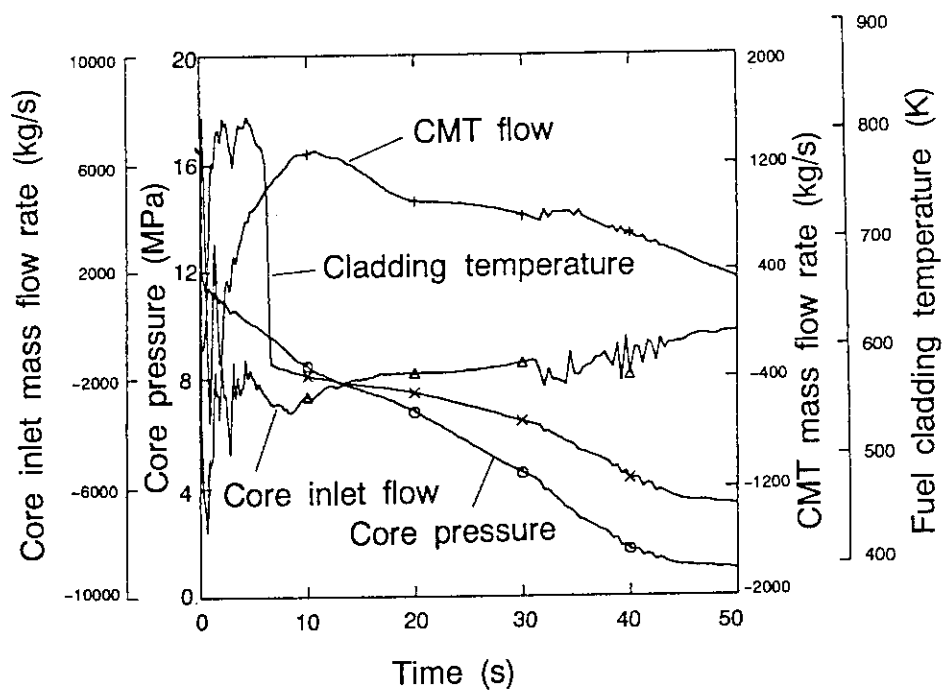


Fig. 4.3.2 Thermal-hydraulic behaviors calculated for JPSR under 200% large break LOCA

#### 4.4 Preliminary Design of Passive Residual Heat Removal and Containment Cooling System for JPSR

T. Iwamura and Y. Murao

In order to reduce manpower in operation and maintenance and influence of human errors on reactor safety, passive residual heat removal and containment cooling system which does not require any auxiliary systems or components of safety class are adopted in JAERI Passive Safety Reactor (JPSR). As a result, emergency diesel generators and active components such as valves and pumps can be eliminated.

Figure 4.4.1 shows the concept of passive residual heat removal and containment cooling system. The horizontal arrangement of major components is shown in Fig.4.4.2. As shown in these figures, two units of residual heat exchanger are installed outside the pressure vessel and each unit has a natural circulation loop connected to a gravity coolant injection pool cooled by air cooler units outside the containment. Each residual heat exchanger is connected to the upper plenum and the downcomer with normally-closed active and passive valves including a check valve. The check valve is opened by gravity force when the discharge pressure of circulation pump is decreased. Other type of passive valve is also equipped in parallel. The valves of air cooler lines are always open and therefore the pool cooling system is always functional. In order to cool the air and/or discharged steam in the containment, air cooling pipes are installed inside the containment wall and connected to the air cooler natural circulation lines as shown in Fig.4.4.1. The core residual heat is removed by the residual heat exchangers through single-phase natural circulation lines under high or low pressure and then transferred to the gravity coolant injection pool by single-phase or two-phase natural circulation under containment pressure. The pool is cooled by natural circulation of water under atmospheric pressure and the heat is transferred to the air coolers as final heat sink.

Heat removal capacity of the passive system has been evaluated by assuming one-dimensional flow under steady-state condition. It was found that one unit of residual heat exchanger has a heat removal capacity of 6% of full power when the primary system is in the hot conditions and 0.3% in the cold conditions.

Figure 4.4.3 shows the heat removal capacity of containment cooling system under various number of air cooler units and air temperatures. The heat removal capability

increases with the pool water temperature. When the available number of air cooler units is four and air temperature is as high as 30 °C, the containment cooling system can remove 1% of full power at the pool temperature of 75 °C. When six air cooler units are available, the heat removal capacity becomes 1.8 % at 80 °C of pool temperature. When the air temperature is as low as 0 °C, the heat removal capacity increases up to 2.1 % at 80 °C of pool temperature. The heat imbalance between heat from the residual heat exchanger and heat to the air coolers is stored in the pool in a certain time. Therefore the gravity coolant injection pool works as a heat reservoir.

Figure 4.4.4 shows the calculated responses of the pool water temperature and the heat removal capacity comparing with the decay heat transient under a large break LOCA condition. In the calculation, following assumptions are made. 1) All of the energy stored in the primary coolant system is discharged to and stored in the gravity coolant injection pool at initiation of LOCA event. 2) The steam discharged from the break of primary coolant piping is completely condensed in the pool. 3) The steady natural circulation in the containment cooling system is established at 1000 seconds after the initiation of LOCA. As shown in Fig. 4.4.4, the pool temperature increases to 51.4 °C just after initiation of LOCA and then increases gradually to the maximum of 69 °C at 15,000 seconds.

After reaching the maximum value, the pool temperature continuously decreases, indicating that long term cooling condition is established.

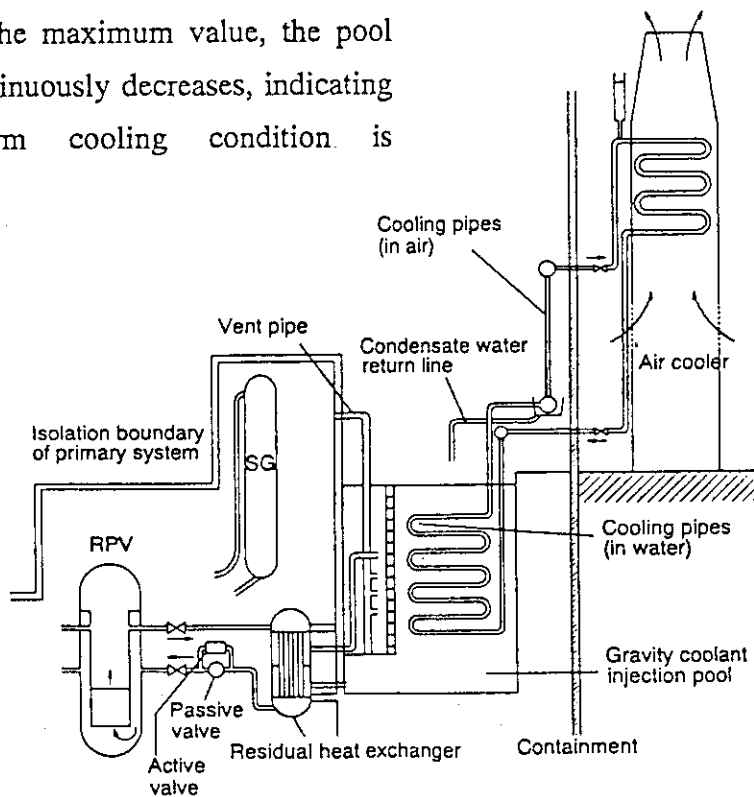


Fig.4.4.1 Passive residual heat removal and containment cooling system

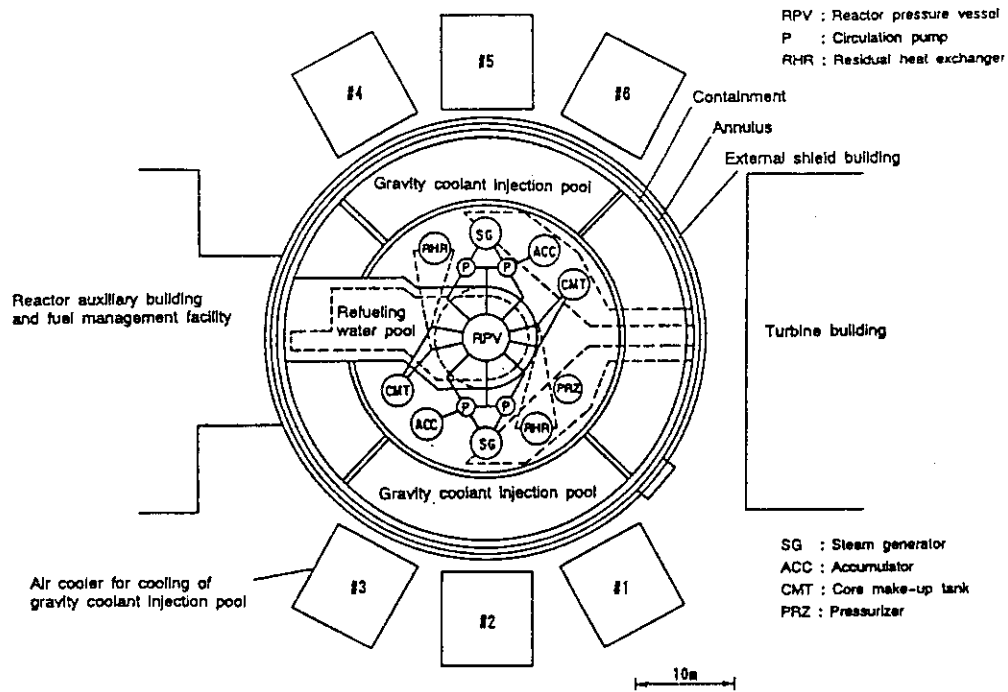


Fig.4.4.2 Horizontal arrangement of major components

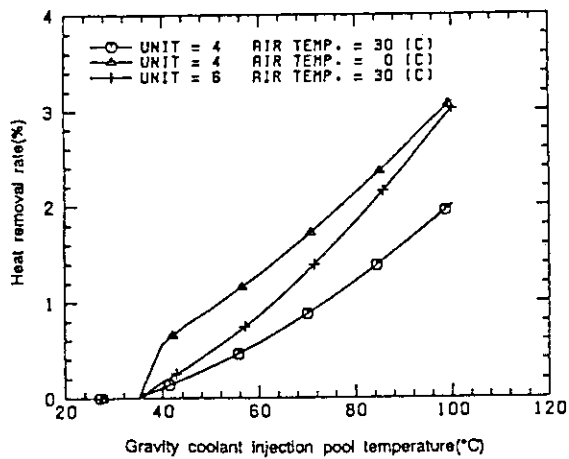


Fig.4.4.3 Heat removal capacity of passive containment cooling system

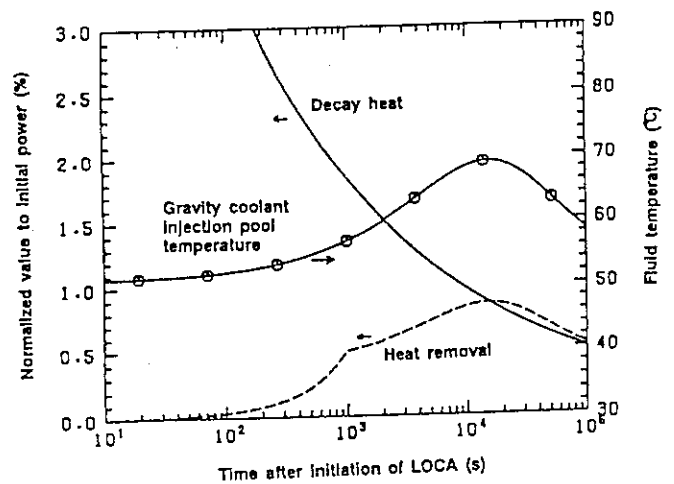


Fig.4.4.4 Response of passive containment cooling system under LOCA event



#### 4.5 Outline of Emergency Coolant Injection Systems and Preliminary Test for Core Makeup Tank for JPSR

Y. Murao, H. Watanabe, F. Araya, T. Iwamura and K. Kunii

This section describes outline of passive emergency coolant injection systems adopted in JPSR which is under development at JAERI and results derived from the preliminary experiment for the core makeup tank.

##### Outline of passive emergency coolant injection systems

JPSR is designed to adopt three kind of passive emergency coolant injection system: core makeup tanks (CMTs), accumulator tanks and gravity coolant injection pools.

Two CMTs are adopted with the objective to keep the core coolable under high pressure conditions like the high pressure injection system in the ordinary PWRs. Each of CMTs has a pressure equalizing line connected with the upper plenum and an injection line connected with the upper plenum, and is actuated by opening of an actively-operated valve or a passively-operated valve which are mechanically opened by sensing lower water level than a given level. The water contained in the CMTs is injected by a driving force of a natural circulation. The CMT contains the borated water. Therefore CMT actuated by the actively-operated valve can be also used as a backup shutdown system.

JPSR has two accumulators just like those of the ordinary PWRs. When the system pressure decreases to a certain level, the accumulators are driven for supplying coolant to the primary system by pressurized nitrogen and actuated by opening check valves. The accumulators also contains the borated water.

The primary coolant system is covered with an inner containment. A large volume of gravity coolant injection pool is placed outside of the inner containment in the containment. This pool is used for heat sink of decay heat and for absorber of heat and iodine from the inner containment in loss-of-coolant accidents (LOCAs). Accordingly the additional containment spray is unnecessary. This pool is also used for reservoir for backup water injection. Therefore the pool is connected with the cold legs of the primary loops through check valves to inject water to the primary system by gravity force when the primary system pressure is equal to the containment pressure. In certain conditions actively operated depressurization valves are opened by logical signal as a backup system. And passive devices and active valves for injecting water in the pool by steam quencher to absorb the energy of the fluid. The volume of water in the pool is large enough to flood the primary system up to the level of the pressure vessel nozzles for main coolant piping to ensure natural circulation between the primary system and the pool. The pool is filled with the borated water not to dilute the borated water injected into the primary

system in emergency. The pool is also used for heat sink of normal operating system and cooled by the in-containment air coolers.

#### Preliminary test for core makeup tank

As described above, the CMTs are designed to be actuated by sensing low water level and to supply the subcooled borated water to the upper plenum. The CMTs are simply actuated by opening the passive valve which is activated by decrease in coolant density in the vertical pipe of the pressure equalizing line due to decrease in water level in the upper plenum. Figure 4.5.1 shows the atmospheric test apparatus which consists of a simulated CMT, a simulator of the pressure vessel (PV simulator) with a boiler. The steam generation in the reactor core is simulated by injection of steam from the boiler to the PV simulator through a steam injection line. Decrease in coolant in the pressure vessel is modeled by discharging the water from the PV simulator through a discharge line. The experiment is initiated by discharging the water from the PV simulator by opening the valve. The valves in the steam injection line and pressure equalizing line are also coincidentally opened. The CMT is filled with subcooled water before initiation of the experiment. The steam flow rate in the pressure equalizing line and the fluid temperatures in the CMT are measured.

Figure 4.5.2 shows the results derived by an experiment under the conditions of the PV pressure and temperature of 0.15MPa and 383K and the CMT temperature of 298K. As shown in this figure, large steam flow is observed at early period of the experiment. This is because the steam is condensed on the water surface in the CMT. The temperature transients show that the steam condensation continuously occur. These data implies that the condensation and the pressure drop in the pressure equalizing line affect the injection characteristics of the CMT. In order to detailedly investigate the phenomena, a large scale experiment is planned to be carried out.

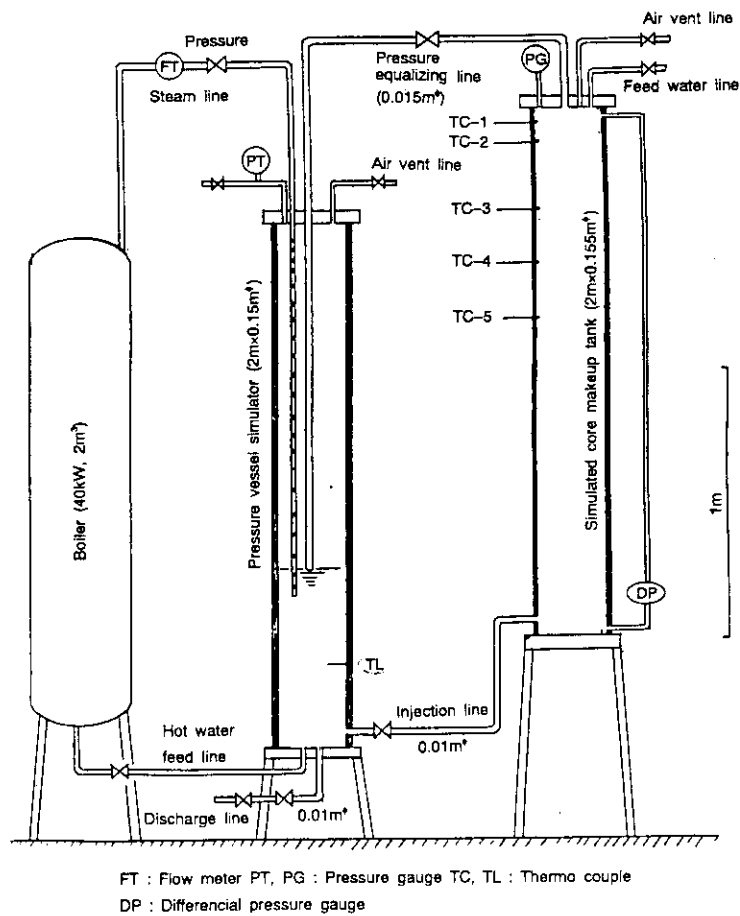


Fig. 4.5.1 Test apparatus for core makeup tank

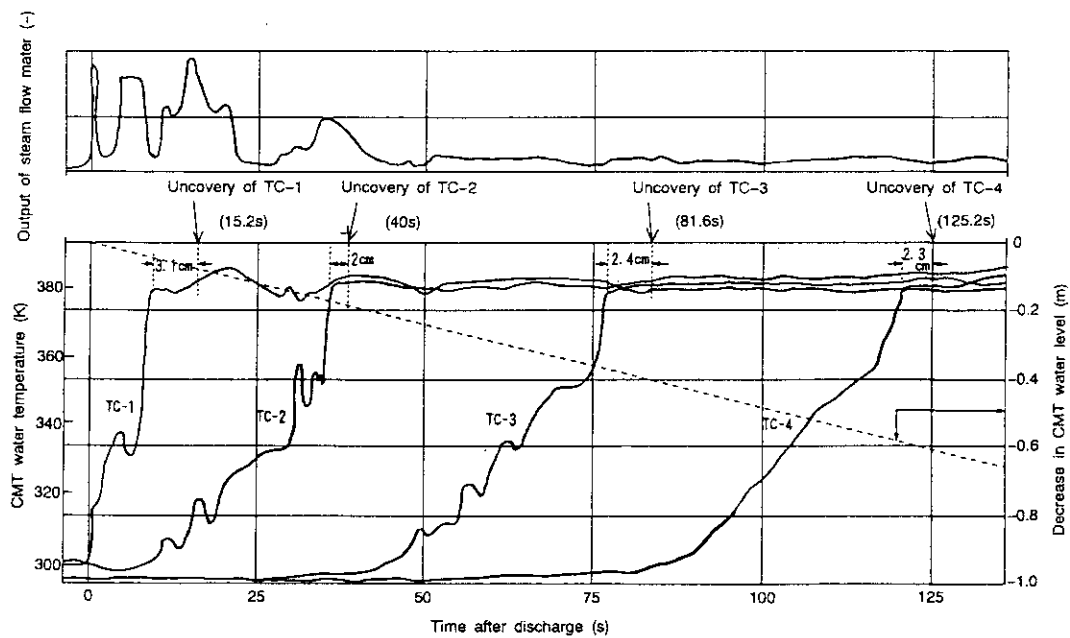


Fig. 4.5.2 CMT water temperature and steam flow injected into PV simulator (PV simulator pressure and temperature of 0.15 MPa, 383 K and CMT temperature of 298 K)

#### 4.6 Analysis for Making Distributions of Temperature and Velocity in Downcomer Uniform for JPSR Design

K. Kunii and Y. Murao

On the preliminary design of passive residual heat removal system for JAERI Passive Safety Reactor (JPSR)<sup>1)</sup>, the driving-force of natural circulation enough to remove the residual heat has been estimated by means of a steady state one-dimensional analysis for thermal fluid flow. In that estimation, the temperature distribution of coolant in downcomer shaping a three-dimensional annulus has been assumed to be uniform required to obtain an enough driving-force. In the present analysis, by applying a three-dimensional numerical analysis code for thermal fluid flow instead of one-dimensional one, first, the temperature distribution in downcomer in case of the natural circulation was analyzed. Second, based on that result, in case that the temperature distribution had the deviation possible to cause lack of driving-force of the natural circulation in comparison with the required one enough to remove the residual heat, a method to make the temperature distribution uniform was investigated.

The following analytical model was adopted: analyzed region of vertical thin-rectangular flow pass transformed from the real vertical annulus one, meshes of  $28 \times 4 \times 54$  (in circumference, radius and height directions in downcomer, respectively), STREAM as a single-phase three-dimensional thermal fluid flow analysis code (adopting  $k-\varepsilon$  turbulence model).

Under the basic conditions of downcomer, such as outline and inlet flow rate etc., being set in the preliminary design of the passive residual heat removal system, three-dimensional numerical analyses for the flow pattern and temperature distribution in downcomer were performed. Fig. 4.6.1 shows a temperature distribution in downcomer. A deviation on temperature distribution exists in the lower part in downcomer. Because of that deviation, it was possible to arise the lack of driving-force of the natural circulation in comparison with the required one. Taking account of these result and estimate, a method in order to make the temperature distribution uniform was investigated by means of installing some small baffles and/or vertical plates (shown in Fig. 4.6.2) at the inlet part in downcomer. The baffles and/or vertical plates were installed in order to make the flow patterns uniform, which contribute to form the temperature distribution dominantly, in both circumference and radius directions in

downcomer. Figs. 4.6.3a,b show temperature distributions in downcomer in cases of installing the baffles (g) and (d) shown in Fig. 4.6.2, respectively. The temperature distribution with the baffle (g) has less deviation than that without baffle(Fig. 4.6.1). However, that with the baffle (d) has more deviation than that without baffle. The temperature distributions with other baffles and/or vertical plates shown in Fig. 4.6.2 had almost same deviation as that with the baffle (d) shown in Fig. 4.6.3b. Therefore, the baffle (g) is the most effective to make the temperature distribution uniform in all the baffles and/or vertical plates shown in Fig.4.6.2.

The following conclusions were obtained:

- (1) By performing the three-dimensional numerical analyses for thermal fluid flow in downcomer, it was found that the deviation of temperature distribution from the uniform one arose in the case without baffle. The result was not consistent with the assumption in the one-dimensional analysis. According to such a result, it was possible to arise the lack of driving-force of natural circulation in the passive residual heat removal system in comparison with the required one.
- (2) An effective method to make the temperature distribution uniform by installing the baffle (g) at the inlet part in downcomer was proposed analytically. It could be expected to obtain an enough driving-force of the natural circulation by adopting this method.

#### Reference

- 1) Iwamura T. and Murao Y.: Study on JAERI Passive Safety Reactor (JPSR) (4) - Preliminary Design of Passive Residual Heat Removal System -, Autumn Meeting of the Atomic Energy Society of Japan, D47, 1993(in Japanese).



## 4.7 Concept of Passive Safe Reactor SPWR

K. Sako, T. Oikawa and J. Oda\*

SPWR (System-integrated PWR) is a passive safe reactor proposed by JAERI. This reactor is being designed since 1986 as a next generation power plant.

SPWR employs a new concept which can provide highly passive safety, easy operation/maintenance and economic competitiveness using experience and technology already obtained in the course of the existing LWR development.

The basic feature of SPWR is an integrated PWR with poison tanks filled with highly borated water (boric acid water) in place of control rods for reactor shutdown.

Figure 4.7.1 shows the concept of SPWR and Fig. 4.7.2 shows the concept of safety systems which are selected as the most rational ones as the result of design study for few years.

The reactor consists of reactor pressure vessel, reactor core, integrated steam generator, main coolant pump and pressurizer. The reactor pressure vessel covered with the water-tight shell is installed in the water-filled containment vessel.

The SPWR employs passive systems, as basic safety functions such as reactor shutdown, short-term decay heat removal (or safety injection), and long-term decay heat removal. The accident mitigation can be achieved by using the passive safety systems such as Passive Reactor Shutdown System, Pressure Balanced Injection System, Containment Water Cooling System, and active Automatic Depressurization System.

### References

- 1) "SPWR Reactor System Description and Development", IAEA TECDOC "Status report on small and medium power reactors", to be published.
- 2) Sako K., et al.: "Passive Safe Reactor SPWR", Proc. ANP'92, Int. Conf. on Design and Safety of Advanced Nuclear Power Plants, Tokyo (1992).
- 3) Araya F., et al.: "Safety Analysis of Highly Passive Safe Reactor SPWR", *ibid.*
- 4) Oikawa T., et al.: "Design Review of SPWR with PSA Methodology", Proc. 2nd ASME/JSME Int. Conf. on Nuclear Engineering, San Francisco (1993).
- 5) Oda J. et al.: "Conceptual Design of Fuel Exchange System for SPWR", Proc. SMiRT Conf., Tokyo (1991).

---

\* Ishikawajima-Harima Heavy Industries Co. LTD.

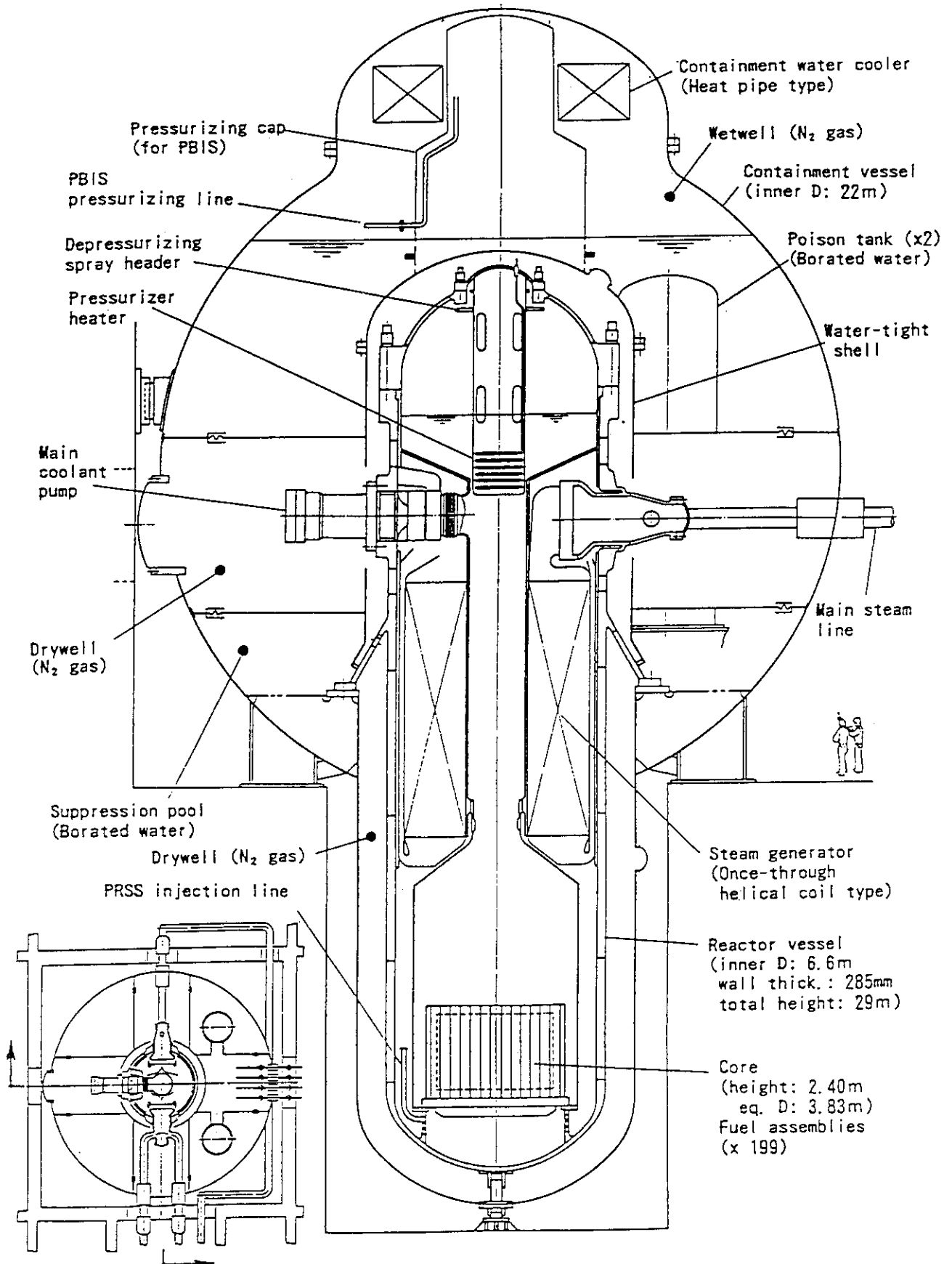


Fig. 4.7.1 Concept of SPWR (600MWe)



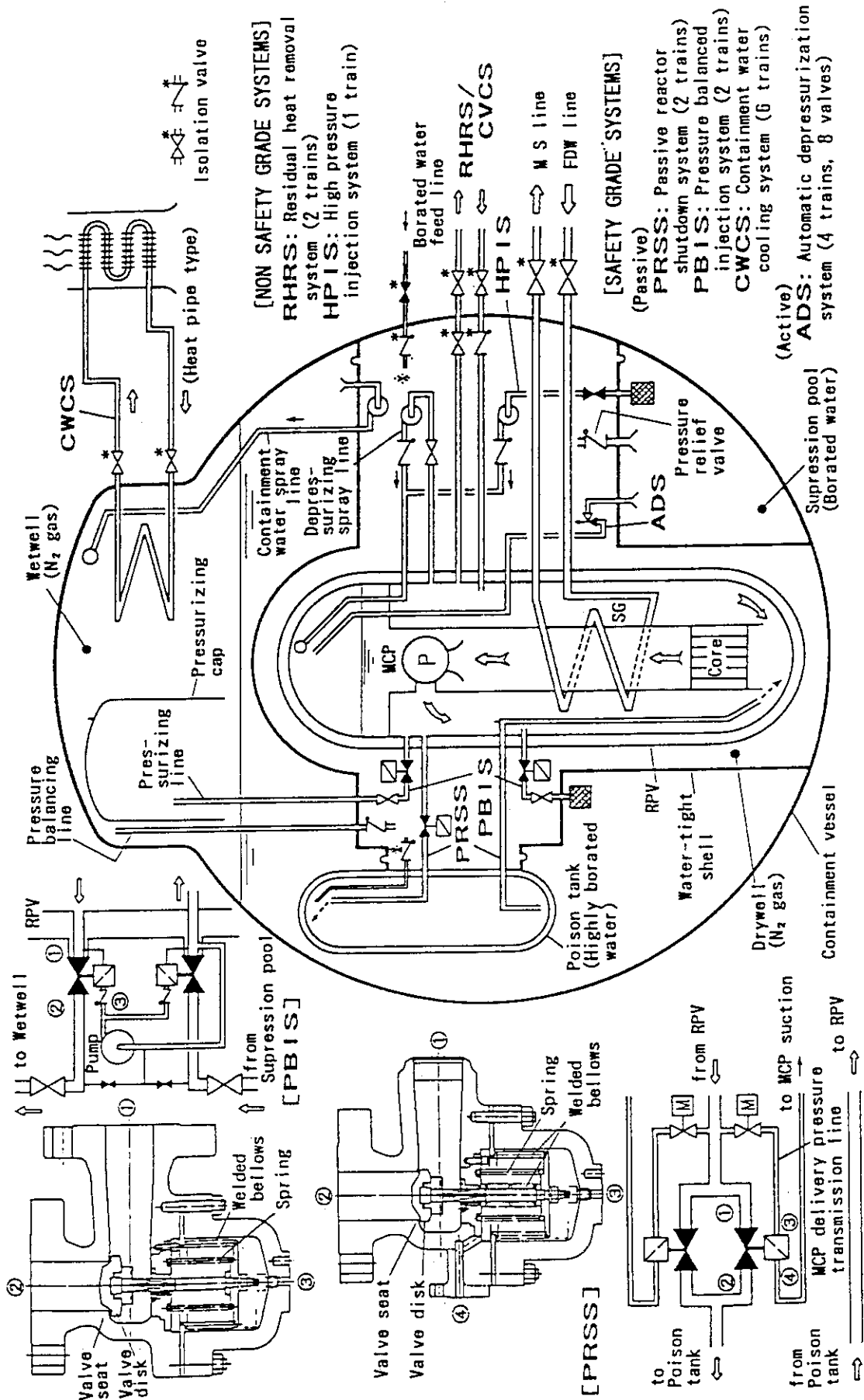


Fig. 4.7.2 Concept of SPWR Safety Systems

## 4.8 Seismicity and Economy for Inherent Safety Lead-Cooled Fast Reactor

H. Takano, H. Akie, K. Hirota\* and Y. Kamishima\*

A design study of lead-cooled fast reactor (LCFR) with nitride fuel assemblies has been performed to improve the safety, fuel cycle cost and transmutation of minor actinide in comparison with sodium-cooled MOX fuel FBR.<sup>1,2)</sup> Figure 4.8.1 shows the concept of the lead-cooled reactor. The core, core support structure and primary heat transport system components are installed in a reactor vessel. The primary heat exchanger is the steam generator and its helical coil tubes encircle the center part of the reactor which includes the core and hot coolant plenum. The primary pumps are located at the cold region of the primary coolant flow path. The coolant flows along the arrows in the figure. Here, the feasibility for the plant construction of LCFR is studied in the view point of seismicity and plant cost.

### Seismic Design Condition and Analysis

The heavy weight of lead coolant increases a seismic loading of the reactor vessel significantly. Therefore, the following countermeasures are adopted in the plant design to meet severe seismic condition:

- a) The plant is settled on soft soil (the Quaternary period's soil) for reducing response acceleration.
- b) Horizontal seismic support at a bottom of the reactor vessel.
- c) Minimized diameter of the reactor vessel for reducing its weight and results in reducing seismic shear stress.

In seismic load condition, the value 2G is used as the horizontal response acceleration of S2 earthquake at the vessel support level, considering that the plant should be settled on soft soil (the Quaternary period's soil).

Design conditions of the reactor are as follows: diameter: D=9000 mm, height: H=17000 mm, wall thickness: t=100 mm, material: Modified 316SS, vessel wall temp.: 480° C, support system: hung by flange/bottom support.

---

\* Mitsubishi Atomic Power Industries, Inc., Tokyo

For the seismic analysis, an axisymmetric analysis model of the reactor system is established as Fig. 4.8.2. The fluid-structure interaction effect is considered in the vibration analysis.

The result of seismic study is as follows: The required minimum wall thickness is approximately 80 mm, and the reactor vessel with 100 mm thickness will have the integrity against the seismic loading. And this 100 mm thickness also satisfies the requirement on manufacture ability, which is to be smaller than 130 mm. As a result, the reactor structure has the integrity against 2G seismic acceleration condition.

### Economics

It is very difficult to estimate the economics of the lead-cooled reactor at this study level, therefore, the possibility of reducing commodities is discussed. By utilizing the remarkable features, such as thinner radiation shields due to high shielding capability and chemically inert coolant use, the total cost of the lead-cooled plant will be reduced more 10% than that of Na-cooled plant, because the commodities of the plant facilities, such as the containment, the heat transfer system, and the reactor facilities and building will be reduced so much. As shown in Fig.4.8.3, the hatched area of Na-cooled plant will be eliminated in case of the lead-cooled plant.

### References

- 1) Takano H., et al.: " A Concept of Self-Completed Fuel Cycle Based on Lead-Cooled Nitride-Fuel Fast Reactors," Seventh International Conference on Emerging Nuclear Energy Systems, ICENES'93, Sept. 20 - 24, Makuhari, 1993, World Scientific, p.308 (1994).
- 2) Takano H., et al.: " A Design Study for Inherent Safety Core, Seismicity and Heat Transport System in Lead-Cooled Nitride Fuel Fast Reactor," Proc. Inter. Topical Meeting on Advanced Reactor Safety, ARS'94, April 17-21, 1994, Pittsburgh, Vol. 1, p.549 (1994).

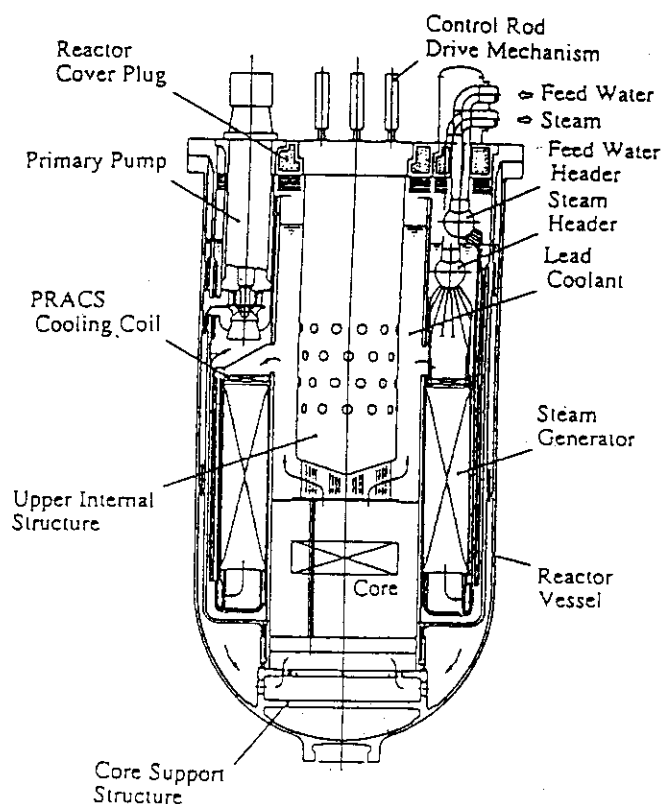


Fig.4.8.1 Concept of lead-cooled fast reactor

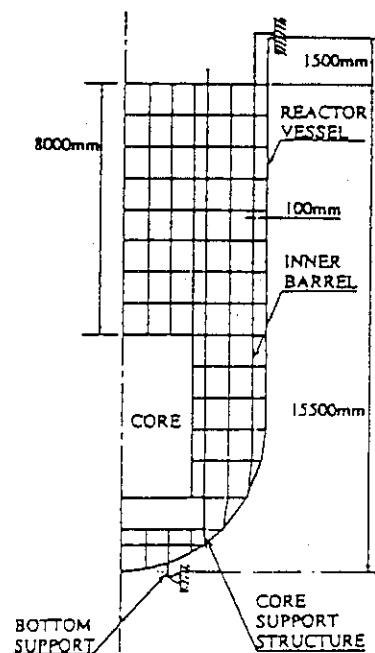


Fig.4.8.2 Analysis model of seismic design

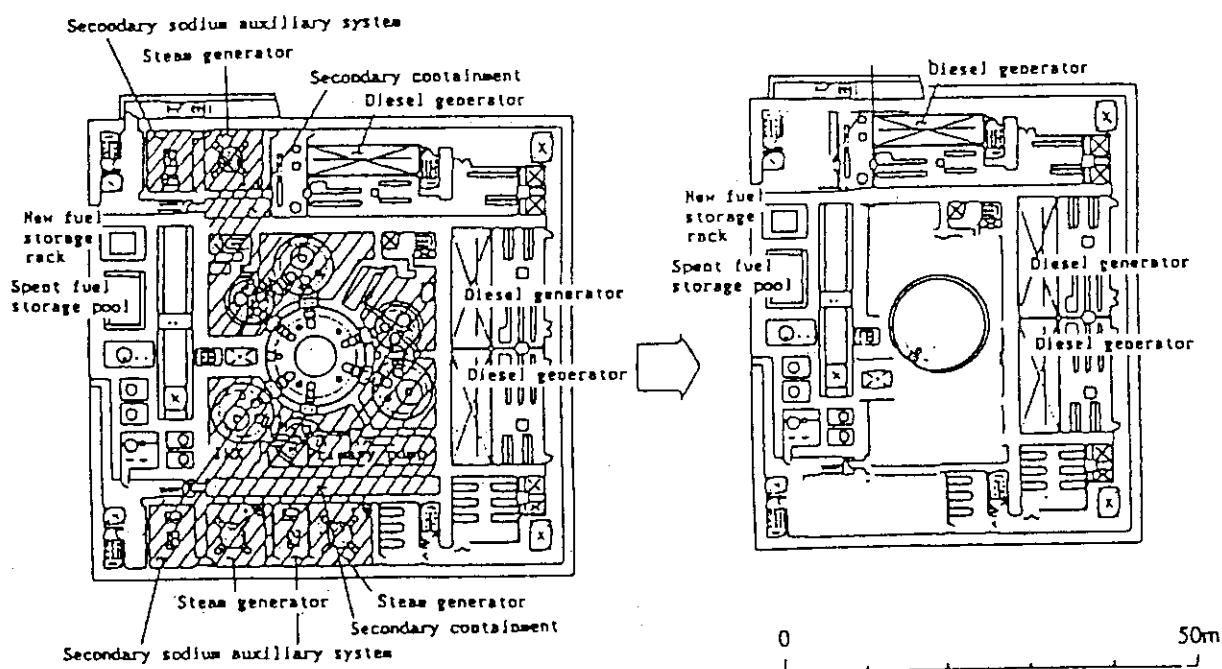


Fig.4.8.3 Comparison of plant facilities between Na- and lead-cooled fast reactors

#### 4.9 Burnup and Reactivity Coefficient Calculation of PWR Core Loaded with Weapons Pu Once-through Burning Fuel of $\text{PuO}_2\text{-ZrO}_2(\text{Y,Gd})\text{-Al}_2\text{O}_3$ Type

H. Akie, H. Takano and Y. Sugo\*

A new idea of once-through weapons plutonium burning fuels, based on thorium  $\text{ThO}_2$  and zirconia  $\text{ZrO}_2$ , was proposed and discussed<sup>1,2,3)</sup>. The fuels are expected to have a different plutonium transmutation characteristics from the usual MOX fuel, because of the different fuel compositions of very high content of Pu-239, and particularly of difference in fertile material. The plutonium transmutation characteristics of the fuels in LWR, FBR and HTGR have been investigated by performing simple cell burnup calculations<sup>1,2,3)</sup>. It was shown that the conventional LWRs are considered to be suitable for the once-through weapon grade plutonium burning. It was estimated that such LWRs can transmute about 99% of Pu-239 and 85% of total Pu in initial loaded plutonium from nuclear warheads. In the discharged fuels, about 2/3 of plutonium was Pu-240 and Pu-242, and the plutonium quality becomes completely poor.

In the zirconia based fuel,  $\text{PuO}_2\text{-ZrO}_2(\text{Y,Gd})\text{-Al}_2\text{O}_3$ , there is not fertile nuclide such as thorium, and fissile nuclide such as U-233 is not produced. In the pin cell burnup calculation in the previous work<sup>1,2,3)</sup>, there was a difficulty in the accurate estimation of discharge burnup. In order to accurately estimate the discharge burnup and plutonium transmutation characteristics, two-dimensional core burnup calculation was performed for the  $\text{PuO}_2\text{-ZrO}_2(\text{Y,Gd})\text{-Al}_2\text{O}_3$  fueled PWR. The results are shown in Table 4.9.1. The discharge burnup is estimated to be about 1400 days. Nearly the same plutonium transmutation characteristics is obtained as the pin cell calculation, namely 83% of total plutonium and 98% of Pu-239 can be transmuted. The transmutation rate is 0.90 tonne/GWe/300days for total plutonium and 0.99 tonne/GWe/ 300days for Pu-239.

As it was pointed out in the previous work, the void reactivity of the  $\text{PuO}_2\text{-ZrO}_2(\text{Y,Gd})\text{-Al}_2\text{O}_3$  fueled LWR is close to zero. The Doppler reactivity and the delayed neutron fraction  $\beta_{\text{eff}}$  are also small. The more accurate calculation of void reactivity, Doppler reactivity and  $\beta_{\text{eff}}$  was done on the basis of the core burnup calculation. As shown in Table

---

\* Information Technologies Japan Inc., Tokyo

4.9.2, the void and Doppler reactivities are negative both at the beginning and at the end of burnup cycle. The  $\beta_{\text{eff}}$  is small to be 0.29%  $\Delta k/k$  at the beginning of cycle and increases to 0.35%  $\Delta k/k$  because of the increase of Pu-241 amount. As the reactivity coefficients are very small, it seems necessary to perform reactor kinetics analyses to confirm the effects of the reactivities and the  $\beta_{\text{eff}}$ .

#### References

- 1) Akie H., Muromura T. and Takano H. : "A New Concept of Once-through Type Plutonium Burning", Reactor Engineering Department Annual Report (April 1, 1992 - March 31, 1993), JAERI-M 93-181, Japan Atomic Energy Research Institute, pp.77-79 (1993).
- 2) Akie H., Muromura T., Takano H. and Matsuura S. : " A New Concept of Once-through Burning for Nuclear Warheads Plutonium", Proc. 7th Int. Conf. on Emerging Nuclear Energy Systems (ICENES'93), 20-24 September 1993, Makuhari, Chiba, Japan, pp.298-302 (1994).
- 3) Akie H., Muromura T., Takano H. and Matsuura S. : "A New Fuel Material for Once-through Weapons Plutonium Burning", Nucl. Technol., to be published (1994).

Table 4.9.1 Amount of plutonium isotopes normalized to 1 GW electric power estimated for  $\text{PuO}_2\text{-ZrO}_2(\text{Y,Gd})\text{-Al}_2\text{O}_3$  fueled PWR by two-dimensional core burnup calculation (per 1 GW electric power, per 300 days)

	Amount of Pu isotopes and minor actinides (tonne/GWe)			
	BOL(0 day)	BO2C(450 days)	BO3C(900 days)	EOL(1360 days)
Pu-238	-	0.004	0.010	0.013
Pu-239	4.57	1.46	0.487	0.089
Pu-240	0.295	0.651	0.534	0.292
Pu-241	0.025	0.388	0.358	0.219
Pu-242	-	0.081	0.165	0.204
total Pu	4.89	2.58	1.55	0.817
total Am	-	0.031	0.055	0.065
total Cm	-	0.009	0.027	0.046

BOL : Beginning of Life, BO2C : Beginning of 2nd Cycle,  
BO3C : Beginning of 3rd Cycle, EOL : End of Life.

Table 4.9.2 Void and Doppler reactivities and the effective delayed neutron fraction ( $\beta_{\text{eff}}$ ) estimated for  $\text{PuO}_2\text{-ZrO}_2(\text{Y,Gd})\text{-Al}_2\text{O}_3$  fueled PWR based on two-dimensional core burnup calculation

	BOEC	EOEC
Void reactivity( $\%\Delta k/k$ )		
moderator density 100%	0.0	0.0
60%	-0.322	-9.74
30%	-3.42	-28.6
5%	-17.7	-92.6
Doppler reactivity( $\%\Delta k/k$ )		
fuel temperature 1200K	-0.0982	-0.201
900K	0.0	0.0
600K	0.107	0.209
300K	0.253	0.467
$\beta_{\text{eff}}$	$2.87 \times 10^{-3}$	$3.50 \times 10^{-3}$

BOEC : Beginning of the Equilibrium Cycle, EOEC : End of the Equilibrium Cycle.

#### 4.10 An HTGR - MHD Combination for High Efficiency Power Generation

T. Takizuka, H. Yasuda, T. Ogawa and T. Hiraoka

A conceptual study has been conducted on a high efficiency power plant which is a combination of a high temperature gas cooled reactor (HTGR) and a magneto-hydrodynamic (MHD) generator. The proposed HTGR-MHD plant has four identical helium loops, each loop having components as depicted in Fig. 1. The plant generates an electric power of 860 MWe at 57.3% efficiency.

The main feature of the HTGR core design is to supply outlet coolant of a very high temperature at a low operating pressure and a reasonably low pressure drop across the core. This is needed for the reactor exit gas to drive directly the MHD generator. The reactor has a pebble-bed type core. Fuel pebbles are continuously fed from the top of the core and gradually move downward as the burnup proceeds, and are eventually taken out from the bottom of the core. Design parameters of the fuel pebble and the reactor core were determined from neutronic and thermal - hydraulic analyses. A concept of the fuel element is presented in Fig. 2. A number of tiny fuel particles coated with multiple layers of pyrolytic carbon and ZrC are embedded in the graphite matrix of the pebble. Inner region of the pebble is unfueled to reduce the temperature peaking in the pebble. Vertical cross-section of the HTGR is schematically shown in Fig. 3. The flat core, 5 m in diameter by 2 m in height, leads to a moderate core pressure drop. Helium gas at 919 K and 0.79 MPa enters the reactor, flows downward through the core, and is heated up to 2300 K. A small amount of helium gas flow at 403 K is extracted from helium compressors which are supplied with 303 K gas, and used to cool the reactor vessel and internal metallic components. Reactivity control is made by vertical movement of control blades inserted into the graphite radial reflector. Control rods are inserted into the core for cold shutdown. The core design parameters are summarized in Table 1.

The plant employs an MHD generator with linear channel geometry. The MHD generator is composed of a nozzle, a generator section, a diffuser, a super-conducting magnet, a cryostat, and associated support structures. Electrodes are made of copper and are cooled by water. The magnetic flux density is 5 T at the center of the channel. Superconductor is made of NbTi, immersed in a pool of liquid helium.

The length of the generator section is 6.5 m, and the channel cross sections are  $0.7 \times 0.7 \text{ m}^2$  at the inlet and  $1.2 \times 1.2 \text{ m}^2$  at the outlet. For an electrical conductivity of working gas of 5 S/m, the generator produces electricity of 214.8 MWe per unit at a flow rate of 51.2 kg/s. The gas is seeded with cesium to enhance the ionization.



The turbine is driven by the high pressure gas at 1443 K from the regenerative heat exchanger (RHX). The compressor is four-stage inter-cooled to reduce the compression work. The motor-generator is provided for uses on startup and in certain emergency cases. Both the capacity and the operating temperature of the turbomachine are within the range of current state of open-cycle gas turbine power plant. The auxiliary cooling system is provided to remove the core decay heat in the remote event of total loss of forced circulation.

The heat balance of the HTGR - MHD plant is analyzed for a given HTGR exit gas temperature of 2300 K. In this analysis, MHD energy conversion characteristics were derived from the design of a fossil-fired closed cycle MHD power plant[4]. The plant efficiency of 57.3% can be obtained with the HTGR exit gas at 2300 K and 0.5 MPa. The electrical power of 860 MWe is generated for the HTGR thermal power of 1500 MWt. The entire primary system is arranged within a space of 50 x 50 m<sup>2</sup>, and contained in a reactor building.

Thermodynamic cycle employed for the HTGR-MHD system is the direct Brayton cycle. Absence of intermediate loops and steam turbines makes the plant configuration very simple and improves the economy. An analysis was also made on an HTGR-GT cycle with the same turbine inlet temperature and compressor outlet pressure as those for the HTGR-MHD cycle. The calculated HTGR-GT efficiency is 57.2%, almost equal to that of the HTGR-MHD. An option of combining with bottoming steam cycle would improve the efficiency of the HTGR-GT plant at the expense of complicating the plant configuration and arrangement.

The proposed system is a somewhat straightforward extrapolation of current HTGR and MHD technology. The major R&D issues identified in this study are:

- (1) High-temperature and long lifetime coated fuel particle (up to ~2600 K)
- (2) Non-equilibrium plasma physics
- (3) MHD generator design high pressure ratio
- (4) High pressure ratio He compressor and high-temperature (~1500 K) He turbine
- (5) Large capacity (~270 MW) RHX.

Table 1 HTGR Parameters

Rated Reactor Power	1500 MWt
Fuel Type	Spherical Pebble
Pebble Diameter	50 mm
Core Diameter x Height	5.0 m x 2.0 m
Core Power Density	38.2 MW/m <sup>3</sup>
Core Inlet Pressure	0.79 MPa
Core Pressure Drop	0.15 MPa
Core Coolant Velocity	19.5 m/s
Coolant Flow Rate	204.8 kg/s
Coolant Temperature in/out	919/2300 K
Maximum Fuel Temperature	2600 K

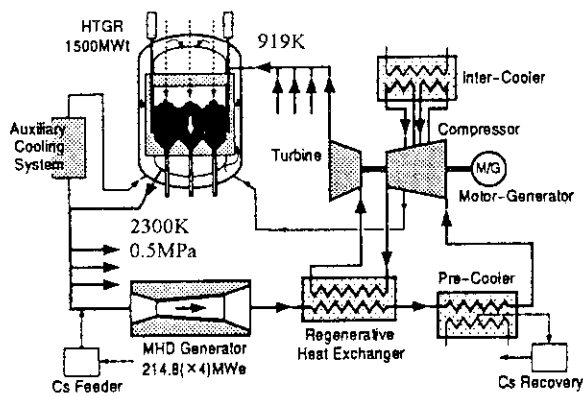


Fig. 1 HTGR-MHD Plant Flow Diagram

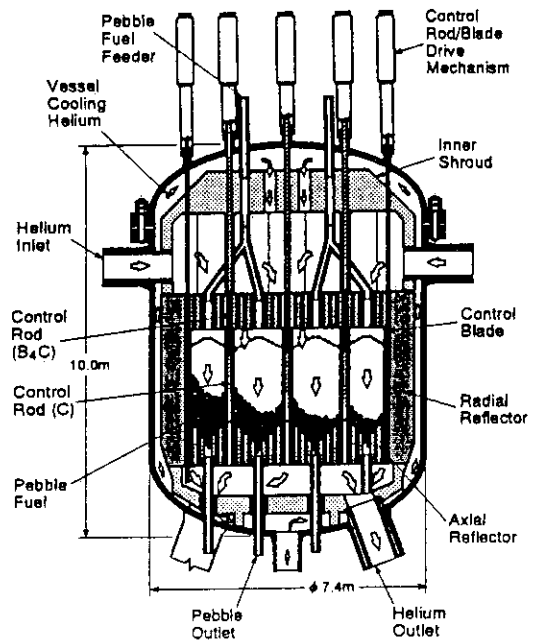


Fig. 3 Cross Section of HTGR

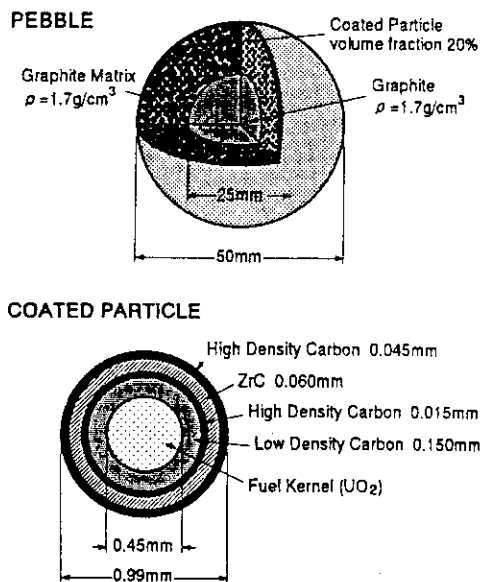


Fig. 2 HTGR Fuel Element

#### 4.11 A Liquid Metal Cooled Pebble-Bed Reactor for a Moon Base

H. Yasuda, T. Takizuka and T. Ogawa

A concept of small power generating system with a liquid metal cooled pebble-bed reactor has been studied for use in a moon base at the consolidation and utilization phases. 1),2),3) In the present study, the design was put emphasis on the safety during a launch from the earth and efforts were made to minimize the specific mass. The reactor thermal power was fixed at 10 MWt. A Rankine cycle was chosen as the plant thermo-dynamic structure.

A pebble bed reactor was adopted considering that this system can be launched without fuel and loaded in bulk on the moon base. This feature has the advantage that the criticality accident would not occur even if the system should fall down on the earth by any failure.

Pebble fuel which consists of coated particles and graphite matrix is adopted because of its refractory characteristics and FP retention capability. A reactor with this type of fuel can be operated at high temperature which can realize a low mass system. The core is cooled by liquid lithium which has a very low vapor pressure at the operating temperature. Therefore the system can be operated at a relatively low pressure and will be a low mass system. Electric power is generated by a potassium steam turbine which has a high conversion efficiency. The potassium turbine is operated at a low pressure compared with that of a gas turbine system. From the above consideration, a lithium cooled pebble bed reactor with a potassium Rankine cycle turbine generator is chosen as the power plant. A system diagram is shown in Fig. 1. Cross section of the pebble bed reactor is shown in Fig. 2. The fuel pebbles are dropped into the core before an initial start-up through a part of lithium flow path at the top of core. The pebbles are directly cooled by liquid lithium which is highly-enriched in lithium-7 having a small neutron absorption cross section. The pebble-bed core has a fast spectrum and its reactivity is controlled by neutron absorber drums. The axial reflectors in a form of BeO pebbles, have a large effect on reducing core height and axial power peaking.

The concept of fuel element is shown in Fig. 3. It is similar to that of HTGR except that the pebble has a smaller diameter and has a Nb-NbC coating prepared for lithium cooling. Specifications of the reactor system are presented in Table 1. It can be pointed out that a core of 1.1 m diameter and 1.1 m height will be practical. Neutronic calculation gave the performance data shown in Table 2. Ten years operation is feasible from the viewpoint of reactivity balance.

The secondary coolant is potassium which is vaporized in a tubeless steam generator (potassium boiler). The heat of the lithium coolant is directly transferred to the potassium

coolant in the potassium boiler. In this system, the lithium coolant is circulated upward by jet pumps which are driven by the potassium coolant. This direct mixing idea is introduced by the fact that lithium and potassium do not make any chemical compound. Although the potassium vapor can be separated from the lithium flow at the free surface of lithium coolant. A small amount of potassium which has not been evaporated in the boiler may be carried down by the lithium flow. The effect of this carry-down on the core nuclear performance was evaluated. Any notable influence was not observed by the potassium liquid content in lithium of about 5%. A reactor vessel contains potassium boiler for reducing the total mass. The reactor vessel is cooled by the fed-back potassiums coolant. This cooling path is effective in reducing the radiant heat loss from the reactor vessel wall to environment or to the control drums and at the same time, effective in pre-heating the potassium itself. As the reactor structure material, a niobium-zirconium alloy is used considering the material strength at high temperature. A nickel base alloy was selected as the turbine structural material considering the characteristics of its erosion endurance and strength at high temperature. The adiabatic turbine efficiency of 0.9 was obtained.

As a heat dissipation component, was adopted a panel type radiator which works as a condenser in the potassium loop. Titanium was used as the material of the condenser radiator to reduce the mass. The necessary dimensions of the condenser radiator are 8m in height and 14m in width. The condenser radiator is placed along or parallel to the equator of the moon to realize a stable performance by receiving weak sunshine.

A rough mass estimation resulted in 17 Mg for the whole system. A thermal-hydraulic calculation gave the operating conditions as written in Fig. 1. The thermal efficiency of 20% was obtained from the calculation.

## References

- 1) Yasuda H., et al.: "Small Reactor Power System for Lunar Base (I)" 11th ISAS Space Energy Symposium, February (1992).
- 2) Yasuda H., et al.: "Conceptual Study of Small Reactors for Space Use" Proc. of SR-TIT, 349 (1992)
- 3) Nei H., et al.: "A Liquid Metal Cooled Pebble Bed Reactor for a Moon Base" Proc. of ICENES '93 359 (1994)

TABLE 1 Specification of Reactor System

Thermal power	10 MW
Reactor core	Diameter 110 cm
	Height 110 cm
	Uranium mass 503 kg
	C/U atom ratio 35.8
Structural material	Nb-Zr alloy
Reflector	
Axial	
Material	BeO pebble (3cm dia.)
Thickness	25 cm
Lateral	
Material	Be
Thickness	28 cm
Control drum	Diameter 24 cm
	Number of drums 18
	Position In lateral reflector
	Material B <sub>4</sub> C(80% <sup>10</sup> B) and Be
Primary coolant	Material Lithium-7
	Inlet temp. 1123 K
	Outlet temp. 1203 K
	Flow rate 3.9 m <sup>3</sup> /min

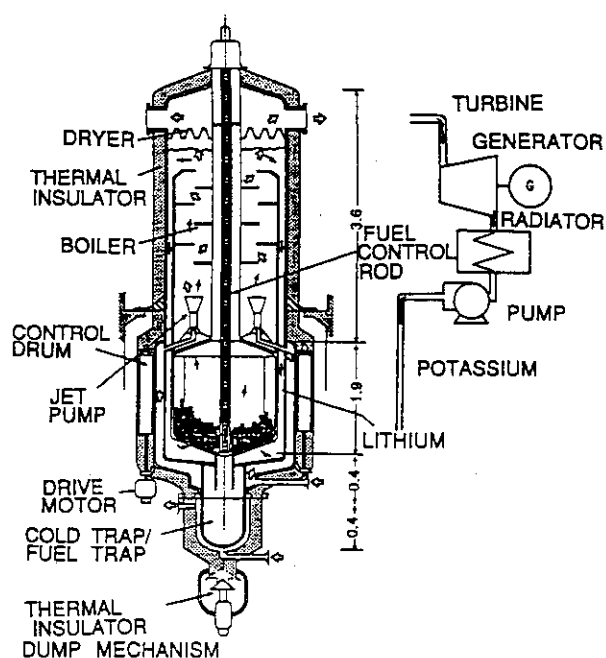


TABLE 2 Core Neutronic Performance Data

Criticality	
Initial hot shutdown Keff	0.973
Burnup reactivity for 10 years	6.75 % ΔK
Control drum reactivity	9.16 % ΔK
Feedback reactivity	
Whole core void reactivity (EOL)	-5.9 % ΔK
Doppler coefficient (BOL)	-1.9 x 10 <sup>-3</sup> T·dK/dT
Power density	
Maximum power density / peaking	
BOL	21.0 W/ cm <sup>3</sup> / 2.20
EOL	17.6 W/ cm <sup>3</sup> / 1.84
Burnup (after 10 y full operation)	
Average	7.5 at. %
Maximum	11.6 at. %
Maximum fast fluence (> 80 KeV)	2.5 x 10 <sup>22</sup> / cm <sup>2</sup>
<sup>235</sup> U inventory	
BOL	432 kg
EOL	380 kg

Fig. 2 Cross section of Lithium-Cooled Pebble Bed Reactor (Tubeless Type Boiler)

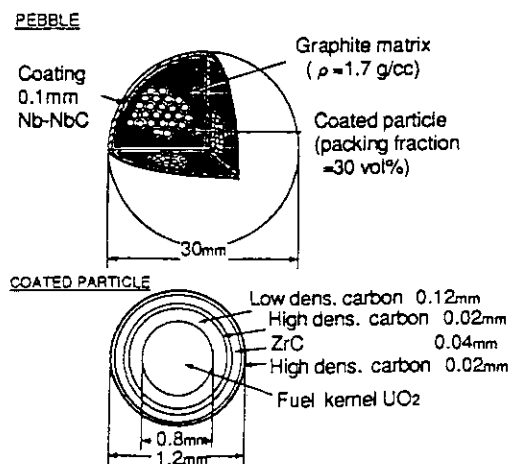


Fig. 3 Fuel Element

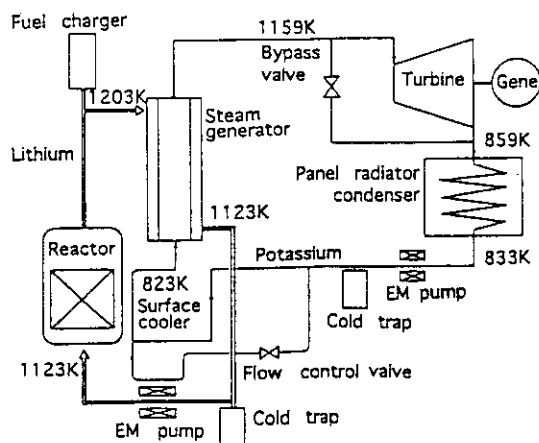


Fig. 1 System Diagram of Lithium-Cooled Pebble Bed Reactor for Moon Base

## 5. Fusion Neutronics

Since the JAERI/USDOE Collaborative Program was being terminated in Oct. 1993, a big effort paid to summarize the achievements for ten years, and to prepare joint reports and papers. At the same time, two workshops were held in both Japan and US in order to introduce the results to the fusion neutronics community world-widely. One of the major results is the development of a methodology to give a "safety factor" to the fusion nuclear designers. Since 1988, additional activities started under this collaboration. They were the induced radioactivity and nuclear heating experiments and their analyses. Both give us very nice benchmark data for the validation of induced radioactivity calculation code systems and Kerma data, respectively.

Under the ITER/EDA R&D program, a series of bulk shield experiments, shown in **Chapter 6**, has been started based on the 93 & 94 Tasks. A new series of benchmark experiments on induced radioactivity and nuclear heating are being performed also as the 93 & 94 Tasks. There are two additional activities under the ITER program. One is the D-T neutron irradiation effect on  $\text{Al}_2\text{O}_3$  insulator. The other is D-T neutron irradiation effect on functional materials for components used in diagnostics.

In order to obtain the information of neutron spectrum below 100 keV, a new technique has been developed using the relation between slowing down time and energy. The technique was applied successfully to the measurement of low energy neutron spectrum in a iron assembly. By way of experiment, fiber scintillation detectors were tested for fusion neutronics application. Further study should be expected to improve the performance.

Two cross section libraries based on JENDL-3.2. One is JSSTDDL-J3.2 (neutron : 295,  $\gamma$ -ray : 40) for ANISN/DOT, and the other is FSXLIB-J3.2 for MCNP. Data tests of JENDL-3.2 for fusion neutronics application are being performed under the activity of the Subcommittee on Fusion Reactor. This data test activity will be continued by the end of next fiscal year.

The IEA Cooperative Programmer on Nuclear Technology of Fusion Reactors has been ready for initiation. One of Subtasks under this Programmer, "Neutronics", is led by FNS/JAERI as the international activity followed to the JAERI/USDOE Collaborative Program. The action plan is being discussed among the participating countries.

This Chapter is contributed by Fusion Neutronics Laboratory.

## 5.1 Completion of the JAERI/USDOE Collaborative Program on Fusion Blanket Neutronics - Blanket Integral Experiment -

Y. Oyama, C. Konno, Y. Ikeda, F. Maekawa, H. Maekawa and  
the joint reserach group<sup>1</sup>

The JAERI/USDOE Collaborative Program on Fusion Blanket Neutronics has been completed in October of 1993. One of the main subjects of the program was to study a tritium breeding ratio (TBR) issue in a fusion blanket by blanket integral experiments. The program started in 1994 officially, but the preparatory work preceded before. The blanket integral experiments were performed in three phases that corresponded to the levels simulating three kinds of geometrical aspects for fusion reactor blankets. The experiments directed rather to engineering view points. The goal was settled in obtaining a guide line of the reactor design for neutronics parameters, e.g., tritium breeding ratio.

In the phase I,<sup>1)</sup> the plane geometry using a cylindrical test blanket was examined for various configurations of the test blankets. At the same time, this phase was very important to develop the measurement techniques and to accumulate the experience of the collaboration itself. Most of the basic measurement techniques, e.g., small sphere NE213 spectrometer and Li-glass scintillator for tritium production, were developed in this phase. The experiments used the rotating neutron target and the small target cell (2nd target room) at the FNS Facility. This arrangement suggested us that the room return background was not negligible for neutronics information from the test blanket, i.e., the room was one of the key elements in the experiment. This was really not desirable in the program purpose. Then the next phase experiments were planned carefully to eliminate that effect and to get more direct information about the reactor blankets.

The phase II experiment<sup>2)</sup> was conducted by a closed geometry in which the rotating target and the test blanket were surrounded by a container made of lithium carbonate. This container acts as shielding material of the test blanket against the room returned neutrons, and at the same time, reduces source neutrons incident to the room wall. In addition, reflected neutrons from the container cavity to the test blanket well simulated those of the reactor. This arrangement provided very reliable experimental data, so that this phase played a main role of the program for testing material configurations. The experiments with various beryllium configurations and with heterogeneous configurations were conducted. Measurements techniques were also established in this phase. Especially, zonal tritium production rate

---

<sup>1</sup> M. Nakagawa, T. Mori, T. Nakamura, et al. from JAERI and M. A. Abdou, M. Z. Youssef, et al. from the US.

measurement technique and small proton recoil gas proportional counter were developed.

In the phase III<sup>3)</sup>, the line source scheme was developed and used for annular blanket geometry experiment which simulated a part of toroidal blanket. In this arrangement, the blanket geometry relevant to the plasma source was more focused on, e.g., the blanket configuration with graphite armor and a large opening port were simulated. Table 5.1.1 summarizes the items of the experimental arrangements for all phases.

All calculations and experiments through the collaboration program were compared between them by the US and the Japan teams. The ratios of the calculated to experimental values (C/E) of the volume integrated tritium production, corresponding to local TBR, were compared for all experiments and plotted as probability distribution function as shown in Fig. 5.1.1.<sup>4)</sup> The distribution shown in the figure includes the prediction uncertainties (C/E-1 in percentage) of local TBR for all techniques and calculation codes, taking account of both experimental and calculational errors, and that is very similar to a Gauss distribution. From this graph, confidence levels are determined for the design safety factor chosen for the design. The hatched area denotes the probability that one would underestimate the TBR for the selected safety factor (risk level).

Consequently all the experimental and calculated results were summarized on the probability distributions. These distributions give good guidance how the design calculations are reliable. A series of the comprehensive papers will be appeared in a special issues of Fusion Technology.

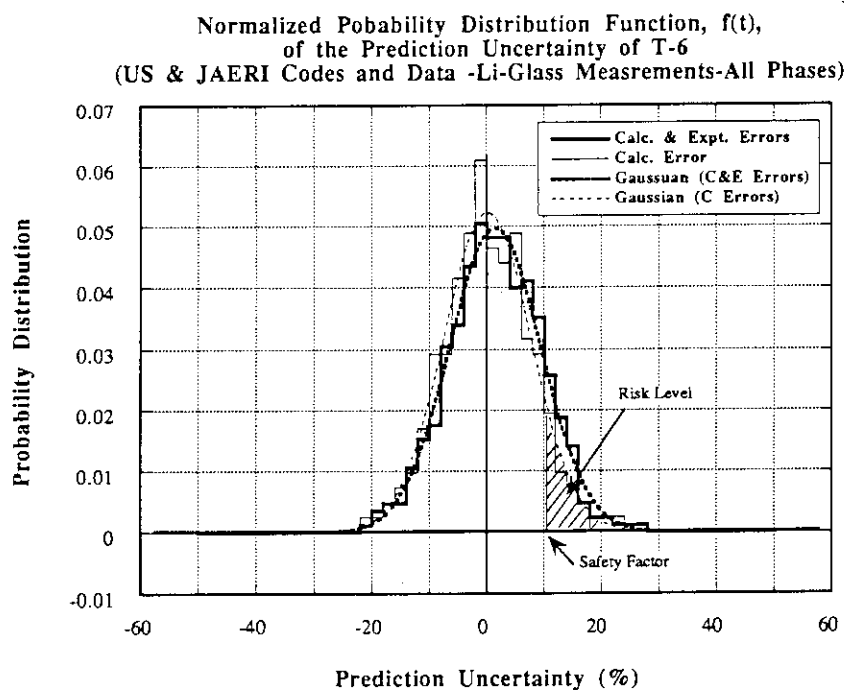
## References

- 1) Nakamura T. and Abdou M.A.: Fusion Technol., 10, 541(1986)
- 2) Oyama Y., et al.: Fusion Eng. Des., 9, 309 (1989);idem., Fusion Technol, 15, 1293 (1989)
- 3) Oyama Y., et al.: Fusion Technol.,19, 1979 (1991)
- 4) Youssef M.Z., et al.: " Fusion Integral Experiments and Analysis and The Determination of Design Safety Factors, Part II: Application to the Prediction Uncertainty of Tritium Production rate From The USDOE/JAERI Collaborative Program on Fusion Blanket Neutronics", to be published in Fusion Technology.



**Table 5.1.1 Configurations of the JAERI/USDOE Collaborative Experiments**

	Phase-I	Phase-II	Phase-III
Neutron Source	Point $3 \times 10^{12}$ n/s	Point $3 \times 10^{12}$ n/s	Line $1.5 \times 10^9$ n/cm/s
Configuration	Open / Slab Test Blanket in the wall	Closed / Sphere-like Test Blanket enclosed by Lithium Carbonate	Cylinder Annular Blanket
Distance between Source & Test Blanket	250 cm	78 cm	21.3 cm
Test Blanket	Li <sub>2</sub> O 60 cm-thick Cylinder	Li <sub>2</sub> O 60 cm-thick Rectangular	Li <sub>2</sub> O / Li <sub>2</sub> CO <sub>3</sub> 40 cm-radial thickness
Material	Be-Multiplier First Wall	Be-Multiplier Be-Coverage Heterogeneity	Armor-Layer Port Openings
Number of Experiments	9	8	3

**Fig. 5.1.1** Probability distributions for prediction uncertainty in local tritium breeding ratio estimations

## 5.2 Completion of JAERI/USDOE Collaborative Program on Fusion Neutronics

### --- Induced Radioactivity and Nuclear Heating Experiments ---

Y. Ikeda, A. Kumar\*, C. Konno, K. Kosako\*\*, Y. Oyama, F. Maekawa,  
M. Z. Youssef\*, M. A. Abdou\* and H. Maekawa

In view of the importance in data validation for induced radioactivity calculations along with the KERMA data, the induced radioactivity and nuclear heating experiments have been conducted as the new technical items proposed in the framework of the JAERI/USDOE Collaborative Program on Fusion Blanket Neutronics since 1988.<sup>1-4)</sup> These experiments have been carried out as the stand-alone experiments in parallel to the major topics of blanket integral experiments. As the program has been completed in 1993, the relevant efforts and the most significant outcome obtained throughout the experimental endeavor are summarized.

#### Induced radioactivity experiments

The first experiment was conducted utilizing the simulated fusion neutron field in the Phase IIC experimental assembly. Additional experiments were performed through Phase-III A, B and C in the experimental series of the collaboration program. Extensive measurements were carried out on materials of importance of the fusion structural materials. The measured values have been finalized as the benchmark data for the induced radioactivity calculation code as well as the cross section libraries. The present status of the prediction accuracy in the calculations with THIDA-2, REAC\*2&3, RACC, DKR-ICF has been clearly shown by the C/E representation for all calculations. The summary of the C/E values for radioactivity levels on materials investigated is given in Fig. 5.2.1. The experimental data have been summarized in numerical form and distributed to the potential users through IAEA. The series of endeavor has demonstrated the significant importance of the benchmark experiment for the validation of activation cross section libraries.

#### Nuclear heating experiments

Extensive efforts have been devoted to the technical development and the demonstration for direct nuclear heating measurement with a micro-calorimeter in D-T neutron fields. The calorimetric system consists of thermal sensors of thermistor and Pt-RTD (Resistance

---

\* University of California, Los Angeles

\*\* Sumitomo Atomic Energy Ind., Ltd.

Thermo Detector), material probes of interest, thermal insulators with vacuum chamber and polystyrene foam and high sensitive voltmeters. A temperature rise due to the nuclear heating, which was as low as  $10^{-5}$  °K/sec, was successfully detected by the system. The materials investigated included  $\text{Li}_2\text{CO}_3$ , graphite, Al, Ti, Fe, SS304, SS316, Ni, Zn, Zr, Nb, Mo, Sn, W and Pb. The overall uncertainty in the experimental data ranged from  $\pm 5\%$  to  $15\%$ . The measurements were compared with calculations with various KERMA library data. The C/E values are plotted in Fig. 5.2.2. It was found that the calculation based on JENDL-3 gave reasonable agreements with experimental data. In conclusion, it was demonstrated that experimental data for the KERMA data validation has been provided for the first time in this collaborative program.

#### References

- 1) Kumar A., Abdou M. A., Ikeda Y. and Nakamura T. :Fusion Technology, 19 (1991) 1909-1918.
- 2) Ikeda Y., et al. :“Joint Report of JAERI/USDOE Collaborative Program on Fusion Neutronics -Induced Radioactivity Measurements in Fusion Neutron Environment -,” JAERI-M 93-018 (1993), UCLA-ENG-91-32, UCLA-FTN-53
- 3) Kumar A., et al. :Fusion Eng. and Design, 18 (1991) 397.
- 4) Ikeda Y., et al. :Fusion Technology, 21 (1992) 2190.

Table 5.2.1 Summary document of the experimental progress

Items	1988	1989	1990	1991	1992	1993
Induced Radioactivity						
Phase-II C	----->					
Long-lived activation		----->				
Phase-III A		-->				
Phase-III B			----->			
Phase-III C				----->		
Summary report						----->
Nuclear Heating						
Single probe test -I		--> --->				
Single probe			----->			
Single probe				----->		
SS304 assembly					--->	
Summary report						----->

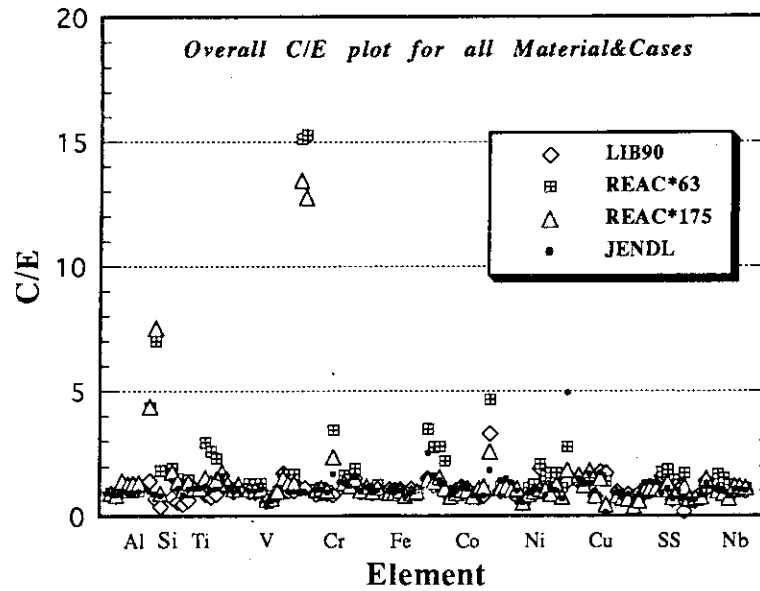


Fig. 5.2.1 Induced radioactivity C/E summary

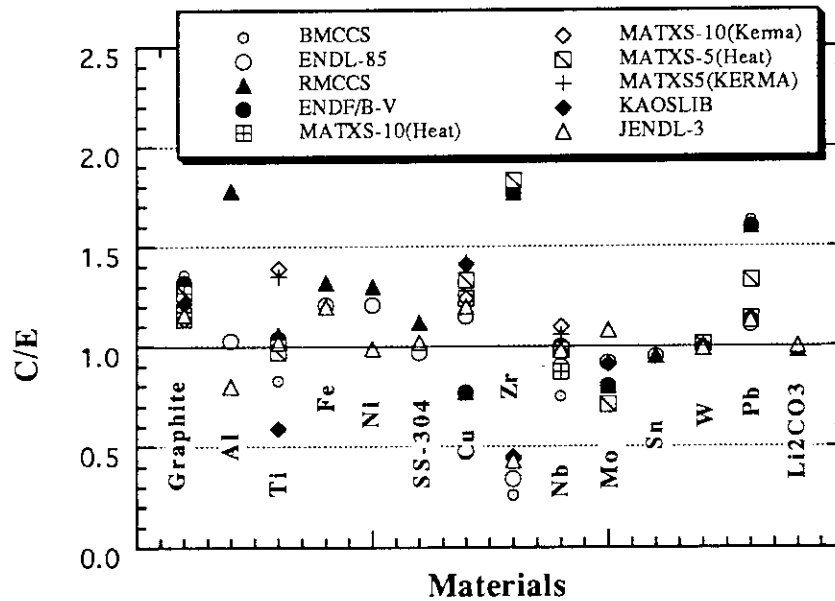


Fig. 5.2.2 Nuclear heating C/E summary

### 5.3 Measurement of Low Energy Neutron Spectrum in Iron Assembly for Verification of Evaluated Nuclear Data

F. Maekawa, C. Konno, Y. Oyama and A. Iwai

Iron is the most essential structural material for fusion and fission applications. For verifying nuclear data of iron, benchmark experiments<sup>1,2)</sup> were carried out for an iron cylindrical assembly utilizing the Fusion Neutronics Source (FNS) facility. Neutron spectra above 3 keV and activation reaction rates were measured so far in the assembly by the proton recoil detectors and the foil activation technique, respectively. In this kind of benchmark experiments, however, neutron spectrum below 3 keV has not been measured yet. Hence neutron spectra below 3 keV has been measured in the iron experimental assembly.

The neutron slowing down time method<sup>3)</sup> was adopted to the experiment. The experimental assembly of 1000 mm in diameter and 950 mm in thickness made of iron was placed at 200 mm from the tritium target of FNS. D-T neutron pulses of 0.5  $\mu$ s width and 200  $\mu$ s repetition rate were injected to the assembly. A BF<sub>3</sub> gas proportional counter was placed inside the assembly at positions of 110, 210, 310, 410, 610 and 810 mm from the front surface to measure time-dependent <sup>10</sup>B(n, $\alpha$ ) reaction rates. The time-dependent reaction rate measured at each position was converted into energy spectrum by using a relation between neutron slowing down time and its mean energy. The relation was determined experimentally by applying the resonance filter technique. Finally, the neutron spectra were normalized to those per source neutron considering the neutron yield and the detector efficiency. Total error of the spectrum at each energy was estimated as less than 10 %.

In order to examine accuracy of the evaluated nuclear data libraries and the transport codes, benchmark calculations of the experiment were performed with MCNP-4 and DOT-3.5. Continuous energy cross section libraries based on JENDL-3.1, -3.2 and ENDF/B-IV were used for MCNP calculations. Two group cross section sets were adopted for DOT calculations. Both were processed from the JSSTD library based on JENDL-3.1 with the self-shielding correction factors, but in different energy group structures of 125 and 175 groups.

Measured neutron spectra at 210 mm and 810 mm are shown in Fig. 5.3.1 with those by MCNP calculations. It is clearly seen that agreements between the calculated spectra with JENDL-3.2 and the measured ones are fairly good not only for their shapes but also their absolute values. Figures 5.3.2 and 5.3.3 show the ratios of the MCNP calculation to the experiment (C/Es) for integrated neutron flux for each decade of energy between 1 eV and 1 MeV. Figure 5.3.4 shows the C/Es of <sup>197</sup>Au(n, $\gamma$ ) reaction rate. The C/Es of the integrated flux below 1 keV agree within 10 % with those of the <sup>197</sup>Au(n, $\gamma$ ) reaction rate, which has much sensitivity to neutrons at 4.9 eV. This fact suggests a consistency between the present

spectrum measurement and the former activation rate measurement.

As for the energy range below 1 keV, the JENDL-3.2 calculation agrees with the experiment within about 10 % at all measurement positions. On the other hand, the calculation with JENDL-3.1 underestimates the flux by a few tens of percentage near the front surface of the assembly, and the ENDF/B-IV calculation is smaller than the experiment by about 30 % at all positions. In the energy range between 10 keV and 1 MeV, the C/Es by JENDL-3.2 are closer to unity than those by JENDL-3.1. A prediction accuracy of low energy neutron flux below 1 MeV is much improved by JENDL-3.2 within about 10 %.

Figure 5.3.5 is the ratios of the integrated flux by DOT to that by MCNP. This figure illustrates an effect of group-wise cross section. The DOT calculation with 125 groups differs by 40 % from the MCNP calculation in the energy range between 10 and 100 keV, while the DOT calculation with 175 groups agrees with the MCNP within 20 % in the energy range between 1 eV and 1 MeV.

#### References

- 1) Oishi K., et al.: Proc. 7th Int. Conf. on Radiation Shielding, Bournemouth, 9331-340 (1988).
- 2) Konno C., et al.: Fusion Eng. Des., 18, 297-303 (1991).
- 3) Maekawa F. and Oyama Y.: "Development of Measurement Technique for Neutron Spectrum in Energy Region of eV in Large Assemblies", JAERI-M 93-181, pp. 96-98 (1993).

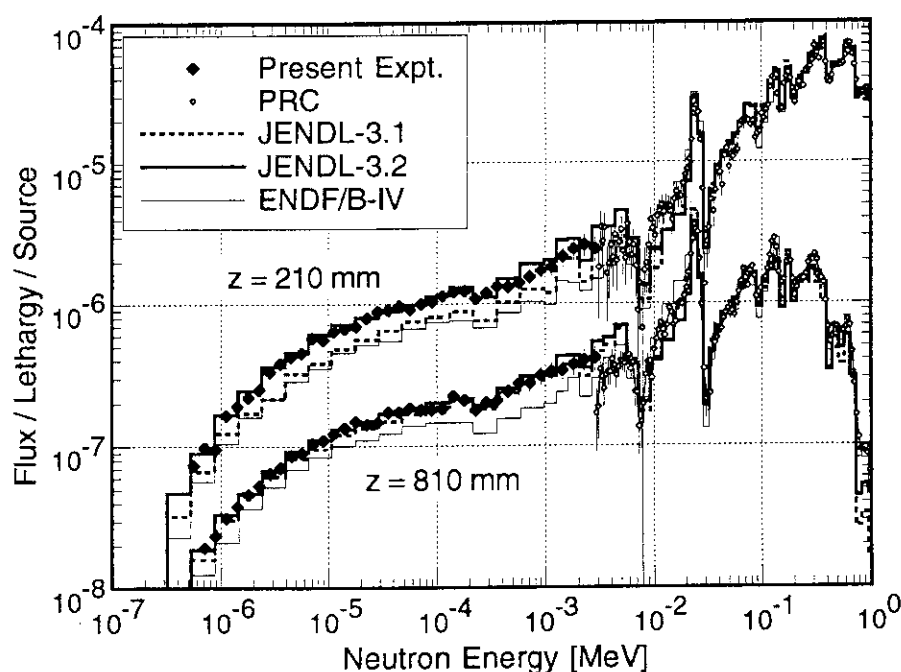


Fig. 5.3.1 Measured neutron spectra in comparison with calculated ones by MCNP.

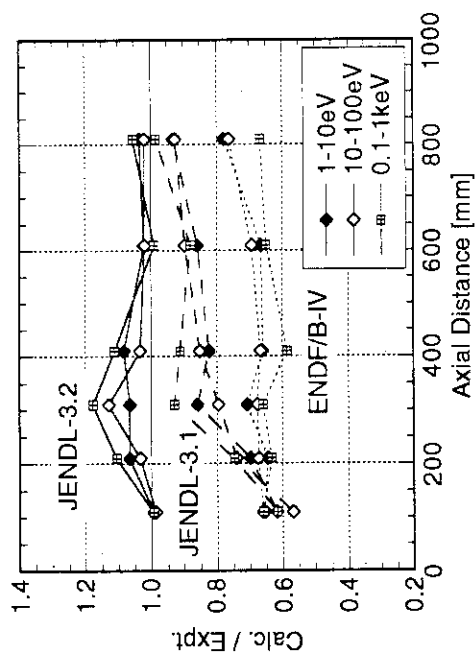


Fig. 5.3.2 Ratios of integrated flux below 1 keV by MCNP calculation with three different libraries to those by experiment.

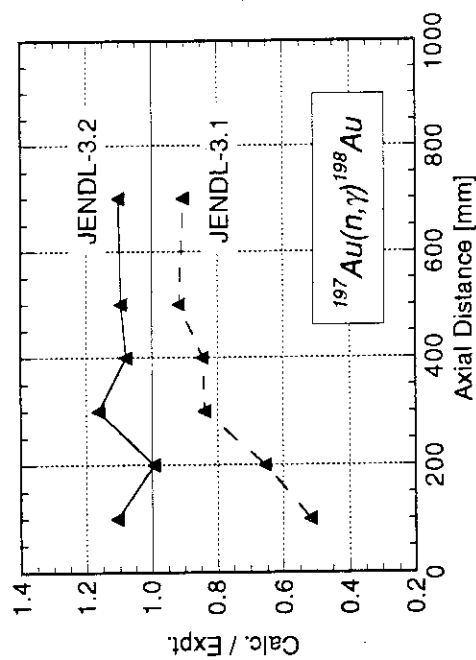


Fig. 5.3.4 Ratios of  $^{197}\text{Au}(n,\gamma)^{198}\text{Au}$  reaction rate by MCNP calculation with two different libraries to those by experiment.

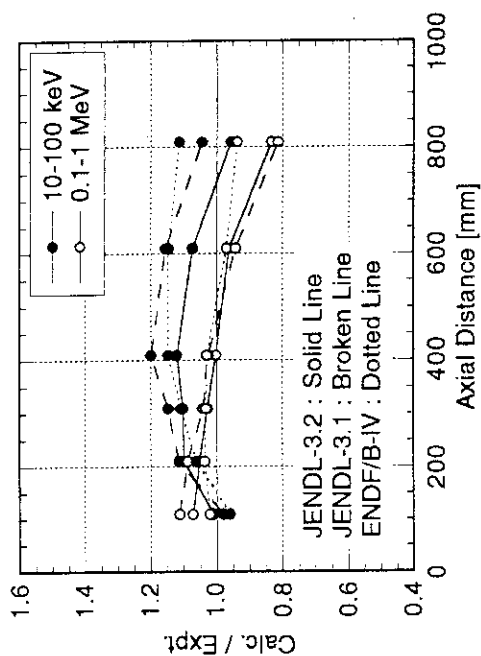


Fig. 5.3.3 Ratios of integrated flux above 10 keV by MCNP calculation with three different libraries to those by experiment.

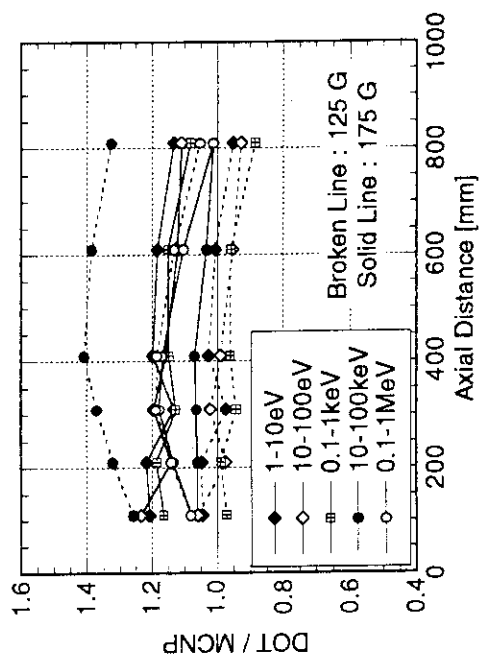


Fig. 5.3.5 Ratios of integrated flux by DOT calculation with 125 and 175 energy groups to those by MCNP calculation.

## 5.4 Verification of Secondary Gamma-ray Data in JENDL-3 through Analysis of Benchmark Experiments at FNS and OKTAVIAN

F. Maekawa, Y. Oyama and K. Kosako\*

Since the release of JENDL-3.1, the previous version of JENDL-3, in 1990, re-evaluation work of JENDL-3 has been progressed, and the latest version of JENDL-3, JENDL-3.2, was released in June of 1994. As an activity of Shielding Integral Working Group of Japanese Nuclear Data Committee, secondary gamma-ray data in JENDL-3 were tested by benchmark calculations of existing experiments. Two series of integral experiment with D-T neutron source were adopted; i) FNS/JAERI clean benchmark experiments <sup>1,2)</sup> with three experimental assemblies of Cu, W and type 316 stainless steel (SS316) and ii) OKTAVIAN/Osaka University pulse sphere experiments <sup>3)</sup> for LiF, CF<sub>2</sub>, Al, Si, Ti, Cr, Mn, Co, Cu, Mo, W and Pb. For the first step, the calculations based on JENDL-3.1 were compared <sup>4)</sup> with the experiments so as to recognize accuracies of secondary gamma-ray data in JENDL-3.1. Problems of the data were pointed out through the comparisons, and their results were fed back to the evaluators to modify them. For the second step, validity of secondary gamma-ray data in JENDL-3.2 were examined.

The continuous energy Monte Carlo code MCNP-4 was used to calculate gamma-ray spectra. Some subroutines of MCNP-4 were modified to identify which nucleus and neutron reaction were occurred, or in which cell a photon was generated. This modification enable us to easily point out which part of secondary gamma-ray data is inconsistent in the case of a disagreement between a calculation and an experiment is found. For example, a calculated gamma-ray spectrum denoted as total contribution in Fig. 5.4.1 is classified into three components; gamma-rays from i) LiF, ii) stainless steel container of LiF powder and iii) tritium target. It is seen that contribution of the container is not small comparing with that of LiF itself especially in a high energy region above 5 MeV. Figure 5.4.2 shows calculated gamma-ray spectra for Nb pile. The total spectrum is classified into each gamma-ray production reaction. This figure illustrates that gamma-rays by inelastic scattering and (n,2n) reactions dominate the total spectrum.

Results of the data testing with OKTAVIAN experiments are as followings. Secondary gamma-ray data of F and Co were given in JENDL-3.2 for the first time. Since Li nuclei emit gamma-rays of 0.478 MeV only, gamma-rays from LiF above

---

\* Atomic Energy Data Center (Present affiliation: Sumitomo Atomic Energy Industries, Ltd.)



0.5 MeV in Fig. 5.4.1 are emitted by F. An agreement between the calculated and the measured spectra is good for LiF. Calculation with the first evaluation for Co does not agree with the experiment as shown in Fig. 5.4.3. The data of Co were re-examined and improved as shown in the figure. Measured and calculated spectra for W by JENDL-3.1 and -3.2 are compared in Fig. 5.4.4. Spectra by both evaluations are almost the same and slightly larger than the experiment between 1 and 2 MeV. In the other energy ranges, both JENDL-3 seems to be consistent. Gamma-ray spectra for Pb is presented in Fig. 5.4.5. A strange peak is seen in the spectrum by JENDL-3.1. This peak was disappeared in JENDL-3.2 through some iteration of evaluation and benchmark calculation. Results of the benchmark test with OKTAVIAN experiments are summarized that the calculations with JENDL-3.2 represent the experiments very well for LiF, CF<sub>2</sub>, Al, Si, Co, Mo and Pb, but there are still unreasonable data for Ti, Cr, Mn, Nb and W.

Measured and calculated gamma-ray spectra in W for the FNS experiment are presented in Fig. 5.4.6. An agreement between JENDL-3.2 and experiment is good while JENDL-3.1 is about five times larger than the experiment. As for W, the differences between JENDL-3.1 and -3.2 are considerably large in the FNS experiment while they are very small in the OKTAVIAN experiment. This fact is explained by the difference of neutron spectra between the two experiment. Since 14 MeV neutrons are dominant in the spherical pile of OKTAVIAN experiment, most of gamma-rays are generated by 14 MeV neutrons. On the other hand, in the FNS experiment, most part of neutrons are in a low energy region below 1 MeV and contribution of (n, $\gamma$ ) reaction to the total gamma-ray production is very large. Secondary gamma-ray data for (n, $\gamma$ ) reaction can be tested only by FNS experiment, and those in JENDL-3.1 are not appropriate. Through the benchmark tests for Cu, W and SS316, secondary gamma-ray data of the materials are validated except for some inconsistent data.

## References

- 1) Maekawa F., et al.: "Benchmark Experiment on a Copper Slab Assembly Bombarded by D-T Neutrons," JAERI-M 94-38 (1994).
- 2) Konno C., et al.: Fusion Technol., 21, pp. 2169-2173 (1992).
- 3) Yamamoto J., et al.: "Gamma-ray Energy Spectra Emitted from Spheres with 14 MeV Neutron Source," JAERI-M 94-14, pp. 32-62 (1994).
- 4) Maekawa F., et al.: "Verification of Gamma-ray Data in JENDL-3.1 through Analysis of OKTAVIAN Experiment," Proc. Int. Conf. on Nucl. Data for Sci. and Technol., Gatlinburg, USA, May 9-13, 1994.

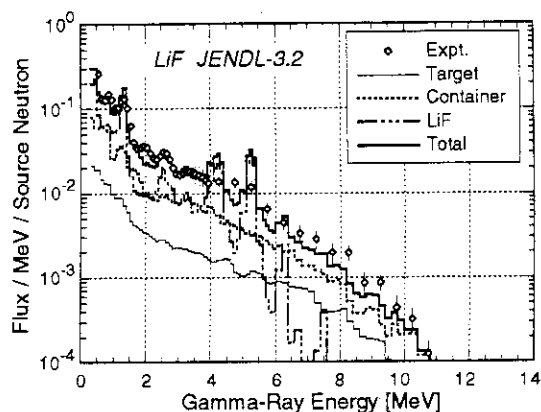


Fig. 5.4.1 Measured and calculated leakage gamma-ray spectra from the LiF pile.

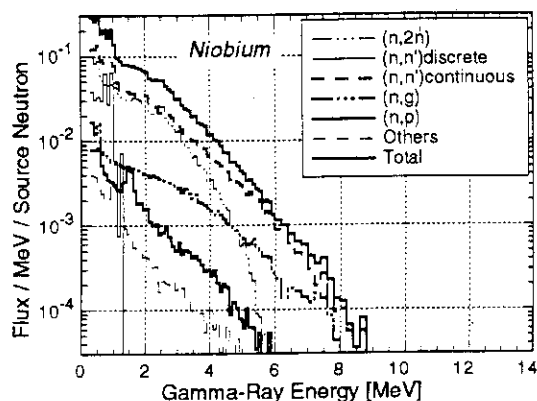


Fig. 5.4.2 Calculated gamma-ray spectra for Nb separating contributions from each gamma-ray production reaction.

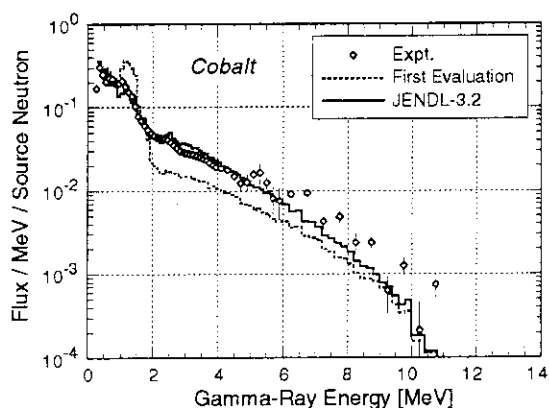


Fig. 5.4.3 Measured and calculated leakage gamma-ray spectra from the Co pile.

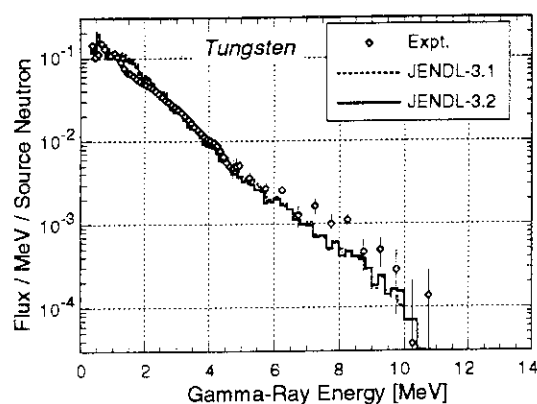


Fig. 5.4.4 Measured and calculated leakage gamma-ray spectra from the W pile.

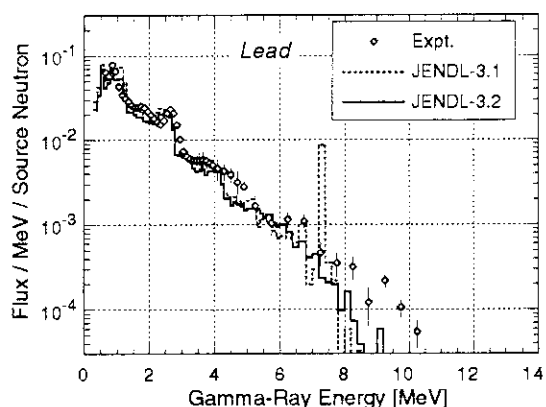


Fig. 5.4.5 Measured and calculated leakage gamma-ray spectra from the Pb pile.

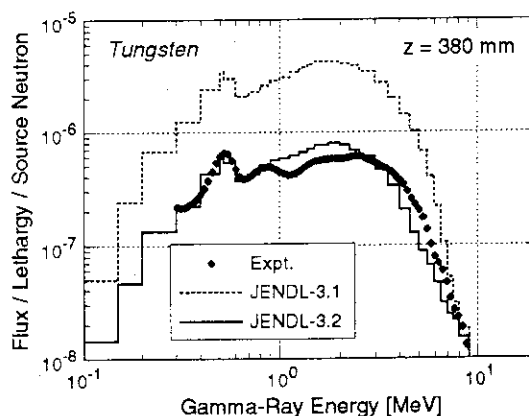


Fig. 5.4.6 Measured and calculated gamma-ray spectra in the W assembly.

## 5.5 Integral Test of Kerma Data for SS304 Stainless Steel in the D-T Fusion Neutron Environment

Y. Ikeda, A. Kumar\*, K. Kosako, C. Konno, Y. Oyama, F. Maekawa,  
M. Z. Youssef\*, M. A. Abdou\* and H. Maekawa

An experiment of nuclear heating in a SS304 assembly was carried out at FNS under the framework of JAERI/USDOE collaborative program on fusion neutronics. The experimental configuration was expected to be suitable to validate calculations in the spectrum where the D-T neutron contribution is less important on nuclear heating, and the associated  $\gamma$ -ray and slow neutron contributions are dominant. **Figure 5.5.1** illustrate the cross sectional view of the assembly made of SS304 core region, side  $\text{Li}_2\text{CO}_3$  enclosure and polyethylene insulator. Cubic blocks of SS304 with unit dimensions ( $51 \times 51 \times 51 \text{ mm}^3$ ) were contained in a SS304 stainless steel box. The assembly was placed in close vicinity of the D-T neutron source in order to maximize the neutron flux levels inside the SS304 core. Thermistor sensors ( $10 \text{ k}\Omega$ ) were attached on the first three blocks. The  $100 \text{ }\Omega$  RTD was attached on the side of the last block at depth range of 170 - 220 mm. The signals of resistance changes were measured with the voltmeters of Keithley-181, 182, 182 and Solatron-7081. Sampling times of 50 s were applied to increase the effective output of the temperature rise. The long pulsed D-T neutron operation of 5 min. was applied to discriminate the background drift composed by slow components due to radiation, heat conduction, self-joule heating in the resistance. The derivatives of temperature changes in the SS-304 blocks are shown in **Fig. 5.5.2**. The data at position closest to the D-T neutron source display the highest values with strong overshoots and undershoots at the beginning and the end of the neutron pulse irradiation, respectively. Considering relatively low thermal conductivity of SS-304 and steep gradient of the neutron flux over the block with 51 mm length, the variation in the derivatives during irradiation is explained by heat transfer from the front to rear sides of the block. The effect due to the heat flow was also observed in the data at the second block even though the neutron flux gradient at this position was expected to be much smaller than that at the first block. The nuclear heating was derived from the first rise in the temperature changing rate.

In order to estimate the temperature change during a sampling time of 50 s, a heat transport code ADINAT<sup>1)</sup> was used. The heat source distribution was given by the result of neutron and  $\gamma$ -ray flux calculated by DOT3.5<sup>2)</sup> with FUSION-J3<sup>3)</sup> cross section library based on JENDL-3<sup>4)</sup>. Differences in the temperature changing rate during the first sampling time were examined by changing the sampling time. The temperature rise at the end of the first

---

\* University of California, Los Angeles

sampling decreases as the sampling time increase. A correction factor for the data with 50 s sampling time was derived assuming that the data with 1 s sampling time gives the ideal temperature rise without heat flow. As the experimental data to be analyzed were obtained by correcting measured data with the factors derived at all positions. Experimental analysis was carried out to examine adequacy of the current data relevant to the nuclear heating. Neutron and  $\gamma$ -ray fluxes were calculated by the two dimensional transport code DOT3.5 with FUSION-J3. The experimental system was modeled by a R-Z cylindrical geometry and P5-S16 approximation was applied. The neutron KERMA data were created from JENDL-3 by direct method counting all contributing reaction cross section. The KERMA for  $\gamma$ -ray was derived from DLC-995).

The experimental data before and after correction for the heat flow are plotted in Fig. 5.5.3 along with the calculation. The neutron and  $\gamma$ -ray fractional contributions are given separately in addition to the total heating rate. This results clearly demonstrate that the heat transfer consideration is essential in determining the heating rate when the large size detector is used. The agreement between the calculation and the experiment suggests that the nuclear data of SS304, employed in this analysis, seems to be adequate. Emphasis should be placed on the fact that the  $\gamma$ -ray contribution to the heating rate becomes dominant as the depth of the position increases, as seen in Fig. 5.5.3.

As regards the similarity of the neutron and  $\gamma$ -ray spectra at 215 mm in the present assembly to those in the shielding structure of fusion reactors, it is worthwhile to note that the experimental data can be used for the direct verification of the data and method to be applied in the design calculation. The present study show the possible direction of applying the calorimetric method on the total nuclear hearing measurement for validating the design calculation. In the nuclear heating at the deeper region, e.g., at the interface between the shield structure and following insulator and super conducting magnet, the uncertainty largely depends on the uncertainty in the neutron and  $\gamma$ -ray flux spectrum calculation.

## References

- 1) Users Manual, "ADINAT, A Finite Element Program for Automatic Dynamic Incremental Nonlinear Analysis of Temperature," ADINA Engineering, Inc. (1984)
- 2) Rhoades W. A. and Mynatt F. R. : "The DOT III Two-Dimensional Discrete Ordinates Transport Code," ORNL/TM-4280 (1979).
- 3) Maki K., et al. : "Nuclear Group Constant Set FUSION-J3 for Fusion Reactor Nuclear Calculations Based on JENDL-3," JAERI-M 91-072 (1991).
- 4) Shibata K., e al. : "Japanese Evaluated Nuclear Data Library, Version-3," JAERI-1319 (1990).

- 5) Roussin R. W., et al., "Description of DLC-99/HUGO Package of Photon Interaction Data in ENDF/B-V Format," ORNL/RSIC-46 (ENDF-335) (1983).

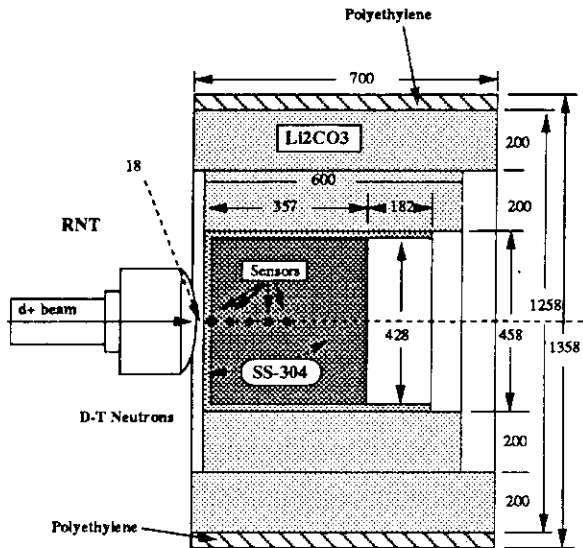


Fig. 5.5.1 Cross sectional views of the SS304 assembly.

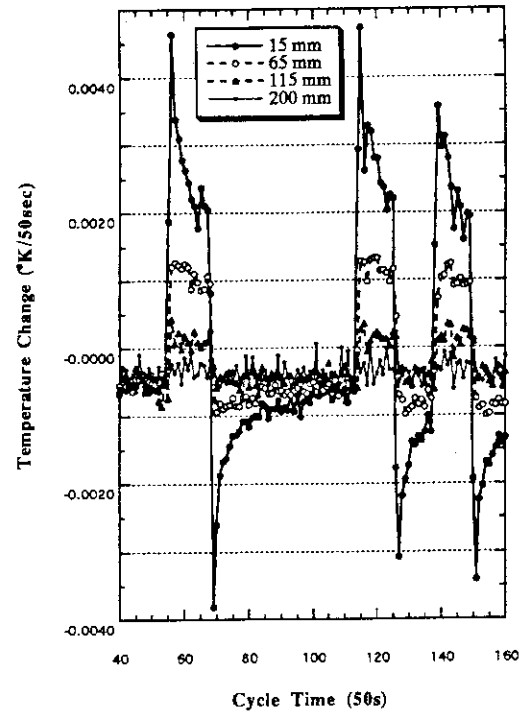


Fig. 5.5.2 Temperature changing rate in the SS304 probes due to D-T neutron irradiation.

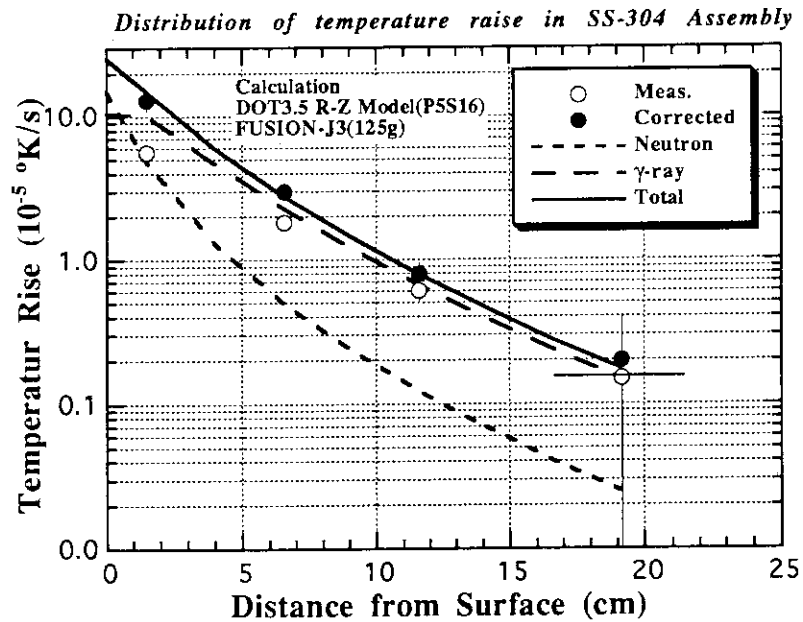


Fig. 5.5.3 Measured and calculated nuclear heating distribution in the SS304 assembly.

## 5.6 Experiment and Analysis of Induced Radioactivity Characteristics in a Large SS-316 Stainless Steel Shielding Materials Bombarded with 14 MeV Neutrons

Y. Ikeda, C. Konno, F. Maekawa, Y. Uno, Y. Oyama, K. Kosako\* and H. Maekawa

Induced radioactivity in D-T fusion environment is recognized as one of the most critical issues from the safety point of view. Validation of the relevant nuclear data and calculation methods by experimental data is highly needed to assure objectively the reliability of the design calculation. New integral experiments on the induced radioactivity in a large SS-316 shield assemblies were conducted to provide integral experimental data of induced radioactivity associated with SS-316. The differences of the cooling time, neutron spectra and cross section libraries were factored into the consideration in experimental analyses. As the neutron transport code, DOT3.5 and MCNP were employed coupled with the JSSTD<sup>1)</sup> and FSXLIB-J3<sup>2)</sup> cross section libraries based on the JENDL-3 nuclear data file<sup>3)</sup>. ACT4 of the THIDA code system<sup>4)</sup> with the JENDL activation library<sup>5)</sup> as well as the FENDL activation library<sup>6)</sup>, and the REAC\*3 code<sup>7)</sup> with the associated cross section library, were used for the activation calculations.

Figure 5.6.1 shows the SS-316 assembly for the fusion shielding experiments. Dimensions of the assembly were 1200 mm in diameter and 1118 mm in thickness for the test region, to which a source reflector cavity of 203 mm in thickness was attached. The experimental holes for sample insertion were filled with same SS-316 materials. The D-T neutron was generated via the  $^3\text{H}(\text{d},\text{n})^4\text{He}$  reaction by using FNS. Nominal D-T neutron yield at the source was about  $2 \times 10^{11}$  n/s. Samples of SS-316 placed at 406.4 and 609.6 mm from the surface of the test region along the central axis of the assembly were irradiated with D-T neutrons for 10 hours. After irradiation, induced radioactivities were measured with Ge detectors at different cooling times from several hours to about 8 months. Experimental data were derived as the decay rate of the radionuclide per unit weight of SS-316 (Bq/g). The experimental values were normalized by the source neutron intensity of  $1.0 \times 10^{11}$ /s. The radionuclide was identified by  $\gamma$ -ray energies and their intensity relationship. The decay rate was derived from  $\gamma$ -ray counts, detector efficiency,  $\gamma$ -ray emission probability and other necessary corrections.

The observed  $\gamma$ -ray lines were mostly associated with the decay of radioactivities produced via (n, $\gamma$ ) reactions. This is simply because the high energy neutron flux was attenuated by SS-316 layer of least 400 mm in thickness in front of the sample location, resulting

---

\* Sumitomo Atomic Energy Ind., Ltd.

in relatively small reaction rates of threshold type reactions. On the other hand, a fractional contribution of low energy neutron flux increases with the depth in the SS-316. In Fig. 5.6.2, experimental data at the position of 406.4 mm are plotted with corresponding decay curves calculated by the ACT4/JENDL activation library. At a short cooling time,  $^{56}\text{Mn}$  was the most dominating activity in both positions, followed by  $^{99}\text{Mo}$  and  $^{187}\text{W}$ . At cooling time of several days, the  $^{99}\text{Mo}$  kept the largest contribution, followed by the  $^{51}\text{Cr}$ . The  $^{56}\text{Mn}$  disappears quickly due to its short half-life. After 8 months cooling time, only four activities with appreciably long half-lives,  $^{54}\text{Mn}$ ,  $^{58}\text{Co}$ ,  $^{59}\text{Fe}$  and  $^{60}\text{Co}$ , were observed.

The ACT4 and REAC\*3 were used as the inventory codes. The activation cross section library based on the JENDL activation file with 125 neutron energy groups and the 175 energy group library installed in the REAC\*3 code system were used for the induced radioactivity calculations. In addition to those libraries, the FENDL activation library was tested for comparison, utilizing ACT4 as the inventory code. The multi-group FENDL library with 125 energy group structure was created from the point wise EFNDL file to be applied in the ACT4 calculation. The experimental analysis gave following results: (1) Uncertainty due to neutron spectrum impacted on prediction accuracy for the (n, $\gamma$ ) reaction products. (2) Uncertainty due to ambiguity in number densities of minor constituents should be seriously taken into account in the overall prediction uncertainty. (3) There were large discrepancies in the cross sections of  $^{98}\text{Mo}(n,\gamma)^{99}\text{Mo}$  and  $^{186}\text{W}(n,\gamma)^{187}\text{W}$  between JENDL and REAC175.

## References

- 1) Hasegawa A. : "JSSTD-295n-104g; a Common Nuclear Group Cross Section Library Based on JENDL-3 Nuclear Data File," JAERI-M 91-062 (1991) 15.
- 2) Kosako K., Oyama Y. and Maekawa H. : "FSXLIB-J3: MCNP Continuous Energy Cross Section Library Based on JENDL-3," JAERI-M 91-187 (1991).
- 3) Shibata K., et al. : "Japanese Evaluated Nuclear Data Library, Version-3," JAERI-1319 (1990).
- 4) Seki Y., et al. : "THIDA-2: An Advanced Code System for Calculation of Transmutation, Activation, Decay Heat and Dose Rate," RSIC computer code collection, CCC-410 (April 1987).
- 5) Y. Nakajima : "JENDL Activation Cross Section File," JAERI-M 91-032 (1991) 43-57.
- 6) Pashchenko A.B. : "Status of FENDL activation file and plans for the future developments," Proc. Int. Workshop on Nuclear Data for Fusion Reactor Technology, Del Mar, California, USA, 3 - 6, May 1993.
- 7) Mann F. M. : "REAC\*3 Nuclear Data Libraries," Proc. Intl. Conf. on Nucl. Data for Sci. and Technol., Jülich, Germany, 12-17 May 1991, 936-938.

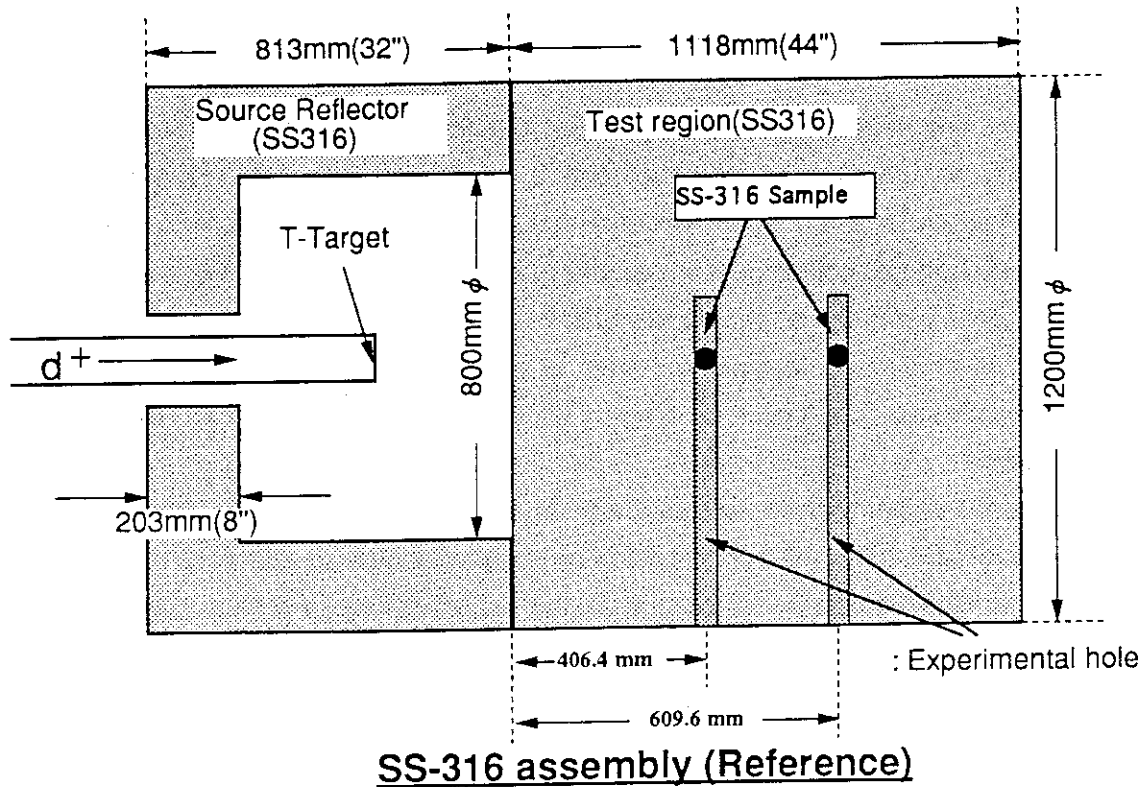


Fig. 5.6.1 Cross sectional view of the SS-316 assembly and sample position.

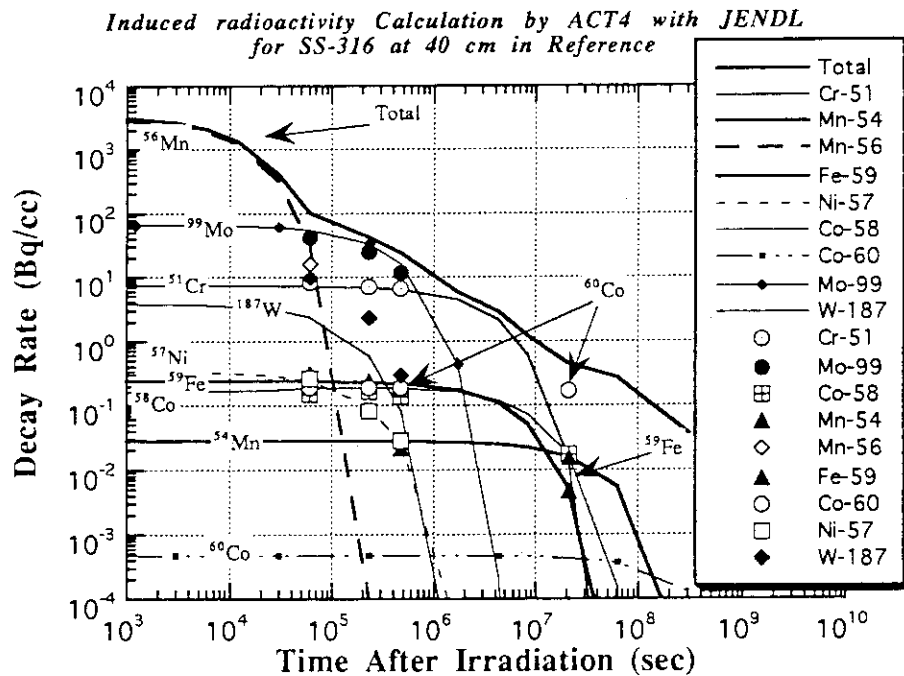


Fig. 5.6.2 Measured radioactivities and calculated decay curves at position A.



## 5.7 Performance Test of Fiber Scintillation Detectors for Fusion Application

Y. Oyama, F. Maekawa, A. Tanaka<sup>\*1</sup> and M. Takada<sup>\*2</sup>

For a fast neutron spectroscopy, recoiled protons are usually measured to obtain the incident neutron spectrum. In such a method, the unfolding procedure is necessary to obtain neutron spectrum from the recoil spectrum using response matrix. This procedure limits the energy resolution and accuracy of the method. For 14 MeV neutrons, the range of knock-on proton is about 3 mm in an organic scintillator. If fiber scintillator with a diameter less than this range is used so as to enter the edge in parallel to the longitudinal direction, only forward recoils stop fully inside the fiber. This special situation gives two advantages for the measurement:

- 1) Recoils escaping from the scintillator do not release their energy fully to the scintillator. Thus the light emission response of neutrons incident to the edge along fiber shows single peak structure similar to the full energy peak as shown in Fig. 5.7.1 (calculated by a Monte Carlo simulation).<sup>1)</sup>
- 2) Angular distribution of recoil for high energetic neutrons has a strong forward anisotropy. Thus combining the above feature of recoil escape, the angular dependence of this detector strongly shows directivity.

To examine the above basic features of fiber scintillators, two kinds of detectors were fabricated and tested for D-T neutrons. The scintillators tested are summarized in Table 5.7.1. In the case of liquid scintillator, glass capillaries are bundled and filled by liquid scintillator as shown in Fig. 5.7.2. For plastic fiber scintillator, the plastic was covered by Teflon sheet and 1 mm-thick aluminum foil to isolate each fiber so as to avoid proton crossing two fibers. These detector responses were measured by D-T neutrons.

The measured pulse height distributions are very different from the calculations. The energy resolutions are worse than the calculations and there is no peak structure as Fig. 5.7.1. In addition, for glass capillary detector, the maximum pulse of the injection at 90 degree is larger than that at 0 degree. This may be explained by the two regions of the detector, the capillaries and the reservoir of disk shape. The reservoir region has larger efficiency than expected.

For the directivity of efficiency for neutron incident angle, only plastic fiber detector showed such characteristics. However, as shown in Fig. 5.7.3, the measured directivity was

---

\*1 Summer student from Nagoya Univ.,

\*2 Summer student from Tohoku Univ.

modest than the calculation. From the measurement, FWHM is about 40 degree for 2 mm diameter fiber and close to the calculation, but the observed one does not decrease the efficiency at larger angles as the calculation shows no efficiency at 90 degree.

In conclusion, the present fiber scintillators show poor energy resolution and there existed no peak structure. This may be due to characteristics of light transmission inside the fiber. The directivity can be obtained at forward but at large angles the secondary emission and interference among fibers should increase the background. In addition, low light yield can not neglect the neutron induced background of photomultiplier. In a further study, the directivity can be improved by more careful detector design and then an application is expected to a detector for neutron camera with self-collimation. However, the feasibility for a detector with full energy peak feature was not confirmed by the present scintillators.

#### Reference

- 1) Oyama Y., et al.: Nucl. Instrum. Meth., A256, 333 (1987)

Table 5.7.1 Two types of fiber scintillators

I.D.	Type	Size
BCF-10	Plastic scintillation fiber	2 mm dia. x 30 mm long, Teflon coat and 1mm-thick Al cover
BC-599	Liquid scintillator	1.15mm inner dia. x 25 mm long 0.26mm thick glass capillaries

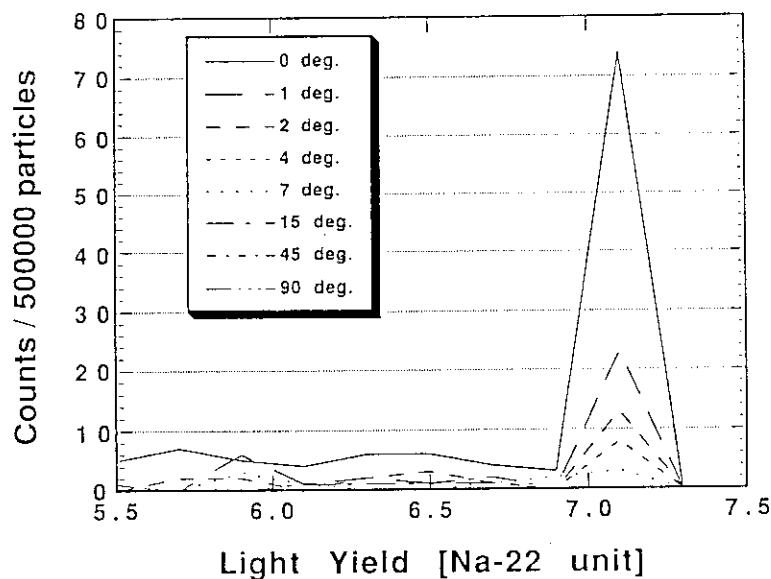


Fig. 5.7.1 Pulse height response calculated for 0.25 mm-diameter fiber

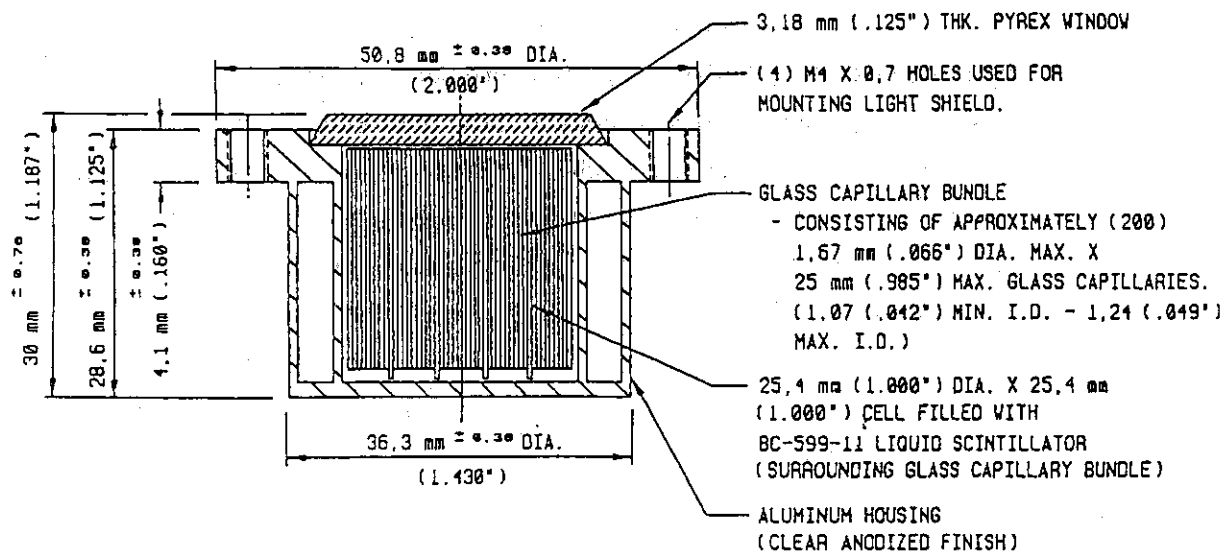
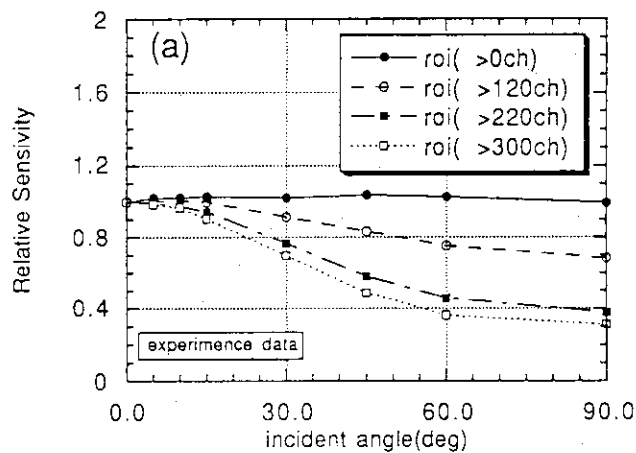
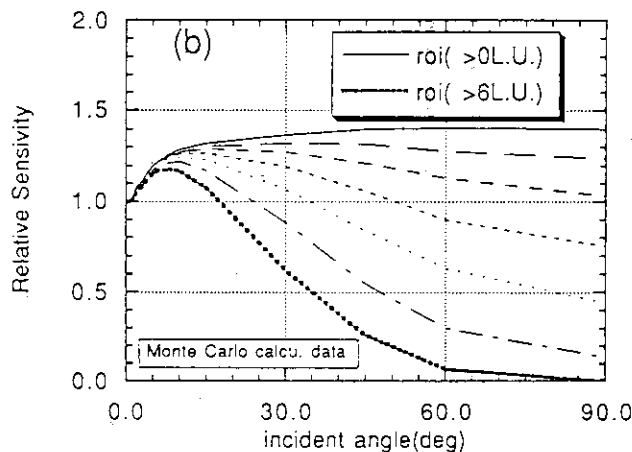


Fig. 5.7.2 Structure of fiber shape detector with glass capillaries and liquid scintillator



(a) Measured directivity response



(b) Calculated directivity response

Fig. 5.7.3 Measured and calculated directivity responses

## 6. Radiation Shielding

Experimental works at TIARA have been continued to verify the data and model codes for neutron transport calculations in intermediate energy. The deep penetration experiments of quasi-monoenergetic 41 and 64 MeV neutrons for iron and concrete were analyzed with the HETC-KfA2 code, and the MORSE-CG and DOT3.5 codes with the group constant HILO86 for indicating the serious effect of elastic scattering model in the HETC-KfA2.

Comprehensive attenuation data were calculated for point isotropic monoenergetic neutron sources up to 400 MeV in water, ordinary concrete and iron using the ANISN code and the group constant HILO86R to employ the data in a point kernel code PKN-H for shielding calculations of high energy neutrons. Stopping power tables were calculated for charged particles from 10 eV/amu to 10 GeV/amu using the codes: STOPPING, SPAR and RSTAN/RSHEV, which were used for evaluating the equivalent dose and detector responses for higher energy neutrons and various charged particles.

Development of the code system has been continued to calculate the equivalent doses in a mathematical phantom and the fluence to effective dose conversion factors to photons and neutrons up to 10 GeV based on the ICRP-60 recommendation. A couple of calculations were carried out for 100 MeV to 10 GeV neutrons for a slab phantom to compare it with the existing data.

In the framework of ITER/EDA blanket/shielding R&D, survey calculations with respect to the bulk shielding for the SCM were performed to design the experimental configuration at FNS with the ANISN and the group constant FUSION-40. Besides, benchmark shielding experiments were continued for a SS316 assembly with annular void at FNS to validate the MCNP and DOT3.5 codes together with the FSXLIB-J3 and JSSTD L libraries.

The activities of 6.1 to 6.4 were conducted in Shielding Laboratory, and those of 6.5 and 6.6 in Fusion Reactor Physics Laboratory.

## 6.1 Measurement and Analyses on Neutron Transmitted Through Iron and Concrete Shields in Intermediate Energy Region

H. Nakashima and JAERI-Universities Collaboration Working Group for Accelerator Shielding Study

It is essential to confirm the nuclear data and methods in the intermediate energy region for accelerator shielding designs. Therefore, a series of accelerator shielding experiments has been carried out using the 90 MV AVF cyclotron TIARA at Takasaki site in JAERI.

Neutron spectra transmitted through iron and concrete shields were measured using the quasi-monoenergetic neutron source settled in the cyclotron facility as shown in Fig. 6.1.1. Neutrons generated by protons accelerated to 67 and 43 MeV at the Li target of 2 MeV loss thickness passed through the iron collimator of 10 cm in diameter and 225 cm long, and bombarded the iron and concrete shields of 120 cm wide, 120 cm high and 20 to 200 cm thick. The pulse height distributions were measured by 5"φ x 5" BC501A liquid scintillation detector set just behind the shields. Neutron spectra were obtained by an unfolding method using the FERDO-U code with the measured response matrix and its error matrix. Neutron intensity monitors, a Faraday cup and fission chambers, calibrated to the absolute value of the generated neutron using a counter telescope have been operated during the experiments.

The transmitted neutron spectra were calculated using the two-dimensional discrete ordinates code DOT3.5 and the Monte Carlo code MORSE-CG with the HILO86 group constants set up to 400 MeV having  $P_5$  Legendre expansions<sup>1)</sup>. The source neutron spectrum measured by the counter telescope was used in calculations as a point isotropic source at the position of the Li target. In DOT3.5 calculations the first collision source calculated by the GRTUNCLE code was also utilized to remove ray effects. The calculated spectra are compared with the measured ones behind the iron and concrete shields on the beam axis at the peak neutron energy of 64.3 MeV in Figs. 6.1.2 and 6.1.3, respectively. The calculated results comparatively agree with the measurements, although the calculations in the energy region lower than the peak energy are slightly larger than the measurements, because the breakup neutron region in the measured source

neutron spectrum by the counter telescope includes the inelastic scattering component from the Si detector of the counter telescope. As a results, it is certified that the design methods in the energy region up to 20 MeV are available to the shielding designs in intermediate energy region less than about 70 MeV.

The HILO86 library gives the preferable results, which was calculated by the HETC code and the optical model for elastic scattering cross sections and adjusted to experiments. On the other hand, the HETC-KFA2<sup>2)</sup> calculations without a built-in elastic scattering option, which means to use only the intra-nuclear-cascade-evaporation model, largely overestimate the measured spectra as shown in Figs 6.1.2 and 6.1.3. The HETC calculations with the elastic scattering option utilizing the same data as the elastic cross sections in the HILO86 library still overestimate the measurements. Thus, it is implied that the contribution of elastic scattering is very important in this energy region and the handling of elastic scattering reaction in the HETC code should be modified.

## References

- 1) Alsmiller R.G., Jr., Barnes J.M. and Drischler J.D., "Neutron-Photon Multigroup Cross Sections for Neutron Energies <400 MeV (Revision 1)," ORNL/TM-9801 (1986).
- 2) Cloth P., et al., "HERMES A Monte Carlo Program System for Beam-Materials Interaction Studies", FA-IRE-E AN/12/88 (1988).

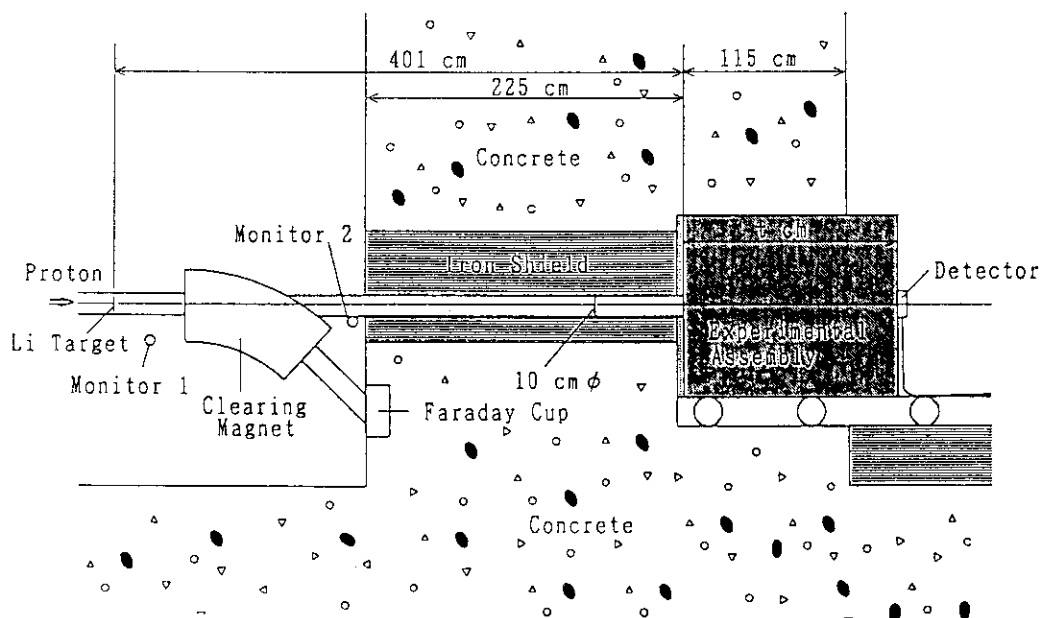


Fig. 6.1.1 Vertical view of experimental arrangement.

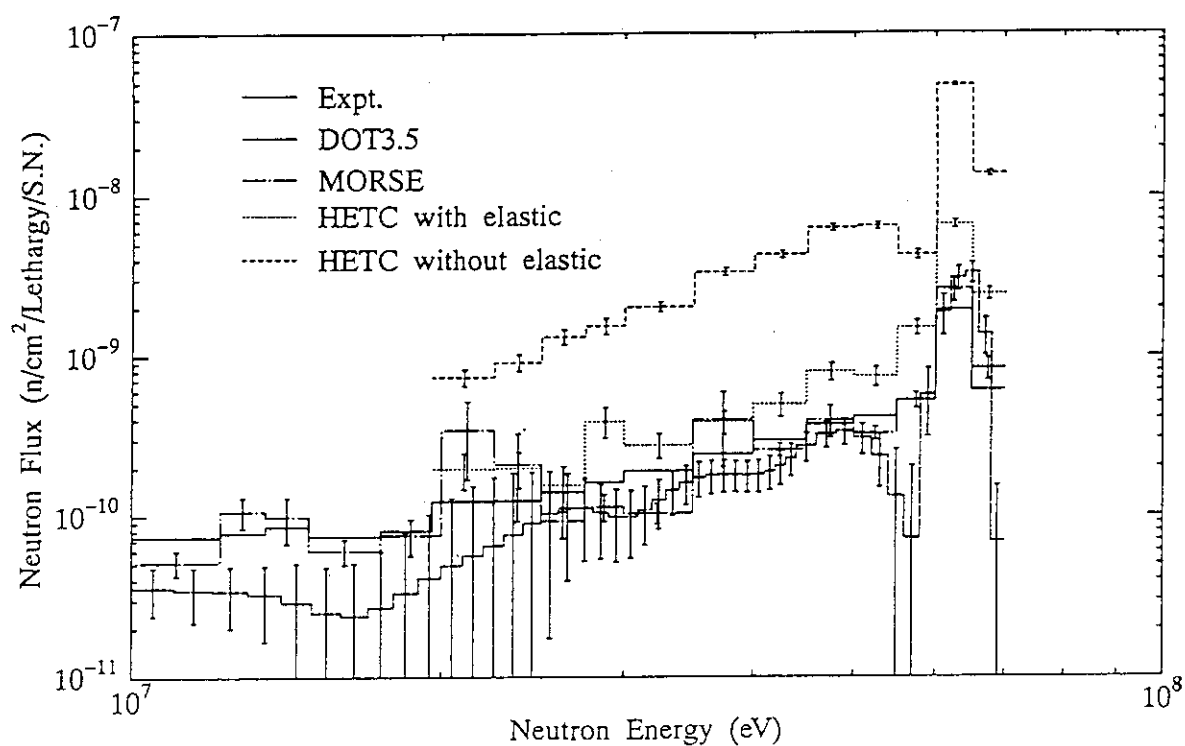


Fig. 6.1.2 Comparison of measured and calculated spectra of neutron transmitted through the concrete shield of 100 cm thick at the peak neutron energy of 64.3 MeV.

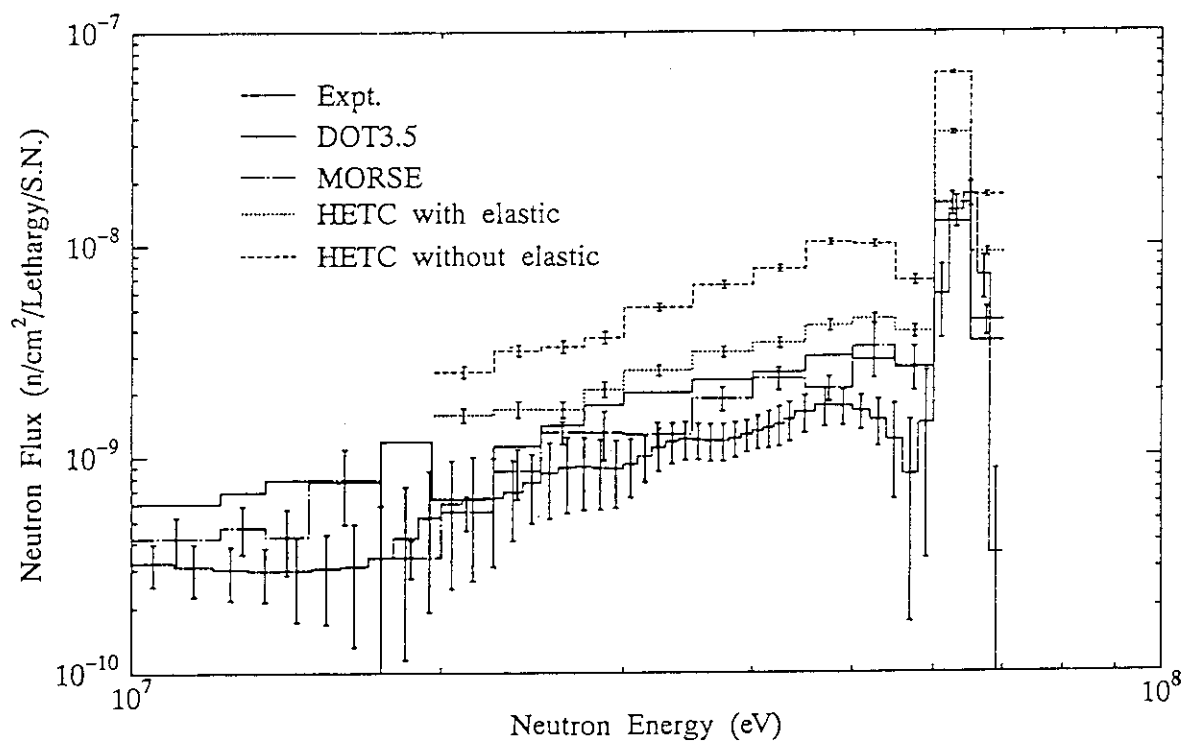


Fig. 6.1.3 Comparison of measured and calculated spectra of neutron transmitted through the iron shield of 70 cm thick at the peak neutron energy of 64.3 MeV.

## 6.2 Attenuation Data of Point Isotropic Neutron Sources up to 400 MeV in Water, Ordinary Concrete and Iron

H. Kotegawa, A. Hasegawa, Y. Nakane, H. Nakashima, Y. Sakamoto and S. Tanaka

Comprehensive attenuation data of dose equivalent for point isotropic monoenergetic neutron sources up to 400 MeV in infinite shields of water, ordinary concrete and iron has been calculated using the ANISN-JR code and a neutron-photon multigroup macroscopic cross section HILO86R<sup>1)</sup>, as shown in Fig.6.2.1<sup>2)</sup>.

The calculated dose equivalent  $H_j(r)$  in spherical geometry was fitted to an exponential formula empirically, as following,

$$H_j(r) = \exp(G_j(r)) / 4\pi r^2 \quad (6.2.1)$$

where  $j$  is energy index corresponding to source neutron energy. The  $G_j(r)$  is expressed with 4th order polynomial formula, as follows, making possible to use for point kernel codes,

$$G_j(r) = \sum_m a_{mj} \cdot r^{m-1} \cdot \theta_+(r) + (b_j \cdot r + g(r)) \cdot \theta_-(r) \quad (6.2.2)$$

where the summation is performed about  $m$  from 1 to 5, and

$$\theta_+(r) = \{ |r_{cj} - r| - (r_{cj} - r) \} / 2 \cdot |r_{cj} - r| \quad (6.2.3)$$

$$\theta_-(r) = 1 - \theta_+(r) \quad (6.2.4)$$

$$g(r) = \ln(4\pi r^2) \quad \text{for water and concrete} \quad (6.2.5)$$

$$= 0 \quad \text{for iron,} \quad (6.2.6)$$

and

$a_{mj}$  :  $m$ -th fitting parameters for energy index  $j$ ,

$b_j$  : a fitting parameter for energy index  $j$ ,

$r_{cj}$  : conjunction radius for energy index  $j$ .

The important feature of the fitting formula is that dose equivalent  $H_j(r)$  is represented by 1) 4th order polynomial exponent formula at inner region of conjunction



radius  $r \leq r_0$ , 2) exponential formula with an attenuation length  $1/b$  at outer region of  $r \leq r_0$ , 3) different exponential formula between water/concrete and iron using the function  $g(r)$  at outer region of  $r \leq r_0$ , and 4) without the buildup factor which shows a drastic variance strongly depending on source neutron energy. The third term means that neutron dose equivalent  $H(r)$  at far distance from source in water and concrete attenuates as  $\sim \exp(-r/\lambda_0)$ , and in iron attenuates as  $\sim \exp(-r/\lambda_0)/r^2$ , in which  $\lambda_0$  is independent on thickness of shield, according to an observation of the calculated dose equivalent attenuation.

Additional data, so called infinite medium effect  $C_H$ , to calculate a dose equivalent in finite shielding geometry was also calculated in order to correct the effect due to infinite medium, for instance, giving the maximum correction of 0.23 in the region far more 400 cm distance from neutron source of 400 MeV in iron shield. Figure 6.2.2 shows an infinite medium effect  $C_H$  of neutron dose equivalent in iron in 3-dimensional description.

This parameterized attenuation data set ( $a_m, b, r_0, C_H$ ) assure, consequently, that it is capable to calculate neutron and secondary gamma-ray dose equivalents with good accuracy from near source to far distance region where the dose equivalent becomes negligible small.

These parameters will be installed in point kernel code, PKN-H<sup>3)</sup>, for quick and easy calculation of neutron and secondary gamma-ray dose equivalent with good accuracy in water, ordinary concrete and iron shields of 3-dimensional configuration for intermediate energy neutron up to 400 MeV.

## References

- 1) Kotegawa H., et al.: "Neutron-Photon Multigroup Cross Sections for Neutron Energies up to 400 MeV: HILO86R -Revision of HILO86 Library-", JAERI-M 93-020(1993).
- 2) Kotegawa H., et al.: "Attenuation Data of Point Isotropic Neutron Sources up to 400 MeV in Water, Ordinary Concrete and Iron", JAERI-Data/Code 94-003(1994).
- 3) Kotegawa H., et al.: "PKN-H", JAERI-Data/Code 94-XXX(1994), (to be published).

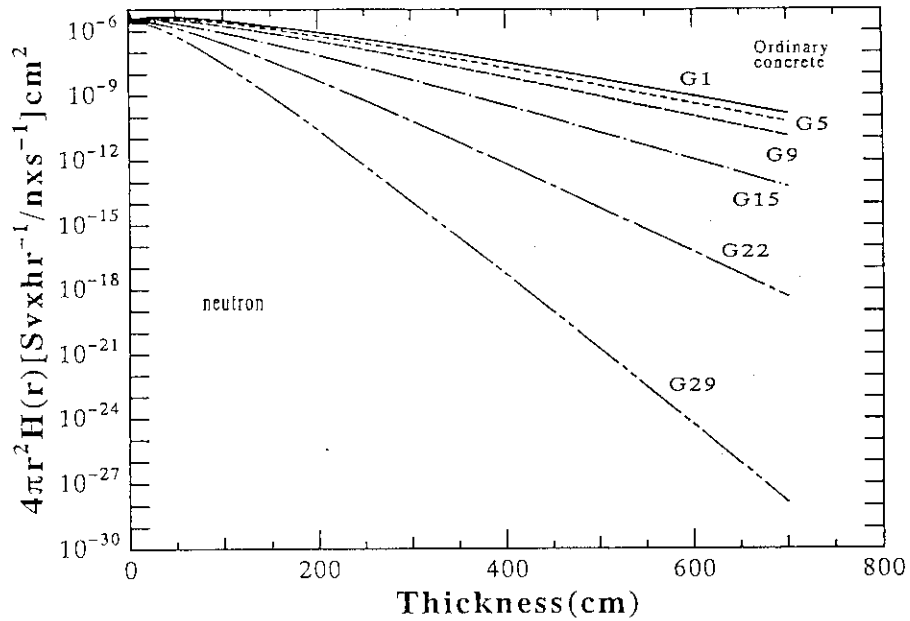


Figure 6.2.1 Neutron dose equivalents in ordinary concrete for isotropic monoenergetic neutron sources.

( G1 = 400 ~ 375 MeV, G5 = 300 ~ 275 MeV, G9 = 200 ~ 180 MeV,  
G15 = 100 ~ 90 MeV, G22 = 50 ~ 47.5 MeV and G29 = 19.6 ~ 14.9  
MeV)

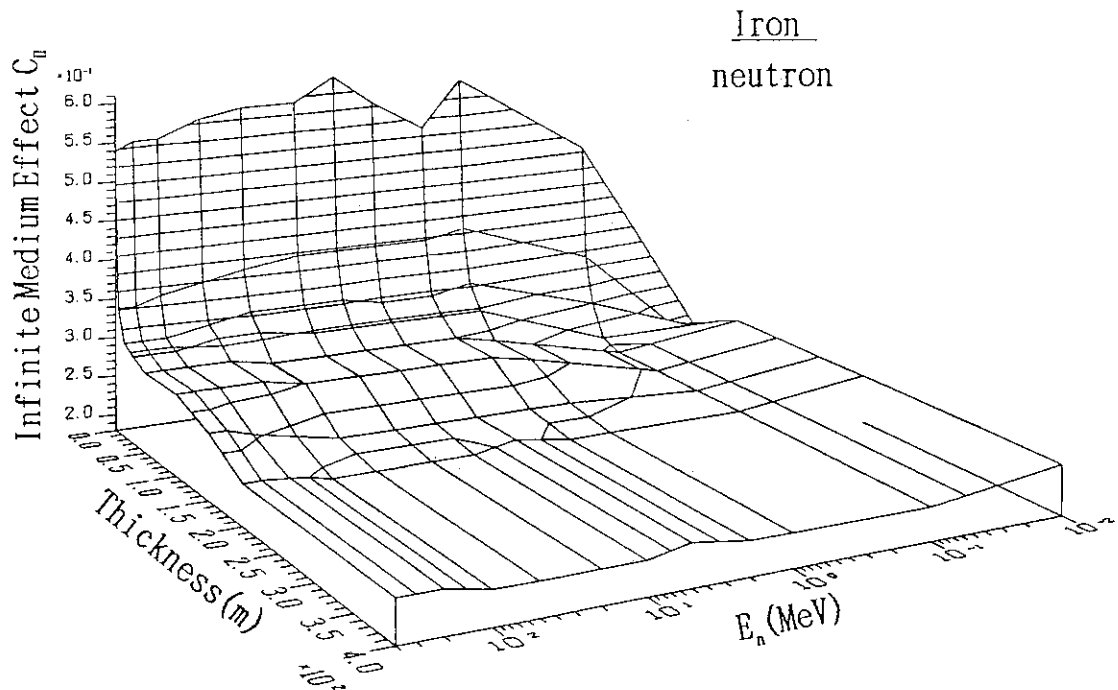


Figure 6.2.2 Infinite medium effect  $C_H$  of neutron dose equivalent in iron in 3-dimensional description.

### 6.3 Stopping Power of Charged Particles from 10 eV/amu to 10 GeV/amu

Y. Nakane, S. Furihata\*, S. Iwai\*\* and S. Tanaka

It is important to calculate stopping power for a variety of particle and material types in the wide energy ranges for the calculations of the dose conversion factors, detector responses and accelerator shielding designs. Therefore, electric collision stopping power ( $S_e$ ), nuclear collision stopping power ( $S_n$ ) and total stopping power in 15 kinds of materials were calculated for 10 kinds of charged particles from 10 eV/amu to 10 GeV/amu with three kinds of calculation codes: STOPPING<sup>1)</sup>, SPAR<sup>2)</sup> and RSTAN/RSHEV<sup>3)</sup>.

The characteristics of these codes are summarized in Table 6.3.1. The combination of these codes makes possible to calculate stopping power of all kinds of projectiles and materials in the wide energy region. At particle energies from 10 MeV/amu to 10 GeV/amu, stopping power was calculated with the RSTAN/RSHEV code for ten kinds of particles: muon, pion, p, d, t,  $\alpha$ ,  $^6\text{Li}$ ,  $^7\text{Li}$ ,  $^{12}\text{C}$ ,  $^{16}\text{O}$  in ten kinds of elements: H<sub>2</sub>, He, Be, C, Al, Fe, Cu, W, Pb and U, and five kinds of materials: water, phantom, LiF-TLDs (TLD-100 and TLD-700) and SSNTD (Solid State Neutron Track Detector). On the other hand, at particle energies from 10 eV/amu to 10 MeV/amu, stopping power was obtained with the SPAR code for muon and charged pion, and electric collision and nuclear collision stopping power was separately calculated with the STOPPING code for other eight kinds of particles, because nuclear collision stopping power is effective below a few hundred keV/amu.

The calculated total stopping power for deuteron particle in water with the RSTAN and STOPPING codes is shown in Fig. 6.3.1, which has a hump around 100 keV/amu and decreases monotonously as a function of particle energy. Both calculations are smoothly joined in the energy region between 1 and 100 MeV/amu including the connecting energy (10 MeV/amu).

The ratios of total stopping power with the STOPPING code to that with the

---

\* Mitsubishi Research Institute, Inc.

\*\* Mitsubishi Atomic Power Ind., Inc.

RSTAN/RSHEV code are shown in Fig. 6.3.2 at the connecting energy for p,  $\alpha$ ,  $^{12}\text{C}$ ,  $^{16}\text{O}$  in 10 elements and water. The ratios are dependent upon the target materials and are large in Fe, Cu and W especially, while the ratios become larger with increasing the charge of incident particle. Nevertheless, the both codes are in agreement less than 10 percent except for the case of  $^{16}\text{O}$  particles in W. Therefore, the STOPPING calculations were adopted in the stopping power table.

#### References

- 1) Ziegler J.F., Biersack J.P. and Littmark U. : "The Stopping and Range of Ions in Solids, Volume 1 of The Stopping and Ranges of Ions in Matter", Pergamon Press (1985).
- 2) Bichsel H. : private communication.
- 3) Armstrong T.W. and Chandler K.C. : "SPAR, a FORTRAN program for computing stopping powers and ranges for muons, charged pion, protons, and heavy ions", ORNL-4869 (1973).

Table 6.3.1 Characteristics of calculation code of stopping power for charged particles

Code	RSTAN / RSHEV	STOPPING	SPAR
Particle	$\pi^+$ , $\mu^+$ , p, $\bar{p}$ , d, t, $^3\text{He}$ , $^4\text{He}$ , $^6\text{Li}$ , $^7\text{Li}$ , $^9\text{Be}$ , $^{10}\text{B}$ , $^{11}\text{B}$ , $^{12}\text{C}$ , $^{13}\text{C}$ , $^{14}\text{N}$ , $^{15}\text{N}$ , $^{16}\text{O}$ , $^{17}\text{O}$	except $\pi$ , $\mu$	$\pi$ , $\mu$ , p, Heavy Ions ( $A > 2$ )
Energy Range (MeV/amu)	0.5 ~	$10^{-13} \sim 10^2$	$0 \sim 10^6$
Target (compounds)	$Z < 57$ / $Z \geq 57$ (possible) / (impossible)	except gases (possible)	except gases (possible)
$S_e$ , $S_n$ Calculation	$S_e$ Calculation only	$S_e$ and $S_n$ Calculation	$S_e$ Calculation ( $S_n$ consideration at lower energy region)

\* This code was modified by our laboratory to calculate compounds.

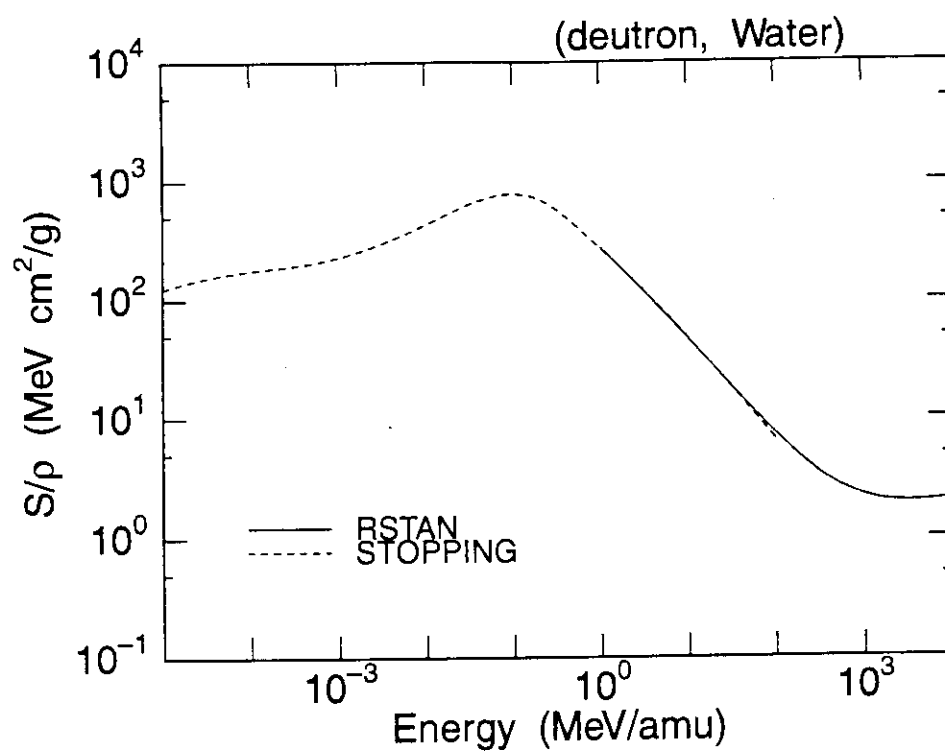


Fig. 6.3.1 Total stopping power for deuteron in water

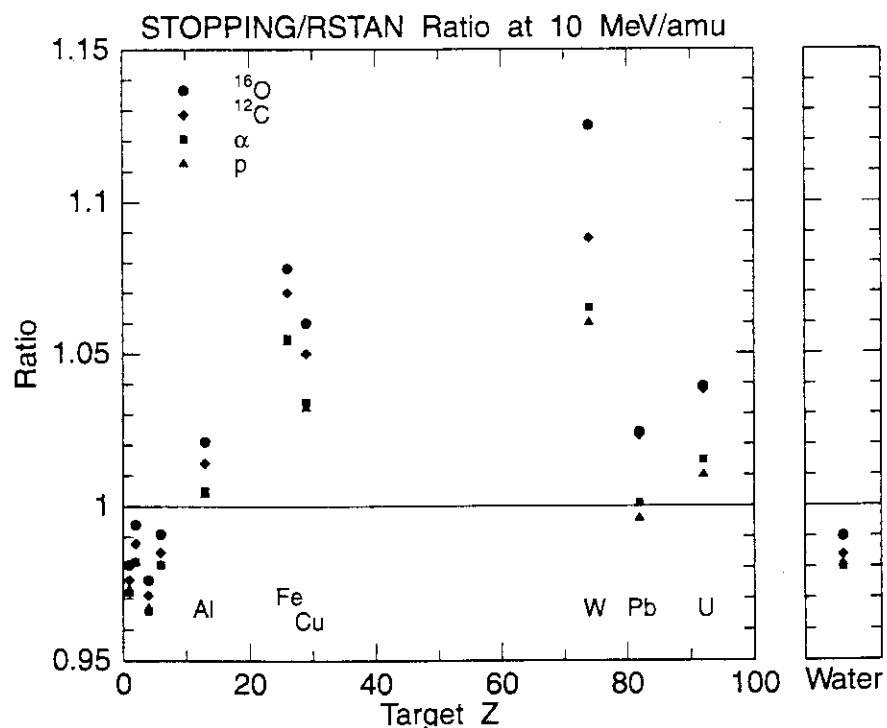


Fig. 6.3.2 The ratios of the stopping power with STOPPING to that with RSTAN at 10 MeV/amu

## 6.4 Evaluation of Fluence to Dose Equivalent Conversion Factors for High Energy Radiations (II)

Y. Sakamoto, S. Tanaka, N. Yoshizawa <sup>\*</sup>, O. Sato <sup>\*</sup>, S. Furihata <sup>\*</sup>, T. Uehara <sup>\*\*</sup>  
and S. Iwai <sup>\*\*</sup>

Along with increase of large scale high energy accelerator facility, from the point of view of radiation protection, an establishment of approach to evaluation of effective dose irradiated by high energy neutrons has come up to an important problem.

In present study, the method to calculate effective quality factors based on ICRP 60 <sup>1)</sup> has been developed. Effective quality factors are defined by weighed average quality factors for charged particles from incident energy to zero energy by the spectral distribution of the absorbed dose in tissue. They can be calculated for any kind of particles from quality factor (Q) - linear energy transfer (LET) relationships of charged particle in water. When a human body is irradiated by high energy neutrons, various kinds of secondary particles (heavy ions of nuclear fragments, high energy nucleons and mesons) with wide energy distributions are produced in nuclear reactions. In evaluation of the effective dose by high energy neutrons, the energy depositions by these secondary particles take effect considerably. Therefore, effective quality factors have been calculated for 186 charged particles up to Z=26 with energy range from 0.2 eV to 10 GeV including charged pion and muon <sup>2)</sup>. These particles were decided from nuclei of the materials used in the MIRD-5 mathematical human body phantom <sup>3)</sup>.

Fluence-to-dose-equivalent conversion factors have been calculated for broad parallel beams of monoenergetic neutrons of 100 MeV, 1 GeV and 10 GeV incident on a 30-cm-thick slab of ICRU four-element tissue (H: 10.1 w/o, C: 11.1 w/o, N: 2.6 w/o, O: 76.2 w/o, density: 1g/cm<sup>2</sup>) using Monte Carlo code HERMES <sup>4)</sup> with effective quality factors. Depths where absorbed doses and dose equivalents show maximum increase with incident neutron energy. In Table 6.4.1, the fractional contributions of various kinds of particles to the maximum dose equivalents using the Q-L relationships in ICRP 60 are compared with those using the Q-L relationships in ICRP 21 <sup>5)</sup> for each neutron energy.

---

<sup>\*</sup> Mitsubishi Research Institute, Inc.

<sup>\*\*</sup> Mitsubishi Atomic Power Industries, Inc.

Heavy ions dominate in dose equivalents for all incident neutrons. Secondary protons contribute to dose equivalent next to heavy ions. The contributions of charged pions increase with incident neutron energy. For all incident neutron energies, the sum of the contributions of photons generated from neutrons below 15 MeV, muons, electrons and positrons is less than about one percent.

In Fig.6.4.1, calculated maximum dose equivalents are compared with those of ICRP 51<sup>6)</sup> as a function of incident neutron energies. The present calculations are 20% - 40% smaller than those in ICRP 51. In ICRP 51, the quality factors for all heavy ions and any ion energy approximated to 20 were used. In present study, effective quality factors are used which are calculated for wide energy range and various charged particles.

#### References

- 1) ICRP Publication 60. 1990 Recommendations of the International Commission on Radiological Protection, Pergamon Press, Oxford (1991).
- 2) Sato O., et al.: "Evaluation of fluence to Dose Equivalent Conversion Factors for High Energy Radiations (II)", JAERI-M 93-147 (1993).
- 3) Snyder W.S., et al.: "Estimates of specific absorbed fractions for photon sources uniformly distributed in various organs of heterogeneous phantom. NM/MIRD Pamphlet No.5 (revised)", J. Nucl. Med. 19. Supplement: 5-67 (1987).
- 4) Cloth P., et al.: "HERMES A Monte Carlo Program System for Beam-Materials Interaction Studies", KFA-IRE-E AN/12/88 (1988).
- 5) ICRP Publication 21, "Data for Protection against Ionizing Radiation from External Sources", Pergamon Press, Oxford (1973).
- 6) ICRP Publication 51, "Data for Use in Protection Against External Radiation", Pergamon Press, Oxford (1987).

Table 6.4.1 Fractional contribution by various kinds of particles to the maximum dose equivalent produced by neutrons normally incident on a 30 cm-thick slab of ICRU four-element tissue.

Particles	Incident Neutron Energy					
	100 MeV		1 GeV		10 GeV	
	Fractional Contribution					
Q-L relations	ICRP60	ICRP21	ICRP60	ICRP21	ICRP60	ICRP21
secondary protons	33.3%	38.1%	38.1%	42.8%	33.2%	36.4%
charged pions	0.0%	0.0%	3.5%	3.9%	9.8%	10.5%
muons	0.0%	0.0%	0.1%	0.1%	0.1%	0.1%
heavy ions	42.0%	41.1%	45.2%	42.0%	48.2%	45.6%
electrons and positrons	1.3%	1.4%	0.6%	0.7%	0.4%	0.4%
neutrons below 15 MeV	23.3%	19.4%	12.5%	10.5%	8.4%	6.9%
photons *	0.1%	0.1%	0.1%	0.1%	0.0%	0.0%
maximum dose equivalent	pSv/(neutron/cm <sup>2</sup> )					
	376	340	986	896	1,840	1,720

\*photons generated from neutrons below 15 MeV

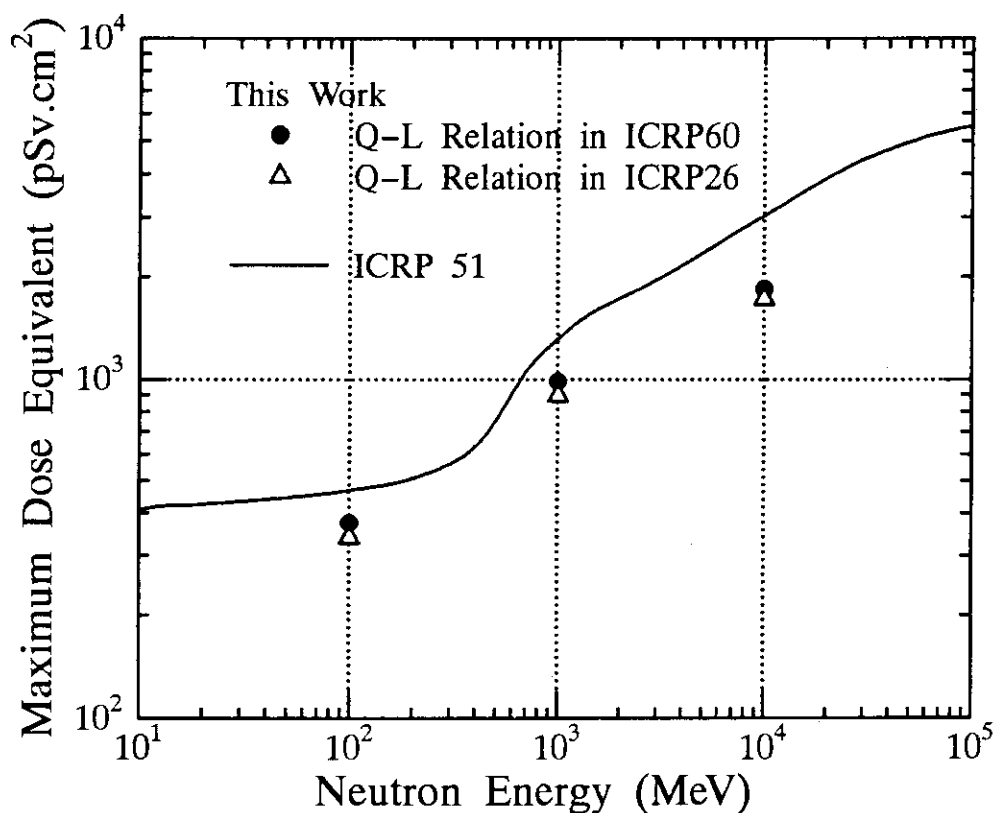


Figure 6.4.1 Calculation results of maximum dose equivalent for normally incident neutrons on a 30 cm-thick slab of ICRU four-element tissue compared with ICRP51.



## 6.5 Survey Calculation for Bulk Shielding Experiments (2)

### ———— Mock-up Experiment ————

C. Konno, F. Maekawa, A. Iwai and H. Maekawa

In the framework of the ITER/EDA blanket/shielding R&D, the Joint Central Team (JCT) proposed to carry out the mock-up shielding experiment. As the part of the '94 R&D Task, the pre-analysis was performed on the mock-up experiment which was expected to be executed at FNS.

The objective of the survey calculation was to determine how to simulate the shielding structure of the ITER. The model of the survey calculation was based on the latest design<sup>1)</sup> of the shielding blanket in ITER/EDA. Figure 6.5.1 shows the models used in the survey calculation. The model (a) is the model of the latest design of the shielding blanket in ITER/EDA and the model (b) is the simplified one of the model (a). In the model (c), the thickness of SS316/water zone is shortened by 400 mm, since the thickness of the SS316/water zone is too thick to measure neutron and gamma-ray data at the super conducting magnet (SCM) region by using FNS. The one-dimensional Sn transport code ANISN and group constant FUSION-40<sup>2)</sup> (42 groups for neutron and 21 groups for gamma-ray) were adopted. Figures 6.5.2 and 6.5.3 show the calculated neutron spectra at the surface of the first wall and at the depth of 50 mm inside the SCM region, respectively. The neutron spectra at the surface of the first wall are different between the model (a) and model (b)/(c) since the ratio of SS316 to water is different among them at the front part of SS316/water region, while the neutron spectra at the depth of 50 mm inside the SCM region are quite similar. It is concluded that the model (c) is a better model for the latest design of the shielding blanket in ITER/EDA regarding the neutron environment at the SCM region. Figure 6.5.4 shows the experimental assembly for the mock-up experiment actually executed at FNS. The SCM region is made of the layer structure simulating the latest design<sup>3)</sup> of the TF coil in ITER as shown Fig. 6.5.4. The calculation of the two dimensional Sn code DOT3.5 using FUSION-J3 suggests that a void can be substituted for liquid helium in the toroidal field (TF) conductor from the neutronics point of view.

#### References

- 1) "ITER Reference Blanket-Shield Design and Advanced Concept", ITER TAC-4-07 (1994).
- 2) Maki K., et al. : " Nuclear Group Constant set FUSION-J3 for Fusion Reactor Nuclear Calculations Based on JENDL-3," JAERI-M91072 (1991) ( in Japanese).
- 3) "Superconducting Coils and Mechanical Structures", ITER TAC-4-09 (1994).

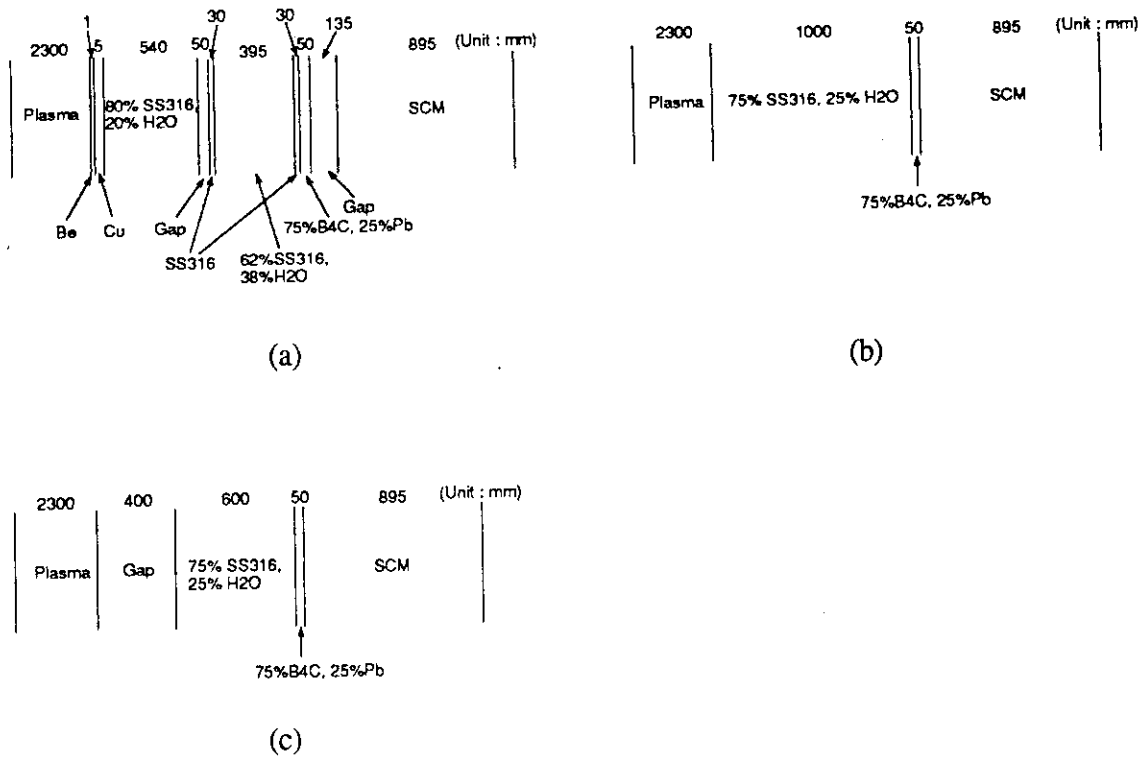


Fig. 6.5.1 Models for Survey Calculations

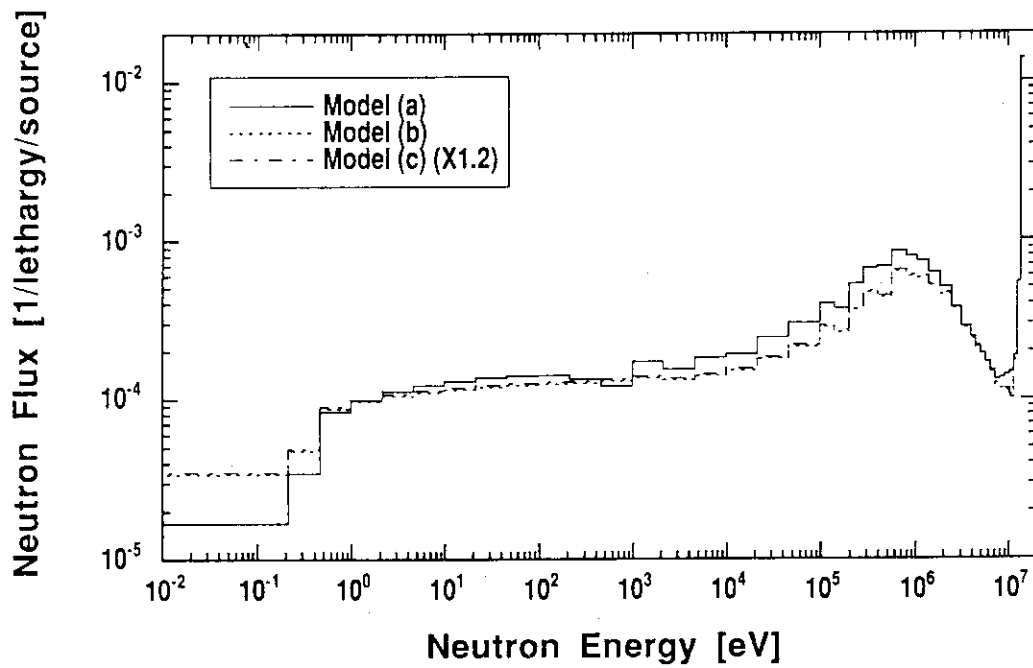


Fig. 6.5.2 Calculated Neutron Spectra at the surface of first wall

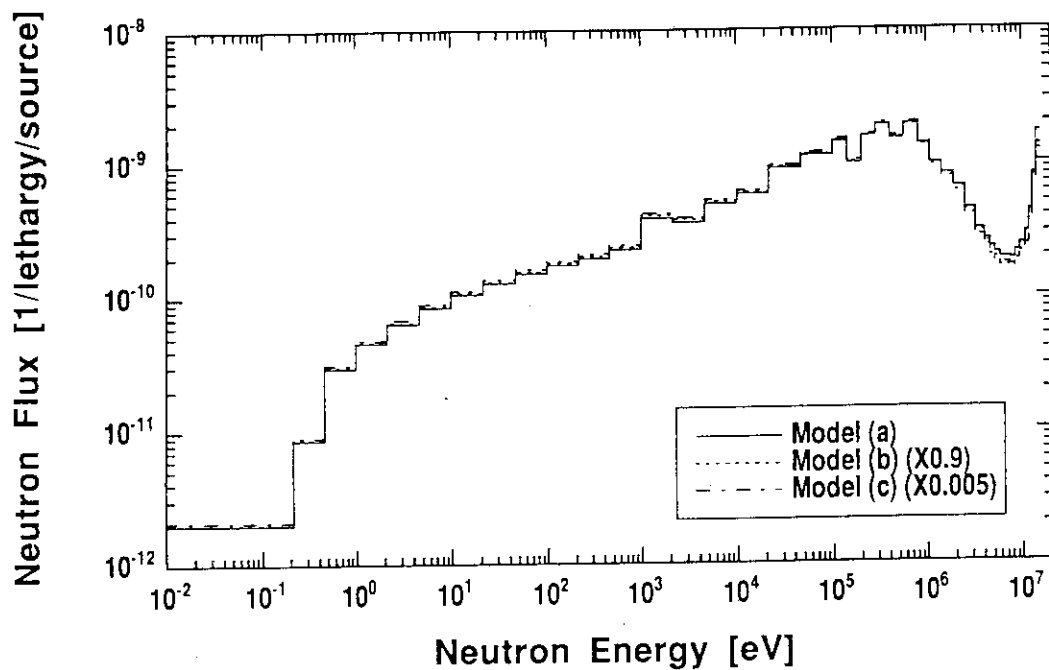


Fig. 6.5.3 Calculated Neutron Spectra at the depth of 50 mm inside the SCM region

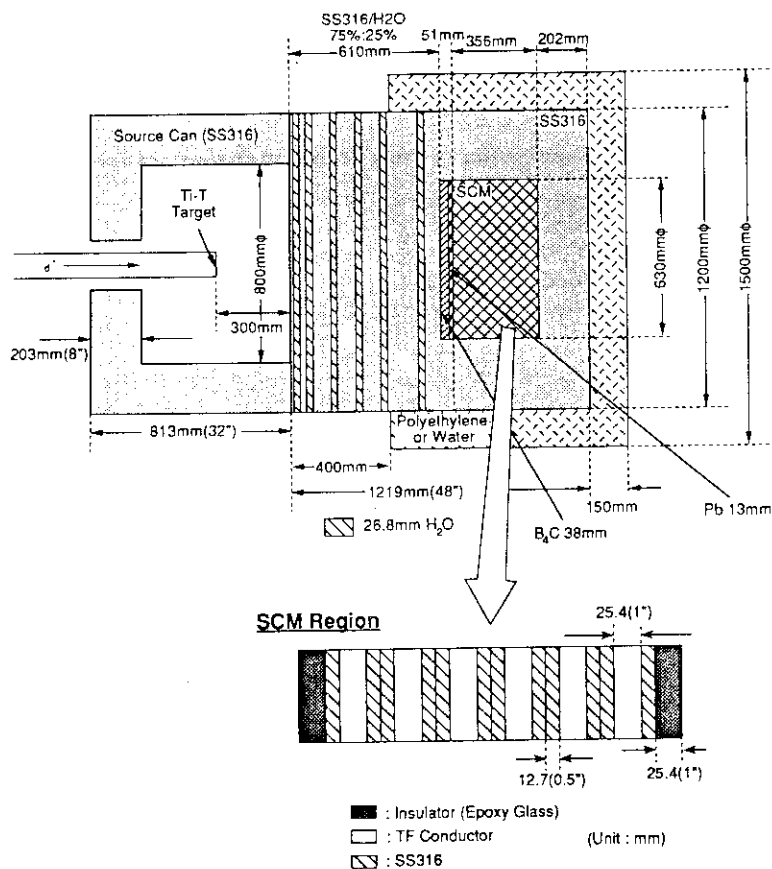


Fig. 6.5.4 Experimental Assembly of the Mock-up Experiment

## 6.6 Bulk Shielding Experiments on a Large SS316 Assembly with Voids

C. Konno, F. Maekawa, Y. Ikeda, Y. Oyama, Y. Uno and H. Maekawa

In next fusion reactors such as ITER, there will be some voids at joints of the shielding modules. Although these voids influence shielding performance, very few experiments have been performed so far. The shielding benchmark experiment was planned in order to examine experimentally the void effects on shielding performance and validate neutron transport codes.

The experiment was executed at the Fusion Neutronics Source (FNS) facility. The basic experimental assembly was a cylindrical assembly (test region) of SS316 (1.2 m in diameter and 1.12 m in thickness) with a source reflector of 0.2 m-thick SS316, which was the same as one of the SS316 bulk shielding experiments<sup>1)</sup>. Two different kinds of voids were made at the depth of 254 mm from the front surface of the test region of the basic experimental assembly. One was a cylindrical void (150 mm  $\phi$  x 102 mm), and another was an annular void (300 mm in outer diameter, 160 mm in inner diameter, 102 mm in thickness). The void size and position were determined based on the calculational survey<sup>2)</sup>. Figure 1 shows the experimental assembly with the annular void. Neutron fluxes over 10 MeV and from 10 keV to 1 MeV were measured using a 14 mm-diam. NE213 spectrometer and a small proton recoil gas proportional counters (19 mm in diameter and 127 mm in effective length), respectively. Gamma-ray heating rate was measured by thermoluminescent dosimeters (TLD). As neutron spectrum indices,  $^{235}\text{U}$  fission and activation reaction rates ( $^{27}\text{Al}(n,\alpha)^{24}\text{Na}$ ,  $^{93}\text{Nb}(n,2n)^{92m}\text{Nb}$ ,  $^{115}\text{In}(n,n')^{115m}\text{In}$ ,  $^{197}\text{Au}(n,\gamma)^{198}\text{Au}$ ) are measured by a fission chamber and foils of Al, Nb, In and Au, respectively. The measurements were performed along the center line and along two radial lines at distances of 50 and 254 mm from the void as shown in Fig. 6.6.1. The measurements were also executed using the assembly without voids. The void effects were presented by the ratio of the data with void to without void.

The analysis on the experiment was performed using the Sn code DOT3.5 ( $P_5$  expansion) and the Monte Carlo code MCNP. The cross section libraries were JSSTD<sup>3)</sup> (reduced to neutron 125 groups and gamma 40 groups, with self-shielding correction) and FSXLIB-J3<sup>4)</sup>, which were based on JENDL-3.1. S8 and S16 angular quadratures were used in the DOT3.5 calculation.

Figures 6.6.2 and 6.6.3 show the ratios of the measured and calculated neutron fluxes over 10 MeV in the cylindrical and annular void assemblies to those without void, respectively. The effects due to the void is very large (two to four times). The peaking due to the void in



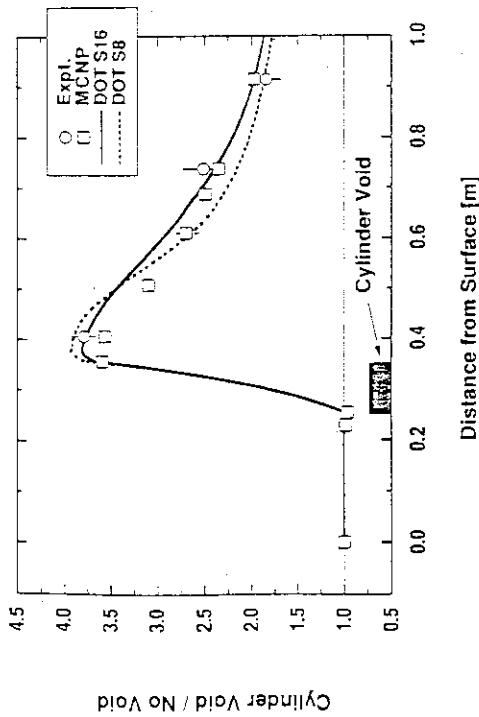


Fig. 6.6.2 Ratio of measured and calculated neutron fluxes over 10 MeV in the cylindrical void assembly to the no void data along the center line.

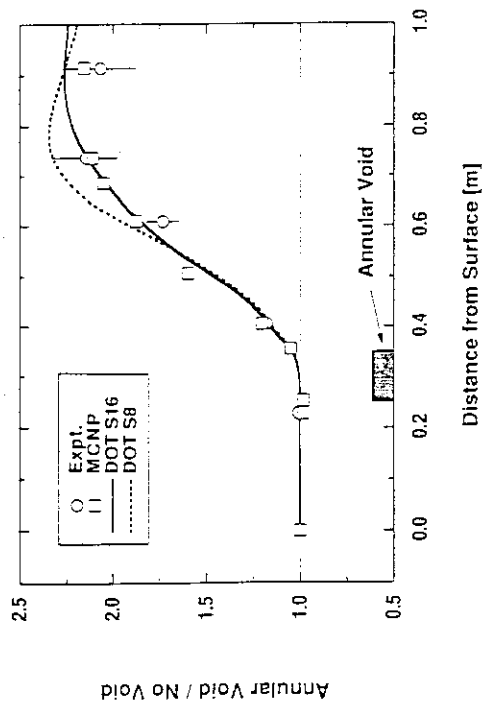


Fig. 6.6.3 Ratio of measured and calculated neutron fluxes over 10 MeV in the annular void assembly to the no void data along the center line.

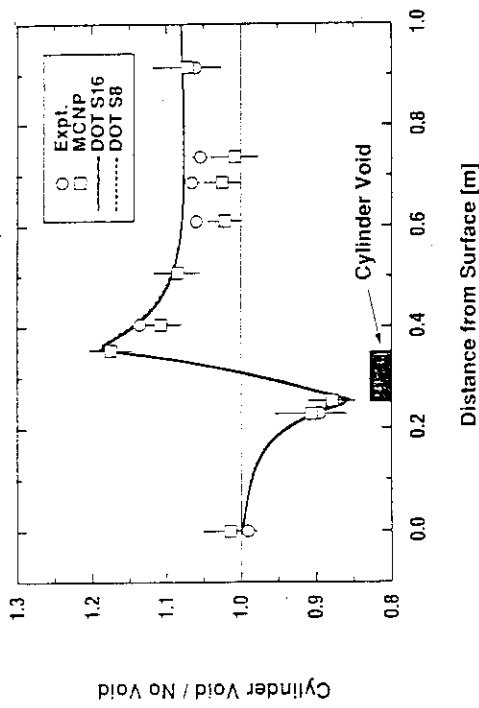


Fig. 6.6.4 Ratio of measured and calculated  $^{235}\text{U}$  fission-rate in the cylindrical void assembly to the no void data along the center line.

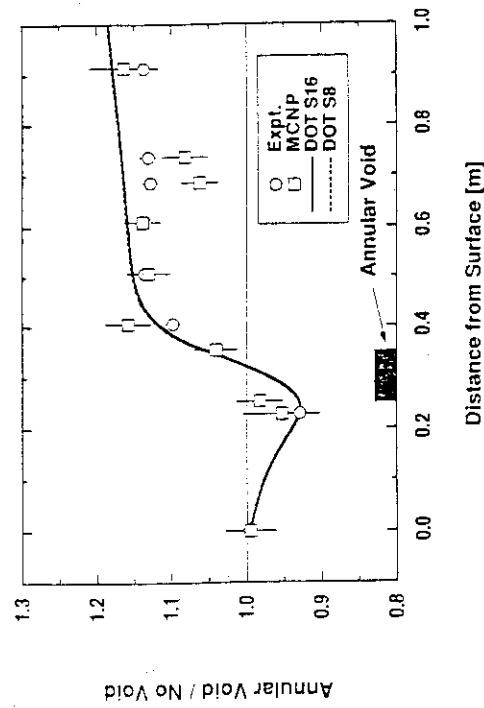


Fig. 6.6.5 Ratio of measured and calculated  $^{235}\text{U}$  fission-rate in the annular void assembly to the no void data along the center line.

## 7. Reactor and Nuclear Instrumentation

In reactor instrumentation, works were carried out in relation to the construction of HTTR (high-temperature engineering test reactor). Nicrosil-nisil thermocouples with various sheath materials were tested in high-temperature He atmospheres in an outpile electric furnace and an incore irradiation capsule to investigate the stability of their electromotive forces. Absorption characteristics of a charcoal filter for noble-gaseous fission products were investigated in the course of performance tests of fuel failure detection system.

As concerns advanced reactor instrumentation, a new-type position-sensitive fission counter was proposed. The counter has an anode of signal-transmission delay-line structure; and theoretical analyses were tried out to reveal the relation between pulse-signal propagation time and electrode structure. Also proposed was a new method of nondestructive measurement for assessment of material degradation of reactor pressure vessels (RPVs). This method deals with changes of magnetic coercivity of RPV steel due to neutron irradiation. A new device utilizing a cylindrical hybrid system of superconductor and ferromagnetic substance was developed for selective detection of magnetic-flux sources appeared around defects in metallic components and structures.

In nuclear instrumentation, works were devoted to R & D of nondestructive measuring methods for assessment of  $\alpha$ -radioactivity of TRU waste drums. The method requires precise estimation of spontaneous fission rate and ( $\alpha$ , n) neutron emission rate for a given waste composition-matrix, and thus an analytical method was proposed and evaluated as compared with experiments. The work pointed out the importance of study of ( $\alpha$ , n) neutron emission rate for waste control and disposal. Also, the statistical analysis of long term background neutron counting was tried out and interesting features were revealed.

As to the fundamental research in the field of instrumentation and measurement, light emission characteristics of various scintillator were investigated in terms of the emission light spectra and decay times to make clear the light emission characteristics in the region of relatively long wavelength. Also, an uninvasive means was explored to measure the beam current profile, and a new method was proposed for the inverse estimation of current distribution from the magnetic fields. The method utilizes ingenious combination of neural network and genetic algorithm, and its effectiveness was proved by computer simulation.

All the above were performed in Sensing Technology Laboratory.

## 7.1 Analysis of Background Count Rates in a Neutron Detection System

H. Gotoh, M. Haruyama, M. Takase and Y. Sugimoto

The authors have been using a passive neutron detection system for the development of measuring systems of transuranic elements in radioactive wastes for more than six years. Although the system has been working well for waste drums containing more than about 10mg plutonium, it is necessary to lessen the background counts if we want to realize a more sensitive detection system. The authors have started to analyze all background data taken already during more than six years. Present results are preliminary and only phenomenological.

The system was completed in February 1988 and was tuned up in the most favorable condition. Figure 7.1.1 shows one of the background data taken in multichannel scaling(MCS) mode at that time. The dwell time of the MCS was 10 s/channel and each channel stored total counts registered in every 10 seconds. The time behavior of background in 40,950 s ( $\cong 11.4$  hours) after the start of measurement was recorded in the figure. The average count was 16.48 and the average counting rate of background was estimated to be 1.648. Spikes are seen here and there. Those are attributed to cosmic rays or electrical noises.

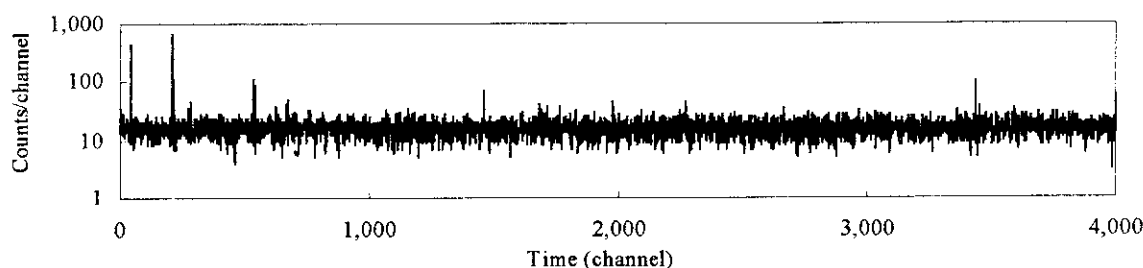


Fig.7.1.1 Multichannel scaling data of background counts. The first channel stores total counts during the first 10 s, the second channel does those during the next 10s, and so on.

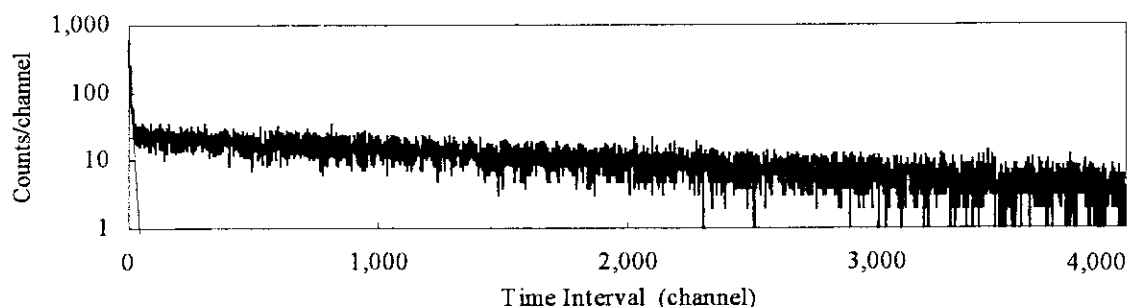


Fig.7.1.2 A distribution of time intervals between pulses. The measurement was performed by using a pulse interval analyzer (PIA).



The time intervals between all pulses were recorded parallel with the data of Fig. 7.1.1 for 36,000s. The distribution of time intervals is shown in Fig. 7.1.2. The time scale is 300  $\mu$ s/channel. A sum of two exponential functions with two different time constants is fitted to the distribution. The smaller time constant was 1.397 ms and the larger one was 684 ms. The total counts of the smaller time constant was 2,467 counts and that of the larger one was 52,981 counts. The sum of both components was 55,449 counts yielding total counting rate of 1.540 cps. This value is smaller than the value of 1.648 cps obtained with the MCS measurement. This means some of counts in spikes are lost at the PIA measurement.

The system was set at an underground room with a ceiling with 50cm thick ordinary concrete in the beginning and moved to the first floor with a ceiling of concrete slate. Figure 7.1.3 shows a time behavior of background counting rates after the system movement. The curve BGCPS corresponds to the counting rate of MCS measurement, the curve FASTCPS to that of smaller time constant, the curve SLOWCPS to that of the larger time constant and the curve TOTALCPS to the sum of FASTCPS and SLOWCPS. The background counting rate increased to about four times of that in the underground case.

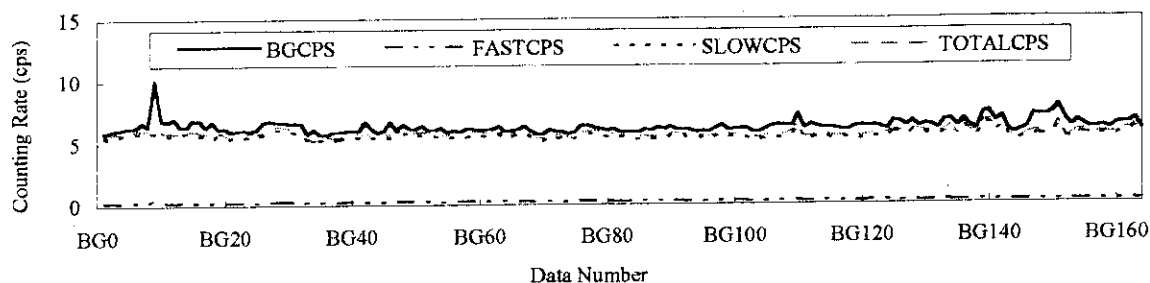


Fig. 7.1.3 A time behavior of background counting rates.

Many experiments were performed after the system movement. Figure 7.1.4 shows a distribution of numbers of background counts in 15s measurements after the system movement. The total number of events amounts to 363,668. We see that the distribution is composed of two components. One is a Gaussian type distribution and the other an inverse power function type tail. The curve drawn in the figure is the Poisson distribution with an average 90 which is the count in 15s counting expected from the average counting rate of 6.0cps. The width of the Gaussian type distribution is wider than that of the Poisson distribution. This will be caused by the long term fluctuation of neutron background. The tail will be caused by cosmic rays and electrical noises in wide sense. The latter will come from noises in commercial power supply, noises from electric apparatus for the system, noises from electric tools in the neighborhood and pulse breakdown in high voltage circuits for  $^3\text{He}$  counters.

Although the system was carefully designed and constructed against electrical noises, the

system was moved to a less favorable situation. And six year passage has a possibility of changing the condition of high voltage insulation. The removal of electric noises will be an important task for the authors.

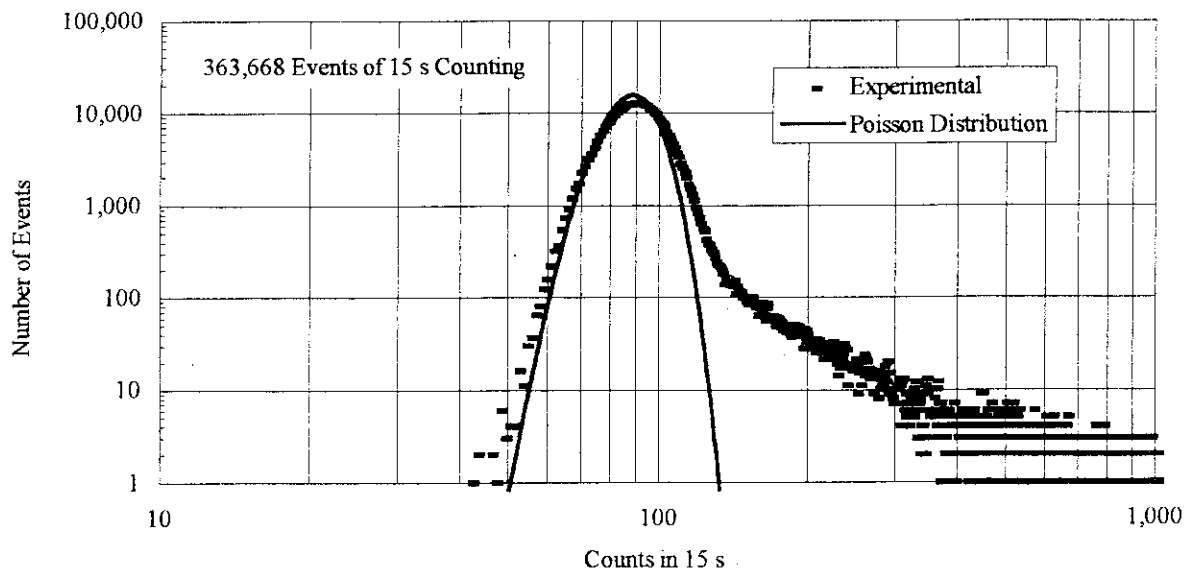


Fig.7.1.4 A time behavior of background counting rates.

## 7.2 Simultaneous Estimation of Spontaneous Fission Rate and $(\alpha, n)$ Neutron Emission Rate

H. Gotoh, M. Haruyama, M. Takase and Y. Sugimoto\*

In passive neutron method, the measuring process is mathematically interpreted as a mapping  $f$  from the direct product space of the time rate of  $(\alpha, n)$  reactions and spontaneous fission rate to the direct product space of a time-uncorrelated count rate and a time-correlated count rate :

$$C = f(R), \quad (1)$$

where  $R = \begin{pmatrix} (\alpha, n)R \\ SF R \end{pmatrix}$ ,  $C = \begin{pmatrix} \text{uncorrelated } C \\ \text{correlated } C \end{pmatrix}$ ,  $(\alpha, n)R$  is the time rate of  $(\alpha, n)$  reactions and  $SF R$  is the spontaneous fission rate. The analyzing process is interpreted as the inverse mapping  $f^{-1}$  of the mapping  $f$ . Although the mapping and the inverse mapping are curved in large scope, both are expected to be linear in a proper local scope.

If we have three standards  $R_i$  ( $i=0,1,2$ ) in a neighborhood of an unknown sample  $R$ , then we have the following three relations:

$$\begin{pmatrix} \text{uncorrelated } C_1 - \text{uncorrelated } C_0 \\ \text{correlated } C_1 - \text{correlated } C_0 \end{pmatrix} = \frac{\partial f}{\partial R} \Big|_{R=R_0} \cdot \begin{pmatrix} (\alpha, n)R_1 - (\alpha, n)R_0 \\ SF R_1 - SF R_0 \end{pmatrix}, \quad (2)$$

$$\begin{pmatrix} \text{uncorrelated } C_2 - \text{uncorrelated } C_0 \\ \text{correlated } C_2 - \text{correlated } C_0 \end{pmatrix} = \frac{\partial f}{\partial R} \Big|_{R=R_0} \cdot \begin{pmatrix} (\alpha, n)R_2 - (\alpha, n)R_0 \\ SF R_2 - SF R_0 \end{pmatrix}, \quad (3)$$

and

$$\begin{pmatrix} \text{uncorrelated } C - \text{uncorrelated } C_0 \\ \text{correlated } C - \text{correlated } C_0 \end{pmatrix} = \frac{\partial f}{\partial R} \Big|_{R=R_0} \cdot \begin{pmatrix} (\alpha, n)R - (\alpha, n)R_0 \\ SF R - SF R_0 \end{pmatrix}. \quad (4)$$

Equation (4) can be rewritten for the estimate of the unknown  $R$ :

$$\begin{pmatrix} (\alpha, n)R \\ SF R \end{pmatrix} = \frac{\partial f}{\partial R} \Big|_{R=R_0}^{-1} \begin{pmatrix} \text{uncorrelated } C - \text{uncorrelated } C_0 \\ \text{correlated } C - \text{correlated } C_0 \end{pmatrix} + \begin{pmatrix} (\alpha, n)R_0 \\ SF R_0 \end{pmatrix}. \quad (5)$$

From (2) and (3) we obtain an expression for the inverse of  $\frac{\partial f}{\partial R} \Big|_{R=R_0}$  :

$$\frac{\partial f}{\partial R} \Big|_{R=R_0}^{-1} = \begin{pmatrix} (\alpha, n)R_1 - (\alpha, n)R_0 & (\alpha, n)R_2 - (\alpha, n)R_0 \\ SF R_1 - SF R_0 & SF R_2 - SF R_0 \end{pmatrix} \cdot \begin{pmatrix} \text{uncorrelated } C_1 - \text{uncorrelated } C_0 & \text{uncorrelated } C_2 - \text{uncorrelated } C_0 \\ \text{correlated } C_1 - \text{correlated } C_0 & \text{correlated } C_2 - \text{correlated } C_0 \end{pmatrix}^{-1}. \quad (6)$$

And we finally obtain

$$\begin{pmatrix} (\alpha, n)R \\ SF R \end{pmatrix} = \begin{pmatrix} (\alpha, n)R_1 - (\alpha, n)R_0 & (\alpha, n)R_2 - (\alpha, n)R_0 \\ SF R_1 - SF R_0 & SF R_2 - SF R_0 \end{pmatrix} \cdot \begin{pmatrix} \text{uncorrelated } C_1 - \text{uncorrelated } C_0 & \text{uncorrelated } C_2 - \text{uncorrelated } C_0 \\ \text{correlated } C_1 - \text{correlated } C_0 & \text{correlated } C_2 - \text{correlated } C_0 \end{pmatrix}^{-1} \cdot \begin{pmatrix} \text{uncorrelated } C - \text{uncorrelated } C_0 \\ \text{correlated } C - \text{correlated } C_0 \end{pmatrix} + \begin{pmatrix} (\alpha, n)R_0 \\ SF R_0 \end{pmatrix}. \quad (7)$$

The authors' passive neutron system measures the distributions of all time intervals between pulses detected as shown in Fig.7.2.1. The distribution is separated into two exponential

\* Present address: Miyama Co. Ltd., Ooarai-machi, Ibaraki-ken

components. The total count of the slower component  $_{\text{slow}}C$  corresponds to the time-uncorrelated count and the total count of the faster component  $_{\text{fast}}C$  corresponds to the time-correlated count. The measurement shown in Fig.7.2.1 was performed on a sample made of plutonium with an isotopic composition of 20.37%  $^{240}\text{Pu}$  in a counting time of 1,800s. The total count of the slower component with time constant 0.680ms was 25,523 and that of the faster component with time constant 4.117 ms was 430,631.

The time interval distribution can be calculated using the neutron detection efficiency  $\varepsilon$ , the system dieaway time  $\tau$ , the spontaneous fission rate  $_{\text{SF}}R$  and the  $(\alpha, n)$  reaction rate  $_{(\alpha, n)}R$  with a mathematical expression<sup>1)</sup>.

Three pairs (880, 220), (890, 220) and (880, 230) was selected for three standards  $(_{(\alpha, n)}R_i, _{\text{SF}}R_i)$  ( $i = 0, 1, 2$ ), and three pairs (418, 712, 27,778), (421, 974, 27,814) and (424, 482, 29,108) were obtained for  $(_{\text{uncorrelated}}C_i, _{\text{correlated}}C_i)$  ( $i = 0, 1, 2$ ) after computation with the mathematical expression and curve fitting. The pair  $(951.1 \pm 16.6, 204.9 \pm 7.7)$  was finally obtained for  $(_{(\alpha, n)}R, _{\text{SF}}R)$  of the unknown using (7).

From the specification of the sample, spontaneous fission rate was calculated and the result was  $205 \text{ s}^{-1}$  which should be compared with  $204.9 \pm 7.7 \text{ s}^{-1}$  described above. The  $(\alpha, n)$  reaction rate was also calculated from the specification with a computer program for  $(\alpha, n)$  reaction rate<sup>2)</sup> regarding the sample as pure  $\text{PuO}_2$  and considering  $^{241}\text{Am}$  accumulation after the analysis of isotopic compositions. The result was  $911 \text{ s}^{-1}$  which should be compared with  $951.1 \pm 16.6 \text{ s}^{-1}$  described above.

Although detailed analysis is now continuing, it is interesting that the time interval measurement with the mathematical aid on time interval distribution saves physical standards of transuranic material.

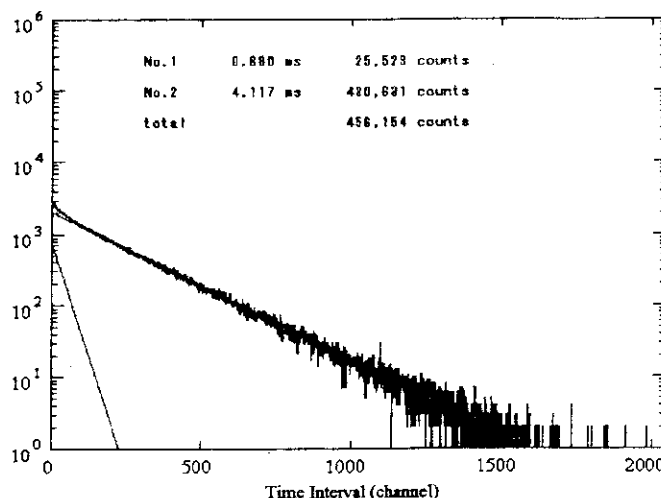


Fig.7.2.1 A distribution of time interval taken for a plutonium sample. The time-correlated count is by the count of the faster component and the time-uncorrelated count is given by the count of the slower component. The dwell time is 20 $\mu$ s/channel.

## References

- 1) Gotoh H., et al.: JAERI-M 91-138 pp.130-132 (1991)
- 2) Gotoh H., et al.: JAERI-M 93-181 pp.127-128 (1993)

### 7.3 A New Method of Nondestructive Measurement for Assessment of Material Degradation of Aged Reactor Pressure Vessels

K. Ara, N. Nakajima\* and N. Ebine\*

As about forty years have rolled on since the commencement of electric power generation by light water reactors, great concern about how one should assess the residual life of nuclear power plant is aroused today. Concurrently hopes of plant life extension are being encouraged with support of today's highly developed technologies in manufacturing of reactor components and management of reactor operations, though these originated from difficulties in finding new sites for plant construction.

As concerns the plant life, the reactor pressure vessel (RPV, hereafter) is the most important reactor component because it is one of the components that cannot be replaced when degraded and hence its failure is not considered in plant safety assessments. A serious problem of radiation embrittlement, however, exists in RPVs, and this brings about an important subject of how one should assess properly the degradation of RPVs in aging. Generally the degradation has been assessed by means of impact testing of Charpy coupons, i.e., surveillance test specimens made of the same material as RPV, settled and irradiated in the reactor between the core and the RPV inner wall. In this way of assessment, the following problems are becoming serious today. Acceleration feature of Charpy coupons tests, uncertainty of stress-induced effects, and lack of Charpy coupons.

Under these circumstances, a nondestructive measuring method to assess directly the degradation of RPVs is required to be explored and developed. The authors propose a new nondestructive method MIM (Magnetic Interrogation Method) by which changes of magnetic coercivity of RPV steel due to neutron irradiation are measured in relation to changes of material properties of and other aging phenomena in RPV.

The schematic representation of a measuring system in MIM is shown in Fig. 7.3.1. A part of RPV is magnetized from the side of its inner wall through its overlay clad by a magnetic yoke. Then one measures a magnetic field distribution pattern on the surface of RPV through a magnetization process as shown in Fig. 7.3.2. From the measured pattern one estimate inversely the coersivity distribution in the direction of thickness of RPV steel with an aid of magnetostatic field analysis.

This type of problems is generally called as the ill-posed inverse problem and cannot be solved uniquely. We therefore introduce very effective and realistic strong constraint; that is,

---

\*Reactor Component Reliability Laboratory,  
Department of Reactor Safety Research

we fix the form of coersivity distribution function,  $f_c(t, [p_1-p_j])$ , and hence inversely estimate parameters  $[p_1-p_j]$  from the measured magnetic field distribution patterns. Here,  $t$  is a position in the RPV steel, and  $[p_1-p_j]$  state parameters related to the degree of radiation-induced hardning.

In the implementation of above process, the following two conditions must be satisfied: i) a mathematical model of the hysteresis magnetization characteristics of RPV steel can be provided, and ii) the thickness of overlay clad can be measured nondestructively with some other means.

The authors have just started works to confirm experimentally the feasibility of MIM. The first subject being made clear is the possibility of nondestructive measurement of overlay clad thickness with a MIM hardware system, and the second the possibility of obtaining measurement patterns that reflect uniquely coercivity distributions in RPV steel.

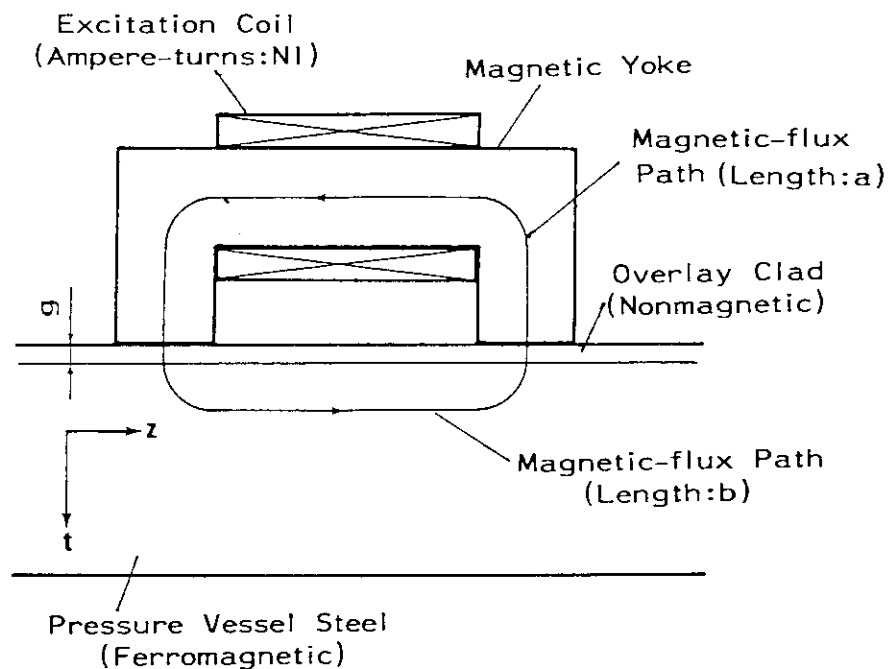


Fig. 7.3.1 Schematic representation of a measuring system

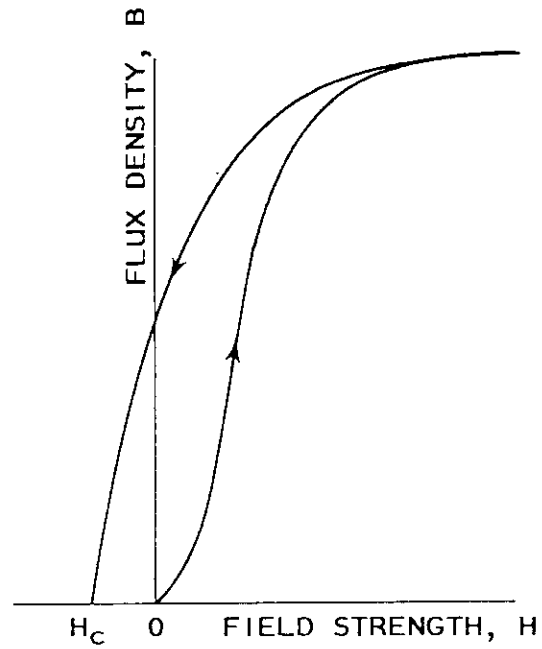


Fig. 7.3.2 A magnetization process by which RPV steel is first magnetized from zero to saturation and then demagnetized until the magnetization becomes zero again

## 7.4 High Temperature Tests of Nicrosil-Nisil Thermocouples

M. Yamada and K. Ara

Nicrosil-nisil thermocouples (N-TCs), as shown in Fig. 7.4.1, were fabricated with metal-sheaths of five different alloys; i.e., inconel 600, incoloy 800, incoloy 825, hasteloy X and nicrosil. The N-TCs were then tested at high temperature environments in an out-pile electric furnace and an incore irradiation capsule, to examine their applicability to incore gas temperature measurement in HTTR.

The out-pile high temperature tests were lasted for 20,000 hours at 1200 °C in He atmosphere. During the tests, the furnace temperature was monitored with a reference R-type TC, that was occasionally calibrated at Ag point (961.93 °C); and the temperature indications by N-TC test samples (27 samples in total) were recorded and compared with the indication by the reference R-TC. Typical test results are shown in Fig. 7.4.2. The N-TCs with the nicrosil sheaths showed the most stable characteristics as that their emf drifts were about -2%. The ones with the inconel 600 and incoloy 825 sheaths showed the drifts of about -3.5%, and those with the incoloy 800 sheaths the worst of -6%. The N-TCs with the hasteloy X sheaths showed two different trends: 2 of 8 samples showed drifts less than -1% but the others about -6%. The cause of this strange phenomenon is not clear.

After the tests, some of the samples were dismantled, and analyses of TC element wires were carried out by means of the energy dispersive X-ray spectroscopy (EDX). One found that the samples which showed large emf drifts contained chemical elements such as Cr, Mn and Fe of sheath materials in their element wires. This proved that the causes of emf drifts were the diffusion of chemical elements from the sheath to the element wires. Hence one can understand the test result that the N-TC having nicrosil sheath showed the most stable long-term emf characteristic.

The incore irradiation tests were performed for the N-TC samples having nicrosil sheaths at about 1000 °C in JMTR. The total irradiation time was 2127 hours that resulted in the fast neutron fluence of  $1.2 \times 10^{21} \text{ n/cm}^2$  and the thermal neutron fluence of  $9.8 \times 10^{20} \text{ n/cm}^2$ . The temperature indications of sample TCs were calibrated during each reactor shutdown by heating up the irradiation capsule and inserting a nonirradiated reference K-TC into the capsule. The test results are shown in Fig. 7.4.3. The emf drifts of about +2% were observed. After the irradiation tests, the capsule was dismantled and the post irradiation emf calibration tests were performed at 1000 °C. The results are shown in Fig. 7.4.4 where small emf drifts of +0.4% in average are presented.

In conclusion one can say that the N-TC with the nicrosil sheath seems to meet the specifications that are required to the incore gas temperature measurement in HTTR.



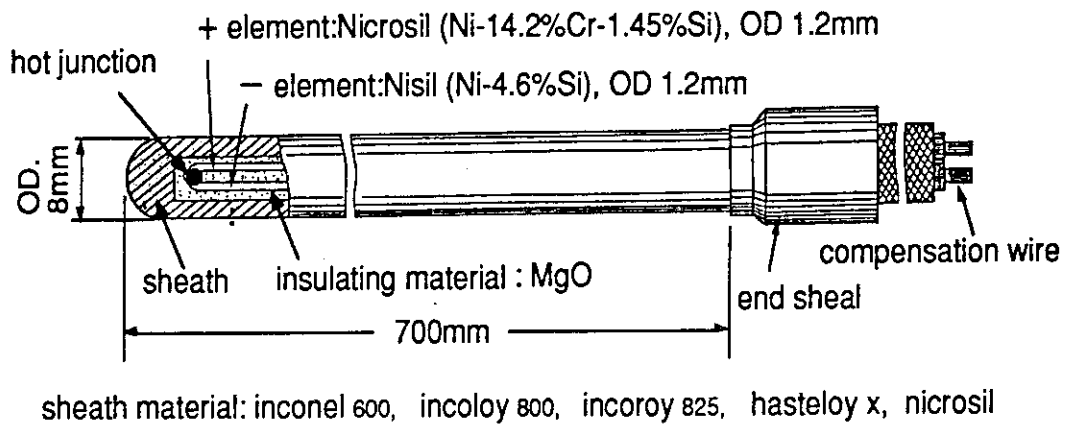


Fig.7.4.1 Fabricated sample thermocouples

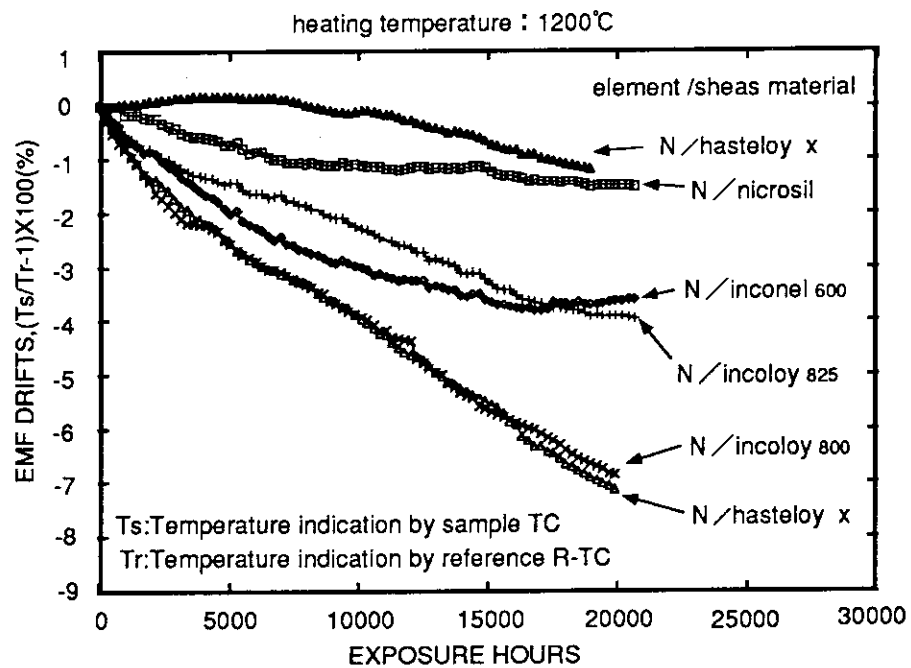


Fig.7.4.2 Typical results of out-pile high-temperature test

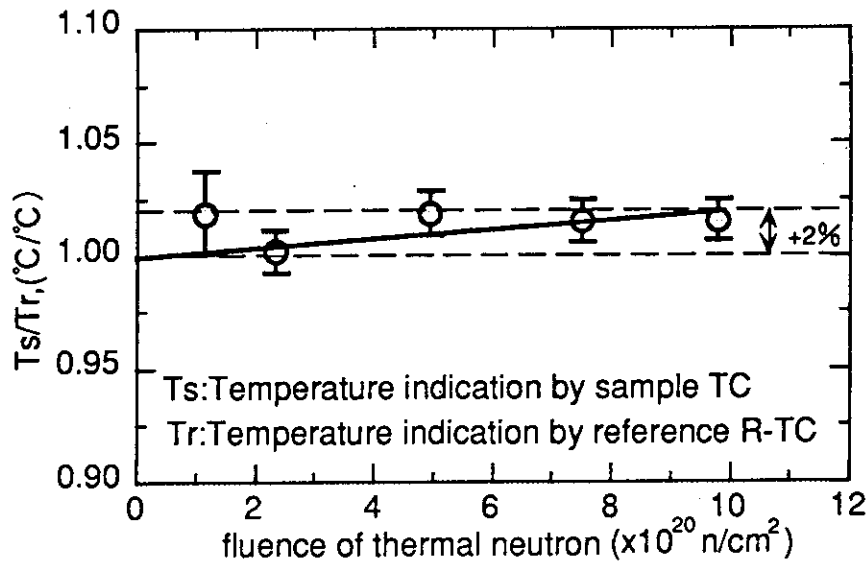


Fig.7.4.3 Results of incore irradiation test

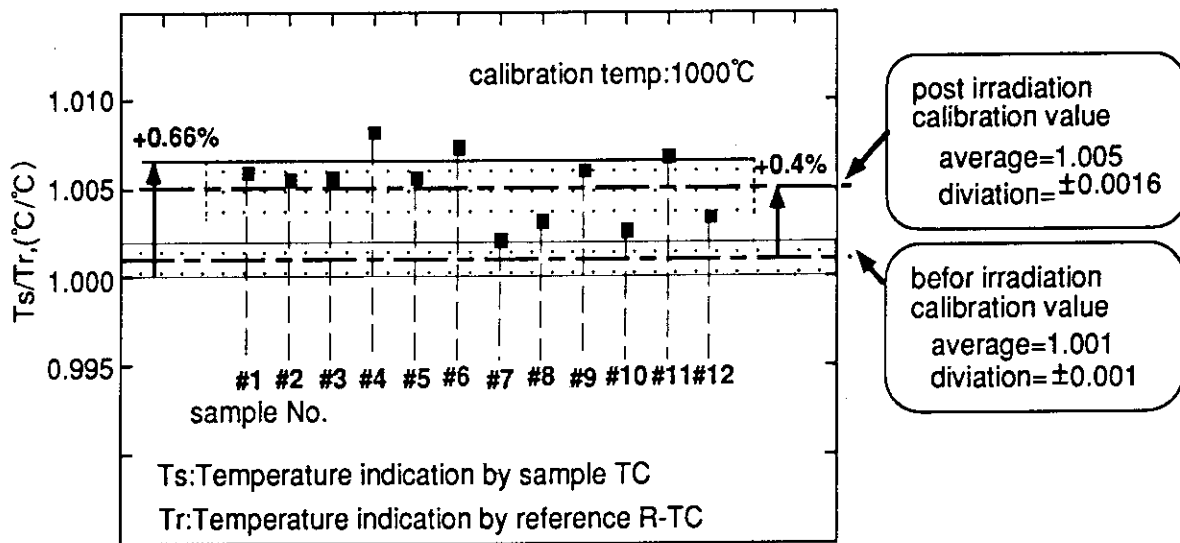


Fig.7.4.4 Result of post irradiation calibration

## 7.5 Measurement of Scintillation Emission Spectra

H. Yagi, H. Itoh and M. Yamada

The experimental investigations have been performed for the scintillation response that include the relation between the emission spectra and the decay time. As the first stage, the emission spectra of the typical inorganic scintillators have been measured. These results support the development of X-ray image sensor that is integrated scintillator on the semiconductor photo detector for the synchrotron radiation. It is necessary to know the relation between the emission spectra and the decay time, for the development of the advanced phoswich detector that is applied to measure the  $\alpha$  emit nuclide.

The scintillators were excited by X-ray and the scintillation emission light was analyzed by the photo spectrometer with a line sensor. The general configuration of the apparatus is shown in Figure 7.5.1. The X-ray generator has an iron target and was operated on the acceleration voltage of 35kV and the beam current of 15mA. The emission light by X-ray excitation was focused on the inlet slit (3mm x 200mm). The passed light was dispersed by the diffraction grating and projected on the Image Intensifier (I.I) coupled with line sensor. The electrons emitted by photo cathode of the I.I were amplified by the Micro Channel Plate (M.C.P). The multiplied electrons excite the phosphor and its luminescence induces the photo current in the line sensor. The I.I has the multi-alkali photo cathode response that is sensitive from 195 to 850nm. The total spectral sensitivity response using for the spectral correction is shown in figure 7.5.2 compared to the S11 and the S20(bi-alkali) as well known photo cathode response. The specified sensitivity of the I.I is 150mA/lm, the electron multiplication factor of the M.C.P is the maximum 700 times. The data processor executes the dark current subtraction, the sensitivity correction and the indication. Because of the lower sensitivity of this photo cathode on the long wave length region, the dark current of the region over the 700nm is evaluated about 10 times large to the region of 400nm. As the results of sensitive correction, the spectral dependency of photo cathode was excepted from the spectral data. Therefore, the wave length (energy) distribution of the emitted photon counts was obtained.

The typical test results of the emission spectra for the scintillators of NaI(Tl), CsI(Tl) and CsI(Na) excited by X-ray are shown in Figure 7.5.3. The comparisons of normalized emission spectra profile of BaF<sub>2</sub>, CaF<sub>2</sub>(Eu), BGO, CdWO<sub>4</sub> and NaI(Tl) are shown in Figure 7.5.4. The integral value (total photon counts) of the photon counting distribution gives a quantum efficiency of the scintillation emission. The relative emission efficiency (%) compared with NaI(Tl) was evaluated with the typical photo cathode response and compared to the Scintillation Phosphors Catalog of the Harshaw Research Laboratory. These results are summarized in Table 7.5.1.

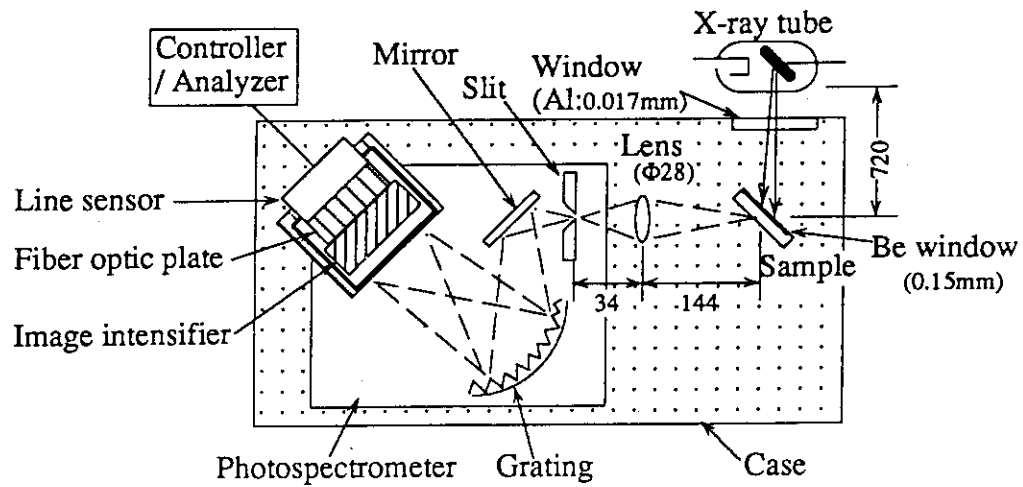


Figure 7.5.1 Configuration of experiment apparatus for the measurement of the scintillation emission spectra.

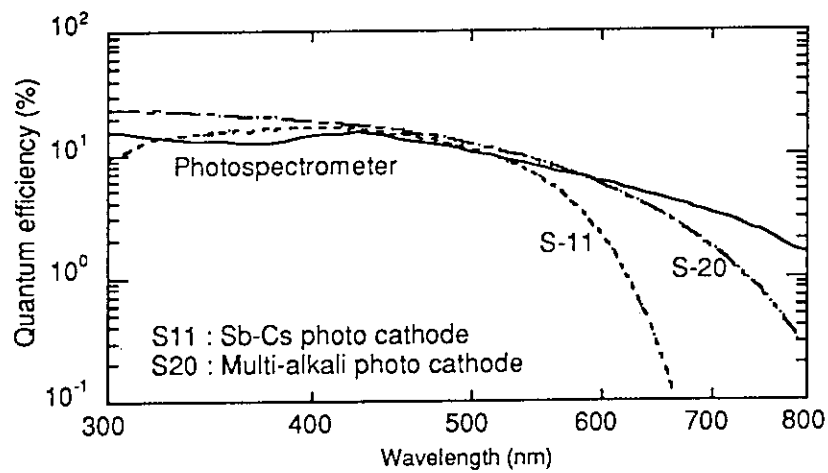


Figure 7.5.2 Total spectral sensitivity response of the photo spectrometer upgraded by the Image Intensifier is compared to the S11 and the S20(multi-alkali) response.

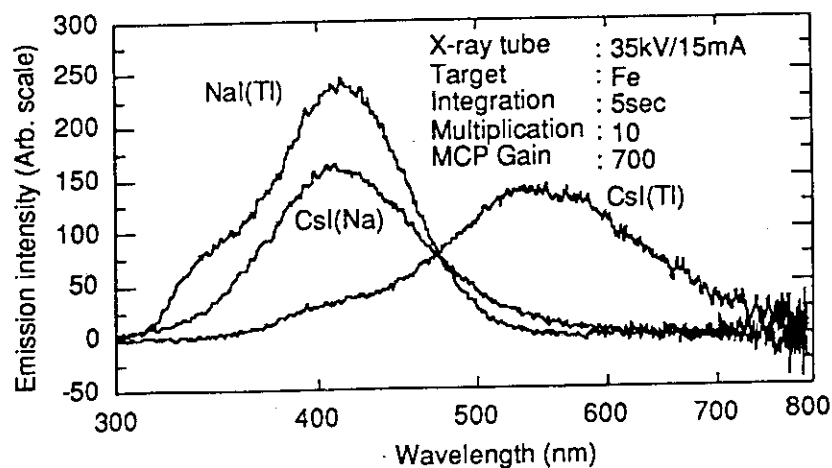


Figure 7.5.3 The emission spectra for the scintillators of NaI(Tl), CsI(Tl) and CsI(Na)

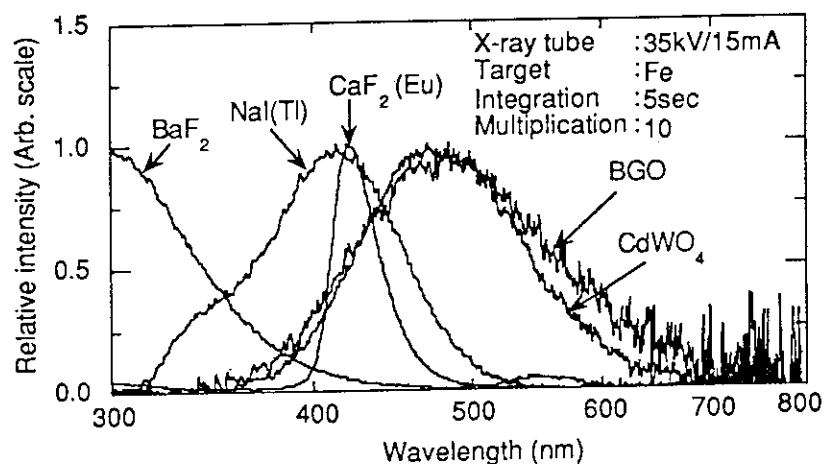


Figure 7.5.4 Comparison of the normalized emission spectra profile of BaF<sub>2</sub>, CaF<sub>2</sub>(Eu), BGO, CdWO<sub>4</sub> and NaI(Tl)

Table 7.5.1 The relative efficiency referred to the NaI(Tl) are evaluated with the S11 and S20 photo cathode response.

Scintillator	Wavelength of Max. Emission* <sup>2</sup> (nm)	Relative Emission Efficiency (%) <sup>*1</sup>			
		Ratio of total photon counts	Evaluated with S20	Evaluated with S11	Evaluated with S11 by Harshaw
NaI(Tl)	413 (410)	100	100	100	100
CsI(Tl)	551 (565)	114	55	48	45
CsI(Na)	409 (420)	74	70	71	85

\*1 : Compared with NaI(Tl)

\*2 : ( ) referred to Harshaw Scintillation Phosphors Third Edition, (1975)

## 7.6 Absorption Characteristics of an Activated Charcoal Filter for Noble-Gas FPs Having Short Half-Life

M. Katagiri, M. Kishimoto, H. Yoshida, H. Ito, K. Iimura and T. Saruta

In an in-pile irradiation experiment for nuclear fuels, a charcoal filter is installed into a sampling gas line in order to remove iodides contained in the sampling gas. Therefore, it is necessary to correct radioactivity concentrations measured at down stream of the filter by using the passing rate for the charcoal filter. However, since an activated charcoal is used at the temperature below 0 °C to remove not only activated iodides but also noble-gas FPs, the absorption coefficients of activated charcoals have been measured in the temperature range from 50 °C to -70 °C <sup>1)2)</sup>.

Therefore, we measured the absorption coefficients of an activated charcoal in the temperature range from 26 °C to 140 °C at which the charcoal filter is used in practice. For these measurements, we used the noble-gas FPs having short half-life.

The measurements of absorption coefficient were carried out by using noble-gas FPs produced at the irradiation test in the JMTR. A schematic diagram of an experimental apparatus is shown in Fig. 7.6.1. The structure

of a charcoal filter used for the measurements is shown in Fig. 7.6.2. The activated charcoal is a cylinder of 10 mm diameter and 40 mm length. The weight is 2.2 grams. The temperature of the charcoal filter was changed by a sheath heater and a temperature controller.

Passing rates as function of the carrier-gas flow rate and the temperature were measured by the experimental apparatus. Sampling gas flow rates are 15 cm<sup>3</sup>/min, 25 cm<sup>3</sup>/min,

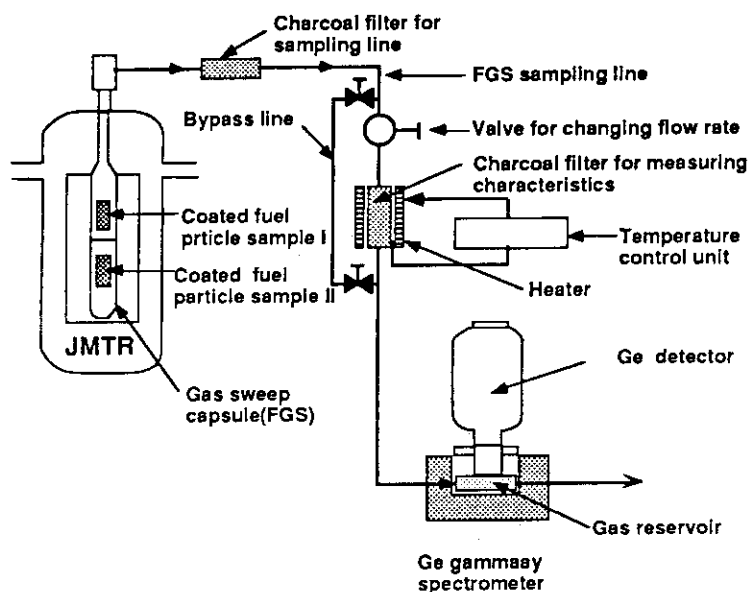


Fig.7.6.1 A schematic diagram of an experimental apparatus for measurements of absorption coefficient of an activated charcoal

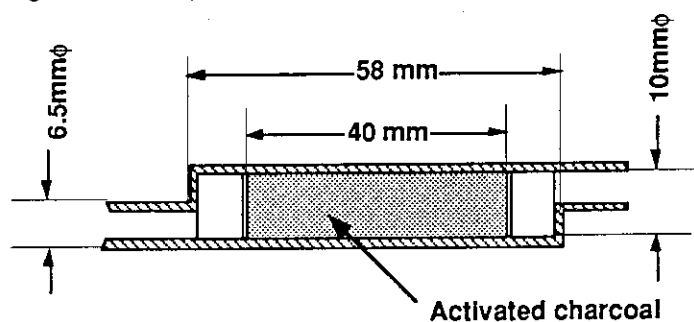


Fig. 7.6.2 Structure of a charcoal filter

50 cm<sup>3</sup>/min and 100 cm<sup>3</sup>/min. The temperature of the charcoal filter was changed in the range from 26 °C(room temperature) to 140 °C with the interval of about 20 °C.

First, base radioactivity concentrations of noble-gas FPs were measured with each carrier-gas flow rate by bypassing a charcoal filter. Next, the radioactivity concentrations of noble-gas FPs passing through the charcoal filter were measured in the condition of various temperatures. The passing rates were obtained by dividing the measured concentration by the base concentration.

By analyzing measurement results, the dependencies of the passing rates on carrier-gas flow rates were obtained with each temperature. Analyzed noble-gas FPs are <sup>88</sup>Kr, <sup>89</sup>Kr, <sup>135m</sup>Xe and <sup>138</sup>Xe. The analysis results at 26 °C, 60 °C, 100 °C and 140 °C are shown in Fig.7.6.3. These results shows the following;

- 1) the passing rate for xenon is smaller than that for krypton in same condition;
- 2) the dependence of the passing rate for nuclide having short-life on the carrier-gas flow rate is large;
- 3) noble-gas FPs are not absorbed at the temperature more than 140 °C by an activated charcoal.

The absorption coefficients obtained by the push model and the mixed model were compared with the results obtained by D.A. Collins et al <sup>1)</sup>. They measured the absorption characteristics of the activated charcoal

in the temperature range from 50 °C to -70 °C by using stable krypton gas and xenon gas. The adsorption coefficients for <sup>89</sup>Kr and <sup>135m</sup>Xe measured at the sampling gas flow rate of 100 cm<sup>3</sup>/min were compared with the referenced data in the almost same condition. The comparison results are shown in Fig. 7.6.4.

The absorption coefficients of the referenced data are between the absorption coefficients obtained by both methods. The gradient of the referenced coefficients and the

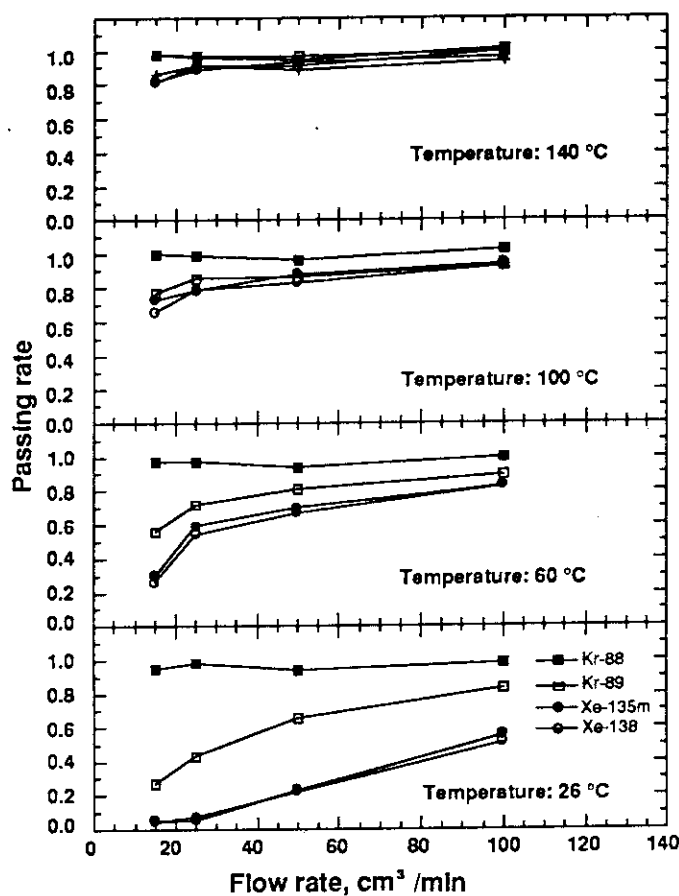


Fig.7.6.3 The dependencies of the passing rates on carrier-gas flow rates at 26 °C, 60 °, 100 °C and 140 °C

measured coefficients is almost same below 100 °C. Therefore, it is estimated that the practical absorption coefficient are between absorption coefficients calculated by both absorption models.

Consequently, it is concluded that it is necessary to correct amounts absorbed by a charcoal filter in order to obtain the precise radioactivities of noble-gas FPs in a sampling line.

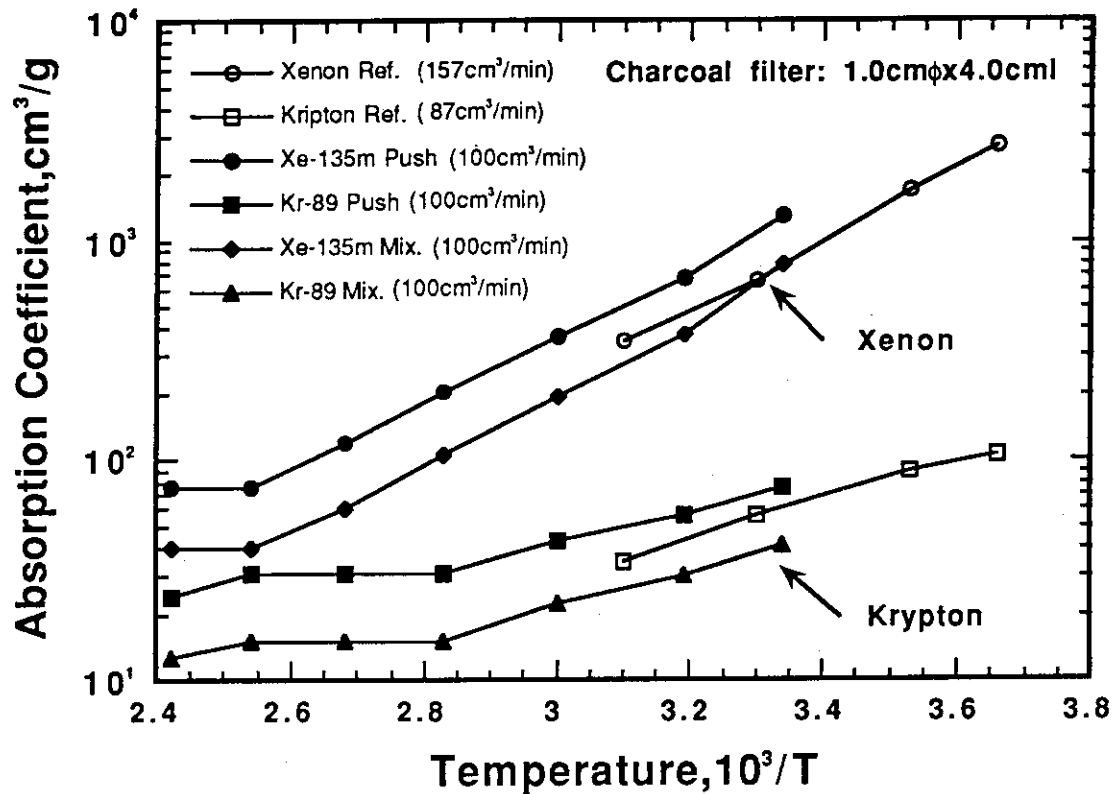


Fig.7.6.4 The comparison results with measured adsorption coefficients and the referenced data<sup>1)</sup> for  $^{89}\text{Kr}$  and  $^{135\text{m}}\text{Xe}$

#### References

- 1) Collins D.A. et al.: TRG Report 1578(W), 1967.
- 2) Sakai E., et al.: IEEE, Trans. Nucl. Sci. Vol. NS-31, No.1, 757, 1984.



## 7.7 A selective detection method of magnetic-flux sources using a system of superconductors, ferromagnetic substance and a magnetic sensor

K. Sakasai, M. Kishimoto and K. Ara

When cracks exist in metallic substance, they can be considered as magnetic dipoles by magnetizing the substance or letting currents flow in it. Therefore many attempts have been made to detect the cracks using the results of the magnetic field measurement of the dipoles. However, localization of the magnetic sources, so called the inverse problem in magnetic field measurement, is known as a problem which has no unique solution. On the other hand, the authors have introduced a new method for selective detection of magnetic dipoles by utilizing superconductors and ferromagnetic substance<sup>1)</sup>.

The proposed method to detect magnetic dipoles in a limited area is shown in Fig.7.7.1. The superconducting cylinder has an axial electric insulated line (i.e., an open slit) to block the flow of circumferential shielding currents. The detectable region with the system is that being cut out by the cylinder. The sensor can detect selectively magnetic fields produced by magnetic dipoles in the region. The effectiveness of the system have been confirmed and already reported<sup>2)-4)</sup>.

For improvement of the effectiveness of the system, a ferromagnetic cylinder will be useful when it is installed outside the superconducting cylinder in Fig.7.7.1, since the magnetic fields through the electric insulated line of the superconducting cylinder will be shielded by the ferromagnetic cylinder. This modified system of superconducting and ferromagnetic cylinders have been studied using a magnetic field analysis code based on the integral element method. The calculation model is shown in Fig.7.7.2. In the analysis z-component of the magnetic fields detected by the sensor were calculated as a function of the position of the magnetic dipole. The magnetic sensor is a flux-gate type magnetometer so that weak magnetic field can be measured. We assumed that the thickness of both superconducting and ferromagnetic cylinders can be neglected and the ferromagnetic

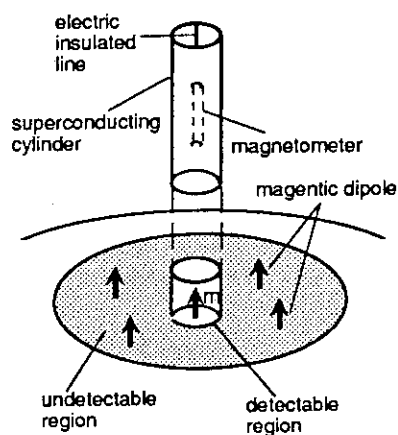


Fig.7.7.1 Detection of magnetic dipoles in a limited area

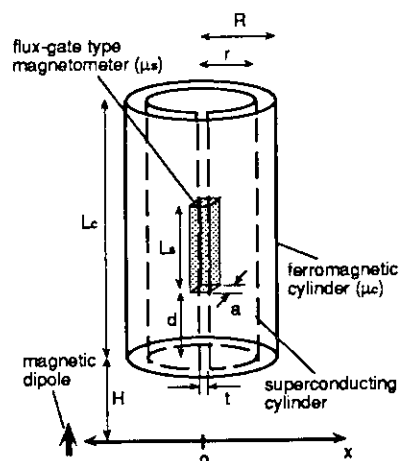


Fig.7.7.2 Calculation model

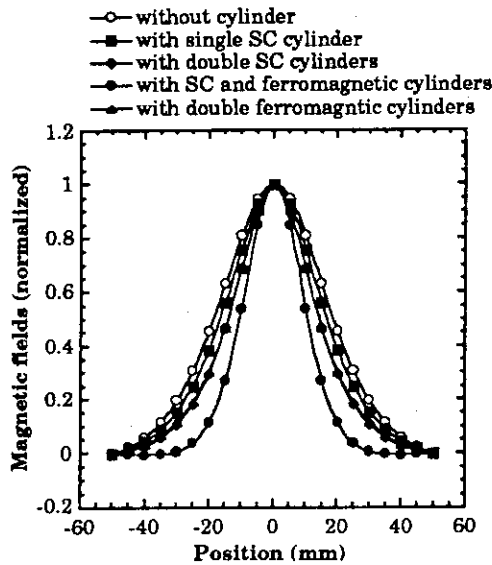


Fig.7.7.3 Results of the calculation of single dipole

value. For comparison, in the figure, are also shown the results of the cases with single superconducting cylinder, double superconducting cylinders and double ferromagnetic cylinders without changing the size of the cylinders. One can easily see that the curve of the case with superconducting and ferromagnetic cylinders has a more sharp peak than that of any other case. When spatial resolution of the sensor is defined as a full width of half maximum of the peak, the spatial resolutions of the cases with superconducting and ferromagnetic cylinders and without any cylinders are 2.09cm and 3.85cm, respectively. It means that the spatial resolution of the sensor is improved by introducing superconducting and ferromagnetic cylinders.

Figure 7.7.4 shows the result of another case that two magnetic dipoles are fixed at  $x=15\text{mm}$  and  $x=-15\text{mm}$ . In this case, the two dipoles have the same intensity and the magnetic fields detected by the sensor are calculated as a function of the position of the sensor. It is easily confirmed that the two dipoles can be clearly recognized with the considered system, though they cannot without any cylinders.

As a result of the above calculations, it is concluded that the sensor with superconduct-

Table 7.7.1 parameters used for calculation

Parameters	value	Parameters	value
R	4.0 mm	a	0.3 mm
r	3.0 mm	d	10.0 mm
Lc	50.0 mm	t	0.2 mm
H	20.0 mm	$\mu_c$	$1.3 \times 10^5$
Ls	20.0 mm	$\mu_s$	$1.3 \times 10^5$

cylinder is magnetized only in its surface. In the figure,  $\mu_s$  and  $\mu_c$  are the permeability of the sensor core and ferromagnetic cylinder, respectively.

Several cases were analyzed changing the parameters in Fig.7.7.2. As an example of the calculations, the results of the case with the parameters listed in table 7.7.1 are shown in Fig.7.7.3 as compared with those of the case without any cylinders, where the fields are normalized with the peak

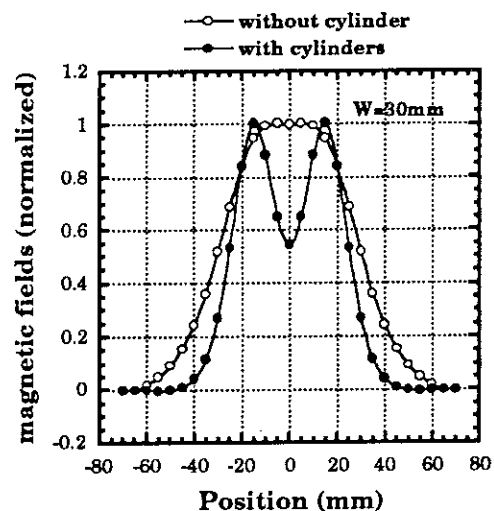


Fig.7.7.4 Results of the calculation of two dipoles

ing and ferromagnetic cylinder can measure magnetic dipoles selectively. Since the degree of the effectiveness of the system greatly depends on the system configuration, it is necessary to optimize the configuration. So extensive calculations are under planning together with actual experiments.

#### References

- 1) Sakasai K. and Ara K. : J. Mag. Soc. Jpn., 16, 337(1992)
- 2) Sakasai K. and Ara K. : JAERI-M 91-138, 136(1991)
- 3) Sakasai K., Kishimoto M. and Ara K. : JAERI-M 92-125, 135(1992)
- 4) Sakasai K., Kishimoto M. and Ara K. : JAERI-M 93-181, 144(1992)

## 7.8 Inverse Estimation of Current Distribution from Magnetic Field Using a Combination Method of Neural-Network and Genetic Algorithm

M. Kishimoto

### Inverse Problem in Electromagnetism

The author has been studying the feasibility of non-destructive measurement of the beam profile for intense ion accelerators using the inverse estimation method of the current distribution from the magnetic fields by means of the Genetic Algorithm.1)

This paper proposes the new inverse estimation method of current distribution from measured magnetic fields by a combination method of genetic algorithm (GA) and Neural Network.

### Inverse Estimation of Current Distribution from Magnetic Fields

We consider the estimation problem of the current distribution as the optimum allocation problem of the currents in the cross-section of the current distribution area.1)2)

In Fig.7.8.1, when the magnetic field that measured at measuring point is  $B_m$ , we define the following error evaluation function to evaluate the fitness.

$$\text{Fitness} = |\mathbf{B}_m - \mathbf{B}|^2$$

To solve the inverse estimation problem of the current distribution from the magnetic fields is regarded as to find the current distribution that make this fitness equal to zero.

To verify the effectiveness of the estimation method of current distribution by GA and Neural Network, Computer simulations were carried out. Fig.7.8.2 shows the example of the simulation results.

### References

- 1) M.Kishimoto.: JAERI-M 93-181,135,(1994)
- 2) Maki Kishimoto.,et al. : Simulation and Design of Applied Electromagnetic Systems,Elsevier Science B.V.,209-212,1994

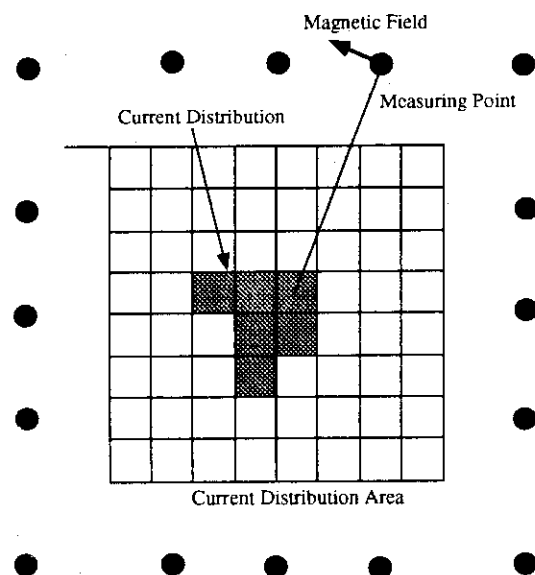
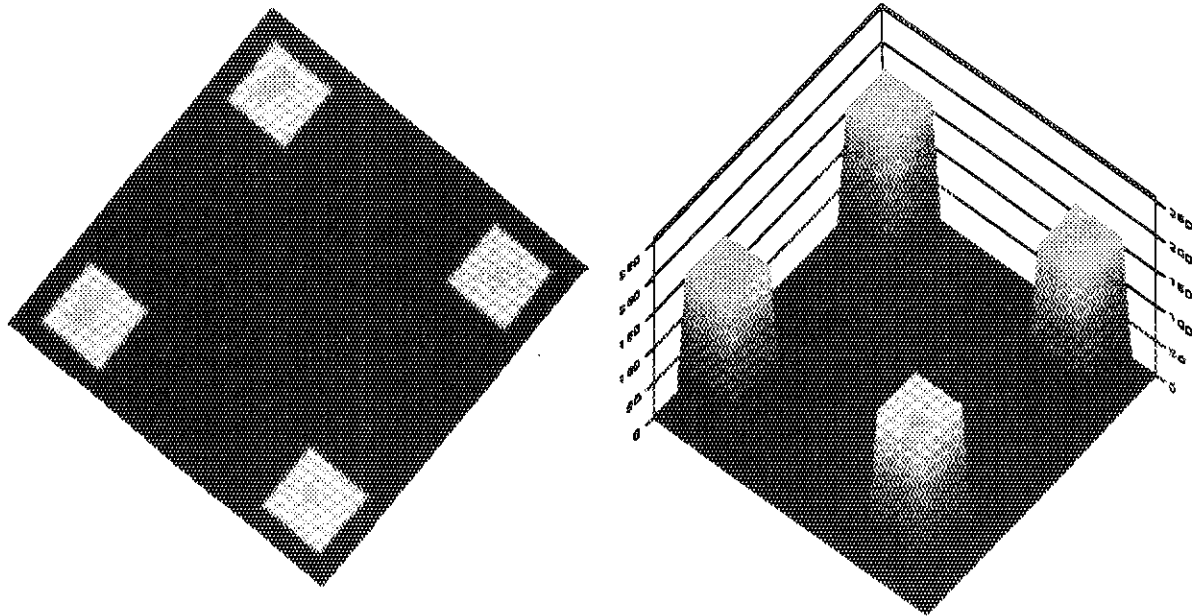
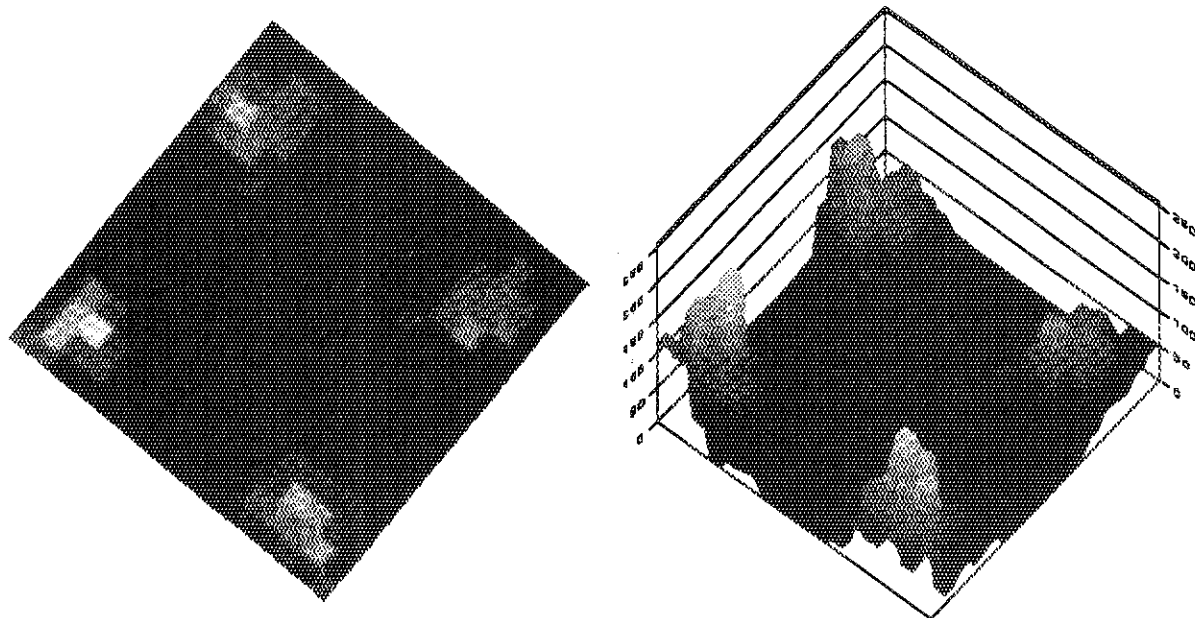


Fig.7.8.1 System of Measurement.



Real Current Distribution



Estimated Result

Fig.7.8.2 Computer Simulation Result

## 7.9 Study of Position Sensitive Fission Counter with Transmission Delay Line Structure

H. Yamagishi

A position Sensitive Fission Counter (PSFC) with transmission delay line (DL) structure was investigated for development of neutron sensors to measure neutron flux distribution in test reactors and critical assemblies. Also, this technology using the DL structure is useful to develop new type neutron sensors installed outside vessel for wide range power monitoring systems in advanced reactors such as the Passive Safe Reactor. The neutron sensor of fission counter type has some merits that it operates in high gamma-ray background, at high temperature condition and in a wide range of neutron flux more than 10 decades. The PSFC, designed using the technology of pulse interval measurement, provides high signal-to-noise ratio because it makes smaller attenuation for signal pulses compared with position sensitive proportional counter with an anode wire of very high electric resistance.

The schematic structure of PSFC is illustrated in Fig. 1. The electrodes of PSFC are constructed with a solenoidal anode and a cylindrical cathode to make DL structure. The PSFC provides two kinds of signals by each fission event in the counter. The signals are a fast propagation pulse from the cathode and a delayed pulse from the solenoidal anode. Since propagation delay of signal pulse is proportional to propagation length of the solenoidal anode, the position of each detected neutron is encoded as interval between the fast pulse and delayed pulse. Equation-1 gives the propagation constant,  $\gamma$ , on a general transmission line. Where  $R$  and  $L$  are series resistance and inductance per unit length of conductor.  $C$  and  $G$  are capacitance and leakage conductance per unit length of insulator on the transmission line. If  $R=G=0$  are given such as a lossless line, pulse propagation velocity,  $v$ , and propagation delay time per unit length,  $\tau_d$ , are given by equation-2 and 3. In case of the PSFC,  $R$  and  $G$  are quite smaller than  $\omega L$  or  $1/\omega C$ . Thus  $\tau_d$  on the PSFC is given to equation-3. On the PSFC constructed with triaxial structure as shown in Fig. 1,  $L$  and  $C$  are given by equation-3 and 4.

$$\gamma = \sqrt{(R + j\omega L)(G + j\omega C)} \quad \text{----- (1)}$$

$$\tau_d = \sqrt{LC} \quad [\text{s/m}] \quad \text{----- (2)}$$

$$L = \mu\pi n^2 \frac{(a_3^2 - a_1^2)(a_2^2 - a_1^2)}{a_3^2 + a_2^2 - 2a_1^2} + \frac{\mu}{2\pi} \frac{\ln(a_3/a_1)\ln(a_2/a_1)}{\ln(a_3a_2/a_1^2)} \quad [\text{H/m}] \quad \text{----- (3)}$$

$$C = \frac{2\pi\epsilon}{\ln(a_2/a_1)} \quad [\text{F/m}] \quad \text{----- (4)}$$

Where  $\mu$  and  $n$  are permeability and turns of solenoid.  $\epsilon$  is dielectric constant. The  $\tau_d$  is calculated as a function of electrode gap from 0.5mm to 5mm. In the calculation, characteristic

impedance was fixed  $50\Omega$ . The calculation results for cathode diameters of 10, 20 and 30mm are shown in Fig. 2. The  $\tau_d$  was 37.6ns/m at 0.7mm of the electrode gap. In case of characteristic impedances of 75 and  $93\Omega$ , each  $\tau_d$  at 0.7mm of electrode gap width was 56.4 and 69.9ns/m. If difference time resolution of electronics for measurement of pulse interval is about 0.5ns, PSFC provides position detecting resolution of about 10mm.

After this study, it was found that the PSFC with electrodes of the DL structure provides a high position resolution for measurement of neutron flux distribution. Also the counter with the transmission line structure provides flux signals with broad bandwidth without reflection pulses because it was made impedance matching to signal cables and the electronics.

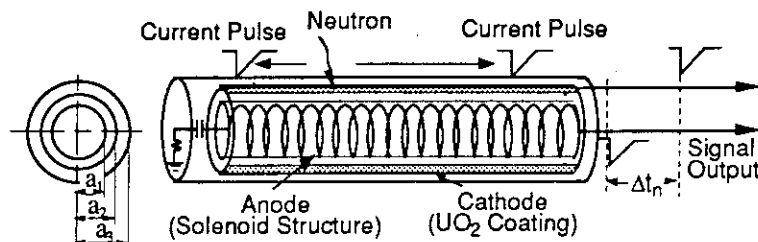


Fig. 1 Structure of Position Sensitive Fission Counter

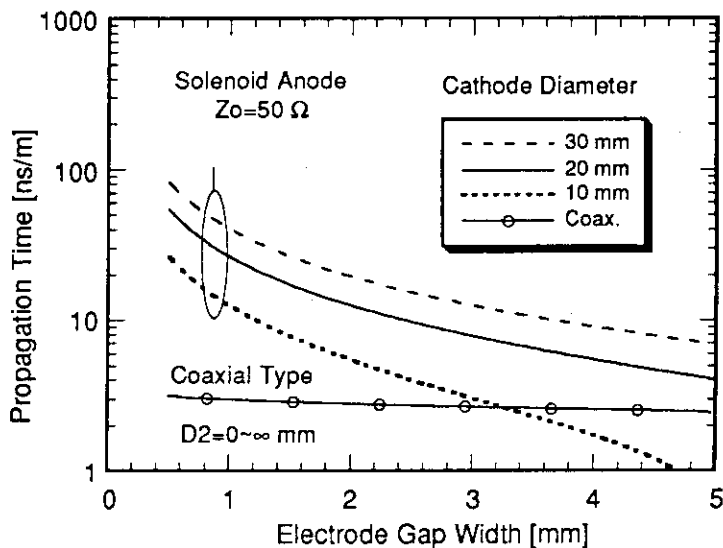


Fig. 2 Calculation Results of Pulse Propagation Time as a Function of Electrode Gap Width

## 8. Reactor Control, Diagnosis and Robotics

A new methodology to estimate the time-varying net reactivity has been proposed; it applies an optimal filtering technique based on  $H_\infty$  estimation theory. The methodology has been tested by using computer simulated reactor model and has been compared to other techniques, such as Kalman filtering techniques.

The performance of the automatic control system of NSRR is investigated experimentally and theoretically in connection with the power oscillation. Although the detailed mechanism of the oscillation cannot be identified, the measured signals imply that the origin of the oscillation is a sort of backlash. A simplified reactor dynamic model with backlash simulates the dynamics of the NSRR power oscillation.

A real-time nuclear power plant monitoring applying artificial neural network has been developed for Borssele Nuclear Power Plant. The adopted artificial neural network has a three-layered feedforward structure and the real-time adaptive learning function as well as its inherent learning function. It proved to give an alarm when the operational condition comes to newly experienced stage for the network, i.e., the monitoring function has been verified.

The analysis of the reactor noise data of the nuclear-powered ship Mutsu obtained in the experiments of the dynamics identification using pseudo-random input signals conducted during her experimental navigation is being continued. This year, the results from the first experiment has been summarized analyzing their signal forms and spectral pattern in order to make a data base.

The benchmark analysis of acoustic noise signals for detection of sodium/water reaction due to sodium leak was continued. This year, the test data was synthesized in JAERI and distributed to the participants.

For the recognition in hazardous environment, the ultrasonic imaging is being studied. One of the most important concerns on the technique is the resolution of the image, which is largely influenced by compensation of the transducer signal's distortion. The three types of the compensation methods have been compared carefully.

The increasing requirements of the manipulators with sophisticated motion motivates the design of the redundant manipulator with more than necessary degrees of freedom. The nominal synthesis problem for a redundant manipulator has been considered; it utilizes an additional task variable called the arm angle which is independent of the end-effector motion and parameterizes the manipulator redundancy.

Control and A.I. Laboratory is in charge of this chapter.



## 8.1 Filtering of Net Reactivity Based on $H_\infty$ Estimation Theory

K. Suzuki, J. Shimazaki and K. Watanabe

This article presents an optimal filtering technique in an  $H_\infty$  setting and gives some results from the computer simulated time-varying net reactivity by the  $H_\infty$  optimal filtering technique.

The filtering problem involves state estimation of system using the past measurements. The celebrated Kalman filtering approach offers the optimal filtering algorithm for estimating all the states of a linear system when the power spectral density of the noise is known and it has been deeply entrenched in the control literature. Here, we consider the estimation problem with an  $H_\infty$  performance criterion formulated in a minimax problem where the maximum "energy" in the error over all noise trajectories is minimized. Let us consider the  $H_\infty$  optimal filtering problem of the following linear time-invariant system:

$$\frac{d}{dt}x(t) = Ax(t) + Bw(t) , \quad (8.1.1)$$

$$y(t) = Cx(t) + Dw(t) , \quad (8.1.2)$$

where  $x(t)$  is the state,  $y(t)$  is the observation and  $w(t)$  denotes the noise. It is assumed that the matrices  $A$ ,  $B$ ,  $C$  and  $D$  have appropriate dimensions. Let the quantities to be estimated be given such as :

$$z(t) = Lx(t). \quad (8.1.3)$$

The problem then becomes obtaining an estimate  $\hat{z}(t)$  of  $z(t)$  using the measurement signal  $y(t)$ . We adopt the following worst-case performance measure:

$$J := \sup_{0 \neq w \in L_2} \frac{\|z - \hat{z}\|_2^2}{\|w\|_2^2}, \text{ with } x(0)=0. \quad (8.1.4)$$

Thereupon the following problem will be addressed : given  $\gamma > 0$ , does there exist a filter with the initial condition given by  $x(0)=0$ ,  $J < \gamma^2$  ? If it does, find a realization of the filter. This problem is solved as follows: If there exists a positive semi-definite and symmetric matrix  $P_\infty$  that satisfies the following Riccati type equation:

$$AP_\infty + P_\infty A^T - P_\infty (C^T C - \frac{1}{\gamma^2} L^T L) P_\infty + BB^T = 0, \quad (8.1.5)$$

$$A - P_\infty (C^T C - \frac{1}{\gamma^2} L^T L) \text{ is stable}, \quad (8.1.6)$$

one filter for which  $J < \gamma^2$  is given as follows:

$$\frac{d}{dt} \hat{x}(t) = A \hat{x}(t) + P_\infty C^T [y(t) - \hat{x}(t)], \hat{x}(0)=0, \quad (8.1.7)$$

$$\hat{z}(t) = L \hat{x}(t). \quad (8.1.8)$$

Adopting the state equation of net reactivity driven by fictitious noise described above, we can represent the dynamics of a reactor system by the following state equations:

$$\frac{d}{dt} n(t) = -\frac{\beta}{\Lambda} n(t) + \sum_{i=1}^6 \lambda_i c_i(t) + \frac{\beta}{\Lambda} \rho(t), \quad (8.1.9)$$

$$\frac{d}{dt} c_i(t) = \frac{\beta_i}{\Lambda} n(t) - \lambda_i c_i(t), \quad i=1,2,\dots,6, \quad (8.1.10)$$

$$\frac{d}{dt} \rho(t) = w_p, \quad (8.1.11)$$

where  $n(t)$ := neutron density,  $c_i(t)$ := density of the  $i$ -th group precursor,  $\rho(t)$ := net reactivity,  $\beta_i$ := portion of neutrons generated by the  $i$ -th group of precursors,  $\beta$ := portion of delayed

neutrons,  $\lambda_i$ := decay constant for the  $i$ -th precursor,  $\Lambda$ := life time,  $w_p$ := disturbance term.

Figure 8.1.1 presents a comparison between the reactivity estimate obtained by the  $H_\infty$  optimal filtering method and those obtained by the Kalman filtering technique when 10 cents of reactivity disturbance in the form of step function was inserted and when 6% of measurement noise was assumed.

#### Reference

- 1) Suzuki K., Shimazaki J. and Shinohara Y. : Estimation of Net Reactivity Based on  $H_\infty$  Estimation Theory, J. Atom. Ener. Soci. Japan, **36**, 79(1994).

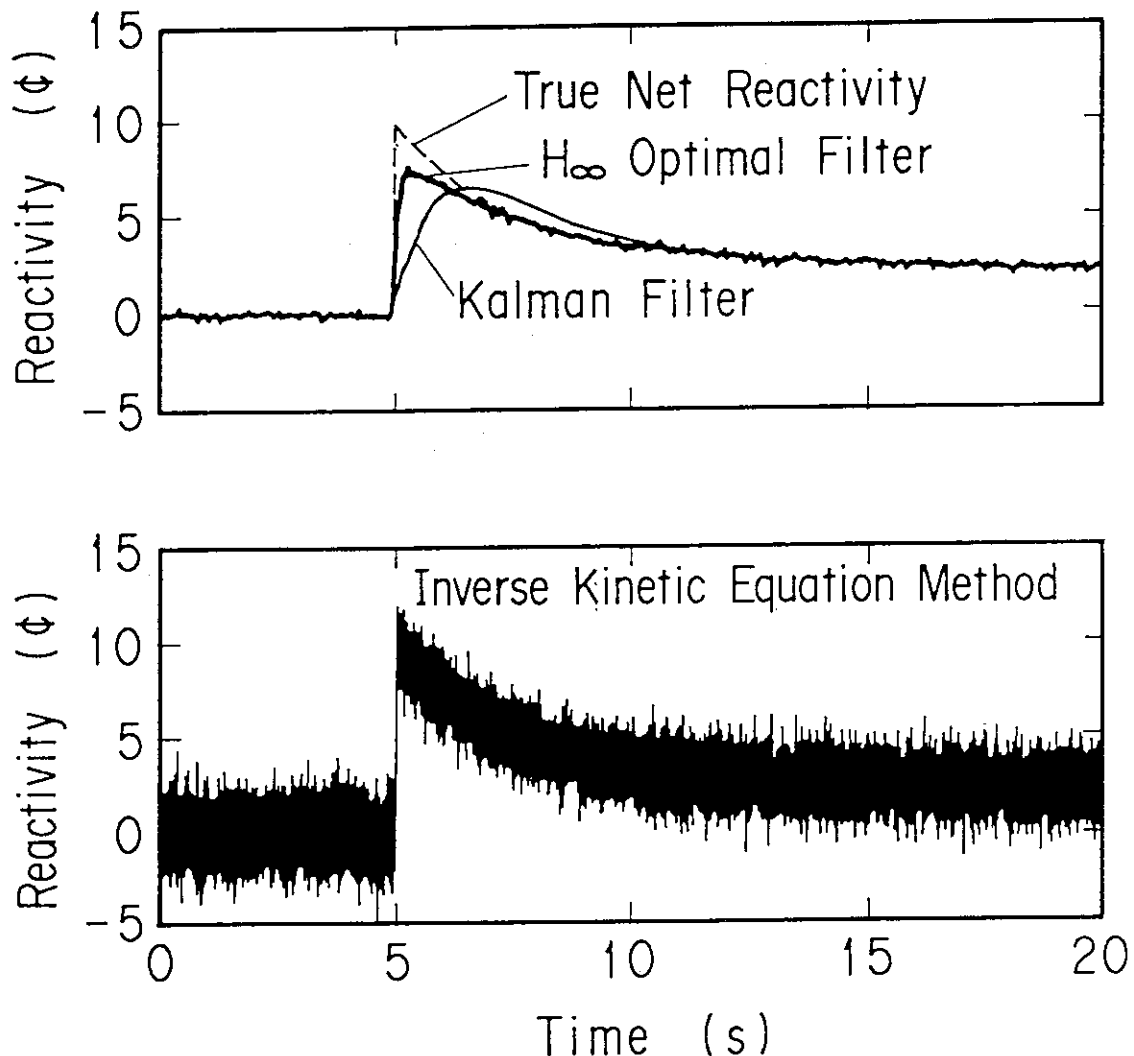


Fig. 8.1.1 Reactivities estimated by the  $H_\infty$ -, inverse kinetic- and Kalman-techniques

## 8.2 Modeling of Nonlinear Power Oscillation in NSRR

T. Suzudo and Y. Shinohara\*

The NSRR is a TRIGA-type pulsed reactor installed in 1975 at JAERI for fuel research. The power was observed to oscillate at  $\sim 0.2$  Hz when regulated by the automatic control system at a high power level. Various experimental analyses suggested that the poor characteristics of the automatic control system caused this instability, but the mathematical explanation was not known.

It is known that negative feedback never cause oscillatory motion without phase lag. Therefore, the element which causes phase lag in the feedback loop is presumably the origin of the power oscillation. The automatic control system of the reactor power is shown in Fig. 8.2.1; it is composed a two-stag servo system: the Master Servo system and six parallel Slave Servo systems. With a data set of signals measured at several points of the automatic control system (Fig. 8.2.1) and we can compare the phase angles of the signals, which leads to the rough location of the phase lag. By this method, we have found that the phase of the neutron-flux signal is almost reverse that of the Master Servo output signal. The Master Servo system is composed of an amplifier and a motor with feedback by a tacho generator, thus as long as it works properly there is never a large enough phase lag to cause oscillation at the frequency of  $\sim 0.2$ . This suggests that the malfunction of the servo system caused the phase lag. We, unfortunately, do not have a means for a more detailed investigation of the malfunction from the experimental data because the interior signals of the Master Servo system are lacking and the whole automatic control system has already been dismantled. Therefore, we have been restricted to finding a simple mathematical expression which gives similar characteristics. Further investigation shows that the Master Servo system possesses a nonlinear dynamics

---

\*Nuclear Power Engineering Corp., Tokyo

qualitatively similar to backlash, although this does not quantitatively embody the experimental data.<sup>1)</sup>

We anticipated that the origin of the phase lag would be a backlash and established a phenomenological model for the NSRR dynamics. For the neutronic dynamics we use a point kinetic equation, because there is no spatial dependence in the power oscillation. The dynamics of the Master Servo system are supposed to be represented by a simple second-order differential equation, but we added the backlash element to the designed dynamics. The Slave Servo system is also represented by a second-order system according to the design feature. The total reactivity is assumed to vary in proportion to the Slave Servo output signal's deviation from its steady state value. See Ref. 1) for more detail of the modeling.

The model has an infinite number of equilibrium points, including the steady state, forming a line of finite length. Therefore the reactor power can easily be changed by a small perturbation, which seems to correspond to the large fluctuation in the actual reactor. When the amplifier's gain of the Master Servo system increased, the NSRR power proved to cause a persistent oscillation called a limit cycle<sup>2)</sup>. The model also causes a limit cycle motion for a large value of the gain. Finally we compare the temporal evolution from the actual plant and the model induced by white noise in Fig. 8.2.2. Both signals' oscillatory motions seem intermittent, and their frequencies vary a lot. In addition, there exists a rough relationship between the amplitude and the frequency in both signals; that is, when amplitude is large the frequency is also large. Consequently the results from the numerical analyses using the model agreed qualitatively with the measured signals, and the nonlinearity, which caused the reactor power to become unstable, has been embodied analogically.

## References

- 1) Suzudo T. and Shinohara Y.: Ann. Nucl. Energy, 21, 5, 291(1994).
- 2) Suzudo T., Hayashi K. and Shinohara Y.: J. Nucl. Sci. Technol., 30, 8, 727(1993).

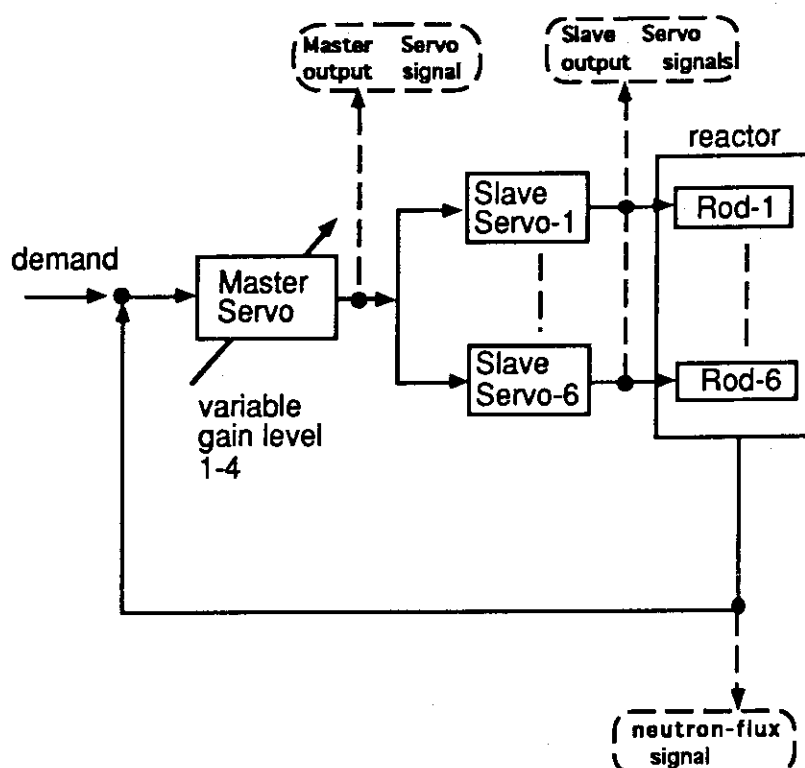


Fig. 8.2.1 NSRR automatic control system and signals measured in the experiment.

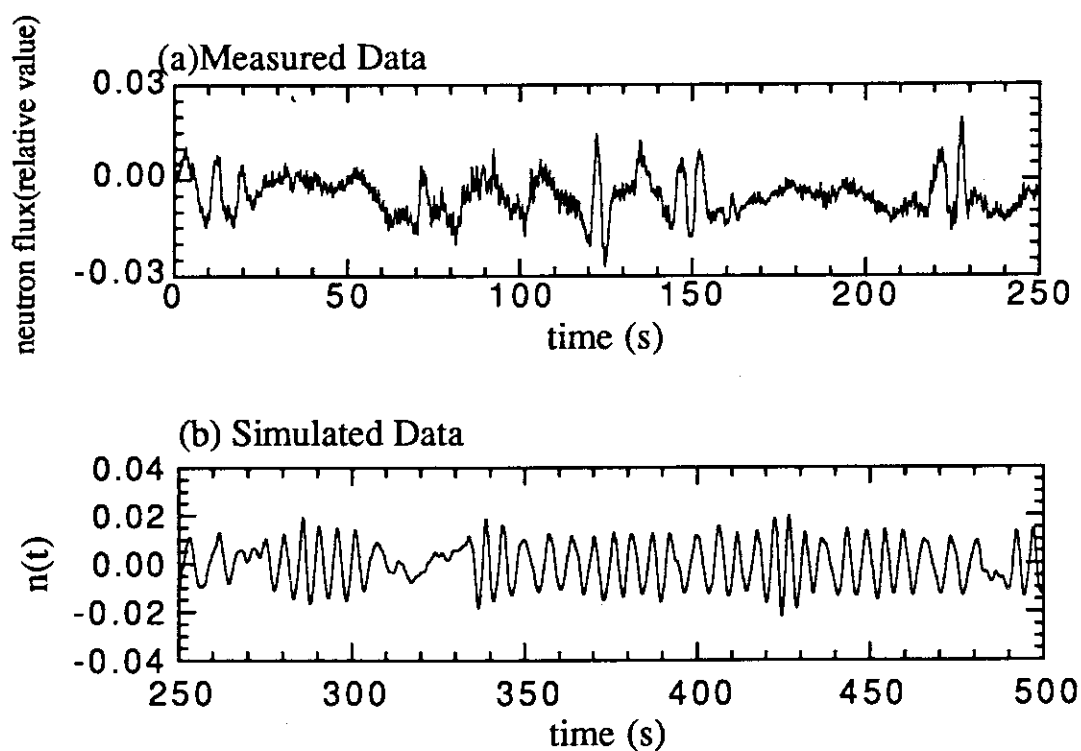


Fig. 8.2.2 Comparison of measured data and simulated data.

### 8.3 Real-time Nuclear Power Plant Monitoring with Neural Network

K. Nabeshima, E. Türkcan\* and Ö. Ciftcioglu\*\*

The major advantages provided by artificial neural network (ANN) are that systems can be modelled by means of measurement information obtained from a multi-output process system, that explicit modelling is not required and that the modelling is not restricted to linear systems. In addition, ANN can respond quickly to anomalous operational conditions. ANN with real-time adaptive learning has been developed for the plant wide monitoring of Borssele Nuclear Power Plant (NPP) so that robust and sensitive on-line monitoring is achieved in real-time environment.

A schematic representation of the reactor with measured signals is shown in Fig.8.3.1. Our ANN adopts a three-layered feedforward structure with 12 inputs, 8 nodes in the hidden layer and 12 outputs. Figure 8.3.2 shows the ANN structure. Standard backpropagation algorithm with sigmoidal nonlinearity is used for learning and adaptive learning. The auto-associative ANN structure requires as many output nodes as it is used at the input nodes so that during the learning each pair of input/output nodes fulfills the supervised learning requirements. A set of sensory signals at a certain time is applied to the learning pattern.

For initial learning 1825 patterns covering start-up, steady-state and shut-down are used. During the learning, the patterns are introduced to the network randomly and the number of iterations is 2000 where each iteration includes all the patterns. After the initial learning, real-time monitoring and adaptive learning starts progressing. The real-time process signals are introduced to the network as input, and plant condition is monitored through the network response at the output. At the same time the learning of the network is performed in adaptive form so that the sensitivity of the network's failure detection is enhanced in the course of the operation.

To illustrate real-time monitoring system's performance, the results obtained from two process signals are given in Figs. 8.3.3 and 8.3.4. At the time point of ~550x30s, a periodic maintenance, called 'rinsing' procedure is performed. Because this maintenance condition is not learned by the network, it cannot identify this operation and the difference between the measured (input) and estimated (output) value exceeds the tolerant level as seen in Fig. 8.3.3. This is not observed at the generated electric power, see in Fig. 8.3.4. This is because this operation causes the same oscillation in SG1 and SG2 but in reverse phase, so

---

\* Netherlands Energy Research Foundation ECN, The Netherlands

\*\* Istanbul Technical University, Turkey

that these two effects to the power are canceled each other.

The study demonstrates that complex and dynamic system like NPP can be modelled by ANN with the help of the measurement information only. As mentioned above, such a computational model can be used for monitoring of the system and has several important advantages compared to conventional applied monitoring.

## References

- 1) K. Nabeshima, E. Türkcan and Ö. Ciftcioglu: ECN-RX--93-066, The Netherlands, 1993.
- 2) K. Nabeshima, E. Türkcan and Ö. Ciftcioglu: AIR'94, May 30-June 1, 1994, Tokai.

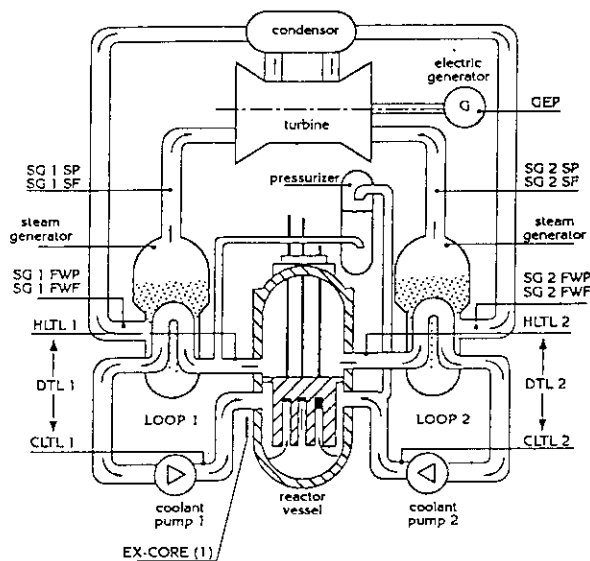


Fig.8.3.1 Schematic representation of NPP

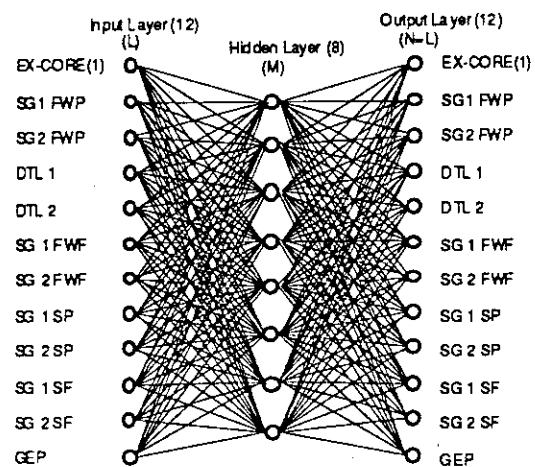


Fig.8.3.2 Neural network structure

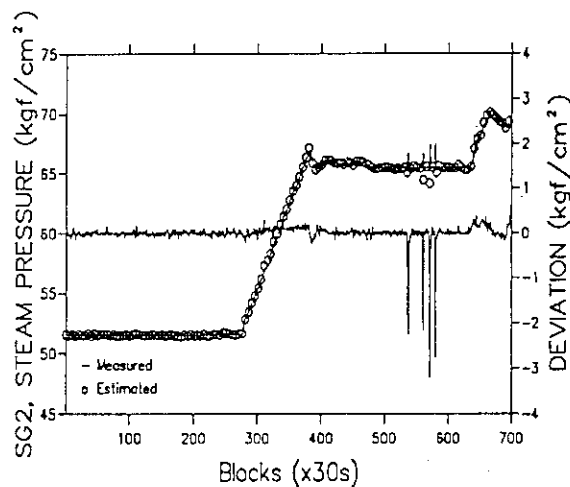


Fig.8.3.3 On-line monitoring(steam pressure)

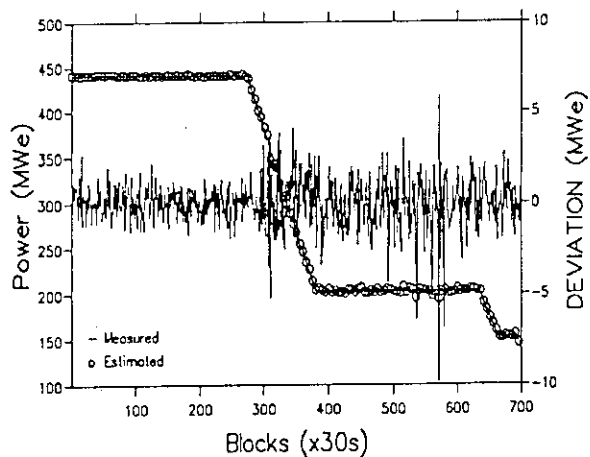


Fig.8.3.4 On-line minotoring(electric power)



## 8.4 Noise Analysis for Plant Dynamics Identification of Nuclear Ship Mutsu (II)

K. Hayashi, J. Shimazaki, K. Nabeshima and Y. Shinohara\*

To identify the plant dynamics of the nuclear ship Mutsu, dynamics experiments using pseudo random binary sequence (PRBS) have been conducted at her experimental navigation. The experiments using reactivity or load disturbance by manual operation of the control rod or the main steam valve were performed under three operational conditions of the plant; (1) at 70 % of nominal reactor power and quiet sea, (2) 50 % and quiet sea, and (3) 70 % and normal sea. The reactor plant signals and ship motion signals measured under the above mentioned conditions have been analyzed by using statistical methods.

In this year, we summarized the results of the first experiment in view points of the experimental procedures and conditions for PRBS experiment and analyzed the signal wave forms and the spectral patterns for all measured signals in order to make a fundamental data base as the reference data set for dynamics analysis of Mutsu plant.

We found from the above analysis that the manipulation signal following the PRBS has distortions in its wave forms when the time delay in the manipulator is a relatively large, but this effect to the dynamics analysis is very small and could be ignored because the distortion is only related to high frequency components and the manipulation signal still keeps low frequency components that characterize the PRBS as shown in Fig. 8.4.1. For the reactivity PRBS experiment under a single rod driven mode, each rod signal does not follow the PRBS but the group total of rod signals follows it as shown in Fig. 8.4.2.

From the results of the first experiments, we confirmed that the procedures and experimental conditions determined prior to the experiment were suitable for performing the PRBS experiment, that the plant state remained quite stable even if the PRBS disturbances were applied, and that the quality of the measured data is adequate for the purpose of dynamics analysis.

In addition, the graphical data base of the wave forms and the spectral patterns obtained from the first experiment are useful in the comparative analyses among the first, the second and the third experiments.

### Reference

- 1) Hayashi K., et al. : "Reactor Dynamics Experiment of N. S. Mutsu Using Pseudo Random Signal (I) The First Experiment, " JAERI-M 93-194, (1993) (In Japanese)

---

\* NUPEC, Tokyo

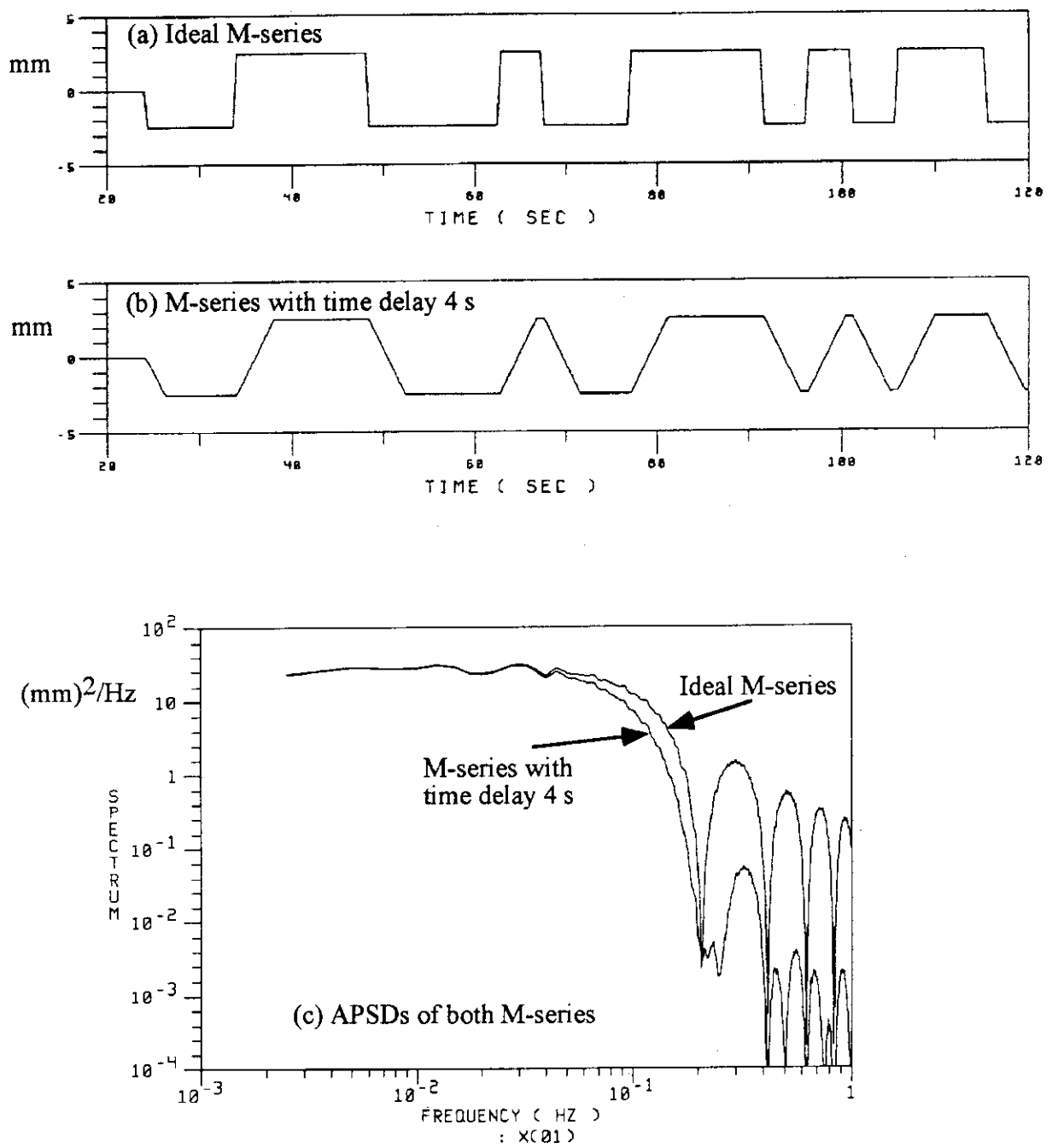


**Fig. 8.4.1** Effects of wave form distortion in the manipulation signal

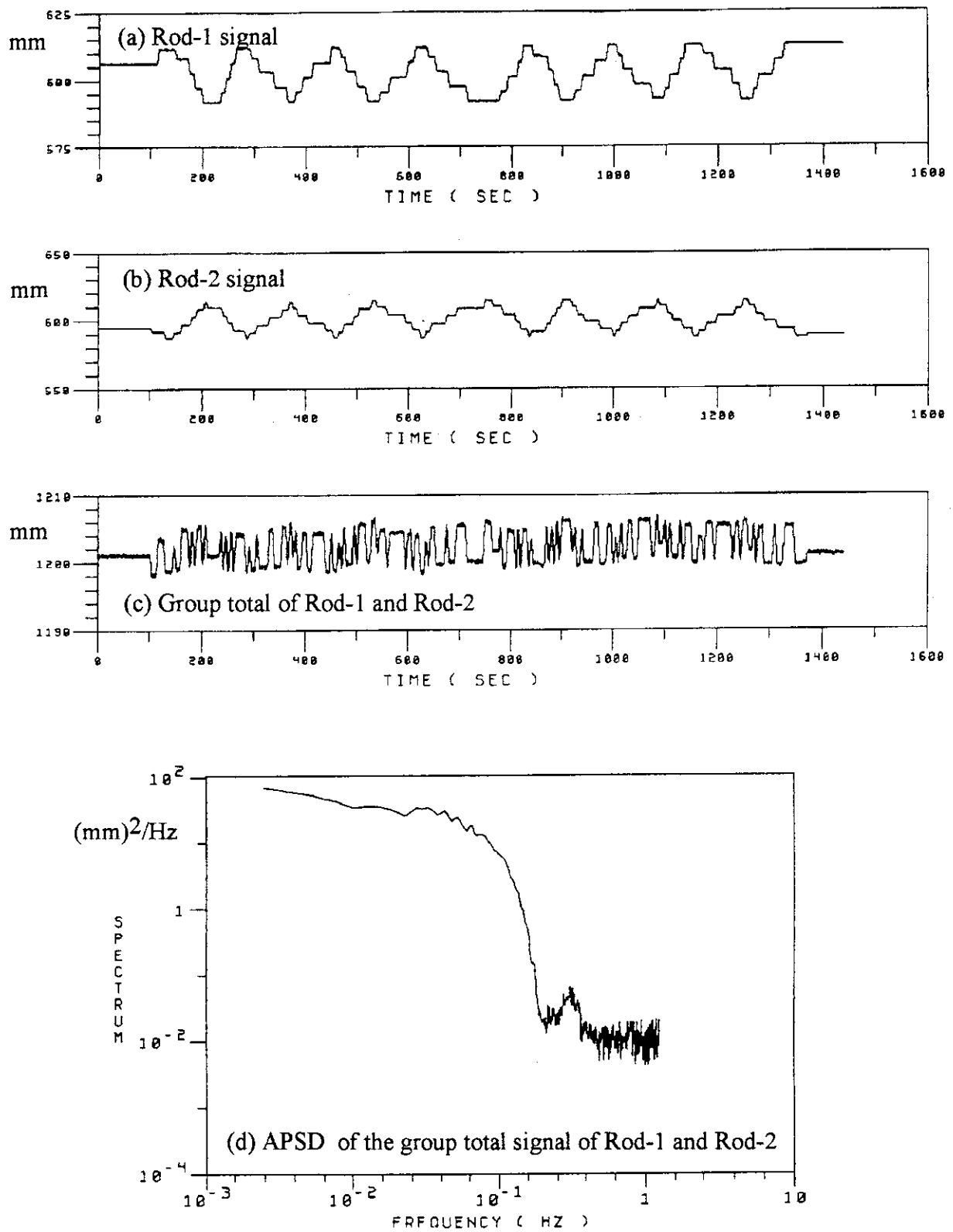


Fig.8.4.2 Characteristics of the group total signal of Rod-1 and Rod-2

## 8.5 Data Synthesis for 1993 Benchmark Test on Detection of Sodium/Water Reaction

K. Hayashi, K. Watanabe, Y. Fujii and Y. Shinohara\*

In the IAEA extended coordinated research program on acoustic signal processing for the detection of sodium boiling or sodium/water reaction in LMFBR, the working group has been performing benchmark tests on the detection methods since 1989. The main objective of the benchmark tests concerns how to detect an onset of sodium/water reaction from acoustic signals with high sensitivity and accuracy. The performances and detection margins of various detection methods have been evaluated through cross comparisons among the test results. The 1993 benchmark test was performed using the test data synthesized by JAERI.

For the 1993 benchmark test, we synthesized the test data in the similar manner to the previous benchmark test as follows; the leak signal of about 5 seconds was superimposed somewhere upon the background signal of 30 seconds. The amplitude of the leak is adjusted so as to obtain the selected signal-to-noise ratio.

Two analog magnetic tapes were supplied from AEA Technology in UK and CEA Cadarache in France for the data synthesis. Each tape contains both acoustic signals; six leak noise signals from ASB loop in Germany and six background noise signals from PFR Steam Generator Units in UK. The mean leak rates of the leak noise signals were 1.8 g/s in the first tape and 3.8 g/s in the second tape.

To choose a leak signal and a background signal for the data synthesis, we checked wave forms and spectral patterns of all leak and background noise signals recorded on each experimental data tape, then we selected a candidate sensor signal for each leak and background noise signals. Next, we checked stationarity of these signals to choose the recording time spans to be used for the synthesis. The stationarity of the selected signals was checked using the real time Root Mean Squares method with a hybrid computer calculating the rms value for each short time span of every 5 seconds for whole signal record of about 300 seconds. From the results, we chose two stationary time-spans in each experimental data.

Finally, the test data for both mean leak rates were synthesized by using an analog computer from the selected leak and background noise signals with four different signal-to-noise ratios ranging from -12dB down to -24dB. The different start times and durations were set for each case. The first data set synthesized for the case of 1.8 g/s were recorded on File No. 3, 4, 5, 6 together with two reference data on No. 1, 2 in the tape to participants. The second data set for 3.8 g/s were recorded on File No. 9, 10, 11, 12 together with two reference data on File No. 7, 8.

---

\* NUPEC, Tokyo.

We set the tasks for the benchmark test as follows;

- 1) Determine the start time and duration of the leak signal in File No. 3, 4, 5, 6, 9, 10, 11 and 12. The time should be counted relative to each start point of the background noise.
- 2) Estimate the detection margin above the background noise and the signal-to-noise ratio in each test data, if possible.

After we distributed the test data tape to the participants, we ourselves tried the task by using Twice-Squaring method; it is a relatively simple nonlinear signal processing in time domain, and consists in band-pass filtering and squaring of signal in two folds.

The signal wave form and the spectral pattern were examined for the background noise signals in File No. 1 and 7 and the leak signals in File No. 2 and 8, at first, in order to tune the parameters of Twice-Squaring method for these reference file data. On the basis of these results, the pass-bands for the first and second band-pass filters in Twice-Squaring process were set [2.0,3.6kHz] and [4.0,8.0kHz], respectively. The threshold value  $L$  for deciding the signal states were determined as  $L=6.5$  for the first data set and  $L=5.9$  for the second data set.

The results of the Twice Squaring analysis for the eight test data files are given in Table 8.5.1. It is concluded that Twice Squaring method can detect reliably the leak signals with signal-to-noise ratio down to -16 dB, unless the background noise signal contains high pulsive components.

Table 8.5.1 The start time and duration of the leak noise signal

File No.	Test No.	Start Time(s)	Duration Time(s)	Detection Margin [max]dB	S/N dB
3	1	-	-	< 0	-
4	2	15.0s	4.0s	6	-12
5	3	-	-	< 0	-
6	4	-	-	< 0	-
9	5	13.5 s	3.5 s	6	-12
10	6	-	-	< 0	-
11	7	16.5 s	0.5 s	0	-20
12	8	16.0 s	1.0 s	0	-16

#### Reference

- 1) Hayashi K., et al. : "The Results of 1993 Benchmark Test on Detection of Sodium/Water Reaction," Presented for Research Coordination Meeting on Acoustic Signal Processing for the Detection of Sodium Boiling or Sodium/Water Reaction in LMFBF, Vienna, 9-10 December 1993.

## 8.6 Compensation of Ultrasonic Signal Distortion with Various Deconvolution Methods

N. Ishikawa

Deconvolution signal processing is utilized to improve the resolution of ultrasonic imaging. The improvement is attained by compensating the signal distortion caused by transducer. This processing is useful especially when the ordinary ultrasonic transducer, which has narrow band characteristics of transduction, is used. In this report, the characteristics of three types of deconvolution methods (the prefilter + direct inverse method, the Wiener filter method and the FIR filter method) are compared to see the compensation capability of narrow band characteristics of transducer.

### Signal Distortion Process

The transmitter is driven by the electric signal  $u(t)$ . The ultrasonics is received by receiver and transformed into electric signal  $g(t)$ . The relation between  $g(t)$  and  $u(t)$  is represented by  $g(t)=x(t)*u(t)$ , where  $x(t)$  denotes the electro-acoustic conversion characteristics of transducer, and symbol  $*$  denotes the convolution with respect to time. Frequency domain representation of this relation is  $G(\omega)=X(\omega)U(\omega)$ . The conversion characteristics  $x(t)$  is the cause of signal distortion. Received signal  $g(t)$  is expressed by the convolution of  $x(t)$  and  $u(t)$ . Note that the measurement using received signal  $g(t)$  is influenced by the characteristics of  $x(t)$  and  $u(t)$ .

### Deconvolution Methods

For deconvolution processing, it is necessary to realize the inverse characteristics of  $X(\omega)U(\omega)$  so as to eliminate the effect of  $X(\omega)$  and  $U(\omega)$ . Since this inverse emphasizes the high frequency component, this processing is very sensitive to noise contained in the signal. In general, some bandwidth limitation is incorporated to prevent the effect of noise. In the following the three methods used are explained.

Prefilter+direct inverse method (Method I): Deconvolution of  $g(t)$  is calculated as  $g_{dec}(t)=F^{-1}[\tilde{G}(\omega)/G(\omega)]$ , where  $F^{-1}$  denotes the inverse Fourier transform, and  $\tilde{G}(\omega)=W(\omega)G(\omega)$ ;  $W(\omega)$  is bandpass filter for prefiltering  $g(t)$  to reduce the effect of noise.

Wiener filter method (Method II): Deconvolution of  $g(t)$  is calculated as  $g_{dec}(t)=F^{-1}[H(\omega)G(\omega)]$ , where  $H(\omega)$  is Wiener filter provided by  $H(\omega)=G'(\omega)/\{G'(\omega)G(\omega)+\gamma\}$ ; the parameter  $\gamma$  plays a role of reducing the noise sensitivity and symbol  $'$  represents complex conjugate.

FIR filter method (Method III): Above two methods apply calculation in frequency domain to the deconvolution. On the other hand, this method applies calculation in time-domain. Deconvolution is obtained by  $g_{\text{dec}}(t)=h(z^{-1})g(t)$ , where  $h(z^{-1})$  is the FIR filter. Details of this method is presented in Ref 1).

#### Comparison

Figure 8.6.1 shows the received signal  $g(t)$  as  $u(t)$  is 40kHz burst signal whose duration is 8 periods. Signal is sampled at the sampling frequency 200kHz, and deconvolution is calculated as digital manner. Figure 8.6.2 is deconvolution result of Method I.  $W(\omega)$  is chosen as the Butterworth type bandpass filter whose pass band is the range of 34–46kHz. Method I shows poor characteristics in both wave shape and noise property. The reason why this method is so sensitive to noise is that this processing is based on direct inversion. Figure 8.6.3 is the result of Method II for  $\gamma=0.5$ ; its performance is much better than method I. Figure 8.6.4 is the result of Method III in which the filter designed is bandlimited to 6kHz so as to reduce the noise sensitivity. In order to compare the noise performance of each method, the index  $NP = \sum g_{\text{dec}}(t)$  is introduced, and shown in each figure.

#### Reference

1)Ishikawa N., et al.: "Basic Experiment on Preprocessing of Ultrasonic Signal by Inverse Filtering Technique", JAERI-M 92-172(1992) (in Japanese).

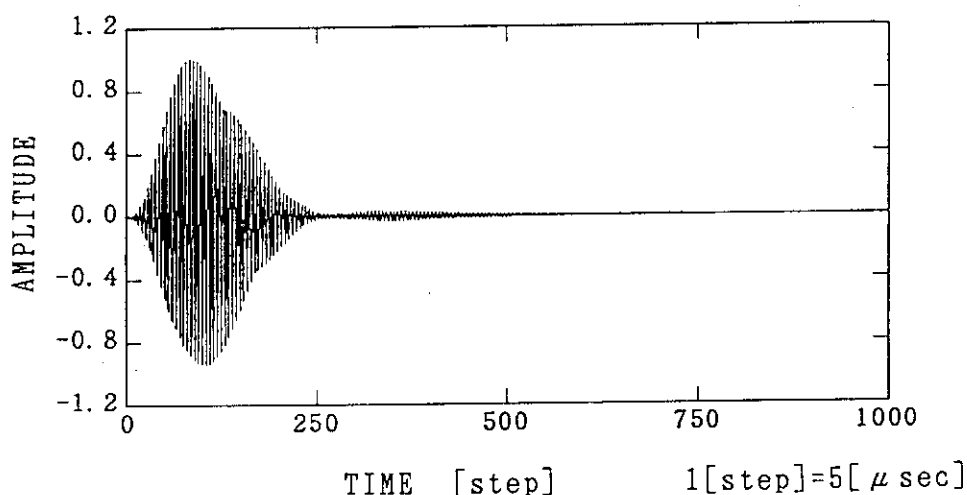


Fig. 8.6.1 Received signal

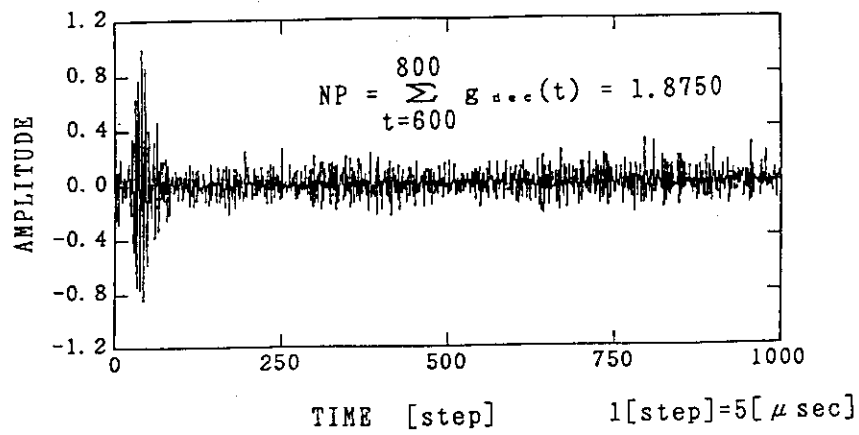


Fig. 8.6.2 Deconvolution by prefilter and direct inverse

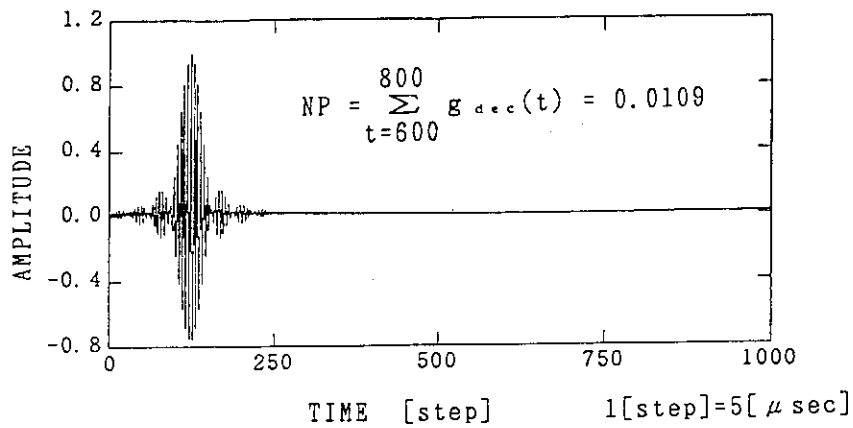


Fig. 8.6.3 Deconvolution by Wiener filter

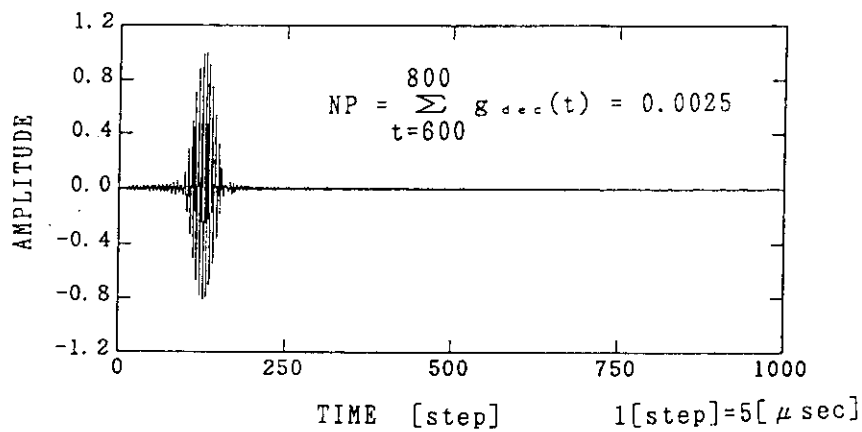


Fig. 8.6.4 Deconvolution by FIR filter



## 8.7 One Consideration for a Class of Redundant Manipulator

S. Sasaki

In recent years, the increasing application of robotic mechanisms has been directed to a variety of tasks requiring sophisticated motion in complex environments, such as working in hazardous or cluttered environment, exploring unpredictable regions, carrying radioactive materials, transporting heavy loads, executing repeated and dull work, etc. As well known, however, a non-redundant manipulator cannot have the ability to achieve other goals while completing the specified end-effector motion. These motivate the design of redundant manipulators with more than necessary degrees of freedom (DOF) to improve their dexterity and flexibility. Usually, joint velocity control depends on the choice of generalized inverse used. The most commonly used generalized inverse is the pseudoinverse derived based on the concept of least-squares minimum norm. However, this pseudoinverse technique cannot provide conservative joint motions for a task of tracking a closed path in the task space. Most of studies are focused on using homogeneous solutions of the Jacobian equation to improve its control. Needless to say, the amount of computation in such approaches seems to be considerable.

Herein we consider the nominal synthesis problem for a redundant manipulator using a different scheme (from a geometrical standpoint of arm motion). When the arm is in a kinematically nonsingular configuration, there exists one excess joint DOF for the task of the manipulator having seven actuators. As a result, for a fixed end-effector frame, there is generally a one-dimensional subset of joint space (a self-motion manifold) that maps to this configuration. For convenience, an additional task variable  $\phi$  (or called the arm angle) independent of the end-effector motion is introduced to resolve the manipulator redundancy. Using the shoulder, elbow and wrist position denoted by S, E and W, respectively, the arm angle  $\phi$  is defined by the angle from the reference plane containing the z-axis unit vector and shoulder-wrist line SW to the SEW arm plane. With this angle  $\phi$  as a parameterization of manipulator redundancy, a self-motion is described by a rotation of the plane SEW about the line SW. Due to establishment of the elbow position, the first three joint angles will be found readily. This situation will be understood with ease from a natural redundancy in the elbow motion of the human arm. Note that the arm angle  $\phi$  is undefined when the arm is either nearly fully outstretched or folded, where  $\phi$  ceases to parameterize the redundancy. Together with this parameter  $\phi$ , the present joint arrangement of anthropomorphic arms with no offsets allows to successfully derive the unique articulated solution. Also, since the parameter  $\phi$  under consideration is expressible analytically using the two plane equations, it may be useful in the future singularity analysis.

## 9 Heat Transfer and Fluid Flow

There are three major subjects of research associated with heat transfer and fluid flow. The first subject is the development and verification of the best-estimate codes for thermal-hydraulic analyses of light water reactors (LWRs). The REFLA/TRAC code is a best-estimate code with two-fluid model being developed at the JAERI to provide advanced predictions of thermal hydraulic behaviors during postulated accidents in LWRs, using the TRAC-PF1 code developed by the USNRC as the framework of the code with adopting physical models developed at the JAERI. In the FY 1993, the assessments of predictive capability of the code were intensively performed and were summarized in the technical reports for the large break loss-of-coolant accident (LOCA) of pressurized water reactors (PWRs), the small break LOCA of PWRs and the multidimensional in-core thermal hydraulics during the reflood phase of PWRs. The COBRA-TF code has also been improved as the detailed analysis code of thermal hydraulic behavior in the subchannels of fuel assembly, especially for accurate prediction of critical heat flux with respect to the entrainment and thermal fluid mixing models. The code is a three field best-estimate code being developed originally by the USNRC. Besides, the analyses of density wave instability were performed for the homogeneous saturated two-phase flow in the once-through steam generator as one of the flow instability problems encountered in LWRs.

The second subject is on the fundamental studies such as the mechanism of critical heat flux (CHF) in the fuel assembly and two-phase flow structures in the vertical and horizontal channels. For making clear the effects of spacer grids on the CHF and for developing a mechanistic model of countercurrent flow limitation in vertical channels, flow visualization experiments were carried out by means of the neutron radiography in the JRR-3M research reactor in the JAERI. Quantitative evaluations were also carried out for the falling water mass flux and the CHF in various kinds of vertical channels.

The last subject is the transient thermal-hydraulic demonstration test program which is the second part of the large scale reflood test program, aiming at the verification of the core integrity during the design basis events of LWRs. The demonstration test facility was initiated to be built in 1993. The test is scheduled to start in 1996 and end in 2000.

This chapter was written by the staffs of Heat Transfer and Fluid Flow Laboratory.

## 9.1 Large Scale Reflood Test Program

T. Iguchi, H. Akimoto, M. Okazaki, T. Okubo, A. Ohnuki, K. Nakajima, H. Watanabe, Y. Watanabe, T. Sato and Y. Sudo

It was planned to perform "Transient thermal-hydraulic demonstration test program" as a part of "Large scale reflood test program" sponsored by Science and Technology Agency of Japan. Transient thermal-hydraulic test program started in April, 1993 and is scheduled to complete in March, 2000.

The purpose of the test program is to demonstrate the core integrity during unexpected transients and accidents, i.e. design basis events (DBEs), of light water reactors (LWRs). To demonstrate the integrity, a test facility which can simulate the transient in-core thermal-hydraulic behavior during DBEs is constructed and simulation tests are to be performed with the test facility. The focused LWRs are pressurized water reactors (PWRs), boiling water reactors, and their improved ones.

Schedule of the test program is shown in Fig.1. The construction of the test facility will be completed in 1995. The tests will start after that.

In 1993, following activities (1) - (3) were performed.

### (1) Design and construction of the test facility

The test facility was designed to have capability enough to simulate the transient in-core thermal-hydraulic behavior during DBEs. The designed test facility is shown in Fig.2. The test facility can supply coolant controlled at specified pressure, temperature and mass flow rate into a test section which simulates the core of reactors.

The major dimensions of the test facility are as follows.

- |    |  |                               |
|----|--|-------------------------------|
| 1) | Maximum pressure                       | 19.5MPa                       |
| 2) | Maximum wall temperature               | 647K                          |
| 3) | Fluid                                  | Demineralized water, Steam    |
| 4) | Maximum flow rate into core            | 10kg/s                        |
| 5) | Core power                             | 6MW                           |
| 6) | Cooling capacity                       | 5MW                           |
| 7) | Range of steady condition controllable |                               |
|    | 1) Flow rate into core                 | 5 - 100% of maximum flow rate |

- 2) Subcooling at core inlet                      5 – 100K  
 3) Pressure    0.1 – 19.5MPa
- 8)      Range of transient condition controllable

The range includes the transient conditions (Pressure, core power, flow rate and coolant temperature) supposed during DBEs.

(2)      Investigation of code predictability

In order to perform simulation tests, it is necessary to know the core boundary conditions (Pressure, core power, flow rate and coolant temperature). It is planned to obtain the core boundary conditions through prediction with reliable analysis codes, for example J-TRAC code. Hence, calculation with the code was performed for major selected DBEs (Primary pump seizure accident, loss of flow accident, unexpected pressure reduction and SG pipe rupture accident of PWRs) and predictability of the code was investigated. It was found that the predicted result with the code agreed fairly well to that with a safety evaluation code.

(3)      Supplemental tests

In order to evaluate the predictability of J-TRAC code on basic two-phase flow characteristics, a two-phase flow experiment was performed. The detail is described in the following section.

Fiscal year	1993	1994	1995	1996	1997	1998	1999
Demonstration test • Test facility  • Test	Design & construction						
	Modification						
	Test						
Code	Evaluation of predictability						
	Calculation of DBEs						
Supplemental test	Two-phase flow tests						

Fig. 1 Schedule of "Transient thermal-hydraulic demonstration test program"

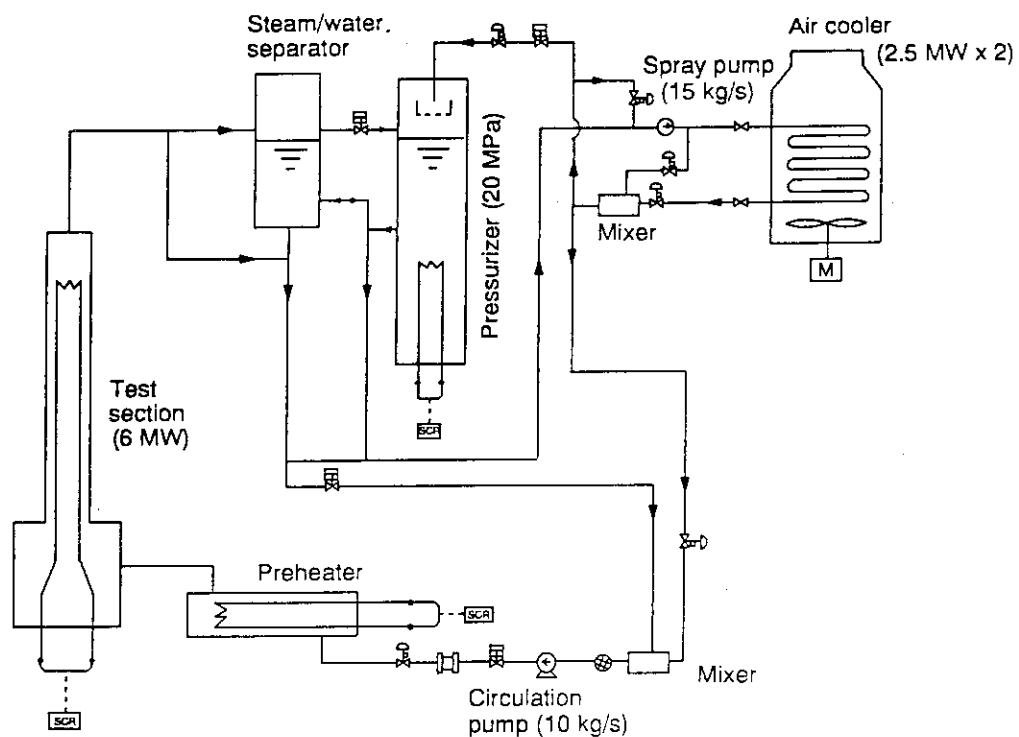


Fig. 2 Transient thermal-hydraulic demonstration test facility

## 9.2 Development of REFLA/TRAC Code for Accident Analyses of Light Water Reactor

### - Assessment of Predictive Capability for Large Break LOCA of PWR -

A. Ohnuki, H. Akimoto and Y. Murao

The REFLA/TRAC code is a best-estimate code being developed at JAERI for the simulation of transient thermal hydraulic behaviors in light water reactors.<sup>1)</sup> The REFLA/TRAC code uses the TRAC-PF1 code<sup>2)</sup> as the framework of the code and uses physical models developed at JAERI based on physical understanding of phenomena<sup>3)</sup>. Since 1984, several models have been implemented to the TRAC-PF1 code at JAERI including reflood model, condensation model, interfacial and wall friction models, critical flow model through orifice plate, etc.<sup>1)</sup> These models are synthesized in a program in order to assess predictive capability and understand the application limit of models. This report presents assessment results of REFLA/TRAC code for the transients related to a large break loss-of-coolant accident (LBLOCA) in a pressurized water reactor (PWR).

The assessment calculations were performed for separate effect tests and integral tests using relatively large scale test facilities as summarized in Table 9.2.1. The predictive capability can be evaluated for the critical flow phenomena, the condensation phenomena in the cold leg and the whole transient of LBLOCA through the assessment calculations.

The assessment results were summarized as follows:

#### Critical flow

The REFLA/TRAC code has predictive capability more than that of the TRAC-PF1 code as shown in Fig. 9.2.1.

#### Condensation phenomena in cold leg

- (1) The predictive accuracy is improved for the fluid temperature at cold leg outlet of downcomer side as shown in Fig. 9.2.2.
- (2) The calculation became more stable by suppression of an overestimation of pressure oscillation in the cold leg and the calculational speed became faster.

#### Whole transient of LBLOCA

The REFLA/TRAC code has predictive capability equal to or more than that of the TRAC-PF1 code. The predictive accuracy is improved for so-called ECC bypass phenomena

and for the clad surface temperature during reflood phase as shown in Fig. 9.2.3. The calculational speed was faster than that by the TRAC-PF1 code due to a stable calculation during the reflood phase.

The assessment results in this report indicate that the REFLA/TRAC code can predict the LBLOCA transients of PWR with good accuracy and faster calculational speed than that of the original TRAC-PF1 code.

## References

- 1) Akimoto H., et al.: Assessments of REFLA/TRAC Code for Various Postulated Accidents in PWR, Fifth International Topical Meeting on Reactor Thermal Hydraulics (NURETH-5), Salt Lake City U.S.A. (1992).
- 2) Liles D.R., et al.: TRAC-PF1/MOD1 Correlations and Models, NUREG/CR-5069 LA-11208-MS (1988).
- 3) Akimoto H. and Murao Y.: J. Nucl. Sci. Technol., 29[7], 642-655 (1992).
- 4) Ericson L., et al.: NUREG/CR-2671, MXC-301 (1982).
- 5) Okubo T., et al.: JAERI-M 85-026 (1985).
- 6) Mayinger F., et al.: Nucl. Eng. Design, 145, 47-61 (1993).
- 7) Reeder D.L.: NUREG/CR-0247 TREE-1208 (1978).

Table 9.2.1 Tests examined in this report

Critical flow test	Marviken test <sup>4)</sup> Inner diameter: 0.5 m Initial pressure: 5 MPa
Condensation test	Cylindrical test facility(CCTF) <sup>5)</sup> Inner diameter: 0.16 m Upper plenum test facility(UPTF) <sup>6)</sup> Inner diameter: 0.7 m
Integral test of LBLOCA	LOFT test <sup>7)</sup> L2-5, LP-02-6

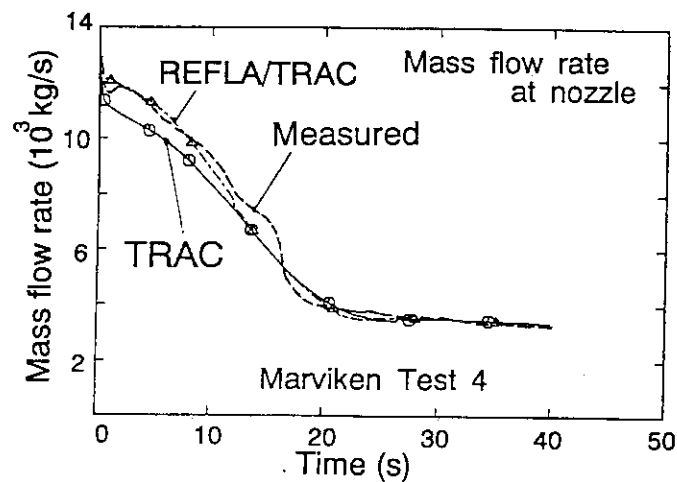


Fig. 9.2.1 Comparison of critical flow rate

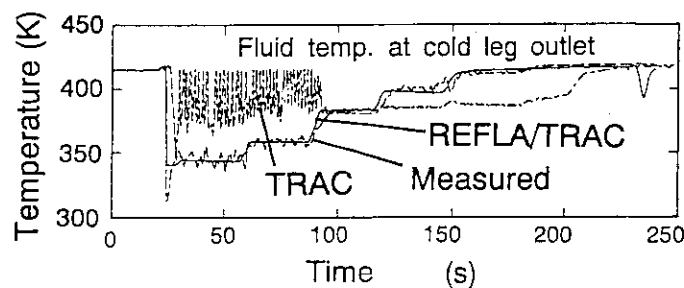


Fig. 9.2.2 Comparison of fluid temperature at cold leg outlet of downcomer side

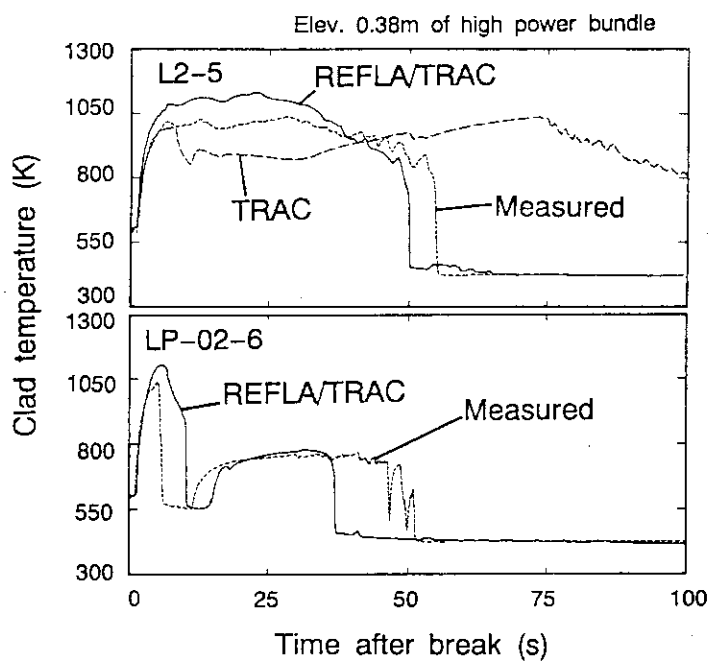


Fig. 9.2.3 Comparison of clad surface temperature in integral tests



### 9.3 Development of REFLA/TRAC Code for Accident Analyses of Light Water Reactor – Analysis of Large Break LOCA in a 4-loop PWR –

H. Akimoto, A. Ohnuki and Y. Murao

The REFLA/TRAC code is a best estimate code being developed at Japan Atomic Energy Research Institute (JAERI) to provide advanced predictions of thermal hydraulic behaviors during postulated accidents in light water reactors. The REFLA/TRAC code uses the TRAC-PF1/MOD1<sup>1)</sup> code as the framework of the code and uses physical models developed at JAERI. Several models have been implemented at JAERI including reflood model, condensation model, countercurrent flow model, interfacial and wall friction models, etc. The REFLA/TRAC code has been assessed to validate for various transients encountered in postulated accidents in pressurized water reactors (PWRs) using data from various simulation tests for two phase critical flow, direct contact condensation at cold leg, countercurrent flow, core reflood, large and small break loss of coolant accident (LOCA).<sup>2)</sup> In these assessment calculations, it was confirmed that the REFLA/TRAC code can predict major phenomena during postulated accidents in PWRs with good accuracy and reasonable computational cost.

To evaluate the safety margin of emergency core cooling system (ECCS) quantitatively, the REFLA/TRAC code was applied for large break LOCA in a four-loop PWR. Table 9.3.1 summarizes major calculational conditions. A double-ended cold break was assumed. The conservative assumptions for initial and boundary conditions as in licensing calculations were adapted. A best-estimated prediction with conservative conditions was intended in this analysis.

Figure 9.3.1 shows clad temperature where peak clad temperature is predicted. The WREM code is one of typical programs used in licensing calculations. The REFLA/TRAC code predicts peak clad temperature at 32.5 s when the reflood of the core was started. On one hand, the WREM code predicts peak clad temperature at about 100 s during the reflood. The REFLA/TRAC code predicted lower clad temperature than the WREM code. The difference of clad temperature transients is caused by the differences in the physical models during the reflood because the REFLA/TRAC code uses a best-estimate model which was confirmed by the large-scale reflood tests performed at JAERI while the WREM code uses a conservative model for licensing calculations. The result demonstrates

the conservativeness of the current safety evaluation method.

The peak clad temperature is predicted to be 1205 K at 32.5 s by the REFLA/TRAC code. The temperature is lower than the maximum allowable clad temperature ( 1473 K ) by about 250 K. The assessment study showed that The REFLA/TRAC code can predict the peak clad temperature within an error of 50 K in large break LOCA of PWR.<sup>2)</sup> Therefore, the present study suggests that the ECCS of PWR has a safety margin of about 200 K against the large-break LOCA.

#### References

- 1) Safety Code Development Group: TRAC-PF1/MOD1; An Advanced Best-Estimate Computer Program for Pressurized Water Reactor Thermal-Hydraulic Analysis, NUREG/CR-3858 LA-10157-MS R4, (1986).
- 2) Akimoto, H., et al.: Assessment of REFLA/TRAC Code for Various Postulated Accidents in PWR, Proc. of the Fifth International Topical Meeting on Reactor Thermal Hydraulics, September 21-24, Salt Lake City, UT, USA, pp.1797-1803.

Table 9.3.1 Major calculational conditions

Item	Condition
Break	Double-ended break at cold leg
Initial reactor power	102 % of nominal power
Power peaking factor	2.32
Emergency core cooling system	Single failure of low pressure injection system
Delay time for start-up of diesel generator	32 s
Primary coolant pump	No power supply after break
Decay heat model	Apply model in TRAC code
Critical flow model	Apply model in TRAC code

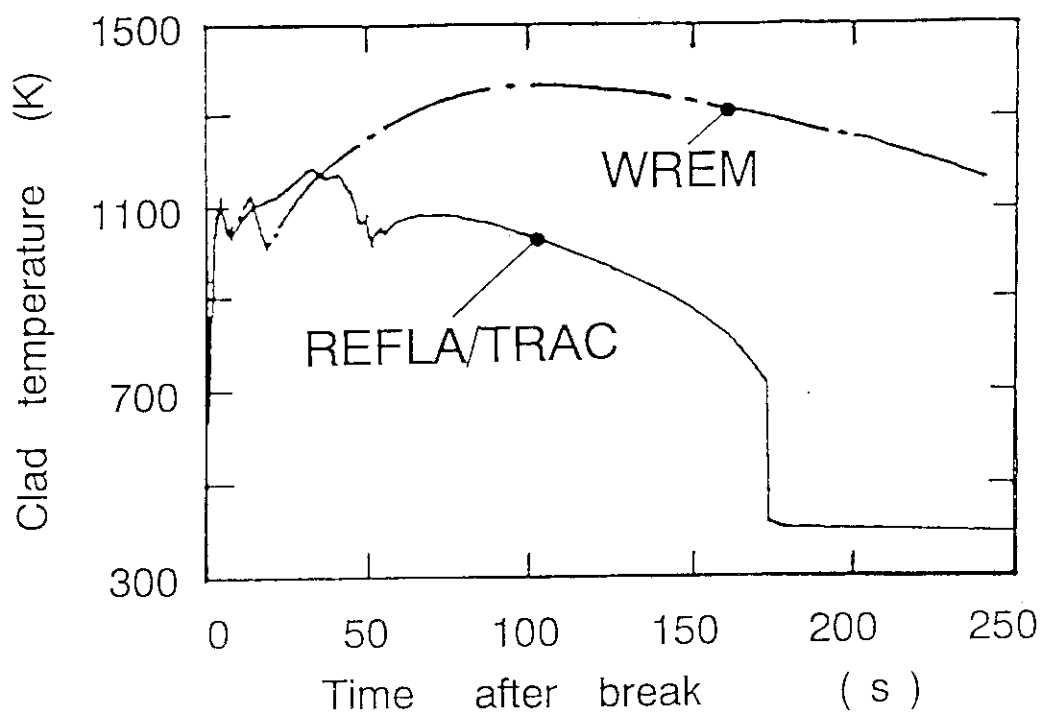


Fig. 9.3.1 Comparison of clad temperature between WREM and REFLA/TRAC codes

## 9.4 Assessment of Models in COBRA-TF Code for Turbulent Mixing in Single-Phase Flow

T. Okubo

The COBRA-TF code<sup>1)</sup> was developed to provide a detailed best estimate thermal hydraulic analysis of a Light Water Reactor (LWR) core for design basis accidents and anticipated transients. Since it provides a two-fluid three-field representation of the two-phase flow, *i.e.* continuous vapor, continuous liquid and entrained liquid, instead of the homogeneous representation used in the previous versions of the COBRA code, it can appropriately analyze the film-mist flow behavior, which we are interested in from the point of view of the prediction of the film dryout phenomenon expected in the reactor core.

Prior to apply the code to the analyses on the film dryout phenomenon, some assessment calculations and subsequent improvement on the liquid entrainment and deposition models in the COBRA-TF code have been performed<sup>2)</sup>. This is because these models significantly affect the film dryout phenomenon.

Other models important in the prediction of the film dryout phenomenon are for the fluid mixing, *i.e.* the turbulent mixing and the void drift. Therefore, in order to assess the turbulent mixing model first, some calculations have been performed against basic fluid mixing experiments<sup>3)</sup> conducted with the single-phase water flow.

Schematic of the experiment is shown in Fig. 9.4.1. This is a simple basic experiment and test section consists of two flow channels with the equivalent geometry. Only the difference is the fluid temperature at the inlet of the test section. The length of the node is set 50 mm in the calculations. Fluid temperatures and velocities are given at the inlet, and the pressures are given at the exit.

Calculated results are shown in Fig. 9.4.2 for the channel gap width of 1.5 mm and 3.0 mm. In the calculations, the turbulent mixing coefficients, *i.e.*  $\beta$ , were set 0.0118 and 0.0042 for the gap of 1.5 mm and 3.0 mm, respectively, based on the suggested values from the experiments<sup>3)</sup>. As shown in these figures, calculated results, *i.e.* average fluid temperatures along the axial direction, are in good agreement with the experimental data.

However, it should be noted the key parameter of  $\beta$  was not given by a generalized method based on the geometry and so forth but was given as a input constant value. In order

to see the sensitivity of  $\beta$  on the calculated results, other two calculations have been performed with the swapped  $\beta$  values. The results from them are shown in Fig. 9.4.3. As shown in the figure, the sensitivity is rather high. Therefore, it is important to establish a generalized method to determine the value of  $\beta$  in the turbulent mixing calculation. Otherwise, it would be difficult to achieve a precise prediction on the fluid mixing for a new system, for which the  $\beta$  value is not given.

#### References

- 1) Thurgood M.J., et al. : "COBRA/TRAC – A Thermal-Hydraulics Code for Transient Analysis of Nuclear Reactor Vessels and Primary Coolant Systems", NUREG/CR-3046 (1983).
- 2) Ezzidi A., Okubo T. and Murao Y. : "Improvement of COBRA-TF Code Models for Liquid Entrainments in Film-Mist Flow", JAERI-M 93-133 (1993).
- 3) Hori K., Kato S. and Kitahara T. : "A Study on Turbulent Mixing in Single-Phase Flow across One Gap between Subchannels with Equivalent Cross Section" (in Japanese), *Proc. JSME*, **814-11**, 97-100 (1981).

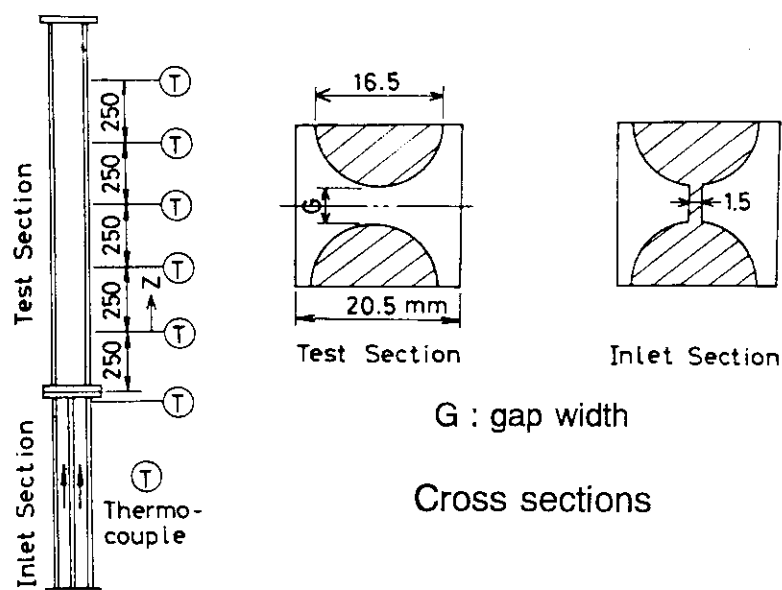


Fig. 9.4.1 Schematic of single-phase turbulent mixing experiments<sup>3)</sup>

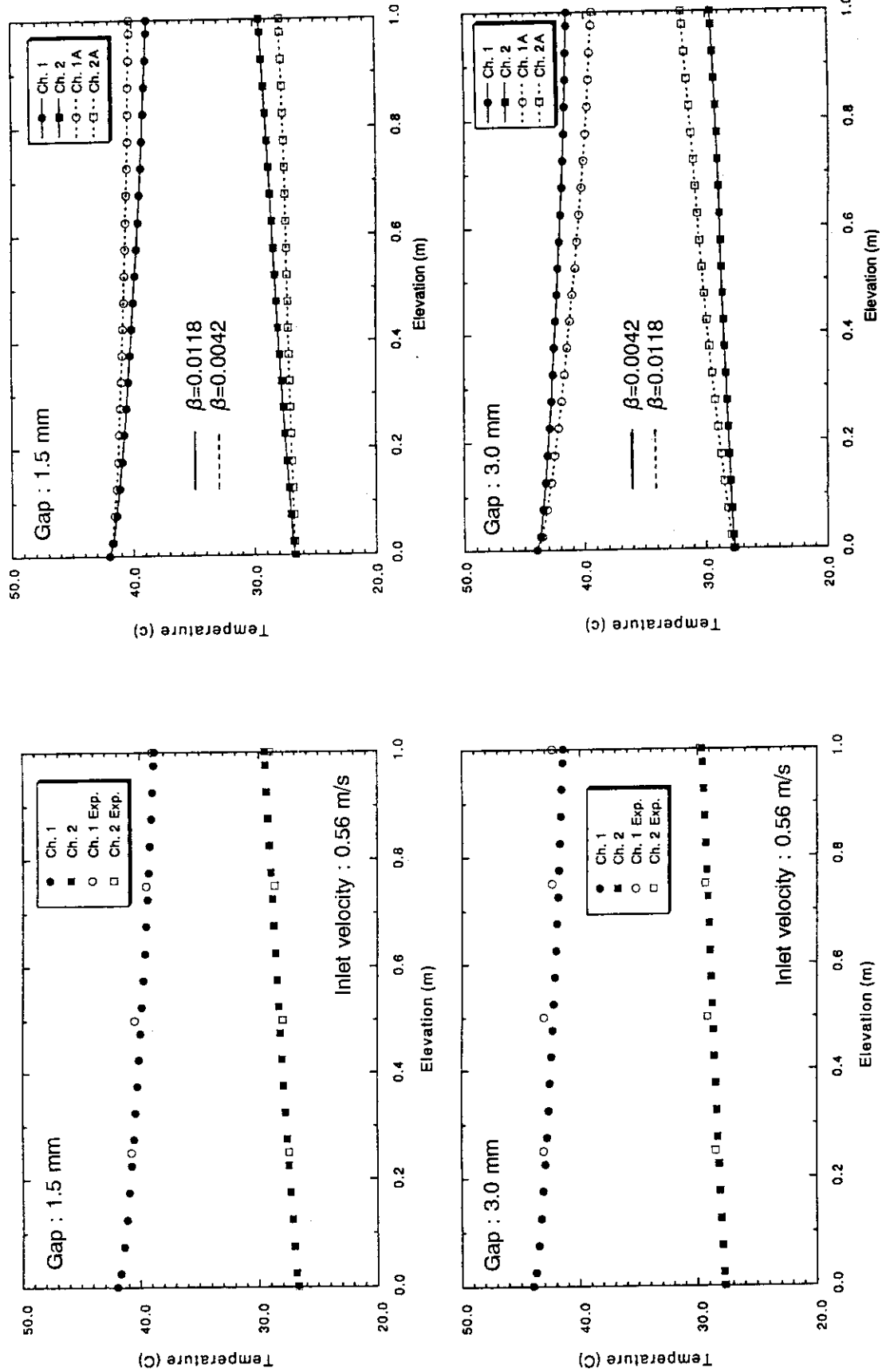


Fig. 9.4.2 Comparison of fluid temperatures between calculations and experimental data

Fig. 9.4.3 Comparison of calculated fluid temperatures with different  $\beta$  value

## 9.5 Analysis of Density Wave Instability in a Boiling flow Using a Characteristic Method.

M. Okazaki

It is known that density wave instability in a boiling flow starts when flow rate is decreased or external heating rate is increased from a certain boundary condition of steady state flow. In order to make analysis of the flow behavior, it is necessary to strictly describe the essential phenomena of the propagation of density and pressure, which take place in an unsteady boiling flow.

In principle, characteristic method can solely deal with the physical aspects occurred in the unsteady boiling flow rigorously through the derivation of characteristic equation. However, the past works<sup>(1)~(2)</sup> to develop the characteristic method have not succeeded in making a practical use. The reasons can be considered as in one case<sup>(1)</sup> it fails to derive a characteristic curve as a realistic sonic speed, and in another case<sup>(2)</sup> it fails to derive a characteristic equations as rigorous expressions of flow change induced by a thermodynamical state change.

In this report, the characteristic curve expressed by a sonic speed is derived assuming no phase change and isentropic change of each phase in the pressure propagation process for a realistic model of sonic speed in the homogeneous saturated two-phase flow. Moreover the characteristic equation are derived so that the phase change rate in the saturated two-phase flow and the state change occurred in the pressure propagation process are rigorously expressed by using thermodynamical laws.

For homogeneous saturated two-phase flow, the following characteristic equations are derived.

$$\begin{aligned}
 \text{along } \frac{dz}{dt} = u, \quad r \frac{Dx}{Dt} + H \frac{DP}{Dt} &= \left( \frac{1}{\rho_m} \frac{\partial P_f}{\partial z} + \frac{\partial q_E}{\partial z} \right) u \\
 \text{along } \frac{dz}{dt} = u + a_x, \quad \frac{1}{a_x} \frac{dP}{dt} + \rho_m \frac{du}{dt} &= \frac{a_x}{a_{ds}^2} \frac{DP}{Dt} + a_x \frac{v_g - v_l}{v_m^2} \cdot \frac{Dx}{Dt} - \frac{\partial P_f}{\partial z} \\
 \text{along } \frac{dz}{dt} = u - a_x, \quad -\frac{1}{a_x} \frac{dP}{dt} + \rho_m \frac{du}{dt} &= -\frac{a_x}{a_{ds}^2} \frac{DP}{Dt} - a_x \frac{v_g - v_l}{v_m^2} \cdot \frac{Dx}{Dt} - \frac{\partial P_f}{\partial z}
 \end{aligned}$$

where  $\frac{D}{Dt} = \frac{\partial}{\partial t} + u \frac{\partial}{\partial z}$

$$\frac{1}{a_x^2} = \left( \frac{\partial \rho_m}{\partial P} \right)_{x,s} = \frac{1}{v_m^2} \left\{ \frac{x v_g^2}{a_g^2} + \frac{(1-x) v_l^2}{a_l^2} \right\}$$

$$\frac{1}{a_a^2} = \left( \frac{\partial \rho_a}{\partial P} \right)_{sa} \quad (\text{Suffix } a = g, l)$$

$$\frac{1}{a_{ds}^2} = \frac{1}{a_{sg}^2} \left( \frac{ds_g}{dp} \right)_{sat} + \frac{1}{a_{sl}^2} \left( \frac{ds_l}{dp} \right)_{sat}, \quad \frac{1}{a_{sa}^2} = \frac{x_a v_a^2}{v_m^2 a_a^2} \left( \frac{\partial P}{\partial s_a} \right)_{\rho_a}$$

$$H = \left\{ x \left( \frac{ds_g}{dp} \right)_{sat} + (1-x) \left( \frac{ds_l}{dp} \right)_{sat} \right\} T_{sat}$$

$a_x$ : Sonic velocity for saturated two-phase flow	m/s		
$h$ : specific enthalpy	J/kg	$T$ : Temperature	K
$P$ : Pressure	Pa	$u$ : Flow velocity	m/s
$q$ : Heat for entropy increase	J/kg	$v$ : Specific volume	m <sup>3</sup> /kg
$s$ : Specific entropy	J/kg·K	$x$ : Flow quality	m/s
$t$ : Time	sec	$\rho$ : Density	kg/m <sup>3</sup>

Unsteady Flow calculations are made for a test pipe shown in Fig.1 with both ends are opened and at one end thermodynamical states and flow quality are kept constant. At the another end pressure is gradually decreased causing start of outflow. The boundary conditions of pressure and heating rate given for the pipe are shown in Fig.2 and Fig.3, and the given values for the each calculation condition are shown in Table.1. First, for the verification of validity of characteristic equation, two-phase flow changes of quality and velocity caused by pressure decrease are examined to check the mass and energy conservation in a steady flow with no external heat in No.1 calculation. Calculated results show approximately 1% decrease in mass and energy fluxes, respectively between flow inlet and outlet. We consider the conservation of mass and energy is attained by this degree of errors in the present calculation. In No.2 calculation, flow oscillation occurred in the early stage decreases gradually as shown in Fig.4, because flow rate is large due to large pressure difference between inlet and outlet. In No.3 calculation, flow rate is made smaller than in No.2 case by increasing the outlet pressure. Then, density wave oscillation continues with no decrease as shown in Fig.5. In No.4 calculation, the length of non-



heating region is made longer in the vicinity of inlet and made shorter in the vicinity of outlet. Moreover, the flow rate is decreased by making outlet pressure higher. The amplitude of density wave oscillation becomes smaller than in No.3 as shown in Fig.6.

## References

- 1) Banerjee S. and Hancox W.T. : Int. J. of Multiphase Flow., 4, 437 (1978)
- 2) Gidaspow D., et al. : Nucl. Sci. and Eng., 84, 179 (1983)

Table. 1. Boundary conditions for saturated two-phase flow  
 $N = 160$ ,  $t_{\text{end}} = 20$  sec,  $l_T = 20.0$  m,  $x_0 = 5 \times 10^{-4}$ ,  $P_0$   $P_E$   $P_{E1}$  (MPa)

No.	$l_{\phi 1}$	$l_{\phi 2}$	$t_{p1}$	$t_{p2}$	$t_{p3}$	$P_0$	$P_E$	$P_{E1}$	$\phi_0$	$C_{F1}$	$t_{F1}$	$t_{F2}$	$t_{F3}$
1	—	—	2.0	2.0	2.0	3.5	2.8	2.8	0.0	—	—	—	—
2	2.0	5.0	0.2	3.0	5.0	3.5	2.5	2.0	$10^4$	0.1	0.6	0.8	6.2
3	2.0	5.0	0.2	2.5	8.0	3.5	2.75	2.0	$10^4$	0.1	0.6	0.8	6.2
4	3.0	2.0	0.2	2.5	8.0	3.5	2.8	2.0	$10^4$	0.1	0.6	0.8	6.2

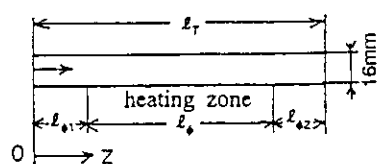


Fig. 1. Test Pipe

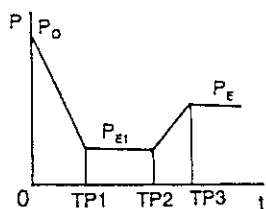


Fig. 2. Pressure Change at one end vs. Time

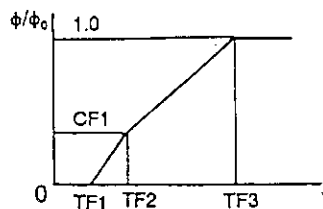


Fig. 3. Heat Flux Change vs. Time

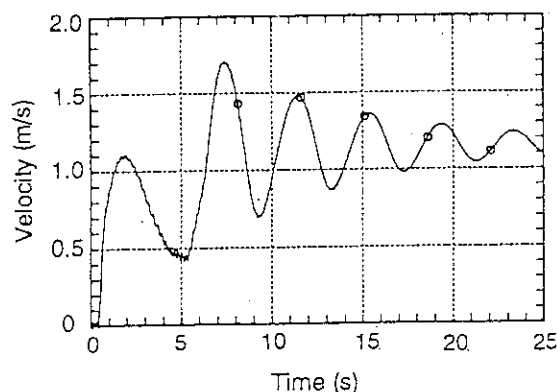


Fig. 4. Velocity change at  $Z=0.2$ m in a boiling flow No. 2 in Table 1

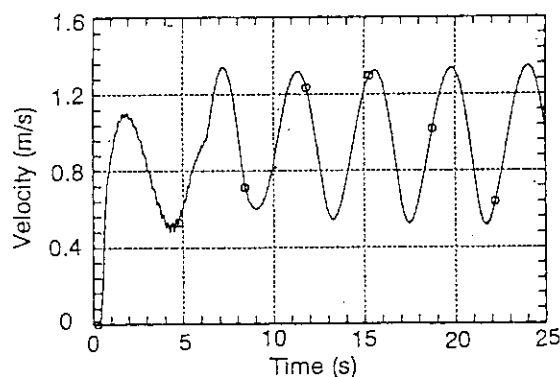


Fig. 5. Velocity oscillation at  $Z=0.2$ m in a boiling flow No. 3 in Table 1

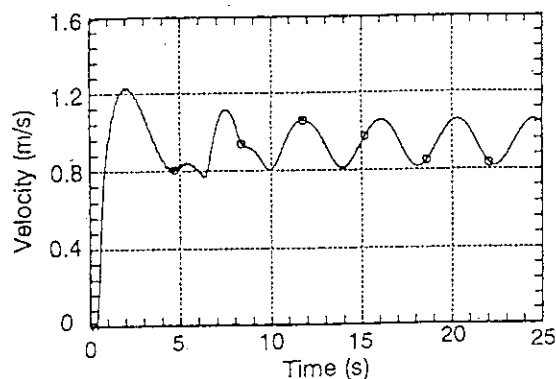


Fig. 6. Velocity oscillation at  $Z=0.2$ m in a boiling flow No. 4 in Table 1

## 9.6 Analysis of Cooling Limit of Rotating Target for DT Neutron Source at FNS

H. Akimoto, Y. Ikeda and J. Kusano

A new rotating target for DT neutron source has been developed to increase the neutron generation rate more than  $10^{13}$  n/s at FNS(Fusion Neutronics Source).<sup>1)</sup> Figure 9.6.1 illustrates the structure of the rotating target. A deuteron beam is irradiated to the tritium, absorbed in titan, to produce the neutron due to the DT reaction. To attain the neutron generation rate more than  $10^{13}$  n/s, a high intensity beam of about 40 kW should be irradiated on the target surface. The heat flux reaches about  $100 \text{ MW/m}^2$  if the beam is focused in  $4 \text{ cm}^2$ . The upper limit of the neutron generation rate is determined by the cooling performance of the target because tritium, absorbed in titan, is lost due to diffusion when titan temperature is higher than  $300^\circ \text{C}$ .

An analysis was performed to understand the mechanism of the cooling limit of the rotating target. In the analysis, performed were unsteady temperature response analysis of rotating target with the TRAC-PF1/MOD2<sup>2)</sup> code, derivation of analytical model for thermal design of rotating target, and evaluation of parameter effect on cooling limit with the analytical model.

The cooling behavior of the rotating target is determined by the heat conduction inside the structural material and heat transfer on the cooling surface. To understand the mutual relation between the heat conduction and the heat transfer, a calculation was performed using the TRAC code, which can handle the unsteady heat conduction problem combined with the heat transfer on the cooling surface. Figure 9.6.2 shows an example of calculated results. The calculation shown in Fig. 9.6.2 was performed under conditions listed below; Titan thickness =  $10 \text{ }\mu\text{m}$ , Copper thickness =  $0.5 \text{ mm}$ , Rotation speed =  $1200 \text{ rpm}$ , Radius of irradiated part =  $5 \text{ cm}$ , Width of cooling flow path =  $10 \text{ mm}$ , Flow path height =  $0.5 \text{ mm}$ , Water velocity =  $10 \text{ m/s}$ , Water temperature =  $300 \text{ K}$ , and Pressure =  $0.1 \text{ MPa}$ . A location on the rotating target is heated for  $1.5915 \text{ ms}$  every  $50 \text{ ms}$  under these conditions.

When the beam irradiation starts ( $1.449254 \text{ s}$ ), wall temperature starts to increase and a steep temperature profile is established inside the structure. A linear temperature profile is calculated in the titan part in the irradiation period. The maximum temperature of titan is predicted when the irradiation is terminated. The heat flux at the cooling

surface,  $q_c$  increased from  $1.4 \text{ MW/m}^2$  to  $4.9 \text{ MW/m}^2$  in the irradiation period. The heat flux at the cooling surface is only about 5 % of the heating heat flux,  $q_0$  ( $100 \text{ MW/m}^2$  in Fig. 9.6.2). It is found that the temperature response in the irradiation period can be treated assuming no cooling by the coolant.

In the period following the beam irradiation termination, the temperature profile inside the structure is flattened and almost flat temperature profile is established in a few milliseconds. The cooling heat flux reaches the maximum right after the nearly-flat temperature profile is established. The temperature of the structure drops gradually keeping the flat temperature profile in the successive period.

The calculated results with the TRAC code revealed the mutual relation between the heat conduction and the heat transfer on the cooling surface. Based on the understanding from the calculation, an analytical model for thermal design of the target was derived using the analytical solutions for the simplified heat conduction equation assuming no cooling in the irradiation period and uniform temperature in the cooling period. As the design criteria, two conditions were adapted, that is,

- (1) the maximum temperature at titan surface is lower than  $300^\circ \text{C}$ , and
- (2) the heat flux on the cooling surface is lower than the burnout heat flux.

The first condition is named maximum temperature limit and second is burnout limit, respectively. It is found from the parametric evaluation that the cooling limit of the rotating target can be increased when copper is used as the structure material. The cooling limit is increased as thinner titan, higher rotation speed, greater radius, larger irradiation area, higher coolant pressure, and higher coolant velocity are established. It is also found that maximum cooling limit can be reached when copper thickness is between 1 and 2 mm.

Based on the parametric evaluation results, a test design of the rotating target was performed with the parameter selection shown in Table 9.6.1. Thicker copper, higher coolant velocity, and larger target radius were selected compared to the current design. Fig. 9.3.3 shows the predicted cooling limit for the test design. The cooling limit is calculated to be 37 kW at the inner part the target. The cooling limit corresponds to the neutron generation rate of  $2 \times 10^{13} \text{ n/s}$ . These results suggest that the neutron generation rate more than  $10^{13} \text{ n/s}$  is attainable by the rotating target.

## References

- 1) Tanaka, S., et al.: Development of New Rotating Target System for 14 MeV Neutron Irradiation Experiments, JAERI-M 86-105, (1986), (in Japanese).
- 2) Los Alamos National Laboratory : TRAC-PF1/MOD2 Code Manual, NUREG/CR-5673 LA-12031-M, (1992).

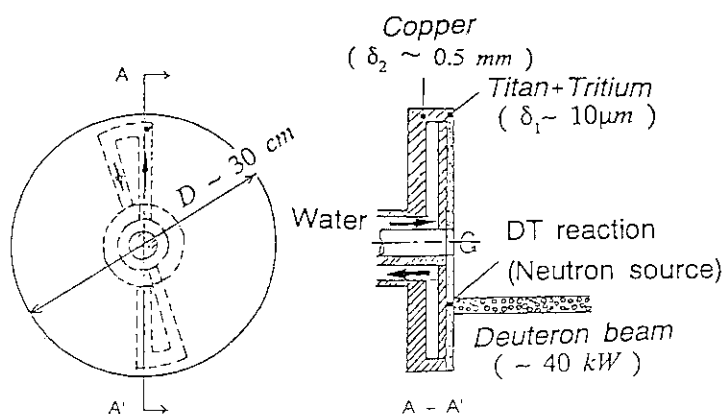


Fig. 9.6.1 Structure of rotating target

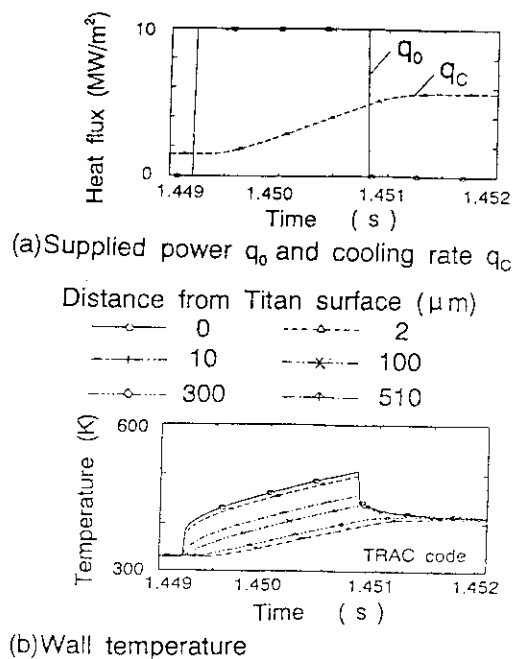


Fig. 9.6.2 Cooling behavior

Table 9.6.1 Specification of test design

Parameter	Value
Titan thickness	7 $\mu\text{m}$
Copper thickness	2 mm
Rotating speed	2000 rpm
Radius of irradiated part	8~18 cm
Irradiated area	3 $\text{cm}^2$
Flow path height	1 mm
Water velocity	10 m/s
Water temperature	300 K
Exit pressure	0.1 MPa

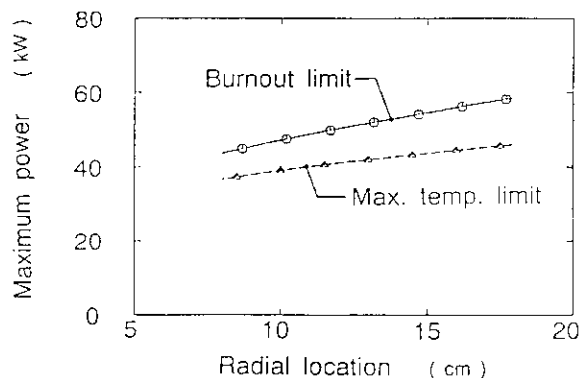


Fig. 9.6.3 Cooling limit for test design

## 9.7 Evaluation of Falling Water Mass Flux under Countercurrent Flow Limitation in Vertical Circular Tubes

Y. Sudo

The countercurrent flow limitation (CCFL) or flooding in vertical channels such as circular tubes, rectangular channels and annular channels is an important phenomenon which governs the capability of core cooling in the postulated loss-of-coolant accident of light water reactors, directly determining the mass flux of emergency core cooling water effectively supplied into the core, which is falling down against upward steam flow in the downcomer and in the upper part of the core of the pressurized water reactors (PWRs) or other type nuclear reactors<sup>1) 2)</sup> and many studies have been carried out so far. However, the mechanism of CCFL and the quantitative evaluation of CCFL condition have not been made clear enough and the objective of this study is, therefore, to make clear the mechanism of the CCFL and to evaluate quantitatively the falling water mass flux under CCFL condition in vertical circular tubes, proposing a new analytical model for the CCFL mechanism, which was compared with the existing experimental results obtained for an air-water system under about atmospheric pressure.

Based on steady state momentum balances for both gas phase and liquid phase in the separated two-phase flow across the entire circular tube shown in Fig.9.7.1, the following correlation of the dimensionless upward air velocity,  $j_g^*$  vs the dimensionless downward water velocity,  $j_l^*$  could be introduced, including the effects of void fraction  $\alpha$ , tube diameter  $D$ , tube length  $L$ , densities of air and water  $\rho_g$  and  $\rho_l$ , interfacial friction factor  $f_i$  and wall friction factor  $f_w$ .

$$\frac{2}{\alpha^{5/2}} \left\{ j_g^* + \frac{\alpha}{1-\alpha} \left( \frac{\rho_g}{\rho_l} \right)^{1/2} j_l^* \right\}^2 f_i + \frac{2}{(1-\alpha)^2} j_l^{*2} f_w + \frac{1}{2} \left( \frac{D}{L} \right) \frac{1-\alpha}{\alpha^2} j_g^{*2} + \frac{1}{2} \left( \frac{D}{L} \right) \frac{1}{1-\alpha} j_l^{*2} = 1 - \alpha$$

where  $j_g^* = j_g / [ g D ( \rho_l - \rho_g ) / \rho_g ]^{1/2}$ ,

$j_l^* = j_l / [ g D ( \rho_l - \rho_g ) / \rho_l ]^{1/2}$

and  $j_g$  is the superficial average air velocity,  $j_l$  the superficial average water velocity and  $g$  the acceleration of gravity. The friction factor  $f_i$  was determined based on the

experiment of Bharathan, et al<sup>3)</sup> and friction factor  $f_w$  was determined corresponding to the laminar, transition and turbulent flow regimes.

The feature of this analytical model is : (1) The interfacial friction factor  $f_i$  is defined based on the relative velocity of air and water, (2) the friction factor  $f_w$  is not constant but is corresponding to the flow regime of water flow and (3) momentum balances are considered across the entire tube. It was assumed that the CCFL condition was given by maximizing the falling water mass flux equivalent to  $j_i^*$  with respect to the void fraction.  $\alpha$ , that is,  $\partial j_i^* / \partial \alpha = 0$ .

Figure 9.7.2 illustrates the analytical results obtained for channels of  $D = 0.019$  and  $0.14$  m with tube length  $L = 1.54$  m, diameters of upper and lower plenum  $D_o = D_2 = 0.33$  m under atmospheric pressure, showing the corresponding flow regime of water flow. The analytical results show a clear tendency that a larger diameter gives a larger  $j_i^*$  for a constant  $j_g^*$ . Figure 9.7.3 and 9.7.4 illustrate the comparisons of analytical results with the existing experimental results<sup>4)</sup> for the channels of air-water system with  $L = 1.52$  m and  $D_o = D_i = 0.33$  m under atmospheric pressure, showing the effect of tube diameter of  $0.019$  to  $0.14$  m. The comparisons clearly show the analytical results give a systematic tendency that a larger diameter gives a smaller  $j_i^*$  for a constant  $j_i^*$ , which is the same tendency as the experiments and it is emphasized that the relationship between  $j_g^{*1/2}$  and  $j_i^{*1/2}$  is not of a straight line for a given diameter but it rather seems that it depends on the water flow regimes.

#### References

- 1) Sudo Y., et al. : J. Nucl.Sci. Technol. 21-1,32-41(1984).
- 2) Sudo Y., et al. : JSME Int. J.Ser.II,34-2,169-174(1990).
- 3) Bharathan D., et al. : "Air-water countercurrent annular flow" , EPRI Report NP-1165(1979).
- 4) Richter H., et al. : Int. J.Multiphase Flow,7,647-658(1981).

Figure 10 is a graph showing the relationship between the friction factor  $j_g^{*1/2}$  (y-axis) and the friction factor  $j_i^{*1/2}$  (x-axis) for a vertical tube. The y-axis ranges from 0 to 1, and the x-axis ranges from 0 to 1. Two curves are plotted for different tube diameters:  $D = 0.019\text{m}$  (upper curve) and  $D = 0.14\text{m}$  (lower curve). The curves are labeled with values of  $\alpha$  (0.65 to 0.98). The graph is divided into Laminar, Transition, and Turbulent regions by vertical lines. The upper curve is labeled 'Laminar' and 'Transition' with arrows. The lower curve is labeled 'Turbulent'.

Figure 10 is a log-log plot showing the normalized velocity profile  $j_g^{1/2}$  (y-axis) versus the normalized axial distance  $j_t^{1/2}$  (x-axis). The y-axis ranges from 0.5 to 1.0, and the x-axis ranges from 0 to 1.0. The plot includes experimental data points for three different diameters  $D$ : 0.025m (open squares), 0.051m (half-filled squares), and 0.14m (filled squares). Solid lines represent the 'This Analysis' for various values of  $\alpha$  (0.7, 0.75, 0.8, 0.85, 0.9, 0.95). A dashed line is also shown for  $D = 0.025m$ . The plot is for  $L = 1.52m$  and  $D_0 = D_2 = 0.33m$ .

— 242 —

## 9.8 Analytical Study on Critical Heat Flux under Countercurrent Flow Limitation in Vertical Channels

Y. Sudo

The quantitative evaluation of critical heat flux (CHF) in the vertical heated channels such as circular tubes, rectangular channels and annular channels, whose bottom, ends are closed or into which no coolant enters at the bottom, that is, under the countercurrent flow limitation (CCFL)<sup>1) 3)</sup>, is very important from the viewpoint of making clear the cooling capability of core under the natural circulation in the postulated loss-of-coolant accident of light water reactors.<sup>2)</sup>

In this study, a new analytical model was proposed for the evaluation of CHF under CCFL and was compared with the existing experimental results under about atmospheric pressure<sup>2), 5)-11)</sup>, whose major run conditions are listed in Table 9.8.1.

The following correlation on the dimensionless CHF  $q_{CHF}^*$  was introduced under the assumption that the CHF is the heat flux by which all of water falling down against the upward steam flow is evaporated under the CCFL condition in the channels,

$$q_{CHF}^* = 0.25 (D_h / L) (D_h / \lambda)^{\frac{1}{2}} (1 + \Delta T_{in}^*) (\rho_l - \rho_g)^{\frac{1}{2}} j_l^*$$

where  $q_{CHF}^* = q_{CHF} / h_{fg} [\lambda (\rho_l - \rho_g) \rho_g g]^{\frac{1}{2}}$ ,

$$j_l^* = j_l / [g D_e (\rho_l - \rho_g) / \rho_l]^{\frac{1}{2}}, \lambda = [\sigma / (\rho_l - \rho_g) g]^{\frac{1}{2}}$$

and  $D_h$  is the equivalent heated diameter,  $D_e$  equivalent hydraulic diameter,  $\Delta T_{in}^*$  dimensionless inlet subcooling,  $q_{CHF}$  critical heat flux,  $h_{fg}$  latent heat of evaporation, and  $\rho_g$  densities of water and steam and  $j_l$  superficial average water velocity. The  $j_l^*$  in the above correlation is given by the relationship of  $j_g^*$  vs  $j_l^*$  in the vertical channels under the CCFL condition where  $j_g^* = j_g / [g D_e (\rho_l - \rho_g) / \rho_g]^{\frac{1}{2}}$ . Figure 9.8.1 illustrates analytical results of  $j_g^*$  vs  $j_l^*$  in the vertical circular tubes under atmospheric pressure, and the  $j_l^*$  at the CHF is obtained as the intersection of  $j_g^* = (\rho_l / \rho_g)^{\frac{1}{2}} j_l^*$  and the relationship of  $j_g^*$  vs  $j_l^*$  as shown in Fig. 9.8.1 for each tube diameter. Figure 9.8.1 shows a systematic tendency that a larger diameter gives a smaller  $j_l^*$  for the same



$j_g^*$ . Figure 9.8.2 also illustrates the  $j_g^*$  at the CHF for the vertical annular channels under atmospheric pressure, giving the effect of channel dimensions. Figures 9.8.3 and 9.8.4 show the comparisons of analytical results obtained thus and the existing experimental results <sup>2),5)11)</sup> on CHF under CCFL. Figure 9.8.3 shows the comparison for the case of circular tubes and Fig.9.8.4 for the case of rectangular and annular channels. It is observed that the analytical results give a rather good prediction to the experimental results for a variety of run conditions listed in Table 9.8.1.

## References

- 1) Sudo Y., et al.: J. Nucl. Sci. Technol. 21(1),32-41(1984).
- 2) Sudo Y., et al.: J. Nucl. Sci. Technol. 22(8),604-618(1984).
- 3) Sudo Y., et al.: JSME Int. J. Ser.II,34(2),169-174(1990).
- 4) Bharathan D., et al.: EPRI Report NP-1165(1979).
- 5) Chang S.H., et al.: Nuclear Eng. & Design 132,225-237(1991).
- 6) El-Genk M.S., et al.: Int. j. Heat Mass Transfer, 31-11,2291-2304(1988).
- 7) Katto Y. and Hirano T., et al: Int. J. Heat Mass Transfer, 34-4/5,993/1001(1991).
- 8) Motomura Y.,et al.: Preprint of Fall Meeting of AESJ,A26(1993).
- 9) Mishima K.: "Boiling burnout at low rate and low pressure conditions" ,Doctoral dissertation, Kyoto Univ.,Japan(1984).
- 10) Kusuda H. and Imura,H.: Bulletin of the JSME,17-114,1613-1618(1974).
- 11) Frea W.J. : Preprint of 4th Int. Heat Transfer Conference,V.B5.10(1970).

Table 9.8.1. Major run conditions of CHF experiments investigated in this study

Ref.No	Channel	dimension	Length	Pressure	Tin	$q_{CHF}$
No	Type	( mm )	L(mm)	(MPa)	(°C)	(-)
1 11	Circular	D = 2.5	88	0.1	100	0.068
2 10	Circular	10.7, 28.4	200~1000	0.1	74~100	0.008~0.022
3 9	Circular	6.0	344	0.1	30~60	0.0097~0.01
4 5	Circular	6.0, 8.8	720	0.1	20 ~70	0.0035~0.0047
5 7	Circular	8, 10	300~900	0.1~0.2	100~120	0.0045~0.018
6 2	Rectangular	W= 50 S=2.25,2.8,5	375 750	0.1	30 ~90	0.0051~0.01
7 8	Rectangular	W=40,S =1.03	360	0.1	20	0.011
8 9	Rectangular	W=40,S =2.4	350	0.1	20 ~86	0.0064
9 6	Annular	Di=12.7 Do=20,21.8,25.4	500	0.12	43 ~74	0.018~0.039
10 9	Annular	Di=20.5,Do=26	860	0.1	36	0.0051~0.0055
11 10	Annular	Di=6.5 ~19.1	200~1000	0.1	32 ~100	0.0032~0.013

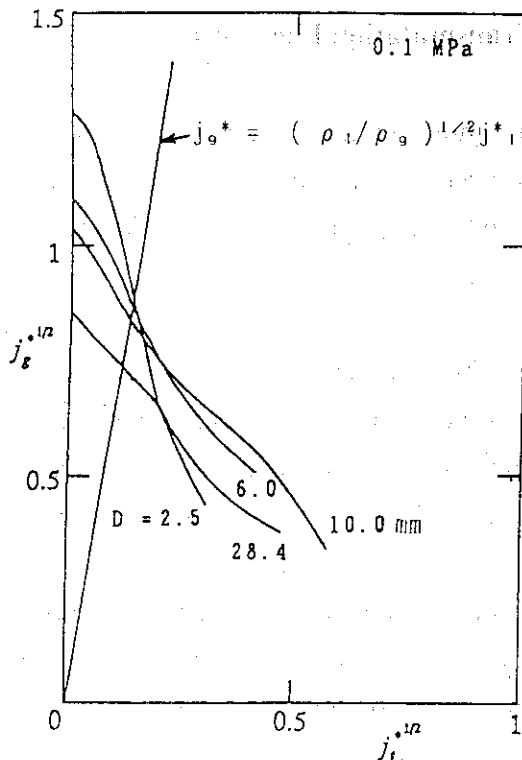


Fig. 9.8.1 Effect of tube diameter on the relationship of  $j_g^*$  vs  $j_l^*$  under CCFL condition in vertical circular tubes

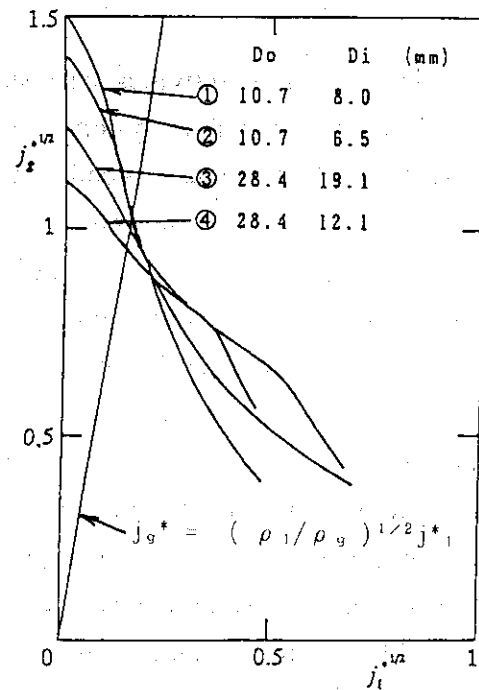


Fig. 9.8.2 Effect of inner and outer diameters on the relationship of  $j_g^*$  vs  $j_l^*$  under CCFL condition in vertical annular channels

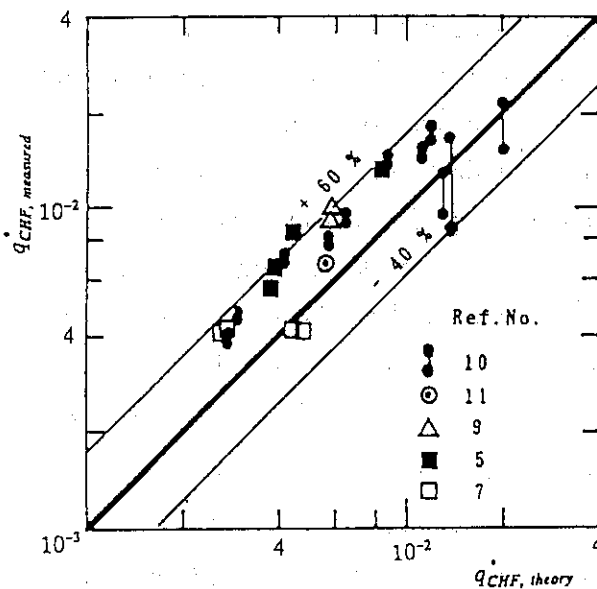


Fig. 9.8.3 Comparison of existing experimental results and analytical results on CHF under CCFL condition in vertical circular tubes

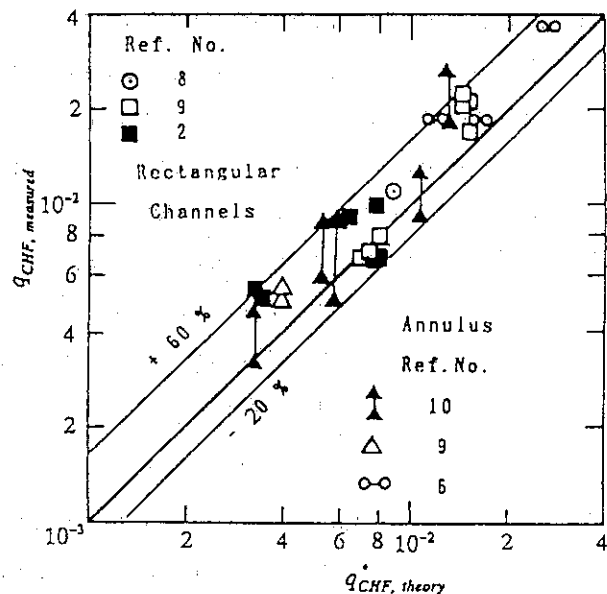


Fig. 9.8.4 Comparison of existing experimental results and analytical results on CHF under CCFL condition in vertical rectangular and annular channels

## 10. Transmutation System and Partitioning -Transmutation Fuel Cycle

The research activities are summarized as three research subjects of (1) the reactor-based transmutation system, (2) the accelerator-based transmutation system with the relevant basic researches such as code development and spallation experiment and (3) assessment of partitioning process for transmutation.

The first subject has the design study on the burner reactor and the fuel cycle facility taking into account the partitioning and transmutation (P-T) fuel cycle. The design study of the burner reactor with hard neutron spectrum and high neutron flux has been made. From the viewpoint of reactor physics it has been apparent that the transmutation by the burner reactor is more excellent in practicability and efficiency than the transmutation using the power reactor such as LWR and FBR.

In the second subject the conceptual design studies on MA (minor actinide) molten salt transmutation system and MA & LLFP (long-lived fission product) liquid metal target-graphite blanket transmutation system driven by an intense proton accelerator have been carried out. In the molten salt system the arrangement of the compact heat exchangers and inner reflector in the core vessel and the installation of fuel salt supplying system, secondary cooling system and beam duct on the core vessel cover have been designed from the viewpoint of engineering practicability. The preliminary calculations on neutronics and thermal characteristics have been carried out for the liquid metal target system which has several advantages of small inventory, on-line charging and processing and simultaneous transmutation of both MA and LLFP. The benchmark studies on the spallation product distribution and the double differential cross section for neutron or proton emission induced by the high energy proton bombardment were made to examine and upgrade the accuracy of some predictions computed by some cascade codes. In the spallation experiment using the synchrotron facility at KEK the energy spectra of neutrons escaped from the thick lead target irradiated by protons with energies of 500 MeV and 1.5 GeV were measured to check and upgrade the accuracy of predictions obtained by the cascade codes and compared with the old experimental data by Cierjacks. The detecting efficiency and the response function of NE-213 scintillation counter on  $\sim 65$  MeV neutrons were measured at the cyclotron in the Takasaki Research Establishment to improve the counter efficiency to neutrons with energy of tens MeV.

In the last subject concerning to the partitioning process preceding to the transmutation, the present status about the group separation technology, in particular, the high temperature chemical method was reported.

In this chapter Transmutation System Laboratory is in charge of the paragraphs 10.1-10.5 and Thermal Reactor Physics Laboratory in charge of the paragraphs 10.6-10.8.

## 10.1 Conceptual Design Study on Minor Actinide Molten Salt Transmutation System Driven by an Accelerator

T. Nishida, H. Takada, T. Takizuka, Y. Kato, H. Katsuta and T. Sasa

In designing the accelerator-based Minor Actinide (MA) molten salt target/core transmutation system, it became obvious that the system can transmute MA  $\sim 250$  kg/y, which is exhausted from ten units of 3 GWt LWR, with thermal power of 800 MW.<sup>1)-3)</sup> In the present report<sup>4),5)</sup> the heat balance in the core has been reevaluated to optimize the heat exchanger size and to keep the large temperature difference between the outlet of primary coolant (NaCl-(Pu,TRU)Cl<sub>3</sub>: 64-36 mol%, melting point :453 °C) and the inlet of secondary coolant (NaBF<sub>3</sub>-NaF: 92-8 mol%). The temperature at the cold leg on the primary cooling system has gone up from 570 °C to 600 °C, while the corresponding temperature in the secondary cooling system have been reduced from 500 °C to 480 °C since the melting point of secondary coolant molten salt occurs between 454 °C and 458 °C. The flow rate of the fuel salt in core and the secondary coolant are 2.42 m<sup>3</sup>/s and 2.84 m<sup>3</sup>/s, respectively. The design study has been done for the compact plate-fin type heat exchanger with fin thickness of 6 mm and fin pitch of 1.2 mm. This heat exchanger has the heat transfer rates of 31493 W/m<sup>2</sup>°C in the primary side and 34280 W/m<sup>2</sup>°C in the secondary side, where the heat transfer area of 420 m<sup>2</sup> and the effective height of about 540 mm are required. Taking into accounts the optimization expected in near future, the dimensions of heat exchangers has been determined to be outer radius of 220 cm, inner radius of 140 cm and the effective height of 60 cm, which is required to remove the total heat generated in the core. In the annular zone between inner and outer reflectors in the core vessel, three cooling lines, each of which consists of a cold-leg type pump and a segmented heat exchanger, have been arranged symmetrically to the vessel axis as shown in Fig. 10.1.1. The secondary coolant flows down through the outer annulus with width of 10 cm at velocity of 9.79 m/s.

The structures inside the core vessel are the lower plenum part and the cylinder supporting the inner reflector and the cooling components such as heat exchangers and primary pump. The lower plenum is the flat two-fold cylinders including the cooling pipes from the heat exchanger & pump to the core bottom and the drain tank for fuel molten salt dumping. The primary coolant flow goes up from inlet holes located at the lower plenum to upper outlet holes connecting with heat exchangers, cooling the target/core and the beam window. The thickness of cylindrical internal reflector for protecting the cooling components from high neutron flux may be decided on the base of results of neutronics calculations but is

desired to be not so thick from the viewpoint of heat removal. The bottom reflector like disc is embedded below the lower plenum. The upper reflector above the core vessel makes also the role of the shielding cover, on which the beam duct & beam window and the secondary coolant pipe line are installed. For replacing the internal installations the beam duct with the beam window is taken off to attach the machine removing the pump and heat exchanger with remote control, after the fuel molten salt has been dumped out from the core to the drain tank and covered by an inert gas.

This system configuration has been adjusted to have the core region with 120 cm in height and 220 cm in radius, including the inner reflector, compact heat exchanger and primary pump, and the top, bottom and outer reflectors in thickness of 20~40 cm with the beam window at the center of the top reflector. Figure 10.1.2 illustrates the vertical cross sectional view of total arrangement around the molten salt transmutation core.

#### References

- 1) Kato Y., et al. : Proc. OECD/NEA Specialist Meeting of Accelerator-based Transmutation (1992).
- 2) Takada H., et al. : JAERI-M 92-125, p.221(1992).
- 3) Takada H., et al. : JAERI-M 93-181, p.219 (1993).
- 4) Nishida T., et al. : Proc. ICENES' 93 (1993).
- 5) Katsuta H., et al. : Proc. OECD/NEA Inter. Inform. Exchan.Meeting, p.242 (1993).

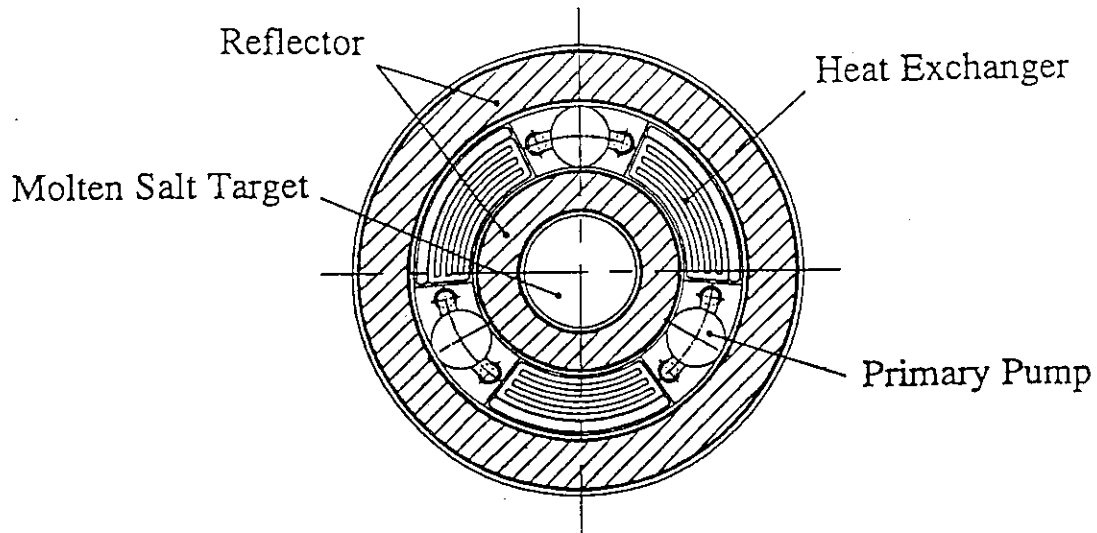


Fig.10.1.1

Arrangement of three primary cooling systems(heat exchanger, primary pump) installed in the core vessel

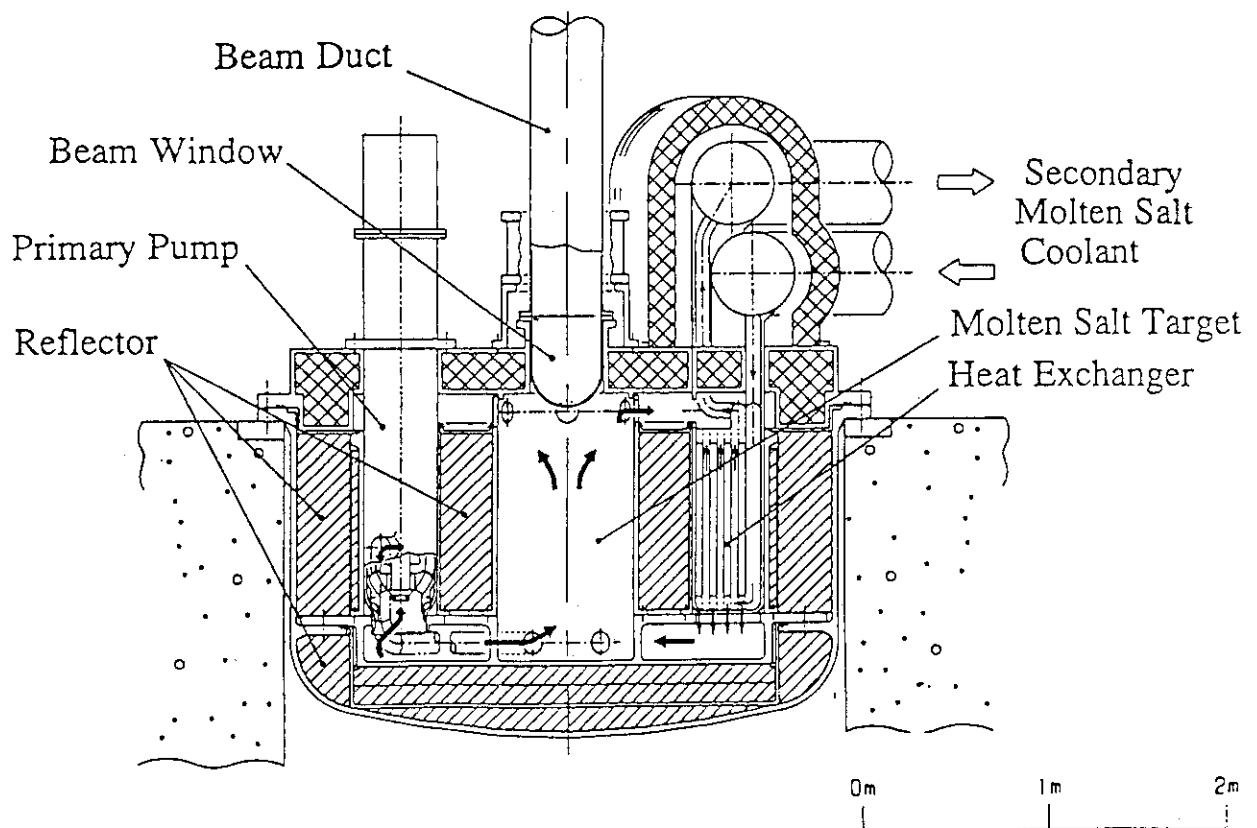


Fig.10.1.2

Vertical view around the MA molten salt transmutation core driven by a proton accelerator.

## 10.2 Conceptual Design of Accelerator-based Liquid TRU-alloy Target and Molten-salt Blanket Transmutation System

T. Sasa, K. Katsuta, T. Takizuka, T. Nishida, Y. Kato and H. Takahashi\*

Conceptual design of accelerator-based transmutation system with TRU-alloy target and molten-salt blanket is performed. This system is composed of a subcritical core driven by a high-current proton accelerator as illustrated in Fig.1. The core is composed of a liquid TRU-alloy target, blanket region with graphite moderator, molten-salt plenum and proton beam duct. Several tens of neutrons are produced by spallation reaction between target material and high energy proton. TRUs and some fission products (FPs) are transmuted in the target region by spallation reaction, fission reaction and neutron absorption reaction. In the blanket region, liquid TRU-alloy flows upward through the channels in graphite moderator with molten-salt flow. Heat and FPs produced by the reactions in the TRU-alloy are transferred to the molten-salt through the direct contact between the two liquids in the channel. The molten-salt is separated from the TRU-alloy liquid at the upper plenum due to the difference of density and led outside to external heat exchangers and FP separation processor as shown in Fig.1.

In this study, Pu-Co-Ce alloy which are researched in LAMPRE program<sup>1)</sup> at LANL are chosen for consideration. The alloy has the melting temperature around 450°C in the composition range of (15-45)Pu-25Co-(60-40)Ce in mol%. The chemical properties of plutonium and neptunium are very close, so plutonium in the alloy is considered to be easily substituted by neptunium without significant change in the melting temperature of the alloy. The composition ratio of plutonium to neptunium of 1 to 2.6 is adopted from the TRU fuel composition at the steady state of burning in the Actinide Burner Reactor<sup>2)</sup>. To transmute technetium, 1% of technetium was added to the alloy by substitution of cobalt, and we adopted the following composition for the liquid TRU-alloy, (11-32.5)Np-(4-12.5)Pu-24Co-(60-30)Ce-Tc.

Molten-salt of  $\text{Li}_2\text{BeF}_4$  studied in MSR program<sup>3)</sup> at ORNL is selected for coolant. Concentration of TRU in the molten-salt has to be low enough to reduce the leakage of TRU from the system components. Solubility of Pu ( $\text{PuF}_3$ ) in  $\text{Li}_2\text{BeF}_4$  was measured to be about 0.5 atomic percent at 600°C.

An effective neutron multiplication factor  $k_{\text{eff}}$  from 0.90 to 0.95 is preferred from the viewpoint of safety and transmutation effectiveness. The  $k_{\text{eff}}$  was calculated as a function of neptunium concentration in the TRU-alloy. The cascade simulation code NMTC/JAERI was

---

\* Brookhaven National Laboratory

used for the calculation in the energy range from 15 MeV to 1.5 GeV. In the energy range below 15 MeV, the calculation was performed with two-dimensional Sn code TWOTRAN-II with ENDF/B-IV. For a typical value of  $k_{\text{eff}}$  around 0.93, the composition of the TRU-alloy is represented by 12.5Np-4.8Pu-24Co-57.7Ce-Tc. For this composition, the 890 kg of TRU is loaded to the core and 16% of TRU is transmuted annually.

Neutron spectrum in core was also calculated by NMTC/JAERI and Monte Carlo transport code MCNP-4 with JENDL-3 as shown in Fig.2. The neutron spectrum in target region is as hard as those in the fast reactors and molten-salt plenum region has relatively high thermal neutron flux. In this result, transmutation of FPs is expected effectively in the molten-salt plenum region as well as that of TRUs in the target region.

Thermal-hydraulic performance of the core was calculated. The maximum power that can be removed from the core by forced circulation of the molten-salt coolant is 455 MWt based on the following parameters for the molten-salt of  $\text{Li}_2\text{BeF}_4$ ; the density of  $2000 \text{ kg/m}^3$ , specific heat of  $2300 \text{ J/kg}\cdot^\circ\text{K}$ , flow velocity of  $7 \text{ m/s}$  and temperature rise of  $200^\circ\text{K}$  through the blanket. The velocity of the liquid TRU-alloy driven by the molten-salt flow through blanket is calculated to be  $1.9 \text{ m/s}$ , assuming the friction factor of 0.16 at the interface of two fluids.

For the thermal power of 182 MW in the target region and 273 MW in the blanket region, the temperature rise of the liquid TRU-alloy is about  $200^\circ\text{K}$  through the target. Assuming the direct contact heat transfer coefficient of  $60,000 \text{ W/m}^2\cdot^\circ\text{K}$  between the two fluids, the liquid alloy temperatures at the blanket inlet and outlet are  $1250^\circ\text{C}$  and  $1050^\circ\text{C}$ , respectively, for the molten-salt inlet temperature of  $550^\circ\text{C}$ .

## References

- 1) Hannum W.H. and Kirkbride L.D. : LA-3384-MS (1966)
- 2) Mukaiyama T. and Gunji Y. : Proc. Information Exchange Meeting on Actinide and Fission Product Separation and Transmutation (1990)
- 3) McNeese L.E. : ORNL-5018 (1974)



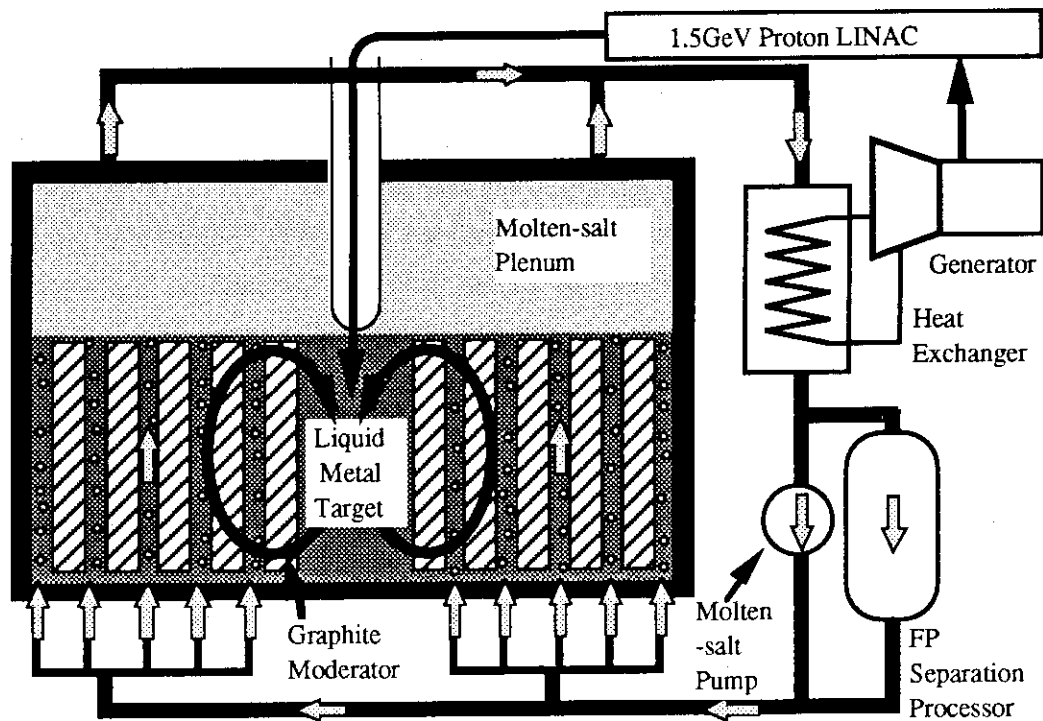


Fig.1 Accelerator-based Liquid TRU-alloy Target and Molten-salt Blanket Transmutation System

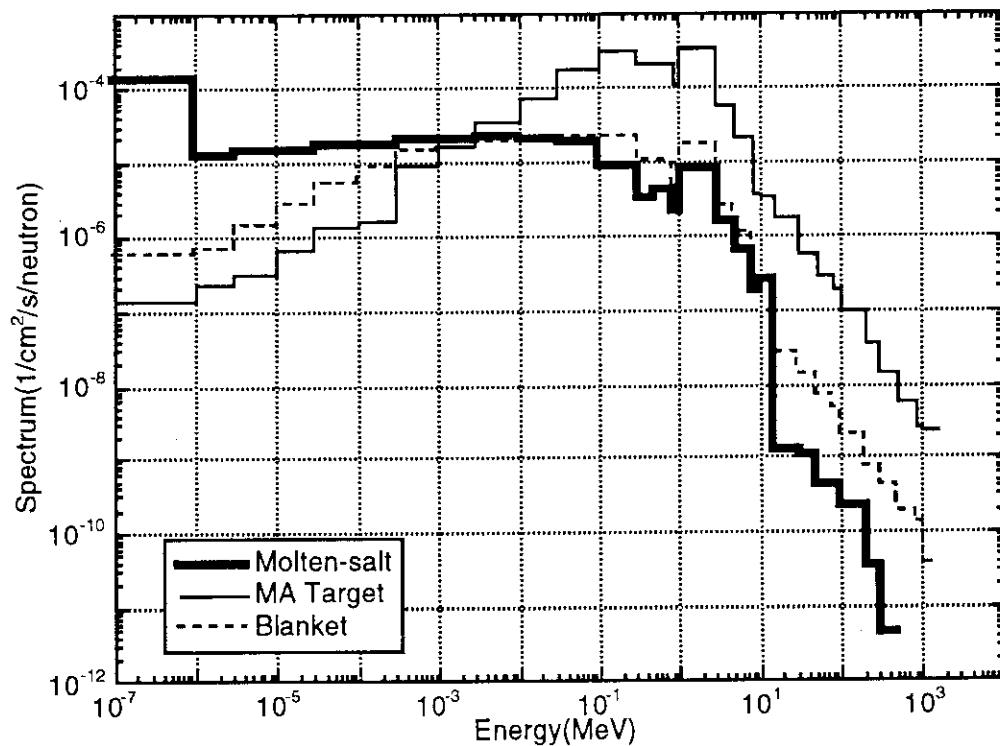


Fig.2 Calculated Neutron Spectrum by NMTC/JAERI and MCNP-4

### 10.3 Minor Actinide Burner Reactor and Influence of Transmutation on Fuel Cycle Facilities

T. Mukaiyama and T. Ogawa

Two concepts of minor actinide burner reactors were previously proposed by the authors, one with metal fuel core and the other with nitride particle fuel core. These reactors have very hard neutron spectrum and very high neutron flux which are effective and efficient for fissioning of minor actinides.<sup>1,2,3)</sup> In these burner reactors, however,  $\beta_{\text{eff}}$  was very small and the sodium void coefficient of a metal fuel reactor was positive and large. To improve the safety characteristics, the design of the original ABRs was modified.

In the new design, MA alloy fuel is replaced with the MA nitride fuel and sodium is replaced with liquid lead as a coolant. The nitride fuel can be processed with the pyrochemical reprocessing and hence, the fuel cycle facilities can be very compact. In the lead-cooled ABR with MA nitride fuel (L-ABR), coolant density coefficient is always negative.

To increase  $\beta_{\text{eff}}$ , uranium is added as a part of fuel material.  $^{238}\text{U}$  has the largest  $\beta$  value but is not adequate as fuel material of ABR because the ABR is a system to burn MA and  $^{238}\text{U}$  is a source nuclide of MA. In the modified ABR, therefore, Pu is replaced with enriched uranium.

The reactor design parameters of modified ABRs are summarized in Table 1.  $\beta_{\text{eff}}$  values and neutron generation time of the modified ABRs are significantly larger than those of the original ones. Significantly hard neutron spectra are also achieved. As far as the Doppler effect is concerned, no improvement was attained because only small amount of  $^{238}\text{U}$  is contained in the fuel and the neutron spectrum is very hard.

In Table 2, the transmutation characteristics are compared between two types of ABRs together with thermal and fast power reactors. For the MA transmutation in power reactors, the concentration of MA is limited to 0.2% and 5% of heavy metal for U-PWR and fast reactors, respectively so that the addition of MA will not affect major reactor design parameters such as enrichment, coolant void coefficient etc.

The negative value of burnup ratio of U-PWR implies the more MA generation than MA burnup. The large discrepancy between transmutation ratio and burnup ratio in power reactors indicates the larger conversion of Np into Pu than in ABRs. The net MA burnup per 1GWt a year of ABRs is significantly larger than that of power reactors because in ABRs the major fuel material is MA.

For the MA transmutation using power reactors, not only reactor performance and fuel manufacturing but also the influence of transmutation on the fuel cycle facilities should be taken into account. To evaluate the effect of MA addition to the fuel, the analysis was carried out to calculate the increase of decay heat, neutron emission, and  $\gamma$ -ray intensity. In Table 3, the effect of MA addition to the fuels of power reactors, namely, U-PWR, MOX-PWR and FBR, is summarized. In this analysis, the effect of MA addition was calculated for both fresh and spent fuel. The increase of decay heat is caused by the generation of  $^{244}\text{Cm}$  and the increase of neutron emission is caused by the generation of higher Cm isotopes and  $^{252}\text{Cf}$ .

As a result of increase of these Cm, Cf, for all of the MA transmutation scheme in power reactors shown in Table 3, the radiation shielding design change will be needed not only for the fresh fuel handling (manufacturing and transportation) but also for the spent fuel handling (transportation and reprocessing). This may cause the increase of cost of the electricity generation. In the case of ABRs, the shielding and the decay heat removal are much severer problem than the MA transmutation in power reactors since the concentration of MA is very high in ABRs. The fuel cycle facilities for

ABRs, however, are very compact and the required number of these facilities is small because nitride fuel can be reprocessed by pyrochemical process and the amount of material to be handled is smaller compared with those of conventional fuel cycles. Therefore, the economy of MA transmutation may be favorable for the ABRs even if the resources required to develop ABRs are larger those that for MA transmutation in power reactors.<sup>3)</sup>

#### References

- 1) T. Mukaiyama, Y. Gunji: "Characteristics of minor actinide transmutation in minor actinide burner reactors and power reactors", Proc. of Information Exchange Meeting on Actinide and Fission Product Separation and Transmutation, OECD/NEA, p326(Mito, 1991).
- 2) T. Mukaiyama, T. Takano, T. Takizuka, T. Ogawa and M. Osakabe: "Conceptual study of actinide burner reactors", Proc. Int. Reactor Physics Conf. (Jackson Hole, 1988), Vol. IV, p369.
- 3) T. Mukaiyama, H. Yoshida and Y. Gunji: "Minor actinide transmutation using minor actinide burner reactors", Proc. Int. Conf. on Fast Reactors and related Fuel Cycles "FR'91", Vol. II, 19-6 (Kyoto, 1991).

Table 1 Reactor design parameters of modified Actinide Burner Reactors

	L-ABR <sup>1)</sup>	P-ABR <sup>2)</sup>
Fuel concept	pin-bundle	coated particle
material	(64NpAmCm-36U <sup>3)</sup> ) <sub>1.0</sub> N <sup>4)</sup> <sub>1.0</sub>	(65NpAmCm-35U <sup>3)</sup> ) <sub>1.0</sub> N <sup>4)</sup> <sub>1.0</sub>
MA initial loading, kg	918	2870
MA/U	588/330	1865/1005
Reactor power, MWth	180	1200
Coolant material	Lead	Helium
Neutron flux, 10 <sup>15</sup> n/cm <sup>2</sup> · sec	3.1	6.6
Core averaged mean neutron energy, keV	700	700
Reactivity (% δk/k)		
Coolant-void reactivity/core	-1.3	----
Doppler reactivity/core (δt=300℃)	-0.01	-0.01
Kinetic parameters		
$\beta_{\text{eff}}$	2.6x10 <sup>-3</sup>	2.6x10 <sup>-3</sup>
$L_p$ , sec	1.3x10 <sup>-7</sup>	1.5x10 <sup>-7</sup>
Cycle length, full-power days	550	300
MA burnup, %/cycle	11	13

1) L-ABR:MA nitride fuel with lead cooling burner reactor

2) P-ABR :MA particle fuel with He cooling burner reactor

3) 90% enriched uranium

4) <sup>15</sup>N enriched

Table 2 Comparison of MA transmutation in various reactors

		MA Burner Reactors		Power Reactors		
		L-ABR	P-ABR	U-PWR	MOX-FBR	LMR <sup>1)</sup>
Output	(MWt)	180	1200	3410	2600	2632
Cycle length <sup>2)</sup>	(EFPD)	550	300	850	1368	900
Core averaged						
Fast neutron flux	( $\times 10^{15} \text{n/cm}^2 \cdot \text{s}$ )	3.1	5.9	0.37	4.1(3.0)*	6.1(4.1)*
Mean neutron energy	(keV)	720	720	thermal	480	490
MA loaded	(kg)	573	1865	180 <sup>3)</sup>	1450 <sup>3)</sup>	1200 <sup>3)</sup>
MA transmutation ratio <sup>4)</sup>	(%/cycle)	16.0	18.8	9.0	33.5	29.8
MA burnup ratio <sup>5)</sup>	(%/cycle)	11	13	-23.8	8.8	8.3
MA transmutation	(kg/1GW · year)	278	292	1.7	40.9	44.5
MA burnup	(kg/1GW · year)	191	202	-4.4	10.7	12.4

1) Metal fuel FBR

2) Effective fuel irradiation time

3) Concentration of MA in fuel ; 0.2% for U-PWR, 5% for MOX-FBR and LMR

4) MA transmutation ratio = {MA(BOC) - MA(EOC)} / MA(BOC)

5) MA burnup ratio = (MA fissioned - MA generated) / MA(BOC)

Values of 4) and 5) are those for the equilibrium cycle in ABRs, and average values of 1 to 10th cycle for power reactors.

\*) Values in the parentheses are for the outer core

Table 3 Effect of MA addition to power reactor fuel handling

Reactor/Fuel	Ratio of value of MA added fuel to that of normal fuel		
	Decay heat	Neutron emission	Photon intensity
U-PWR (0.2wt%) <sup>a</sup>			
fresh fuel(U235:4wt%) <sup>b</sup>	$3.6 \times 10^3$	$8.3 \times 10^4$	$1.3 \times 10^3$
spent fuel(45GWD/t) <sup>c</sup>	1.5	4	1
MOX-PWR (0.5wt%)			
fresh fuel(Pu:6.5wt%)	1.4	4.8	1.2
spent fuel(45GWD/t)	1.5	1.7	1
MOX-FBR (5wt%)			
fresh fuel(Pu:30wt%)	2.2	$1.0 \times 10^2$	2.1
spent fuel(80GWD/t)	2.8	19	1

a: minor actinides(MA) fraction in fuel (HM weight %)

b: fuel enrichment

c: fuel burnup (cooling time : 10 years)

## 10.4 Overall Assessment of Partitioning Process (I) : Status of Partitioning Technology

Y. Kondo and T. Takizuka

In order to collect a good grounding in assessment of the partitioning process, present and future trends on the partitioning technology were surveyed. Technical feasibility of the partitioning process was discussed for some scenarios to reduce the hazard associated with waste management.

### (1) Partitioning for volume reduction of high level waste glass

If Mo (major constituent of yellow phase) and Sr and Cs (heat generated nuclides) could be separated from high level liquid waste (HLLW) prior to vitrification, volume of the vitrified waste would have been minimized. The present status of partitioning technology may be matured enough to accomplish this scenario<sup>1)</sup>.

### (2) Partitioning for lightening the burden of high level waste management

Separation of long-lived nuclides such as TRU makes it possible to lighten the burden of high level waste management, because the volume of TRU waste would be extremely reduced. TRU can be separated from HLLW by several solvent extraction processes, such as DIDPA process<sup>2)</sup>, TRUEX process<sup>3)</sup>, HDEHP process<sup>4)</sup> and CTH process<sup>5)</sup>. This scenario also appears to be feasible based on the use of currently identified partitioning technology.

### (3) Partitioning and transmutation option as an alternative waste management strategy

The permanent presence of very toxic radio nuclides for thousands of years in geologic repositories was deemed a risk, which ought to be avoided. Alternative scenarios comprising the separation of TRU from HLLW (partitioning) and transmutation of these nuclides in LWR, FBR and HTGR received considerable attention. Fig.10.4.1 shows the schematic diagram of P-T (partitioning-transmutation) fuel cycles. P-T cycle normally requires two partitioning process, partitioning process for LWR fuel and transmutor fuel, because the chemical and physical properties of transmutor fuel are very different from LWR fuel.

Some solvent extraction processes, which were attached to the PUREX process through the high level liquid waste, have been designed as the partitioning process for LWR fuel in the U.S., Europe and Japan. DIDPA process<sup>2)</sup>, TRUEX process<sup>3)</sup>, HDEHP process<sup>4)</sup> and CTH process<sup>5)</sup> had been proposed as the partitioning process for LWR fuel in the 1970s and 1980s. The chemistry of different partitioning methods for the HLLW has been extensively tested in the laboratory. The separation of TRU appears to be feasible using processing technology that has been experimentally verified at the laboratory level and much of which has been verified at the hot, production-scale level. The engineering data,

concerned about separation efficiency, amount of secondary waste, decomposition rate of solvent and so on, have been accumulated at JAERI.

It is desired that the partitioning process for the transmutor fuel should be designed as the process exclusive to the individual transmutation system. An alternative partitioning technology based on pyrometallurgical processing received considerable attention. The pyrometallurgical process has many advantages such as simple operation, low amount of secondary waste, compact body and high critical safety. The pyrometallurgical processing of metallic fuels for the Integral Fast Reactor (IFR)<sup>6)</sup> and a pyrometallurgical partitioning process for aqueous HLLW<sup>7)</sup> have been proposed in U.S. and Japan. These processes involve electrorefining of spent fuel by a cadmium anode, solid and liquid cathodes, and a molten salt electrolyte (LiCl - KCl) at 500°C. It is obvious that these process are still in the exploratory stage and cannot yet be considered as proven, even at the conceptual level. The pyrometallurgical process has the advantage involve to no water mixture which is favorable for critical safety but are very sensitive to oxygen and moisture ingress into the equipment. The technical data concerned about pyrometallurgical process have been accumulated in U.S. and Japan. These efforts will soon prove the technical feasibility of the pyrometallurgical process.

#### References

- 1) Horner D.E., et al.: Nucl. Sci. Eng., 17, 234(1963).
- 2) Morita Y., Tani S. and Kubota M.: Proc. International Symposium Advanced Nuclear Energy Research - Near-Future Chemistry in Nuclear Energy Field -, 234 (1989).
- 3) Horwitz E.P. and Schulz W.W.: Proc.Int.Meeting on Solvent Extraction and Ion Exchange AERE. Harwell. Conf. 85-09-47-2, DE-85, 009647, 137(1985).
- 4) Mannone F. and Dworschak H.: CEC-JRC report SA/-1-07-03-84-02, (1984).
- 5) Lilijenzin J.O., et al.: Int. Solvent Extr. Conf., 3, 1(1980).
- 6) Battles J.E., Miller.W.E. and Gay E.C.: Am. Nucl.Soc. Meeting 1991 ,342(1991).
- 7) Inoue T. and Tanaka H.: *Kinzoku*, 1990-9, 36(1990). (in Japanese)

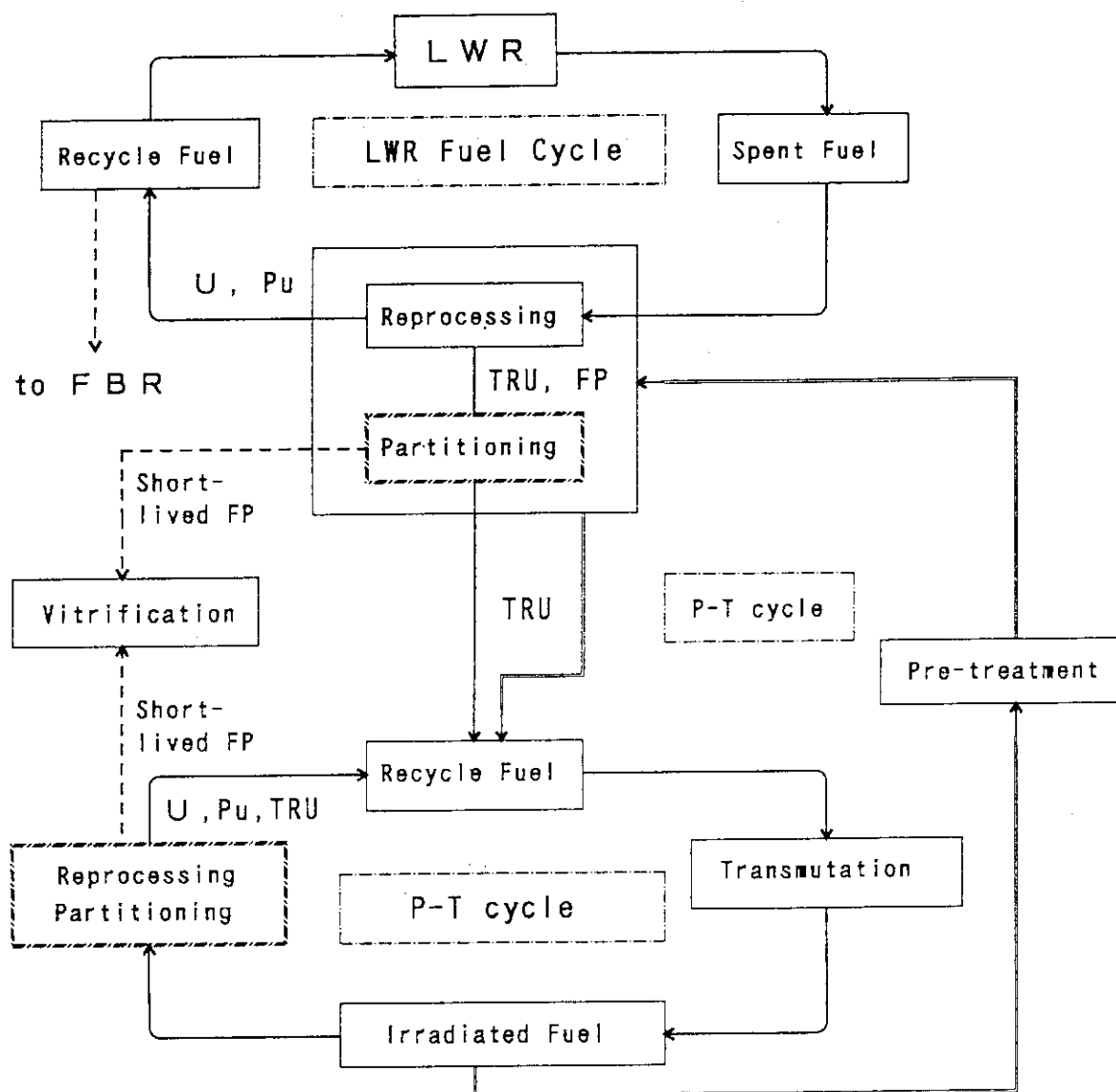


Fig.10.4.1 Schematic diagram of P-T cycle

## 10.5 Benchmark Calculations for the Cascade Codes NMTC/JAERI and NUCLEUS

T. Nishida, H. Takada, N. Yoshizawa\*, Y. Nakahara, K. Ishibashi\*\*,  
H. Kadotani\*\*\* and E. Suetomi\*\*\*

Several benchmark calculations have been carried out to examine and upgrade the accuracy of predictions calculated by the Monte Carlo Cascade codes NMTC/JAERI<sup>1)</sup> and NUCLEUS<sup>2)</sup>, which were developed for a target and a nucleus calculations respectively at JAERI and are used for the accelerator-based transmutation research.

The subroutines calculating the high energy fission reaction<sup>3)</sup> in the spallation cascade process using the Nakahara model has been transplanted from NMTC/JAERI into the HERMES code system including another cascade code HETC/KFA2 with the Atchison's fission model, to directly intercompare both model's predictions of reaction products computed under the same parameter conditions for nuclear reactions except fission. The mass distributions of yield of reaction products and the intensity of emitted particles in the cascade process have been computed for thin and thick targets of uranium and neptunium metals irradiated by protons with the incident energies of 590, 800 and 1500 MeV. Figure 10.5.1 shows the mass distributions of spallation and fission products calculated by using both fission models for a thin neptunium target irradiated by a 800 MeV proton. The Nakahara model gave the asymmetric mass distribution of fission products with long tail creeping under the evaporation component above the mass number  $A = 150$ , while Atchison model predicted the symmetric mass distribution of fission products around  $A = 100$  with the higher maximum and less evaporation components than the Nakahara model. This result implies that the Atchison model gives higher ratio of fission width to neutron emission width than the Nakahara model does. The discrepancy should be adjusted by comparing these calculation data with more accurate experimental ones which may be measured in the near future. In the intensities of emitted neutrons in the cascade process, there are no differences between both models.

The nucleon-nucleon inelastic scattering cross sections with one pion production, the pion-proton elastic scattering cross section and the recoil nucleon Double Differential Cross sections (DDX), which are used in the intranuclear cascade calculation, were calculated on the basis of the recent phase shift data analyzed by the partial wave method.<sup>4),5)</sup> The original NMTC data, compiled several tens years ago by Bertini et al.<sup>6)</sup> have been replaced by these

---

\* Mitsubishi Research Institute Inc.

\*\* Faculty of Engineering, Kyushu University

\*\*\* Century Research Center, Inc.



new cross sections. The benchmark calculations were made for the energy spectre of emitted neutrons and the mass distribution of reaction products using the new data and the Bertini's ones of inelastic scattering cross sections when a 800 MeV proton is injected on the lead bulk as seen in Fig 10.5.2. The significant differences between them have not been observed for both mass distribution and neutron spectra. So update of these cross sections gives little influences on the number of neutrons escaped from the heavy metal target such as a tungsten bulk used in the transmutation system.

On the other hand the DDXs for neutron emission induced by a 80 MeV proton incidence on a zirconium nucleus,<sup>7)</sup> which were calculated by NUCLEUS and HETC/3STEP, have been compared with experimental one<sup>8)</sup> as shown in Fig. 10.5.3 (a). In the spectrum at the forward emission angle of 25° above 20 MeV, these codes overpredict the experimental DDX by a factor of 2. This discrepancy results from the fact that the quasi-elastic p-n collision cross section used in the intranuclear cascade calculation is estimated to be too large. The calculations reproduce the experimental data at 45° quite well even above 20 MeV. In the spectrum at the backward emission angles of 95° and 145° above 20 MeV, NUCLEUS underpredicts the experimental result by about one order of magnitude, while the HETC/3STEP code achieves the good agreement with the experimental one. On the contrary DDXs for proton emission in the case of the same proton incident energy and nucleus are compared in Fig. 10.5.3 (b). The calculation results agree with the experimental data at 25°. By taking the preequilibrium emission process in the 2 step intranuclear cascade model into account, HETC/3STEP has reproduced the proton DDX at the backward emission angles of 95° and 145° above 20 MeV better by one order than NUCLEUS. As seen from these results, NUCLEUS gives the yield of nucleons emitted below 15 MeV much larger than HETC/3STEP.

## References

- 1) Nakahara Y. and Tsutsui T. : JAERI-M 82-198 (1982)
- 2) Nishida T., Nakahara Y. and Tsutsui T. : JAERI-M 86-116, (1986)
- 3) Nishida T., Takada H., Nakahara Y., Takizuka T., Yoshizawa N. and Iwai S. : PSI Proc. 92-02, ISSN 1019-6447, p.535 (1992).
- 4) Arndt R. A. and L. D. Roper L. D. : Phys. Rev. D, 28(1), p.97 (1983).
- 5) Arndt R. A., et al. : Phys. Rev. D, 35(1), p.128(1987).
- 6) Bertini H.W. : Phys. Rev., 131, p.1801 (1963).
- 7) Takada H., et al. : Jour. Nucl. Sci. Technol. 31(1), p. 80-82 (1994).
- 8) Trabandt M., et al. : Phys. Rev. C, 39, p.452(1989).

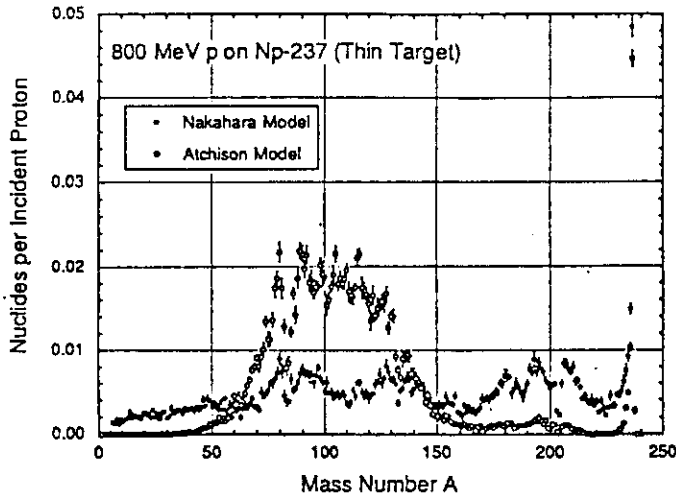


Fig. 10.5.1

Mass distributions of spallation products  
calculated by both fission models

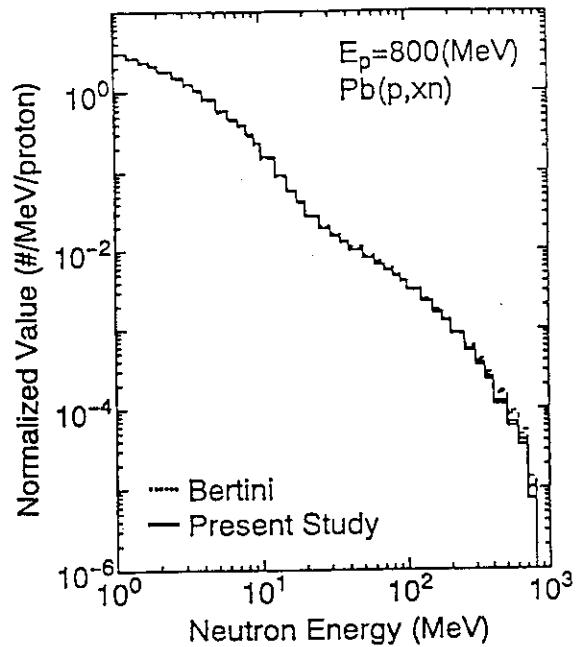


Fig. 10.5.2

Neutron energy spectra calculated on the  
basis of old and new cross section data

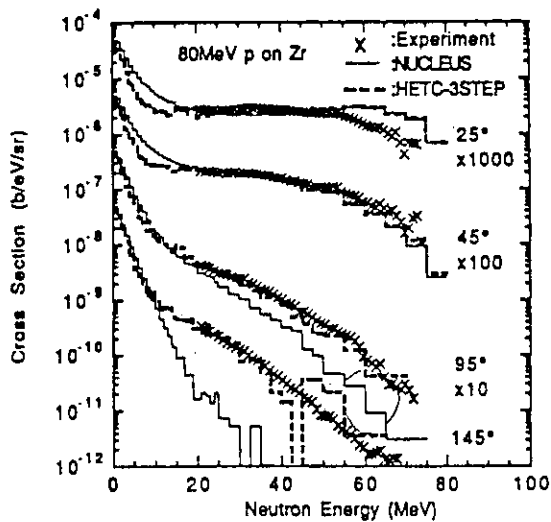


Fig. 10.5.3 (a)

Neutron DDX for 80 MeV proton incidence  
on a Zr nucleus

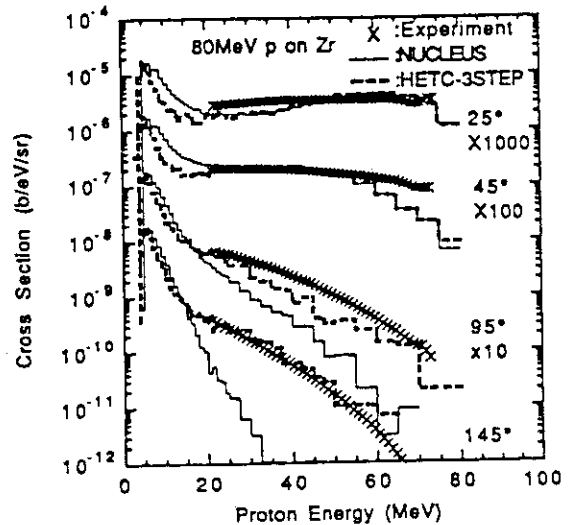


Fig. 10.5.3 (b)

Proton DDX for 80 MeV proton incidence  
on a Zr nucleus

## 10.6 Investigation of Nuclide Production Cross Sections for the Analysis of Integral Spallation Experiment.

H. Takada, T. Fukahori, K. Hasegawa, T. Sasa and S. Meigo

An integral spallation experiment with a lead assembly has been performed at the 500 MeV booster proton synchrotron facility of National Laboratory for High Energy Physics. The size of the assembly is 60 cm in diameter and 100 cm in length. The tungsten target of 16 cm in diameter and 30 cm in length is installed in the assembly. Protons are injected perpendicularly on the target through the beam incident hole of 10 cm in diameter and 20 cm in length. In order to study the transport phenomenon of spallation neutrons in the assembly, the activation method with high purity metallic samples was employed. The experimental procedure is the same as that described in the previous report<sup>1)</sup>. The spatial distribution of the reaction rates of nuclide production in Nb and Pb samples has been obtained in FY-1993. A detailed calculation has also been carried out to study the accuracy of Nucleon Meson Transport Code NMTC/JAERI<sup>2)</sup>.

In the calculation, the assembly is divided into 5 regions for radial direction and 40 for axial one. The interval of a cell was chosen to be 1.5 cm in width and 2.5 cm in length for a position at which samples were placed. In order to estimate neutron flux at the sample position, the Monte Carlo codes of NMTC/JAERI and MCNP-4.2<sup>3)</sup> were employed. NMTC/JAERI simulates the transport of nucleons and mesons with the energy higher than 20 MeV and MCNP-4.2 treats neutron transport below 20 MeV. The following energy group structure was employed: 20 groups with the lethargy width of 0.05 from 20 to 70 MeV and 30 groups with the lethargy width of 0.075 above 70 MeV. The reaction rates of nuclide production in the samples are given by the product of the value of the neutron flux and the nuclide production cross section. The nuclide production cross sections were calculated values with NUCLEUS<sup>4)</sup> which is the nuclear reaction calculation part of NMTC/JAERI in the energy region above 20 MeV because of lack of evaluated data, whereas the cross sections in JENDL 3.1 were used for the energy region below 20 MeV. For comparison, the nuclide production cross section was calculated with the codes of ALICE-85<sup>5)</sup> and ALICE-F<sup>6)</sup>.

The calculated production cross sections of  $^{57}\text{Ni}$ ,  $^{56}\text{Co}$  and  $^{54}\text{Mn}$  from  $\text{natNi}$  are shown in Figs.10.6.1 to 10.6.3, respectively. The calculated and the experimental reaction rates at a radial position of 10 cm are compared in Figs.10.6.4 to 10.6.6 for the reactions of  $\text{natNi}(n,x)^{57}\text{Ni}$ ,  $\text{natNi}(n,x)^{56}\text{Co}$  and  $\text{natNi}(n,x)^{54}\text{Mn}$ . For the production cross section of  $^{57}\text{Ni}$ , ALICE-F does not estimate the cut off energy correctly. This code gives lower reaction rate than NUCLEUS. For the reaction rate of  $^{56}\text{Co}$ , ALICE-F and NUCLEUS give almost the

same results. The calculations overestimate by about 60% for the reactions of  $^{nat}\text{Ni}(n,x)^{57}\text{Ni}$  and  $^{nat}\text{Ni}(n,x)^{56}\text{Co}$  in comparison with the experiment. On the other hand, the calculation underestimates the experimental reaction rate of  $^{54}\text{Mn}$ . It is confirmed that the results of ALICE-85 deviate from the experimental ones further than those of ALICE-F and NUCLEUS.

It is found from this study that the calculated results of ALICE-F and NUCLEUS agree with the experimental ones with a factor of 2 for the reaction rates in Ni samples. Further investigations are required because there still remains some differences between the calculated nuclide production cross sections.

## References

- 1) Takada H., et al.: JAERI-M 93-181, 210(1993).
- 2) Nakahara Y. and Tsutsui T.: JAERI-M 82-198 (1982).
- 3) Driesmeister J. F.: RSIC-CCC-200 (1991).
- 4) Nishida T. et al.: JAERI-M 86-116 (1986).
- 5) Blann M.: UCID, 20169 (1985).
- 6) Fukahori T.: JAERI-M 92-039, 114 (1992).

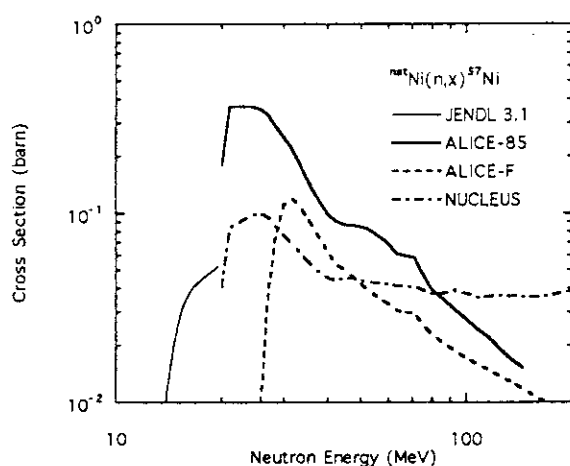


Fig.10.6.1 Production cross section of  $^{57}\text{Ni}$  from  $^{nat}\text{Ni}$ .

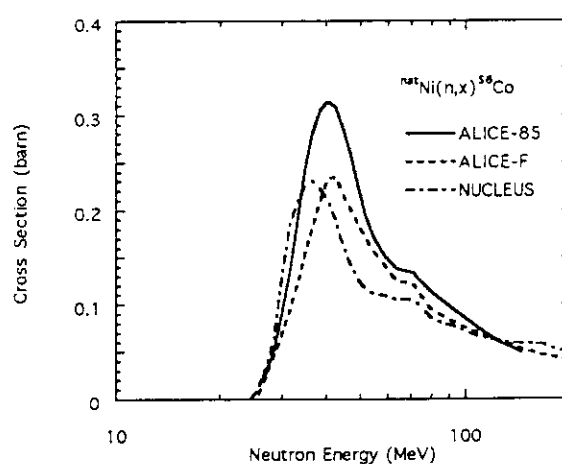


Fig.10.6.2 Production cross section of  $^{56}\text{Co}$  from  $^{nat}\text{Ni}$ .

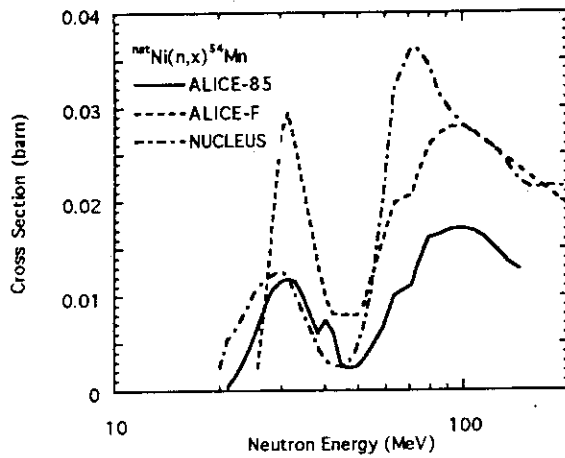


Fig.10.6.3 Production cross section of  $^{54}\text{Mn}$  from  $\text{natNi}$ .

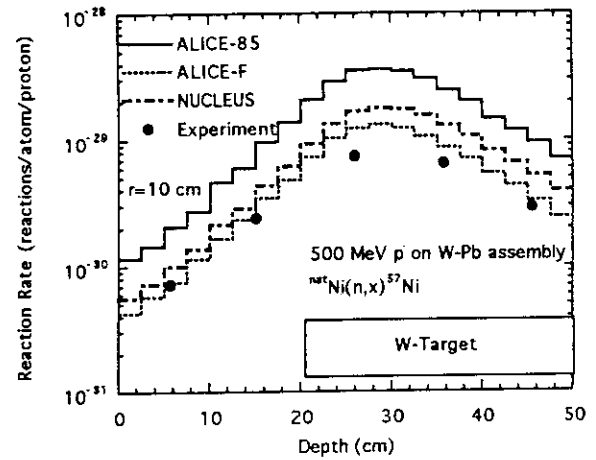


Fig.10.6.4 Experimental and calculated reaction rate of  $^{57}\text{Ni}$  production in  $\text{natNi}$  sample at radial position of 10 cm for 500 MeV proton incidence on tungsten target installed in lead assembly.

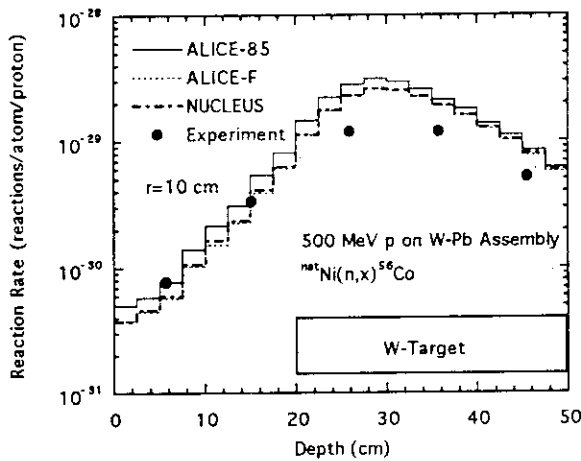


Fig.10.6.5 Experimental and calculated reaction rate of  $^{56}\text{Co}$  production in  $\text{natNi}$  sample at radial position of 10 cm for 500 MeV proton incidence on tungsten target installed in lead assembly.

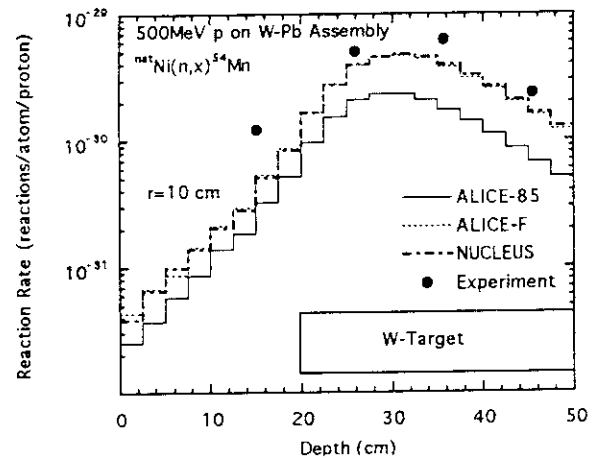


Fig.10.6.6 Experimental and calculated reaction rate of  $^{54}\text{Mn}$  production in  $\text{natNi}$  sample at radial position of 10 cm for 500 MeV proton incidence on tungsten target installed in lead assembly.

## 10.7 Measurements of Neutron-Production Double-Differential Cross Sections for Incident Protons of 0.8, 1.5 and 3.0 GeV

S. Meigo, H. Takada, S. Chiba, K. Ishibashi\*, T. Nakamoto\*, N. Matsufuji\*,  
K. Maehata\*, N. Shigyo\*, Y. Wakuta\*, Y. Watanabe\*\*, M. Numajiri†  
and T. Nakamura‡

In order to ensure and improve the nucleon-meson transport calculation codes which are used for the neutronics calculation of the accelerator driven actinide transmutation system, we started the measurement of neutron-production cross section for the reaction (p,xn) by the GeV region protons which were supplied by the  $\pi$  2 beam line at National Laboratory for High Energy Physics (KEK). In 1992, we obtained the data for C and Pb target using 0.8, 1.5 and 3 GeV protons.<sup>1)</sup> For covering a variety of wide target materials, the measurement was carried out with the targets of Al, Fe, and In. A cross section calculation has also been made with the HETC<sup>2)</sup> code which is a nucleon-meson transport calculation code based on the intranuclear-cascade and evaporation (INCE) model. The calculated results are compared with the measured ones.

The time of flight (TOF) method was used to measure energy spectra of neutrons from the target. NE-213 scintillators with different sizes ( $\phi 5'' \times 5''$  and  $\phi 2'' \times 2''$ ) were employed as neutron detectors. The experimental arrangement is illustrated in Fig. 10.7.1. The intensity of the incident protons was about  $10^5$  particles/pulse. Because the protons and the pions were generated as the secondary particles at an internal target placed in the accelerator ring of the 12 GeV proton synchrotron, the incident protons were distinguished from pions using a pair of TOF scintillators (Pilot U) located at a separation distance. Veto detectors were installed in front of all neutron detectors in order to reject charged-particle events in the neutron detectors.

The detection efficiency of the neutron detectors was calculated using the SCINFUL<sup>3)</sup> code for the energy region below 80 MeV. Above 80 MeV neutrons, the efficiency was calculated by the Cecil<sup>4)</sup> code of which the result was modified to smoothly connect to that of SCINFUL at 80 MeV. This calculated efficiency agrees with the data measured at LANL<sup>5)</sup> within 10%. This efficiency was employed to determine the neutron spectrum.

The Al, Fe and In targets were 15, 18 and 20 g/cm<sup>2</sup> thick respectively. The neutron scattering effect in the target, which distorted the measured value, was evaluated with the HETC code and was found to be several percent for the double differential cross section.

---

\* Department of Nuclear Engineering, Kyushu University

\*\* Department of Energy Conversion, Kyushu University

† National Laboratory for High Energy Physics (KEK)

‡ Cyclotron RI Center, Tohoku University

Since the experimental error was larger than the contribution of the scattering effect, the experimental data were not corrected for this effect.

The present data of double differential cross section (DDX) are shown with the calculated results in Figs. 10.7.2 to 10.7.7. For the incident protons energy of 0.8 GeV, the calculated results are in good agreement with the experimental ones. The agreement is better for the results of In than for those of Al and Fe. With increasing protons energies to 3 GeV, the HETC code overestimates the neutron production DDX in the energy region around 10 MeV. The discrepancy is commonly observed in all directions.

#### References

- 1) Ishibashi K., et al. : JAERI-M 93-046, p.82 (1992).
- 2) Cloth P., et al. : "HERMES, High Energy Radiation Monte Carlo Elaborate System", KFA-IRE-E AN/12/88 (1988).
- 3) Dickens J.K. : "SCINFUL: A Monte Carlo Based Computer Program to Determine a Scintillator Full Energy Response to Neutron Detection for En Between 0.1 and 80 MeV", ORNL-6462 (1988).
- 4) Cecil R.A., Anderson B.D. and Madey R. : Nucl. Instr. Meth., 161, 439 (1979).
- 5) Meier M., et al. : Nucl. Sci. Eng., 110, 289 (1992).

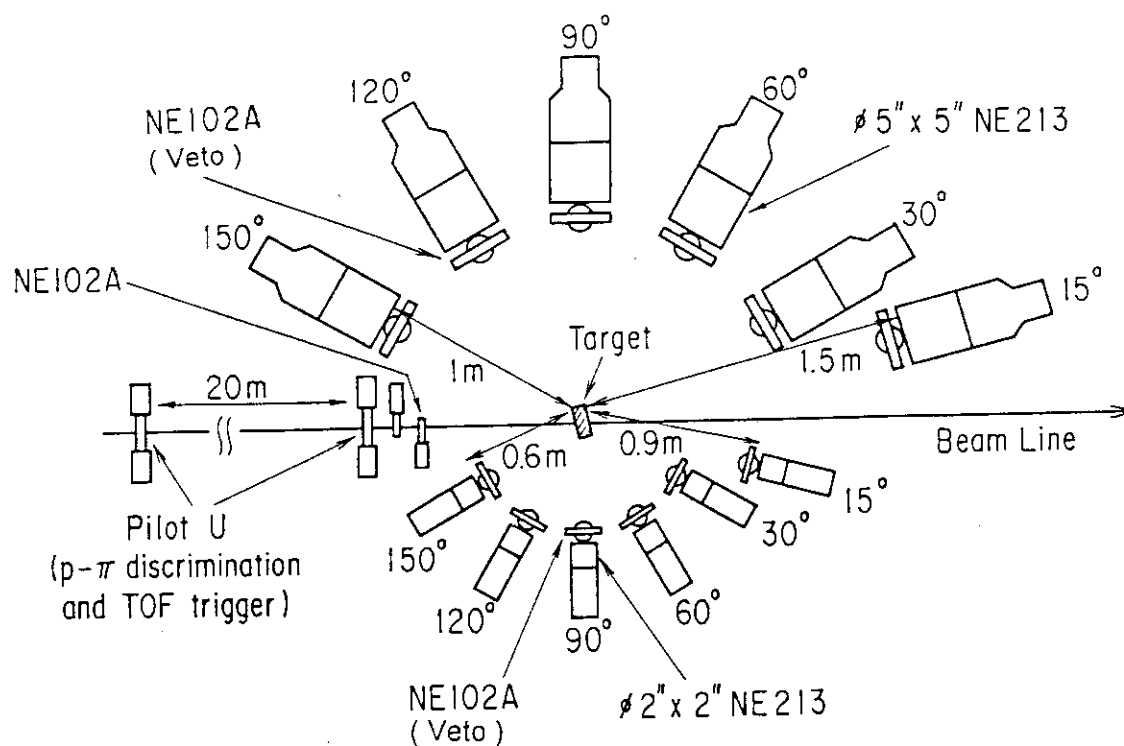


Fig. 10.7.1 Illustration of the experimental arrangement.

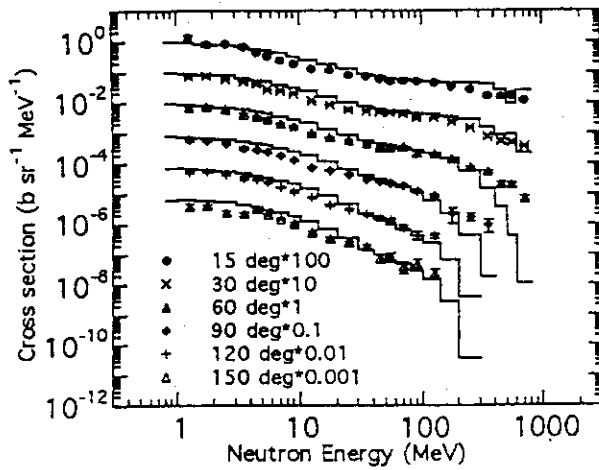


Fig. 10.7.2 DDX of Al at 0.8 GeV. Lines show calculation results by HETC.

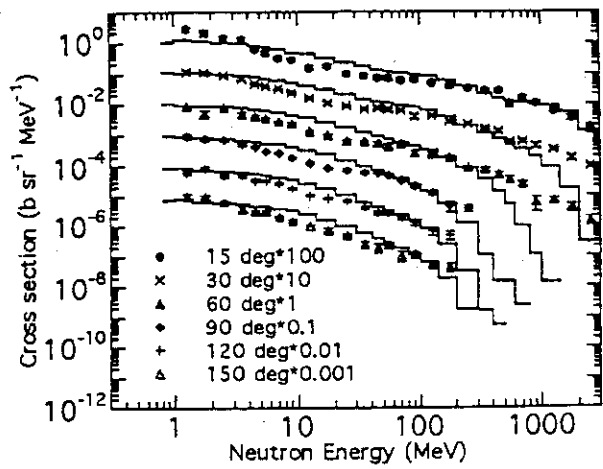


Fig. 10.7.3 DDX of Al at 3.0 GeV. Lines show calculation results by HETC.

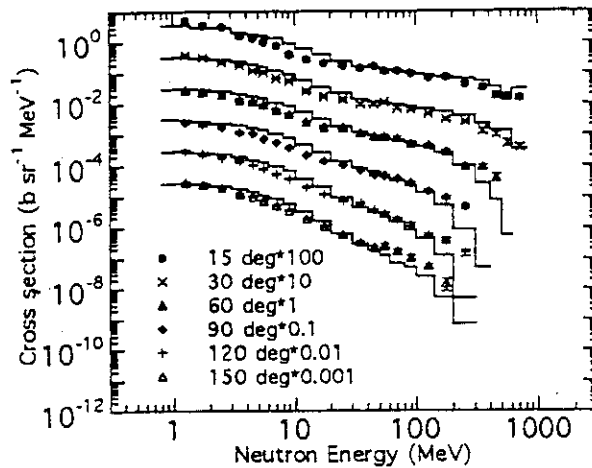


Fig. 10.7.4 DDX of Fe at 0.8 GeV. Lines show calculation results by HETC.

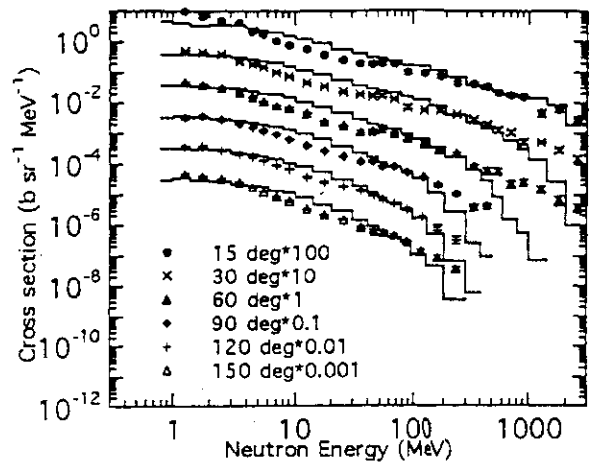


Fig. 10.7.5 DDX of Fe at 3.0 GeV. Lines show calculation results by HETC.

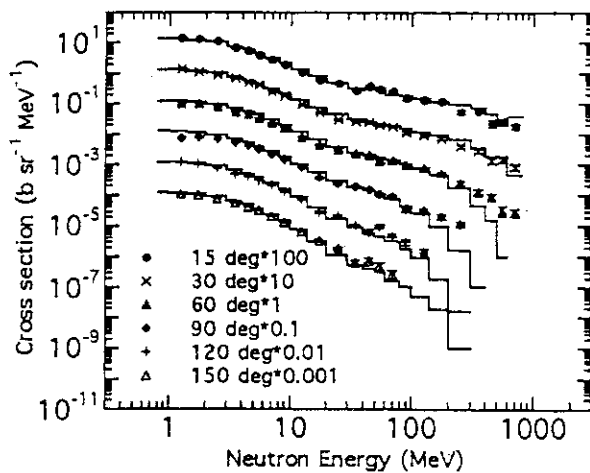


Fig. 10.7.6 DDX of In at 0.8 GeV. Lines show calculation results by HETC.

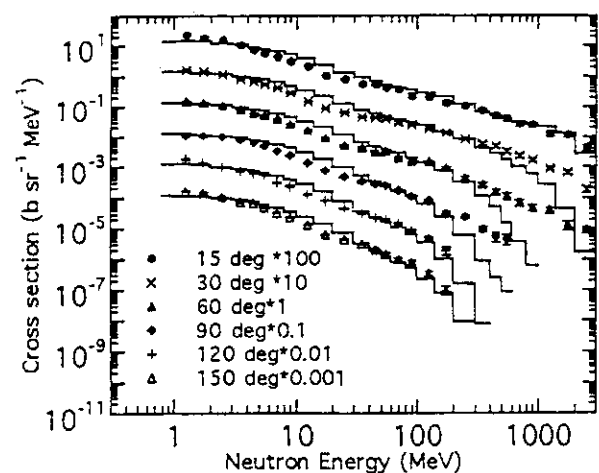


Fig. 10.7.7 DDX of In at 3.0 GeV. Lines show calculation results by HETC.



## 10.8 Measurements of the Absolute Detection Efficiency of NE-213 Scintillator for 20-100 MeV Neutrons

S. Meigo, H. Nakashima, S. Chiba and S. Tanaka

In the experimental determination of neutron spectrum by using an organic scintillator, is often used the detection efficiency calculated by such codes as SCINFUL<sup>1)</sup> and Cecil<sup>2)</sup>. In the energy range above 20 MeV, the calculated efficiency is less accurate than in the energy range below 20 MeV, because of the inaccurate library cross sections for the carbon and of the uncertain light output data of the charged particles. In order to verify the calculation accuracy, the absolute efficiency and the response function of the NE-213 scintillator are measured at a neutron energy 65 MeV.

The measurement was carried out at TIARA (Takasaki Ion Accelerator for Advanced Radiation Application) with 65 MeV quasi-mono-energetic neutrons produced by the  ${}^7\text{Li}(p,n){}^7\text{Be}$  reaction. The experimental arrangement is shown in Fig. 10.8.1. A time of flight (TOF) method was applied to neutron spectrum measurements by a NE-213 scintillator of 5" dia. and 5" thick. The bias level of the detector was set to a half-height of the Compton edge of  ${}^{60}\text{Co}$   $\gamma$ -ray. In order to measure absolute flux of the mono-energetic neutron, a proton-recoil telescope (PRT) is used, because its detection efficiency is calculated precisely relying only on the well-known n-p scattering cross section and the geometry.

The response of the NE-213 scintillator to 65 MeV neutrons is shown in Fig. 10.8.2 where the abscissa is a light output in a unit of 1 MeV electron equivalence (MeVee). The response calculated with SCINFUL agrees with measured results except for the deuteron peak due to the C(n,d) reaction. The difference of deuteron peak position between the experimental and the SCINFUL results indicates that the light output of deuterons is underestimated. In this work, therefore, the light output of deuterons was revised. From the light output of protons used in the SCINFUL code and the stopping power data<sup>3)</sup>, the light output data of deuterons was modified by Murray and Meyer's<sup>4)</sup> suggestion that the light output per unit energy deposited would be described accurately by taking account of its dependence on the stopping power. The responses calculated with SCINFUL using the revised light output of deuterons agree with the experimental data for 5 to 65 MeV neutrons. This modification, however, did not improve the value of the absolute efficiency of the  ${}^{60}\text{Co}$ -bias noticeably.

The experimental and calculated absolute efficiencies of  ${}^{60}\text{Co}$ -bias are shown in Fig. 10.8.3. Vervinski's data<sup>5)</sup>, which are well known, are also shown in Fig. 10.8.3. The SCINFUL using the revised light output of deuterons reproduces the experimental value within the experimental error. The SCINFUL could predict the absolute efficiency with 10% accuracy in the region from 3 to 65 MeV. On the other hand, the Cecil code of the Kent State

University version does not reproduce well the experimental values. This is because the Cecil code includes the library with a small number of reaction channels and inaccurate reaction cross sections in comparison with the SCINFUL code. Further measurements are planned for 20 MeV to 100 MeV neutrons at JAERI Tandem accelerator and TIARA.

#### References

- 1) Dickens J.K. : "SCINFUL: A Monte Carlo Based Computer Program to Determine a Scintillator Full Energy Response to Neutron Detection for En Between 0.1 and 80 MeV", ORNL-6462 (1988).
- 2) Cecil R.A., Anderson B.D. and Madey R. : Nucl. Inst. and Meth. , 161, 349 (1979).
- 3) Janni J. F. : Atomic Data and Nuclear Data Tables, 27, 150 (1982).
- 4) Murray R.B. and Meyer A. : Phys. Rev., 122, 815 (1961).
- 5) Vervinski V.V., et. al. : "The Response of Some Organic Scintillators to Fast Neutrons", Proc. American Nuclear Society Special Session on Fast Neutron Spectroscopy, San Francisco (1964).

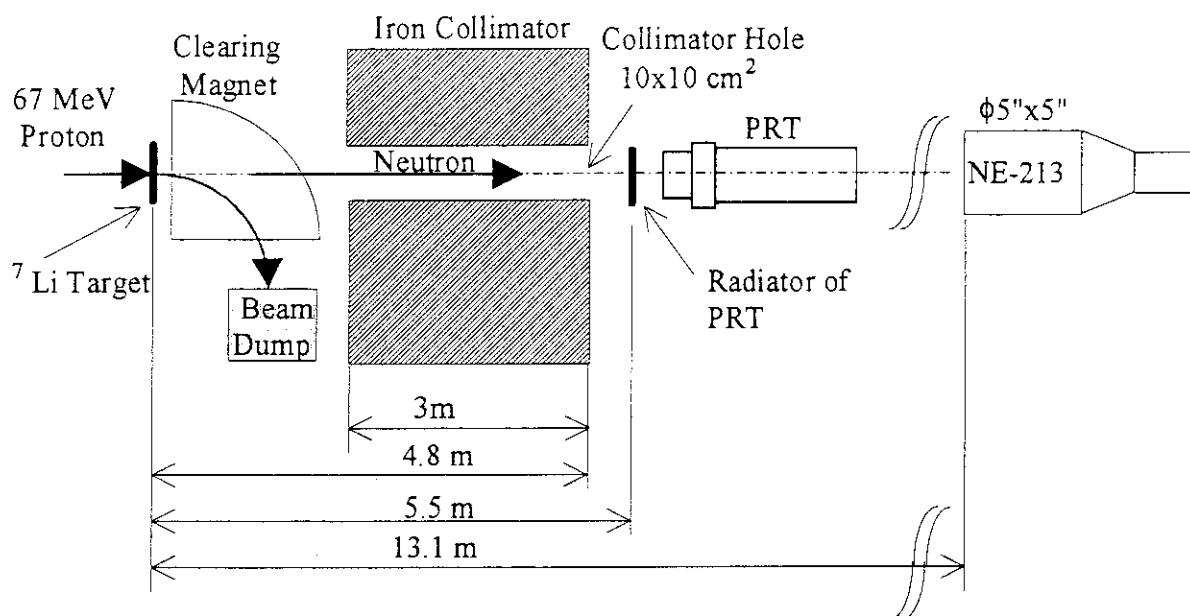


Fig. 10.8.1 Illustration of the experimental arrangement.

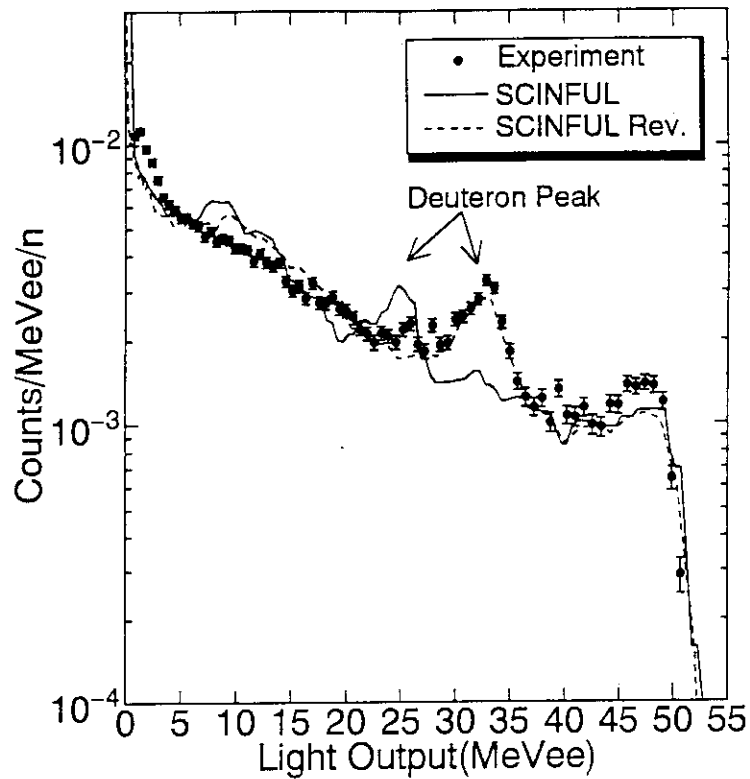


Fig 10.8.2 Calculated and experimental responses of the NE-213 scintillator (5"φx5") to 65 MeV neutrons.

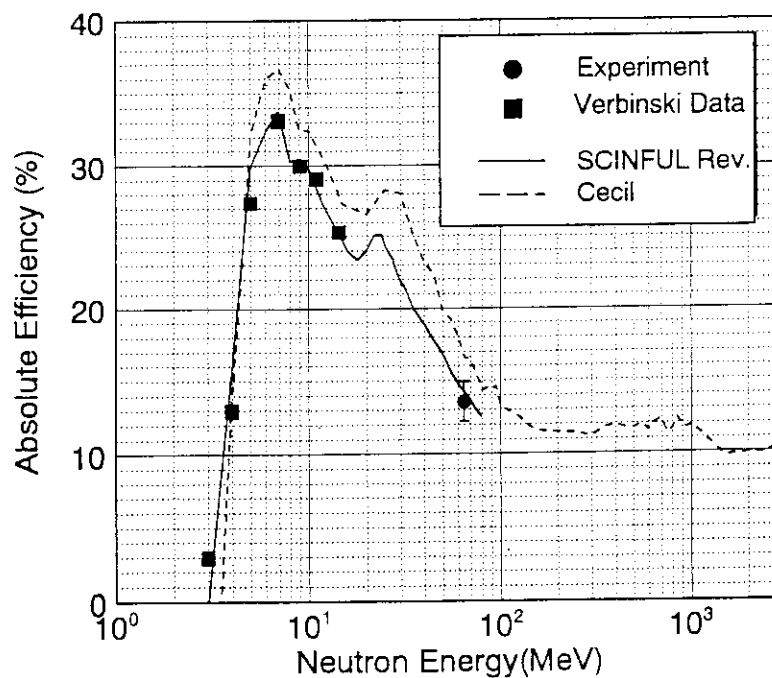


Fig. 10.8.3 Calculated and experimental neutron detection efficiency of the NE-213 scintillator (5"φx5") biased at a half-height of Compton edge of  $^{60}\text{Co}$  γ-ray.

## 11. Development of Proton Linear Accelerator, FEL and Superconducting Booster

Development of a low energy portion for high intensity proton accelerator (BTA) has been carried out. An injector consists of a multi cusp type ion source, a low energy beam transport and a radio frequency quadrupole (RFQ). The accelerating current of 52mA with a duty factor of 5% was achieved in the first beam test. The characteristics of the RFQ such as the transverse beam profile, transmission, and beam current were measured as functions of the input beam parameters (e.g., ion source acceleration voltage, matching, input current) and of the RF power (RFQ vane voltage).

The hot test model of a drift tube linac (DTL) with 9 cells has been developed to examine the cooling capability and RF characteristics. The resonance frequency and Q value were measured to be 201.178MHz (design value, 201.25MHz) and 42,100 (83% of the calculated value), respectively. The test result indicated that the RF power of 127kW is needed to obtain prescribed average field strength of 2MV/m. Deviation of average field strength measured with the bead perturbation method was within 2.3%.

The design studies of a 100kW proton beam stop for the BTA were carried out. A unidirectional carbon-fiber composite (C/C) material was considered for the target material because it has superior characteristics in the thermal conductivity and strength. A finite element model calculation gave the satisfactory results with the thermal displacement and thermal strain.

A prototype FEL (Free Electron Laser) has been constructed using a superconducting RF linac, aiming at long pulse lasing in the infrared region by a 15 MeV electron beam. The RF tests of the cavities were finished with satisfactory result; Q value  $> 2 \times 10^9$  at  $E=5\text{MV/m}$ . A new undulator with vertical undulation plane was constructed with Nd-Fe-B permanent magnets. The optical resonator consists of two Au-plated Cu mirrors confront with each other with a separation of 14.395 m.

The construction of superconducting booster for the tandem accelerator was completed in October 1993. The booster is an independently phased linac composed of 46 superconducting resonators made of niobium and copper. Beam acceleration was succeeded with beams of  $\text{Cl}^{10+}$  to 261MeV by using 25 resonators operated at field gradients of 3MV/m. The spectrum showed that the beam bunch width was 0.3ns and that 80% of the incident beams were bunched.

The chapters of 11.1–11.5, 11.6 and 11.7 were separately prepared in charge of Accelerator Engineering Laboratory, Free Electron Laser Laboratory and Accelerator Division, respectively.

## 11.1 A Progress in the High Intensity Proton Linear Accelerator Development

M. Mizumoto, K. Hasegawa, H. Oguri, N. Ito, J. Kusano, Y. Okumura, T. Ono, H. Murata, K. Sakogawa\* and M. Kawai\*\*

For the accelerator-based nuclear waste transmutation as a part of the OMEGA project, the high intensity proton linear accelerator (ETA: Engineering Test Accelerator) with an energy of 1.5 GeV and an average current of 10 mA has been proposed. The main characteristics of this accelerator is to accelerate the high intensity beam current. In the conceptual and detailed design of the system, much attention has been paid in order to maintain the beam spill as small as possible. As the research and development (R&D) work for the accelerator components, the low energy portion of the accelerator structures are studied since 1991 because the beam quality is mainly determined at the low energy part<sup>1,2</sup>). The block diagram of the R&D components is shown in Fig. 11.1.1. For the high intensity accelerator, it is of particular importance to maintain the good beam quality (low emittance; small beam size and divergence) to avoid the damage and activation of the accelerator structures.

Electromagnetic properties and heat removal problems are also important issues for the structural and mechanical design, because accelerator is required for high peak power and high duty (repetition rate x pulse width) operation. The full mock-up test structure of RFQ and hot test model of DTL, which are both operated by the full RF power, have been fabricated. The electromagnetic characteristics were measured with the electromagnetic field distribution and electric discharge property, and the thermal characteristics were also measured with temperature distribution, outgas condition and attainable vacuum range. The beam acceleration test with high brightness ion source and RFQ was made successfully with the beam current of 52 mA (peak) and 5 % duty. The preparatory work for high power test of the DTL hot-test model was also carried out together with the utility (electricity and water) supplies. These progresses are described in the separated reports.

As one of the main R&D components for the accelerator development, an RF source has been developed. The system was designed to generate 1MW peak power (pulse width is 1.2ms and repetition rate is 100Hz) at 201.25 MHz. The tetrode of EIMAC 4CM2500KG, which was developed for fusion plasma heating at JT-60, is

---

\* Mitsubishi Heavy Industries, Ltd.

\*\* Toshiba Corporation

used as a high power amplifier (HPA) with multistage amplifier configuration. The input and output circuits are  $3/4$  wave length coaxial cavities. The HPA is driven by a 60 kW intermediate amplifier (IPA of RS2058CJ) which is fed by a master oscillator and a 3 kW solid state drive amplifier. The accelerating voltage and phase control loop are made with an accuracy of  $<0.1\%$  in amplitude and  $<1^\circ$  in phase. The block diagram of the RF source system is shown in Fig. 11.1.2.

The peak powers of 1 MW at 0.6 % duty and 830 kW at 12 % duty were obtained in a high power test using a dummy load. In the conditioning process, the original RF coupler had to be modified by changing the geometry and windows due to the multipactoring occurred. The sufficient power for the RFQ to generate an accelerating voltage (363 kW) and to compensate the beam loading (100 kW) was delivered through the modified RF coupler

The conceptual and optimization studies for the high energy accelerator ETA have been carried out in collaboration with the Los Alamos National Laboratory. The accelerator cavities and RF system for high  $\beta$  structures dominate the accelerator size and construction cost for the ETA. The main issue for the conceptual and optimization

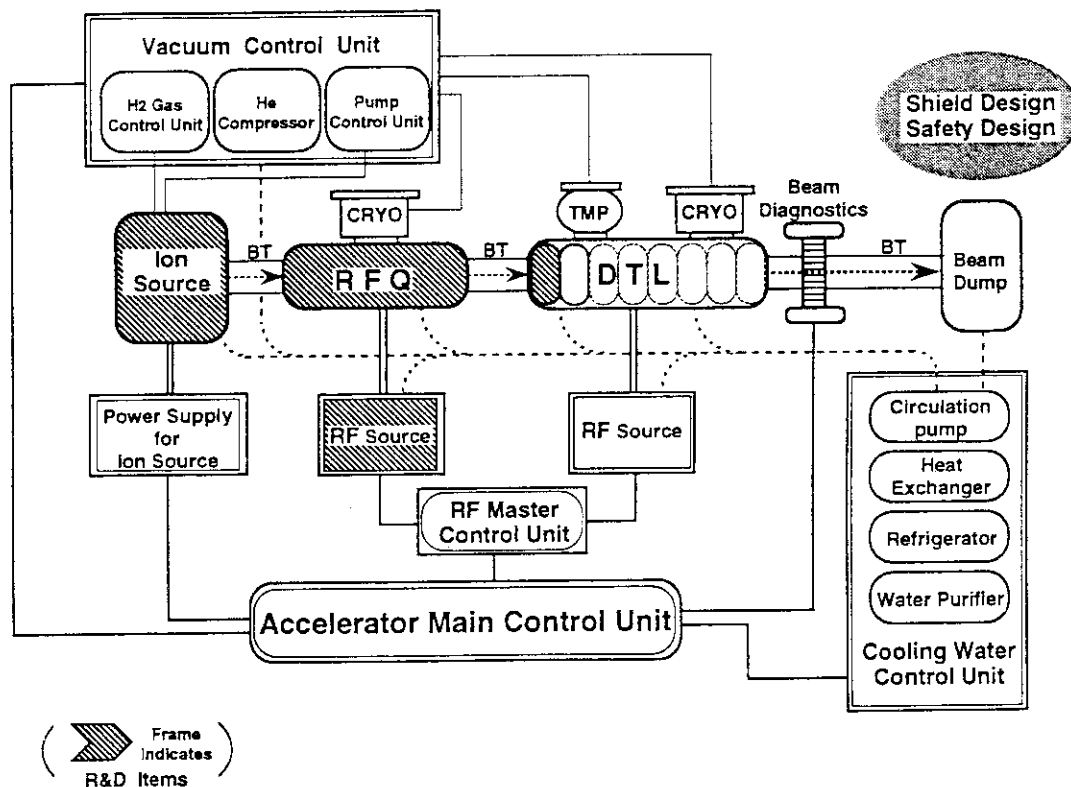


Fig.11.1.1 The block diagram of the BTA.



## 11.2 First Beam Test of the JAERI Radio Frequency Quadrupole (RFQ)

K. Hasegawa, M. Mizumoto, N. Ito, H. Oguri, J. Kusano and H. Murata

The JAERI 2 MeV Radio Frequency Quadrupole (RFQ) is one of the main injector components for the Basic Technology Accelerator(BTA)<sup>1)</sup>. The RFQ is designed to accelerate 100 mA of protons with a duty factor of 10 %. To study the characteristics of the RFQ, the first beam test was carried out after the low power tuning and the high power conditioning.

### Low Power Tuning

After the mechanical alignment of the vanes, relative field distribution was measured using the perturbation method. The phase shift, which is proportional to the square of the electric field, was measured by introducing a plastic perturbator. The end tuners and the fixed tuner positions were adjusted to minimize the field variation along the longitudinal position and quadrant-to-quadrant differences. Longitudinal field variations are shown in Fig. 11.2.1. Fields at the position of 2200 mm were about 7 % higher than that at the entrance end, and quadrant-to-quadrant differences were < 2.5 %. These field variations and differences do not significantly affect the beam performance, which was predicted with the beam simulation code of PARMTEQ.

### High Power Conditioning

The tank had a conditioning so as to accept an RF high power. The vacuum pressure was kept in the middle of  $10^{-6}$  Torr range to avoid sparking with RF power in the tank, where it was  $10^{-7}$  Torr without RF. The RF wave-forms from the directional coupler and the pickup loop were used as a monitor of the multipactoring and sparking. A TV camera was also used to observe sparks in the tank. X-ray energy end-point was measured by a 3"  $\phi$  X 3" NaI(Tl) detector, since X-rays from the RFQ tank are supposed to be bremsstrahlung of the electrons which are emitted by the RF electric field on the vane surface. This measurement confirmed that the input RF power of 273 kW gave the designed intervane voltage of 113 kV.

### First Beam Test

The first beam test was carried out at the test shop of Sumitomo Heavy Industries, Ltd. in Ehime Pref. The injector for the RFQ consists of a multi-cusp type ion source<sup>2)</sup> and a low energy beam transport (LEBT). Proton beam was injected and beam current at the downstream of the RFQ was measured. The characteristics of the RFQ such as the transverse beam profile, transmission and beam current were studied as functions of the input beam parameters (e.g., ion source acceleration voltage, beam matching, input current) and of the RF power (RFQ vane voltage).



Transmission rate as a function of the ion source acceleration voltage is shown in Fig.11.2.2. This result is consistent with the PARMTEQ code predictions although measured transmission was approximately 15 % lower at 100 keV. Two main reasons are considered to be overestimate the RFQ input beam current; one should correct the ion source proton fraction, and inadequate secondary electron suppression of the Faraday cup in the LEBT. To obtain the RFQ transmission correctly, the proton fraction and more accurate beam current measurement will be planned in the next step beam test. The beam energy spectrum from the RFQ was measured using a magnetic energy analyzer. Figure 11.2.3 shows the beam energy spectra for several intervane voltages. The peak energy is reduced and the energy spread is broadened as the intervane voltage is reduced.

The acceleration current of 52 mA with a duty factor of 5 % was achieved in the first beam test. The RFQ and the RF source have been reassembled in JAERI. The higher duty operation will be scheduled in FY-1994.

#### References

- 1) Hasegawa K., et al.: "Design Study on an RFQ for the Basic Technology Accelerator in JAERI ", 1992 Linear Accelerator Conference, Ottawa, Canada, AECL-10728, pp.314-316 (1992)
- 2) Okumura Y., et al.: "Development of a High Brightness Ion Source for the Proton Linear Accelerator (BTA) at JAERI", *ibid.*, pp.645-647

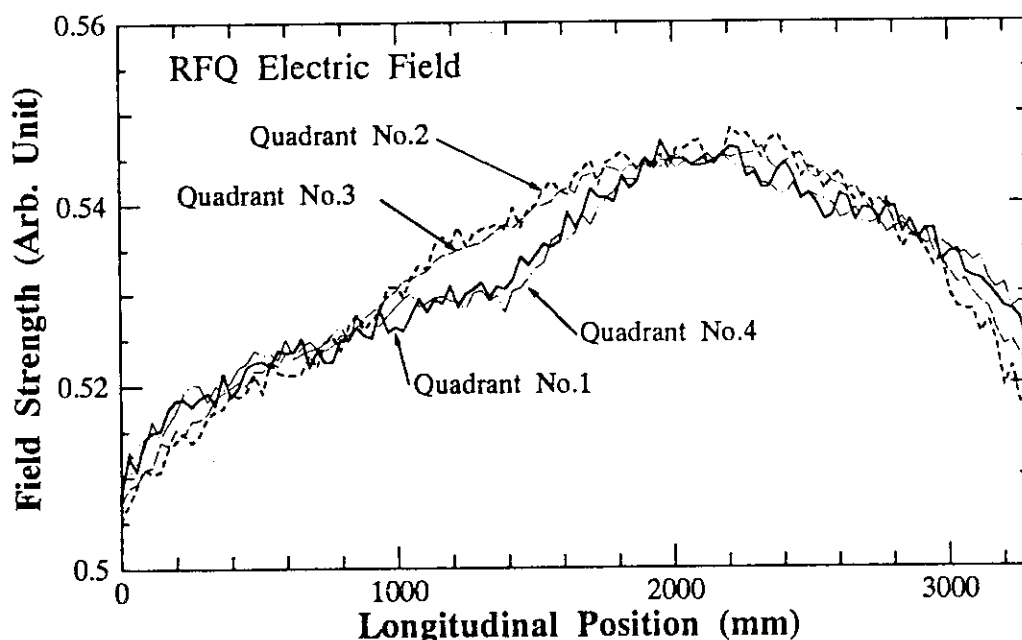


Fig. 11.2.1 Relative electric field along the position in the RFQ

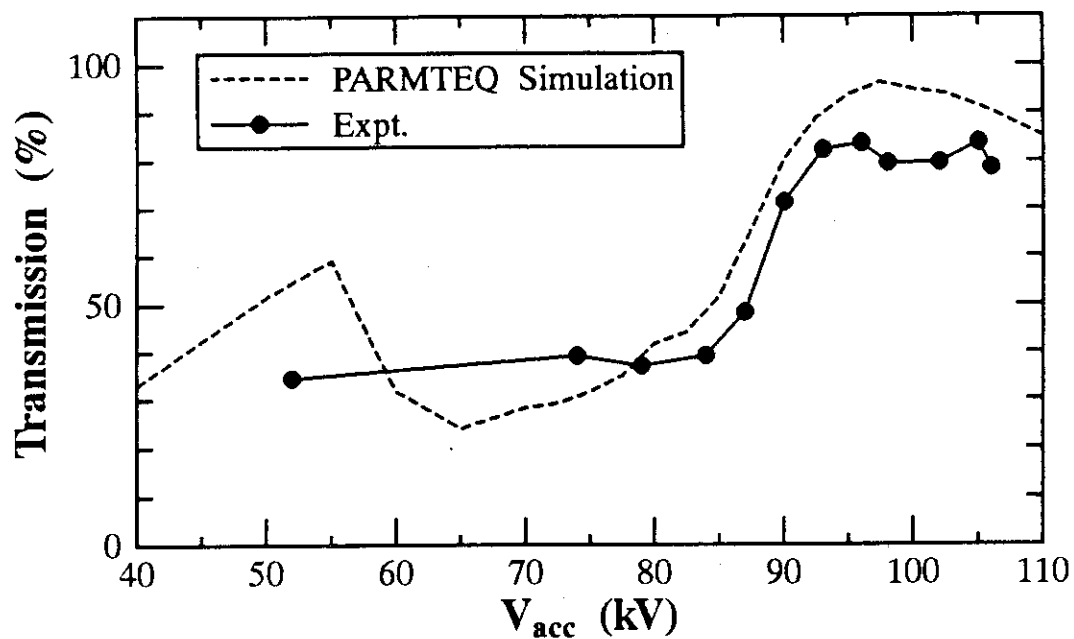


Fig.11.2.2 Transmission rate as a function of the ion source acceleration voltage

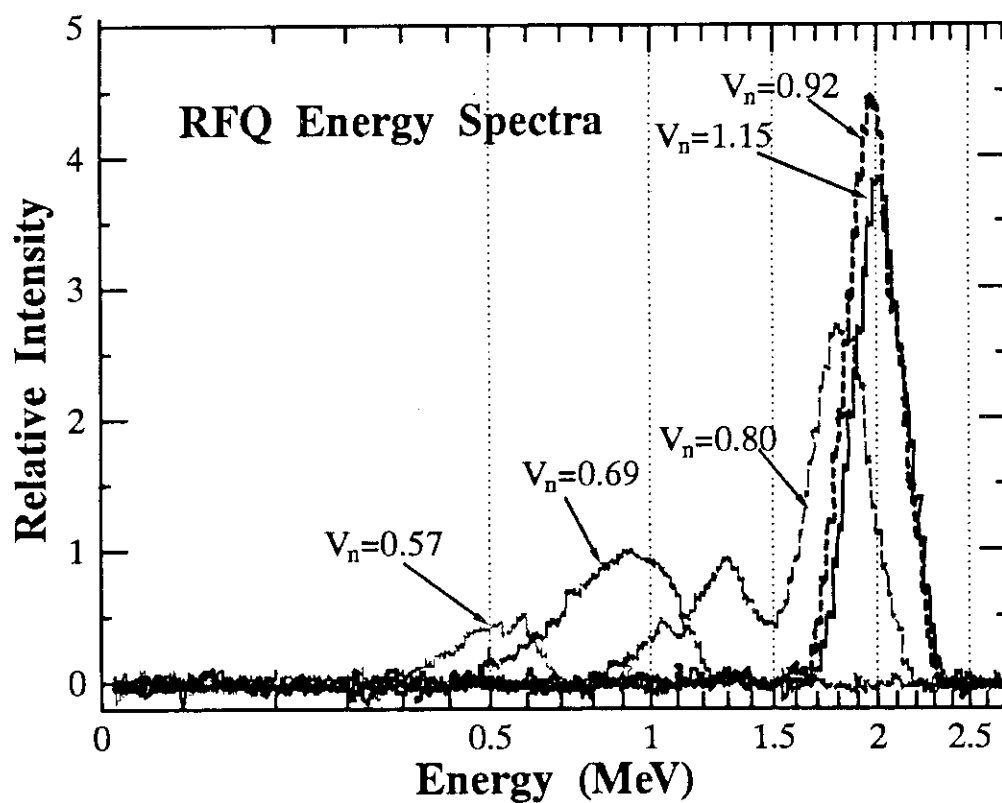


Fig.11.2.3 RFQ beam energy spectra for five relative vane voltages

## 11.3 Development of a Drift Tube Linac for the Basic Technology Accelerator

### —— Fabrication and RF Characteristics ——

N. Ito, K. Sakogawa\* and K. Hasegawa

The hot test model of a drift tube linac (DTL) with 9 cells has been developed to examine the cooling capability and RF characteristics<sup>1)</sup>. Elements of the hot test model, i.e., a tank, drift tubes (DTs), two quadrupole magnets and a tuner, have been fabricated. The elements were assembled to examine RF characteristics in the cold tests at the clean room of Mitsubishi Heavy Industries, LTD. in Hiroshima prefecture.

Figure 11.3.1 illustrates the cross sectional view of the hot test model which is 893 mm in inner diameter and 1005.5 mm in length. The electromagnetic quadrupoles, whose characteristics have been already reported<sup>2)</sup>, were installed in the first and the second DTs (DT#0 and #1). Each DT (DT#1 to #8) are supported by the single stem. Figure 11.3.2 shows the displacements of the DTs from the beam axis in the transverse plane: the alignment errors were within 0.1 mm as shown in Fig. 11.3.2. The alignment errors in the longitudinal direction were also confirmed to be within 0.08 mm.

After the assembling, a cold test was carried out to examine the RF characteristics, i.e., resonant frequency, Q value and electric field distribution on the beam axis. The resonant frequency was measured to be 201.178 MHz (designed value: 201.25 MHz) when the tuner stroke was 100 mm. Figure 11.3.3 shows measured frequency shifts as a function of the tuner stroke compared with the calculated values by the three dimensional electromagnetic calculation code system of MAFIA. The measured frequency shifts are in good agreement with those by the calculation. In Fig. 11.3.3, total frequency shift was about  $\pm 200$  kHz, which is enough to compensate frequency change due to the RF heating. Measured Q value of the hot test model was 42100, which is 83% of the calculated value by SUPERFISH code. The result indicates that the RF power of 127 kW is needed to obtain prescribed average field strength of 2 MV/m. Electric field distributions on the beam axis were measured by means of bead perturbation method with an aluminum spherical bead of 7 mm in diameter. Figure 11.3.4 shows typical result of the field distribution measurement, where vertical values are

---

\* Mitsubishi Heavy Industries, LTD.

normalized to prescribed field strength using the stored energy calculated by SUPERFISH code. The RF field is exited in the gap regions as shown in Fig. 11.3.4. An average field strength in the total region have been deduced to be 2.03 MV/m which is in good agreement with the designed value of 2 MV/m; this proves our proper experimental method. Deviation of an average field strength in each cell has been measured to be within 2.3 %.

In FY-1994, the hot test model will be reassembled to perform the high power test at JAERI.

### References

- 1) Yokobori H., et al.: Reactor Eng. Dep. Annual Report, 215, JAERI-M 92-125 (1992).
- 2) Hasegawa K. and Sakogawa K.: Reactor Eng. Dep. Annual Report, 201, JAERI-M 93-181 (1993).

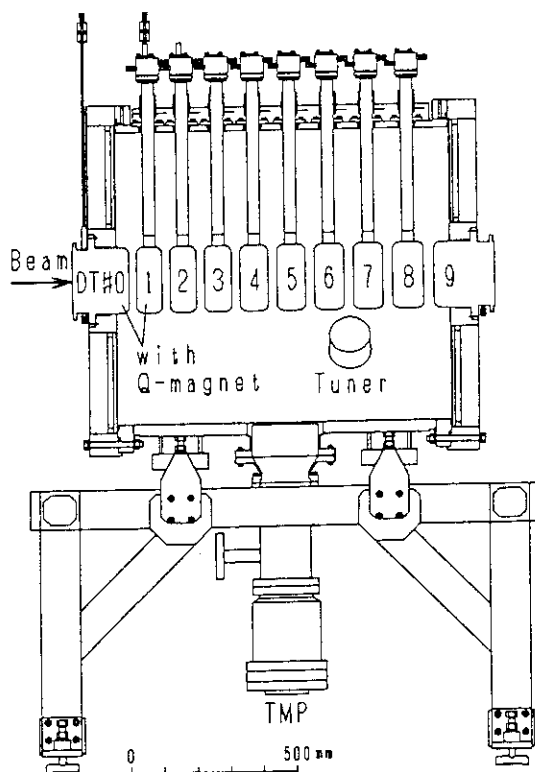


Fig.11.3.1 Cross sectional view of the DTL hot test model

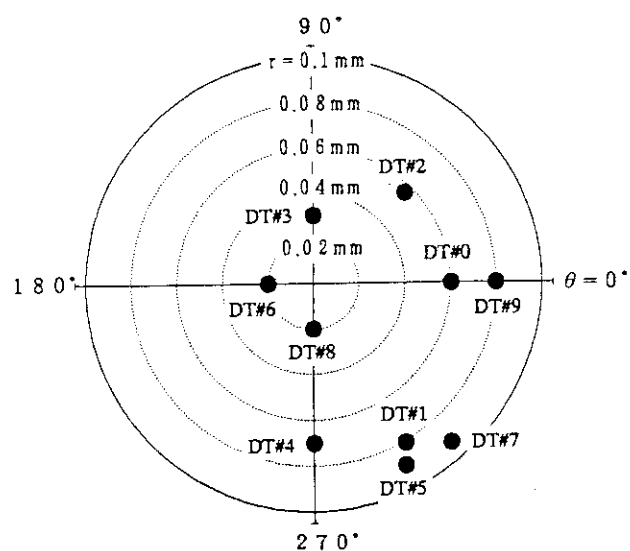


Fig.11.3.2 Displacements of the DTs from the beam axis in the transverse plane

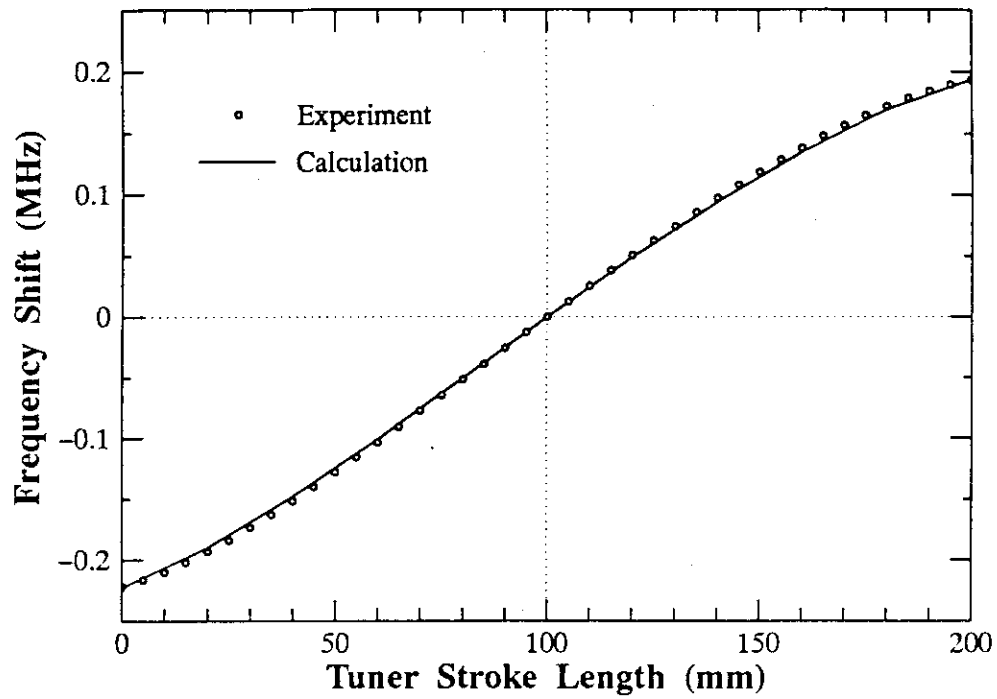


Fig.11.3.3 Measured frequency shifts as a function of tuner stroke length compared with the calculated values

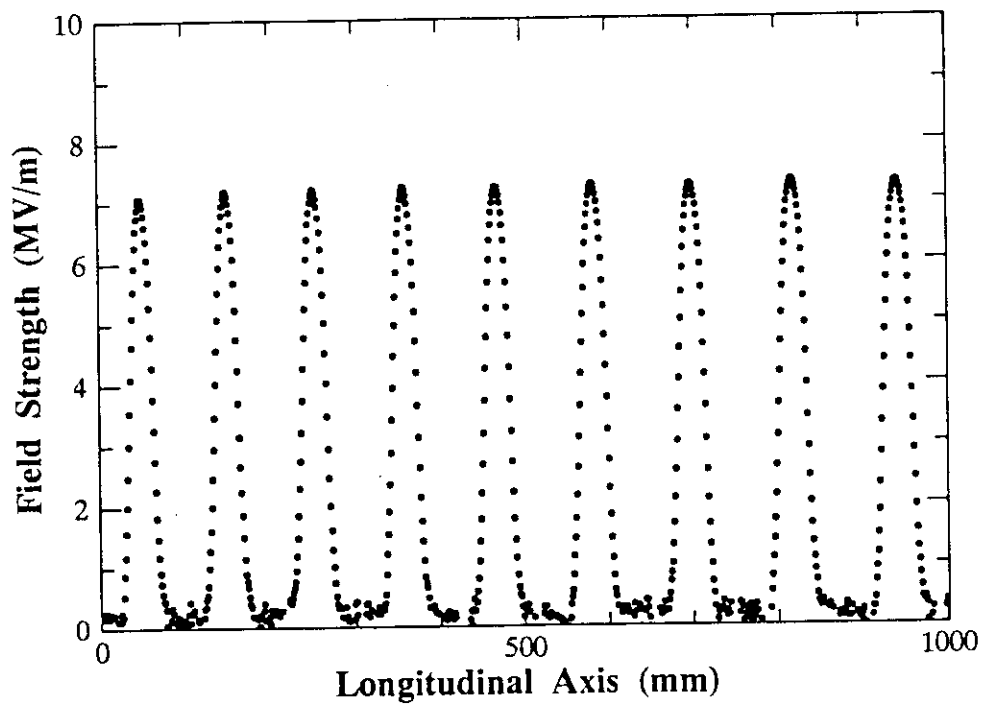


Fig.11.3.4 Electric field distribution on the beam axis measured by bead perturbation method

## 11.4 Performance of a High Brightness Hydrogen Ion Source for the BTA

H. Oguri, J. Kusano, Y. Okumura and N. Ito

A high brightness hydrogen ion source for the high intensity proton linear accelerator BTA has been developed since 1991 at JAERI. The ion source consists of a multicusp plasma generator and a two stage beam extraction system so as to produce high brightness (high current and low emittance) beam. The basic performance tests demonstrated that the ion source satisfies the requirements for the BTA ion source<sup>1)</sup>. In February 1994, an RFQ beam test was performed<sup>2)</sup>. The ion source was successfully operated as the RFQ beam injector. The performance of the ion source during the RFQ beam test is described.

For stable beam extraction at 100 kV during the beam test, the electrode gap length of the ion source was expanded by 4 mm in length. Figure 11.4.1 shows the new perveance characteristic together with the previous data<sup>1)</sup>. Optimum beam current decreased by 35 % in comparison with the previous value of 140 mA at 100 kV.

An arc efficiency  $\eta$ , defined by the ratio of acceleration current  $I_{acc}$  to the arc discharge power  $P_{arc}$ , was measured. Figure 11.4.2 shows the result of the arc efficiency as a function of the neutral hydrogen gas flow rate injected into the ion source. The arc efficiency was high when the gas flow rate was low. It reached 18 mA/kW at 5 SCCM. Lower gas flow rate operation induced an instability of the arc discharge. We chose 4 SCCM, where the stability was found to be good.

A beam profile was measured by a two dimensional 32 channel wire type monitor installed in the vacuum chamber at 2.4 m downstream from the ion source. The distance between the wires is 2 mm in the central region and 4 mm in the outer region. Figure 11.4.3 shows a typical beam profile measured at the vacuum pressure of  $3 \times 10^{-5}$  Torr in the beam drift region. No beam focusing elements were used in this figure. The Gaussian fitting curve in the Fig. 11.4.3 reproduces the data with the e-holding half width beam divergence  $\omega_{1/e}$  of 8.5 mrad. It is consistent with the previous data which was measured by a multichannel calorimeter<sup>1)</sup>. Such a small beam divergence was obtained without focusing elements. This is because the space charge force was neutralized by the electron in the beam plasma in the beam drift region<sup>3)</sup>. During the beam test, the beam size visually observed by the Balmer radiation which was emitted from the hydrogen atoms.

The proton yield was measured by a momentum mass analyzer installed at 1.5 m downstream from the ion source. The measured proton yield was 75 % at an acceleration current of 75 mA. The result supported the previous data measured by the Doppler-shifted spectroscopy<sup>1)</sup>, where the proton yield increases with the acceleration current and reaches

85 % at 140 mA. In addition, one can expect further enhancement of the proton yield by using the magnetic filter effect<sup>4)</sup>.

We will start the second RFQ beam test at JAERI in October 1994, and then investigate the detailed performance of the ion source.

#### References

- 1) Oguri H., et al.: Reactor Eng. Dep. Annual Report, JAERI-M 93-181 (1993)
- 2) Hasegawa K., et al.: Reactor Eng. Dep. Annual Report, (April 1, 1993 - March 31, 1994) (1994)
- 3) Oguri H., et al.: "Development of a High Brightness Ion Source for the Basic Technology Accelerator (BTA)", JAERI-M 92-200 (1992) (in Japanese)
- 4) Okumura Y. and Watanabe K.: "Design of a High Brightness Ion Source for the Basic Technology Accelerator (BTA)", JAERI-M 92-024 (1992)

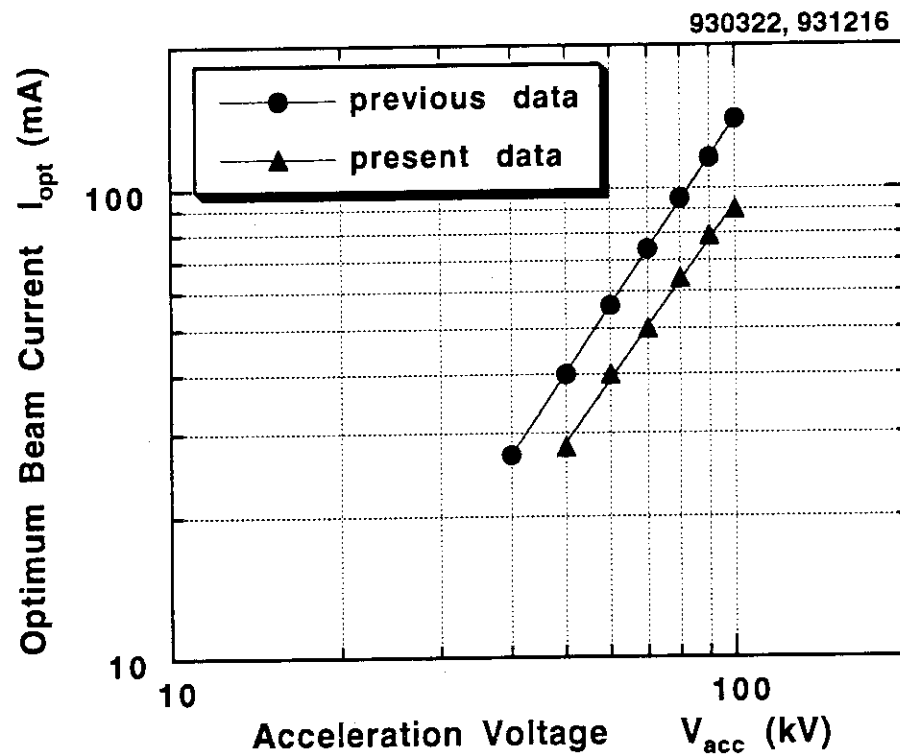


Fig. 11.4.1 Perveance characteristic of the ion source

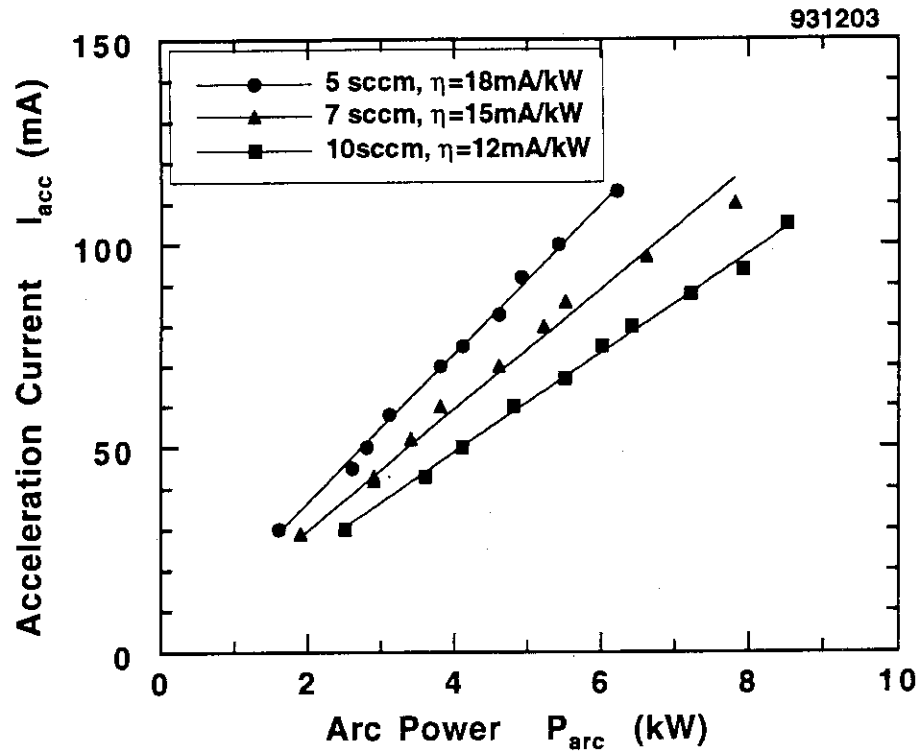


Fig. 11.4.2 Arc efficiency as a function of the neutral hydrogen gas flow rate

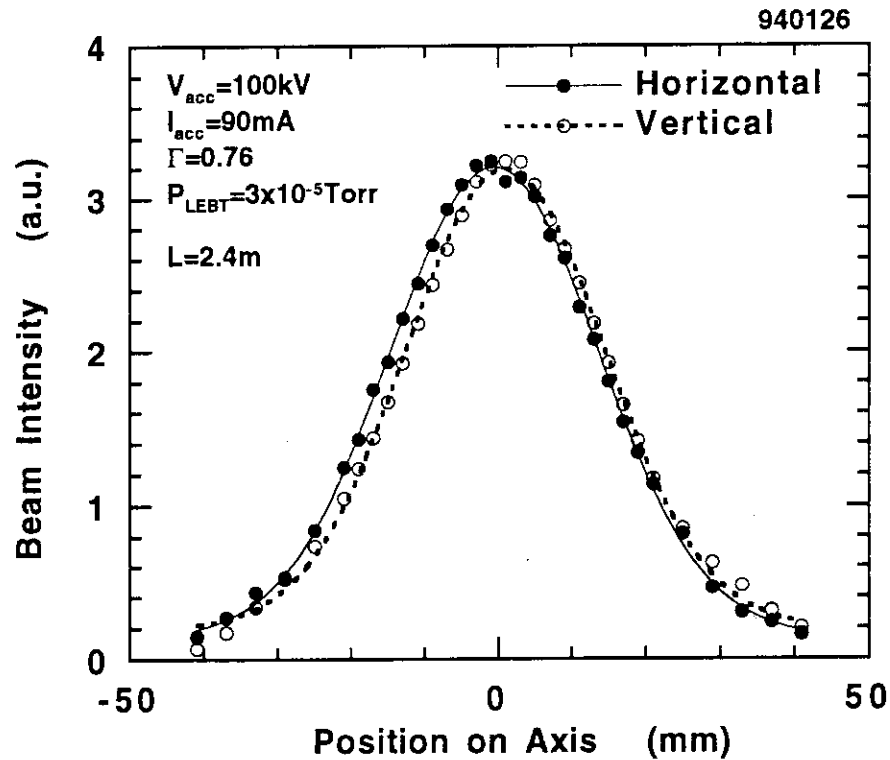


Fig. 11.4.3 Typical beam profile of the ion source



## 11.5 Design of 100kW Proton Beam Stopper for BTA at JAERI

M. Kawai\*, K. Sakogawa\*\*, M. Mizumoto, J. Kusano, K. Hasegawa, H. Oguri,  
N. Ito and H. Murata\*\*\*

The design study of the 10 MeV proton linear accelerator BTA (Basic Technology Accelerator) pulse-operated with a peak current of 100 mA, 100 Hz repetition rate and 1 ms duration is being made<sup>1)</sup> together with the R&D study<sup>2)</sup> on accelerator components, as one of the activities of the OMEGA project. For its high energy beam transport system needed is a beam stopper which can absorb 100 kW heat in average due to proton beam. In the present work, the conceptual design has been made by considering thermal performance.

The proton beam of BTA is very collimated to about 10 mm in diameter at the exit of DTL and there is almost no material to directly absorb such a high heat flux. In order to reduce input heat flux to a moderate level that is taken in intense-beam stoppers of FMIT prototype<sup>3)</sup> and JT-60 NBI<sup>4)</sup> or a diverter design of fusion reactor ITER<sup>5)</sup>, we adopted such stopper configuration as shown in Fig. 11.5.1: the beam size is enlarged to 30 cm and 20 cm in diameter, and the incident angle  $\alpha=15$  and 20 degree for 1.68 MW/m<sup>2</sup> and 5.00 MW/m<sup>2</sup>, respectively. Copper is used as a base plate of the beam stopper. However, it has a problem to generate large amounts of secondary neutron due to Cu(p,n) reaction with 10 MeV proton. For carbon, major constituent <sup>12</sup>C does not generate neutron because of high Q value of (p,n) reaction, although minor constituent <sup>13</sup>C does. Thus, carbon sheathing is adopted to suppress neutron generation. Especially, unidirectional carbon-fiber composite (C/C) material, for example MFC-1, is superior in thermal conductivity compared to graphite. Weak point of MFC-1 is not strong to tensile stress perpendicular to the fiber. Accordingly, as a sheath, we select a small tile with 5x5 cm<sup>2</sup> square and composed of multi-layers of 10 mm thick MFC-1, 3 mm W-30Cu and 3 mm Cu. A tile or a module made of tiles can be replaced without so much trouble when it is broken. Tungsten alloy of W-30Cu has nearly the same thermal expansion coefficient as MFC-1 and is mechanically strong, so that it can absorb thermal stress from copper expansion together with inelastic deformation of copper. Coolant system is composed of 24 channels, arrayed with a 1 cm pitch in copper plate. The water channel

---

\* Toshiba Corporation

\*\* Mitsubishi Heavy Industries, Ltd.

\*\*\* Sumitomo Heavy Industries, Ltd.

is of a non-circular geometry having a cross sectional area of  $0.643 \text{ cm}^2$  as shown in Fig. 11.5.1. Individual channels are connected with others on the fringe of the stopper and make four loops. Feed water temperature is  $25^\circ\text{C}$  and flow velocity is  $4 \text{ m/s}$ .

Thermal performance of the beam stopper is analyzed with both the analytic approach and the finite element model (FEM) calculations. Under the assumption of Gaussian distribution for proton beam, we estimate temperatures of water and stopper materials at the principal points of the stopper with a one-dimensional thermal conduction model associated with heat removal by random flow in straight channel. Then, detailed analysis is made by using the ABAQUS code. For the calculation, the parameters of material properties are taken from Ref. 5. Heat transfer coefficient of the film at the copper-water interface of cooling channel with non-circular shape is estimated to be  $24.2 \text{ kW}/(\text{m}^2 \cdot \text{K})$  by the equation of Dittus-Boelter. The temperatures of water at the places of beam center are  $29.1^\circ\text{C}$  and  $37.3^\circ\text{C}$  for the input heat flux of  $1.68 \text{ MW/m}^2$  and  $5 \text{ MW/m}^2$ , respectively. The ABAQUS calculation with two-dimensional model gives  $437^\circ\text{C}$  on the surface of MFC-1 and  $170^\circ\text{C}$  in the cooling channel film for  $5 \text{ MW/m}^2$ . They satisfy the design criterion: the former below  $1,000^\circ\text{C}$  and the latter below  $180^\circ\text{C}$  which shows saturation vapor pressure of  $10 \text{ atm}$  with a constrain that we admit a subcool boiling.

Figure 11.5.2 shows the thermal displacements calculated by ABAQUS with three-dimensional model for  $1.68 \text{ MW/m}^2$  heat flux. Table 11.5.1 gives the results for maximum values of thermal displacement and thermal strain. For  $5 \text{ MW/m}^2$ , tensile stress to MFC-1 is  $0.008 \text{ kgf/mm}^2$ , and is satisfactorily smaller than the ultimate strength of  $0.3 \text{ kg/mm}^2$ . On the other hand, the MISES stress  $16.2 \text{ kgf/mm}^2$  for copper exceeds the yield strength of  $0.2\%$  inelastic deformation so that deformation of copper will be inevitable. Further calculation by replacing W-30Cu of the second layer with copper shows that the maximum tensile stress to MFC-1 increases to  $0.133 \text{ kgf/mm}^2$  at the bottom of MFC-1 where temperature is  $308^\circ\text{C}$ . The stress at the brazing temperature of about  $800^\circ\text{C}$  to join layers is straightforward estimated to be  $0.36 \text{ kgf/mm}^2$ . This value has a potential to split the fiber composite. Accordingly, the buffer layer is desirable to absorb such a thermal strain. Besides, for the cooling system, output water temperature becomes  $48.4^\circ\text{C}$  and the pressure drop is estimated to be  $1.94 \text{ atm}$  by using the friction coefficients represented by the Moody chart.

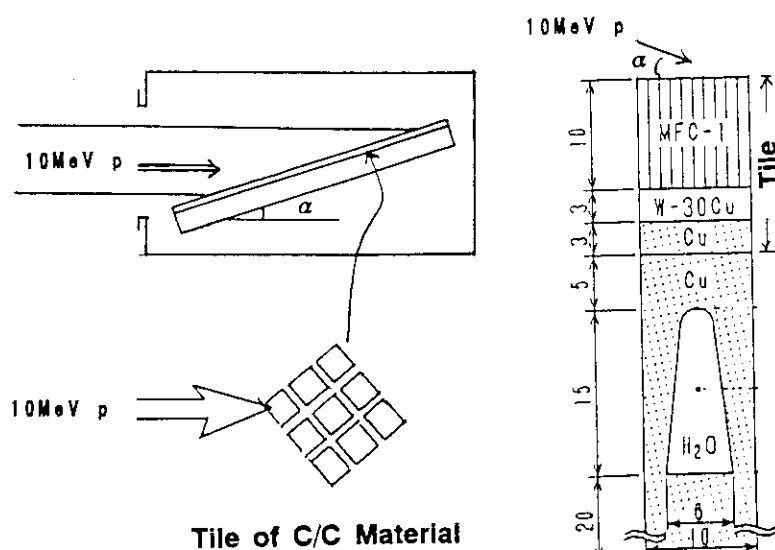
The present analysis confirms that the beam stopper is of no problem from view point of thermal performance. Further studies are needed on an optimization of stopper and cooling system, fabrication method and a behavior of C/C material under proton beam.

## References

- 1) Mizumoto M., et al.: "High Intensity Proton Linear Accelerator for Nuclear Waste Transmutation," Proc. 7th Int. Conf. on Emerging Nuclear Energy System, 20-24 September 1993, Makuahari, p.453 (1993).
- 2) Hasegawa K., et al.: "Status of the R&D for the Basic Technology Accelerator in JAERI," Proc. of 9th Symp. on Accelerator Science and Technology, 25-27 August 1993, Tsukuba, p.56 (1993).
- 3) Liska D.: private communication.
- 4) Miya K., et al.: J. of Atomic Energy Soc. of Japan, **29**, 855 (1987) [in Japanese].
- 5) Smid I., et al.: JAERI-M 93-149 (1993).

Table 11.5.1 Maximum thermal displacement and strain.

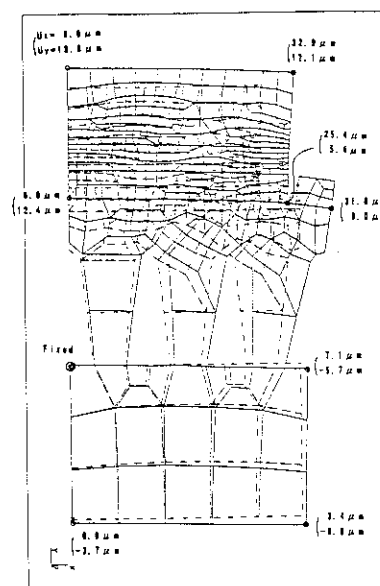
	1.68 MW/m <sup>2</sup>	5.00 MW/m <sup>2</sup>
Thermal Displacement Perpendicular	32.9 $\mu\text{m}$	103.2 $\mu\text{m}$
Parallel	18.8 $\mu\text{m}$	59.3 $\mu\text{m}$
Tensile Stress in MFC-1 Layer	-0.025 to 0.002 kgf/mm <sup>2</sup>	-0.090 to 0.008 kgf/mm <sup>2</sup>
Mises Stress in W-30Cu Layer	4.61 kgf/mm <sup>2</sup>	13.8 kgf/mm <sup>2</sup>
Mises Stress in Copper Layer	5.42 kgf/mm <sup>2</sup>	16.2 kgf/mm <sup>2</sup>



(a) whole geometry

(b) basic module

Fig. 11.5.1 Concept of beam stopper

Fig. 11.5.2 Thermal displacement  
for 1.68 MW/m<sup>2</sup>

## 11.6 Status of the JAERI Free Electron Laser Facility

M. Ohkubo, M. Sugimoto, M. Sawamura, R. Nagai, M. Takao\*, R. Kato, E. Minehara and Y. Suzuki

### Introduction

A free electron laser (FEL) is a promising machine to produce nearly monochromatic powerful light of variable wave length, which will be useful for the basic research and application, such as physics and chemistry, isotope separation, waste processing, therapy, communication and so on.

In JAERI, Tokai, a prototype FEL has been constructed using a superconducting RF linac, aiming at long pulse lasing in the infrared region by a 15 MeV electron beam. The FEL was installed in the retired 5.5 MeV Van-de-Graaf target room and a newly added accelerator room. Cutaway view of the JAERI FEL facility is shown in Fig. 1.

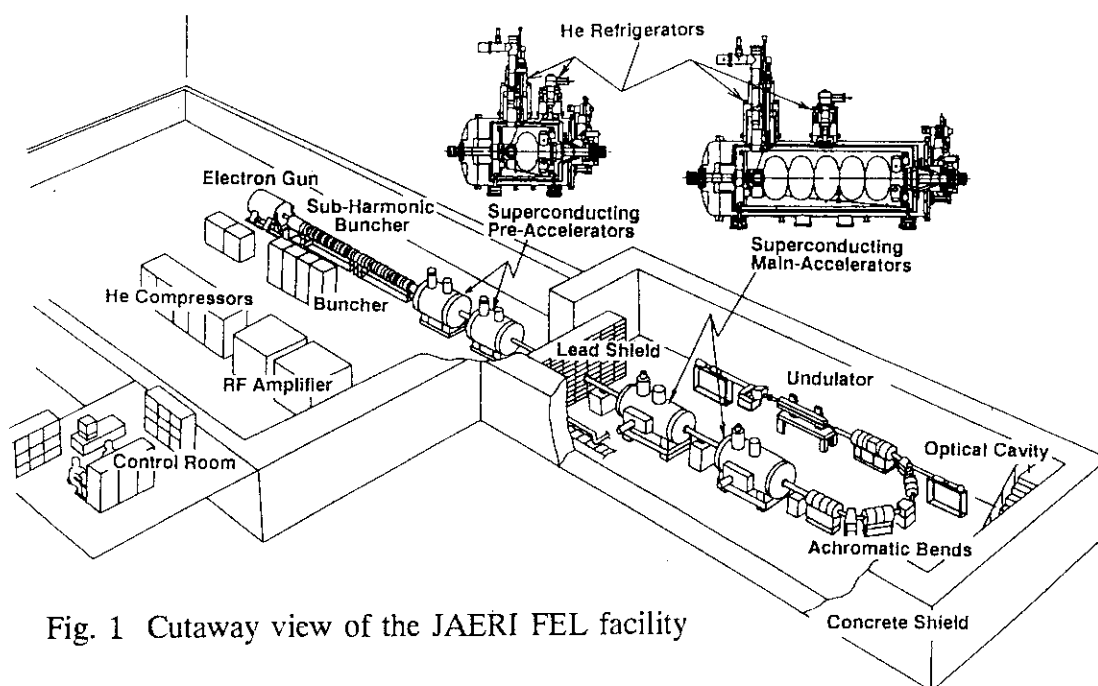


Fig. 1 Cutaway view of the JAERI FEL facility

### Status of FEL Facility

An FEL produces light by a high energy electron beam which excites laser oscillation through an undulator. The laser light is confined in optical resonator and part of it is

---

\* Contract Researcher

extracted through a coupling window. The FEL consisted of a electron gun, subharmonic buncher (SHB), superconducting pre- and main- accelerators (SCA) and refrigerators, beam transport, vacuum, RF, undulator and optical resonator, accelerator control, and radiation shielding and safety systems.

#### (1) Electron Gun and Subharmonic Buncher

The electron gun has been operated stably at 200 kV, 0.1 A with 2ns micropulse with a repetition rate 10 Hz. Reduction of amplitude modulation in long macropulse is under consideration. The electron beam from the gun was velocity modulated by an RF field in the subharmonic buncher (83.3MHz), and was time-focused at the pre-accelerator. Many solenoid coils were placed along the beam duct to focus the electron beam. In addition, degaussing coils were set to compensate earth magnetic field in the region from the gun to the main accelerator.

#### (2) Superconducting accelerators (SCA)<sup>1)</sup>

The superconducting accelerators, (designed by JAERI, produced by Siemens (interatom), Germany) have been installed in January 1993. They were cooled down to liquid helium temperature with closed loop refrigerator successfully. First in the world, this type of refrigerator were applied to the accelerator cavities. There are two pre-accelerators (SCPA) with single cavity, and two main-accelerators (SCMA) with five cavities. RF tests of these cavities were performed with satisfactory results: Q values  $> 2 \times 10^9$  at  $E = 5 \text{ MV/m}$ . Overhaul of the refrigerators is made every 8000 hours of operation time.

#### (3) RF Control and RF amplifiers<sup>2)</sup>

For the beam acceleration, three frequencies were used; 10.4125 MHz for the electron gun, 83.3 MHz for the SHB, and 499.8 MHz for the SCA. To reduce irregular phase deviation among these frequencies, a frequency dividing method was adopted instead of the frequency multiplication method. All transistorized 4 and 50 kW RF amplifiers for the SCPA and SCMA were operated successfully. To stabilize output power of the RF amplifiers, additional high power RF circulators are under construction to shut off reflected power from the cavities.

#### (4) Beam Transport System

In order to transport electron beam from the gun to the undulator, solenoid coils, steering dipoles, quadrapole doublets (QD), quadrapole triplets (QT), 60 deg. bending magnets

etc. were placed based on the beam transport calculations. A momentum filter, composed of four dipole magnets, were placed between the SCPA and SCMA. Ion pumps and turbo molecular pumps kept vacuum less than  $1 \times 10^{-8}$  Torr in the beam duct and accelerator cavities. Quadrupole mass filters were installed to analyze and to monitor the residual gases. Beam profiles were monitored at several points, by inserting luminescent screen in the beam and observing it by TV cameras through vacuum tight transparent windows. Beam current was non-destructively picked up by amorphous core current transformers, placed at several points along the beam ducts.

#### (5) Undulator and Optical Resonator

A new undulator with vertical undulation plane was constructed with Nd-Fe-B permanent magnets. The optical resonator consisted of two Au-plated Cu mirrors confront with each other with a separation of 14.395 m. The mirror alignment and control systems were placed on two optical benches, between which the undulator was placed. Detectors for the infrared light is under preparation.

#### (6) Accelerator Control System<sup>3)</sup>

Many components of the accelerator were controlled and logged through LAN system on the displays of the personal computers. The control program was based on Windows Operation System, and parameters can be set by a mouse or by a key board.

#### (7) Radiation Shield and Safety System

During operation of the accelerator, strong gamma rays are produced in the accelerator room. Maximum intensity was estimated to be 20 mSv/h at 1m at the center of the room. To keep irradiation dose for the staff below 50mSv/y, a radiation shielding for the accelerator room, and an interlock system for the hazardous region was made. We have gotten a license for the operation of FEL facility from the Science and Technology Agency, Japan, in July 1993.

#### References

- 1) Kikuzawa N., et al.: Nucl. Instr. Methods. A331(1993)276
- 2) Sawamura M., et al.: Nucl. Instr. Methods. A341(1994)391, *ibid.* A331(1993)323
- 3) Sugimoto M.: Nucl. Instr. Methods. A331(1993)340

## 11.7 Status of Superconducting Booster

S. Takeuchi

The superconducting booster for the tandem accelerator was completed in October 1993 after 4 year research and development and 6 year construction since 1984. Beam testing has started with a successful result.

The booster is an independently phased linac composed of 46 superconducting resonators made of niobium and copper. The booster structure is illustrated in Fig. 1. Forty of them are used for acceleration and housed in ten cryostats, four for bunching and two for de-bunching. Forty-four resonators are all the same. Their frequency is 129.8 MHz. Their optimum beam velocity is 10 % of the light velocity and the acceptable lowest velocity is 5 %. The bunching system is a double drift harmonic buncher. Two resonators for bunching have the frequency of 259.6MHz. The booster is equipped with two 250 watts helium refrigerators and liquid helium transfer lines. By the end of FY 1992, all the resonators, their cryostats and refrigerators have been set ready for use.

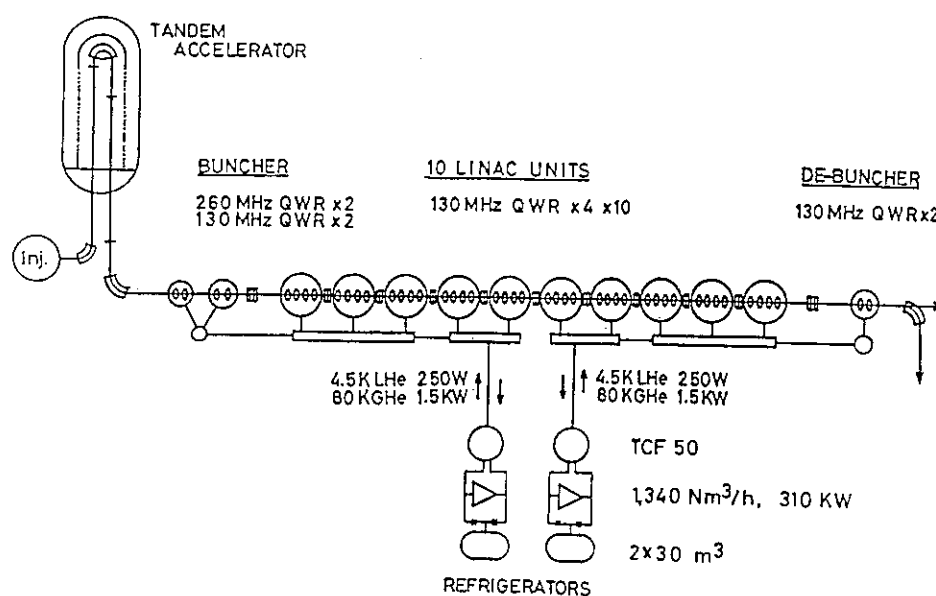


Fig. 1 Booster structure diagram

From the end of FY 1992 to October of this fiscal year, installation work of various components, such as beam line components, their control circuits, safety interlocks systems, resonator control modules, rf power amplifiers, rf cables and control cables, was done.

In the meantime, refrigerating systems with resonators were operated three times for learning operation, for optimizing control parameters of the systems and for resonator testing

without beams. Several difficulties were found in the test runs. We could not have enough flow of liquid helium to the 5th unit of the linac. We had to open its flow adjusting valve much wider than others. One (A) of the refrigerating systems had instability in cold box; one of two expansion turbines continued a harmful oscillation of rotating frequency and was changed to a new one. The system B was troubled for a while with noise causing a big change of rotating frequency of turbines. In addition to the test runs, an annual inspection by ourselves, which is obliged by law, was done for the first time with the whole high pressure system.

Resonator Q values were measured in the test runs of the refrigerating systems. In off-line tests, an appreciable Q-degradation occurred with our niobium resonators, when the cooldown rate was smaller than 20K/h at about 120K<sup>1)</sup>. With the refrigerators that cool down the resonators at a rate of 10 K/h, we found that the first 16 resonators had severe Q-degradation of 30 - 70 % compared to the fast cooldown data. But, the last 24 resonators, which were built one year later than the first 16 ones, had no severe Q-degradation. This is believed to be improved by feeding nitrogen gas bubbles into the electro-polishing solution in the final surface treatment of niobium in order to prevent hydrogen from entering niobium walls<sup>2)</sup>. The accelerating fields for the Q-degraded resonators were 3 - 5 MV/m with an rf input of 4 watts. We found another problem that many of the resonators had lower frequencies than the tunable range of 129.800-129.815MHz. The frequency adjustment we did at the room temperature was found to be not appropriate. The part which was deformed with too much stress recovered to some extent in thermal cycles.

On October 26, 1993, every thing had been completed for beam acceleration and the booster facility was inspected with respect to the radiation safety and approved by the authority for the safety law. The next day, beams of Cl<sup>10+</sup> from the tandem accelerator were injected into the booster and passed through it, successfully. In November, beam acceleration test was carried out with beams of Cl<sup>10+</sup> 164MeV( $\beta = v/c = 0.1$ ) from the tandem. The beams were bunched well. An energy-and-time spectrum was measured by a detector composed of Au target and Si detector located at the entrance of the linac. The spectrum showed that the beam bunch width was 0.3 nS and that 80 % of the incident beams were bunched. In acceleration, resonator field amplitudes and phases were set one by one by monitoring beam-bunch phase shifts at beam-bunch phase detectors located after No.3, No. 6 and No.10 linac units. The phase detectors worked very well in the resonator phase setting. As a result of the first acceleration test, we succeeded in accelerating the beams to 261 MeV by using 25 resonators operated at accelerating field gradients of 3 MV/m and at a frequency of 129.796 MHz. The energy spectrum measured at the end of the linac is shown in Fig. 2, in which every spectrum after resonator setting is superimposed.



The rest 15 resonators were not used mainly because their frequencies were lower than 129.796 MHz and partly because the 5th unit was out of liquid helium. The refrigerating system A had a big change of helium pressure on the resonator walls, when an rf power

input was increased and liquid helium levels in the cryostats recovered to the full after some decrease. It caused a big frequency change (nearly 100 Hz) to the resonators and made it difficult to lock resonator phases at high accelerating field gradients.

Then, all the cryostats except the 259.6 MHz sub-bunching unit were opened. With most of the resonators, frequencies were re-adjusted by a right method of deforming outer conductors. Supports were put on end-plates which are the most pressure sensitive walls of the resonators. They decreased the frequency change by a factor of 5. The work has finished by the end of FY 1993 and the cooldown for the second beam acceleration testing started.

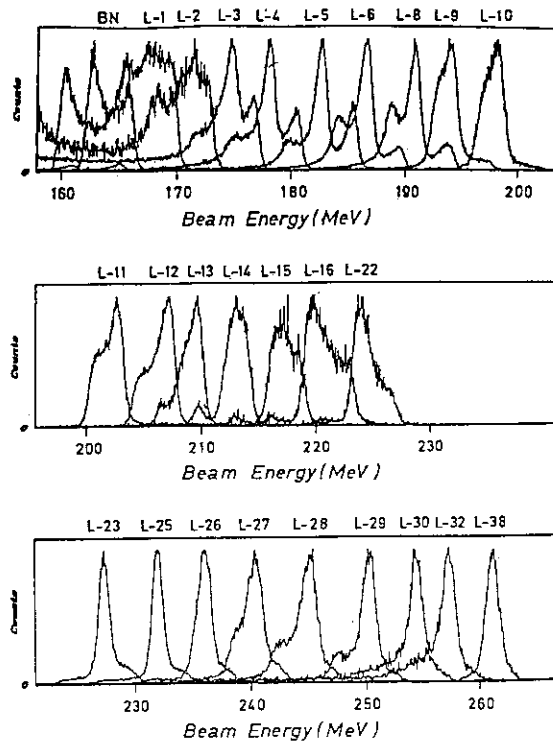


Fig. 2 Superimposed beam energy spectrum during resonator set-up

We repeat testing with different heavy ions till a recoil mass spectrometer is installed in the target room and ready for experiments in a year. A complete test result for the booster performance will be presented in the next annual report.

#### References

- 1) Ishii T., Shibata M. and Takeuchi S.: Nucl. Instr. and Methods A328(1993)231-235.
- 2) Shibata M.: to be published in "Proc. of the 6th Workshop on RF Superconductivity, CEBAF, Oct. 1993"

## 12. Facility Operation and Technique Development

Operations of three reactor engineering facilities and three accelerator engineering facilities were carried out as scheduled, such as Fast Critical Assembly (FCA), Very High Temperature Critical Assembly (VHTRC), Heat Transfer and Liquid Flow Facility, Fusion Neutron Source (FNS), Tandem Accelerator and Electron Linac. Main activities of each facility of this fiscal year are summarized briefly below.

(1) FCA was operated according to various purposes of experiments, and recorded the operation time of 445 hours. As for maintenance activities, besides annual and monthly inspections a part of the safety system such as the lighting conductor and argon gas fire-extinguish system were renewed or overhauled. The monthly inspection and the physical inventory verification of nuclear fuel materials were carried out without problem by the safeguard authority.

(2) VHTRC was operated as scheduled, especially for measurements of wholecore temperature coefficient reactivity up to 200°C, aiming at the verification of the calculation accuracy for HTTR, and recorded the operation time of 680 hours. The data base of the operation and the experiment data completed.

(3) Heat Transfer and Liquid Flow Facility was operated for various experiments such as DNB tests using the high pressure water loop, two-phase fluid flow tests and spacer effect test in two-phase flows. Besides these operations, the multi-dimensional fluid flow mock-up loop, the two-phase flow plenum test loop and the ultra high heat flux test loop were installed as scheduled.

(4) FNS was operated as scheduled according to various requirements of experiments and recorded the operation time of 608 hours. Exhaust tritium gas was processed in safe by the tritium adsorption processor (TAP). The fiber optic cable control system was adopted newly to the ion source voltage control. As for technique developments, a new test target disk having highly cooling performance was manufactured and its performance will be tested next fiscal year.

(5) Tandem Accelerator was operated as scheduled and recorded the operation time of 4138 hours. The beam performance of the tandem booster is under the test. This facility is expected to be used widely by customers of various fields and to contribute greatly execution of their experiments. Electron Linac was also operated and recorded the 366 hour beam time. Electron Linac terminated the operation and was shutdown on 31 Dec. 1993. Over twenty years of operation, this linac was operated safely and was utilized for researches of various fields.

## 12.1 Operation Report of FCA

K. Satoh, K. Hayasaka, H. Sodeyama, K. Kurosawa, A. Ohno and H. Watanabe

Operation of Fast Critical Assembly (FCA) was carried out in accordance with the experiment schedule on the FCA XVII-1 assembly. Operations of 82 times were carried out in 72 days. During the operation, the reactor scrammed once owing to commercial power failure. The total operation time was 445 hours and the integrated power 2.5 kWh. A total number of 4,828 criticality operations has been recorded at the end of this fiscal year since the first achievement of criticality on the 29th of April 1967. Following to the safety regulation for operation, two days were devoted to the monthly inspection and about 10 weeks to the annual inspection from May 1993. Routine maintenance activities were done in those days to provide maximum operation days for the experiments.

As for maintenance activities, the lighting conductor on the reactor dome was renewed, which is one of safety protection systems. The control system of the crane in the reactor room was also renewed so as to meet the lately revised wireless telegraphy act. Argon gas fire-extinguish system as an emergency system was overhauled. The soundness of the argon gas pressure containers was checked using an endoscope and no defect was found. The performance of the valves was also checked under the pressure of 160 kg/cm<sup>2</sup>. After conformation of soundness of the whole system, Argon gas was refilled up to 150 kg/cm<sup>2</sup> at 35°C. So far no leakage was observed.

As for the physical protection (P/P), the management of the entrance and exit was done restrictively and the system was maintained properly. All P/P control systems in the local guard booth and the battery for the case of commercial power loss were renewed in the renewal plan.

In connection with safeguard, IAEA and NSB\* carried out monthly inspection under the international treaty. The Physical Inventory Taking (PIT) of the fuels performed from the 15th to the 18th of June by means of item counting, weighing and non-destructive assay. IAEA and NSB made the Physical Inventory Verification (PIV) from the 21st to the 23rd of June. No anomaly was confirmed.

---

\* NSB: Nuclear Safety Bureau

## 12.2 Operation Report of VHTRC

S. Fujisaki, M. Takeuchi, T. Ono and H. Watanabe

VHTRC-4, VHTRC-6 and VHTRC-7 cores were assembled to obtain experimental data for the verification of the HTTR design accuracy. Core temperature coefficient measurements were performed two times on VHTRC-4 and VHTRC-6 core. Burnable poison rods of 18 pairs were arranged in the core region of VHTRC-6 core to measure the fuel rod worths and control-safety rod worths. The operations for this purpose were completed as scheduled without any problem disturbing execution of the experiment.

The results of the operation were as follows ;

- 1) Operations of 286 times in 94 days,
- 2) Critical operations of 251 times,
- 3) Total operation time of 680 hours,
- 4) Integrated power of 163 WH.

One scram was recorded due to earthquake during the operations. The integral operation time is 4055 hours at the end of this fiscal year since the first achievement of criticality on May 13, 1985.

According to the safety regulation for operation, one day was devoted to the monthly inspection and about 8 weeks to the annual inspection from October to November.

The major activities relating to the maintenance and document were as follows ;

- 1) Installation of the compact counter drive mechanism for axial reaction rate distribution measurements,
- 2) Continuation of the database work relating to the operation and the experiment data of VHTRC.

As for fuel management, Physical Inventory Taking (PIT) was carried out from May 9 to May 10 by means of item counting. IAEA and NSB made the Physical Inventory Verification (PIV) under the international treaty on May 13 and November 11. No anomaly was confirmed. The maintenance activity was also taken on the physical protection (p/p) system. The sensitivity and function of the system were examined and calibrated.

### 12.3 Operation Report of FNS

S. Tanaka, C. Kutsukake, Y. Abe, M. Seki, J. Kusano and H. Watanabe

Operation of the Fusion Neutronics Source(FNS) was carried out for a series of experiments including ones relating to ITER, as scheduled. The total operation time was 653 hours in this fiscal year. A new record on neutron generation of  $9.4 \times 10^{17}$  was marked in the operation of the heavy irradiation experiment using the rotating target, of which tritium activity being nominal 29.6 TBq.

As for maintenance activities, the control circuit of the accelerator was inspected every four month. The target assembly of the 80° beam line was replaced with a new one, owing to the inexpedient structure. As electric discharge often happened to both the low(3mA) and high(20mA) current ion source, damaged parts in the ion source were renewed and then characteristic performance recovered.

As for renewal activities, the fiber optic cable control system was newly applied to the ion source voltage control, aiming at easy and fine control. The special caution was paid on the design and manufacture of the noise resistant circuit, and a great effort was taken to protect it from the noise in actual operation. In addition to the activity, regulator system for beam extraction voltage control was renewed and two turbo molecule pumps were replaced with magnetic-float-type turbo molecule pumps (maintenance free pump) to reduce tritium waste.

#### Tritium Handling

Six small tritium targets with 370 GBq and one tritium target with 24TBq were used for experiments at the 80° beam line and for heavy irradiation experiment at the 0° beam line, respectively. The Tritium Adsorption Processor(TAP) system processed a total amount of 2.2 TBq tritium in exhaust gas from the vacuum system of the accelerator. Three rotating tritium targets and 44 small targets were canned and transferred to the waste processing facility.

#### Development

Development of a high-quality and long-lived target to accommodate the FNS future plan was progressed under the commercial contract base with VALDUC center of France Commissariat a L'Energie Atomique(CEA). In parallel with the above development, a new test target disk having highly cooling performance was manufactured by the electroforming. Its performance will be tested next fiscal year.

## 12.4 Operation Report of Heat Transfer and Fluid Flow Test Facilities

H. Watanabe, K. Nakajima, T. Satoh, Y. Watanabe and H. Watanabe

In FY-1993, operation and maintenance as well as design & construction of Heat Transfer and Fluid Flow Test Facilities were successfully achieved as schedules.

As for the operations of test facilities, the following five tests were performed.

- 1) DNB (Departure from Nucleate Boiling) test with high pressure water loop.
- 2) Two-phase flow test with horizontal-pipe test loop.
- 3) Test of spacer effect in two-phase flow with the neutron radio graphy loop.
- 4) Test of flow instability in boiling channel.
- 5) Test of effectiveness of new ECCS concept (Core Make-up Tank) for the passive safety reactor.<sup>1)</sup>

As for the maintenance of test facilities, annual inspections of the pressure vessels, the high pressure gas production system and the steam generator located at both of the Large Scale Reflood Test Building and Chemical / Mechanical Engineering Building were carried out.

As a result, those pressure vessels passed the inspection by the labor standard office without any problems.

As for the design and construction of test facilities, the following four facilities were newly constructed.

- 1) Multi-dimensional fluid flow mock-up loop.
- 2) Two-phase flow plenum test loop.
- 3) Ultra high heat flux test loop.
- 4) A part of the CCFT-II facility such as pressurizer tank, recirculation pumps, 2.5MW air-coolers, etc.

Radio isotopes used in the large scale reflood test facility was disposed and legal procedure was completed based on the regulation on prevention from radiation hazard.

### Reference

- 1) Murao. Y., et al. : Study on Concept of JAERI Passive Safety Reactor (JPSR) (5), Fall Meeting of the Atomic Energy Society of Japan, D48, 1993 (in Japanese).

## 12.5 Operation Report of Tandem Accelerator and Electron Linac

T. Yoshida, S. Shoji and C. Kobayashi

### Tandem Accelerator

The scheduled operation of the tandem accelerator for experiments was performed through the past one year containing two short periods for the scheduled maintenance. The accelerator ran with smoothly throughout the year. The accelerator running time was 4137.6 hours. The following are summary of the operation from April 1, 1993 to March 31, 1994.

The construction of the tandem booster has almost completed in November 1993. The beam test is under going successfully. This item will be reported in other paragraphs.

#### 1) Time distribution by terminal voltage

> 16 MV	75 days	38.7 %		11-12MV	12 days	6.2 %
15-16	62	32.0		10-11	3	1.5
14-15	13	6.7		9-10	4	2.1
13-14	9	4.6		4 - 9	3	1.5
12-13	10	5.2		< 8	3	1.5

#### 2) Time distribution by projectile

<sup>1</sup> H	11 days		<sup>18</sup> O	6 days		<sup>54</sup> Fe	3 days
<sup>2</sup> H <sub>2</sub>	1		<sup>19</sup> F	6		<sup>56</sup> Fe	7
<sup>7</sup> Li	7		<sup>28</sup> Si	2		<sup>58</sup> Ni	19
<sup>11</sup> B	2		<sup>31</sup> P	3		<sup>59</sup> Co	9
<sup>12</sup> C	9		<sup>32</sup> S	5		<sup>63</sup> Cu	9
<sup>13</sup> C	11		<sup>35</sup> Cl	17		<sup>79</sup> Br	1
<sup>14</sup> N	1		<sup>37</sup> Cl	9		<sup>127</sup> I	13
<sup>16</sup> O	27		<sup>45</sup> Sc	6		<sup>198</sup> Au	6

#### 3) Time distribution by activity

Operation for research	194 days
Atomic and solid state physics (34 days)	
Radiation effects in materials (19 )	

Nuclear chemistry	(27 )	
Nuclear physics	(86 )	
Fast neutron physics	( 8 )	
Radiation chemistry	( 4 )	
Detector development	( 3 )	
Accelerator test	(11 )	
Others	( 2 )	
Voltage conditioning		4 days
Operation training		2 days
Scheduled maintenance (2 tank openings)		85 days
Unexpected repair (1 tank opening)		10 days
Holidays and vacation		70 days

### Electron Linac

The electron linac was operated for the experimental researches with the 366.4 hour beam time from April 1, 1993 to December 31, 1993. The following are summary of the operation.

#### Time distribution by activity

Positron Experiment (Emission of mono-energetic Positron)	14 days
JSR injection	12 days
Neutron Radiography	17 days
Test and Development of Detectors	9 days

After over twenty years operation, it became difficult to operate and maintain due to deteriorate of the accelerator components and the peripheral system. The electron linac was shut-down on December 31, 1993.



### 13. Activities of Research Committees

Several research committees are organized to promote research activities. Name and task of each research committee are as follows:

#### Japanese Nuclear Data Committee

The committee is organized to promote evaluation of nuclear data and production of group constants. The committee takes a task of compiling the activities of the International Nuclear Data Committee and the OECD/NEA Nuclear Science Committee. The committee is also required to exchange information on nuclear data with the OECD/NEA Data Bank and domestic research institutions. A symposium is held annually to discuss research activities on nuclear data.

#### Research Committee on Reactor Physics

The Committee is organized to discuss research activities on reactor core analysis method and neutronics of new concept reactors.

#### Atomic and Molecular Data Committee

The committee is organized to promote compilation and evaluation of atomic and molecular data for controlled fusion research. Three working groups are organized under the committee. Workshops on atomic and molecular data are held to discuss current problems relevant to fusion research.

#### Research Committee on Advanced Reactors

The committee is organized to review and discuss reactor concepts and fuel cycle with emphasis on Pu utilization and passive reactor safety.

#### Research Committee on Partitioning and Transmutation

The committee is organized to discuss research activities on partitioning and transmutation.

Members of the committees are consist of staff of JAERI and experts on the relating research fields.

### 13.1 Activity of Japanese Nuclear Data Committee

Y. Kikuchi

The Japanese Nuclear Data Committee, which was organized to promote compilation and evaluation of nuclear data, has about 150 members in Atomic Energy Society of Japan. The committee consists of three subcommittees, six standing groups, steering and counseling committees.

The Committee Meeting was held in July 1993 to discuss the nuclear data activity in the previous fiscal year and plans for the fiscal year 1993. Furthermore, discussion was made on several topics including the NEANSC Think Tank meeting, the status of JENDL-3.2 and the international activity on nuclear data.

The activities of subcommittees and standing groups are briefly summarized below.

#### **Subcommittee on Nuclear Data**

##### Evaluation and Calculation System WG

The Integrated Nuclear Data Evaluation System (INDES) is under development with knowledge engineering technology. Discussion was made about nuclear model parameters such as optical potentials and level density. The microscopic optical model could be applied to data evaluation. It was required to study models of nuclear fission in the high energy region.

##### High-Energy Nuclear Data Evaluation WG

Methods of the high-energy data evaluation were discussed. Actual work was divided into two energy regions of up to 50 MeV and up to a few GeV. Nuclear data of several elements were evaluated up to 50 MeV for the ESNIT project. A review was made of several computer codes applicable to high-energy data evaluation.

##### Photonuclear Reaction Data WG

Data evaluation has been made up to 140 MeV. The results are published as a JAERI-Data report.

##### Evaluation of Covariance Data WG

Covariance matrices of the (n,p) and (n,2n) reactions on  $^{46}\text{Ti}$  were obtained by using the GMA code. Errors of the total and inelastic scattering cross sections of  $^{238}\text{U}$  were

estimated from nuclear model calculations. The code system which estimates errors of optical model calculations was implemented on a workstation at the Nuclear Data Center. Discussion was made about the covariance matrices used for the JENDL-3.1 evaluation.

#### Activation Cross Section WG

A benchmark test has been being performed of the JENDL Activation Cross Section File by comparing with the measurements at FNS. The results will be used to modify evaluated data. The WG decided to join the coordinated research program on International Reference Data Library of Nuclear Activation Cross Sections promoted by IAEA.

#### PKA Spectrum WG

Kerma factors of the neutron-induced reactions on  $^{12}\text{C}$  were calculated by using a Monte Carlo code developed at Kyushu University. The WG decided to employ the same method for evaluation of light nuclides such as  $^6\text{Li}$ ,  $^9\text{Be}$ ,  $^{14}\text{N}$  and  $^{16}\text{O}$ . Examined was the accuracy of the PKA spectra calculated with the ESPERANT code.

#### Fission Product Nuclear Data WG

Revision of the FP data was performed for JENDL-3.2, and a benchmark test has been made.

#### WG on Revision of JENDL-3 Heavy-Nuclide Data

Revision work for JENDL-3.2 was performed.

#### WG on Revision of JENDL-3 Gamma-ray Production Data

Revision work for JENDL-3.2 was performed.

#### **Subcommittee on Reactor Constants**

#### Fission Reactor Integral Test WG

Benchmark tests of JENDL-3.2 were performed for thermal and fast reactors.

#### Shielding Integral Test WG

Various integral measurements were analyzed by using the iron data in JENDL-3.2, and it was found that the evaluated data reproduced the measurements quite well. Benchmark tests of gamma-ray production data contained in JENDL-3.2 were performed by using the integral measurements at FNS and OKTAVIAN. A research has been started on group constants and benchmark tests for high-energy nuclear data applicable to accelerator-driven transmutation.

#### Dosimetry Integral Test WG

A review was made of the evaluated data contained in the JENDL Dosimetry File. Reevaluation of the data has been performed.

### **Subcommittee on Nuclear Fuel Cycle**

#### Decay Heat Evaluation WG

Calculation of beta-ray heating and delayed neutrons was performed.

#### WG on Evaluation of Nuclide Generation and Depletion

It was decided to make the ORIGEN-2 library based on JENDL-3.2 in cooperation with the Decay Heat Evaluation WG. At first, the COMRAD library is created, and then it is converted to the ORIGEN-2 library.

### **Standing Groups**

#### ENSDF Group

Mass chain evaluation for  $A = 123, 125$  and  $126$  has been finished.

#### Group on A&M Data and Nuclear Data for Medical Use

The group was reorganized in 1993. Data needs from medical use are surveyed.

#### JENDL Compilation Group

Compilation of JENDL-3.2 was performed.

#### CINDA Group

The literature on neutron data published in Japan was surveyed. In 1993, eighty-five entry records were created and they were sent to the NEA Data Bank.

#### Editorial Group of "Nuclear Data News"

"Nuclear Data News No. 45-47" were issued.

### 13.2 Activities of the Research Committee on Reactor Physics

T. Hiraoka, K.Tsuchihashi, H. Maekawa and S. Tanaka

The committee reviews research works related to reactor physics in Japan and supports the activities of Nuclear Science Committee of OECD/NEA. It conducts the following three sub-committees. The sub-committee on reactor system discusses topics both of theoretical and experimental reactor physics of fission reactors. The activities of subcommittee on fusion reactor involve neutronics and diagnostics of fusion reactors. The scope of subcommittee on shielding involves mainly radiation shielding and protection of fission reactors and accelerators.

During the FY1993, the 63th meeting of the Research Committee on Reactor Physics (RCRP) was held in July 1993. The meeting was devoted to review the work relating the cooperative study on thorium fuel cycle supported by Grant-in-Aid for Scientific Research by Ministry of Education, Science and Culture of Japanese government. In the program, the following subjects were involved: 1) nuclear data for the thorium fuel cycles, 2) design study of Th/U-233 fuelled reactors, 3) critical experiments of these reactors and their analyses, 4) a preliminary study of fusion-fission hybrid with thorium and 5) thorium fuel developments, thorium fuels, irradiation tests. The summary report edited by Prof. I. Kimura was published. As to the activities related to NEA NSC, there were the status reports of three working parties on physics of plutonium recycling, advanced computing for nuclear applications and international evaluation cooperation of nuclear data. Brief summary was introduced on the 4th meeting of NEA NSC held in June 1993 at Paris.

The 38th meeting of Sub-committee on Reactor System was held in July 1993. Under the topic of measurement of C8/F, a review of various measurements, two measurements performed at TCA and FCA by counting  $\gamma$  ray from irradiated fuel, and a foil measurement at FCA were presented. As the first issue in a series of introductions of reactor core design and core management software for commercial reactors, the system of Hitachi Energy Research Institute was introduced. This system consists of a group constant processing code, a Monte Carlo and a deterministic code for assembly design, a neutronics-thermal hydraulics coupled nodal code and a nodal kinetics code for core design and analysis, and a sub-channel analysis code for evaluation of thermal margin. Several topics were introduced

from M&C + SNC '93 meeting at Karlsruhe, Seminar on Monte Carlo method at Saclay and Int. Conf. on transport theory at Bologna.

The 39th meeting was held in March 1994. As the second issue in the series of introductions of reactor core design and fuel management software for commercial reactors, the system of Mitsubishi Atomic Power Industry was presented. Core management is performed by the CBCF code to evaluate critical boron concentration at the nominal operation from plant operation information and by the INFANT code to evaluate on-line characteristics like power distribution from in-core instrumentation. Core design having been performed by the conventional codes is now covered by PHOENIX for assembly analysis and ANC for 3D nodal diffusion. Under the topic of utilization of neutron field, planning of a variable spectrum field at KUCA, status of neutron therapy and planning of a medical irradiation purpose reactor were introduced. The RERTR program for JRR-4 where medical irradiation is planned was also introduced in this topic.

The 40th meeting of the Subcommittee on Fusion Reactor was held on August 19, 1993. Following two meetings were reported; (1) International Workshop on Nuclear Data for Fusion Reactor, and (2) IAEA-CRP on long-lived radioactivity production cross section. After the regular meeting, one and half days spent for the Japan/US workshop on Fusion Neutronics. The purpose of the workshop was to introduce the achievements of JAERI/USDOE collaborative program on Fusion Blanket Neutronics for ten years to Japanese neutronics community. A similar meeting was held at UCLA in October 1993 as International Workshop.

The 41st meeting was held in March 28, 1994. Present status of ITER/EDA and the IEA Cooperative Program on Fusion Reactor Technology were reported. Outline of two IAEA meetings was also reported; one was the FENDL meeting held in November at JAERI/Tokai and the other was the meeting on benchmark experiments for data testing held in December at IAEA/Headquarters.

Benchmark problems based on FNS and OKTAVIAN experiments were compiled by the Working Group and published as JAERI-M 94-014.

The 35th meeting of the Subcommittee on Shielding was held in July 1993 to introduce the experimental facilities in TIARA. A quasi-monoenergetic neutron experimental facility was fixed for shielding experiments and cross section measurements to 20 - 90 MeV neutrons, and penetration experiments on iron and concrete were made with neutrons of 43

and 67 MeV protons to verify the HILO86 group constant and model codes. Another three times of working group meeting were held to prepare the issue to be presented and discussed at the OECD/NEA specialists' meeting on Shielding Aspects of Accelerators, Targets and Irradiation facilities held in April 1994 at Arlington, USA.

### 13.3 Activity of Atomic and Molecular Data Committee

T. Shirai

The Atomic and Molecular (A&M) Data Committee is organized to promote activities on A&M data for the research and development of controlled thermonuclear fusion. The committee consists of members from JAERI, universities and other research institutions. The three working groups, particle-material interaction, atomic collision and atomic structure, are organized under the research committee according to differences in these specialty fields.

In collaboration with the A&M Data Committee, compilation and evaluation work is continued for making the 4th edition of Japanese Evaluated Atomic and Molecular Data Library (JEAMDL-4) as a five-year project from 1992. The activities of these three working groups are briefly summarized below.

Particle-material interactions relevant to the particle-recycling in the plasma edge have been surveyed and reviewed for the carbon materials. A workshop was held on particle-material interactions such as plasma-facing materials, radiation damages in carbon materials, trapping, emission and permeation of hydrogen in metals. Domestic literatures published during the last year were surveyed to collect numerical data of particle-material interaction data.

Analytical least squares fits have been made to the recommended cross sections for excitation and spectral line emission in collisions of H, H<sub>2</sub>, He and Li atoms and ions with atoms and molecules as is presented in 1.18 of this report. A similar work is now in progress for the ionization and charged particle production collisions. In parallel data compilation have been continued for recent experimental data for these collision processes in order to compare with the recommended data and to examine the validity of the analytical formulas used for extrapolation.

Critical evaluation of spectroscopic data of particular interest to the fusion community has been finished for Ti through Cu and Mo and now in progress for the Kr ions. These monographs will be put into one volume with addition of more recent data to the earlier compilations.



## 13.4 Activities of the Research Committee on Advanced Reactors

T. Tone, K. Tsuchihashi and Y. Murao

The Research Committee on Advanced Reactors (RCAR) was founded in 1990, and renovated in FY1993 to more broadly review and discuss reactor concepts and fuel cycle with emphasis on Pu utilization and passive reactor safety. At its 4th meeting in January 1994, in order to cover these new activities, the RCAR approved the establishment of two Subcommittees on Pu Utilization Reactors and on Research and Development of Passive Safety Reactor, following the abolition of the previous two Subcommittees on High Conversion Light Water Reactor (LWR) and on Advanced LWR Technology Program. The RCAR is chaired by Director General of Tokai Research Establishment (Mr. S. Matsuura). The RCAR and its three subcommittees comprise members from Japan Atomic Energy Research Institute (JAERI), universities, Power Reactor and Nuclear Fuel Development Corporation (PNC), and industries including utilities and reactor manufacturers.

### 1. Subcommittee on Pu Utilization Reactors

Subcommittee on Pu Utilization Reactors was established to discuss and exchange information about utilization of Pu in advanced reactors coupled with fuel reprocessing. Reactor type should be broad enough to include current LWRs, Pu active storage reactors, and FBRs. The head is Professor A. Kanazawa, Nagoya University. It was recommended at the third RCAR meeting that the discussion should cover all the activities performed in Japan.

The first meeting of the subcommittee was held in January 1994. The topic discussed first was Pu utilization in the next generation LWR. General remarks on effective utilization of uranium and plutonium in LWRs were introduced on the basis of the investigation program performed by Nuclear Power Engineering Corporation with the support of MITI. It was followed by the presentations of the research work related to the program by Toshiba Corporation, Hitachi Ltd. and MAPI. In the second topic of once-through type Pu burner LWRs, expected chemical property of thorium and zirconia fuels and their burnup characteristics were presented as a proposal for the disposition of weapons grade plutonium.

The second meeting of the subcommittee was held in February 1994 where the topic

was a self-completed fuel cycle. First, the concept characterized by nitride (may be metallic) fuelled FBR, and high temperature pyro-chemical reprocessing was proposed as a new fuel cycle to satisfy simultaneously the conditions of economy, safety and breeding. It was followed by presentations on mass-flow analysis, design study of nitride fuelled FBR, PIE result of nitride fuel and high temperature pyro-chemical reprocessing. The topic was closed after the introduction of status and planning on the nitride-fuelled lead-cooled FBR program in Russia.

## 2. Subcommittee on Research and Development of Passive Safety Reactor

The subcommittee was founded in FY1993. The objective is to review the planning and results of research and development activities of passive safety reactor project of JAERI. The head is Professor M. Akiyama, the University of Tokyo. In this fiscal year, a meeting was held in January 1994. Here, the reviews of an integral-type test reactor and a loop-type passive safety reactor were identified as the major tasks.

The test reactor is a prototype of the system-integrated PWR (SPWR) which is a medium size passive safety reactor and the advanced marine reactor (MRX) which is a small scale integral-type PWR with passive safety features. A conceptual design of the test reactor is in progress and will be completed in 1996. Experimental studies are under way to investigate the important thermal-hydraulic phenomena of the test reactor including natural circulation, DNB characteristics, gravity driven coolant injection system, and steam condensation. The design and related research works of the test reactor will be discussed in next fiscal year.

A new concept of loop-type passive safety LWR (JPSR: JAERI Passive Safety Reactor) was presented at the subcommittee meeting. The JPSR has the following features: an inherent matching nature of core heat generation and heat removal, in-vessel control rod drive mechanism units, low power density core, once-through steam generators, elimination of chemical shim, a large volume pressurizer, passive residual heat removal systems, passive engineering safety systems and elimination of emergency diesel generators. The present states of transient analyses, design of passive heat removal system and results of nuclear calculations were explained and discussed at the meeting.

### 3. Subcommittee on Improvement of Core Thermal-Hydraulic Analysis Codes

The subcommittee was founded in FY1990. The objective is to evaluate the predictive capability of the present thermal-hydraulic analysis codes. The head is Professor H. Ninokata, the Tokyo Institute of Technology. In this fiscal year, a meeting was held in January 1994.

It was agreed that the attending organizations should perform bench-mark calculations to investigate the capability of various subchannel analysis codes. The proposed bench-mark problems are as follows: (1) subchannel mixing between two channels simulating the single-phase mixing experiment by Hori, et al.<sup>1)</sup> and the two-phase mixing experiment by Sato, et al.<sup>2)</sup>, (2) subchannel mixing among many channels simulating the Ispra 4 X 4 rod bundle experiment<sup>3)</sup>, (3) critical heat flux experiment simulating the JAERI 7-rod CHF experiments<sup>4)</sup>, (4) droplet entrainment and deposition simulating the low pressure air-water experiment by Cousin, et al.<sup>5)</sup> and the high pressure steam-water experiment by Keeys, et al.<sup>6)</sup>

In this fiscal year, the subchannel analysis results of problems (1) and (4) were presented by JAERI, Mitsubishi heavy industries, Nuclear fuel corporation, Hitachi and Toshiba corporation. The remaining problems will be discussed in next fiscal year. The summary of bench-mark calculations will be issued as an internal report of JAERI.

#### References

- 1) Hori K., et al.: Proceedings of JSME Kansai meeting 814-11, 97-100 (1981).
- 2) Sato Y., et al.: JSME Journal 56-528, 2327 (1990).
- 3) Herkenrath H., et al.: NEUR 7575 EN (1981).
- 4) Iwamura T., et al.: NURETH-6, Grenoble 571 (1993).
- 5) Cousins L.B., et al.: AERE-R 4926 (1965).
- 6) Keeys R.K.F., et al.: ARER-R 6293 (1970).

### 13.5 Activities of the Research Committee on Partitioning and Transmutation

H. Yoshida, H. Katsuta, M. Kubota, T. Mukaiyama, T. Takizuka and M. Mizumoto

The first meeting of the Research Committee on Partitioning and Transmutation was held in FY 1991 to review and discuss the R&D program and activities on partitioning and transmutation of actinides and fission products at JAERI, and the related national and international cooperation. This Committee consists of about 30 formal members from JAERI, other national institutes, universities and nuclear companies. Two Research Sub-Committees on Partitioning and Transmutation are attached to discuss the technical subjects by the relevant specialists.

In the fourth meeting of the Committee held in FY 1993, the Program Sub-Committee and the Program Working Group were established to take over the expediting and coordinating tasks of the OMEGA Program Team that was dissolved at the end of FY 1992 after the expiration of its two and a half year term. In the fifth meeting, the progress of OMEGA Program and the outline of the International Conference on Future Nuclear System( GLOBAL' 93) held in Seattle, USA were reported. The progresses of R&D on partitioning and transmutation were discussed in each Sub-Committee respectively.

Main topics addressed in the Sub-Committee on Partitioning were the followings:

1. Separation of Am and Cm from rare earth by selective back-extraction from the DIDPA solvent with a DTPA solution.
2. Back-extraction of U from the DIDPA solvent with sodium carbonate and the recovery of U from the sodium carbonate solution.
3. Solid formation in HLLW by its concentration and denitration and the filtration characteristics of the precipitate.

Main topics addressed in the Sub-Committee on Transmutation were the followings:

1. High intensity proton accelerator development including a 2 MeV beam acceleration test with ion source and RFQ, and the conceptual and optimization studies for the 1.5 GeV Engineering Test Accelerator.
2. Design studies on the accelerator-based transmutation systems including solid system, molten salt system and liquid metal system, and spallation integral experiments with 500 MeV proton beam at the National Laboratory for High Energy Physics.
3. Researches on basic properties of TRU fuels such as metallic alloy, nitride particle, and chloride molten salt.
4. Analyses of irradiated actinide fuels with mass spectroscopy, gamma-ray spectrometry and alpha spectrometry.

## Publication List

### 1. Nuclear Data, and Atomic and Molecular Data

- 1) Chiba S. and Smith D.L.: "Some Comments on Peelle's Pertinent Puzzle", JAERI-M 94-068, p.5, (1994)
- 2) Nakagawa T.: "ENDF Format for Covariance Matrices", *ibid.*, p.13, (1994)
- 3) Shibata K.: "Sensitivities of Nuclear Model Calculations and Parameter Covariances", *ibid.*, p.51, (1994)
- 4) Miyano K.: "Nuclear Data Sheets Update for A=126", Nucl. Data Sheets, 69, 429 (1993)
- 5) Derrien H.: "R-Matrix Analysis of  $^{239}\text{Pu}$  Neutron Transmission and Fission Cross Sections in Energy Range from 1.0 keV to 2.5 keV", J. Nucl. Sci. Technol., 35, 845 (1993)
- 6) Nakagawa T., Fukahori T., Chiba S. and Kikuchi Y.: "Nuclear Data Evaluation for JENDL Actinide File and High Energy Files", Proc. Int. Conf. and Technology Exp. on Future Nuclear Systems GLOBAL '93, Sep. 12-17, Seattle, USA, p.467, (1993)
- 7) Fukahori T., Nakajima Y. and Kikuchi Y.: "Evaluation of Intermediate Energy Nuclear Data for Accelerator System; A Case Study Neutron- and Proton-Induced Reactions in  $^{27}\text{Al}$ ", Proc. 7th Int. Conf. on Emerging Nuclear Energy Systems ICENES '93, Sep. 20-24, 1993, Makuhari, Chiba, Japan, p.449, (1994)
- 8) Mengoni A. and Nakajima Y.: "HERMES: A Personal-Computer Program for Calculation of the Fermi-Gas Model Parameters of Nuclear Level Density", JAERI-M 93-177 (1993)
- 9) Asami T. and Nakagawa T.: "Bibliographic Index to Photonuclear Reaction Data (1955-1992)", JAERI-M 93-195 (1993)
- 10) Nakagawa T.: "JENDL-3 Revision 2", JAERI-M 94-019, p.68, (1994)
- 11) Meigo S., Chiba S. and Fukahori T.: "Characterization of Neutrons Produced from the  $^1\text{H}(^{11}\text{B},n)^{11}\text{C}$  Reaction, *ibid.*, p.243, (1994)
- 12) Kawai M. and JNDC FP Nuclear Data WG: "Reevaluation of FP Nuclear Data for JENDL-3.2", *ibid.*, p. 276, (1994)

- 13) Chiba S., Fukahori T., Watanabe Y. and Koyama Y.: "Evaluation of Neutron Cross Sections of  $^{12}\text{C}$  up to 50 MeV", *ibid.*, p.300, (1994)
- 14) Mengoni. A and Nakajima Y.: "Nuclear Level Density Parameter Systematics Revisited: Nuclear Deformation Effects", *ibid.*, p.337, (1994)
- 15) Matsuyama I., Baba M., Matsuyama S., Kiyosumi T., Sanami T., Hirakawa N., Ito N., Chiba S., Fukahori T., Mizumoto M., Hasegawa K. and Meigo S.: "Measurements of Double-Differential  $\alpha$ -Particle Production Cross Sections Using a Gridded Ionization Chamber —Application of  $^{14}\text{N}(\text{d},\text{n})^{15}\text{O}$  and  $^{15}\text{N}(\text{d},\text{n})^{16}\text{O}$  Neutron Sources—", *ibid.*, p.191, (1994)
- 16) Fukahori T.: "Status of Intermediate Energy Nuclear Data", JAERI-M 94-028, p.53, (1994)
- 17) Ishibashi K., Nakamoto T., Matsufuji N., Machata K., Wakuta Y., Numajiri M., Takada H., Meigo S., Chiba S., Watanabe Y. and Nakamura T.: "Neutron Measurement for the Reactions Induced by High-Energy Protons", *ibid.*, p.66, (1994)
- 18) Chiba S.: "QMD Calculation of Nucleon-Nucleus Reaction Cross Sections", *ibid.*, p.111, (1994)
- 19) Derrien H.: "Revision of  $^{241}\text{Pu}$  Reich-Moore Resonance Parameters by Comparison with Recent Fission Cross Section Measurements", JAERI-M 93-251 (1993)
- 20) Mengoni A. and Nakajima Y.: "Fermi-Gas Model Parametrization of Nuclear Level Density", *J. Nucl. Sci. Technol.*, **31**, 151 (1994)
- 21) Nakagawa T. and Kikuchi Y.: "Evaluation of Nuclear Data of  $^{237}\text{U}$ ,  $^{236}\text{Np}$  and  $^{238}\text{Np}$ ", JAERI-M 94-009 (1994) (in Japanese)
- 22) Katakura J., Oshima H., Kitao K. and Iimura H.: "Nuclear Data Sheets for A=125", *Nucl. Data Sheets*, **70**, 217 (1993)
- 23) Kikuchi Y., Nakagawa T., Takano H. and Mukaiyama T.: "Reliability of Actinoid Nuclear Data and Integral Tests", *J. Atomic Energy Soc. Jpn.*, **211**, **36** (1994) (in Japanese)
- 24) Narita T., Ichimiya T. and Kitao K.: "List of Strong Gamma-Rays Emitted from Radionuclides (Version 2)", JAERI-M 94-059 (1994)
- 25) Cierjacks S. and Shibata K.: "Blind Intercomparison of Nuclear Models for Predicting Charged Particle Emission", NEA/NSC/DOC(93)4 (1994)

- 26) Shibata K.: "Sensitivities of Calculated Cross Sections of  $^{56}\text{Fe}$  to Model Parameters", OECD/GD(94)21 (1994)
- 27) Kawai M., Hasegawa A., Ueki K., Yamano N., Sasaki K., Matsumoto Y., Takemura M., Ohtani N. and Sakurai K.: "Shielding Benchmark Tests of JENDL-3", JAERI 1330 (1994)
- 28) Ito R., Tabata T., Shirai T. and Phaneuf R.A.: "Analytic Cross Sections for Collisions of H, H<sub>2</sub>, He and Li Atoms and Ions with Atoms and Molecules I", JAERI-M 93-117 (1993)
- 29) Hamamoto N., Tanaka T., Itoh A., Imanishi N., Saito M., Haruyama Y. and Shirai T.: "Charge-Changing Collision Cross Sections of Low-Energy Carbon Ions with Carbon Containing Molecules", JAERI-M 93-202 (1993) (in Japanese)
- 30) Ichihara A., Shirai T. and Eichler J.: "Cross Sections for Electron Capture in Relativistic Atomic Collisions", Atom. Data Nucl. Data Tables, **55**, 63 (1993)
- 31) Shirai T., Nakai Y., Nakagaki T., Sugar J. and Wiese W.L.: "Spectral Data and Grotrian Diagrams for Highly Ionized Chromium, Cr V through Cr XXIV", J. Phys. Chem. Ref. Data, **22**, 1249 (1993)
- 32) Janev R.K., Phaneuf R.A., Tawara H. and Shirai T.: "Recommended Cross Sections for State-Selective Electron Capture in Collisions of C<sup>6+</sup> and O<sup>8+</sup> Ions with Atomic Hydrogen", Atom. Data Nucl. Data Tables, **55**, 201 (1993)
- 33) Mengoni A. and Shirai T.: "Vibron Model Description of Vibrational Spectra of the HCO and DCO Molecules", J. Mol. Spectrosc., **162**, 246 (1993)
- 34) Baba M., Kiyosumi T., Iwasaki T., Yoshioka M., Matsuyama S., Hirakawa N., Nakamura T., Tanaka S., Tanaka R., Tanaka S., Nakashima H. and Meigo S.: "Characterization and Application of 20-90 MeV  $^7\text{Li}(p,n)$  Neutron Source at Tiara", Proc. 1993 Symp. on Nuclear Data, JAERI-M 94-019, 200 (1994)
- 35) Ikeda Y. and Konno C.: "Measurements on the Cross Sections for  $^{94}\text{Mo}(n,p)$  &  $^{95}\text{Mo}(n,np)^{94}\text{Nb}$ ,  $^{158}\text{Dy}(n,p)^{158}\text{Tb}$ ,  $^{182}\text{W}(n,n\alpha)^{178\text{m}2}\text{Hf}$  and  $^{187}\text{Re}(n,2n)^{168\text{m}}\text{Re}$  Reactions at 14 MeV Region", Proc. of 2nd IAEA-RCM on Long-Lived Radioactivity Production Cross Section, April 29-30, San Diego, USA, INDC(NDS)-286, 27, (1993)
- 36) Meadows J., Smith D., Haight R., Ikeda Y. and Konno C.: "Results from the Argonne, Los Alamos, JAERI Collaboration", *ibid.*, 13, (1993)

- 37) Kobayashi K., Nakazawa M., Iwasaki S., Iguchi T., Sakurai K., Ikeda Y. and Nakagawa T.: "JENDL Dosimetry File", Proc. of 8th ASTM-EURATOM Symp. on Reactor Dosimetry, Aug. 29 – Sep. 3, 1993, Vail, Colorado, USA
- 38) Ikeda Y., Konno C., Oyama Y., Kosako K., Oishi K. and Maekawa H.: "Absolute Measurements of Activation Cross Section of  $^{27}\text{Al}(n,p)^{27}\text{Mg}$ ,  $^{27}\text{Al}(n,\alpha)^{24}\text{Na}$ ,  $^{56}\text{Fe}(n,p)^{56}\text{Mn}$ ,  $^{90}\text{Zr}(n,2n)^{89m+g}\text{Zr}$  and  $^{93}\text{Nb}(n,2n)^{92m}\text{Nb}$  at an Energy Range from 13.3 to 14.9 MeV", J. Nucl. Sci. Technol., **30** [9] (1993)
- 39) Konno C., Ikeda Y., Oishi K., Kawade K., Yamamoto H. and Maekawa H.: "Activation Cross Section measurements at Neutron Energy from 13.3 to 14.9 MeV Using the FNS Facility", JAERI 1329 (1993)
- 40) Ikeda Y., Konno C., Kosako K., Asai M., Kawade K. and Maekawa H.: "Measurement of the  $^{93}\text{Nb}(n,n')^{93m}\text{Nb}$  Reaction Cross Section at 14.5 and 14.9 MeV", J. Nucl. Sci. Technol. **30** [10], pp.967–973, (1993)
- 41) Ikeda Y., Konno C. and Maekawa H.: "Measurement of Radioactivity Production for  $^{48}\text{V}$ ,  $^{56}\text{Co}$  and  $^{65}\text{Zn}$  via the (p,n) Sequential Reaction Processes in Titanium, Iron and Copper Metals Associated with 14 MeV Neutron Irradiation", Nucl. Sci. Eng., **116**, 19–27 (1994)
- 42) Ikeda Y., Cheng E.T., Konno C. and Maekawa H.: "Measurement of Neutron Activation Cross Sections for the  $^{99}\text{Tc}(n,\alpha)^{99}\text{Mo}$ ,  $^{99}\text{Tc}(n,\alpha)^{96}\text{Nb}$ ,  $^{99}\text{Tc}(n,n'\alpha)^{95}\text{Nb}$  and  $^{99}\text{Tc}(n,n')^{99m}\text{Tc}$  Reactions at 13.5 and 14.8 MeV", Nucl. Sci. Eng., **116**, 28–34 (1994)

## 2. Theoretical Method and Code Development

- 1) Kugo T., Tsuchihashi K. Nakagawa M. and Mori T.: "Development of Intellectual Reactor Design System IRDS", Int. Conf. on Mathematical Methods and Supercomputing in Nuclear Applications (M&C + SNA '93) Apr. 19–23, 1993, Karlsruhe, Vol.2, p.199, (1993)
- 2) Nakagawa M. and Mori T.: "Whole Core Calculations of Power Reactors by Monte Carlo Techniques", *ibid*, Vol.2, p.702, (1993)
- 3) Nakagawa M. and Mori T.: "Whole Core Calculations of Power Reactors by Use of Monte Carlo Method", J. Nucl. Sci. Technol. **30**, 1692 (1993)



## 3. Reactor Physics Experiment and Analysis

- 1) Iijima S., et al.: "Benchmark Physics Experiment of Metallic-fueled LMFBR at FCA(II) —Experiments of FCA Assembly XVVII-1 and Their Analyses—", JAERI-M 93-186 (1993)
- 2) Iijima S., et al.: "Experimental Study of Reactivity Feedback Parameters on Metallic-Fueled LMFBR", Proc. of Japanese-Russian FBR Seminar —General Approaches for Fast Reactor Safety Ensuring— (1993)
- 3) Oigawa H., Okajima S., Mukaiyama T. and Satoh K. "Measurement of Doppler Effect Up to 2000 °C at FCA (1) —Development of Experimental Device for Doppler Reactivity Worth Measurement with Small Sample Heated Up to 1500 °C—", JAERI-M 94-043 (1993)
- 4) Mukaiyama T.: "Nuclear Reactors as Versatile Equipments for Innovative Studies", Journal of the Atomic Energy Society of Japan Vol.35, No.5 (1993)
- 5) Mukaiyama T. and Gunji Y.: "Minor Actinide Transmutation in Fission Reactors and Fuel Cycle Consideration", Proc. 2nd OECD/NEA Information Exchange Mtg. on P-T
- 6) Mukaiyama T.: "Transmutation of Long-Lived Nuclides by Burner Reactors", The Symp. of Japan Atomic Energy Soc., (Aug. 1993)
- 7) Mukaiyama T.: "Minor Actinide Transmutation in Actinide Burner Reactors", Proceedings of Japanese-Russian FBR Seminar, (Sept. 7, 1993)
- 8) Mukaiyama T.: "Influence of Minor Actinide Transmutation on Fuel Cycle Facilities", GLOBAL '93, (Sept. 1993)
- 9) Mukaiyama T.: "Partitioning and Transmutation R&D Program "OMEGA" and Present Status of Transmutation Study at JAERI", IAEA Tech Committee Mtg. on P-T
- 10) Mukaiyama T., Ogawa T. and Gunji Y.: "Minor Actinide Burner Reactor and Influence of Transmutation on Fuel Cycle Facilities", IAEA Tech. Committee Mtg. on P-T
- 11) Mukaiyama T.: "Transmutation of Long Lived Radioactive Waste", Energy Review, (Feb. 1994)

## 4. Advanced Reactor System Design Studies

- 1) Murao Y., Araya F., Iwamura T. and Watanabe H.: "A Concept of Passive Safety Light Water Reactor System Requiring Reduced Maintenance Efforts", presented at ANS Winter Meeting, Nov. 1993, San Francisco
- 2) Murao Y., Araya F., Iwamura T., Okumura K. and Kunii K.: "Concept of Passive Safety Reactor with Inherent Matching Nature of Heat Removal and Core Heat Generation", presented at 71st JSME Spring Annual Meeting, March 1993, Tokyo (in Japanese)
- 3) Murao Y., Araya F. and Iwamura T.: "Transient Characteristics of JAERI Passive Safety Light Water Reactor System", presented at ARS '94 —International Topical Meeting on Advanced Reactor Safety, Apr. 1994, Pittsburgh
- 4) Inabe T., Nakata H., Akie H., et al.: "Conceptual Study of Test Reactor for Fuel Irradiation/Reactor Performance Research", JAERI-M 93-106 (1993) (in Japanese)
- 5) Fujine S., Takano H., et al.: "Conceptual Study of the Future Nuclear Fuel Cycle System for the Extended LWR Age", JAERI-M 93-157 (1993) (in Japanese)
- 6) Fujine S. and Takano H.: "Fuel Cycle System for Pu-Recycling in Very High Burnup LWRs", Proc. GLOBAL '93, Int. Conf. on Future Nuclear Systems, Sep. 12-17, Seattle, Vol.2, p.1157, (1993)
- 7) Takano H. and Fujine Y.: "Minor Actinide Transmutation Light Water Reactor", *ibid*, Vol.2, p.1273, (1993)
- 8) Akie H., Muromura T., Takano H. and Matsuura S.: "A New Concept of Once-through Burning for Nuclear Warheads Plutonium", 7th Int. Conf. on Emerging Nuclear Energy Systems (ICENES '93), Sep. 20-24, 1993, Makuhari, World Scientific, p.298, (1994)
- 9) Takano H., Akie H., Handa M. and Hiraoka T.: "A Concept of Self-Completed Fuel Cycle Based on a Lead-Cooled Nitride Fuel Fast Reactors", *ibid.*, p.308, (1994)
- 10) Takizuka T., Yasuda H., Ogawa T., Hiraoka T., Nei H., Mawatari K. and Aoki K.: "An HTGR-MHD Combination for High Efficiency Power Generation", Proc. 7th ICENES '93, 321 (1993)

## 5. Fusion Neutronics

- 1) Maekawa F., Konno C., Kosako K., Oyama Y., Ikeda Y. and Maekawa H.: "Importance of Self-Shielding Effect on Shielding Design of Fusion Devices", *Fusion Technol.*, pp.1419-1423, (1993)
- 2) Pulpan J.: "Wall Effect Correction for a Small Cylindrical Proportional Counters", *JAERI-M 93-115* (1993)
- 3) Oyama Y., Kosako K. and Maekawa H.: "Measurement and Calculations of Angular Neutron Flux Spectra from Iron Slabs Bombarded with 14.8 MeV Neutrons", *Nucl. Sci. Eng.*, **115** [1] pp.24-37, (1993)
- 4) Ikeda Y.: "Measurement of Nuclear Heat Deposition in Structural Materials due to 14 MeV Neutron by a Microcalorimeter", *Houshasen*, **19**(3), 39 (1993)
- 5) Maekawa F. and Oyama Y.: "Techniques of Integral Experiment and Methods for Validation of Evaluated Nuclear Data Libraries for Secondary Gamma-Ray Data under D-T Neutron Field", *Proc. of the 1993 Symposium on Nuclear Data*, *JAERI-M 94-019*, pp.369-374, (1994)
- 6) Ikeda Y.: "Integral Test of JENDL Activation Library for Fusion Application", *ibid.*, pp.79-94, (1994)
- 7) Maekawa F., Konno C., Oyama Y., Ikeda Y. and Maekawa H.: "Benchmark Experiment on a Copper Slab Assembly Bombarded by D-T Neutrons", *JAERI-M 94-038* (1994)
- 8) Sub-Working Group of Fusion Reactor Physics Subcommittee: "Collection of Experimental Data for Fusion Neutronics Benchmark", *JAERI-M 94-014* (1994)
- 9) Oyama Y., Konno C., Ikeda Y., Maekawa F., Kosako K., Maekawa H., M.A. Abdou, M.Z. Youssef and A. Kumar: "Phase III Experiments of the JAERI/USDOE Collaborative Program on Fusion Blanket Neutronics", *JAERI-M 94-015* (1994)
- 10) Kuriyama K., Tomizawa K., Koga K., Hayashi N., Watanabe H., Ikeda Y. and Maekawa H.: "Thermally Stimulated Current in Test Neutron Irradiated Semi-insulating GaAs: Ga Anti-site Related New Frap", *App. Phys. Lett.*, **63**(14), 4 (1993)
- 11) Hoek M., Nishitani T., Ikeda Y. and Morioka A.: "Initial Results from Neutron Yield Measurements by Activation Technique at JT-60U", *JAERI-M 94-002* (1994)

## 6. Radiation Shielding

- 1) Suzuki T., Hasegawa A., Tanaka S. and Nakashima H.: "Development of BERMUDA: A Radiation Transport Code System, Part II. Gamma Rays Transport Codes", JAERI-M 93-143 (1993)
- 2) Sato O., Furihata S., Uehara T., Yoshizawa N., Iwai S., Tanaka S. and Sakamoto Y.: "Evaluation of Fluence to Dose Equivalent Conversion Factors for High Energy Radiations (II), —Establishment of the Evaluation of the Q Values for High Energy Charged Particles and Evaluation of the Dose Equivalent Conversion Factors for High Energy Photons—", JAERI-M 93-147 (1993) (in Japanese)
- 3) Nakane Y., Furihata S., Iwai S. and Tanaka S.: "Stopping Power of Charged Particles from 10 eV/amu to 10GeV/amu", JAERI-M 93-152 (1993) (in Japanese)
- 4) Yamaji A. and Sakamoto Y.: "Comparison between Measured and Design Dose Rate Equivalents on Board of Nuclear Ship MUTSU", J. Nucl. Sci. Technol., Vol.30, No.9, 926 (1993)
- 5) Tian D., Hasegawa A., Nakagawa T. and Kikuchi Y.: "Benchmark Tests of Principal Fissile Nuclide Data in JENDL-3 with Simple Fast Critical Assemblies", J. Nucl. Sci. Technol., Vol.30, No.11, 1087 (1993)
- 6) Nariyama N., Tanaka S., Yoshizawa M., Hirayama H., Ban S., Nakashima H., Namito Y. and Nakane Y.: "Responses of LiF TLDs to 10 – 40 keV Monoenergetic Photons from Synchrotron Radiation", Radiat. Prot. Dosim., Vol.49, No.4, 451 (1993)
- 7) Sakamoto Y.: "Photon Cross Section Data PHOTX for PEGS4 Code", Proc. of the Third EGS4 User' Meeting in Japan, KEK-Proc-93-15, 77 (1993) (in Japanese)
- 8) Ban S., Hirayama H., Namito Y., Tanaka S., Nakashima H., Nakane Y. and Nariyama N.: "Calibration of Silicon PIN Photodiode for Measuring Intensity of 7 – 40 keV Photons", J. Nucl. Sci. Technol., Vol.31, No.2, 163 (1994)

## 7. Reactor and Nuclear Instrumentation

- 1) Kishimoto M., Sakasai K. and Ara K.: "Estimation of Current Distribution from Magnetic Fields by Combination Method of Genetic Algorithm and Neural-Network",

- Tran. IEEE, C, Vol.113, No.9 (1993) (in Japanese)
- 2) Ara K., Katagiri M., Wakayama N., et al.: "Development of Water Level Gauge with Binary Coding Thermocouples and its Application to Measurement of In-Vessel Reactor Water Level", J. At. Energy Soc. Japan, Vol.35, No.11 (1993) (in Japanese)
  - 3) Katagiri M., Kishimoto M., Ito H., Yoshida H., et al.: "A Nuclide-Separation Wire Precipitator for Measurements of Noble-Gas Fission Products", Nucl. Inst. Meth. in Phy. Res., A, No.327 (1993)
  - 4) Ara K., et al.: "Development of Eddy Current Testing Method with Detection of Disturbed Magnetic Flux", IEEE, MAG-93-96 (1993) (in Japanese)
  - 5) Kishimoto M., Sakasai K. and Ara K.: "The Inverse Estimation of Current Distribution Using Combination Method of GA and Neural-Network", IEEE, MAG 93-167 (1993) (in Japanese)
  - 6) Ara K., Nakajima N. and Ebine N.: "A Proposal on Non-Destructive Measuring Method for Embrittlement of Reactor Pressure Vessel", IEEE, MAG-93-218 (1993) (in Japanese)
  - 7) Ara K., Sakasai K., Kishimoto M., Ebine N. and Nakajima N.: "A Nondestructive Measuring Method for Estimating the Thickness of Overlay-Clad of Reactor Pressure Vessel", IEEE, MAG-94-24 (1994) (in Japanese)
  - 8) Sakasai K., Kishimoto M. and Ara K.: "On Spatial Transfer Function between Magnetic Fields and their Sources", J. Mag. Soc. Japan, Vol.18, No.2 (1994) (in Japanese)
  - 9) Ara K., Katagiri M., Ito H. and Sakasai K.: "AC Magnetic-Flux Penetration in Sintered  $\text{Bi}_2\text{Sr}_2\text{CaCu}_2\text{O}_x$  High-Tc Superconductors, by Using a Planar Coil", J. Mag. Soc. Japan, Vol.18, No.2 (1994) (in Japanese)
  - 10) Sakasai K., Kishimoto M. and Ara K.: "Experiment for Directional Detection of Magnetic Flux Sources by a System of High Tc Superconductors and a Magnetic Sensor", J. Mag. Soc. Japan, Vol.18, No.2 (1994) (in Japanese)
  - 11) Kishimoto M., Sakasai K. and Ara K.: "Inverse Estimation of Beam Current Distribution for Accelerators Using the Combination Method of Genetic Algorithm and Neural Network", the 3rd MAGDA Conference in Osaka, A24-2 (1994) (in Japanese)

- 12) Yamagishi H.: "Theoretical Study on Position Sensitive Fission Counters Designed with a Transmission Delay Line Structure", JAERI-M 93-151 (1993) (in Japanese)
- 13) Yamagishi H.: "Electronics and Pulse Counting Error of Position Sensitive Fission Counters with a Transmission Delay Line Structure", JAERI-M 94-010 (1994) (in Japanese)

#### 8. Reactor Control, Diagnosis and Robotics

- 1) Suzuki K.: " $H_{\infty}$  Control and its Application to Nuclear Plant", JAERI-M 93-169 (1993) (in Japanese)
- 2) Suzuki K., Shimazaki J. and Shinohara Y.: "Application of  $H_{\infty}$  Control Theory to Power Control of a Nonlinear Reactor Model", Nucl. Sci. Eng., 115, 142 (1993)
- 3) idem: "Estimation of Net Reactivity Based on  $H_{\infty}$  Estimation Theory", J. Atom. Ener. Soc. Japan, 36[1] 79 (1994) (in Japanese)
- 4) Suzudo T.: "Time-Series Analysis of Nonlinear Power Oscillation in NSRR", JAERI-M 93-137 (1993) (in Japanese)
- 5) Suzudo T., Hayashi K. and Shinohara Y.: "Methodology of Nuclear Reactor Monitoring and Diagnostics Using Information Dimension —Application to Power Oscillation", J. Nucl. Sci. Technol., 30[8], 727 (1993)
- 6) Hayashi K., et al.: "Reactor Dynamics Experiment of N.S. Mutsu Using Pseudo Random Signal (I) The First Experiment", JAERI-M 93-194 (1993) (in Japanese)
- 7) Hayashi K., et al.: "The Results of 1993 Benchmark Test on Detection of Sodium/Water Reaction", presented for Research Coordination Meeting on Acoustic Signal Processing for the Detection of Sodium/Water Reaction in LMFBR, Dec. 9-10, 1993, Vienna

#### 9. Heat Transfer and Fluid Dynamics

- 1) Sudo Y. and Kaminaga M.: "A New CHF Correlation Scheme Proposed for Vertical Rectangular Channels Heated from Both Sides in Nuclear Research Reactors", Trans. ASME J. Heat Transfer, Vol.115, No.2 (1993)

- 2) Ezzidi A., Okubo T. and Murao Y.: "Improvement of COBRA-TF Code Models for Liquid Entrainments in Film-Mist Flow", JAERI-M 93-133 (1993)
- 3) Ohnuki A., Akimoto H. and Murao Y.: "Assessment of TRAC-PF1/MOD1 and TRAC-PF1/MOD2 Codes for Thermal-Hydraulic Behavior in Pressure Vessel during Reflood in SCTF Test with an Inclined Radial Power Distribution", JAERI-M 93-138 (1993)
- 4) Ohnuki A., Akimoto H. and Murao Y.: "Assessment of TRAC-PF1/MOD1 Code for Thermal-Hydraulic Behavior in Pressure Vessel during Reflood in SCTF Test with a Radial Power Distribution", JAERI-M 93-139 (1993)
- 5) Akimoto H., Ohnuki A. and Murao Y.: "Assessment of One Dimensional Reflood Model in REFLA/TRAC Code", JAERI-M 93-240 (1993) (in Japanese)
- 6) Iguchi T.: "Void Fraction in a PWR Fuel Bundle during Reflood Phase —Evaluation of Equivalent Diameter Effect by Air Water Test—", JAERI-M 94-008 (1994) (in Japanese)
- 7) Akimoto H., Ikeda Y. and Kusano J.: "Development of Thermal Design Method of Rotating Target for DT Neutron Source", JAERI-M 94-016 (1994) (in Japanese)
- 8) Ohnuki A., Akimoto H. and Murao Y.: "Development of REFLA/TRAC Code for Engineering Work Station", JAERI-M 94-026 (1994) (in Japanese)
- 9) Akimoto H., Ohnuki A. and Murao Y.: "Assessment of Predictive Capability of REFLA/TRAC Code for Large Break LOCA Transient in PWR Using LOFT L2-5 Test Data", JAERI-M 94-037 (1993) (in Japanese)
- 10) Iwamura T., Watanabe H. and Murao Y.: "Critical Heat Flux Experiments under Steady-State and Transient Conditions and Visualization of CHF Phenomenon with Neutron Radiography", presented at Sixth International Topical Meeting on Nuclear Reactor Thermal Hydraulics, Oct. 1993, Grenoble
- 11) Murao Y., Iguchi T., Sugimoto J., Akimoto H., Iwamura T., Ohkubo T. and Ohnuki A.: "Thermal-Hydraulic Model for Reflooding Phenomena in a PWR-LOCA", presented at Sixth International Topical Meeting on Nuclear Reactor Thermal Hydraulics, Oct. 1993, Grenoble
- 12) Iwamura T., Watanabe H. and Murao Y.: "Steady-State and Transient DNB Experiments for Triangular-Pitched Rod Bundle", presented at 71st JPME Fall Annual

Meeting, Oct. 1993, Hiroshima (in Japanese)

- 13) Murao Y., Iguchi T., Akimoto H. and Iwamura T.: "Large-Scale Multi-Dimensional Phenomena found in CCTF and SCTF Experiments", Nuclear Engineering and Design, 145 (1993)
- 14) Yadigaroglu G., Nelson R.A., Teschendorff V., Murao Y., Kelly j. and Bestion D.: "Modeling of Reflooding", Nuclear Engineering and Design, 145 (1993)

#### 10. Transmutation System and Partitioning-Transmutation Fuel Cycle

- 1) Nishida T., Takada H., Takizuka T., Meigo S., Katsuta H. and Kato Y.: "Minor Actinide Transmutation System with an Intense Proton Accelerator", Proc. 7th ICENES '93, 419 (1993)
- 2) Katsuta H., Sasa T., Takizuka T., Kato Y., Nishida T. and Takahashi H.: "A Concept of Accelerator Based Incineration System for Transmutation of TRU and FP with Liquid TRU-alloy Target and Molten Salt Blanket", Proc. 7th ICENES '93, 424 (1993)
- 3) Katsuta H., Kato Y., Takizuka T., Takada H., Nishida T. and Yoshida H.: "A Continuous Transmutation System for Long-Lived Nuclides with Accelerator-Driven Fluid Target", Proc. Inter. Inform. Exchange Meeting on Actinide and Fission Product Separation and Transmutation, NEA/P&T REPORT°.7, 243 (1993)
- 4) Takizuka T., Nishida T., Takada H., Meigo S. and Mizumoto M.: "Conceptual Design Study of Accelerator-Based Actinide Transmutation Plant with Sodium-Cooled Solid Target/Core", Proc. Inter. Inform. Exchange Meeting on Actinide and Fission Product Separation and Transmutation, NEA/P&T REPORT°.7, 398 (1993)
- 5) Takada H., Ishibashi K., Yoshizawa N. and Nakahara Y.: "Benchmark Calculation for Double Differential Cross Section of (p,xn) and (p,xp) Reaction", J. Nucl. Sci. Technol., 31, 81 (1994)

#### 11. Accelerator Development

- 1) Oguri H., et al.: "Development of High Brightness Hydrogen Ion Source for BTA", 18th Linear Accelerator Meeting, Tsukuba



- 2) Hasegawa K., et al.: "R&D Works of JAERI BTA", 18th Linear Accelerator Meeting, Tsukuba
- 3) Mizumoto M.: "Application of High Intensity Accelerator in JAERI", 9th Accelerator Technical Meeting, Tsukuba
- 4) Hasegawa K., et al.: "Status of R&D for the Basic Technology Accelerator in JAERI", 9th Accelerator Technical Meeting, Tsukuba
- 5) Mizumoto M., et al.: "Development of Proton Linear Accelerator and Transmutation System", GLOBAL '93, Seattle, USA
- 6) Mizumoto M., et al.: "High Intensity Proton Linear Accelerator for Nuclear Waste Transmutation", ICENES '93, Makuhari
- 7) Minehara E., Nagai R., Sawamura M., Takao M., Kikuzawa N., Sugimoto M., Sasaki S., Ohkubo M., Sasabe J., Suzuki Y., Kawarasaki Y. and Shikazono M.: "JAERI Quasi-CW, and High Average Power Free Electron Laser Driven by a Superconducting RF Linac", Nucl. Instr. Meth. Phys. Res., A331, p.182, (1993)
- 8) Takao M., Sugimoto M., Sawamura M., Nagai R., Kikuzawa N., Minehara E., Ohkubo M., Kawarasaki Y. and Suzuki Y.: "Design Concept for the Second Phase Project of the JAERI Free Electron Laser", *ibid.*, p.218
- 9) Kikuzawa N., Minehara E., Sawamura M., Nagai R., Takao M., Sugimoto M., Ohkubo M., Sasabe J., Suzuki Y. and Kawarasaki Y.: "Recent Progress of the Superconducting Accelerator Module for the JAERI FEL", *ibid.*, p.276
- 10) Sawamura M., Ohkubo M., Minehara E., Nagai R., Takao M., Kikuzawa N., Sugimoto M., Suzuki Y., Kawarasaki Y., Nagatsuka K., Satoh K., Matsumoto H. and Kashiwagi A.: "An RF System Using All Solid State Amplifiers for the JAERI FEL", *ibid.*, p.323
- 11) Sugimoto M.: "Control System with a Software Simulator for JAERI FEL", *ibid.*, p.340
- 12) Sasaki K., Nagai R., Kikuzawa N., Sawamura M., Takao M., Sugimoto M., Minehara E., Ohkubo M., Sugimoto Y. and Kawarasaki Y.: "JAERI PULSE —A Versatile FEL Simulation Code on a Super-Computer", *ibid.*, p.450
- 13) Minehara E., Nagai R., Sawamura M., Takao M., Kikuzawa N., Sugimoto M., Sasaki S., Ohkubo M., Sasabe J., Suzuki Y., Kawarasaki Y., Kato and Shikazono M.: "Commissioning of the JAERI Free Electron Laser", Proc. 18th Linac Meeting Japan, July 21-23, 1993, KEK, Tsukuba, p.16

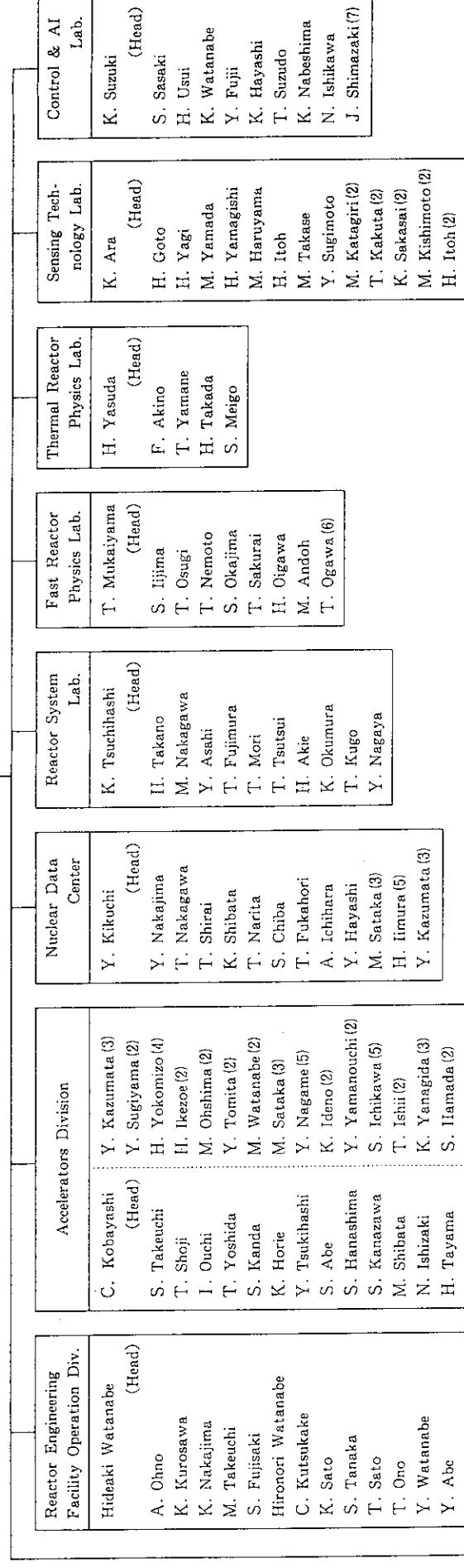
- 14) Sugimoto M.: "HELP System for Control of JAERI FEL", *ibid.* p.343
- 15) Kato R., Nakazato T., Oyamada M., Urasawa S., Yamakawa T., Yoshida, Ikezawa, Ishii, Kanai, Shibata and Takahashi S.: "Suppression of Coherent Synchrotron Radiation in Metallic Shield", *ibid.*, p.411
- 16) Kikuzawa N., Sawamura M., Nagai R., Minehara E., Takao M., Sugimoto M., Ohkubo M. and Suzuki Y.: "Superconducting Accelerator Module for the JAERI FEL", *Proc. 9th Symp. Accelerator Sci. & Technol.*, Aug. 23-27, 1993, KEK, Tsukuba, p.440
- 17) Minehara E., Nagai R., Sawamura M., Kikuzawa N., Sugimoto M., Sasaki S., Ohkubo M., Sasabe J., Suzuki Y. and Kawarasaki Y.: "JAERI Free Electron Laser Program", *ibid.*, p.455
- 18) Sugimoto M., Takao M., Sawamura M., Nagai R., Kato T., Kikuzawa N., Minehara E., Ohkubo M., Kawarasaki Y. and Suzuki Y.: "Progress of the IR FEL Development at JAERI", *Nucl. Instr. Meth. Phys. Res.*, A341, p.41, (1994)
- 19) Sawamura M., Nagai R., Takao M., Minehara E., Kikuzawa N., Kato R., Sugimoto M., Ohkubo M. and Suzuki Y.: "RF Power Tests for JAERI FEL Superconducting Accelerator Modules", *ibid.*, p.391
- 20) Takao M., Sugimoto M., Sawamura M., Nagai R., Kato R., Minehara E., Ohkubo M. and Suzuki Y.: "Recirculation Scheme in the Second Phase of the JAERI FEL Project", *ibid.*, p.394
- 21) Ohkubo M.: "Research on Highly Excited States of Nucleus by Neutrons", *Proc. 5th Int. Symp. "Neutrons as Microscopic Probes"*, March 30, 1993, Mito, JAERI-M 93-228, p.744
- 22) Takao M.: "On FEL Integral Equation and Electron Energy Loss in Intermediate Gain Regime", JAERI-M 94-025 (1994)
- 23) Ohkubo M., Mizumoto M., Nakajima Y. and Mashiko K.: "History of the JAERI Linac Facility for 33 Years (Construction, Research and Shutdown)", JAERI-M 93-250 (1993)
- 24) Shibata M., Ishii T. and Takeuchi S.: "Off-Line Test of Superconducting Resonators of the JAERI Tandem Booster", *Proc. of the 18th Linear Accelerator Meeting in Japan*, Tsukuba, July 1993, p.296
- 25) Takeuchi S., Shibata M., Ishii T., et al.: *Proc. of the 9th Symp. on Accelerator Sci. &*

Technol., Tsukuba, Aug. 1993, p.437

- 26) Takeuchi S., et al.: Proc. of the 5th Japan-China Joint Symp., Oct. 1993, Osaka, p.189
- 27) Shibata M.: "Superconducting RF Activities at JAERI", 6th Workshop on RF Superconductivity, CEBAF, Oct. 1993
- 28) Shibata M.: "RF Performances of Superconducting Resonators for JAERI Tandem Booster", 6th Workshop on RF Superconductivity, CEBAF, Oct. 1993
- 29) Takeuchi S.: "Status and Future of Heavy Ion Accelerator Development at JAERI Tokai", Symp. on Heavy Ion Accelerators, Riken, July 1993)

## 12. Facility Operation and Technique Development

- 1) Ideno K., Sugiyama Y., Ikezoe H., Yamanouchi Y., Hamada S. and Hanashima S.: "Coincidence Measurement of  $3\alpha$ -decays from the  $^{16}\text{O} + ^{12}\text{C}$  Reactions", Autumn Meeting of the Physical Society of Japan, Oct. 5, 1993, Fukuoka
- 2) Ideno K.: "Coincidence Measurements of Three Alpha-Particles Emitted from the  $^{16}\text{O} + ^{12}\text{C}$  Reaction", INS Meetings of Nuclear Study on the Topics: Towards the Unified Understanding of Elastic, Inelastic Scattering and Transferred Reactions of Nuclei; Jan. 7, 1994, Tokyo



Research Committees
Japanese Nuclear Data Committee
Research Committee on Reactor Physics
Atomic and Molecular Data Committee
Research Committee on Advanced Reactor
Research Committee on Partitioning and Transmutation

Shielding Lab.	S. Tanaka (Head)	S. Sakamoto	H. Kotegawa	H. Nakashima	Y. Nakane	N. Sasamoto (4)
Heat Transfer & Fluid Flow Lab.	Y. Sudo (Head)	T. Iguchi	H. Akinoto	M. Okazaki	T. Okubo	A. Ohnuki
Fusion Neutronics Lab.	H. Maekawa (Head)	Y. Ikeda	Y. Oyama	C. Konno	A. Iwai	F. Maekawa
		Y. Uno	Y. Seki (3)	T. Nishitani (9)		
Passive Safety Reactor Systems Lab.	Y. Murao (Head)	T. Iwamura	F. Araya	K. Kunii	N. Ishida (7)	J. Shimazaki (7)
Transmutation System Lab.	T. Takizuka (Head)	T. Nishida	K. Takeuchi	T. Sasa	Y. Nakahara (2)	Y. Katoh (6)
					S. Hamada (3)	K. Hayashi (3)
					M. Akabori (6)	Y. Kondoh (6)
Accelerator Engineering Lab.	M. Mizumoto (Head)	J. Kusano	K. Hasegawa	H. Murata	K. Sakogawa	N. Itoh
					H. Oguri	Y. Okumura (8)
Free Electron Laser Lab.	Y. Suzuki (Head)	M. Ohkubo	E. Minehara	M. Sugimoto	N. Sawamura	T. Kato
					R. Nagai	
Administrative Services	N. Ogino (Administrative Manager)	K. Shibata	K. Ozawa	N. Sekiya	M. Inoue	M. Tsukakoshi
						K. Shinozuka
						H. Yamano
						T. Fujioka
T. Tone	H. Yoshida	S. Moniyama	H. Katsuta (3)			

(No.) : Original Organization of the Shared-Time Members

---

- (1) Dept. of Engineering Services
- (2) Advanced Science Research Center
- (3) Dept. of Materials Science and Engineering
- (4) Dept. of Synchrotron Radiation Facility Project
- (5) Dept. of Radioisotopes
- (6) Dept. of Chemistry and Fuel Research
- (7) Office of Nuclear Ship Research and Development
- (8) Dept. of Fusion Engineering Research
- (9) Dept. of Fusion Plasma Research

## Appendix II Abbreviations

CCTF : Cylindrical Core Test Facility

The CCTF is an experimental facility to study overall primary system response as well as the in-core behavior during the refill and reflood phase of a large cold leg break LOCA.

ECCS : Emergency Core Cooling System

FCA : Fast Critical Assembly

The FCA is a split-table type facility of horizontal matrix structure designed for studying nuclear characteristics of fast reactor. The construction of the FCA was started in 1965 and the first core went critical on 29th April, 1967.

The main features of the facility are summarized as follows:

Type : Split-table type of horizontal matrix structure

Size : 2.8 m × 2.8 m × 1.3 m (each half assembly)

Fuel : Enriched uranium and plutonium (Plate type)

Other material : Sodium, stainless steel, aluminum  
oxide ( $\text{Al}_2\text{O}_3$ ), polystyrene etc. (Plate type)

Maximum power : 2 kW

Assembly name constructed : FCA-I ~ FCA-XVII

Critical experiments using enriched uranium cores were made in 1960s for investigating basic characteristics of fast reactor cores. Mock-up experiments were extensively made in 1970s for the Fast Experimental Reactor JOYO and the Prototype Fast Breeder Reactor MONJU. In 1980s, the main subjects of experiments were the investigation of the core characteristics of an axially heterogeneous large fast breeder reactor and the core physics study on a high conversion light water reactor. From 1989, the reactor physics experiments of metallic-fueled LMFBR have been carried out using the FCA-XVI and XVII cores.

FER : Fusion Experimental Reactor

A next fusion device designed and planned at JAERI.

FNS : Fusion Neutronics Source

The FNS is an accelerator based D-T neutron source installed for the purpose of investigating the neutronics on the D-T fusion reactor blanket and shielding. It provides following three functions to meet experimental requirements:

- 1) High intensity DC point source
- 2) DC point source with wide variation of neutron yield rate
- 3) Pulsed neutron source

The D-T neutrons are generated via  ${}^3\text{T}(\text{d},\text{n}){}^4\text{He}$  reaction. There are two beam lines; one is so called  $0^\circ$  line for high current operation, and the other is so called  $80^\circ$  line for rather low current operation. The major specifications of the FNS accelerator are shown in the following Table.

<<Table>>

Items	$0^\circ$	$80^\circ$
● Beam current	>20 mA	3 mA
● Beam size	<15 mm $\phi$	<15 mm $\phi$
● Pulse width	--	< 2 ns
● Frequency	--	2 MHz
● Peak current	--	40 mA
● Target assembly	Rotating (Water cooled)	Stationary (Water cooled, Air cooled)
● Amount of ${}^3\text{T}$	<37T Bq	370G Bq
● Neutron yield	$4 \times 10^{12}/\text{s}$	$5 \times 10^{11}/\text{s}$

The major experimental subjects are as follows:

- 1) Tritium production rate in the various blanket configurations
- 2) Nuclear heating rate in materials
- 3) Shielding performance for D-T neutrons in the various configurations
- 4) Induced effects on materials by D-T neutrons

HCLWR : High Conversion Light Water Reactor

HTGR : High Temperature Gas-cooled Reactor

HTTR : High Temperature engineering Test Reactor

JAERI is constructing the HTTR to carry out the necessary R&D for establishing and upgrading the HTGR (High Temperature Gas-cooled Reactor) technology basis, and to conduct various innovative basic researches on high-temperature technologies. The HTTR consists of a reactor core, a main cooling circuit, an auxiliary cooling circuit and related components. The size of active core is 2.3 m in diameter and 2.9 m high. The reactor pressure vessel of 13.2 m in height and 5.5 m in diameter contains the core, graphite reflectors, core support structures and core restraint mechanism.

<<Table>> Specification of HTTR

Thermal power	30 MW
Outlet coolant temperature	850°C/950°C
Inlet coolant temperature	395°C
Fuel	3-10wt% enriched UO <sub>2</sub> (coated particle fuel compact)
Fuel element type	Prismatic block (pin-in block)
Primary coolant	Helium gas, 4MPa Downward-flow in core
Pressure vessel	Steel
Number of main cooling loop	1
Heat removal	IHX(10MW) and PWC(30MW)
Containment type	Steel containment

ITER	: International Thermonuclear Experimental Reactor A next fusion device. The ITER Project is conducted by four parties, i.e., Japan, USA, Russia and EU under the framework of IAEA.
JEAMD	: Japanese Evaluated Atomic and Molecular Data Library
JENDL-3	: Japanese Evaluated Nuclear Data Library, version 3, released in 1989.
JENDL-3.2	: Second Revision of JENDL-3, released in 1994.
JMTR	: Japan Materials Testing Reactor
LLFP	: Long-Lived Fission Product
LOCA	: Loss of Coolant Accident
LWR	: Light Water Reactor
MA	: Minor Actinide (Np, Am, Cm)
MHD	: Magneto-Hydro Dynamic
NSRR	: Nuclear Safety Research Reactor
NSSS	: Nuclear Steam Supply System
SCTF	: Slab Core Test Facility The SCTF is an experimental Facility to study two-dimensional effect on thermal hydraulics in the core of full radius during reflood phase of LOCA.
TRU	: Trans-Uranium element (Transuranic nuclide)



VHTRC : Very High Temperature Reactor Critical assembly

The VHTRC is a low-enriched uranium fueled and, graphite moderated and reflected critical assembly. At VHTRC, reactor physics experiments have been carried out mainly for the verification of the neutronics design of the HTTR.

<<Table>> Main features of VHTRC

Type	Split table type of hexagonal prism (prismatic block structure)
Size	2.4 m across the flats and 2.4 m long
Fuel	2, 4 and 6 wt% enriched $\text{UO}_2$ Coated particle fuel compact Pin-in-block type
Moderator/reflector	Graphite
Core temperature	Room temperature to 210°C by electric heaters
Maximum power	10 W
Auxiliary equipments	(1) Sample heating device (Up to 800°C) (2) Pulsed neutron source